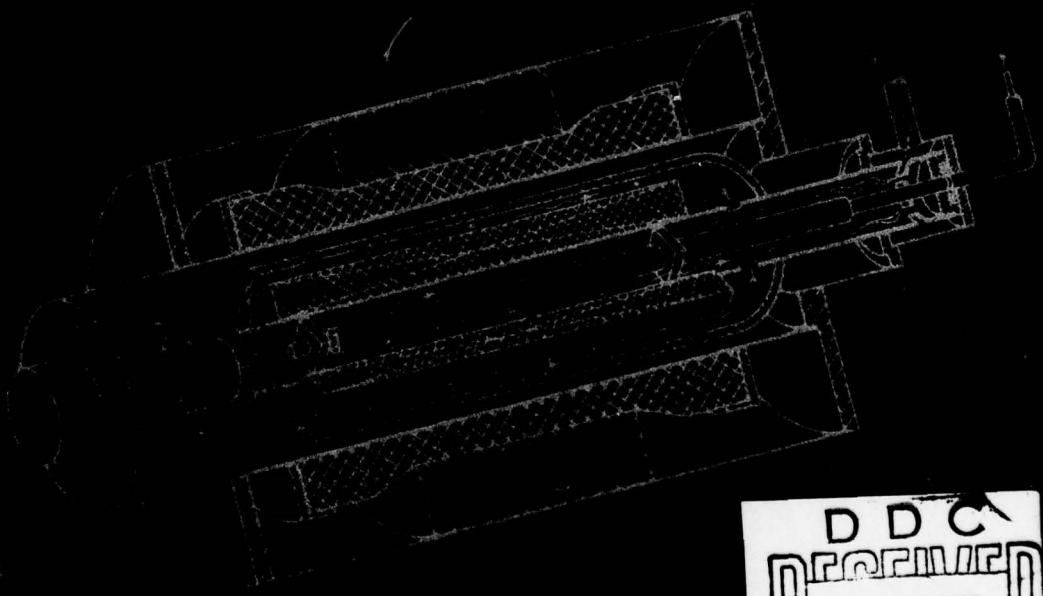
AD A036919

NBS-ARPA

Materials Research for Superconducting Machinery VI



DDC
RECEIVED
MAR 14 1977

DISTRIBUTION STATEMENT A
Approved for public release;
Distribution Unlimited

(12) (6)

SEMI-ANNUAL TECHNICAL REPORTS ON MATERIALS

RESEARCH IN SUPPORT OF SUPERCONDUCTING MACHINERY - VI

(9) Semi-annual technical rept. 1 Mar - 1 Sep 76

1 March 1976 to 1 September 1976

(10)

Edited by

Richard P. Reed and H. M. Ledbetter
National Bureau of Standards

and

Edward C. van Reuth
Advanced Research Projects Agency

DDC
RECEIVED
MAR 14 1977
C

Sponsored by

Advanced Research Projects Agency
1400 Wilson Boulevard, Arlington, VA 22209
ARPA Order No. 2569 - Program Code 5D10

(11) 1 Sep 76 (12) 574 p.

Contracted for 11 September 1975

by

Cryogenics Division, Institute for Basic Standards
National Bureau of Standards, Boulder, CO 80302

Subcontracts to:

Battelle, Columbus Laboratories
National Bureau of Standards, Cryogenics Division
Westinghouse Electric Research & Development Center

(15) ARPA Order-2569

DISCLAIMER

The views and conclusions contained in this document are those of the authors and should not be interpreted as necessarily representing the official policies, either expressed or implied, of the Advanced Research Projects Agency or the U.S. Government.

DISTRIBUTION STATEMENT A
Approved for public release;
Distribution Unlimited

400992 AB

SUMMARY

The sixth semi-annual technical reports are collected from three subcontractors of an ARPA-sponsored program to study the very low-temperature properties of structural materials in support of the development of superconducting machinery. The program is outlined and new research results are reported. Low-temperature results are given for the following properties: elastic, tensile, fatigue and fracture, thermal expansion, specific heat, thermal and magnetothermal conductivity, electrical and magnetic. Effects of processing and fabrication are also considered for some properties; weld and braze-joint properties are included. Tensile and compressive properties at 4 K of selected composite materials are presented.

CONTENTS

	Page
ORGANIZATIONAL CONTACTS	iv
INTRODUCTION	1
PROGRAM DESCRIPTION	1
OUTLINE OF THIRD-YEAR PROGRAM	2
SUMMARY OF EXPERIMENTAL STUDIES	4
HIGHLIGHTS OF RESULTS	5
HANDBOOK	6
PUBLICATIONS	7
TECHNICAL REPORTS BY SUBCONTRACTORS	ff

BATTELLE, COLUMBUS LABORATORIES

Preparation of a Handbook on Mechanical, Thermal, Electrical, and Magnetic Properties of Materials for Superconducting Machinery

Hanby, K. R.
Hucek, H. J.
Thompson, J. K.
Wilkes, K. E.

Low-Temperature Thermal Expansion and Specific Heat Properties of Structural Materials

Collings, E. W.
Jelinek, F. J.

NATIONAL BUREAU OF STANDARDS

Advanced Composites

Kasen, M. B.
Read, D. T.
Schramm, R. E.

Elastic Properties

Ledbetter, H. M.
Read, D. T.

Fracture Mechanics Parameters

McHenry, H. I.
Reed, R. P.
Schramm, R. E.
Tobler, R. L.

Magnetothermal Conductivity

Sparks, L. L.

Thermal Conductivity

Hust, J. G.

WESTINGHOUSE ELECTRIC CORPORATION

Structural Materials for Cryogenic Applications

Daniel, M. R.
Kossowsky, R.
Logsdon, W. A.
Wells, J. M.

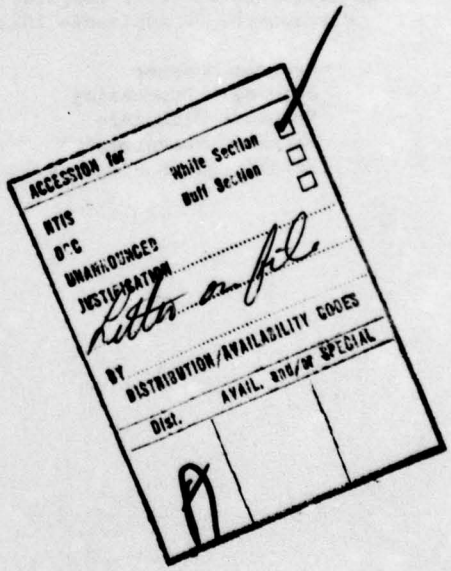


Table 1. Organizational Contacts, ARPA Low-Temperature Properties of Structural Materials

Advanced Research Projects Agency, 1400 Wilson Blvd., Arlington, Virginia 22209

Program Director	Edward C. van Reuth	202-694-4750 694-4750 (FTS)	

National Bureau of Standards, Cryogenics Division, Boulder, Colorado 80302

Program Manager	Richard P. Reed		Ext. 3870
Fracture, Fatigue	Ralph L. Tobler	303-499-1000	Ext. 3421
Elastic	Hassell M. Ledbetter	323-ext. (FTS)	Ext. 3443
Thermal Conductivity	Jerome G. Hust		Ext. 3733
Magnetothermal Conductivity	L. L. Sparks		Ext. 3612
Composites	Maurice B. Kasen		Ext. 3558

Battelle, Columbus Laboratories, 505 King Avenue, Columbus, Ohio 43201

Program Manager (Handbook)	Harold J. Hucek		Ext.6379
Mechanical Properties Data	Harold J. Hucek		Ext.6379
Thermal Properties Data	Kenneth E. Wilkes	614-424-xxxx	Ext.7487
Magnetic Properties Data	J. Ken Thompson	941-xxxx (FTS)	Ext.5399
Physical Properties Meas'ts.	Frank J. Jelinek		Ext.7472
Specific Heat Measurements	Edward W. Collings		Ext.4355

Westinghouse Electric Corporation, Research & Development Center, Beulah Road, Pittsburgh, Pennsylvania 15235

Program Manager	Joseph M. Wells	412-256-7000	Ext. 3467
Joining & Processing	Joseph M. Wells	412-256-7000	Ext. 3633
Fracture Mechanics	William A. Logsdon	412-256-7000	Ext. 3652
Magnetic Measurements	Michael R. Daniel	412-256-7000	Ext. 7267
Metallurgy-Fractography	Ram Kossowsky	412-256-7000	Ext. 3684

INTRODUCTION

This report contains results of a research program designed to fill the need for materials properties data to facilitate design and development of superconducting machinery. The program was conceived and developed jointly by the staffs of the Materials Science Group at the Advanced Research Projects Agency and the Cryogenics Division of the National Bureau of Standards. This ARPA - sponsored program on "Materials Research in Support of Superconducting Machinery" is managed by NBS, with subcontracts to two other laboratories.

PROGRAM DESCRIPTION

The program's objectives are: (1) to evaluate candidate structural materials for use in superconducting electrical machinery by determining their mechanical and physical properties between 4 and 300 K and the effects of processing and joining on these properties; (2) to explore new materials, such as composites, for potential innovative design applications by performing screening tests on their low-temperature properties; (3) to assist the information transfer of the available low-temperature properties data into design use by compiling and publishing existing data; and (4) to assess which materials and properties need further study.

A summary of the third year of the program is shown in Table 2, which describes research efforts at three laboratories. The major thrust has been fatigue and fracture measurements at low temperatures where virtually no data have existed previously. Major material categories include: structural alloys, composites, ferromagnetic alloys, and high-strength high-conductivity alloys.

Table 2. Outline of Third-Year ARPA-Sponsored Program on Materials Research for Superconducting Machinery

Program Area	Organization	Program Description
A. Mechanical Properties		
1. Fracture and Fatigue		
	NBS, Cryogenics	Fracture toughness, fatigue crack-growth rate, fatigue sustained-load crack-growth rate tests from 4-300 K on structural alloys, effects of stress level and frequency.
	Westinghouse	Mechanical, magnetic, electrical loss characterization of alloys proposed for use in DOD-sponsored programs. Mechanical tests include tensile, fracture toughness, fatigue.
2. Effects of Processing and Joining		
a. Processing	Westinghouse	Identification of effects of fabrication and processing techniques on mechanical properties of selected alloys. Variables include industrial melting practices, powder metallurgy techniques, cold working, grain size, and inhomogeneities.
b. Joining	Westinghouse	Mechanical properties of fabricated metal joints, including welding (GTAW, EB, GMAW), brazing, and soldering from 4-300 K. Properties include tensile, notched tensile, fracture toughness, and fatigue crack growth rate in the fused and heat affected zones and the base metal.
3. Elastic Properties	NBS, Cryogenics	Young's shear, bulk moduli; Poisson's ratio; dynamic tests; 4-300 K; structural alloys and composite materials.

Program Area	Organization	Program Description
B. Thermal Properties		
4. Thermal Expansion, Specific Heat	Battelle	Thermal expansion and specific heat measurements on selected insulations and structural alloys and composites.
5. Thermal-Magnetothermal Conductivity	NBS, Cryogenics	Thermal conductivity and thermal conductivity in magnetic fields up to 50 kilogauss from 4-300 K of structural alloys and composites.
C. Composites		
6. Evaluation of Advanced Composites	NBS, Cryogenics	Screening tests (tensile, fatigue at 4 K) on selected candidate metal and non-metal base composites, including B-epoxy, C-epoxy and polyimide, PRD 49-epoxy, borsic-Al, steel-Al.
D. Data Compilation and Evaluation		
7. Handbook	Battelle	Publication of Handbook containing recommended best value data and complete set of references for over 80 additional materials (structural alloys, superconductors, electrical materials, and polymers). Data presented in graphical and tabular formats; mechanical, thermal, electromagnetic properties from 0-300 K.
8. Workshop Meeting	NBS, Cryogenics	Organization of meeting for mutual data sharing and interaction with service agencies and their contractors.

Summary of experimental studies during three-year ARPA-sponsored program on materials research for superconducting machinery; participating laboratories were A = Argonne National Laboratory, GE = General Electric (Schenectady), MM = Martin-Marietta (Denver), NBS = National Bureau of Standards (Boulder), W = Westinghouse (Pittsburgh), B = Battelle Columbus Laboratories.

	Elastic	Fatigue	Flexure	Fracture Toughness, Fatigue-Crack Growth, and/or Tensile	Magnetic	Magneto-thermal Conductivity	Thermal Conductivity	Thermal Expansion, Specific Heat	Tensile, Compressive, Shear
Structural Alloys									
Aluminum 1100	NBS					NBS			
Aluminum 2014	NBS			NBS					
Aluminum 2219	NBS			NBS					
Aluminum 5083	NBS			NBS					
Aluminum 7005	NBS								
Aluminum 7075	NBS								
Inco Lo. Exp. Alloy				W	NBS, W		NBS	B	
Invar	NBS							B	
Stainless 304	NBS	MM		NBS, MM		NBS			
Stainless 304L				NBS					
Stainless 310	NBS	MM		NBS, MM, W+	W	NBS	NBS	B	
Stainless 316	NBS			NBS					
Stainless A286	NBS	MM		NBS, MM, W+				B	
Nitronic 33								B	
Stainless 21-6-9	NBS	MM		NBS, MM					
Pyromet 538*				W+				B	
Pyromet 680								B	
Pyromet 860									
Kromarc 58				W+	W		NBS	B	
Hastelloy B								B	
Hastelloy C								B	
Inconel 600	NBS							B	
Inconel 706				W+				B	
Inconel 718	NBS	MM		NBS, MM, W+	W	NBS			
Inconel X750	NBS			NBS, MM, W+	NBS, W		NBS	B	
Ti-5Al-2.5Sn	NBS			NBS				B	
Ti-6Al-4V	NBS			NBS		NBS		B	
Structural Composites									
Boron/Aluminum	NBS	NBS					NBS	B	NBS
Boron/Epoxy	NBS*	NBS					NBS		NBS
Composite/Metal Joints									GE
Graphite/Al									
Graphite/Epoxy	NBS*						NBS	B	NBS
Kevlar/Epoxy	NBS*							B	NBS
Modmor II/Epoxy			GE#					GE***	
PRD-49/Epoxy			GE#					GE***	
S-Glass/Epoxy	NBS*	NBS	GE#					B, GE**#	NBS
Ferromagnetics									
Armco Iron					W				
Fe-3Si					W				
Fe-3.5Ni	NBS			NBS					
Fe-9Ni	NBS			NBS	W				
Fe-49Ni	NBS			NBS		NBS	NBS		
Fe-78Ni					W				
Fe-Ni-Co	NBS			NBS			NBS		
AISI 410					W				
Superconducting Magnet Materials									
Bakelite							NBS	B	
Copper-Tin						NBS		B	
Copper-Nickel	NBS					NBS		B	
Niobium-Titanium									
NbTi/Cu	NBS								
NbTi/Cu Epoxy	NBS								
Potting Compounds								B	
High-Strength, High-Conductivity Alloys									
Copper								B	
Copper, OFHC	NBS			W+	A, NBS, W	NBS	NBS		
Copper, high purity					A	NBS			
Copper-Al_2O_3								B	
Copper-Zirconium								B	
PD 135(Cu-Cd-Cr)	NBS			W	W				

*Pyromet 538 is equivalent to stainless 21-6-9.
+Results for welds were also obtained at Westinghouse.
*Static results; all other elastic results are dynamic.
**Thermal expansion only.
#Joints.

HIGHLIGHTS OF RESULTS

A general overview of the program is best obtained by examining the individual technical reports contained herein. A summary of materials studied during the three-year program is given in Table 3. The major technical accomplishments are briefly as follows:

The Handbook on Materials for Superconducting Machinery was published in 1974. The second edition of the Handbook was published in December of 1975, and the third edition is due in January of 1977. It includes approximately eighty materials and approximately thirty mechanical and physical properties.

A variety of mechanical properties have been studied for six different composite materials at low temperatures.

Thermal expansion data at low-temperatures have now been obtained for about thirty materials, and low-temperature specific heats have been obtained for eight materials.

Elastic constants at low-temperatures have been determined for about thirty engineering materials, including four composites.

Magneothermal conductivities, including thermal conductivities have been measured at low temperatures for ten materials, and the electrical conductivities of some of these materials have also been measured.

Thermal conductivity measurements on twelve structural materials, including three composites, have also been made.

Fatigue-crack growth-rate data and fracture toughness data have been determined for about twenty-five important structural alloys and weldments. Also, conventional fatigue data were obtained for five alloys. For most of these materials, the usual tensile properties -- elongation, reduction in area, yield strength and ultimate strength -- were also obtained.

Three workshops were held. These workshops brought together research personnel and Department of Defense project staff members. Design-materials interfacing problems were discussed and emphasis was placed on meeting Department of Defense materials needs.

A major new materials conference, the International Cryogenic Materials Conference, was held at Kingston, Ontario, In July 1975. Over 60 technical papers (14 from this program) were presented and the proceedings were published as Volume 22 of Advances in Cryogenic Engineering (Plenum, New York, 1976).

HANDBOOK

One of the important outputs of this program is the Handbook on Materials For Superconducting Machinery. In one volume, it collects information, including data generated by this program, on the low-temperature properties of structural materials of possible use in superconducting machinery. The Handbook project was carried out at Battelle (Columbus Laboratories). It presents in loose-leaf format the mechanical, elastic, thermal, electrical, and magnetic properties of materials for superconducting machinery. Best-value data are presented either graphically or tabularly together with original data and test conditions. It contains data on about seventy metals, alloys, and polymers in various conditions; and it contains about 1000 references to the experimental literature. The principal reference sources were the Materials and Ceramics Information Center (MCIC), the Defense Documentation Center (DDC), and the Cryogenic Information Center (CIC).

Handbooks can be ordered from the National Technical Information Service (NTIS), Operation Division, Springfield, Virginia 22151 by requesting: Handbook on Materials for Superconducting Machinery (November 1974) MICI - HB - 04 and its supplements. The second supplement will be available in January of 1977.

Publications Resulting from the Three-Year ARPA-Sponsored Program on Materials Research in Support of Superconducting Machinery

Semiannual Progress Reports. Most of the results of the program are described in the following six semiannual progress reports available from NTIS, P. O. Box 1553, Springfield, VA 22161:

1. MATERIALS RESEARCH FOR SUPERCONDUCTING MACHINERY, Semi-Annual Tech. Rept., Sept 1973-Mar 1974 (Mar 1974).

Order No.: AD780596 Price: Paper Copy $13.00
Microfiche $ 2.25

2. MATERIALS RESEARCH FOR SUPERCONDUCTING MACHINERY - II, Semi-Annual Tech. Rept., Mar-Sep 1974, A. F. Clark, R. P. Reed, and E. C. van Reuth (Editors) (Oct 1974).

Order No.: ADA004586 Price: Paper Copy $17.25
Microfiche $ 2.25

3. MATERIALS RESEARCH FOR SUPERCONDUCTING MACHINERY - III, Semi-Annual Tech. Rept., Sep 1974-Mar 1975, R. P. Reed, A. F. Clark, and E. C. van Reuth (Editors) (Apr 1975).

Order No.: ADA012365 Price: Paper Copy $12.00
Microfiche $ 2.25

4. MATERIALS RESEARCH FOR SUPERCONDUCTING MACHINERY - IV, Semi-Annual Tech. Rept., Mar 1975-Sep 1975, R. P. Reed, A. F. Clark, and E. C. van Reuth (Editors) (Oct 1975).

Order No.: ADA019230 Price: Paper Copy $16.25
Microfiche $ 2.25

5. MATERIALS RESEARCH FOR SUPERCONDUCTING MACHINERY - V, Semi-Annual Tech. Rept., Sep 1975-Mar 1976, R. P. Reed, H. M. Ledbetter, and E. C. van Reuth (Editors) (Apr 1976).

Order No.: ADA030170 Price: Paper Copy $11.75
Microfiche $ 3.00

6. MATERIALS RESEARCH FOR SUPERCONDUCTING MACHINERY - VI, Semi-Annual Tech. Rept., Mar 1976-Sep 1976, R. P. Reed, H. M. Ledbetter, and E. C. van Reuth (Editors) (Oct 1976).

Order No.: not yet assigned

NBS Semiannual Progress Reports. The following NBS contributions to the above reports are also available in limited quantities from the Cryogenics Data Center, NBS, Boulder, CO 80302:

7. L. L. Sparks, F. R. Fickett, J. G. Hust, P. J. Giarratano, H. M. Ledbetter, E. R. Naimon, W. F. Weston, M. B. Kasen, R. L. Tobler, R. P. Mikesell, R. L. Durcholz, C. W. Fowlkes and R. P. Reed, Semi-Annual Report on Materials Research in Support of Superconducting Machinery, NBSIR 74-359 (1974).

8. R. P. Reed, R. L. Durcholz, F. R. Fickett, P. J. Giarratano, J. G. Hust, M. B. Kasen, H. M. Ledbetter, R. P. Mikesell, E. R. Naimon, R. E. Schramm, L. L. Sparks, R. L. Tobler and W. F. Weston, Semi-Annual Report on Materials Research in Support of Superconducting Machinery, NBSIR 74-393 ((1974).

9. R. P. Reed, J. G. Hust, M. B. Kasen, H. M. Ledbetter, R. P. Mikesell, R. E. Schramm, L. L. Sparks, R. L. Tobler and W. F. Weston, Semi-Annual Report on Materials Research in Support of Superconducting Machinery, NBSIR 75-810 (1975).

10. R. P. Reed, J. G. Hust, M. B. Kasen, H. M. Ledbetter, D. T. Read, E. R. Naimon, R. E. Schramm, L. L. Sparks, R. L. Tobler and W. F. Weston, Semi-Annual Report on Materials Research in Support of Superconducting Machinery, NBSIR 75-828 (1975).

11. R. P. Reed, J. G. Hust, M. B. Kasen, H. M. Ledbetter, D. T. Read, R. E. Schramm, L. L. Sparks and R. L. Tobler, Semi-Annual Report on Materials Research in Support of Superconducting Machinery, NBSIR 76-839 (1976).

12. R. P. Reed, J. G. Hust, M. B. Kasen, H. M. Ledbetter, H. I. McHenry, D. T. Read, R. E. Schramm, L. L. Sparks and R. L. Tobler, Semi-Annual Report on Materials Research in Support of Superconducting Machinery, NBSIR 76-848 (1976).

NBS Publications in the Engineering-Scientific Literature

13. C. W. Fowlkes and R. L. Tobler, Fracture testing and results for a Ti-6Al-4V alloy at liquid helium temperature, Eng. Fract. Mechs. 8 (1976) 487-500.

14. M. B. Kasen, Properties of filamentary-reinforced composites at cryogenic temperatures, in Composite Reliability, ASTM STP 580 (Amer. Soc. Testing Mater., Phila., 1975).

15. M. B. Kasen, Mechanical and thermal properties of filamentary-reinforced structural composites at cryogenic temperatures. I: glass-reinforced composites, Cryogenics 15 (1975) 327-349.

16. M. B. Kasen, Mechanical and thermal properties of filamentary-reinforced structural composites at cryogenic temperatures. II: advanced composites, Cryogenics 15 (1975) 701-722.

17. M. B. Kasen and R. E. Schramm, Primary static mechanical properties of several boron-graphite and glass-reinforced composites at cryogenic temperatures, to be submitted for publication.

18. M. B. Kasen, R. E. Schramm, and D. T. Read, Fatigue of composites at cryogenic temperatures, submitted for publication.

19. H. M. Ledbetter, Anomalous elastic properties of a precipitation-hardened copper alloy, submitted for publication.

20. H. M. Ledbetter, Low-temperature elastic properties of a precipitation-hardened copper alloy, submitted for publication.

21. H. M. Ledbetter, E. R. Naimon, and W. F. Weston, Low-temperature elastic properties of invar, in Advances in Cryogenic Engineering, Vol. 22 K. D. Timmerhaus, R. P. Reed, and A. F. Clark (Eds.) (Plenum, New York, 1976).

22. H. M. Ledbetter and D. T. Read, Orthorhombic elastic constants of an NbTi/Cu composite superconductor, J. Appl. Phys., forthcoming.

23. H. M. Ledbetter and D. T. Read, Low-temperature elastic properties of a 300-grade maraging steel, submitted for publication.

24. H. M. Ledbetter and D. T. Read, Low-temperature elastic properties of a nitrogen-strengthened chromium-manganese stainless steel, submitted for publication.

25. H. M. Ledbetter and W. F. Weston, Low-temperature elastic properties of some copper-nickel alloys, Ultrasonics Symposium Proc., Cat. No. 75 Ch 8 994-4SU (IEEE, New York, 1975) 623-627.

26. H. M. Ledbetter, W. F. Weston, and E. R. Naimon, Low-temperature elastic properties of four austenitic stainless steels, J. Appl. Phys. 46 (1975) 185-194.

27. E. R. Naimon, H. M. Ledbetter, and W. F. Weston, Low-temperature elastic properties of four wrought and annealed aluminum alloys, J. Mater. Sci. 10 (1975) 1309-1316.

28. E. R. Naimon, W. F. Weston, and H. M. Ledbetter, Elastic properties of two titanium alloys at low temperatures, Cryogenics 14 (1974) 246-249.

29. D. T. Read and H. M. Ledbetter, Temperature dependencies of the elastic constants of precipitation-hardened aluminum alloys 2014 and 2219, submitted for publication.

30. D. T. Read and H. M. Ledbetter, Low-temperature elastic properties of a boron/aluminum composite, submitted for publication.

31. D. T. Read and H. M. Ledbetter, Low-temperature elastic constants of an NbTi/Cu composite superconductor, submitted for publication.

32. D. T. Read and R. P. Reed, Effects of specimen thickness on fracture toughness of some aluminum alloys, submitted for publication.

33. R. P. Reed, A. F. Clark, and E. C. van Reuth, A research program on the properties of structural materials at 4 K, in Advances in Cryogenic Engineering, Vol. 22, K. D. Timmerhaus, R. P. Reed, and A. F. Clark (Eds.) (Plenum, New York, 1976).

34. R. P. Reed, R. L. Tobler, and R. P. Mikesell, Fracture toughness and fatigue crack growth rate of an Fe-Ni-Cr superalloy at 298, 76 and 4 K, in Advances in Cryogenic Engineering, Vol. 22, K. D. Timmerhaus, R. P. Reed, and A. F. Clark (Eds.) (Plenum, New York, 1976).

35. R. E. Schramm and M. B. Kasen, Static tensile properties of boron-aluminum and boron-epoxy composites at cryogenic temperatures, in Advances in Cryogenic Engineering, Vol. 22, K. D. Timmerhaus, R. P. Reed, and A. F. Clark (Eds.) (Plenum, New York, 1976).

36. L. L. Sparks, Magnetothermal conductivity of selected pure metals and alloys, in Advances in Cryogenic Engineering, Vol. 22, K. D. Timmerhaus, R. P. Reed, and A. F. Clark (Eds.) (Plenum, New York, 1976).

37. R. L. Tobler, Fatigue crack growth and J-integral fracture parameters of Ti-6Al-4V at ambient and cryogenic temperatures, in Cracks and Fracture, ASTM STP 601 (Amer. Soc. Test. Mater., Philadelphia, 1976) 346-370.

38. R. L. Tobler, Fracture of structural alloys at temperatures approaching absolute zero, Proc. Fourth ICE, Waterloo, Ontario, June 1977, forthcoming.

39. R. L. Tobler, Low temperature effects on the fracture behavior of a nickel-base superalloy, submitted for publication.

40. R. L. Tobler, Cryogenic effects on the fracture mechanics parameters of ferritic nickel-alloy steels, submitted for publication.

41. R. L. Tobler and D. T. Read, Fatigue resistance of a uniaxial S-glass/epoxy composite at room and liquid helium temperatures, J. Comp. Mater. 10 (1976) 32-43.

42. R. L. Tobler and R. P. Reed, Fatigue crack growth rates of structural alloys at four kelvin, in Advances in Cryogenic Engineering, Vol. 22, K. D. Timmerhaus, R. P. Reed, and A. F. Clark (Eds.) (Plenum, New York, 1976).

43. R. L. Tobler and R. P. Reed, Fracture mechanics parameters for a 5083-0 aluminum alloy at low temperatures, submitted for publication.

44. R. L. Tobler and R. P. Reed, Tensile and fracture behavior of a nitrogen-strengthened, chromium-nickel-manganese stainless steel at cryogenic temperatures, submitted for publication.

45. R. L. Tobler and R. P. Reed, Fatigue crack growth resistance of structural alloys at cryogenic temperatures, submitted for publication.

46. R. L. Tobler, R. P. Reed, and R. E. Schramm, Cryogenic tensile, fatigue, and fracture parameters for a solution-annealed maraging steel, submitted for publication.

47. W. F. Weston, Elastic constants of a superconducting-coil composite material. J. Appl. Phys. 46 (1975) 4458-4465.

48. W. F. Weston and H. M. Ledbetter, Low-temperature elastic properties of a nickel-chromium-iron-molybdenum alloy, Mater. Sci. Engg. 20 (1975) 287-290.

49. W. F. Weston, H. M. Ledbetter and E. R. Naimon, Dynamic low-temperature elastic properties of two austenitic nickel-chromium-iron alloys, Mater. Sci. Engg. 20 (1975) 185-194.

Publications of Westinghouse Research Laboratory. Six technical reports were included in Refs. 1-6 above.

50. G. G. Lessman, W. A. Logsdon, R. Kossowski, M. P. Mathur, and J. M. Wells, WRL Rep. 74-9D4-CRYMT-R1 (March 1974).

51. G. G. Lessman, R. Kossowsky, W. A. Logsdon, M. P. Mathur, and J. M. Wells, WRL Rep. 74-9D4-CRYMT-R2 (Sept 1974).

52. J. M. Wells, R. Kossowsky, W. A. Logsdon, and M. R. Daniel, WRL Rep. 75-9D4-CRYMT-R1 (March 1975).

53. W. A. Logsdon, R. Kossowsky, M. R. Daniel, and J. M. Wells, WRL Rep. 75-9D4-CRYMT-R2 (October 1975).

54. J. M. Wells, R. Kossowsky, W. A. Logsdon, and M. R. Daniel, WRL Rep. 76-9D4-CRYMT-R1 (April 1976).

55. J. M. Wells, W. A. Logsdon, R. Kossowsky, and M. R. Daniel, WRL Rep. 76-9D9-CRYMT-R1 (October 1976).

Other WRL technical papers include:

56. W. A. Logsdon, Cryogenic fracture mechanics properties of several manufacturing process/heat treatment combinations of Inconel X750, in Advances in Cryogenic Engineering, Vol. 22 (Plenum, New York, forthcoming).

57. R. Kossowsky, Microstructure of Inconel X750 materials for cryogenic structural applications, ibid.

58. J. M. Wells, Evaluation of Inconel X750 weldments for cryogenic applications, ibid.

59. W. A. Logsdon, J. M. Wells, and R. Kossowsky, Fracture mechanics properties of austenitic stainless steels for advanced cryogenic applications, in Proceedings of the Second International Conference on Mechanical Behavior of Materials (Amer. Soc. Metals, Metals Park, Ohio, 1976).

Publications of Battelle Columbus Laboratories

60. E. W. Collings, F. J. Jelinek, M. P. Mathur, and J. C. Ho, Magnetic and thermal properties of stainless steels and Inconels at cryogenic temperatures, in Advances in Cryogenic Engineering, Vol. 22 (Plenum, New York, forthcoming).

61. F. J. Jelenik and A. Muller, Study of the dimensional behavior of various thin-film dielectric polymers in the temperature range 4.2 to 300 K, ibid.

62. E. W. Collings and R. D. Smith, Specific heats of some cryogenic structural materials -- (1) iron-nickel-base alloys, in preparation.

63. E. W. Collings and R. D. Smith, Specific heats of some cryogenic structural materials -- (2) composites, in preparation.

UCCNM - ERL

SEMIANNUAL TECHNICAL REPORT

on

PREPARATION OF A HANDBOOK ON MECHANICAL, THERMAL, ELECTRICAL, AND MAGNETIC PROPERTIES OF MATERIALS FOR SUPERCONDUCTING MACHINERY

Sponsored by
Advanced Research Projects Agency
ARPA Order No. 2569
Program Code 4D10
Contract No. CST-8303

Contract Monitor
Cryogenics Division
National Bureau of Standards
Boulder, Colorado 80302

November 1, 1976

METALS AND CERAMICS INFORMATION CENTER
A Department of Defense Information Analysis Center
BATTELLE
Columbus Laboratories
505 King Avenue
Columbus, Ohio 43201
Telephone (614) 424-6424

FOREWORD

This research was supported by the Advanced Research Projects Agency of the Department of Defense with Dr. Edward C. VanReuth as Project Monitor. The handbook preparation task was subcontracted to Battelle-Columbus by the Cryogenics Division, National Bureau of Standards under Contract No. CST-8303 with Dr. Richard P. Reed as Program Manager and Contract Monitor.

The research described in this report was carried out under ARPA Order No. 2569 and Program Code 4D10 by the Metals and Ceramics Information Center (MCIC) with K. R. Hanby and H. J. Hucek (614, 424-6379) as the Program Coordinators, and K. E. Wilkes (614, 424-7487) and J. K. Thompson (614, 424-5399) as Principal Investigators. Contract No. CST-8303 includes two tasks. Task I of the current program provides for a compilation of low-temperature property data on an expanded series of selected materials for structural applications in superconducting machinery. These data compilations will be produced as the second revision of the "Handbook on Materials for Superconducting Machinery". Task II provides for determination of thermal expansion and specific heat values at cryogenic temperatures for selected structural alloys. The Semiannual Technical Report on the latter program is presented under separate cover. Overall contract funding was $90,000 with $60,000 for the handbook program and $30,000 for the laboratory study. The effective data of the current contract period was September 10, 1975, and the contract expiration date November 15, 1976.

DISCLAIMER

The views and conclusions contained in this document are those of the authors and should not be interpreted as necessarily representing the official policies, either expressed or implied, of the Advanced Research Projects Agency or the U. S. Government.

PREPARATION OF A HANDBOOK ON MECHANICAL, THERMAL, ELECTRICAL, AND MAGNETIC PROPERTIES OF MATERIALS FOR SUPERCONDUCTING MACHINERY

INTRODUCTION

This report describes the task of preparing the second revision (for producing the third edition) of the handbook and the progress made to date on that task. The end product of this task is a series of new or modified pages which, added to or replacing existing pages in the second edition, will produce an up-to-date handbook covering the materials scope shown in the April 1976 report. The new materials added during this contract period are listed in Table 1. Preparation of a first draft of those pages is scheduled for November 1976, and the published version, to be distributed by MCIC, is expected to be available by January 1977.

SUMMARY

The specific properties that are included in the handbook are listed in the April 1976 report. All the available data covering these properties have been gathered for all of the materials within the project scope. The search for data included all forms of the materials, including sheet, plate, forgings, extrusions, bar, rod, and weldments. All conditions of heat treatment were included. The types of sources that were exploited are listed in Table 2. Table 3 indicates the information centers and indexing and abstracting services that were used in attempts to retrieve pertinent data. In addition, the reference lists in all documents screened on this project, including those accessioned during previous contract periods, were exploited systematically to maximize the recovery of data.

All the data gathered has been analyzed and evaluated. The tables, graphs and other displays of the data have been compiled and are ready for final editing and typing.

NEW FORMATS

The second revision of the handbook contains data on composite materials and weldments which requires some small modifications of format.

The format for presenting mechanical properties of composite materials was devised by Dr. M. B. Kasen of NBS – Boulder, who is responsible for the data search and presentation on composite materials for the current contract period. He has finished his search and his data has been received at Battelle and is being incorporated into the second revision of the handbook.

Data for weldments can be accommodated by the existing format; however, a few additional parameters must be specified over those required for parent metal only. These parameters are: 1) Type of weld (TIG, MIG, electron beam) and filler material, if any, are specified on the line for "Form", 2) Thickness refers then to that of the plate, sheet, or bar from which the weldment is made, 3) The temper of the sheet, plate or bar prior to welding, 4) The condition of the test specimen, "as welded", or specifications of postweld heat treatment, 5) The orientation of the weld on the specimen.

Another change in format was the inclusion of a list of materials or alloys at the beginning of each section along with the codes for all materials listed in that section. Also, in Section 3 the index table has been expanded to three tables–

1. Metals and Alloys
2. Polymers
3. Composites.

PROGRESS

All of the documents accessioned for this program during previous contract periods have been re-examined for data applicable to the present contract period. Reference lists in them have been exploited systematically, new sources identified, and documents ordered.

Many of the items cited previously in the bibliography have, on re-examination, been rejected. Secondary data have been identified for use in filling gaps where appropriate.

Computer printouts from previous searches were looked at again in light of known information gaps, and some items previously rejected were retrieved. All the suitable data retrieved has been evaluated and compiled into tables and figures. The tables and figures are being assembled into the "Second Supplement to the Handbook on Materials for Superconducting Machinery".

The following handbooks, or data collections, have been examined, and secondary data useful for filling gaps identified:

Cryogenic Materials Handbook – Aug. 1968
Damage Tolerant Design Handbook (MCIC)
Alloy 718 Processes and Properties Handbook (DMIC)
DMIC Data Sheets
Structural Alloys Handbook (MPDC)
Aerospace Structural Alloys Handbook (MPDC)
NBS Monograph 13 (1960).

The latest semiannual report for this program has been examined, and pertinent data extracted.

The process of evaluating data tentatively selected for incorporation in the third edition by careful comparison with data already in the handbook has been completed. Data sheets for inclusion have been completed.

Dr. Kasen has already completed and forwarded to Battelle data sheets for incorporation in the handbook covering eight specific composite types, as follows:

Class	Type
Glass - Epoxy	181/Epon 828(CL)
Glass - Epoxy	1581/E-787 (58-68R)
Glass - Epoxy	S-901/NASA Resin 2
Boron - Epoxy	4.0 mil Boron/2387
Boron - Epoxy	5.6 mil Boron/2387
Graphite - Epoxy	AS/NASA Resin 2
Graphite - Epoxy	HT-S/X-904
Boron - Aluminum	5.6 mil Boron/6061

HANDBOOK ON MATERIALS FOR SUPERCONDUCTING MACHINERY— 3rd Edition (2nd Revision)

TABLE 1. NEW MATERIALS ADDED TO THE PROJECT DURING THIS CONTRACT PERIOD

Aluminum

2024
5456

Copper and Copper Alloys

90Cu-10Zn
Aluminum Bronzes, 18 alloys

Nickel and Cobalt and Their Alloys

High purity nickel
Nickel "A"
Inconel 706

Steels and Iron Alloys

1010 Steel
Armco Iron

Stainless Steels

AISI 410
AISI 416

Special Metals and Alloys

Mg-AZ31B

Composites

Glass/Epoxy
Boron/Epoxy
Graphite/Epoxy
Boron/Aluminum
Kevlar Epoxy

TABLE 2. SOURCES OF DATA

Reports of Government-sponsored R&D
(including semiannual reports of this ARPA contract)

Open published literature
(including handbooks, state-of-the-art reports, and conference proceedings)

Private communication

TABLE 3. ACCESS TO DATA

Information Centers

- NBS Cryogenic Information Center
- Metals and Ceramics Information Center (MCIC)
- Defense Documentation Center (DDC)
- Thermophysical and Electronic Properties Information Analysis Center (TEPIAC)
- Copper Data Center
- Iron Information Center
- Plastics Technical Evaluation Center (Plastec)
- Mechanical Properties Data Center (MPDC)

Indexing and Abstracting Services

Chemical Abstracts	
Metallurgical Abstracts	Machine searchable
Engineering Index	through MCIC
Nuclear Abstracts	

SEMIANNUAL TECHNICAL REPORT

on

LOW-TEMPERATURE THERMAL EXPANSION AND SPECIFIC HEAT PROPERTIES OF STRUCTURAL MATERIALS

Sponsored by

ADVANCED RESEARCH PROJECTS AGENCY
ARPA Order No. 2569
Program Code 4D10
Contract No. CST-8303

Contract Monitor

CRYOGENICS DIVISION
NATIONAL BUREAU OF STANDARDS
Boulder, Colorado 80302

by

F. J. Jelinek and E. W. Collings

September 30, 1976

BATTELLE
Columbus Laboratories
505 King Avenue
Columbus, Ohio 43201

SEMIANNUAL TECHNICAL REPORT

on

LOW-TEMPERATURE THERMAL EXPANSION AND SPECIFIC HEAT PROPERTIES OF STRUCTURAL MATERIALS

Sponsored by

ADVANCED RESEARCH PROJECTS AGENCY
ARPA Order No. 2569
Program Code 4D10
Contract No. CST-8303

from

BATTELLE
Columbus Laboratories

F. J. Jelinek and E. W. Collings

September 30, 1976

FOREWORD

This research was supported by the Advanced Research Projects Agency of the Department of Defense and was monitored by the Cryogenics Division, National Bureau of Standards under Contract No. CST-8303. Dr. Richard P. Reed serves as Program Manager and Contract Monitor.

The research was carried out under ARPA Order No. 2569 and Program Code 4D10 by the Materials and Coating Technology and the Metal Science Sections of Battelle-Columbus Laboratories with F. J. Jelinek (614-424-7472) and E. W. Collings (614-424-4355) as Principal Investigators. Contract CST-8303, under the overall coordination of H. J. Hucek, covers both the handbook program and the property measurement program. Only the property measurement program is present here. Effective date of the contract was September 10, 1975, and the contract expiration date is September 10, 1976.

DISCLAIMER

The views and conclusions contained in this document are those of the authors and should not be interpreted as necessarily representing the official policies, either expressed or implied, of the Advanced Research Projects Agency or the U.S. Government.

TECHNICAL REPORT SUMMARY

The development of superconducting electrical machinery requires the suitable engineering property characterization of all candidate materials at cryogenic temperatures. This program involves the determinations of thermal expansion and specific heat for several structural materials in the cryogenic temperature region (4.2 to 300 K).

Materials selected for this study period were supplied through the cooperation of Westinghouse R&D and the National Bureau of Standards. Additional materials were secured from within Battelle or purchased from an appropriate vendor. All materials are appropriately labeled in the text of the report.

Thermal expansion measurements were performed utilizing a fused silica dilatometer with a linear differential transducer as the dilatometer head. The accuracy of the measurement is one percent. Specific heat at low temperatures is measured to one percent by adiabatic calorimetry from a method developed by Nernst. In this method, small increments of heat are supplied to a thermally insulated sample, and the accompanying temperature increase is measured.

PROGRAM PROGRESS

PART I. LOW TEMPERATURE SPECIFIC HEATS OF SOME CRYOGENIC STRUCTURAL MATERIALS

During the current reporting period three alloys and three composites have been added to the list of materials whose low-temperature specific heats have been measured over the temperature range 3-20 K.

Metallic Alloys

Alloys investigated, together with their heat treatment specifications, are listed in Table I. They were supplied by the Westinghouse

TABLE 1. ALLOY SAMPLES MEASURED*

Nitronic 33	STWQ
Nitronic 33	STFC
Inco Low-Expansion (LEA)	STA
Kromarc 58	STQ
Kromarc 58	30 % CW

* The alloys were supplied in the conditions listed by Dr. J. M. Wells of the Westinghouse Research and Development Center, Pittsburgh, Pa.

Heat Treatment Conditions

STWQ - Annealed (solution treated) at 1066°C (1950°F) for 1 hour and water quenched.

STFC - Annealed (solution treated) at 1066°C (1950°F) for 1 hour and slow furnace cooled.

STA - Annealed (solution treated) at 980°C (1800°F) for 1 hour, air cooled, and subsequently aged at 660°C (1225°F) for 8 hours.

STQ - Annealed at 980°C (1800°F) for 1 hour and water quenched.

CW - Reduced at room temperature.

Research and Development Center through the courtesy of Dr. J. M. Wells The principal constituents of these materials are listed in Table 2. Also presented in that table are a set of molar weight (M) values (computed from the full chemical analysis) eventually required in estimating Debye temperatures.

Specific Heat Results on Metallic Alloys

As discussed in previous reports the specific heat data were fitted to a polynomial of the form

$$C = A + \gamma T + \beta T^3 \quad . \tag{1}$$

The temperature-independent term, A, is magnetic in origin and in the austenitic alloys owes its presence to the existence of superparamagnetic clusters. The second parameter, γ, is the electronic specific heat coefficient; while β is the lattic specific heat term from which the Debye temperature, θ_D, may be derived using the formula

$$\theta_D = (1.944 \times 10^6/\beta M)^{1/3} . \tag{2}$$

The results of applying multiple linear regression analysis to the experimental data are summarized in Table 3. The "coefficient" of variability" listed therein is a measure of the appropriateness of the fitting function (in this case the RHS of equation (1)). In early stages of the work various polynomials were tried in attempts to minimize that quantity. The "standard errors" listed are measures of the precisions with which the coefficients have been determined. They tend to reflect scatter in the data, and thus may be relatively small even if a poor fitting function has been selected.

Finally in Table 4 are presented lists of specific heat values computed from the fitted polynomials at each of a set of specified temperatures.

TABLE 2. PRINCIPAL COMPONENTS (>1 wt. pct.) AND CALCULATED MOLAR WEIGHTS OF THE ALLOYS REFERRED TO IN THIS REPORT(1)

Alloy Name	Mn	Fe	Cr	Ni	additional (>1 %)	Molar Weight (M)(2)
Nitronic 33	13.85	64.47	18.00	3.21	-	54.25
Inco LEA	-	55.44	-	39.56	2.9(Nb+Ta); 1.46(Ti)	57.57
Kromarc 58	9.3	49.5	15.5	23.0	2.2 (Mo)	55.99

(1) Data Sources are

Nitronic 33 J. M. Wells and M. W. Hagadorn, "Evaluation of Nitronic 33 Stainless Steel for TFTR Device Applications", Westinghouse Research Report 75-8C3-WETWO-R1, September, 1975.

Inco LEA J. M. Wells, R. Kossowsky, W. A. Logsdon and M. R. Daniels, "Structural Materials for Cryogenic Applications--Third Semi-Annual Technical Report", Westinghouse Research Report 75-9D4-CRYMT-R1, March, 1975.

Kromarc 58 G. G. Lessman, W. A. Logsdon, R. Kossowski, M. P. Mathur, and J. M. Wells, "Structural Materials for Cryogenic Applications--Third Semi-Annual Technical Report", Westinghouse Research Report 75-9D4-CRYMT-R1, March, 1974.

TABLE 3. LOW-TEMPERATURE SPECIFIC HEAT PARAMETERS FOR FOUR ALLOY SAMPLES

$$C = A + \gamma T + \beta T^3$$

	Alloy and Parameter Value			
	Nitronic 33 STFC	Inco LEA STA	Kromarc 58 30 % CW	Kromarc 58 STQ
Coefficient of Variability[1], %	3.5	1.9	1.3	0.9
A, 10^{-1} J/kg-deg.	1.24 ± 0.09[2]	1.80 ± 0.06	1.93 ± 0.06	0.85 ± 0.04
γ, 10^{-1} J/kg-deg.[2]	2.15 ± 0.03	2.18 ± 0.02	3.61 ± 0.02	3.67 ± 0.01
β, 10^{-4} J/kg-deg.[4]	5.11 ± 0.10	6.68 ± 0.08	4.71 ± 0.06	4.58 ± 0.03
θ_D, K	412 ± 3	370 ± 2	419 ± 2	423 ± 1

(1) Coefficient of variability. If large (say greater than 5%) this is a measure of the inappropriateness of the selected polynomial provided that "wild" data have first been recognized and rejected. When small (a few %), i.e. when the "best" polynomial has been selected, it begins to reflect the scatter in the data itself.

(2) Standard error of the regression coefficient (polynomial coefficient). This is a measure of the precision of determination of the coefficients of the selected polynomial and reflects scatter in the data. The standard error may be small even if the coefficient of variability is large.

TABLE 4. LOW-TEMPERATURE SPECIFIC HEATS (FITTED VALUES) FOR FOUR ALLOY SAMPLES AT SPECIFIED TEMPERATURES

$C = A + \gamma T + \beta T^3$

Temperature, K	Alloy and Specific Heat, C (J/kg-deg)*			
	Nitronic 33 STFC	Inco LE STA	Kromarc 58 30 % CW	Kromarc 58 STQ
2.0	0.56 ± 0.02	0.62 ± 0.01	0.92 ± 0.01	0.82 ± 0.01
4.0	1.02 ± 0.02	1.09 ± 0.01	1.67 ± 0.01	1.58 ± 0.01
5.0	1.26 ± 0.03	1.35 ± 0.02	2.06 ± 0.02	1.98 ± 0.01
10.0	2.79 ± 0.05	3.03 ± 0.03	4.27 ± 0.03	4.21 ± 0.02
15.0	5.07 ± 0.09	5.70 ± 0.06	7.20 ± 0.06	7.14 ± 0.03
20.0	8.51 ± 0.15	9.88 ± 0.11	11.18 ± 0.09	11.09 ± 0.05

* The standard errors are indicated - see footnote, Table 3.

Discussion of Metallic Alloy Results

During analysis of the specific heat data two problems emerged, and as yet they remain unsolved. The first was the appearance of a constant term (A) in the specific heat function for the Inco LE alloy, which is ferromagnetic. Secondly, specific heat values for Nitronic 33 STWQ turned out to be extraordinarily high. Although no error was detected in the results of the experiment or its interpretation, conclusions regarding Nitronic 33 in the STQ condition are being held in abeyance pending further investigation.

Composites

The low-temperature specific heats of the three representative reinforced resins listed in Table 5 were investigated. Reinforcing fibers were of S-901 glass, type AS graphite, and boron (5.6 mil); and the materials were supplied by the Cryogenics Division, NBS, Boulder through the courtesy of Dr. M. B. Kasen.

Analysis of Specific Heat Data--S-901 Glass/NASA Resin 2

Using the specific heat data from measurements on the glass/resin composite the relative applicabilities of various fitting functions were explored. Specific heat data were fitted to polynomials of the form:

$$f(n,m,---) \equiv \alpha_n (T/10)^n + \alpha_m (T/10)^m + --- \qquad (3)$$

by a computorized linear regression procedure* which yielded values for the α_i (together with estimates of their precision in terms of standard errors) and, among an array of diagnostic parameters, a quantity referred to as the "coefficient of variability" (henceforth C-of-V) which, provided "wild" data had been eliminated by preliminary applications of the fitting procedure or otherwise, could generally be used as a measure of the appropriateness of the fitting function.

---

* SPSS - Statistical Package For the Social Sciences, Version 6, April 1, 1975. Vogelback Computing Center, Northwestern University.

TABLE 5. COMPOSITE MATERIALS* MEASURED

S-901 Glass (20 End)/NASA Resin 2	-	Fiber Vol. Frac. 60%
Type "AS" Graphite/NASA Resin 2	-	Fiber Vol. Frac. 60%
5.6 mil Boron/5505 Epoxy	-	Fiber Vol. Frac. 50%

* Materials supplied by Dr. M. B. Kasen, Cryogenics Division, NBS, Boulder, Colorado.

The validities of the following fitting functions (as defined in Equation (3)) were investigated:

f(1,3), f(3,5), f(2,3,4), f(2,3,5), f(1,2,3,4),

as well as the effect of dividing the data into "low temperature" (3-6 K) and "high temperature" (6-20 K) groupings. The results of the statistical analyses are summarized in Table 6; and values of specific heat, computed from the functions f(n,m,--) at each of a set of selected temperatures are given in Table 7.

For a given set of data the best fitting function will generally be that which minimizes the C-of-V at more-or-less constant standard error in α_i. With reference to Table 6, and after classifying f(n,m,--) into regions of unacceptability, marginality and acceptability according to whether C-of-V is greater than 6%, between 4 and 6%, or less than 4%, the following functions are deemed unacceptable:

f(1,3) (3-19 K)
f(3,5) (6-19 K).

The following

f(2,3,4), f(2,3,5), f(1,2,3,4),

are regarded as marginal when applied to the entire temperature range of 3-19 K; while the following are acceptable:

f(3,5), f(2,3,4), f(2,3,5)	(3-6 K)
f(2,3,4), f(2,3,5)	(6-19 K)

TABLE 6. MULTI-TERM LEAST-SQUARES FITTING OF SPECIFIC HEAT DATA FOR A GLASS-EPOXY COMPOSITE (S-901 Glass/NASA Resin 2) - - - COEFFICIENTS, α_i, OF THE EXPRESSION

$C = \sum_i \alpha_i (T/10)^i$ J/kg-deg

Function Symbol	Temperature Range (K)	Coefficient of Variability (%)	Regression Coefficients, α_i, J/kg-deg$^{(i+1)}$				
			α_1	α_2	α_3	α_4	α_5
f(1,3)	2.6 - 19	31.6	1.47 ± 0.13		4.10 ± 0.12		
f(2,3,4)	2.6 - 19	5.6		1.49 ± 0.13	7.82 ± 0.26	-2.58 ± 0.11	
f(2,3,5)	2.6 - 19	7.2		2.39 ± 0.13	4.99 ± 0.19		-0.71 ± 0.04
f(1,2,3,4)	2.6 - 19	4.1	-0.73 ± 0.10	4.28 ± 0.40	4.83 ± 0.45	-1.64 ± 0.15	
f(3,5)A	2.6 - 6	1.5			10.99 ± 0.08		-5.84 ± 0.30
f(3,5)B	6 - 19	9.4			7.95 ± 0.16		-1.23 ± 0.06
f(2,3,4)A	2.6 - 6	1.3		-0.01 ± 0.17	12.32 ± 0.80	-5.61 ± 0.91	
f(2,3,4)B	6 - 19	2.8		2.45 ± 0.25	6.27 ± 0.42	-2.00 ± 0.17	
f(2,3,5)A	2.6 - 6	1.4		0.33 ± 0.13	9.89 ± 0.44		-4.15 ± 0.72
f(2,3,5)B	6 - 19	3.1		3.40 ± 0.20	3.78 ± 0.25		-0.50 ± 0.05
f(1,2,3,4)A	2.6 - 6	1.0	-1.68 ± 0.39	12.63 ± 0.30	-17.92 ± 7.13	17.58 ± 5.50	
f(1,2,3,4)B	6 - 19	2.5	-2.21 ± 0.80	8.53 ± 2.21	1.09 ± 1.91	-0.62 ± 0.52	

TABLE 7. LOW-TEMPERATURE SPECIFIC HEAT (FITTED VALUES) FOR A GLASS-EPOXY COMPOSITE (S-901 GLASS/NASA RESIN 2) AT SPECIFIED TEMPERATURES

$C = \sum_i \alpha_i (T/10)^i$ J/kg-deg

Function Symbol	Temperature Range of Validity (K)	Low-Temperature Specific Heat (J/kg-deg) at Temperatures Indicated						Comments
		2.0 K	4.0 K	5.0 K	10.0 K	15.0 K	20.0 K	
f(1,3)	2.6 - 19	0.38 ± 0.03	0.85 ± 0.06	1.25 ± 0.08	5.6 ± 0.3	16.0 ± 0.6	35.7 ± 1.2	(1)
f(2,3,4)	2.6 - 19	0.12 ± 0.01	0.67 ± 0.04	1.19 ± 0.07	6.7 ± 0.5	16.7 ± 1.7	27.2 ± 4.4	(2)
f(2,3,5)	2.6 - 19	0.14 ± 0.01	0.69 ± 0.04	1.20 ± 0.07	6.7 ± 0.6	16.8 ± 2.2	26.8 ± 6.4	(3)
f(1,2,3,4)	2.6 - 19	0.06 ± 0.04	0.66 ± 0.14	1.21 ± 0.22	6.7 ± 1.1	16.5 ± 3.3	28.1 ± 7.8	(3)
f(3,5)A	2.6 - 6	0.09 ± 0.00	0.64 ± 0.01	1.19 ± 0.02				(2)
f(3,5)B	6 - 19			0.96 ± 0.03	6.7 ± 0.4	17.5 ± 1.8	24.2 ± 5.8	(1)
f(2,3,4)A	2.6 - 6	0.09 ± 0.01	0.64 ± 0.10	1.19 ± 0.20				(2)
f(2,3,4)B	6 - 19			1.27 ± 0.13	6.7 ± 0.8	16.6 ± 2.8	28.0 ± 7.1	
f(2,3,5)A	2.6 - 6	0.09 ± 0.01	0.64 ± 0.07	1.19 ± 0.14				(2)
f(2,3,5)B	6 - 19			1.31 ± 0.08	6.7 ± 0.5	16.6 ± 1.7	27.8 ± 4.4	
f(1,2,3,4)A	2.6 - 6	0.05 ± 0.16	0.65 ± 0.80	1.18 ± 1.51				(1)
f(1,2,3,4)B	6 - 19			1.13 ± 1.22	6.8 ± 5.4	16.4 ± 15.3	28.5 ± 34.0	

(1) Unacceptable Fit

(2) Acceptable Fit

(3) Marginal

In judging the applicability of a function to a given set of data it is necessary to consider both C-of-V and the standard error in α_i. Usually the standard error does not change much, but occasionally, as with f(1,2,3,4), (3-6 K) and (6-19 K), the uncertainity of fit is transferred from C-of-V to the standard error to yield unacceptable results.

In constructing the final summarizing tabulation (Table 10) the functions f(2,3,4) (3-6 K) and f(2,3,4) (6-19 K) were utilized.

Analysis of Specific Heat Data--Graphite- and Boron-Reinforced Resins

Two experiments were performed on a sample of graphite/resin within the temperature ranges 4-18 K and 4-17 K respectively; and one on boron/epoxy within the range 3-19 K. Based on the experience described above, the functions f(2,3,4) and f(2,3,5) were fitted to all the specific heat data. In addition, the function f(1,2,3,5) was applied to the graphite/resin data with anticipated unsatisfactory results. Since the graphite/resin was not measured below 4 K, that data set was not subdivided into two temperature ranges. Two ranges were, however, used in analyzing the boron/epoxy data. The results of the regression analyses are given in Table 8, while fitted specific heat values at the specified temperatures are presented in Table 9.

From the standpoint of the regression coefficients (α_i) there is scarcely qualitative agreement between the f(2,3,4) and f(2,3,5) fitting functions; on the other hand since they are in fact both good fits to the data, there is no significant difference between the results of their application within the relevant temperature range.

Summary of the Results on the Composite Data

Although absent in the fitting function for metallic alloys, the presence of a quadratic term in T is essential for a proper description of the specific heat temperature dependences of resinous materials in the

TABLE 8. LOW-TEMPERATURE SPECIFIC HEAT PARAMETERS, α_i, FOR TWO COMPOSITE MATERIALS

$C = \sum_i \alpha_i (T/10)^i$ J/kg-deg

Sample	Function Symbol	Temperature Range of Experiment (K)	Coefficient of Variability (%)	Regression Coefficient, α_i, J/kg-deg$^{(i+1)}$				
				α_1	α_2	α_3	α_4	α_5
Graphite/Resin -Experiment 1	f(1,3)	4-18	19.3	3.29 ± 0.33		4.66 ± 0.22		
	f(2,3,4)		3.1		4.22 ± 0.23	8.64 ± 0.45	-3.49 ± 0.19	
	f(2,3,5)		3.6		5.40 ± 0.20	4.92 ± 0.29		-1.01 ± 0.07
	f(1,2,3,5)		2.5	-2.01 ± 0.31	11.49 ± 0.96	0.29 ± 0.75		-0.40 ± 0.10
Graphite/Resin -Experiment 2	f(2,3,4)	4-17	4.9		2.77 ± 0.39	12.22 ± 0.82	-5.56 ± 0.43	
	f(2,3,5)		5.6		4.38 ± 0.34	6.74 ± 0.53		-1.72 ± 0.14
	f(1,2,3,5)		5.1	-1.63 ± 0.63	9.77 ± 2.11	2.32 ± 1.78		-1.06 ± 0.29
Boron/Epoxy	f(2,3,4)	3-6	0.6		-0.52 ± 0.09	10.50 ± 0.44	-4.60 ± 0.48	
		6-19	1.5		2.14 ± 0.13	4.65 ± 0.21	-1.71 ± 0.08	
	f(2,3,5)	3-6	0.7		-0.22 ± 0.07	8.43 ± 0.24		-3.33 ± 0.36
		6-19	1.9		2.97 ± 0.12	2.51 ± 0.14		-0.43 ± 0.03

TABLE 9. LOW-TEMPERATURE SPECIFIC HEAT (FITTED VALUES) FOR TWO COMPOSITE MATERIALS AT SPECIFIED TEMPERATURES

$C = \sum_i \alpha_i (T/10)^i$ J/kg-deg

		Temperature Range of Experiment (K)	Low-Temperature Specific Heat (J/kg-deg) at Temperatures Indicated						Comments
			2.0 K	4.0 K	5.0 K	10.0 K	15.0 K	20.0 K	
Graphite/Resin -Experiment 1	f(2,3,4)	4-18	0.23 ± 0.01	1.14 ± 0.07	1.92 ± 0.13	9.4 ± 0.9	21.0 ± 3.0	30.2 ± 7.6	(1)
	f(2,3,5)		0.26 ± 0.01	1.17 ± 0.05	1.93 ± 0.09	9.3 ± 0.6	21.1 ± 2.0	28.6 ± 5.4	(1)
	f(1,2,3,5)		0.06 ± 0.11	1.05 ± 0.33	1.89 ± 0.49	9.4 ± 2.1	20.8 ± 5.9	31.5 ± 13.7	(2)
Graphite/Resin -Experiment 2	f(2,3,4)	4-17	0.20 ± 0.02	1.08 ± 0.13	1.87 ± 0.23	9.4 ± 1.6	19.3 ± 5.8	(19.9 ± 15.0)	(3)
	f(2,3,5)		0.23 ± 0.02	1.11 ± 0.09	1.88 ± 0.16	9.4 ± 1.0	19.5 ± 3.6	(16.4 ± 10.1)	(3)
	f(1,2,3,5)		0.08 ± 0.22	1.05 ± 0.71	1.88 ± 1.07	9.4 ± 4.8	19.3 ± 13.9	20.5 ± 33.2	(2)
Boron/Epoxy	f(2,3,4)	3-6	0.06 ± 0.01	0.47 ± 0.05	0.90 ± 0.11				(4)
		6-19			1.01 ± 0.06	5.1 ± 0.4	11.9 ± 1.4	18.4 ± 3.5	(4)
	f(2,3,5)	3-6	0.06 ± 0.00	0.47 ± 0.03	0.89 ± 0.06				(4)
		6-19			1.04 ± 0.05	5.1 ± 0.3	11.9 ± 1.0	18.2 ± 2.6	(4)

(1) Acceptable fit $\lesssim$ 20 K

(2) Unsatisfactory fitting function

(3) Acceptable fit $\lesssim$ 15 K

(4) Acceptable fit $\lesssim$ 20 K

temperature range above 6 K. But below that temperature, according to Tables 6 and 8, good fits are obtained with essentially cubic functions (e.g. row 5, Table 6 and rows 7 and 9, Table 8).

As a summary of the results, specific heat data for the three composites studied, critically selected from Tables 7 and 9, are presented in Table 10.

TABLE 10. SUMMARY OF SPECIFIC HEAT DATA FOR COMPOSITE MATERIALS

Temperature, K	Specific Heat of Composite (J/kg-deg)		
	S-901 Glass/NASA Resin 2	Type "AS" Graphite/NASA Resin 2	5.6 mil Boron/5505 Epoxy
2.0	0.09 ± 0.01	0.23 ± 0.01	0.06 ± 0.01
4.0	0.64 ± 0.10	1.14 ± 0.07	0.47 ± 0.05
5.0	1.19 ± 0.20	1.92 ± 0.13	0.90 ± 0.11
10.0	6.7 ± 0.8	9.4 ± 0.9	5.1 ± 0.4
15.0	16.6 ± 2.8	21.0 ± 3.0	11.9 ± 1.4
20.0	28.0 ± 7.1	30.2 ± 7.6	18.4 ± 3.5

PART II. LOW TEMPERATURE THERMAL EXPANSION OF SOME CRYOGENIC STRUCTURAL MATERIALS

Introduction

Low temperature thermal expansion results are reported for ten materials in the temperature range 4.2 to 300 K. The technique used to perform the measurements was a fused silica dilatometer which has been previously described.

In addition to the four materials furnished by Westinghouse for this study, we have included four composites furnished by NBS and two alloys supplied by Battelle. Table 11 lists these materials with a brief description and/or heat treatment used.

Data Presentation

The results reported in this work are shown as percent contraction versus temperature (K) with all data normalized at the ice point (273 K).

Figure 1 through 10 illustrate the results in graphic form while Tables 12 through 21 contain the specific data in 10 degree intervals.

TABLE 11. LIST OF THERMAL EXPANSION SPECIMENS INCLUDED IN THIS REPORT

COMPOSITES	
5.6 Mil Boron/5505 Epoxy	- Fiber Vol. Frac. 50 %
Type "AS" Graphite/NASA Resin 2	- Fiber Vol. Frac. 60 %
5.6 Mil Boron/6061 Aluminum	- 6061-F Temperature
S-901 Glass (20 End)/NASA Resin 2	- Fiber Vol. Frac. 60 %
ALLOYS	
NITRONIC 33	- ST/FC
NITRONIC 33	- STQ
Ti-6Al-4V	- ANNEALED
A-286	- ST
SMAW-40B	- WELD FILLER*
GTAW-20B	- ACROSS WELD*

* For further identification see Westinghouse section of this semiannual report.

TABLE 12. THERMAL EXPANSION BEHAVIOR OF 5.6 MIL BORON/5505 EPOXY COMPOSITE IN THE TEMPERATURE RANGE 4.2 TO 300 K

T(K)	$\Delta L/L_o$ (%) (longitudinal)	$\Delta L/L_o$ (%) (tranverse)
300	-0.011	-0.063
290	-0.007	-0.037
280	-0.003	-0.016
273	0	0
260	0.005	0.028
250	0.010	0.050
240	0.013	0.071
230	-	0.092
220	0.019	0.110
210	0.022	0.129
200	0.024	0.150
190	0.027	0.169
180	0.030	0.188
170	0.032	0.206
160	0.035	0.221
150	0.037	0.237
140	0.039	0.252
130	0.041	0.267
120	0.042	0.283
110	0.044	0.298
100	0.046	0.310
90	0.048	0.318
77	0.049	0.328
60	0.051	0.336
50	0.053	0.344
40	0.054	0.352
30	0.055	0.359
20	0.056	0.365
10	0.057	0.370
5	0.058	0.372

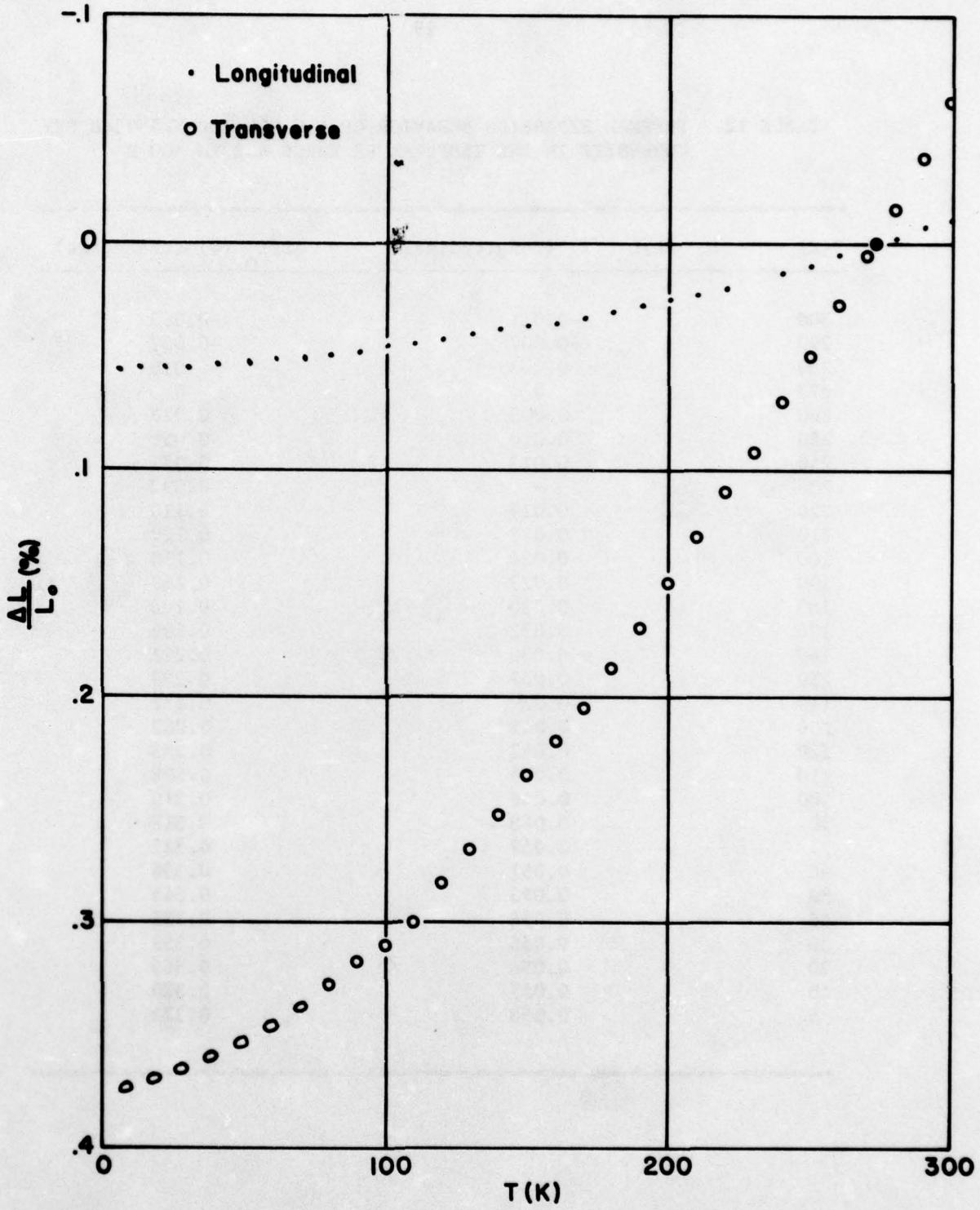


FIGURE 1. THERMAL EXPANSION BEHAVIOR OF 5.6 MIL BORON-5505 EPOXY, NOMINAL FIBER VOLUME FRACTION ABOUT 50 %

TABLE 13. THERMAL EXPANSION BEHAVIOR OF TYPE AS GRAPHITE-NASA RESIN 2 IN THE TEMPERATURE RANGE 4.2 TO 300 K

T(K)	$\Delta L/L_o$ (%) (Longitudinal)	$\Delta L/L_o$ (%) (Transverse)
300	-0.001	-0.031
290	0	-0.019
280	0	-0.009
273	0	0
260	0	0.040
250	0	0.050
240	0	0.059
230	0.001	0.079
220	0.001	0.102
210	0.001	0.126
200	0.002	0.157
190	0.002	0.191
180	0.002	0.227
170	0.003	0.262
160	0.003	-
150	0.003	0.320
140	0.004	0.351
130	0.004	0.375
120	0.005	0.401
110	0.007	0.428
100	0.009	0.454
90	0.011	0.479
77	0.013	0.507
60	0.014	0.526
50	0.015	0.538
40	0.015	0.549
30	0.016	0.557
20	0.016	0.562
10	0.016	0.565
5	0.016	0.568

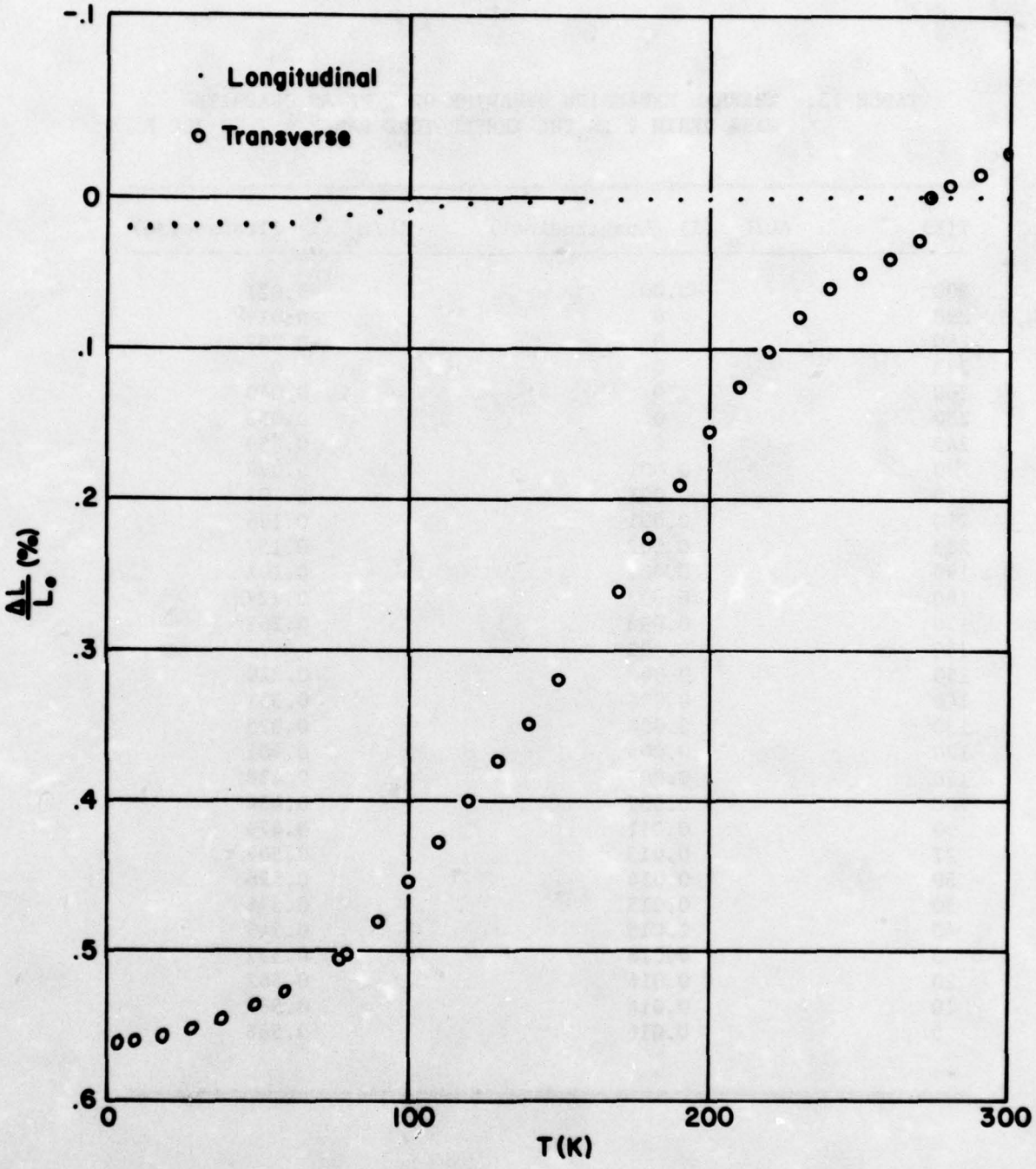


FIGURE 2. THERMAL EXPANSION BEHAVIOR OF TYPE AS GRAPHITE-NASA RESIN 2, NOMINAL FIBER VOLUME FRACTION ABOUT 60 %

TABLE 14. THERMAL EXPANSION BEHAVIOR OF 5.6 MIL BORON/6061 ALUMINUM-F-TEMPER, IN THE TEMPERATURE RANGE 4.2 TO 300 K

T(K)	$\Delta L/L_o$ (%) (longitudinal)	$\Delta L/L_o$ (%) (transverse)
300	-0.012	-0.050
290	-0.008	-0.030
280	-0.003	-0.013
273	0	0
260	0.006	0.025
250	0.010	-
240	0.014	0.059
230	0.017	0.075
220	0.021	0.090
210	0.026	0.106
200	0.030	0.120
190	0.035	0.132
180	0.040	0.145
170	0.045	0.158
160	0.049	0.170
150	0.053	0.181
140	0.057	0.192
130	0.061	0.199
120	0.064	0.210
110	0.067	0.215
100	0.070	0.221
90	0.074	0.228
77	0.077	0.236
60	0.079	0.242
50	0.081	0.247
40	0.083	0.251
30	0.085	0.254
20	0.086	0.257
10	0.087	0.260
5	0.088	0.262

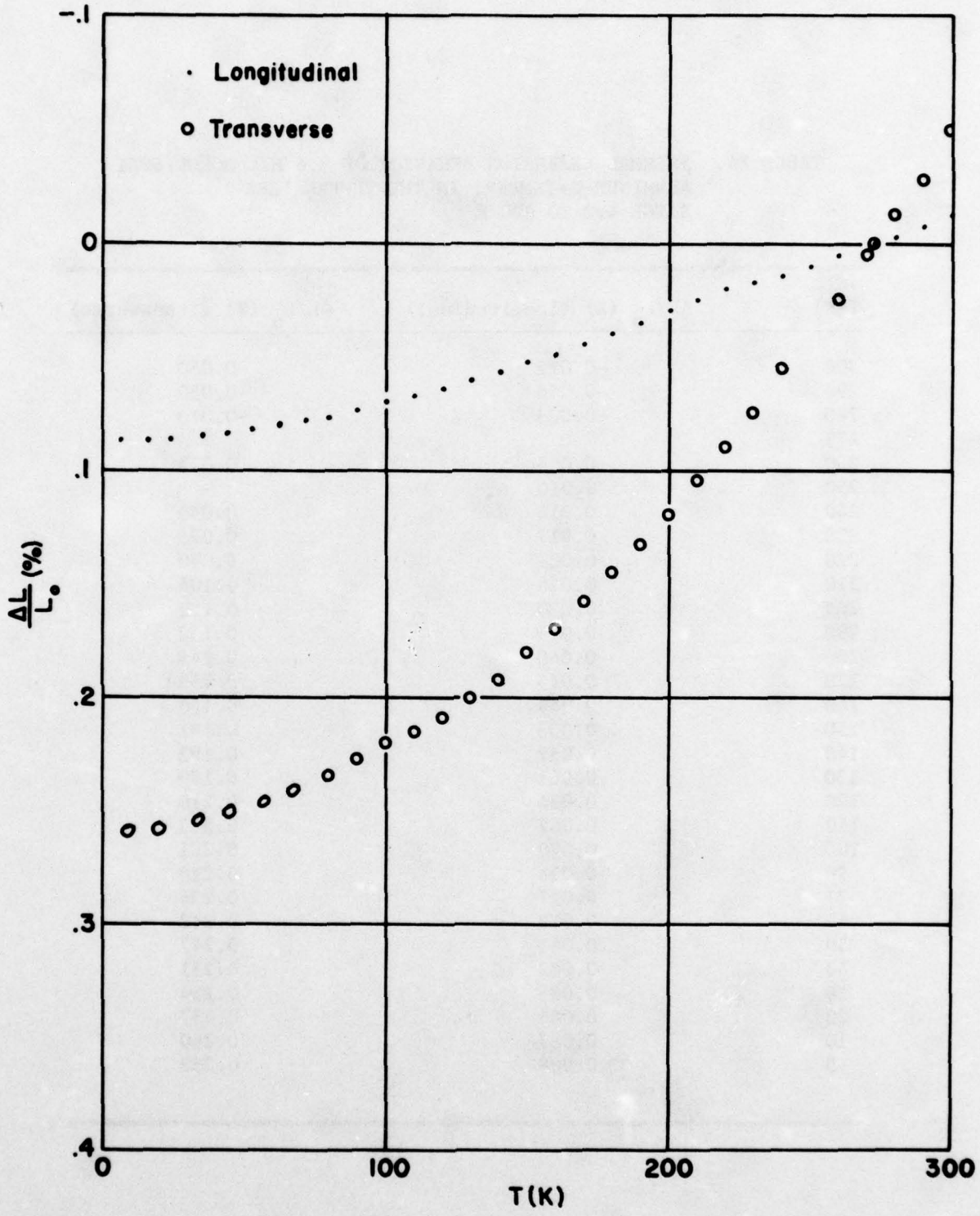


FIGURE 3. THERMAL EXPANSION BEHAVIOR OF 5.6 MIL BORON-6061 ALUMINUM, F TEMPER

TABLE 15. THERMAL EXPANSION BEHAVIOR OF S-901 GLASS-20 END/ NASA RESIN 2 IN THE TEMPERATURE RANGE 4.2 TO 300 K

T(K)	$\Delta L/L_o$ (%) (longitudinal)	$\Delta L/L_o$ (%) (transverse)
300	-0.017	-0.070
290	-0.007	-0.043
280	-0.003	-0.017
273	0	0
260	0.003	0.032
250	0.010	0.056
240	0.013	0.081
230	0.017	0.106
220	0.022	0.130
210	0.027	0.152
200	0.032	0.175
190	0.035	0.194
180	0.039	0.212
170	0.044	0.234
160	0.050	0.255
150	0.052	0.275
140	-	0.294
130	0.055	-
120	0.056	0.331
110	0.057	0.354
100	0.058	0.364
90	0.058	0.376
77	0.060	0.391
70	-	0.403
60	0.061	0.417
50	0.061	0.421
40	0.062	0.438
30	0.062	0.450
20	0.063	0.459
10	0.063	0.466
5	0.064	0 470

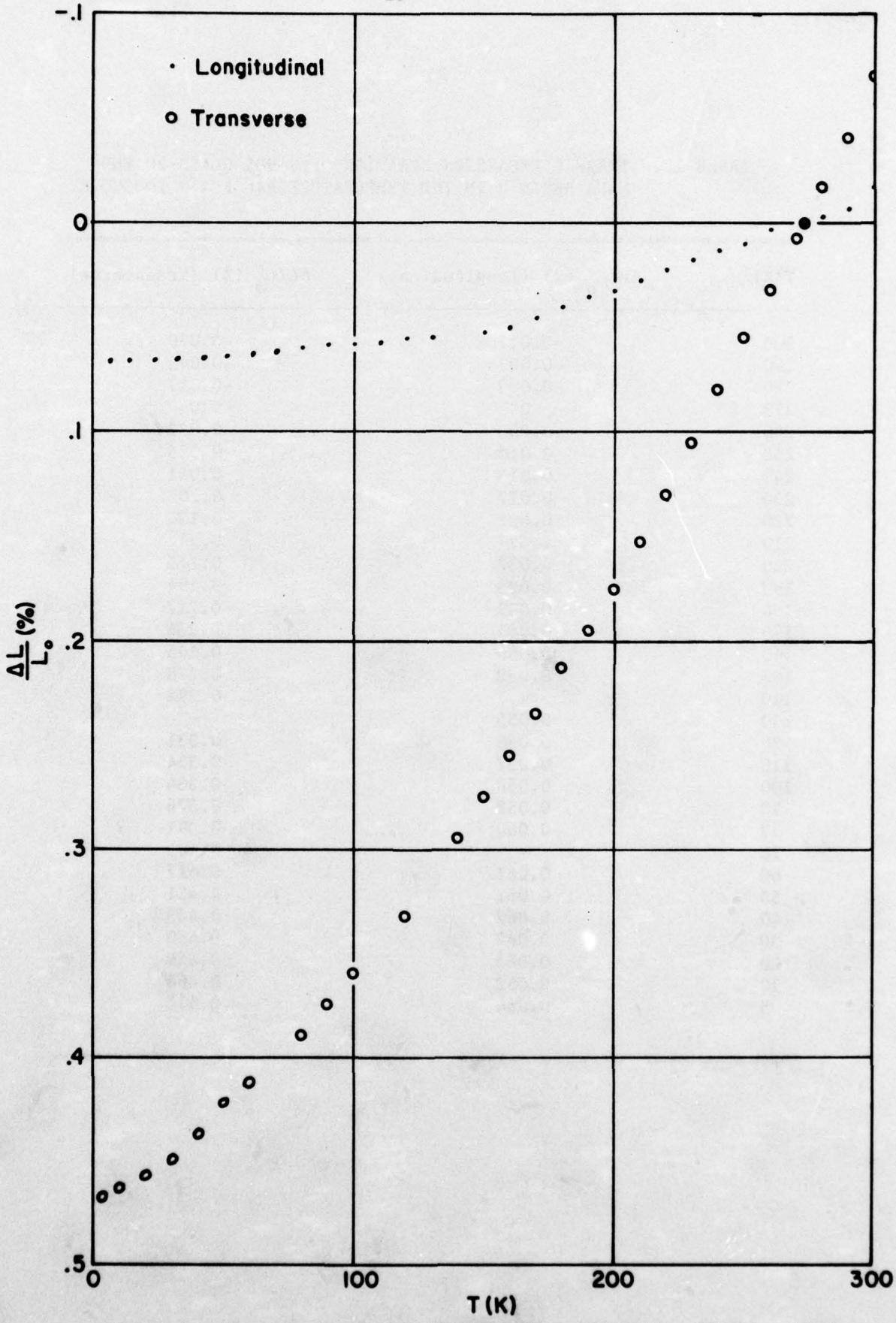


FIGURE 4. THERMAL EXPANSION BEHAVIOR OF S-901 GLASS, 20 END - NASA RESIN 2, NOMINAL FIBER VOLUME FRACTION ABOUT 60 %

TABLE 16. THERMAL EXPANSION BEHAVIOR OF NITRONIC 33-SOLUTION TREATED AND FURNACE COOLED. TEMPERATURE RANGE 4.2 TO 300 K

T(K)	$\Delta L/L_o$ (%)
300	-0.038
290	-0.022
280	-0.007
273	0
260	0.015
250	0.031
240	0.042
230	0.059
220	0.074
210	0.090
200	0.103
190	0.118
180	0.131
170	0.140
160	0.145
150	0.154
140	0.161
130	0.168
120	0.174
110	0.180
100	0.184
90	0.186
77	0.187
60	0.189
50	0.189
40	0.189
30	0.189
20	0.190
10	0.190
5	0.190

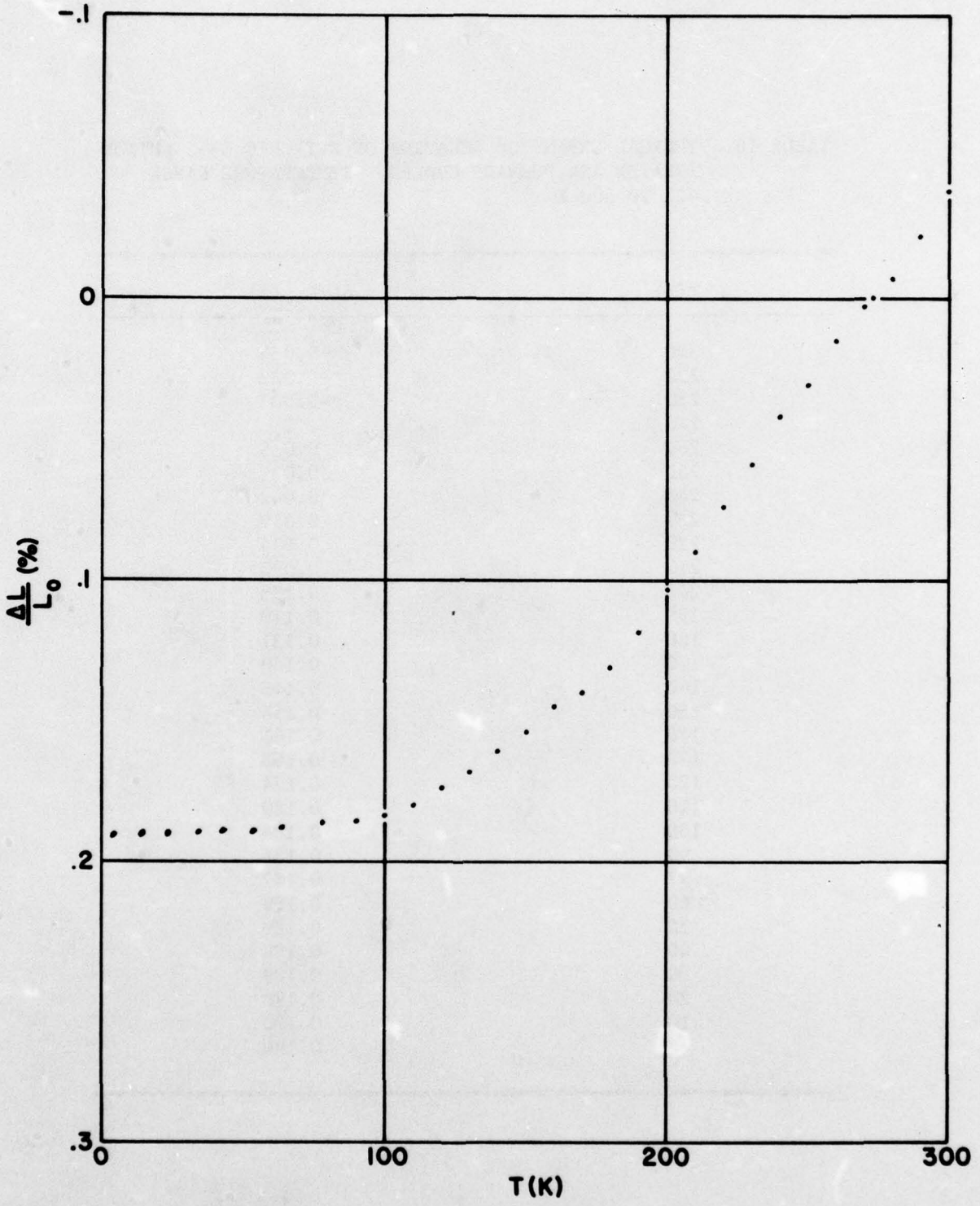


FIGURE 5. THERMAL EXPANSION BEHAVIOR OF NITRONIC 33, SOLUTION TREATED AND FURNACE COOLED

TABLE 17. THERMAL EXPANSION BEHAVIOR OF NITRONIC 33-SOLUTION TREATED AND QUENCHED. TEMPERATURE RANGE 4.2 TO 300 K

T(K)	$\Delta L/L_o$ (%)
300	-0.042
290	-0.028
280	-0.013
273	0
260	0.017
250	0.031
240	0.044
230	0.058
220	0.072
210	0.084
200	0.096
190	0.108
180	0.119
170	0.127
160	0.137
150	0.145
140	0.148
130	0.159
120	0.166
110	0.171
100	0.175
90	0.180
77	0.185
60	0.187
50	0.188
40	0.188
30	0.189
20	0.189
10	0.189
5	0.189

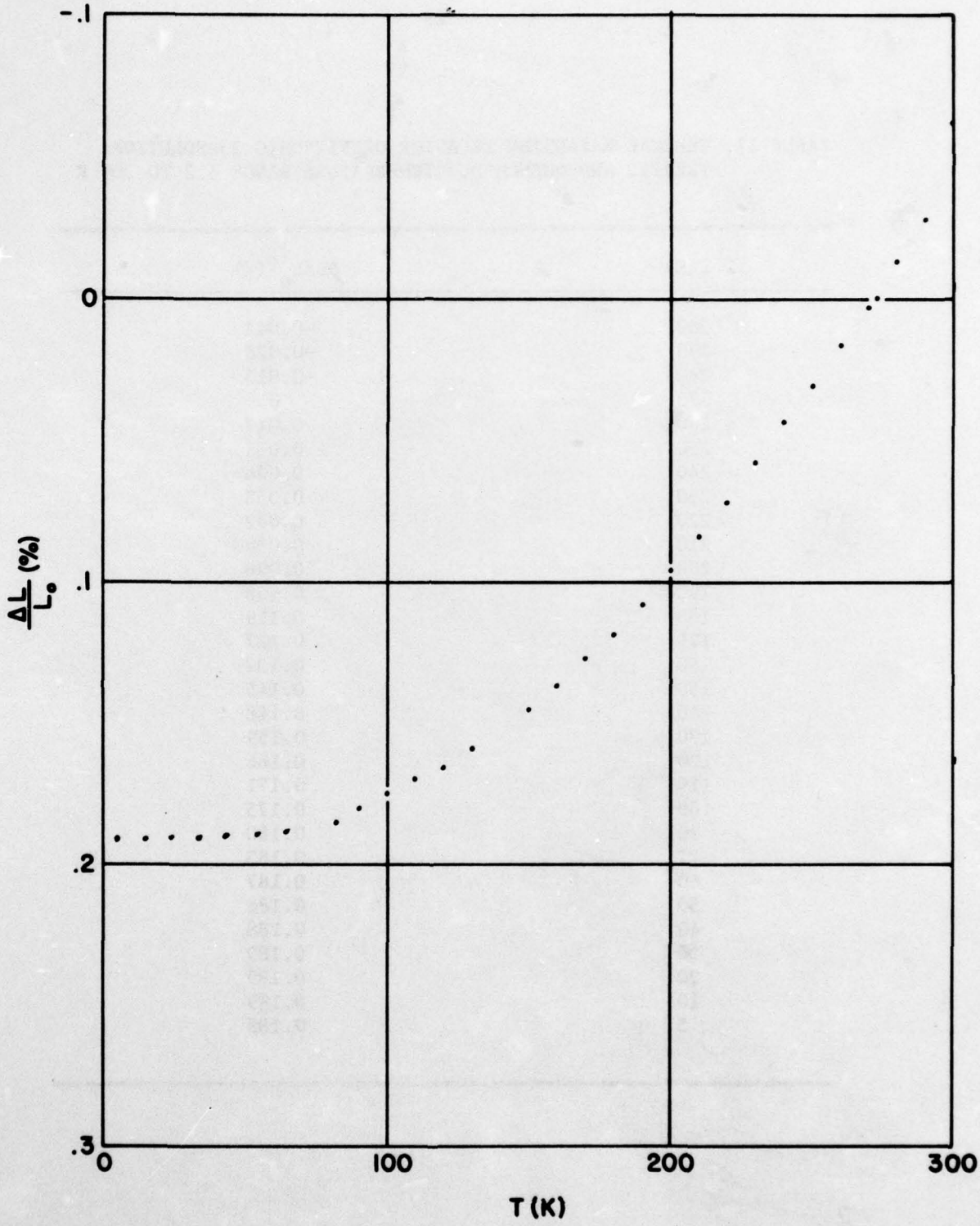


FIGURE 6. THERMAL EXPANSION BEHAVIOR OF NITRONIC 33, SOLUTION TREATED AND QUENCHED

TABLE 18. THERMAL EXPANSION BEHAVIOR OF ANNEALED Ti-6Al-4V IN THE TEMPERATURE RANGE 4.2 TO 300 K

T(K)	$\Delta L/L_o$ (%)
300	-0.024
290	-0.015
280	-0.006
273	0
260	0.011
250	0.020
240	0.028
230	0.036
220	0.044
210	0.054
200	0.061
190	0.070
180	0.077
170	0.085
160	0.091
150	0.098
140	0.105
130	0.111
120	0.117
110	0.120
100	0.125
90	0.127
77	0.131
60	0.136
50	0.138
40	0.139
30	0.140
20	0.141
10	0.142
5	0.142

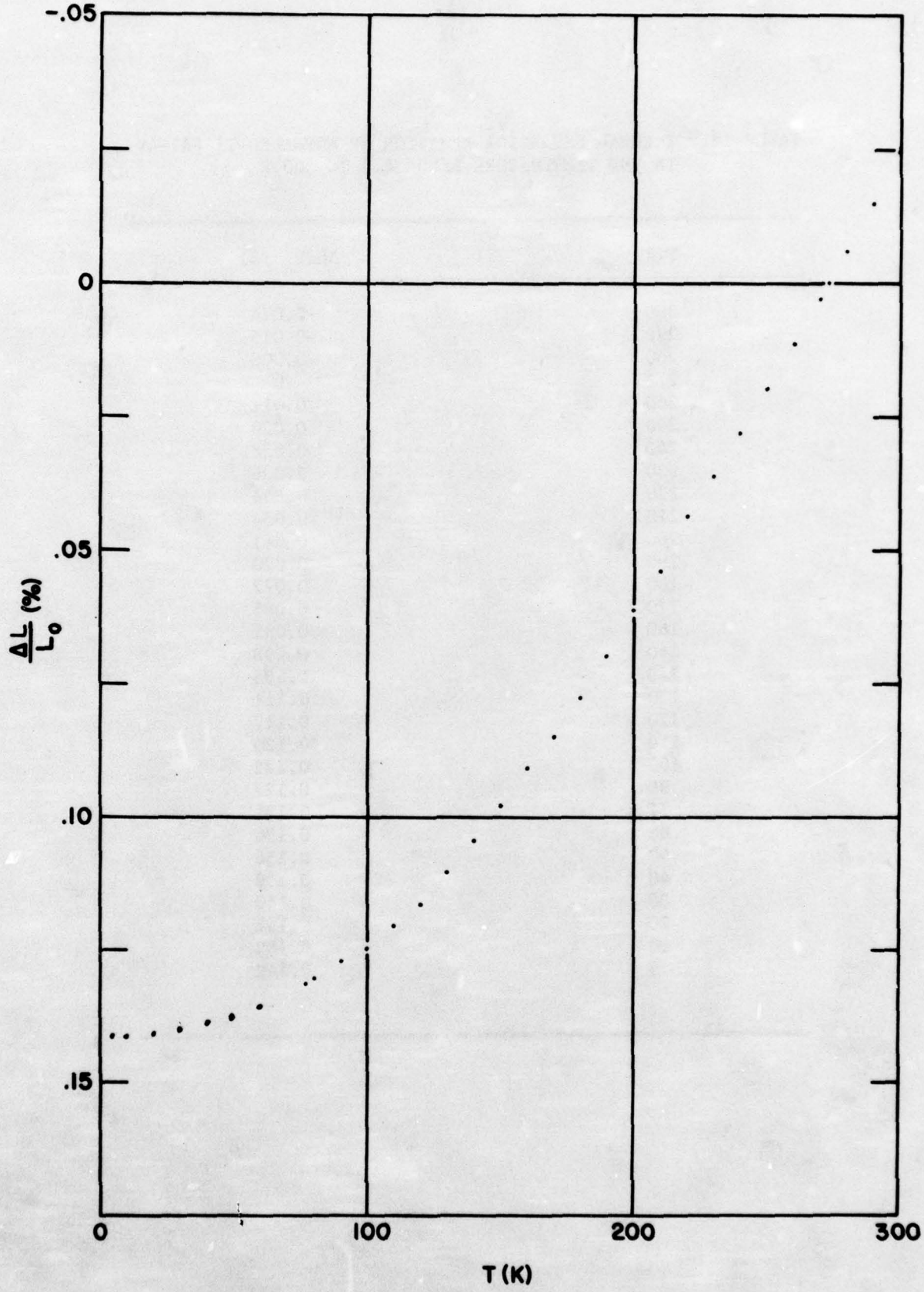


FIGURE 7. THERMAL EXPANSION BEHAVIOR OF Ti-6Al-4V IN THE ANNEALED CONDITION

TABLE 19. THERMAL EXPANSION BEHAVIOR OF SOLUTION TREATED A-286 IN THE TEMPERATURE RANGE 4.2 TO 300 K

T(K)	$\Delta L/L_o$ (%)
300	-0.042
290	-0.025
280	-0.010
273	0
260	0.021
250	0.037
240	0.052
230	0.067
220	0.081
210	0.096
200	0.111
190	0.126
180	0.141
170	0.154
160	0.168
150	0.181
140	0.194
130	0.207
120	0.218
110	0.230
100	0.241
90	0.247
77	0.250
60	0.262
50	0.265
40	0.268
30	0.269
20	0.270
10	0.271
5	0.271

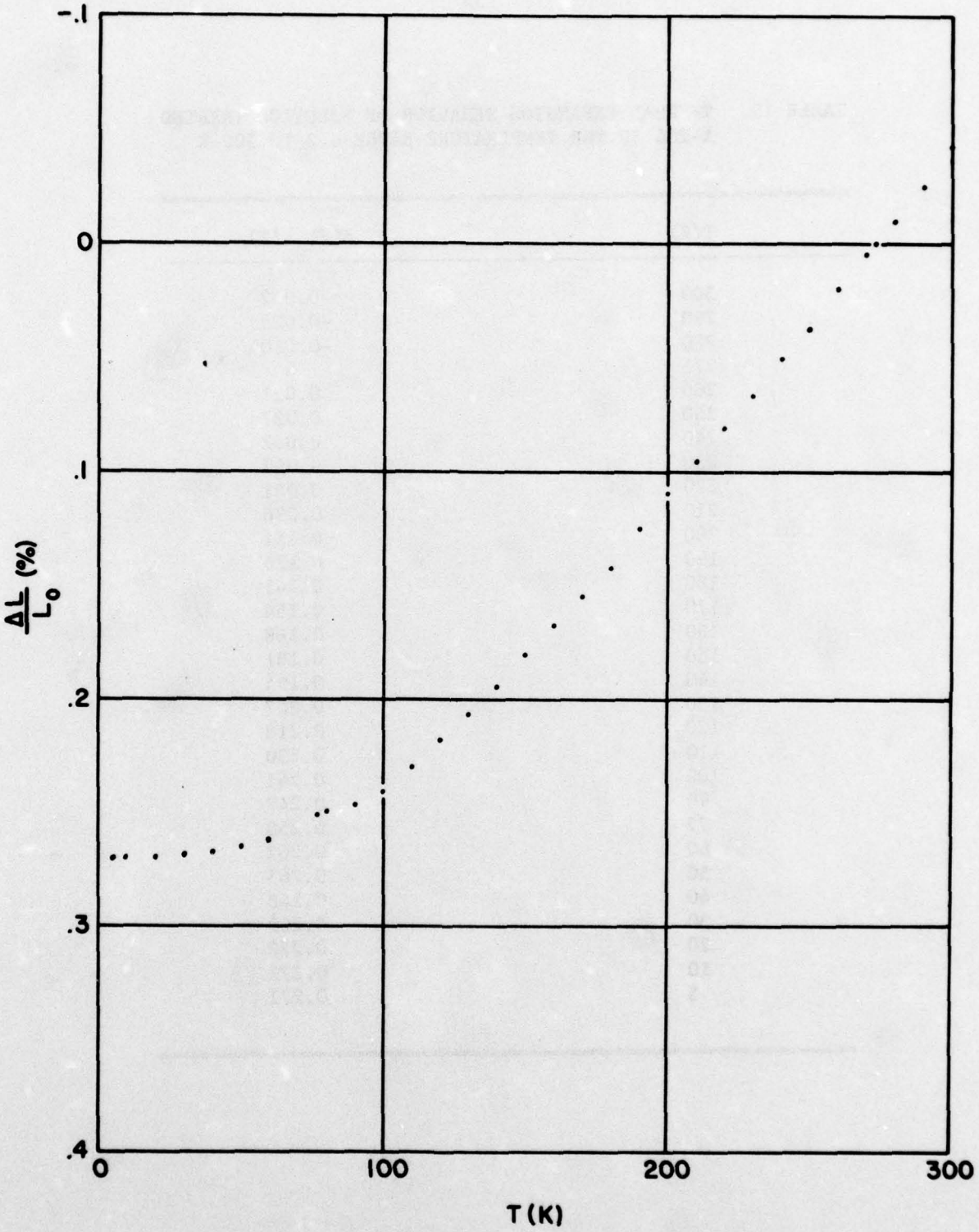


FIGURE 8. THERMAL EXPANSION BEHAVIOR OF ALLOY A-286 SOLUTION TREATED

TABLE 20. THERMAL EXPANSION BEHAVIOR OF SMAW-40B WELD FILLER IN THE TEMPERATURE RANGE 4.2 TO 300 K

T(K)	$\Delta L/L_o$ (%)
300	-0.039
290	-0.024
280	-0.004
273	0
260	0.019
250	0.032
240	0.045
230	0.058
220	0.071
210	0.084
200	0.094
190	0.105
180	0.114
170	0.123
160	0.130
150	0.137
140	0.144
130	0.149
120	0.154
110	0.160
100	0.166
90	0.169
77	0.173
60	0.178
50	0.179
40	0.180
30	0.180
20	0.181
10	0.181
5	0.181

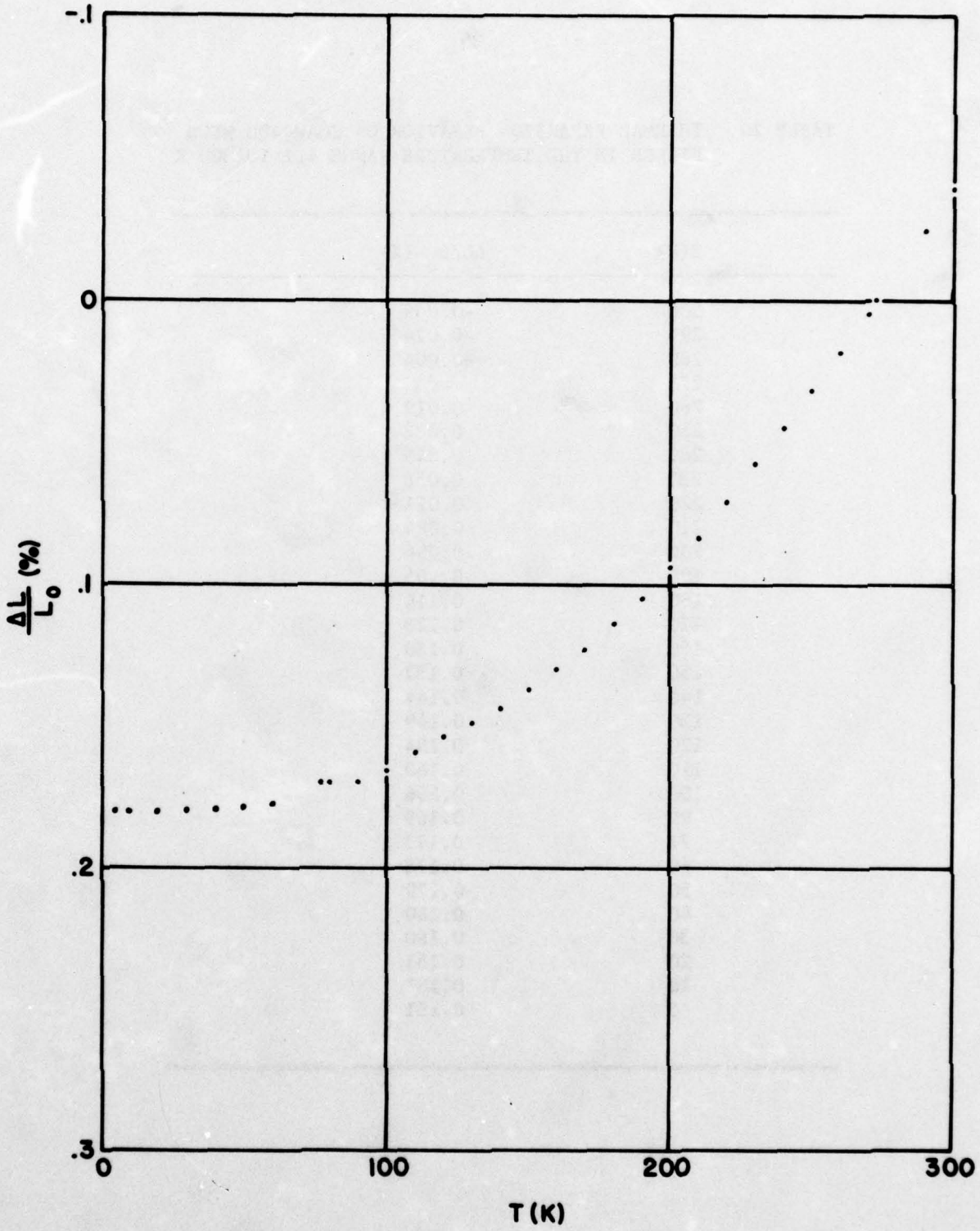


FIGURE 9. THERMAL EXPANSION BEHAVIOR OF SMAW-40B WELD FILLER MATERIAL

TABLE 21. THERMAL EXPANSION BEHAVIOR OF GTAW-20B ACROSS THE WELD IN THE TEMPERATURE RANGE 4.2 TO 300 K

T(K)	$\Delta L/L_o$ (%)
300	-0.043
290	-0.027
280	-0.011
273	0
260	0.020
250	0.034
240	0.049
230	0.063
220	0.077
210	0.092
200	0.105
190	0.117
180	0.128
170	0.138
160	0.148
150	0.157
140	0.166
130	0.174
120	0.182
110	0.189
100	0.195
90	-
77	0.205
60	0.213
50	0.215
40	0.217
30	0.218
20	0.218
10	0.219
5	0.219

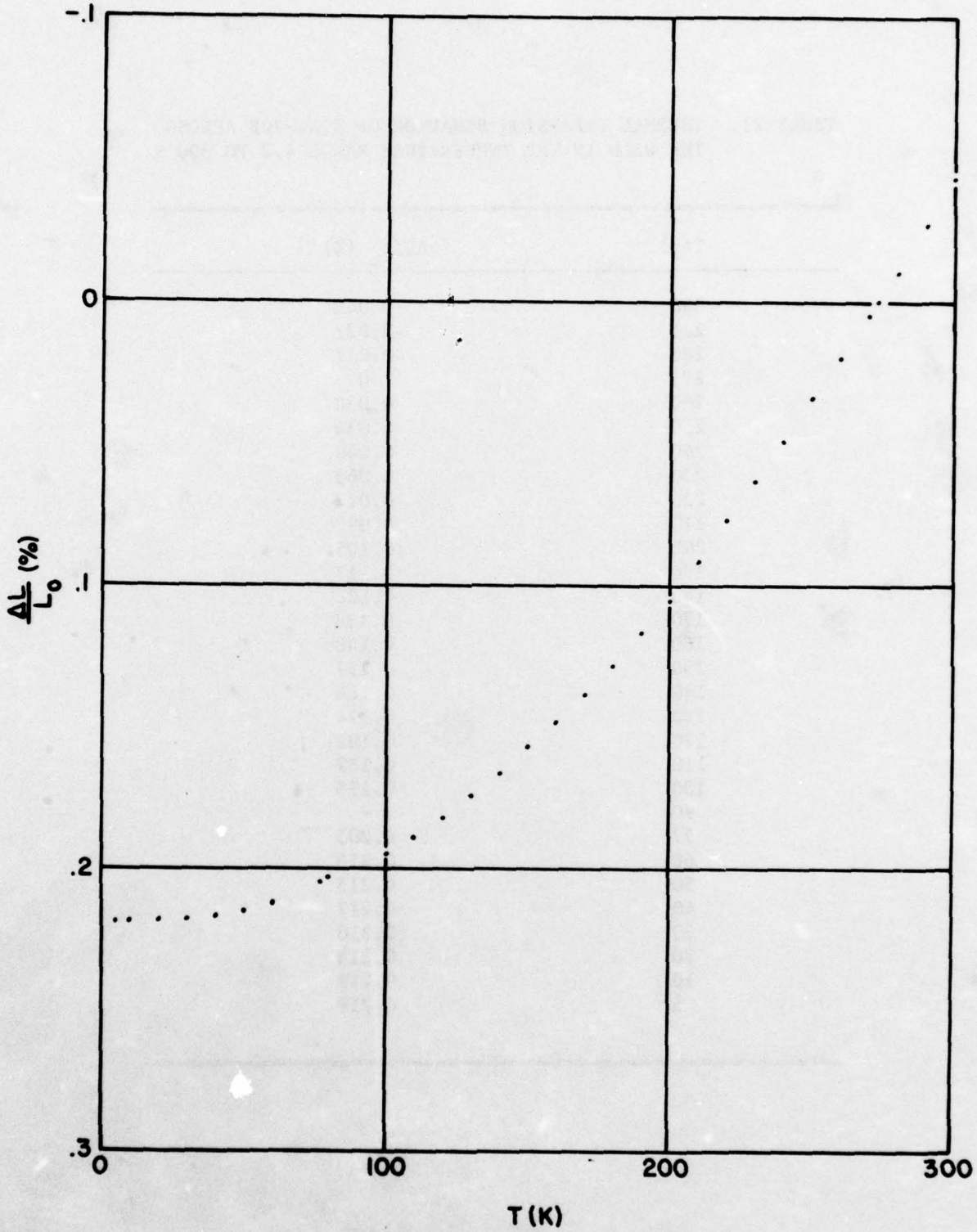


FIGURE 10. THERMAL EXPANSION BEHAVIOR OF GTAW-20B ACROSS THE WELD

NBSIR 76-848

SEMI-ANNUAL REPORT ON MATERIALS RESEARCH IN SUPPORT OF SUPERCONDUCTING MACHINERY

R. P. Reed, J. G. Hust, M. B. Kasen, H. M. Ledbetter, H. I. McHenry,
D. T. Read, R. E. Schramm, L. L. Sparks, and R. L. Tobler

Cryogenics Division
Institute for Basic Standards
National Bureau of Standards
Boulder, Colorado 80302

October 1976

Prepared for :

Advanced Research Projects Agency
1400 Wilson Boulevard
Arlington, Virginia 22209



U.S. DEPARTMENT OF COMMERCE, Elliot L. Richardson, Secretary
James A. Baker, III, Under Secretary
Dr. Betsy Ancker-Johnson, Assistant Secretary for Science and Technology

NATIONAL BUREAU OF STANDARDS, Ernest Ambler, Acting Director

PRECEDING PAGE BLANK-NOT FILMED

SEMI-ANNUAL REPORT ON MATERIALS RESEARCH IN SUPPORT OF SUPERCONDUCTING MACHINERY

Sponsored by
Advanced Research Projects Agency
ARPA Order No. 2569
Program Code 4D10
August 10, 1975 - October 1, 1976

Program Director
Dr. E. C. van Reuth
Materials Sciences
Advanced Research Projects Agency
1400 Wilson Boulevard
Arlington, Virginia 22209

Program Manager
Dr. R. P. Reed
Cryogenics Division
Institute for Basic Standards
National Bureau of Standards
Boulder, Colorado 80302

The views and conclusions contained in this document are those of the authors and should not be interpreted as necessarily representing the official policies, either expressed or implied, of the Advanced Research Projects Agency or of the U.S. Government.

Abstract

Results are reported of a six-month study, ending September 1976, on candidate materials for superconducting-machinery components. The results cover five areas--advanced composites, elastic properties, fatigue resistance and fracture toughness, magnetothermal conductivity, and thermal conductivity. Material properties were studied over the temperature range 4 to 300 K. Materials studied include: aluminum alloy 5083, copper-0.3 cadmium-0.3 tin, copper-28 nickel, iron-48 nickel, 3.5 Ni and 9 Ni steels, titanium-4 aluminum-6 vanadium, titanium-5 aluminum-2.5 tin, stainless steel 21-6-9, several austenitic stainless steels of the 300 series, 300-grade maraging steel, phenolformaldehyde, and the composites boron/aluminum, boron/epoxy, graphite/epoxy, and niobium-titanium/copper. Some notable results of the study are: anomalous elastic properties of stainless steel 21-6-9 due to a Néel transition; complete sets of elastic constants for two composites, B/Al and NbTi/Cu; thermal conductivities of Ti-6Al-4V and Fe-48Ni are reduced by a magnetic field while those of Cu-0.5 Sn and Cu-28Ni are unaffected; a screening method for composites of possible cryogenic use; general trends regarding temperature effects on the fracture toughness and fatigue-crack-growth resistances of structural alloys are correlated with crystal structure class; and the tensile-yield-strength and fracture-toughness data for fourteen commercial structural alloys at 4 K and 295 K are compared demonstrating an inverse relationship between these properties and indicating the optimum combination of properties that are technologically possible. Also, the materials and properties studied experimentally during the three-year program are summarized.

This work was supported by the Advanced Research Projects Agency of the U.S. Department of Defense.

Key words: Aluminum alloys; composites; elastic properties; engineering materials; fatigue; fracture; iron alloys; cryogenic temperatures; maraging steels; mechanical properties; nickel alloys; phenolformaldehyde; stainless steels; superconducting machinery; thermal conductivity; titanium alloys.

Report Contents

Page

ADVANCED COMPOSITES
M. B. Kasen, R. E. Schramm, and D. T. Read 1

ELASTIC PROPERTIES
H. M. Ledbetter and D. T. Read 19

Orthorhombic elastic constants of an NbTi/Cu composite superconductor
H. M. Ledbetter and D. T. Read 23

Temperature dependence of the elastic constants of an NbTi/Cu superconducting composite
D. T. Read and H. M. Ledbetter 48

Low-temperature elastic properties of a 300-grade maraging steel
H. M. Ledbetter 66

Low-temperature elastic properties of a precipitation-hardened copper alloy
H. M. Ledbetter 84

Elastic properties of a boron-aluminum composite at low temperatures
D. T. Read and H. M. Ledbetter 100

Anomalous low-temperature elastic behavior of a nitrogen-strengthened chromium-manganese stainless steel
H. M. Ledbetter 117

FRACTURE MECHANICS PARAMETERS
R. L. Tobler, H. I. McHenry, R. P. Reed, and R. E. Schramm . . 133

Fracture mechanics parameters for a 5083-0 aluminum alloy at low temperatures
R. L. Tobler and R. P. Reed 135

Tensile and fracture behavior of a nitrogen-strengthened, chromium-nickel-manganese stainless steel at cryogenic temperatures
R. L. Tobler and R. P. Reed 162

Cryogenic tensile, fatigue, and fracture parameters for a solution-annealed maraging steel
R. L. Tobler, R. P. Reed, and R. E. Schramm 188

Cryogenic effects on the fracture mechanics parameters of ferritic nickel-alloy steels
R. L. Tobler 214

Note on the fracture properties of Fe-49Ni at cryogenic temperatures
H. I. McHenry and R. E. Schramm 244

Fatigue crack growth resistance of structural alloys at cryogenic temperatures
R. L. Tobler and R. P. Reed 256

Fracture of structural alloys at temperatures approaching absolute zero
R. L. Tobler 279

MAGNETOTHERMAL CONDUCTIVITY
L. L. Sparks 287

THERMAL CONDUCTIVITY
J. G. Hust 305

Disclaimer

Tradenames of equipment and materials are used in this report for clarity and to conform with standard usage in the scientific and engineering literature. Selection of materials for discussion and examination with regard to application in superconducting machinery is based on properties reported in the literature, and must be regarded as preliminary and tentative. In no case does such selection imply recommendation or endorsement by the National Bureau of Standards, nor does it imply that the material or equipment is necessarily the best available for the purpose.

SEMI-ANNUAL REPORT ON MATERIALS RESEARCH IN SUPPORT OF SUPERCONDUCTING MACHINERY

ADVANCED COMPOSITES

M. B. Kasen, R. E. Schramm, and D. T. Read

Cryogenics Division
Institute for Basic Standards
National Bureau of Standards
Boulder, Colorado 80302

October 1976

NBS COMPOSITE-MATERIALS STUDIES DURING ARPA-SPONSORED PROGRAM, SEPTEMBER 1973 TO SEPTEMBER 1976

Subject	ARPA Report No.
Literature Review	1, 2, (4), (5)*
Cryostat Construction	1
Tensile Test Procedures	2, 3, 4
Shear Test Procedures	3, 4
Compression Test Procedures	5
Fatigue Test Procedures	6
Tensile Data, Boron-Epoxy	2, 3, 4
Tensile Data, Boron-Aluminum	3, 4
Tensile Data, Graphite-Epoxy	3, 4
Tensile Data, Glass-Epoxy	4
Tensile Data, Kevlar-Epoxy	4
Shear Data, Boron-Epoxy	4
Shear Data, Boron-Aluminum	3, 4
Shear Data, Graphite-Epoxy	4
Shear Data, Glass-Epoxy	4
Compression Data, Boron-Epoxy	5
Compression Data, Boron-Aluminum	5
Compression Data, Graphite-Epoxy	5
Compression Data, Glass-Epoxy	5
Tensile Fatigue Data, Boron-Epoxy	6
Tensile Fatigue Data, Boron-Aluminum	6
Compression Fatigue Data, Boron-Epoxy	6

*Numbers in parentheses refer to report numbers in which reprint versions of the manuscripts occur. Other numbers refer to preprint versions.

Summary: Advanced Composites

A comparison has been made between the wearout rates of $[0/\pm45/0]_s$ boron-epoxy and boron-aluminum composites in low-cycle fatigue at 295 K and 76 K. Using degradation of modulus as the wearout criterion, these preliminary data indicate that cryogenic temperatures have a negligible effect on either tensile or compressive fatigue performance of boron-epoxy. A similar indication was obtained for boron-aluminum in tensile fatigue.

Contents: Advanced Composites

		Page
1.0	Review	3
2.0	Phase III: Fatigue of Composites at Cryogenic Temperatures	3
	2.1 Introduction	3
	2.2 Experimental Procedures	4
	2.3 Results and Discussion	5
	2.4 Conclusions	6
3.0	References	7
Appendix 1:	List of Symbols	8

1.0 Review

Work on this project was initiated by preparing state-of-the-art reviews on the mechanical and thermal properties of structural composites at cryogenic temperatures (1-3). These reviews suggested that boron-aluminum, boron-epoxy, graphite-epoxy, glass-epoxy and Kevlar 49-epoxy composites warranted further study to characterize key static mechanical properties at cryogenic temperatures. This work was undertaken in a previous experimental portion of the ongoing study (9).

Phase I of the experimental work involved development of apparatus and procedures for obtaining the required data. Phase II encompassed the static characterization work. All of the above work has been completed and has been reported in prior Semi-Annual Reports (see summary table at beginning of this section). Phase III addresses the question of the effect that cryogenic temperatures have on the performance of composite materials under fatigue loading and is the subject of this report.

2.0 Phase III: Fatigue of Composites at Cryogenic Temperatures

2.1 Introduction

The ability of composite structures to withstand cyclic stresses at cryogenic temperatures is crucial to their suitability for use in rotating cryogenic machinery. Very little is presently known on this subject. The few studies that have been undertaken indicate that the fatigue life of glass-cloth-epoxy composites is improved by cooling to cryogenic temperatures, although the overall performance remains unimpressive (4). NBS tests of uniaxial glass-epoxy straps indicate that they are fit for service as thermal stand-offs transitioning from 4 K to 295 K in a superconducting generator (5). The only data known to the authors on the fatigue performance of advanced composites at cryogenic temperatures is restricted to low-cycle hydrostatic testing of filament-wound pressure vessles (6-7).

It is unfortunate that there exists no body of theory permitting prediction of crossply composite fatigue performance from systematically determined uniaxial properties, as is the case for the static mechanical properties. Each layup of a particular type composite must therefore be looked upon as a distinct material having a unique S-N curve. To a large extent, this

problem arises due to the differing strain to failure of the fiber and the matrix. Where the strain capability of the fiber exceeds that of the matrix and where the fiber is of low modulus as is the case for glass-epoxy, the matrix will fracture at relatively low stress levels, even when stressed in the uniaxial fiber direction. This leads to increased damping, fiber-matrix debonding and to relatively poor fatigue performance. Conversely, where the fiber has a low strain capability and high modulus, as with graphite or boron, the fatigue performance in the uniaxial fiber direction is excellent, as the matrix remains intact until fiber fracture. Advanced composites tested in the uniaxial longitudinal direction have almost flat S-N curves at room temperature. However, when advanced composites are crossplied, the failure mode in fatigue becomes a complex function of the anisotropy of a particular layup as well as of the constituent properties, composite quality and other variables.

The above considerations made it evident that the conventional S-N curve approach to studying composite fatigue would be unproductive in the present program. An alternative approach was to seek to answer the more general question of the extent to which cryogenic temperatures affect the fatigue performance of state-ofthe-art composites developed for service at and above room temperature. The development of an efficient means of accomplishing this would permit screening of existing composites for further cryogenic study and might well pinpoint some composite types so insensitive to temperature as to allow existing room temperature fatigue data to be used to predict cryogenic fatigue performance. This report describes the attempts made to achieve this goal.

2.2 Experimental Procedures

Composites begin to wear out when the magnitude of a cyclic applied stress exceeds the elastic limit of any component. Wearout is manifested by an increase in damping (increased internal friction) and in a decrease in modulus. The initial objective of the present work was to determine if modulus changes could be used as a criterion for assessing the state of internal damage in a $[0/\pm45/0]_s$ 5.6 mil boron-epoxy specimen subjected to tensile-tensile and to compressive-compressive low-cycle fatigue at 295 K and 76 K, and in a similar boron-aluminum composite in tensile-tensile fatigue.

The selected composites consisted of eight plies of 0.014 cm (5.6 mil) boron in a matrix of PR-286 epoxy or 6061 aluminum. The commercial suppliers reported 52.1% and 48.4% nominal fiber volume fraction for the boron-epoxy and the boron-aluminum, respectively. Loads were always applied along the 0° fiber direction. This layup was selected to provide reasonable fatigue performance due to the 0° plies while providing wearout by virtue of the inability of the ± 45° plies to sustain the loads.

Specimen configurations were similar to those previously used for static tension and compression studies, Table 1. Sufficient thickness to avoid column bending failure in compression was obtained by removing the scrim cloth and bonding two thickness of boron-epoxy to give 16 plies.

The tensile specimen gripping system which had proved adequate for static testing (8) was inadequate for fatigue, as the specimen tended to pull out of the grips. The 0.16 cm (0.06 in) Ti-6Al-4V serrated gripping plates were replaced with 0.64 cm (0.25 in) thick Inconel X-750 plates, and the 0.48 cm (0.19 in) stainless steel pressure plates were increased to 0.64 cm (0.25 in) thickness. Provisions were made for passing a 0.64 cm (0.25 in) diameter bolt through the grip system and specimen. This bolt was torqued to 16 N·m (12 ft·lb), while the twelve pressure screws on the sides of each grip were torqued to 8 N·m (6 ft·lb) each.

The compressive test fixture developed for static use (9) proved adequate

for the fatigue program. However, the titanium pull rods failed under fatigue and were replaced with stainless steel.

As previously in this study, specimen strain was monitored by gages bonded to the specimen surface. Tensile fatigue specimens had both longitudinal and Poisson's gages, while only a longitudinal gage was used for the compression fatigue specimens. Debonding of the gages was not a problem.

Static mechanical properties of the composite were determined in tension and compression at 295 K and 76 K using methods previously described (9). Fatigue studies utilized a closed-loop electrohydraulic machine, specially adapted for cryogenic work. All tests were run at 30 Hz using a sinusoidal wave form. The experimental procedure was similar to that of Williams, et al. (10). A static stress-strain curve was initially obtained, after which a dynamic stress-strain curve was obtained for comparison. To obtain the dynamic stress-strain curve, we first fatigued (R = 0.1) the specimen for 25,000 cycles at a maximum stress (σ_{max}) that was a small fraction of the ultimate strength. Near the end of this fatigue increment a peak-reading DVM was used to measure the maximum strain (ε_{max}). After fatigue, a quasi-static loading gave the modulus (E_f). The maximum fatigue stress was then increased for another 25,000 cycles and another set of measurements. These stress increases were repeated until specimen fracture.

The 295 K tests were run in ambient air. A small temperature increase ($\sim$ 10°C) was observed after the first few steps, remaining relatively stable for the remainder of the step sequence. The 76 K tests were run immersed in liquid nitrogen.

An attempt was made to measure modulus and damping changes by dynamic methods during several tensile fatigue tests of the boron-epoxy and boron-aluminum composite materials at 295 K and at 76 K. Piezoelectric transducers were attached to opposite ends of the specimen-grip system; one was driven with an electrical signal of variable frequency, and the voltage across the other was monitored as the output signal. This allowed the specimen-grip-load train system to be scanned for mechanical resonances over a 0.5-15 kHz range between load steps.

2.3 Results and Discussion

Static mechanical properties are given in Table 2. Table 3 compares these data with values of tensile strength and moduli predicted by the rule of mixtures, using uniaxial and ± 45° data obtained earlier in this program from the same type composites. The boron-epoxy properties follow the rule of mixtures very well in both strength and modulus. Boron-aluminum follows the rule reasonably well in strength. However, the measured modulus substantially exceeds the predicted value, reflecting the non-linearity between stress and strain in crossplied boron-aluminum composite materials.

Results of the dynamic stress-strain, low-cycle fatigue program appear in Table 4 and in summary in Figs. 1-3. In each of these Figures, plot (a) reflects the strain determined dynamically during a given run, while plot (b) reflects quasi-static strain determined from the slope of a stress-strain curve obtained between each fatigue step. If the dynamic tensile modulus remains unchanged throughout a test, a plot of $\sigma_{max}/\sigma tu$ vs. $\varepsilon_{max}/\varepsilon tu$ should have a slope of 1.0 for a composite with a linear stress-strain curve to fracture. (See Appendix 1 for definition of symbols.) The same is true for the dynamic compressive modulus. Likewise, a plot of E_f/E_o vs. $\varepsilon_{max}/\varepsilon tu$ should have a constant value of 1.0 if the static modulus is unchanging. The same is true for the static compressive modulus. Therefore, deviations from these values were considered as indicators of the extent to which damage was being incurred during the fatigue program.

Fig. 1 (a) indicates that the dynamic tensile modulus of the $[0/\pm45/0]_s$

boron-epoxy was not affected by cyclic loading up to about 76% of its static ultimate strength at either 295 K or 76 K. However, Fig. 1 (b) indicates that a small decrease in static tensile modulus did occur at both temperatures.

The compression fatigue data of Fig. 2 show more scatter than does the tensile data. Nevertheless, Fig. 2 (a) indicates that the dynamic compression modulus is relatively unaffected by cyclic loading below about 60% of its ultimate compressive strength. The data suggest that a modulus reduction may occur at higher stress levels. Test temperature appears irrelevant. Fig. 2 (b) indicates that the static compressive modulus does decline with cyclic loading; in some specimens, the decline began at very low stress levels. Again, no temperature dependence of the modulus change was evident.

Most of the compressive data were obtained by cycling at 30 Hz with 25,000 cycles per increment of stress. As reported on Table 5, several runs were also made at 15 Hz and at 10,000 cycles per increment without a significant difference in result.

The limited amount of data obtained on $[0/\pm45/0]_s$ boron-aluminum during dynamic stress-strain, low-cycle fatigue testing in tension is reported on Table 4 and summarized in Fig. 3. The displacement of the data above the line of slope 1.0 in Fig. 3 (a) does not reflect cyclic stiffening. Rather, it reflects an increase in the slope of the initial part of the stress-strain curve due to the initial cycle to the preload limit indicated on the Figure for the purpose of determining the static modulus. During the cyclic test, the modulus follows the steeper initial slope up to the preload limit, after which it continues at a lesser slope of approximately 1.0, causing the observed displacement of the plotted data. This is an illustration of the non-linearity characteristic of cross-plied boron-aluminum composites. Fig. 3 (a) therefore suggests that the cyclic tensile loading up to about 82% of the static ultimate strength had no significant effect on the dynamic tensile modulus. Fig. 3 (b) indicates that the tensile modulus was likewise unaffected. The temperature of testing appears irrelevant.

Attempts to measure modulus and damping changes by resonance methods during the dynamic stress-strain, low-cycle fatigue program produced inconsistent results. Several maxima of the amplitude of the output signal voltage, each corresponding to a mechanical resonance in the specimen-grip-load train system were observed in the 5-15 KHz range. In most of the tests, the observed frequencies and amplitudes did not exhibit systematic behavior as a function of load step number (increasing stress increment). The boron-aluminum specimen tested at 76 K (specimen 1-3) did exhibit systematic behavior. Fig. 4 shows the frequency (x axis) and amplitudes (y axis) of several resonances after the load step indicated by the numeral at the data point. These load steps correspond to the increasing stress levels for specimen 1-3 listed on Table 4. The systematic decrease in resonance amplitude at those frequencies indicates that damping in this specimen was increased significantly by stress cycling, while the absence of large systematic changes in resonance frequencies indicates that the modulus change was not large, in agreement with Fig. 3 (b). The failure to observe similar systematic behavior in test at 295 K indicates that the damping in the specimens before fatiguing, the sensitivity of the apparatus, or both change significantly on cooling to 76 K.

2.4 Conclusions

A dynamic stress-strain, low-cycle fatigue method has shown itself capable of detecting composite wearout as revealed by modulus changes in a $[0/\pm45/0]_s$ boron-epoxy specimen. However, the method was found to lack the sensitivity required for purposes of screening composite systems for use at cryogenic temperatures. The data suggest that static and dynamic moduli differ, the static modulus providing the most sensitivity to composite wearout. It is

probable that the method would produce more useful results with a composite layup less forgiving in fatigue, i.e., a [0/±45] or a [± 45] orientation.

The wearout rate in boron-epoxy appears to be greater in compression fatigue than in tension fatigue both at 295 K and 76 K, although the substantially larger scatter in data in compression tends to obscure this difference.

The wearout rate as measured by modulus decrease in the $[0/\pm45/0]_s$ boron-epoxy composite used in this study was the same at 76 K as at 295 K. This suggests that the room temperature fatigue data on boron-epoxy composites might serve as a criteria for cryogenic service. However, these preliminary indications must be complimented by additional test work.

Results of the study indicate that $[0/\pm45/0]_s$ boron-aluminum performs well in low-cycle tensile fatigue. No difference in performance was detected between tests conducted at 295 K and at 76 K.

Attempts to use an in-situ dynamic resonance method for evaluating composite wearout was for the most part unsuccessful. However, partial success with a boron-aluminum specimen fatigued in tension at 76 K suggests that the method might prove very useful when apparatus and procedures are perfected.

3.0 References

1. Kasen, M. B., "Properties of Filamentary-Reinforced Composites at Cryogenic Temperatures," Composite Reliability, ASTM STP 580, American Society for Testing and Materials, 1975, pp. 586-611.

2. Kasen, M. B., "Mechanical and Thermal Properties of Filamentary-Reinforced Structural Composites at Cryogenic Temperatures. I: Glass-Reinforced Composites," Cryogenics, 15 (6), 1975, pp. 327-349.

3. Kasen, M. B., "Mechanical and Thermal Properties of Filamentary-Reinforced Structural Composites at Cryogenic Temperatures. II: Advanced Composites," Cryogenics, 15 (12), 1975, pp. 701-722.

4. Brink, N. O., "Determination of the Performance of Plastic Laminates under Cryogenic Temperatures," ASD-TDR-62-794, Air Force Systems Command, WPAFB, Ohio (August 1962) AD 288944.

5. Tobler, R. L. and Read, D. T., "Fatigue Resistance of a Uniaxial S-Glass/Epoxy Composite at Room and Liquid Helium Temperatures," J. Compos. Mater. 10, 32 (1976).

6. Hanson, M. P., "Tensile and Cyclic Fatigue Properties of Graphite Filament-Wound Pressure Vessels at Ambient and Cryogenic Temperatures," NASA TN D-5354, National Aeronautics and Space Administration, Lewis Research Center, Cleveland, Ohio (1969) (N69-31300) (identical to SAMPE 15, 249).

7. Alfring, R. J., Morris, E. E., Landes, R. E., "Cycle-Testing of Boron Filament-Wound Tanks," NASA CR-72899, National Aeronautics and Space Administration, Lewis Research Center A(1971) (N71-38023).

8. Kasen, M. B. and Schramm, R. E., "Advanced Composites," in Semi-Annual Technical Reports on Materials Research in Support of Superconducting Machinery - II; R. P. Reed, A. F. Clark, E. C. van Reuth (Eds.); Nat. Bur. Stds., Boulder, CO; October 1974; ADA004586.

9. Schramm, R. E. and Kasen, M. B., "Advanced Composites," in Semi-Annual Technical Reports on Materials Research in Support of Superconducting Machinery - V; R. P. Reed, A. F. Clark, E. C. van Reuth (Eds.); Nat. Bur. Stds., Boulder, CO; April 1976.

10. Williams, R. S., Reifsnider, K. L., Stinchcomb, W. W., and Turgay, H. T., "The Effect of Frequency and Strain Amplitude on the Fatigue Damage of Boron/Epoxy Fiber-Reinforced Composite Materials," AFOSR-TR-75-1387, AFOSR, Arlington, VA, April 1975, ADA 015479.

APPENDIX 1: LIST OF SYMBOLS

E Elastic modulus measured from quasi-static loading.

E_o Elastic modulus measured prior to fatigue.

E_f Elastic modulus measured after fatigue.

R Ratio of minimum to maximum stress during fatigue cycle.

ε^{cu} Maximum strain measured in quasi-static loading (compression).

ε^{tu} Maximum strain measured in quasi-static loading (tension).

ε_{max} Maximum strain measured during fatigue.

σ^{cu} Maximum stress measured in quasi-static loading (compression).

σ^{tu} Maximum stress measured in quasi-static loading (tension).

σ_{max} Maximum stress measured during fatigue.

ν Poisson's ratio measured in quasi-static loading.

ν_o Poisson's ratio measured prior to fatigue.

ν_f Poisson's ratio measured after fatigue.

Table 1. Nominal specimen dimensions.

Specimen	Length cm	Length in	Width cm	Width in	Thickness cm	Thickness in	Gage Length cm	Gage Length in
Tension	25.4	10.0	2.54	1.0	0.142	0.056	15.2	6.0
Compression	10.2	4.0	0.406	0.160	0.279	0.110	1.3	0.5

Table 2. Static mechanical properties

Test Temp. (K)	E 10^9 N/m^2	E 10^6 psi	ν	σ^u 10^8 N/m^2	σ^u 10^3 psi	ε^u%
$[0/\pm45/0]_s$ Boron-Epoxy						
			Tension			
295	120	17.4	0.755	7.62	110	0.65
295	119	17.2	0.692	7.60	110	0.68*
295	122	17.7	0.806	8.10	117	0.71
76	117	17.0	0.551	8.56	124	0.70
76	133	19.3	0.540	8.61	125	0.70
4	134	19.4	0.580	**	**	**
4	133	19.3	0.561	8.87	129	0.71
			Compression			
295	102	14.8		12.4	180	1.20
295	101	14.7		9.7	141	1.08
$[0/\pm45/0]_s$ Boron-Aluminum						
			Tension			
295	178	25.8	0.295	7.74	112	0.54*
295	179	26.0	0.287	8.53	124	0.60*
295	180	26.0	0.305	7.61	110	0.58
295	159	23.0	0.415	6.34	92	0.51
76	163	23.6	0.350	8.14	118	0.68
4	166	24.0	0.314	8.47	123	0.72*

* Grip Fracture
** No fracture

Underlined values used in calculating data on Figs. 1-3 and Table 5.

Table 3. Comparison between measured properties of $[0/\pm45/0]_s$ boron-epoxy and boron-aluminum and properties predicted by the rule of mixtures.

Material	295 K Predicted σ^{tu}	295 K Measured σ^{tu}	76 K Predicted σ^{tu}	76 K Measured σ^{tu}	295 K Predicted E^t	295 K Measured E^t	76 K Predicted E^t	76 K Measured E^t
Boron-epoxy	128	110-117	130	124-125	17.4	17.4-17.7	17.8	17.0-19.3
Boron-aluminum	119	92-124	146	118	16.3	23.0-26.0	16.3	23.6

$\sigma^{tu} = 10^3$ psi, $E^t = 10^6$ psi

Table 4. Results or dynamic σ-ε tests.

	Fatigue Cycles 10^3	Dynamic σ_{max} $10^8 N/m^2$	Dynamic ε_{max} %	Static E $10^9 N/m^2$	Static ν	$\frac{\sigma_{max}}{\sigma^{tu}}$	$\frac{\varepsilon_{max}}{\varepsilon^{tu}}$	$\frac{E_f}{E_o}$
Boron-Epoxy, specimen 1-8,	0	--	--	130	0.578	--	--	1.00
76 K, $\sigma^{tu} = 8.61 \times 10^8$	25	0.50	0.05	132	0.573	0.06	0.07	1.02
N/m^2, $\varepsilon^{tu} = 0.70\%$, 30 Hz,	50	1.01	0.09	132	0.553	0.12	0.13	1.02
Tension	75	1.51	0.13	132	0.563	0.18	0.19	1.02
	100	2.02	0.17	132	0.568	0.23	0.24	1.02
	125	2.53	0.21	128	0.563	0.29	0.30	0.98
	150	3.03	0.24	126	0.563	0.35	0.34	0.97
	175	3.53	0.29	126	0.580	0.41	0.41	0.97
	200	4.04	0.33	125	0.597	0.47	0.47	0.96
	225	4.54	0.38	124	0.589	0.53	0.54	0.95
	250	5.05	0.41	123	0.593	0.59	0.59	0.95
	275	5.56	0.46	122	0.587	0.65	0.66	0.94
	300	6.06	0.50	120	0.608	0.70	0.71	0.92
	325	6.56	0.52	132	0.641	0.76	0.74	1.02
Boron-Epoxy, specimen 1-3,	0	--	--	117	0.703	--	--	1.00
295 K, $\sigma^{tu} = 8.10 \times 10^8$	25	0.50	0.05	116	0.712	0.06	0.07	0.99
N/m^2, $\varepsilon^{tu} = 0.71\%$, 30 Hz,	50	1.00	0.09	115	0.698	0.12	0.13	0.98
Tension	75	1.50	0.13	115	0.693	0.19	0.18	0.98
	100	2.51	0.23	117	0.715	0.31	0.32	1.00
	125	3.51	0.31	113	0.717	0.43	0.44	0.97
	150	4.01	0.36	113	0.713	0.50	0.51	0.97
	175	4.51	0.40	113	0.728	0.56	0.56	0.97
	200	5.01	--	113	0.740	0.62	--	0.97
	225	5.51	0.50	110	0.739	0.68	0.70	0.94
	250	6.01	0.55	--	--	0.74	0.77	--
Boron-Epoxy, specimen F-7,	0	--	--	137	--	--	--	1.00
76 K, $\sigma^{cu} = 12.0 \times 10^8$	25	1.009	0.07	132	--	0.08	0.08	0.96
N/m^2, $\varepsilon^{cu} = 0.93\%$, 30 Hz	50	2.017	0.14	140	--	0.17	0.15	1.02
Compression	75	3.026	0.22	137	--	0.25	0.24	1.00
	100	4.035	0.28	144	--	0.34	0.30	1.05
	125	5.043	0.34	148	--	0.42	0.37	1.08
	150	6.052	0.42	140	--	0.50	0.45	1.02
	175	7.061	0.54	133	--	0.59	0.68	0.97
	200	8.069	0.75	113	--	0.67	0.81	0.82
Boron-Epoxy, specimen F-18,	0	--	--	156	--	--	--	1.00
76 K, $\sigma^{cu} = 12.0 \times 10^8$	25	1.02	0.06	156	--	0.09	0.06	1.00
N/m^2, $\varepsilon^{cu} = 0.93\%$, 30 Hz,	50	2.05	0.12	148	--	0.17	0.13	0.95
Compression	75	3.07	0.20	144	--	0.26	0.21	0.93
	100	4.10	0.28	140	--	0.34	0.30	0.90
	125	5.12	0.35	139	--	0.43	0.38	0.89
	150	6.15	0.44	139	--	0.51	0.47	0.89
	175	7.17	0.53	133	--	0.60	0.57	0.85
	185.07	8.19	--	--	--	--	--	--

Table 4. continued

	Fatigue Cycles 10^3	Dynamic σ_{max} $10^8 N/m^2$	Dynamic ε_{max} %	Static E $10^9 N/m^2$	Static ν	$\frac{\sigma_{max}}{\sigma_{tu}}$	$\frac{\varepsilon_{max}}{\varepsilon_{tu}}$	$\frac{E_f}{E_o}$
Boron-Epoxy, specimen F-15,	0	--	--	152	--	--	--	1.00
76 K, σ^{cu} = 12.0 x 10^8	10	0.99	0.07	150	--	0.08	0.08	0.99
N/m^2, ε^{cu} = 0.93%, 30 Hz,	20	1.97	0.14	151	--	0.16	0.15	0.99
Compression	30	2.96	0.21	143	--	0.25	0.23	0.94
	40	3.94	0.30	130	--	0.33	0.32	0.85
	50	4.93	0.37	136	--	0.41	0.39	0.89
	60	5.91	0.46	132	--	0.49	0.50	0.87
Boron-Epoxy, specimen F-16,	25	1.02	0.08	--	--	0.09	0.08	--
76 K, σ^{cu} = 12.0 x 10^8	50	2.03	0.15	147	--	0.17	0.16	1.00
N/m^2, ε^{cu} = 0.93%, 15 Hz,	75	3.05	0.24	129	--	0.25	0.25	0.88
Compression	100	4.06	0.31	131	--	0.34	0.34	0.89
	125	5.07	0.39	134	--	0.42	0.42	0.91
	150	6.09	0.48	129	--	0.51	0.52	0.88
	175	7.10	0.57	125	--	0.59	0.61	0.85
	200	8.12	0.64	157	--	0.68	0.69	1.07
Boron-Epoxy, specimen F-6,	0	--	--	134	--	--	--	1.00
295 K, σ^{cu} = 12.4 x 10^8	25	1.015	0.11	145	--	0.08	0.09	1.08
N/m^2, ε^{cu} = 1.20%, 30 Hz,	50	2.029	0.20	135	--	0.16	0.17	1.01
Compression	75	3.044	0.24	133	--	0.25	0.20	0.99
	100	4.058	0.33	128	--	0.33	0.28	0.96
	125	5.091	0.40	128	--	0.41	0.33	0.96
	150	6.088	0.49	122	--	0.49	0.41	0.91
	175	7.102	0.57	121	--	0.57	0.48	0.96
	200	8.117	0.73	106	--	0.65	0.61	0.79
Boron-Epoxy, specimen F-10,	0	--	--	88	--	--	--	1.00
295 K, σ^{cu} = 12.4 x 10^8	25	0.99	0.12	93	--	0.08	0.10	1.05
N/m^2, ε^{cu} = 1.20%, 30 Hz,	50	1.99	0.23	91	--	0.16	0.19	1.04
Compression	75	2.98	0.31	103	--	0.24	0.26	1.16
	100	3.97	0.41	104	--	0.32	0.34	1.17
	125	4.96	0.51	99	--	0.40	0.43	1.12
	150	5.95	0.63	94	--	0.48	0.53	1.07
	175	**6.95**	**0.75**	**87**	**--**	**0.56**	**0.62**	**0.99**
	186.18	7.94	0.95	--	--	0.64	0.79	--
Boron-Epoxy, specimen F-12,	0	--	--	107	--	--	--	1.00
295 K, σ^{cu} = 12.4 x 10^8	10	1.00	0.08	104	--	0.08	0.07	1.02
N/m^2, ε^{cu} = 1.20%, 30 Hz,	20	1.99	0.20	107	--	0.16	0.16	0.99
Compression	30	2.99	0.31	112	--	0.24	0.26	1.04
	40	3.98	0.38	111	--	0.32	0.32	1.03
	50	4.98	0.45	109	--	0.40	0.37	1.01
	60	5.97	0.55	107	--	0.48	0.46	1.00
	70	6.97	0.68	106	--	0.56	0.56	0.98
	80	7.96	0.79	104	--	0.64	0.66	0.97
	90	8.91	0.88	103	--	0.72	0.73	0.96

Table 4. continued

	Fatigue Cycles 10^3	Dynamic σ_{max} $10^8 N/m^2$	Dynamic ε_{max} %	Static E $10^9 N/m^2$	Static ν	$\frac{\sigma_{max}}{\sigma^{tu}}$	$\frac{\varepsilon_{max}}{\varepsilon^{tu}}$	$\frac{E_f}{E_o}$
Boron-Epoxy, Specimen E-11,	0	--	--	132	--	--	--	1.00
295 K, σ^{cu} 12.4 x 10^8	25	1.00	0.09	123	--	0.08	0.07	0.94
N/m^2, ε^{cu} = 1.2%, 15 Hz	50	2.00	0.16	119	--	0.16	0.14	0.91
Compression	75	3.00	0.26	116	--	0.24	0.21	0.88
	100	4.00	0.33	118	--	0.32	0.27	0.90
	125	5.01	0.42	116	--	0.40	0.35	0.88
Boron-Aluminum, specimen	0	--	--	199	--	--	--	1.00
1-3, 76 K, σ^{tu} = 7.61	25	0.56	0.03	197	--	0.07	0.06	0.99
x 10^8 N/m^2, ε^{tu} = 0.58%,	50	1.13	0.07	193	--	0.15	0.11	0.97
30 Hz, Tension	75	1.69	0.10	200	--	0.22	0.18	1.01
	100	2.82	0.17	199	--	0.37	0.30	1.00
	125	3.95	0.25	200	--	0.52	0.44	1.01
	150	5.08	0.33	196	--	0.67	0.58	0.98
	175	6.21	0.42	189	--	0.82	0.72	0.95
Boron-Aluminum, specimen	0	--	--	187	--	--	--	1.00
1-6, 295 K, σ^{tu} = 8.14	25	0.56	0.03	189	--	0.07	0.05	1.01
x 10^8 N/m^2, ε^{tu} = 0.68%,	50	1.11	0.07	188	--	0.14	0.11	1.01
30 Hz, Tension	75	1.67	0.10	188	--	0.21	0.15	1.01
	100	2.79	0.18	186	--	0.34	0.27	0.99
	125	3.90	0.26	184	--	0.48	0.38	0.98
	150	4.46	0.30	183	--	0.55	0.44	0.98
	175	5.01	0.34	185	--	0.62	0.50	0.99

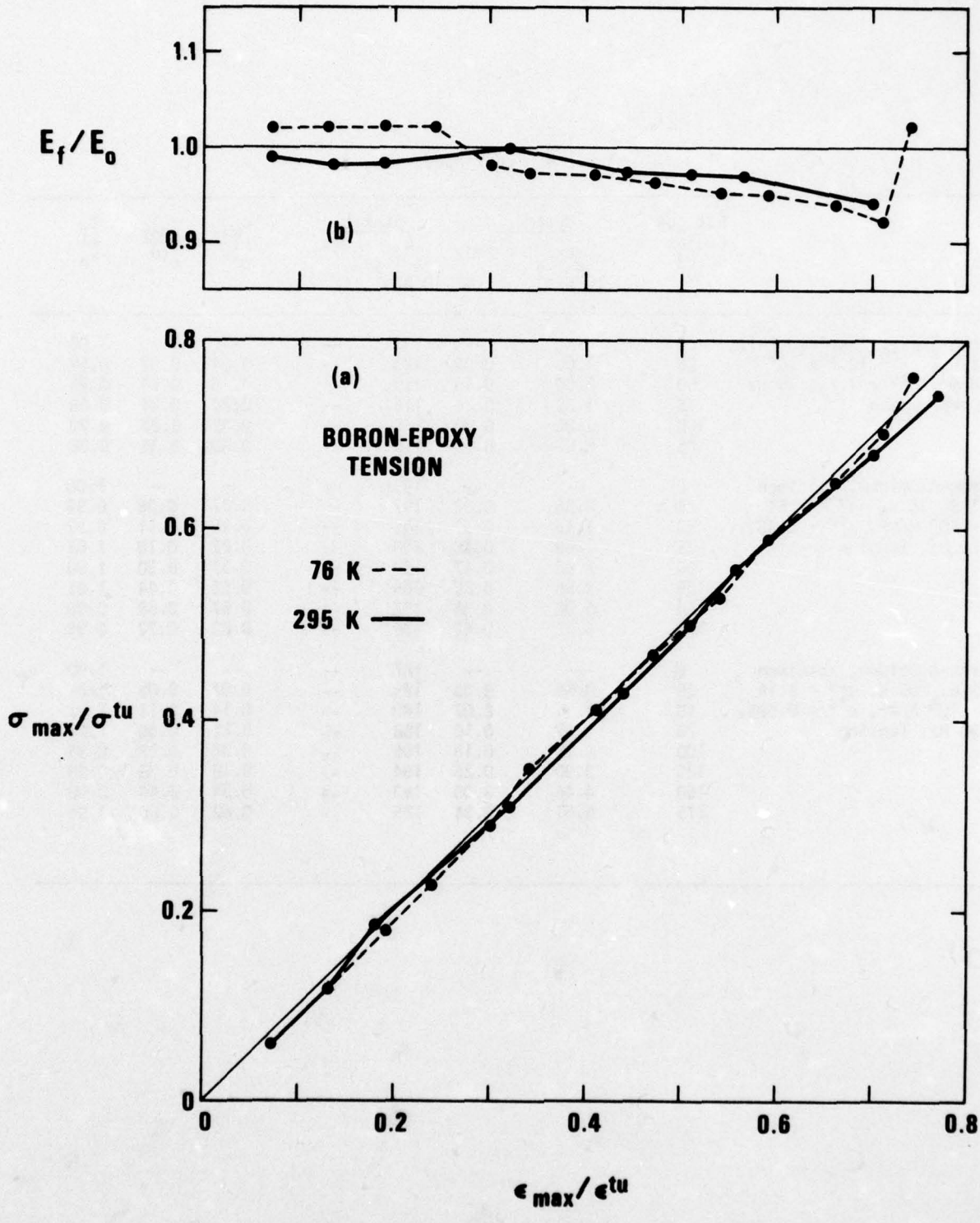


Fig. 1. Relative stress and relative modulus as a function of relative strain for boron-epoxy during tensile fatigue. Each point represents an increment of 25,000 cycles.

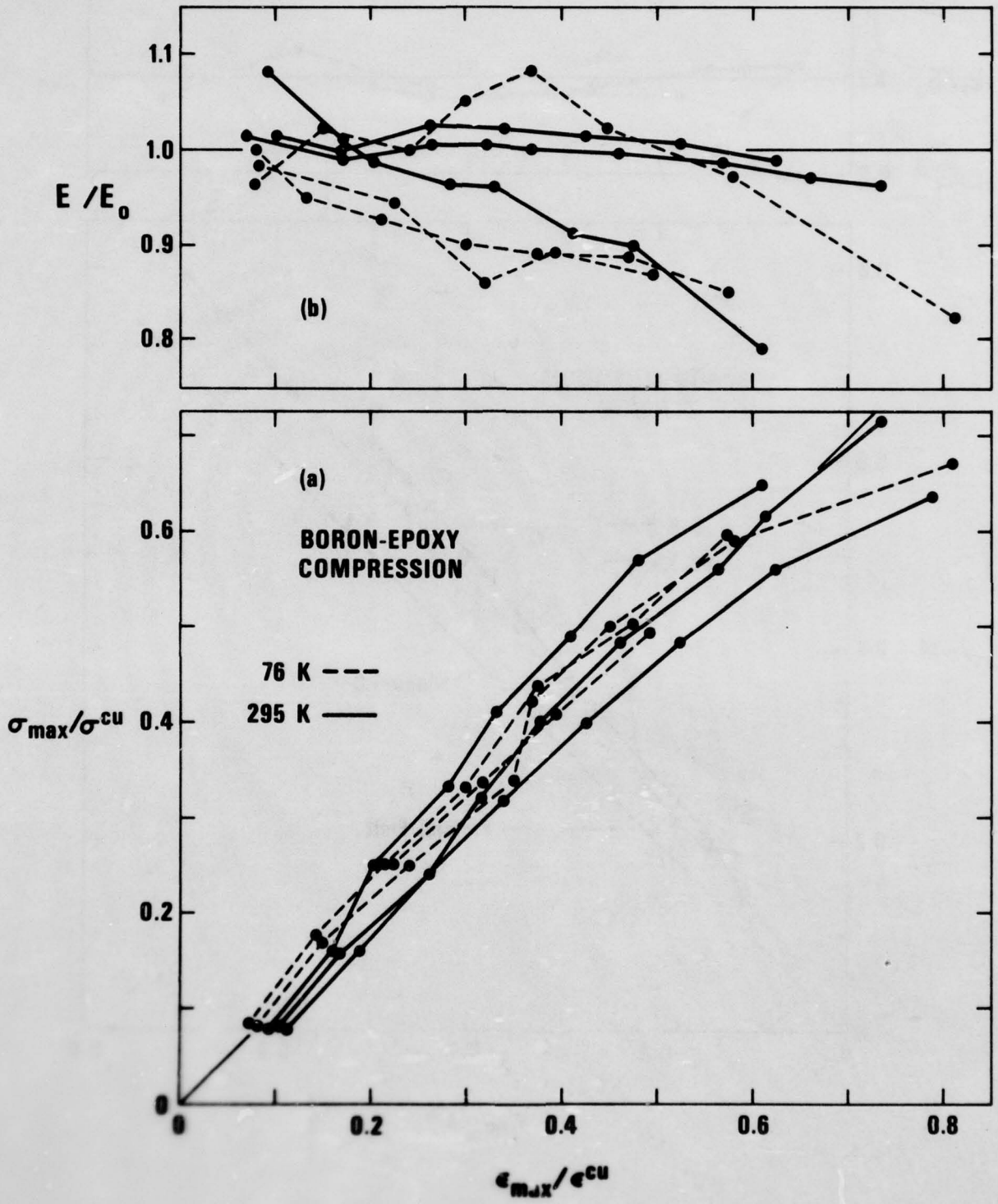


Fig. 2. Relative stress and relative modulus as a function of relative strain for boron-epoxy during compressive fatigue. Each point represents an increment of 25,000 cycles.

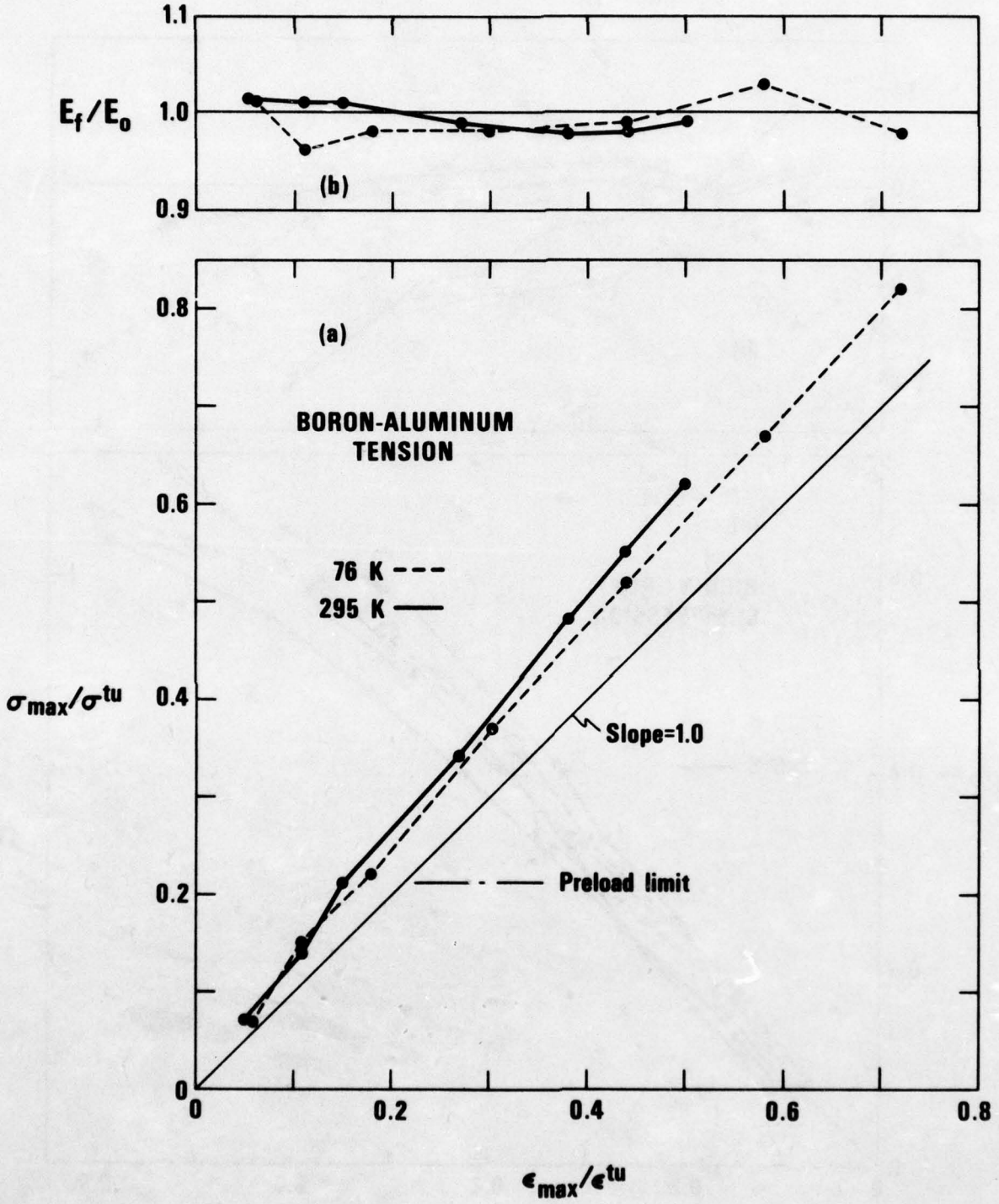


Fig. 3. Relative stress and relative modulus as a function of relative strain for boron-aluminum during tensile fatigue. Each point represents an increment of 25,000 cycles.

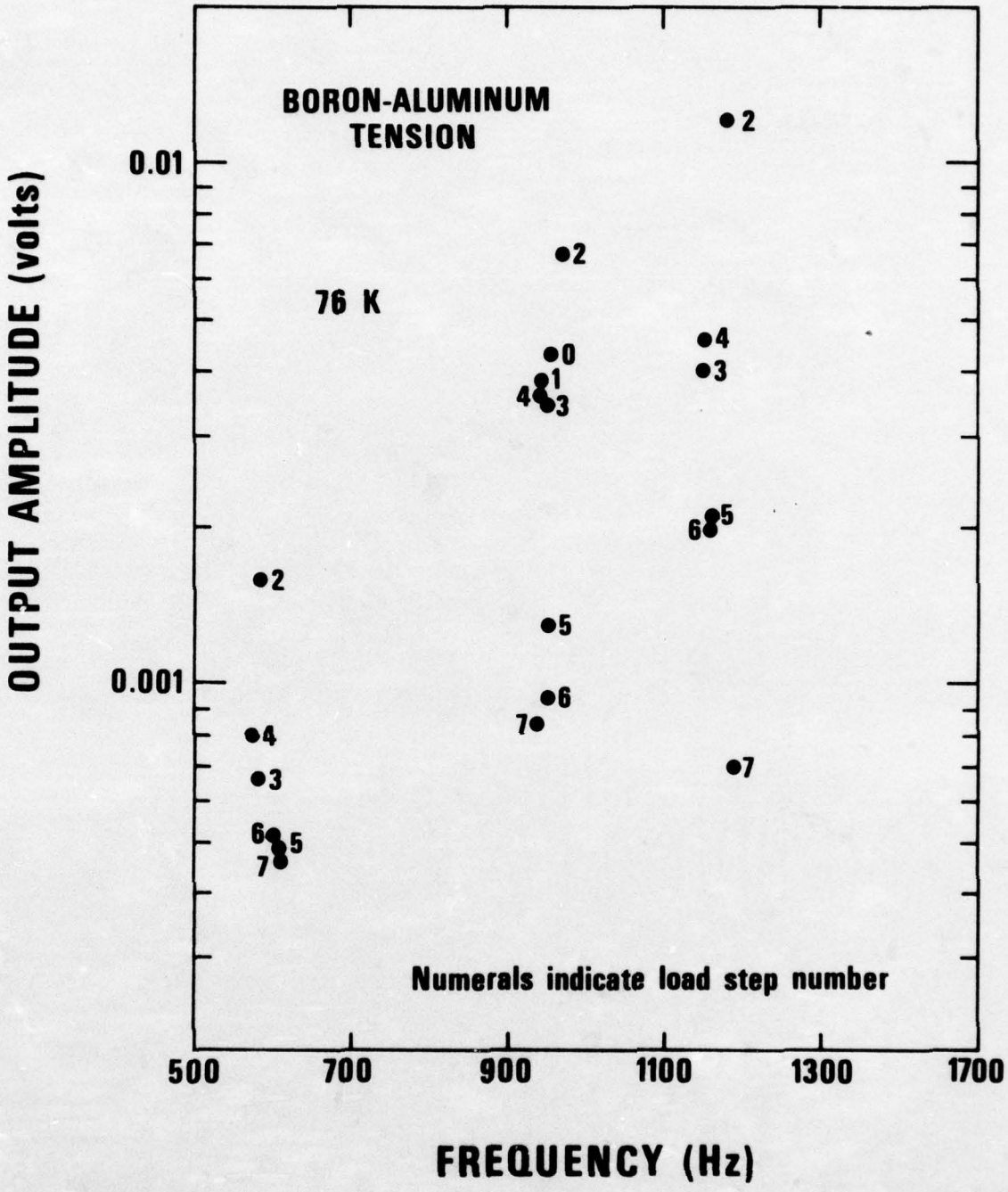


Fig. 4. Frequency and amplitude of three maxima in piezo electric transducer output after the indicated fatigue-stress steps.

PRECEDING PAGE BLANK-NOT FILMED

SEMI-ANNUAL REPORT ON MATERIALS RESEARCH IN SUPPORT OF SUPERCONDUCTING MACHINERY

ELASTIC PROPERTIES

H. M. Ledbetter and D. T. Read

Cryogenics Division
Institute for Basic Standards
National Bureau of Standards
Boulder, Colorado 80302

October 1976

NBS ELASTIC-PROPERTIES STUDIES DURING ARPA-SPONSORED PROGRAM, SEPTEMBER 1973 TO SEPTEMBER 1976.

	Material	ARPA Report No.	Experimental Method(s)
1.	Aluminum alloy 1100	2,(5)*	P**
2.	" " 2019	5	P
3.	" " 2215	5	P
4.	" " 5083	2,(5)	P
5.	" " 7005	2,(5)	P
6.	" " 7075	2,(5)	P
7.	Copper	4	R,P
8.	" -10Ni	4	R,P
9.	" -30Ni	4	R,P
10.	" -0.3Cd-0.3Cr(PD135)	4,6	R,P
11.	Inconel 600	1,(4)	P
12.	" 718	3,(5)	P
13.	" X750	1,(4)	P
14.	Iron-36Ni (Invar)	4	R,P
15.	Maraging steel	6	P
16.	Nitronic 40(21-6-9)	6	R,P
17.	Stainless steel A286	2,(4)	P
18.	" " 304	2,(4)	P
19.	" " 310	2,(4)	P
20.	" " 316	2,(4)	P
21.	Titanium-6Al-4V	1,(2)	P
22.	" -5Al-2.5Sn	1,(2)	P
	Composites:		
23.	Boron/aluminum	6	R
24.	Fiberglass/epoxy	3,(5)	R
25.	NbTi/Cu	6	P,R
26.	NbTi/Cu/epoxy	3,(5)	R

* Numbers in parentheses refer to report numbers in which reprint versions of the manuscripts occur. Other numbers refer to preprint versions.

**P = pulse, R = resonance.

ELASTIC PROPERTIES OF ENGINEERING MATERIALS AT CRYOGENIC TEMPERATURES

H. M. Ledbetter

Six manuscripts on the elastic properties of engineering materials are included in the present report:

1. "Low temperature elastic properties of a precipitation-hardened copper alloy" by H. M. Ledbetter. This manuscript on the cryogenic elastic properties of copper alloy PD 135 complements the manuscript in the fourth semi-annual report that described the anomalous elastic properties of this alloy at room temperature.

2. "Orthorhombic elastic constants of an NbTi/Cu composite superconductor" by H. M. Ledbetter and D. T. Read. This manuscript describes the elastic symmetry of a material used in cryogenic magnets.

3. "Temperature dependence of the elastic constants of an NbTi/Cu superconducting composite" by D. T. Read and H. M. Ledbetter. This manuscript complements item (2), giving the low-temperature elastic constants.

4. "Anomalous low-temperature elastic behavior of a nitrogen-strengthened chromium-manganese stainless steel" by H. M. Ledbetter. This is the first study of the low-temperature elastic properties of this steel. It behaves anomalously because of a paramagnetic-antiferromagnetic transition.

5. "Low-temperature elastic properties of a 300-grade maraging steel" by H. M. Ledbetter.

6. "Elastic properties of a boron-aluminum composite at low temperatures" by D. T. Read and H. M. Ledbetter.

Since this is the final report of the three-year ARPA-sponsored program on materials research for superconducting machinery, it is appropriate to review briefly the entire elastic-properties effort. The table on the previous page summarizes the NBS experimental studies on low-temperature elastic properties. Twenty-six materials were studied in the temperature region 4-300 K: six aluminum alloys; four copper alloys; three inconels; an iron-nickel alloy; a maraging steel; a nitrogen-strengthened stainless steel; two titanium alloys; and four composites: boron/aluminum, fiberglass/epoxy, NbTi/Cu, and NbTi/Cu/epoxy. Some of the special properties of these materials include: precipitation hardening, low thermal expansion, high strength-density ratio, and high strength-thermal conductivity.

NBS PUBLICATIONS ON ELASTIC PROPERTIES, RESULTING FROM ARPA-SPONSORED PROGRAM, SEPTEMBER 1973 TO SEPTEMBER 1976

1. E. R. Naimon, H. M. Ledbetter, and W. F. Weston, Low-temperature elastic properties of four wrought and annealed aluminum alloys, J. Mater. Sci. 10 (1975) 1309-1316.

2. D. T. Read and H. M. Ledbetter, Temperature dependencies of the elastic constants of precipitation-hardened aluminum alloys 2014 and 2219, submitted for publication.

3. H. M. Ledbetter and W. F. Weston, Low-temperature elastic properties of some copper-nickel alloys, Ultrasonics Symposium Proc., Cat. No. 75 Ch 8 994-4SU (IEEE, New York, 1975) 623-627.

4. H. M. Ledbetter, Anomalous elastic properties of a precipitation-hardened copper alloy, submitted for publication.

5. H. M. Ledbetter, Low-temperature elastic properties of a precipitation-hardened copper alloy, submitted for publication.

6. W. F. Weston, H. M. Ledbetter and E. R. Naimon, Dynamic low-temperature elastic properties of two austenitic nickel-chromium-iron alloys, Mater. Sci. Engg. 20 (1975) 185-194.

7. W. F. Weston and H. M. Ledbetter, Low-temperature elastic properties of a nickel-chromium-iron-molybdenum alloy, Mater. Sci. Engg. 20 (1975) 287-290.

8. H. M. Ledbetter, E. R. Naimon, and W. F. Weston, Low-temperature elastic properties of invar, Proc. ICMC, Kingston, Ontario, July 1975 (Plenum, New York, forthcoming).

9. H. M. Ledbetter and D. T. Read, Low-temperature elastic properties of a 300-grade maraging steel, submitted for publication.

10. H. M. Ledbetter and D. T. Read, Low-temperature elastic properties of a nitrogen-strengthened chromium-manganese stainless steel, submitted for publication.

11. H. M. Ledbetter, W. F. Weston, and E. R. Naimon, Low-temperature elastic properties of four austenitic stainless steels, J. Appl. Phys. 46 (1975) 185-194.

12. E. R. Naimon, W. F. Weston, and H. M. Ledbetter, Elastic properties of two titanium alloys at low temperatures, Cryogenics 14 (1974) 246-249.

13. D. T. Read and H. M. Ledbetter, Low-temperature elastic properties of a boron/aluminum composite, submitted for publication.

14. W. F. Weston, Elastic constants of a superconducting-coil composite material, J. Appl Phys. 46 (1975) 4458-4465.

15. H. M. Ledbetter and D. T. Read, Orthorhombic elastic constants of an NbTi/Cu composite superconductor, submitted for publication.

16. D. T. Read and H. M. Ledbetter, Low-temperature elastic constants of an NbTi/Cu composite superconductor, submitted for publication.

ORTHORHOMBIC ELASTIC CONSTANTS OF AN NbTi/Cu COMPOSITE SUPERCONDUCTOR*

H. M. Ledbetter and D. T. Read**

Cryogenics Division
Institute for Basic Standards
National Bureau of Standards
Boulder, Colorado 80302

ABSTRACT

Elastic properties of a niobium-titanium-filament, copper-matrix composite superconductor were studied experimentally. Ultrasonic pulse and resonance measurements showed the material has orthorhombic symmetry and, therefore, nine independent elastic constants. With respect to copper: C_{11}, C_{22}, and C_{33} are about seven percent lower; C_{44} C_{55}, and C_{66} are about fifteen percent lower; the off-diagonal elastic constants are unchanged; and the bulk modulus is about five percent lower. Deviations from isotropic elastic behavior are small.

Key words: Bulk modulus; composite; compressibility; copper; elastic constants; niobium-titanium; Poisson's ratio; pulse method; resonance method; shear modulus; sound velocity; superconductor; Young's modulus.

* Contribution of NBS, not subject to copyright.

**NRC-NBS Postdoctoral Research Associate, 1975-6.

ORTHORHOMBIC ELASTIC CONSTANTS OF AN NbTi/Cu COMPOSITE SUPERCONDUCTOR*

H. M. Ledbetter and D. T. Read**

Cryogenics Division
Institute for Basic Standards
National Bureau of Standards
Boulder, Colorado 80302

I. INTRODUCTION

The purpose of this paper is to report an experimental study of the elastic properties of a composite material, emphasizing elastic symmetry and the value of applying familiar single-crystal methods to composites. This composite contains unidirectional niobium-titanium (NbTi) filaments in a copper (Cu) matrix. It is designed as a superconductor for magnets. Manufacture and morphology suggest that the filament direction is an elastic symmetry axis. Thus, the macroscopic elastic symmetry is orthorhombic, tetragonal, hexagonal, or cubic. Oblique axis systems--triclinic, monoclinic, trigonal--are excluded.

The present study shows that this composite is orthorhombic. But, deviations from isotropy are small. Thus, it can be referred to other co-ordinate axes--for example, hexagonal-- without introducing large errors. Advantages of this simplification are discussed below. Nevertheless, a complete set of nine orthorhombic elastic constants was determined.

Experimentally, two dynamic methods were used: pulse and resonance. Most measurements were made by a pulse method; eighteen ultrasonic wave velocities were measured along the orthorhombic $\langle 100 \rangle$ and $\langle 110 \rangle$ directions. Resonance experiments were done to achieve two ancillary objectives. First, to detect dispersion, the variation of sound-velocity with frequency. Second, to confirm the off-diagonal elastic constants.

It is emphasized that the elastic constants reported here may differ from those of apparently identical composites for reasons discussed below in sections IIIC and VF.

II. WAVE MOTION IN ORTHORHOMBIC MEDIA

Usual crystallographic notations for vectors and elastic constants are used in this report, although all components of the studied composite material are polycrystalline. Symmetries discussed here are strictly macroscopic. The filament direction of the composite is designated [001], and the principal directions perpendicular to the filaments are [100] and [010]. These directions are indicated in Fig. 1.

As stated above, the studied material has orthorhombic symmetry. Materials with orthorhombic symmetry have nine dependent elastic constants. These are displayed in Eq. (1) in the Voigt contracted notation in matrix form.

$$C_{ij} = \begin{bmatrix} C_{11} & C_{12} & C_{13} & 0 & 0 & 0 \\ & C_{22} & C_{23} & 0 & 0 & 0 \\ & & C_{33} & 0 & 0 & 0 \\ & & & C_{44} & 0 & 0 \\ & & & & C_{55} & 0 \\ & & & & & C_{66} \end{bmatrix}, \qquad (1)$$

where the matrix is symmetrical about its main diagonal. The Christoffel equations, which relate the elastic constants to the plane, monochromatic phase velocities, are:[1]

$$(C_{ijkl} n_j n_k - \rho v^2 \delta_{il}) p_l = 0 \qquad (2)$$

where C_{ijkl} is the fourth-rank elastic stiffness tensor, $\underset{\sim}{n}$ is the wave-propagation direction, ρ is the mass density, v is the wave velocity, δ_{il}

is the Kronecker delta, and $\underset{\sim}{p}$ is the displacement vector. It is easy to show that the resulting secular equation is diagonal for the [100], [010], and [001] directions. Thus, waves traveling along $\langle 100 \rangle$ directions are pure modes. Their velocities are determined by C_{11}, C_{55}, C_{66}; C_{22}, C_{44}, C_{66}; and C_{33}, C_{44}, C_{55}; respectively. Thus, all diagonal elastic constants C_{ii} can be determined by propagating waves in $\langle 100 \rangle$ directions. For each direction, there is one longitudinal wave and two shear waves; the three are polarized mutually orthogonally. Thus, checks on each of the three shear elastic constants C_{44}, C_{55}, and C_{66} are available. The off-diagonal elastic constants C_{12}, C_{13}, and C_{23} must be determined by measurements where the $\underset{\sim}{n}$ vectors are oblique to the $\langle 100 \rangle$ directions.

In general, waves traveling along lower-symmetry directions are not pure modes.[2] For $\underset{\sim}{n} = \langle 110 \rangle$, there is a single pure mode whose velocity is determined by $\frac{1}{2}(C_{55} + C_{66})$, $\frac{1}{2}(C_{44} + C_{66})$, and $\frac{1}{2}(C_{44} + C_{55})$ for the [011], [101], and [110] directions, respectively. These provide additional checks on the three C_{ii} shear constants measured along $\langle 100 \rangle$ directions. The two impure modes that propagate along each $\langle 110 \rangle$ direction can be determined from the Christoffel equations.

The $\langle 011 \rangle$ propagation-direction case is now outlined. The Kelvin-Christoffel elastic stiffnesses

$$\Gamma_{il} = C_{ijkl} n_j n_k \tag{3}$$

are for the case $\underset{\sim}{n} = \frac{1}{\sqrt{2}}[011]$:

$$\Gamma_{il} = \frac{1}{2}\begin{bmatrix} C_{55} + C_{66} & 0 & 0 \\ 0 & C_{22} + C_{44} & C_{23} + C_{44} \\ 0 & C_{23} + C_{44} & C_{33} + C_{44} \end{bmatrix}. \quad (4)$$

Thus, one solution is

$$\rho v^2 = \frac{1}{2}(C_{55} + C_{66}), \quad (5)$$

a torsion mode. And the remaining two roots are

$$\rho v^2 = \frac{1}{2}\{C_{22}+C_{33} \pm [(C_{22}-C_{33})^2+4(C_{23}+C_{44})^2]^{1/2}\} + C_{44}. \quad (6)$$

Experimentally, ρv^2 is measured and C_{23} is unknown. Thus, by rearrangement

$$C_{23} = \pm\{[2\rho v^2 - \frac{1}{2}(C_{22}+C_{33}+2C_{44})]^2 - \frac{1}{4}(C_{33}-C_{22})^2\}^{1/2} - C_{44}. \quad (7)$$

The spurious second value of C_{23} from this equation can be discarded on physical grounds. Similarly, [101] and [110] planes can be used to determine C_{13} and C_{12}, respectively. For these cases

$$C_{13} = \pm\{[2\rho v^2 - \frac{1}{2}(C_{11}+C_{33}+2C_{55})]^2 - \frac{1}{4}(C_{33}-C_{11})^2\}^{1/2} - C_{55} \quad (8)$$

and

$$C_{12} = \pm\{[2\rho v^2 - \frac{1}{2}(C_{11}+C_{33}+2C_{66})]^2 - \frac{1}{4}(C_{22}-C_{11})^2\}^{1/2} - C_{66}. \quad (9)$$

Further details on the problem of wave propagation in orthorhombic media were given by Musgrave.[3]

III. EXPERIMENTAL

A. Material

The samples used in this study were cut from a short section of Kryo 210* superconductor supplied by Magnetics Corporation of America. This is a copper-matrix, niobium-titanium-filament composite material. The Cu/NbTi volume ratio is 6:1, and the bar contains 2640 filaments with a twist each 7.6 cm. The distribution of filaments is shown in Fig. 2. The sample obtained for this study was about 20 cm long, 1.0 cm wide, and 0.5 cm thick. Four samples were cut for ultrasonic pulse measurements, one with its surfaces perpendicular to the symmetry axes of the material and three with the largest surface oriented at 45° to two symmetry axes. Sample geometries are shown in Fig. 1. Samples were studied in the as-received condition, that is, optimized by the manufacturer for use as a superconductor. The thermal and mechanical treatments that optimize such superconductors were described by McInturff and Chase.[4] The specimen with {100} surfaces was 0.5 cm by 1.0 cm by 1.0 cm, while the three off-axis specimens had thicknesses of 5 mm, 3 mm, and 2 mm. All specimens were ground sufficiently flat and parallel for ultrasonic study.

B. Procedures

Eighteen different ultrasonic-wave modes could be studied in these four specimens. All eighteen were examined at room temperature using the following procedure. Quartz-crystal transducers either 9.5 mm or 6.4 mm in diameter with fundamental resonance

---

*A trade name is used to describe the studied material; its use is not an NBS endorsement of the product.

frequencies between 5 and 10 MHz were bonded to one sample surface with phenyl salicylate (salol). Ultrasonic pulses were generated and detected in the transducer using an electronic apparatus described previously.[5] The time interval between the arrival of selected pulses from the ultrasonic echo train was measured using an oscilloscope with a delaying time base calibrated against a precision time-mark generator. The ultrasonic echo patterns obtained in this study were of good quality. They had three to thirty well-defined echoes.

Using the velocity v of the ultrasonic wave obtained from the transit time and the path length and the specimen mass density ρ the room-temperature elastic constants were calculated using the relationship

$$C = \rho v^2 \tag{10}$$

a simplified form of Eq. (2), where C is a combination of the C_{ij}'s depending on the mode. Results derived from Eq. (2) for the eighteen modes studied here are given in Table 1.

Resonant-bar elastic-constant measurements were performed on two other specimens at room temperature. These specimens were 4.8 mm diameter cylinders with lengths of 1.9 cm and 3.1 cm prepared with filaments along the specimen axis. In the resonant-bar technique, the sample is excited into longitudinal or torsional resonance by an attached quartz-crystal driver of appropriate mode and frequency. Resonance is detected using a quartz gauge crystal attached to the driver. The driver, gauge, and specimen form a composite oscillator. The appropriate elastic constant of the specimen can be calculated from the resonant frequency of the composite oscillator, the

specimen density, and known properties of the driver and gauge crystals. Since the composite-oscillator resonant frequency is often tens of kilohertz, this technique is sometimes called a kilohertz technique. But, in the literature it is called a composite-oscillator technique.[6]

C. Uncertainties

Experimental uncertainties of the elastic constants are discussed in two parts: imprecision and systematic error. Imprecisions affect many conclusions of the study. Systematic errors do not; they affect slightly only the C_{ij}'s themselves.

Bounds on the C_{ij}'s in Table I are imprecisions expressed as $\pm \sigma$, where σ is the standard deviation based on a normal distribution. For the diagonal C_{ij}'s, these imprecisions are based on two to five pure-mode measurements. Imprecisions of the non-diagonal C_{ij}'s depend both on these values and on an assumed imprecision of 0.005 in the quasi-transverse values of ρv^2. Sources of imprecision include: deviations of specimens from flat and parallel, specimen-length mismeasurement, specimen-to-specimen bond variations, transit-time mismeasurement, and, for this material, specimen imhomogeneity.

There are two principal systematic errors, one arising from the mass density and one from the transducer-bond coupling to the specimen. Maximum error in the mass density is estimated to be less than 0.15 percent. Transit-time error due to the ultrasonic wave traveling through the transducer and the coupling agent is estimated to be less than one percent; and, when corrected for, increases the ρv^2 values. Thus, the overall uncertainty in the C_{ij}'s is estimated to be less than $\pm$ 1.5 percent.

A possible source of sample-to-sample variation in the elastic constants of any composite material is its thermal-mechanical treatment, which may vary considerably for the type of material reported on here. For example, for copper, elastic-constant differences up to ten percent have been reported for annealed and deformed specimens.[7] Such variations can also occur in copper-base composites. Residual stresses of the order of the yield strength may occur in the composite, but simple computations show that these would change the elastic constants by less than one percent.

IV. RESULTS

Results of the study are displayed in the first four tables. In Table I, the observed room-temperature values of ρv^2 are given for eighteen measurement modes. This table also contains expressions for the ρv^2 in terms of the C_{ij}'s. These expressions were derived from the Christoffel equations. When a $\pm$ sign occurs, the + sign corresponds to the longitudinal mode, and the - sign corresponds to the transverse mode. Estimated errors for the derived elastic constants are also in Table I. The basis for estimating these errors was described above.

Results of the resonance studies are in Table II. S_{33} is the reciprocal Young's modulus along the filament direction, and $\frac{1}{2}(S_{44} + S_{55})$ is the reciprocal torsion (or shear) modulus around that direction.

The elastic compliances, the S_{ij}'s, are in Table III along with a summary of the C_{ij} data. The S_{ij}'s were determined by inverting the C_{ij} matrix displayed in Eq. (1) and substituting the C_{ij} values from Table I. Except for S_{44}, S_{55}, and S_{66}, which are simple reciprocals of the corresponding C_{ij}'s, errors in the S_{ij}'s are larger than those in the C_{ij}'s because of error accumulation.

The practical elastic constants (E = Young's modulus, G = shear modulus, and ν = Poisson's ratio) are given in Table IV. These parameters are related to the S_{ij}'s displayed in the matrix equation:

$$S_{ij} = \begin{bmatrix} 1/E_{11} & -\nu_{21}/E_{22} & -\nu_{31}/E_{33} & 0 & 0 & 0 \\ & 1/E_{22} & -\nu_{32}/E_{33} & 0 & 0 & 0 \\ & & 1/E_{33} & 0 & 0 & 0 \\ & & & 1/G_{44} & 0 & 0 \\ & & & & 1/G_{55} & 0 \\ & & & & & 1/G_{66} \end{bmatrix} \quad (11)$$

where the Poisson ratios are defined

$$\nu_{ij} = -S_{ij}/S_{ii} \text{ (no sum)} \quad (12)$$

and the S_{ij} matrix is symmetrical about its main diagonal.

V. DISCUSSION

A. Symmetry

On the basis of its internal and external geometry, the composite appears to be orthorhombic. If an object has three mutually perpendicular two-fold axes, then it belongs to the orthorhombic symmetry system. These rotation axes are labeled x, y, and z in Figs. 1 and 2.

Other possible symmetry systems can be excluded. Triclinic has no symmetry axis. Monoclinic has a single two-fold axis. Trigonal has a single three-fold axis. Clearly, these three systems are less symmetrical than the composite.

Orthorhombic symmetry includes four other symmetry systems: tetragonal, hexagonal, cubic, and isotropic. Relationships among the C_{ij}'s for these systems are listed in Table V together with tests of the relationships. Clearly, from Table V, none of the higher-symmetry systems can be used to describe exactly the observed C_{ij}'s. But the deviations are small for any of these four symmetry choices. Tetragonal is a slightly better choice than hexagonal. The advantage of describing an object by its highest symmetry is that there are fewer independent elastic constants: six for tetragonal, five for hexagonal, three for cubic, and two for isotropic. Thus, measurements and calculations are simplified to various degrees. In Table IV, the present orthorhombic results are also expressed in higher-symmetry co-ordinates to facilitate comparisons with other studies. When necessary, elastic constants were simply averaged.

B. Off-Diagonal Elastic Constants

The off-diagonal ($i \neq j$) elastic constants are more difficult to determine and almost always have higher uncertainties than the diagonal ($i = j$) elastic constants. This problem is reflected in

the present study in Table I. The problem arises because the off-diagonal elastic constants are not related simply to any pure mode of mechanical deformation. This is best shown in the S_{ij} matrix displayed in Eq. (11). All the diagonal S_{ij}'s are related reciprocally to either a Young's modulus or to a shear modulus. But all the off-diagonal terms are related to a Young's modulus and a Poisson's ratio, which is in turn determined by two other elastic constants, as shown in Eq. (12).

In the present study, another difficulty arose in determining the off-diagonal elastic constants. As shown in Table I, different values of the off-diagonal C_{ij}'s were obtained depending on whether the observed ρv_ℓ^2 or the observed ρv_t^2 were substituted into the C_{ij} expressions given in the table. For example, in the [011] direction the quasi-transverse datum gave $C_{23} = 0.715$ while the quasi-longitudinal datum gave $C_{23} = 1.041$. The C_{12} and C_{13} cases are similar. On the basis of small imprecisions of the measurements, and on the basis of the correctness of the value of the third (pure shear) mode, it seemed that the off-diagonal terms should be less uncertain than this and that one of the two values was perhaps correct.

To resolve this uncertainty in the off-diagonal elastic constants, an independent experiment was done. Some of the S_{ij}'s were determined by a resonance method. Dilatational and shear modes were measured on a cylindrical specimen with filaments along the cylinder axis. Results shown in Table II for the torsional mode $\frac{1}{2}(S_{44} + S_{55})$ agree exactly with the value calculated from the C_{ij}'s. (The S_{ij}'s are computed from the C_{ij}'s by inverting the C_{ij} matrix.) Similarly, exact agreement is also obtained for the dilatational mode, S_{33}, if the C_{ij} data from quasi-transverse modes rather than quasi-longitudinal modes are used. Thus, it was concluded that the quasi-transverse velocity data are both correct and consistent with other

data. However, the quasi-longitudinal wave velocities are low by about five percent. This slowing can be interpreted as a longer path length in the specimen due to interactions between the quasi-longitudinal waves and internal boundaries due to the presence of filaments.

C. Comparison with Copper

It is useful to compare the elastic constants of the composite with those of the matrix material, unalloyed copper,[7] to determine the effects of the filaments. Comparative data are shown in Table IV. Both the Young's moduli and the shear moduli of the composite are about fifteen percent lower than those of copper. The compressibility

$$K = \frac{1}{9} \sum_{i,j=1,3} S_{ij} \qquad (13)$$

of the composite is about five percent higher. The off-diagonal C_{ij}'s are identical to the value for copper, within one percent. This result is quite unexpected. And it may be accidental since it has no obvious physical interpretation.

D. Comparison with Previous Studies

The elastic constants of this composite were measured by Sun and Gray[8] using static methods, assuming hexagonal symmetry. Their results are shown in Table IV. Considering the higher inaccuracies usually associated with static methods, the agreement between the two sets of data is good. The static Young's and shear moduli are up to nine percent higher than the values reported here. The largest discrepancy is in ν_{21} and is due probably to error accumulation in the computed static value. Possibly, the differences in the two data sets are real, but this cannot be decided without knowing the uncertainties of the static values. A real

difference is, however, unlikely because, ignoring dispersion effects, dynamic elastic moduli are almost always higher than static elastic moduli, and the opposite effect is observed in this case.

E. Dispersion

No dispersion effects were observed, either in the limited 5-10 MHz region that was studied or in comparing the MHz pulse data with the 60 kHz resonance data. By dispersion is meant the dependence of sound velocity on frequency. Dispersive effects have been reported in many composite materials; they are usually due to either relaxation or resonance effects. Their absence here is attributed to coherent interfaces between the filaments and the matrix and to the small difference in acoustic impedance between the filaments and the matrix. Absence of dispersion is also consistent with the well-defined echo patterns that were obtained.

F. Relationship to Similar Composites

Elastic-property data have not been reported for NbTi/Cu composites with different ratios of NbTi or with different thermal-mechanical treatments. The present data can be applied to other NbTi/Cu composites through predictive schemes that relate the elastic constants of a composite to those of its components. Using the values of the NbTi elastic constants given by Sun and Gray[8] and formulas summarized by them, it follows that the present material obeys <u>approximately</u> simple rules of mixtures. Thus, similar composites would also be expected to follow these rules approximately. The present study is a useful guide to the elastic properties of any NbTi/Cu composite, but it is a source of exact elastic data only for the particular material studied. Even when the filament matrix volume ratio is adjusted for, several other variables remain that can affect elastic properties. These include: the state of mechanical deformation

(the number and distribution of lattice defects), composition of the NbTi filaments, preferred orientations in either the filaments or the matrix, and degree of coherency of the filament-matrix interfaces.

G. Low-Temperature Elastic Constants

Since this composite is intended for use as a superconductor, its low-temperature elastic properties are important. Studies down to liquid-helium temperature are underway in our laboratory, and results will be reported subsequently. Preliminary results are that the composite behaves on cooling approximately like unalloyed copper. But the magnitudes of the elastic constant changes are slightly different, and there are some anomalous effects that are both reproducible and reversible.

VI. CONCLUSIONS

The chief conclusions of this study are:

(1) Ultrasonic (5-10 MHz) waves, both dilatational and shear, can be propagated in an NbTi/Cu composite in directions parallel, perpendicular, and oblique to the filaments.

(2) Except as noted below, usual single-crystal elasticity techniques could be used to establish the complete set of elastic constants of the composite.

(3) Longitudinal waves propagated obliquely to $\langle 100 \rangle$ directions had velocites about five percent lower than expected. Obliquely propagated shear waves traveled with their expected velocities.

(4) The studied composite has orthorhombic symmetry, and, therefore, nine independent elastic constants. But the deviations from isotropy are small.

(5) Compared to copper, the C_{ij} $(i = j)$ of the composite are lower by about seven percent for C_{11}, C_{22}, and C_{33}, and by about fifteen percent for C_{44}, C_{55}, and C_{66}. But the C_{ij} $(i \neq j)$ are about the same. The composite's compressibility is about five percent higher than copper's.

(6) The present dynamic results agree resonably well with existing static measurements.

(7) Advantages of combining pulse-echo measurements and resonance measurements were found.

(8) No dispersion, change of velocity with frequency, was observed.

ACKNOWLEDGMENT

This study was supported by the Advanced Research Projects Agency of the U.S. Department of Defense. G. A. Miranda of Los Alamos kindly contributed a photomicrograph of the studied material. W. H. Gray of Oak Ridge National Laboratory contributed a critical reading of the manuscript.

REFERENCES

1. L. D. Landau and E. M. Lifshitz, Theory of Elasticity (Pergamon, London, 1959), p. 104.
2. J. R. Neighbors and G. E. Schacher, J. Appl. Phys. 38, 5366-5375 (1967).
3. M. J. P. Musgrave, Crystal Acoustics (Holden-Day, San Francisco, 1970), p. 117-123.
4. A. D. McInturff and G. G. Chase, J. Appl. Phys. 44, 2378-2384 (1973).
5. E. R. Naimon, W. F. Weston, and H. M. Ledbetter, Cryogenics 14, 246-249 (1974).
6. J. Marx, Rev. Sci. Instrum. 22, 503-509 (1951).
7. H. M. Ledbetter and E. R. Naimon, J. Phys. Chem. Ref. Data 3 897-935 (1974).
8. C. T. Sun and W. H. Gray, Sixth Symp. Engnrng. Probs. Fusion Res., San Diego, CA, Nov. 1975.

Table I. Room-temperature elastic constants C_{ij} for an NbTi/Cu composite with macroscopic orthorhombic symmetry. The wave-front normal is denoted by $\underset{\sim}{n}$, and the displacement direction by $\underset{\sim}{p}$. Both ρv^2 and C_{ij} have units of 10^{11} N/m^2. Impure modes are denoted by asterisks. Daggers indicate values discarded for reasons discussed in text.

Specimen	Measurement Number	$\underset{\sim}{n}$	$\underset{\sim}{p}$	ρv_ℓ^2	ρv_t^2	C_{ij}	Derived C_{ij}
A	1	100	100	1.834		C_{11}	$C_{11}=1.834\pm0.005$
	2		010		0.404	C_{66}	$C_{66}=0.414\pm0.007$
	3		001		0.407	C_{55}	$C_{55}=0.407\pm0.011$
	4	010	010	1.878		C_{22}	$C_{22}=1.878\pm0.015$
	5		100		0.413	C_{66}	
	6		001		0.413	C_{44}	$C_{44}=0.416\pm0.003$
	7	001	001	1.880		C_{33}	$C_{33}=1.880\pm0.002$
	8		100		0.414	C_{55}	
	9		010		0.419	C_{44}	
B	10	011	011*	1.713		$\left.\begin{matrix}1/2\{C_{22}+C_{33}\pm[(C_{22}-C_{33})^2+4(C_{23}+C_{44})^2]^{1/2}\}\\+C_{44}\end{matrix}\right.$	$(C_{23}=0.715)\dagger$
	11		0$\bar{1}$1*		0.419		$C_{23}=1.041\pm0.040$
	12		100		0.407	$1/2(C_{55}+C_{66})$	
C	13	101	101*	1.740		$\left.\begin{matrix}1/2\{C_{11}+C_{33}\pm[(C_{11}-C_{33})^2+4(C_{13}+C_{55})^2]^{1/2}\}\\+C_{55}\end{matrix}\right.$	$(C_{13}=0.809)\dagger$
	14		$\bar{1}$01*		0.409		$C_{13}=1.039\pm0.040$
	15		010		0.408	$1/2(C_{44}+C_{66})$	
D	16	110	110*	1.744		$\left.\begin{matrix}1/2\{C_{11}+C_{22}\pm[(C_{11}-C_{22})^2+4(C_{12}+C_{66})^2]^{1/2}\}\\+C_{66}\end{matrix}\right.$	$(C_{12}=0.804)\dagger$
	17		1$\bar{1}$0*		0.400		$C_{12}=1.056\pm0.040$
	18		001		0.394	$1/2(C_{44}+C_{55})$	

Table II. Elastic compliances of an NbTi/Cu composite measured by a resonance method. Units are 10^{-11} m^2/N.

S_{ij}	Observed	Calculated from C_{ij}
S_{33}	0.873 ± 0.009	0.878 ± 0.073 from quasi-shear modes (0.692 from quasi-longitudinal modes)
$\frac{1}{2}(S_{44} + S_{55})$	2.398 ± 0.024	2.430 ± 0.041

Table III. Room-temperature elastic stiffnesses C_{ij} and elastic compliances S_{ij} of an NbTi/Cu composite and copper. C_{ij} units are 10^{11} N/m^2; S_{ij} units are 10^{-11} m^2/N. Values in parentheses are derived from $2C_{44} = C_{11} - C_{12}$ and $S_{44} = 2(S_{11} - S_{12})$.

	Composite		Copper[a]	
ij	C_{ij}	S_{ij}	C_{ij}	S_{ij}
11	1.834	0.924	2.006	0.780
22	1.878	0.894		
33	1.880	0.879		
44	0.416	2.404	0.477	2.096
55	0.407	2.457		
66	0.414	2.415		
12	1.056	-0.341	(1.052)	(-0.268)
13	1.039	-0.322		
23	1.041	-0.307		

[a] Ref. 7

Table IV. Practical elastic constants E = Young's modulus, G = shear modulus, ν = Poisson's ratio for NbTi/Cu composite in different co-ordinate systems at room temperature. Units are 10^{11} N/m^2, except ν's, which are dimensionless.

Elastic Constant	Orthorhombic Basis	Tetragonal Basis	Hexagonal Basis	Isotropic Basis	Copper[a] Values	Static Results[b] (Hexagonal Basis)
E_{11}	1.082	1.100	1.100	1.112	1.282	1.22
E_{22}	1.119					
E_{33}	1.138	1.138	1.138			1.19
G_{44}	0.416	0.411	0.411	0.412	0.477	0.448
G_{55}	0.407					
G_{66}	0.414	0.414	(0.398)[c]			(0.431)
ν_{21}	0.381	0.381	0.381			(0.415)[c]
ν_{31}	0.365	0.357	0.357			0.347
ν_{32}	0.349					

[a] Ref. 7

[b] Ref. 8

[c] Quantities in parentheses are derived from given data using $G_{66} = E_{11}/2(1 + \nu_{12})$.

Table V. Checks for various symmetries for NbTi/Cu composite. For hexagonal and cubic cases, relationships (1), (2), and (3) also hold. For isotropic case, all eight relationships must hold; either number (4) or (8) is redundant.

Symmetry System	Relationships	Ratio of L.H.S./R.H.S. for NbTi/Cu
Tetragonal	(1) $C_{22} = C_{11}$	1.024 ± 0.020
	(2) $C_{55} = C_{44}$	0.978 ± 0.014
	(3) $C_{23} = C_{13}$	1.002 ± 0.040
Hexagonal	(4) $C_{66} = \frac{1}{2}(C_{11} - C_{12})$	1.064 ± 0.020
Cubic	(5) $C_{33} = C_{11}$	1.025 ± 0.007
	(6) $C_{12} = C_{13}$	1.016 ± 0.040
	(7) $C_{66} = C_{55}$	1.017 ± 0.018
Isotropic	(8) $C_{44} = \frac{1}{2}(C_{11} - C_{12})$	1.069 ± 0.016

LIST OF FIGURES

Fig. 1. Schematic geometries of four pulse specimens. Filaments along [001] are indicated by striping. The wave-propagation directions (indicated by dashed lines) and displacement vectors are given in Table I. The x, y, and z axes are equivalent to the [001], [010], and [001] axes that are used in the text and tables.

Fig. 2. Photomicrograph showing distribution of filaments. Plane of photo is perpendicular to filaments. Width shown corresponds to 4.3 mm in specimen. Vertical direction is x = [100] and horizontal direction is y = [010].

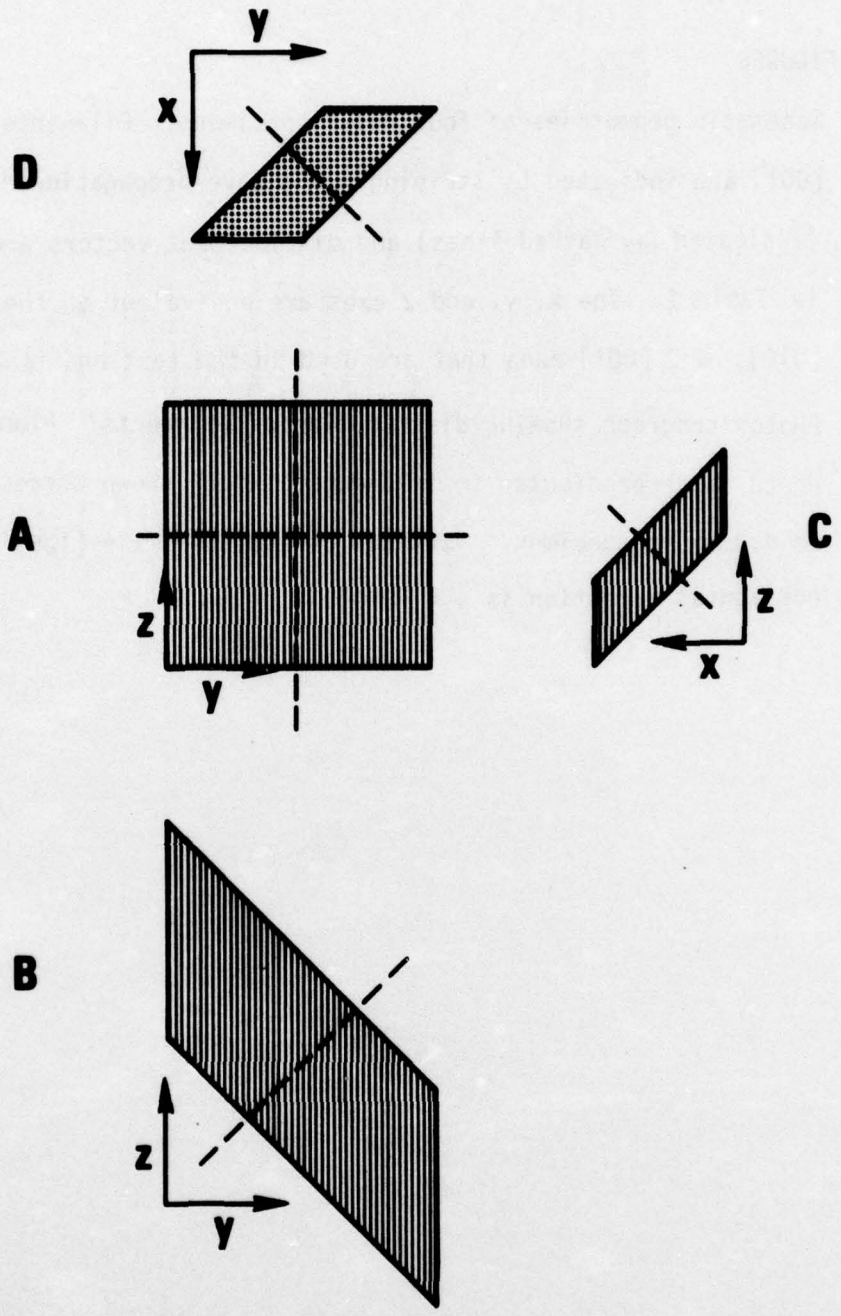


Fig. 1. Schematic geometries of four pulse specimens. Filaments along [001] are indicated by striping. The wave-propagation directions (indicated by dashed lines) and displacement vectors are given in Table I. The x, y, and z axes are equivalent to the [001], [010], and [001] axes that are used in the text and tables.

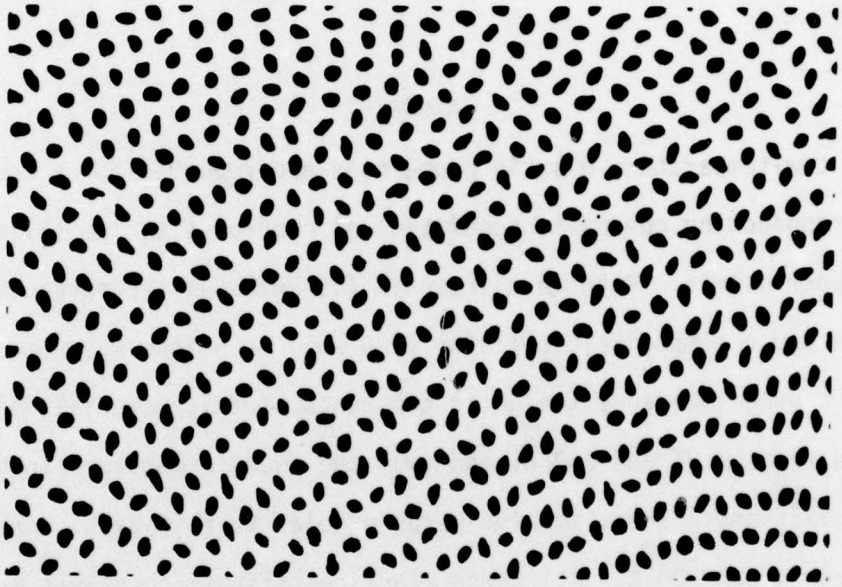


Fig. 2. Photomicrograph showing distribution of filaments. Plane of photo is perpendicular to filaments. Width shown corresponds to 4.3 mm in specimen. Vertical direction is x = [100] and horizontal direction is y = [010].

TEMPERATURE DEPENDENCE OF THE ELASTIC CONSTANTS OF AN NbTi/Cu SUPERCONDUCTING COMPOSITE*

D. T. Read** and H. M. Ledbetter

Cryogenics Division
Institute for Basic Standards
National Bureau of Standards
Boulder, Colorado 80302

ABSTRACT

Low-temperature elastic properties are reported for a commercial superconducting composite consisting of niobium-titanium filaments in a copper matrix. Both an ultrasonic (10 MHz) pulse-superposition technique and a composite oscillator (100 kHz) technique were used. Seven of the nine independent elastic constants of this material were determined between 76 and 300 K; and two, the Young's modulus along the filament axis and a shear modulus perpendicular to that axis, were determined between 4 and 300 K. All these elastic-stiffness constants are about ten percent lower than the corresponding values for copper. All increase about ten percent on cooling from 300 to 4 K. And all have anomalous temperature behavior.

Keywords: Bulk modulus; composite; compressibility; copper; cryogenic tempeatures; elastic constants; niobium-titanium; Poisson's ratio; shear modulus; superconductor; Young's modulus.

* Contribution of NBS, not subject to copyright.

**NRC-NBS Postdoctoral Research Associate, 1975-76.

INTRODUCTION

Superconducting composites consisting of niobium-titanium filaments in a copper matrix are now available commercially for applications in which high electrical-current density must be obtained in high magnetic fields. Components containing these conductors are designed critically. Elastic constants of such conductors are useful for two reasons: for computing the recoverable deflections due to applied loads, and for computing thermoelastic stresses due to either temperature changes or differential thermal contractions. Also, elastic constants provide a valuable characterization of a material. For composite materials, accurate elastic data provide key tests for theories that relate macroscopic elastic properties to elastic properties of constituents.

The particular NbTi/Cu composite reported on here has orthorhombic symmetry, and the room-temperature values of all nine independent elastic constants, the C_{ij}'s, were reported previously.[1] The temperature dependencies to 77 K of seven of these nine were determined in the present study: C_{11}, C_{22}, C_{33}, C_{55}, C_{66}, E_{33}, and $2/(S_{44} + S_{55})$, where E_{33} is Young's modulus along the filament axis and $2/(S_{44} + S_{55})$ is the torsion modulus about that axis. Two elastic constants, E_{33} and C_{66}, were determined to 4 K. The temperature dependencies of the other elastic constants, such as C_{12} and C_{13}, were not determined because they are not measured directly and they have larger errors. Symmetries discussed here are strictly macroscopic. The filament direction of the composite is designated [001], and the principal directions perpendicular to the filaments are [100] and [010]. These directions are indicated in Fig. 1.

EXPERIMENTAL

A. Material

Specimens were cut from a short section of Kryo 210* superconductor supplied by Magnetics Corporation of America. This is a copper-matrix, niobium-titanium-filament composite material. The Cu/NbTi volume ratio is 6:1, and the bar contains 2640 filaments with a twist pitch of 7.6 cm. The section obtained for this study was about 20 cm long, 1.0 cm wide, and 0.5 cm thick. Four specimens were cut for ultrasonic pulse measurements, one with its surfaces perpendicular to the symmetry axes of the material and three with their largest surface oriented at 45° to two symmetry axes. Specimen geometries are shown in Fig. 1. The material was studied in the as-received condition. The thermal and mechanical treatments of such superconductors during manufacture were described by McInturff and Chase.[2] The specimen with {100} surfaces was 0.5 cm by 1.0 cm by 1.0 cm, while the three off-axis specimens had thicknesses of 5 mm, 3 mm, and 2 mm. All specimens were ground sufficiently flat and parallel for ultrasonic study.

Two composite-oscillator specimens were prepared. These were right-circular cylinders 4.8 mm in diameter and 3.1 and 1.9 cm long for the extensional and torsional measurements, respectively.

---

* A trade name is used here to characterize the studied material. Its use is not an NBS endorsement of a particular product.

B. Procedures

The room-temperature elastic constants of the specimens used in this study were reported previously.[1] The temperature dependence of five of these constants, the elastic stiffnesses C_{11}, C_{22}, C_{33}, C_{55}, and C_{66}, were measured using a pulse-superposition technique in which the ratio of the ultrasonic velocity, v, at low temperatures to its value at room temperature was measured every five degrees between room temperature and the lowest temperature obtained during each cooling. These ratios of sound velocities were used to calculate the temperature dependence of the appropriate elastic constant, C, from $C = \rho v^2$ where ρ is the mass density of the specimen. Each sample was cooled by enclosing it in a sample chamber and lowering it gradually into the ullage of a dewar containing either liquid nitrogen or liquid helium. The low-temperature apparatus and techniques were described previously.[3]

The temperature dependencies of the Young's modulus and the torsional modulus were measured using a composite-oscillator technique. Briefly, the resonant frequency is measured of a composite oscillator consisting of the specimen, a quartz-crystal driver, and a quartz-crystal gauge. This composite oscillator is also cooled by putting it in a sample holder and inserting the specimen end into the ullage of a dewar containing either liquid nitrogen or liquid helium. The resonant frequency of the specimen is calculated from the resonant frequency of the composite oscillator, the masses and geometries of the specimen and the sample, and known properties of the gauge and quartz crystals. Froms its resonant frequency, the elastic constant of the sample can be calculated easily. The apparatus and techniques used in such measurements were described previously.[4]

RESULTS

The measured value of E_{33} (Young's modulus along the filament direction) for the NbTi/Cu composite is shown in Fig. 2. Young's modulus, E, of polycrystalline copper is shown for comparison.[5] Young's modulus of the composite is about ten percent lower than that of copper, and it rises with decreasing temperature to a value at 4 K about ten percent above its room-temperature value. Irregularities in the curve for the composite are not observed in copper, and they are significant deviations from the temperature dependence of Young's modulus for ordinary materials, of which copper is a good example. The upturn in the curve below 20 K is believed to be a real effect.

The value of $2/(S_{44} + S_{55})$, the modulus of torsion about the filament axis, is shown in Fig. 3. Shown also is the torsional or shear modulus, G, of copper. It is clear that the temperature behavior of $2/(S_{44} + S_{55})$ is dissimilar to the of E_{33}, and that its approximate relationship to the torsional modulus of copper is nearly the same as the relationship of E_{33} to the Young's modulus of copper. The dashed part of the curve is an extrapolation based on the usual behavior of elastic constants at low temperatures and the behavior of the elastic constants of this composite that were measured to 4 K.

The Poisson ratios of this composite material that relate the strain along the filament axis (produced by a stress along that axis) to the strains perpendicular to the axis were found to be 0.366 and 0.349 along the x and y axes respectively at room temperature.[1] The temperature dependencies of these ratios are not easily measured by dynamic techniques, and they were not measured in this study. However, since Poisson's ratio for copper decreases by two percent on cooling

of the composite are intermediate between those of the two copper moduli. Based on simple rule-of-mixture arguments it follows from Fig. 6 that the shear modulus of NbTi must increase with temperature similar to copper, but the longitudinal modulus of NbTi must increase considerably more than that of copper.

DISCUSSION

In a previous study,[1] it was shown that the room-temperature magnitudes of the elastic constants of this composite can be predicted approximately from a rule of mixtures from the known elastic constants of copper and NbTi. It was also shown that the observed values of the practical elastic constants E_{33} and $2/(S_{44} + S_{55})$ were consistent with the measured values of the elastic stiffnesses, the C_{ij}'s.

Rules of mixtures could not be used to predict the temperature dependence of the composite material studied here because the temperature dependencies of the elastic constants of the niobium-titanium alloy have not been reported. An attempt to obtain such data failed.[6]

Weston[7] reported the temperature dependencies of the elastic constants of an NbTiCu/fiberglass-epoxy coil composite. Although that composite included fiberglass and epoxy, the temperature dependence of its elastic constants reflects that of the NbTi/Cu part, because the stiffness of the fiberglass-epoxy is low and it constitutes only about one-fourth the total volume. The sign and magnitude of the temperature dependencies observed by Weston were about the same as those observed in the present study. For most of the elastic constants, Weston reported very small deviations from the usual temperature behavior of ordinary materials. But, in the Young's modulus along the filaments, Weston found a large deviation from usual temperature behavior. However, none

of the elastic constants of the coil composite studied by Weston showed the type of anomaly observed in the present study.

The observed increase in all the elastic stiffnesses of about ten percent on cooling from 295 K to 4 K is expected for this material. Elastic constants of most metals increase between five and fifteen percent on cooling to zero temperature;[8] the polycrystalline longitudinal modulus C_ℓ of copper increases four percent on cooling. Thus, the sign and magnitude of the observed temperature dependencies of the elastic constants of the NbTi/Cu composite studied here are not surprising.

As shown in Figs. 2-6, all the measured elastic constants reported here have irregular temperature dependencies compared to copper. Experimental evidence for these anomalies is strong: they occur in seven different measured elastic constants; they were observed on measurements made during both heating and cooling; and they occurred in repeated experiments. These anomalies are probably insignificant from the viewpoint of engineering design because they change the elastic constants only a few percent from regular behavior scaled against copper. However, they indicate unexpected behavior of the composite.

The cause of these anomalies is uncertain. Two hypotheses can be suggested. First, since elastic constants are changed by stress, the anomalies may arise from internal-stress changes due to differential thermal contraction during cooling. Second, the anomalies may arise from similar anomalies in the temperature dependencies of the elastic constants of the niobium-titanium filaments. Anomalies similar to those observed here were reported in niobium and in other transition metals, where they are ascribed to the electronic structure,[9,10] and in a niobium-zirconium alloy, where they are attributed to the formation of omega phase.[11]

from 300 to 4 K, a similar change would be expected for Poisson's ratio of the composite.

Attention is now turned from the practical elastic constants to the elastic-stiffness coefficients, the C_{ij}'s. Although C_{11}, C_{22}, and C_{33} were all measured, the data for C_{22} practically coincide with those for C_{33}, so only C_{11} and C_{33}, normalized separately to their 300 K values (given in Table I) are shown in Fig. 4 together with the longitudinal modulus, C_{ℓ}, of copper. The dashed curves are extrapolations. Again, these elastic constants are about seven percent lower than those of copper, and they increase about five percent on cooling. As in the previous cases of the practical elastic constants, anomalous changes in these elastic constants occur during cooling.

The temperature dependence of C_{66}, normalized to 300 K, is shown in Fig. 5. C_{55} was measured between 300 and 76 K; the resulting data nearly coincide with those for C_{66} and they are not shown. C_{55} and C_{66} for the composite material are about fourteen percent lower than the value for copper, and they increase about ten percent on cooling. They also exhibit anomalous temperature behavior. The data point shown as an open square at 4 K in Fig. 5 represents an absolute, rather than a relative, elastic-constant measurement; it confirms the overall elastic-constant change due to cooling.

C_{33} and C_{55}, a longitudinal and a transverse stiffness of the composite material are shown in Fig. 6 together with C_{ℓ} and C_t, the longitudinal and transverse moduli of polycrystalline copper. In both copper and the composite, the transverse (shear) moduli have stronger temperature dependencies than the longitudinal moduli. Surprisingly, the temperature dependencies of both the transverse and longidutinal moduli

CONCLUSIONS

The following principal results and conclusions emerge from the present study:

(1) The Young's modulus along the filaments, E_{33}, increases twelve percent on cooling from 300 to 4 K, compared to eight percent for copper. The extrapolated torsional modulus around the filaments, $G_{\parallel}$, increases nine percent on cooling, the same as copper.

(2) The extrapolated elastic stiffnesses C_{11}, C_{22}, and C_{33} increase five percent on cooling, compared to four percent for copper.

(3) The shear elastic constants C_{55} and C_{66} increase ten percent on cooling, compared to nine percent for copper.

(4) All measured elastic constants are anomalous in their temperature dependencies.

ACKNOWLEDGMENT

This study was supported by the Advanced Research Projects Agency of the U.S. Department of Defense.

REFERENCES

1. H. M. Ledbetter and D. T. Read, submitted for publication.
2. A. D. McInturff and G. G. Chase, J. Appl. Phys. 44, 2378-2384 (1973).
3. E. R. Naimon, W. F. Weston, and H. M. Ledbetter, Cryogenics 14, 246-249 (1974).
4. J. Marx, J. Sci. Instrum. 22, 503-509 (1951).
5. W. C. Overton and J. Gaffney, Phys. Rev. 98, 969-977 (1955).
6. C. N. Reid, J. L. Routbort, and R. A. Maynard, J. Appl. Phys. 44, 1398-1399 (1973).
7. W. F. Weston, J. Appl. Phys. 46, 4458-4465 (1975).
8. R. F. S. Hearmon, in Numerical Data and Functional Relationships in Science and Technology, Group III, Vol. I, K. H. Hellwege and A. M. Hellwege, Eds. (Springer-Verlag, Berlin, 1969).
9. K. J. Carroll, J. Appl. Phys. 36, 3689-3690 (1965).
10. F. H. Featherston and J. R. Neighbors, Phys. Rev. 130, 1324-1333 (1963).
11. C. Goasdue, P. S. Ho, and S. L. Sass, Acta Met. 20, 725-733 (1972).

Table 1. Elastic constants of an NbTi/Cu composite and polycrystalline copper at selected temperatures in units of 10^{11} N/m^2, except ν, which is dimensionless; numbers in parentheses are based on extrapolated data.

	300 K	200 K	100 K	0 K
NbTi/Cu Composite:				
E_{33}	1.138	1.189	1.238	1.287
$G_{\parallel}$	0.417	0.427	0.445	(0.454)
ν_{31}	0.365	---	---	---
ν_{32}	0.349	---	---	---
C_{11}	1.834	1.865	1.908	(1.915)
C_{22}	1.878	1.911	1.952	(1.957)
C_{33}	1.880	1.919	1.965	(1.983)
C_{55}	0.407	0.418	0.436	(0.442)
C_{66}	0.414	0.425	0.442	0.456
Polycrystalline Copper[a]:				
E	1.282	1.329	1.369	1.386
G	0.477	0.496	0.512	0.519
ν	0.344	0.341	0.339	0.338
C_{ℓ}	2.006	2.053	2.093	2.111
C_t	0.477	0.495	0.511	0.518

[a] Ref. 5, arithmetic average of Hashin-Shtrikman bounds.

LIST OF FIGURES

Fig. 1. Schematic geometries of four pulse specimens. Filaments along [001] are indicated by striping. In specimen A, waves were propagated along the [100], and [010] directions; in B along [011]; in C along [101]; and in D along [110].

Fig. 2. Young's modulus of the composite along [001] compared to the Young's modulus of polycrystalline copper.

Fig. 3. Shear, or torsional, modulus of the composite around the [001], or filament, axis compared to the shear modulus of polycrystalline copper.

Fig. 4. Longitudinal elastic stiffnesses of the composite in the [100] and [001] directions compared to the longitudinal elastic modulus of polycrystalline copper.

Fig. 5. A shear modulus of the composite compared to that of polycrystalline copper. C_{66} corresponds to the shear resistance on a (100) plane in a [010] direction, or vice versa.

Fig. 6. Comparison of a longitudinal and a shear elastic constant of the composite. C_{33} is measured in the [001] direction, along the filament axis. C_{55} corresponds to the shear resistance on a (100) plane in a [001] direction or of a (001) plane in a [001] direction. Values for copper are shown for comparison.

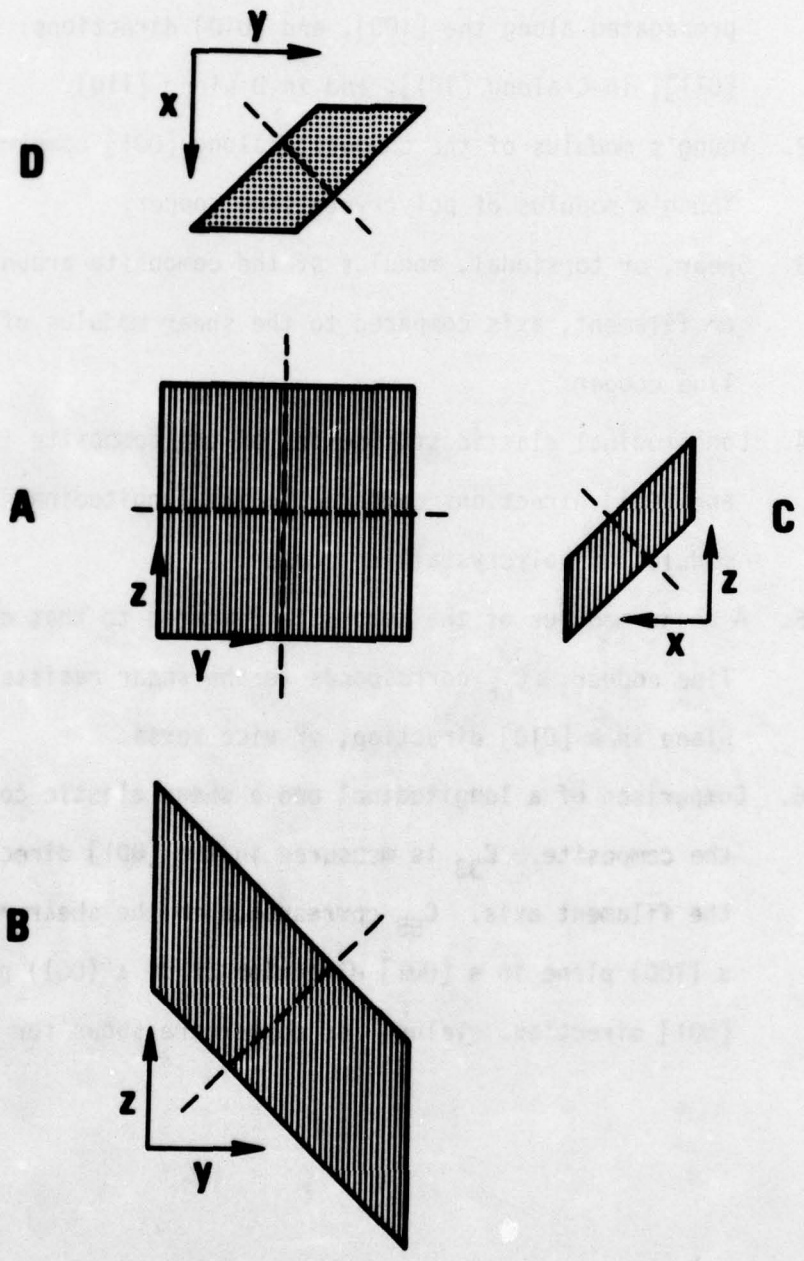


Fig. 1. Schematic geometries of four pulse specimens. Filaments along [001] are indicated by striping. In specimen A, waves were propagated along the [100], [010], and [001] directions; in B along [001]; in C along [101]; and in D along [110].

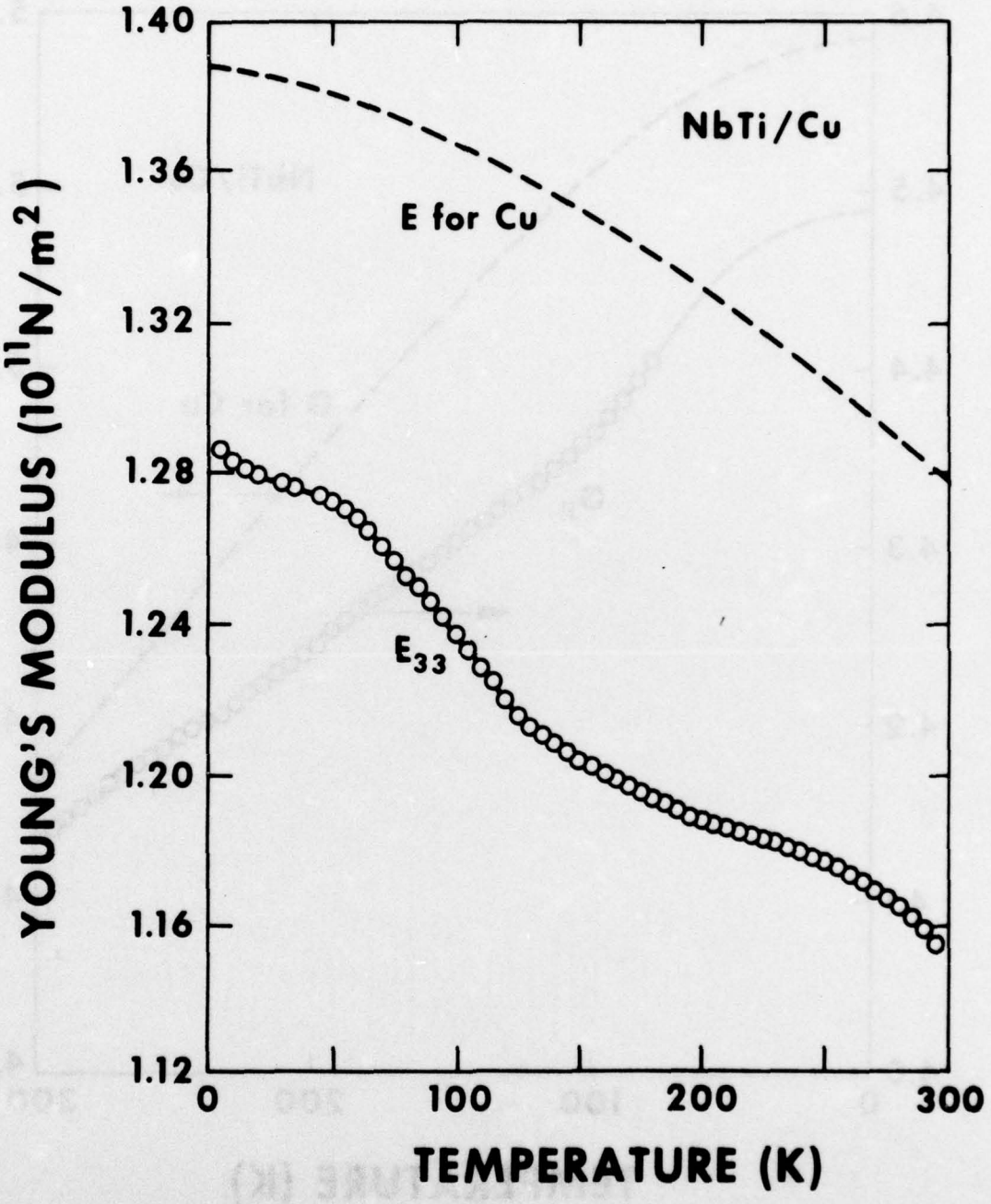


Fig. 2. Young's modulus of the composite along [001] compared to the Young's modulus of polycrystalline copper.

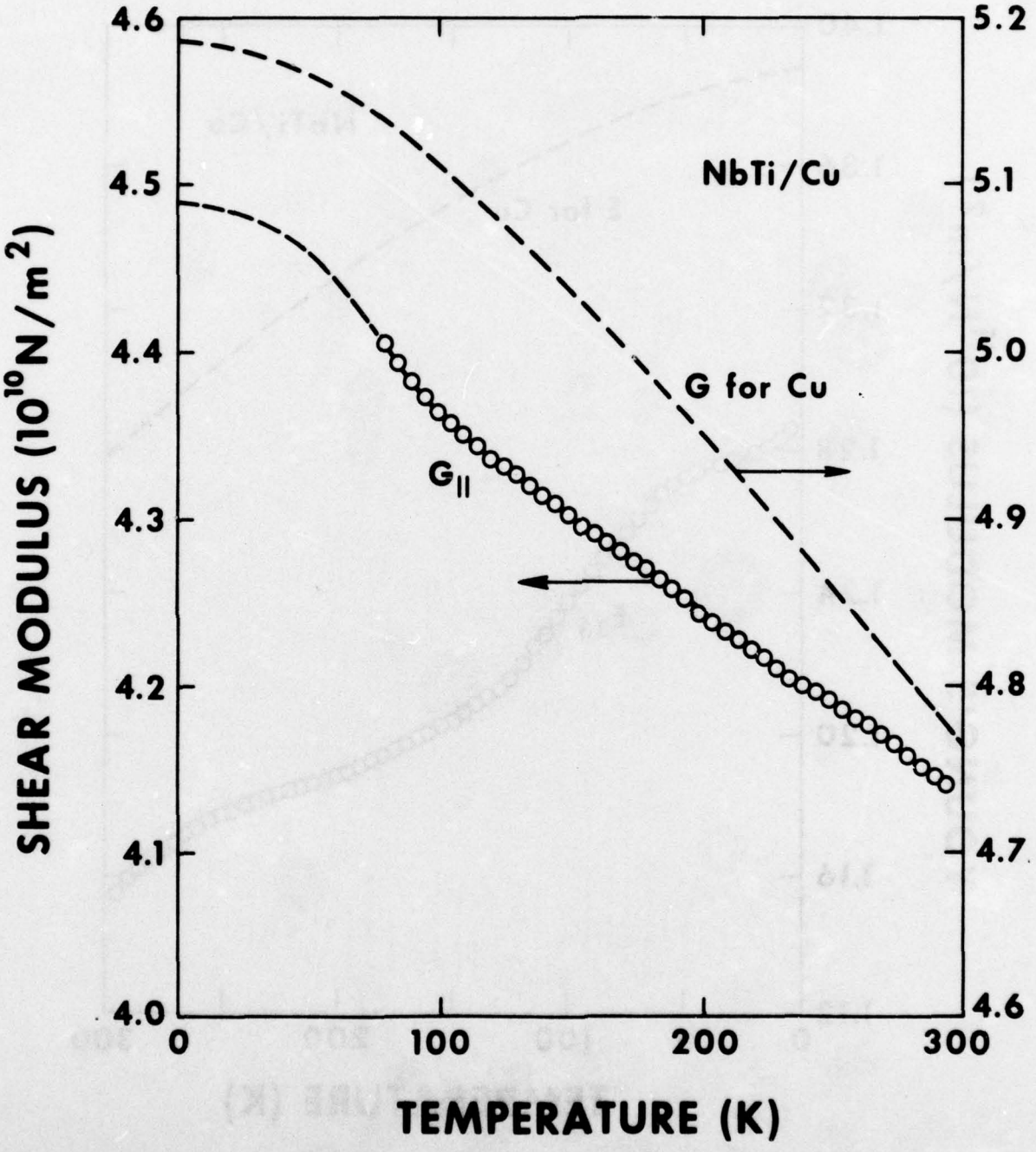


Fig. 3. Shear, or torsional, modulus of the composite around the [001], or filament, axis compared to the shear modulus of polycrystalline copper.

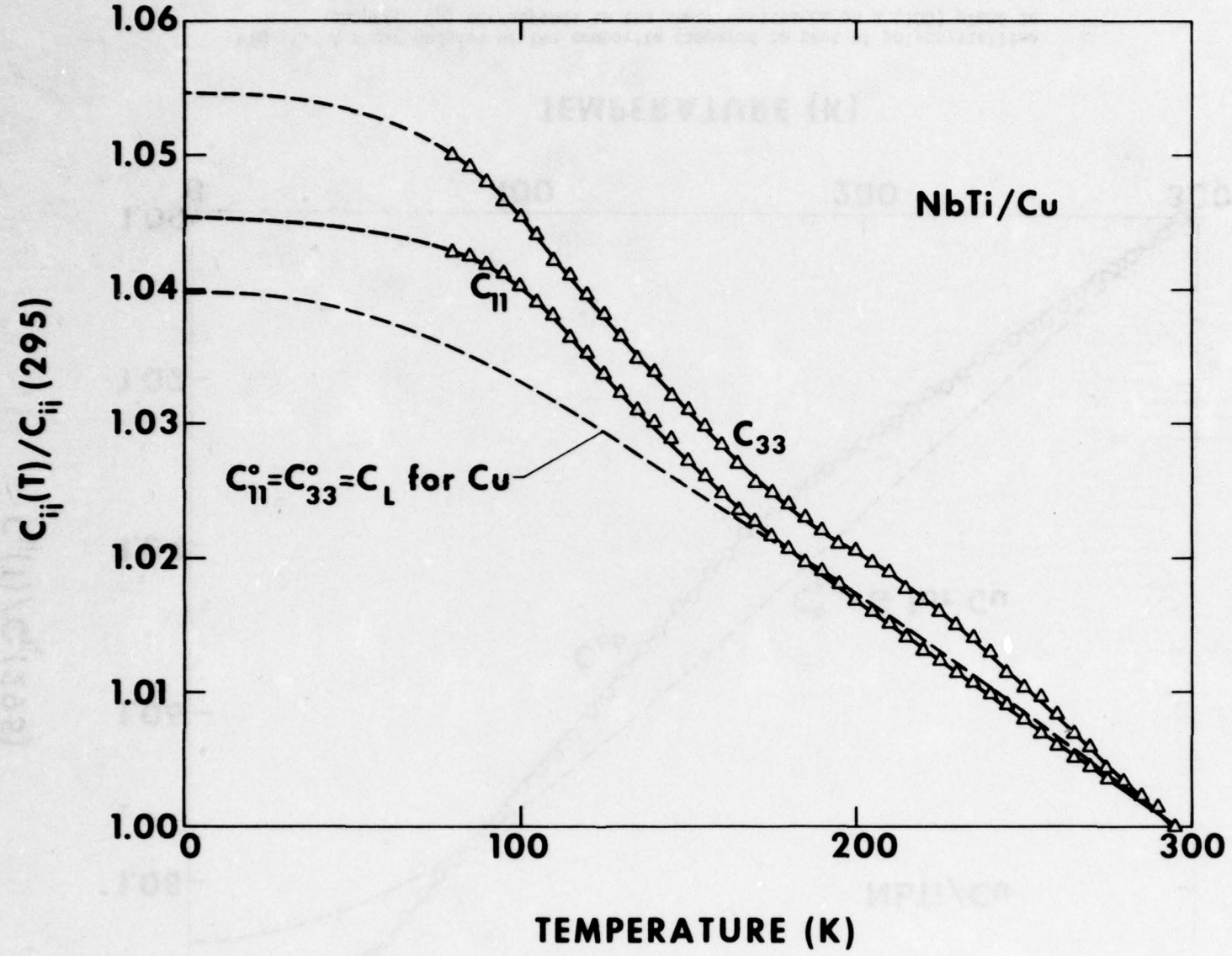


Fig. 4. Longitudinal elastic stiffnesses of the composite in the [100] and [001] directions compared to the longitudinal elastic modulus of polycrystalline copper.

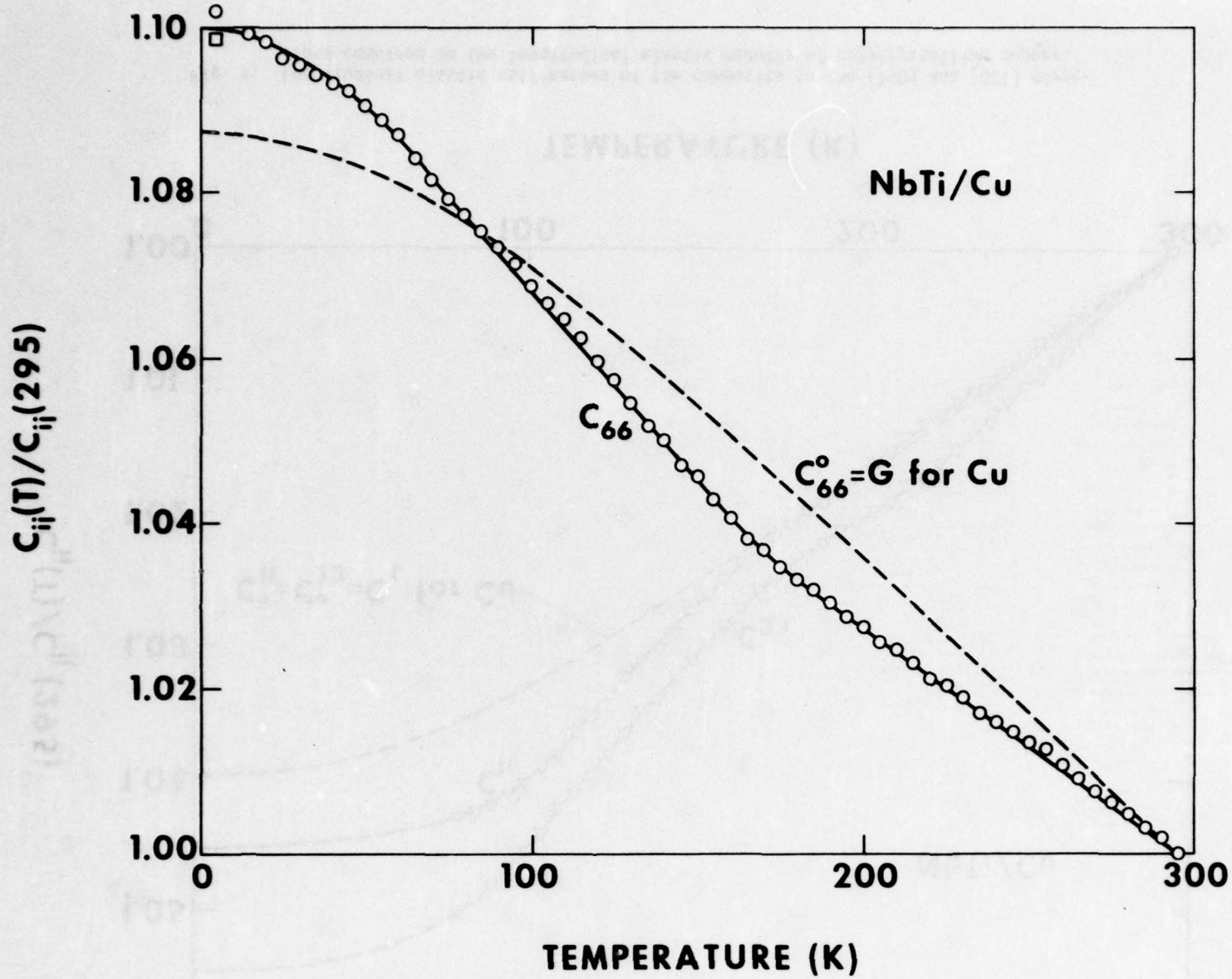


Fig. 5. A shear modulus of the composite compared to that of polycrystalline copper. C_{66} corresponds to the shear resistance on a (100) plane in a [010] direction, or on a (010) plane in a [100] direction.

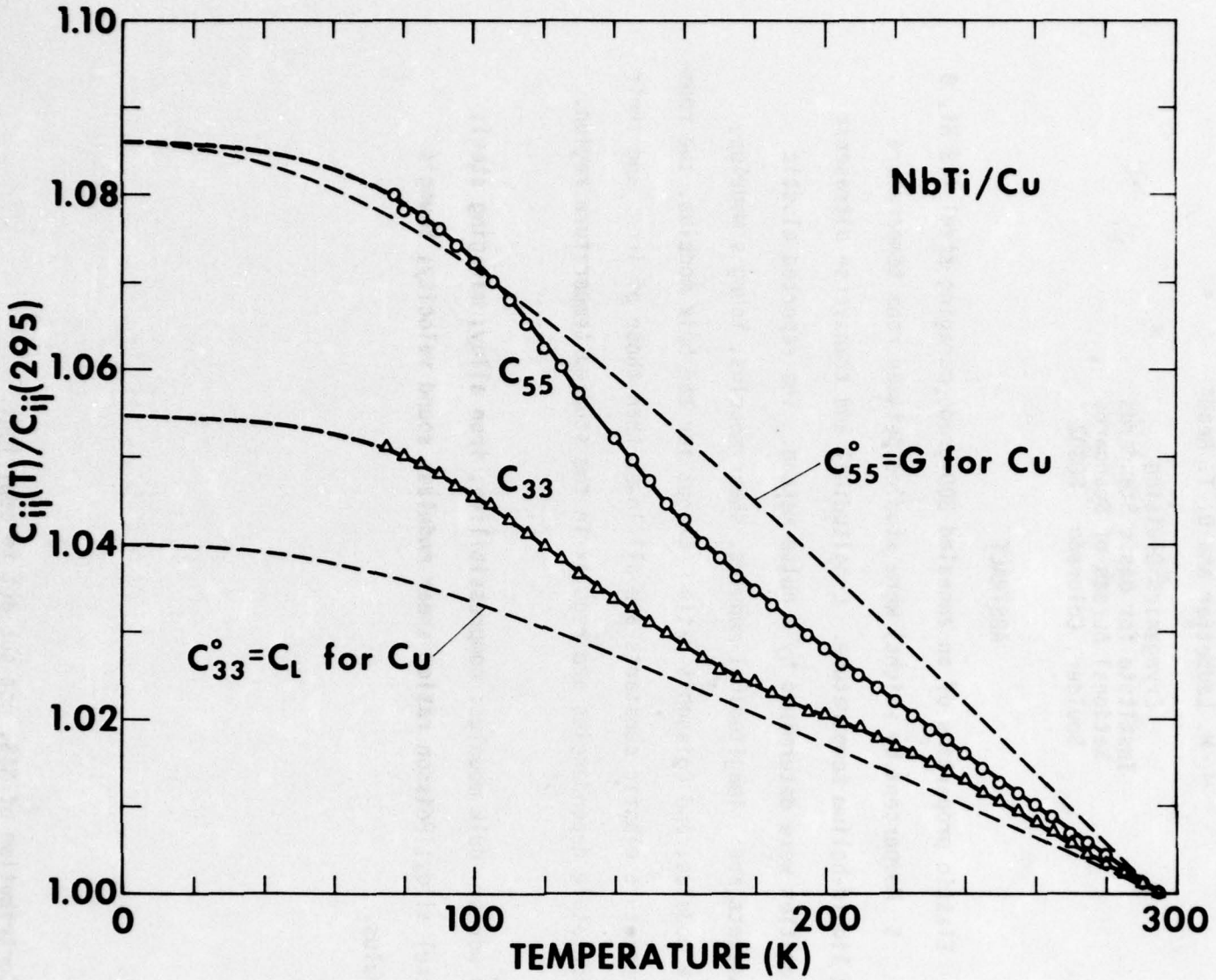


Fig. 6. Comparison of a longitudinal and a shear elastic constant of the composite C_{33} is measured in the [001] direction, along the filament axis. C_{55} corresponds to the shear resistance on a (100) plane in a [001] direction or of a (001) plane in a [100] direction. Values for copper are shown for comparison.

Low-Temperature Elastic Properties of a 300-grade Maraging Steel†

H. M. Ledbetter and D. T. Read*

Cryogenics Division
Institute for Basic Standards
National Bureau of Standards
Boulder, Colorado 80302

ABSTRACT

Elastic properties of an annealed 300-grade maraging steel (18 Ni, 9 Co, 5 Mo percent by weight) were studied between room temperature and liquid-helium temperature. Longitudinal and transverse ultrasonic velocities were determined by a pulse method. The reported elastic constants are: longitudinal modulus, shear modulus, Young's modulus, bulk modulus, and Poisson's ratio. Except for the bulk modulus, the room-temperature elastic constants are all lower than those of iron; and their temperature dependencies are regular in the studied temperature region.

Key words: Bulk modulus; compressibility; iron alloy; maraging steel; nickel alloy; Poisson ratio; shear modulus; sound velocity; Young's modulus.

† Contribution of NBS, not subject to copyright.

* NRC-NBS Postdoctoral Research Associate, 1975-6.

INTRODUCTION

Elastic properties of a 300-grade maraging steel (18 Ni, 9 Co, 5 Mo) were studied between room temperature and liquid-helium temperature. Elastic constants were determined by measuring the velocities of both longitudinal and transverse ultrasonic waves in a polycrystalline aggregate. The following constants are reported here: C_ℓ = longitudinal modulus, G = shear modulus, B = bulk modulus, E = Young's modulus, and ν = Poisson's ratio.

Maraging steels exhibit some of the best available combinations of high strength and high toughness at room temperature.[1] Some alloy steels with high nickel contents also have good toughness at cryogenic temperatures. However, the usual heat treatment of maraging steels would probably embrittle them at these temperatures. Thus, maraging steels would probably be used at low temperatures in their annealed conditions. An annealed 300-grade maraging steel was studied (300 indicates a yield stress of approximately 300 x 10^6 psi). This alloy has a body-centered-cubic crystal structure, and it is ferromagnetic at room temperature. Other grades of annealed maraging steels are expected to be similar elastically because of their similar chemical compositions.

Elastic constants are interesting for two principal reasons. First, elastic constants are related directly to interatomic forces; thus, they are connected with a variety of solid-state phenomena, including maximum attainable strengths, phase stabilities, and lattice specific heats. Second, elastic constants are essential design parameters; the elastic constants must be known to compute deflections due to applied loads or stresses due to temperature changes of constrained components.

While some data on the temperature dependence of the Young's modulus of a 250-grade maraging steel are available[2], data on the other elastic constants (shear modulus, bulk modulus, Poisson's ratio) and on other grades of maraging steel have not been reported. Furthermore, because of the many elastic-constant anomalies exhibited by iron-nickel alloys (both those with higher and lower nickel contents than maraging steels), and because of the complicated chemistry of maraging steels, their elastic behavior cannot be estimated confidently by usual predictive methods. Therefore, detailed experimental studies of the elastic behavior of these alloys are required.

EXPERIMENTAL

Material

The studied material was obtained from a commercial source in the form of a 10 x 23 x 108 cm ingot. The chemical (mill) analysis of the material by weight is: 18.41 Ni, 9.27 Co, 4.95 Mo, 0.002 C, 0.12 Al, 0.01 Mn, 0.006 P, 0.003 S, 0.01 Si, 0.59 Ti, balance Fe. The Rockwell B hardness is 105, and the mass density is 8.188 g/cm^3 as determined by Archimedes's method using distilled water as a standard.

Room-Temperature Sound Velocities

Room-temperature sound velocities were measured by a pulse technique.[3] Briefly, a quartz piezoelectric transducer with a fundamental resonance frequency of 10 MHz was cemented with phenyl salycilate (salol) to one end of a specimen having flat and parallel faces. The specimen in this case was a 1.25 x 1.25 x 1.6 cm parallelpiped with opposite faces ground flat and parallel within 2.5 μm. Ultrasonic pulses about one μs in duration were sent into the specimen by electrically exciting the transducer. The pulses propagated through the specimen, reflected from

the end, and propagated back. The echoes were detected by the transducer and displayed on an oscilloscope. The sound velocity was computed by

$$v = 2\ell/t \qquad (1)$$

where ℓ is the specimen length and t is the transit (round-trip) time. On the oscilloscope, t was the time between subsequent echoes. The oscilloscope was calibrated against a precision time-mark generator. An x-cut quartz transducer was used for longitudinal waves, and an ac-cut quartz transducer was used for transverse waves.

Low-Temperature Sound Velocities

Low-temperature measurements of the sound velocities were made by a pulse-superposition technique.[4] Briefly, the repetition rate of the pulse was increased so that each pulse coincided with the second echo of the preceding pulse. Since the excitation voltage was large compared with the echo voltages, the oscilloscope display consisted of alternating pulses of excitation voltages and "echo" voltages where the "echo" voltage represented the sum of all odd-numbered echoes of the non-superimposed case. Because of interference effects, the envelope of the summed odd-numbered echoes is highly sensitive to small changes in the ultrasonic velocity that are caused, in this case, by cooling.

The transducer-specimen bonding material was a stopcock grease. Temperatures were monitored with a chromel-constantan thermocouple placed near the specimen. Cooling rates were about 2 K/min. The specimen holder was described previously.[5] Cooling was achieved by lowering the specimen-holder assembly stepwise into the ullage of a helium dewar. No thermal contraction corrections were made. For this alloy, the maximum thermal

contraction correction to the elastic constant, which applies at T = 0 K, is 0.3 percent. No correction was made for the transducer-cement-coupling phase shift; the McSkimin[6] analysis gives a correction of less than 0.5 percent in the velocity, assuming a maximum phase shift of π. The transit time was corrected to allow for the thickness of the transducer; this correction is approximately one cycle at 10 MHz; thus, the observed longitudinal-wave and transverse-wave transit times were reduced about 1.0 and 0.5 percent, respectively.

RESULTS

Room-temperature sound velocities are given in Table 1. Velocities were measured in three orthogonal directions for three orthogonal polarizations. The experimental uncertainties in these velocities are estimated to be 0.5%.

Longitudinal and shear elastic constants were computed from the velocities according to

$$C_\ell = \rho v_\ell^2 \tag{2}$$

and

$$G = C_t = \rho v_t^2 \tag{3}$$

where ρ is the mass density. The uncertainty of these elastic constants is estimated to be 1%.

The temperature variations of C_ℓ and C_t are shown in Figs. 1 and 2. Curves in those figures are least-squares fits of the data to the Varshni[7] relationship:

$$C = C^o - \frac{s}{\exp(t/T) - 1} \tag{4}$$

where C is C_ℓ or C_t, C^o, s, and t are adjustable parameters, and T is temperature. The value of C at T = 0 K is C^o, and -s/t is the high-temperature limit of the temperature derivative dC/dT. By invoking an Einstein oscillator model, it can be shown that t is the Einstein temperature. Parameters C^o, s, and t are given in Table II. Average differences between measured and curve values are 0.04 and 0.05 percent for the longitudinal and transverse cases, respectively.

Temperature variations of Young's modulus, the bulk modulus, and Poisson's ratio are shown in Figs. 3-5. These elastic constants were computed from Eq. (4) and the parameters in Table II using the relationships:

$$B = C_\ell - (4/3)G \tag{5}$$

$$E = 9GB/(G + 3B) \tag{6}$$

and

$$\nu = (E/2G) - 1 \tag{7}$$

The experimental uncertainties of these elastic constants are estimated to be ± 1% Values of these elastic constants at selected temperatures are given in Table III, and temperature coefficients of the elastic constants are given in Table IV.

DISCUSSION

The present study is discussed in two parts: the room-temperature elastic constants and the changes of the elastic constants due to cooling to liquid-helium temperature.

As shown in Table III, the Young's and shear moduli of the steel are about twenty percent lower than those of unalloyed iron, the bulk modulus

is about the same, and Poisson's ratio is about ten percent higher. Usually, the elastic-stiffness constants of alloys are lower than those of their base metal. Two of the three principal alloying elements in the steel -- nickel[11] and molybdenum[12] -- lower the elastic stiffnesses of iron, while cobalt raises them.

Nickel has the largest effect of the three. Thus, it is appropriate to compare the elastic constants of the steel with those of the corresponding iron-nickel alloy, and this is done in Table III. Except for the bulk modulus, the elastic constants of the steel are very close to those of an iron-18 nickel alloy. Cobalt and molybdenum seem to have very little effect on Young's modulus, the shear modulus, and Poisson's ratio, that is, on elastic constants that are determined either entirely or largely by the resistance of a material to shear deformations.

The bulk modulus is determined by the resistance of a material to dilatational deformations, and it is surprising that the bulk moduli of the steel and of unalloyed iron are the same. There appears to be no simple explanation for the unexpectedly high bulk modulus of the maraging steel. The usual effects of alloying are that the bulk modulus changes approximately in the same way as Young's modulus and the shear modulus. However, there is no <u>a priori</u> requirement that the bulk and shear moduli change similarly, and the present case is an interesting departure from usual behavior. Possible explanations for this effect may lie in the high bulk modulus of molybdenum, which is fifty percent higher than that of iron. Of all the elastic constants, the bulk modulus would be expected to come closest to a Vegard-law type behavior[13] because it is the most structure-independent elastic constant, depending much more on atomic volume than on other factors. Also, the bulk modulus is the elastic constant least affected by the usual magnetic energies that contribute to the elastic constants of iron-base alloys.[14]

As shown in the figures, the temperature behavior of the elastic constants of maraging steel is quite regular; that is, qualitatively the same as that exhibited by almost all simple metals and alloys. The salient features of regular behavior are: zero slope at zero temperature, as required by the third law of thermodynamics, continuous decrease with increasing temperature, consistent with the softening of interatomic bonding forces due to increased thermal vibrations; and a linear slope at high temperatures.

The regular temperature behavior of the maraging steel is unexpected. While no low-temperature elastic constants have been reported previously for body-centered-cubic iron alloys with so high a nickel content, some data exist for lower nickel content alloys. Weston, Naimon, and Ledbetter[10] reported the low-temperature elastic constants of iron-nickel alloys containing 3.5, 5, 6, and 9 percent nickel. These alloys show regular behavior above about 40 K, but are anomalous at lower temperatures. The anomalies are due, presumably, to magnetic transitions. But the maraging steel shows no such behavior. It is well known that iron-nickel alloys containing more than about 30 percent nickel are face-centered cubic and have very large anomalies in their elastic constants between room temperature and liquid-helium temperature. These anomalies are also due to magnetic effects.[15]

The maraging steel has considerably higher temperature coefficients of Young's modulus and the shear modulus than unalloyed iron, as shown in Table IV. This suggests that the steel has a considerably lower Debye temperature than iron, consistent with the Debye temperatures reported for b.c.c. iron-nickel alloys by Weston, Naimon, and Ledbetter.[10] Practically, this means the elastic stiffness of the steel, upon cooling, increases more than in the case of iron.

CONCLUSIONS

In the present study, several conclusions were reached concerning the elastic properties of annealed 300-grade maraging steel:

1. The Young's modulus, shear modulus, and Poisson's ratio are all about 15 percent lower than the corresponding elastic constants of unalloyed iron. The bulk modulus is the same as that of iron.

2. Except for the bulk modulus, all the elastic constants are essentially the same as those of an iron-18 nickel alloy, implying that the effects of cobalt and molybdenum on the elastic constants are effectively canceled.

3. All the elastic constants show regular behavior over the entire studied temperature range, 4-300 K, indicating the absence of magnetic transitions that have been reported at low temperatures in other body-centered-cubic iron-nickel alloys.

4. Temperature coefficients of Young's modulus and the shear modulus are about 40 percent higher than those of unalloyed iron. This implies a lower Debye temperature for the steel.

ACKNOWLEDGMENT

This study was supported by the Advanced Research Projects Agency of the U.S. Department of Defense.

REFERENCES

1. A Maynée, J. M. Drapier, J. Dumont, D. Coutsouradis and L. Habraken: Cobalt - Containing High-Strength Steels, 1974, p. 50, Centre D'Information Du Cobalt, Brussels.
2. F. R. Schwartzberg, S. H. Osgood, and R. Herzog: Cryogenic Materials Data Handbook, 1968, U.S. Air Force Systems Command (Tech. Doc. Rpt. No. AFML-TDR-64-280).
3. R. T. Beyer and S. V. Letcher: Physical Ultrasonics, 1969, pp. 79-87, Academic, New York.
4. H. J. McSkimin: J. Acoust. Soc. Amer., 1961, Vol. 33, pp. 12-16.
5. E. R. Naimon, W. F. Weston, and H. M. Ledbetter: Cryogenics, 1974, Vol. 14, pp. 246-49.
6. H. J. McSkimin: IRE Trans. Ultrasonics Engr., 1957, Vol. 5, pp. 25-43.
7. Y. P. Varshni: Phys. Rev., 1970, Vol. 2, pp. 3952-3955.
8. J. A. Rayne and B. S. Chandrasekhar: Phys. Rev., 1961, Vol. 122, pp. 1714-1716.
9. H. M. Ledbetter and R. P. Reed: J. Phys. Chem. Ref. Data, 1974, Vol. 2, pp. 531-618.
10. W. F. Weston, E. R. Naimon, and H. M. Ledbetter: in Properties of Materials for Liquefied Natural Gas Tankage, ASTM STP 579, 1975, pp. 397-420, Amer. Soc. Test. Mater., Philadelphia.
11. W. C. Leslie: Metall. Trans., 1972, Vol. 3, pp. 5-26.
12. S. Takeuchi: J. Phys. Soc. Japan, 1969, Vol. 27, pp. 929-940.
13. N. F. Mott: Rep. Prog. Phys., 1962, Vol. 25, pp. 218-243.
14. W. F. Brown: Phys. Rev., 1936, Vol. 50, pp. 1165-1172.
15. G. Hausch: Phys. Status Solidi., 1973, Vol. 15, pp. 501-510.

Table I. Room-temperature acoustic-wave velocities in units of 10^6 cm/s

Propagation Direction	v_ℓ	v_{t_1}	v_{t_2}
x	0.5673	0.2882	0.2879
y	0.5648	0.2881	0.2865
z	0.5589	0.2848	0.2841

Table II. Parameters determined from the Varshni equation

	Longitudinal	Transverse
C^o, 10^{11} N/m^2	2.654	0.7047
s, 10^{11} N/m^2	0.1036	0.05959
t, K	221.9	264.4

Table III. Elastic constants of a 300-grade maraging steel at selected temperatures and those of iron and iron-18 nickel at room temperature in units of 10^{11} N/m^2 except ν, which is dimensionless.

Material	Temp. (K)	E	G	B	ν
Maraging steel, 300-grade	300	1.756	0.663	1.676	0.325
	200	1.806	0.683	1.692	0.322
	100	1.848	0.700	1.708	0.320
	0	1.859	0.705	1.714	0.319
Iron[a]	300	2.140	0.831	1.680	0.288
Iron-18 Ni[b]	300	1.710	0.653	1.463	0.309

a. Ref. 8

b. Ref. 9, 10

Table IV. Temperature coefficients $(1/C)(dC/dT)$ at room temperature in units of 10^{-4} K^{-1}.

Material	E	G	B	ν
Maraging steel	-2.92	-3.18	-0.98	1.04
Unalloyed iron[2]	-2.11	-2.31	-0.90	0.95

a. Computed from data in Ref. 8 using a Voigt-Reuss-Hill arithmetic average.

LIST OF FIGURES

Fig. 1. Longitudinal modulus $C_\ell = \rho v_\ell^2$ for 300-grade maraging steel as a function of temperature.

Fig. 2. Shear modulus $G = C_t = \rho v_t^2$ for 300-grade maraging steel.

Fig. 3. Young's modulus for 300-grade maraging steel.

Fig. 4. Bulk modulus for 300-grade maraging steel.

Fig. 5. Poisson's ratio for 300-grade maraging steel.

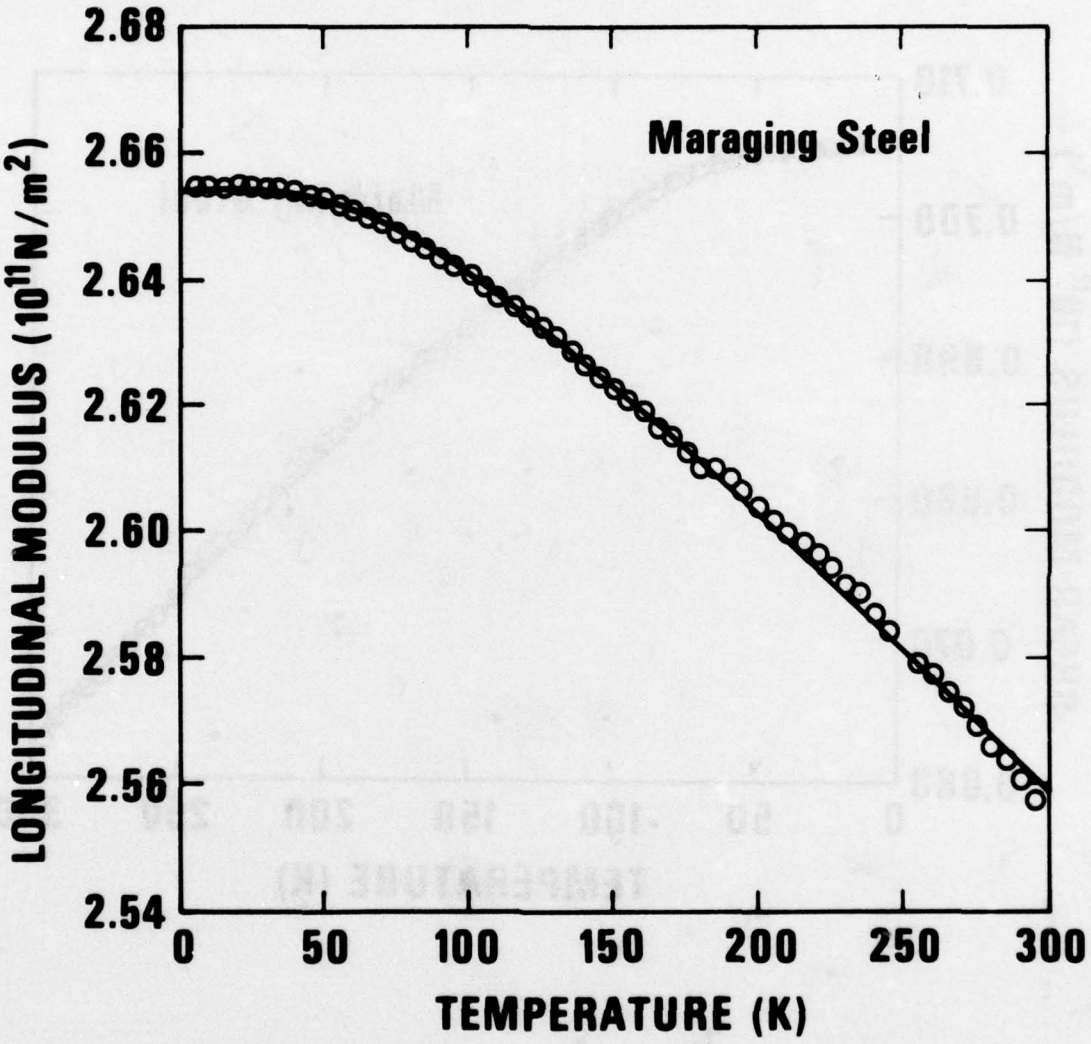


Fig. 1. Longitudinal modulus $C_\ell = \rho v_\ell^2$ for 300-grade maraging steel as a function of temperature.

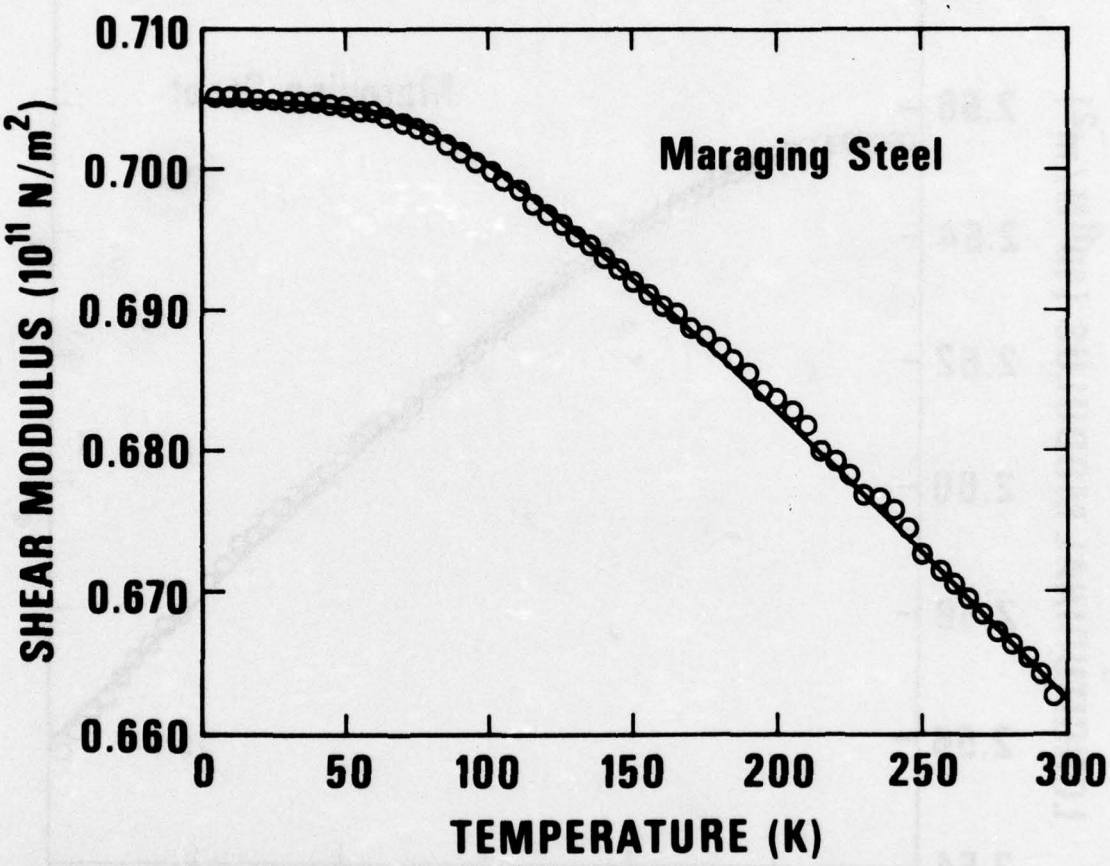


Fig. 2. Shear modulus $G = C_t = \rho v_t^2$ for 300-grade maraging steel.

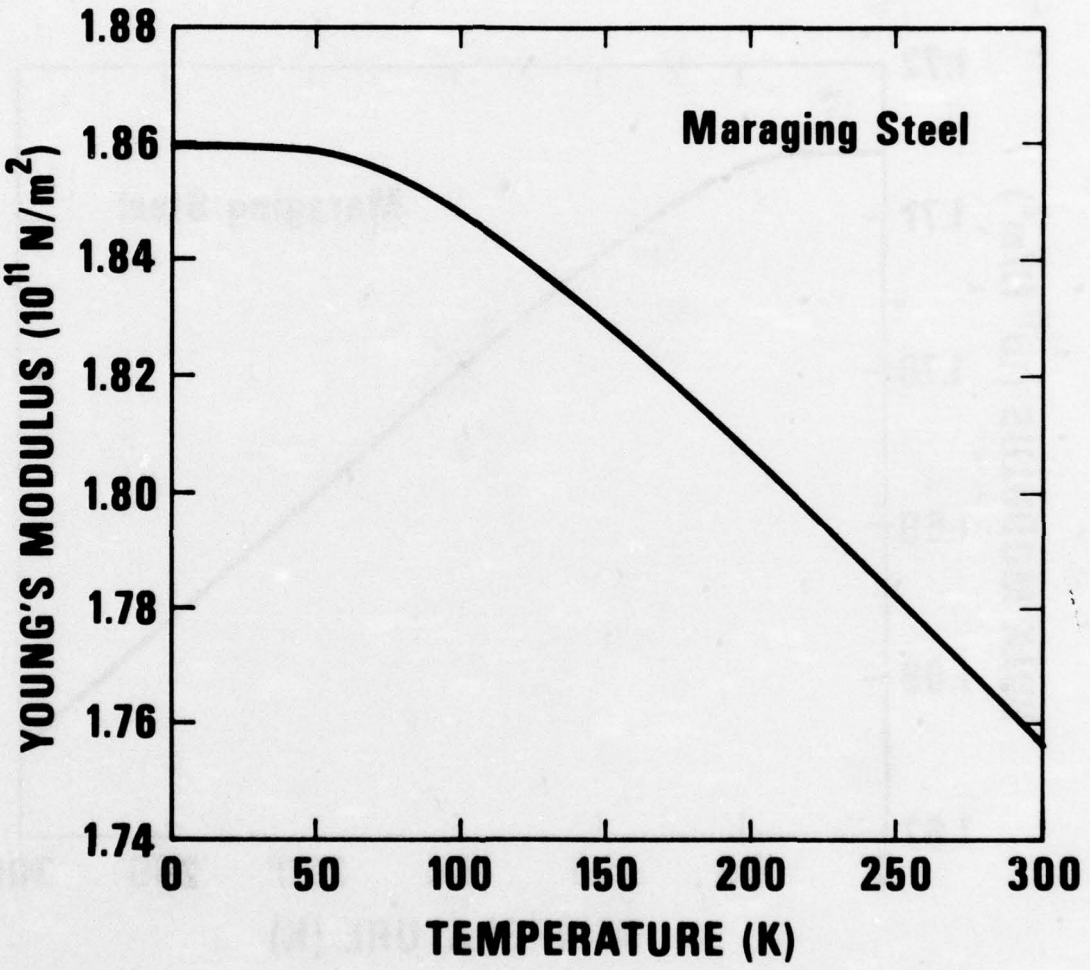


Fig. 3. Young's modulus for 300-grade maraging steel.

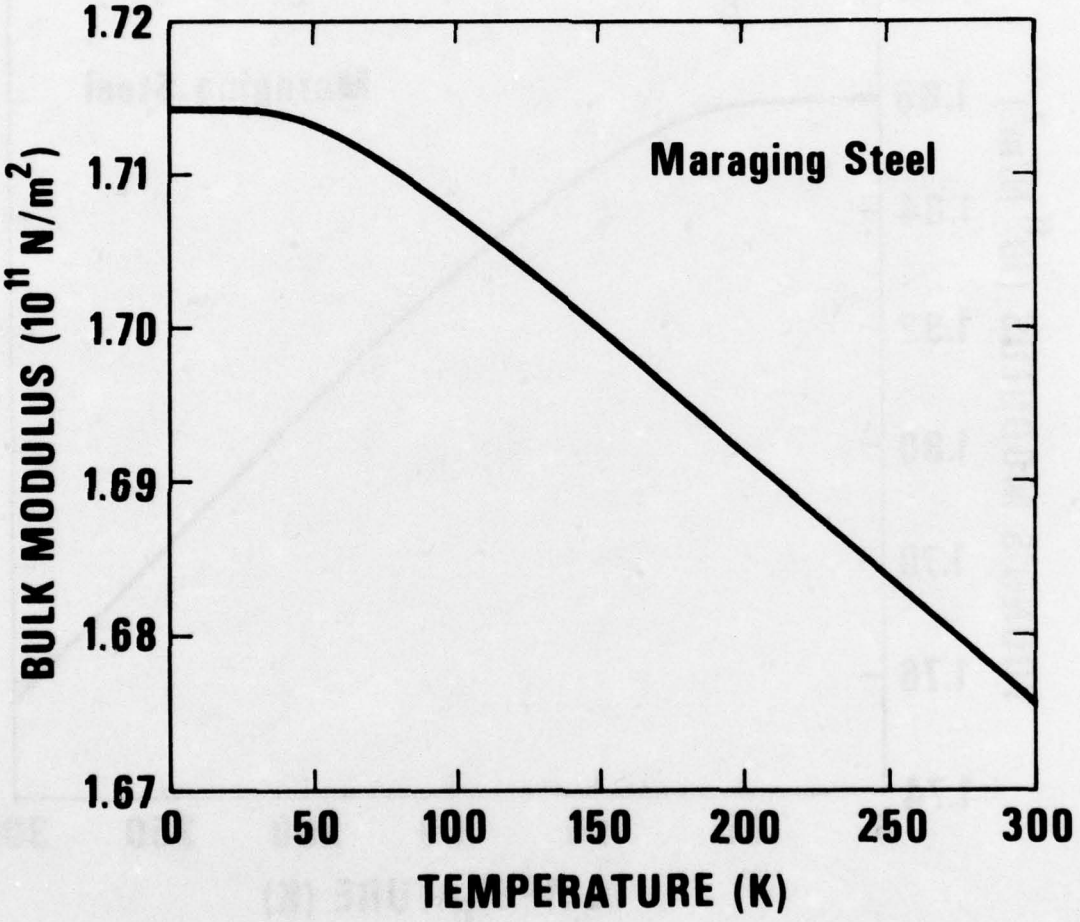


Fig. 4. Bulk modulus for 300-grade maraging steel.

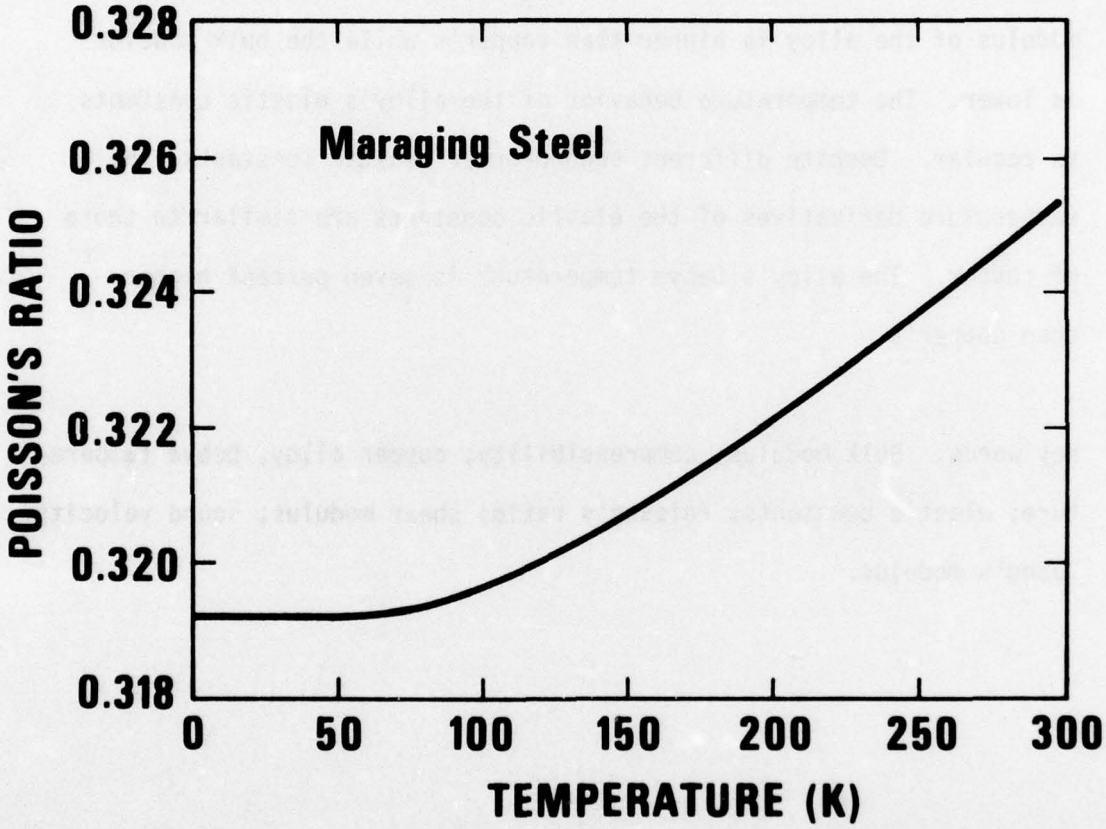


Fig. 5. Poisson's ratio for 300-grade maraging steel.

Low-Temperature Elastic Properties of a Precipitation-Hardened Copper Alloy*

H. M. Ledbetter

Cryogenics Div., Institute for Basic Standards, NBS, Boulder, CO 80302

ABSTRACT

Elastic properties of a copper-cadium-chromium precipitation-hardened alloy differ considerably from those of copper. The shear modulus of the alloy is higher than copper's while the bulk modulus is lower. The temperature behavior of the alloy's elastic constants is regular. Despite different second-order elastic constants, the temperature derivatives of the elastic constants are similar to those of copper. The alloy's Debye temperature is seven percent higher than copper's.

Key words: Bulk modulus; compressibility; copper alloy; Debye temperature; elastic constants; Poisson's ratio; shear modulus; sound velocity; Young's modulus.

* Contribution of NBS, not subject to copyright.

INTRODUCTION

Precipitation is a principal hardening-and-strengthening mechanism in metals and alloys. Precipitates can significantly raise a material's yield strength by pinning the dislocations that initiate plastic flow. Because precipitates occupy a small volume fraction, they usually have little effect on most physical properties, including the elastic constants.

Ledbetter[1] reported recently that a precipitation-hardened copper-0.3 cadmium-0.3 chromium alloy has elastic constants that differ about fifteen percent from copper's. Such large elastic-constant changes in such a dilute alloy are unusual, but not necessarily anomalous. The alloy <u>is</u> anomalous because its shear modulus is higher than copper's while its bulk modulus is lower. Most elastic-constant models predict that the shear and bulk moduli always change in the same direction when affected by metallurgical variables such as composition, temperature, or pressure. Usually, only variables that introduce anisotropies -- mechanical deformation or structural phase transformation, for example -- are expected to change the shear and bulk moduli oppositely. But there are no such anisotropies in a precipitation-hardened alloy; precipitates are usually equiaxed, and no macroscopic elastic anisotropy was detected in the studied alloy.

Deviation of the Cu-Cd-Cr alloy's Poisson ratio from that of copper also represents a significant departure from usual behavior. Köster and Franz[2] pointed out that Poisson's ratio is quite insensitive to most metallurgical variables, including alloying. The reason for this is simple. Poisson's ratio, ν, is given by

$$\nu = \frac{1}{2}\,\frac{3B - 2G}{3B + G} \qquad (1)$$

where B and G denote the bulk and shear moduli, respectively. By differentiation

$$\frac{d\nu}{\nu} = \frac{9GB}{(G + 3B)\,(3B - 2G)}\left(\frac{dB}{B} - \frac{dG}{G}\right) \qquad (2)$$

which gives for $\nu \simeq 1/3$, a typical value for metals, including copper,

$$\frac{d\nu}{\nu} \simeq \frac{4}{9}\left(\frac{dB}{B} - \frac{dG}{G}\right) \qquad (3)$$

Thus, the usually parallel changes in B and G tend to cancel and leave ν unaffected. But opposite changes in B and G affect ν additively. Thus, the precipitation-hardened Cu-Cd-Cr alloy is an exceptional case where a large change in ν can occur in a macroscopically isotropic material.

The low-temperature elastic constants of this alloy are of interest for two reasons. First, how do the alloy's temperature coefficients compare with copper's? Second, what are the alloy's low-temperature elastic constants, which are needed for the cryogenic engineering applications of this material. Because the room-temperature elastic constants are anomalous, no basis exists for scaling the alloy's temperature dependence against copper's temperature dependence. And there is neither a model nor a data base for estimating the alloy's low-temperature elastic constants. In fact, very few low-temperature elastic-property studies have been reported for precipitation-hardened materials.

The main purpose here is to report the elastic constants of a precipitation-hardened Cu-Cd-Cr alloy between room temperature and liquid-helium temperature. Two experimental methods were used: resonance (60 kHz) and pulse (10 MHz). For most purposes, the differences between the dynamic elastic constants reported here and the more familiar static elastic constants determined by stress-strain methods are small; for the shear modulus they are zero at all temperatures; for dilatation-type elastic constants such as the bulk modulus, they are zero at zero temperature, and they increase to a few percent at room temperature.

EXPERIMENTAL

A. Material

The studied material is the same as that reported on previously[1], and it is characterized as follows: The weight-percent chemical composition is: 0.31 Cd, 0.33 Cr, < 0.01 Pb, < 0.01 Fe, < 0.01 Ni, < 0.01 Mn, balance Cu. Mass density determined by hydrostatic weighing is 8.94 g/cm^3. Hardness is 57.5 on a Rockwell 30-T scale. ASTM grain size number is five. The material was produced by the Phelps Dodge Corporation in the form of a flat extrusion 2.5 cm x 10.8 cm in cross-section. The extrusion temperature was 1227 K and the subsequent aging temperature was 866 K for 1 h. The commercial designation of this material is alloy PD 135. (This trade name is used here to identify the material; it is not an NBS endorsement of a particular product).

B. Specimens

For ultrasonic-pulse measurements, a "cube" was prepared measuring 0.9 x 1.3 x 1.3 cm. Opposite faces were ground flat and parallel within 3 μm. For torsional resonance measurements, cylindrical specimens were prepared 0.4 cm in diameter and 2.1 cm long.

C. Methods

Experimental methods used in the present study were described previously[3,4]. Thus, only a brief outline is given here.

Room-temperature pulse measurements were made using McSkimin's[5] method. A quartz transducer with a fundamental frequency between 6 and 10 MHz was bonded to a specimen with salol. X-cut transducers were used for longitudinal waves and ac-cut transducers were used for shear waves. The pulse length was about one μs. The ultra-sound velocity was computed from

$$v = 2\ell/t \qquad (4)$$

where ℓ = specimen length and t = transit (round-trip) time. On an oscilloscope, t was the time between subsequent echoes. The oscilloscope was calibrated with a precision time-mark generator. Elastic constants are computed from the velocities by

$$C = \rho v^2 \qquad (5)$$

where ρ = mass density.

Low-temperature pulse measurements were made with a superposition method[5] where the envelope of the sum of the odd-numbered echoes is maximized by tuning the carrier frequency, f. Neglecting thermal contraction, the change in ultrasonic velocity is

$$\Delta v/v = \Delta f/f \qquad (6)$$

Details of the specimen holder, cooling procedures, and temperature measurements were given previously.[3] Measurements were made at intervals of 5 K with a cooling rate of about 2 K/min.

The torsional (shear) modulus was also measured with a composite-oscillator method[6] during cooling. The oscillator has three components: a quartz-crystal driver, a quartz-crystal gage, and a specimen. The resonant frequency of the specimen is

$$f_s^2 = f_0^2 + (f_0^2 - f_q^2)(m_q/m_s)(r_q/r_s)^2 \qquad (7)$$

where m = mass, r = radius of cylindrical specimen, and the subscripts s, o, and q denote specimen, oscillator, and quartz. For torsional resonance, the shear modulus is then

$$G = 4\rho\ell_s^2 f_s^2 \qquad (8)$$

where ℓ = length. During cooling, the frequency f_o is tuned to the resonance condition, which is determined by a maximum output voltage across a gage crystal.

RESULTS

Results of the present study are shown in Table 1 and in Figs. 1-5. Both the C_1 and the $G = C_t$ data were least-squares fitted to a relationship due to Varshni[7]:

$$C(T) = C^\circ - s/[\exp(t/T) - 1] \qquad (9)$$

where C°, s, and t are adjustable parameters and T is temperature. The fitting-parameter values are given in Table 2. Average differences between measured and curve values are 0.07 and 0.06 percent for the longitudinal and transverse cases, respectively. The elastic constants B, E, and ν were computed from the smoothed results of Eq. (9) and the relationships

$$B = C_1 - (4/3)G \qquad (10)$$

$$E = 9GB/(G + 3B) \qquad (11)$$

and

$$\nu = (E/2G) - 1 \qquad (12)$$

Temperature coefficients of the elastic constants are given in Table 3. Point-to-point 2σ imprecisions in the modulus-temperature data are estimated to be less than 0.1 percent. Uncertainties in the room-temperature experimental moduli are given in Table 1. No significant elastic-constant anisotropy was detected. Resonance results for the shear modulus agreed exactly with pulse results, and they are not reported here.

DISCUSSION

The temperature dependencies of the elastic constants of PD 135 resemble closely those of unalloyed copper,[8] as shown in Figs. 1-5. Both materials exhibit regular behavior: linearity at high temperatures, continuously decreasing slope due to cooling, relative flatness at low

temperatures, and zero slope at zero temperature in accordance with the third law of thermodynamics. Hiki, Thomas, and Granato[9] showed that the temperature derivatives dC/dT depend on elastic constants of second, third, and fourth order. Thus, second-order elastic constants (which are reported here) of two materials can differ considerably, but their temperature derivatives dC/dT can be similar.

The Debye temperature Θ is of considerable interest in a variety of applications, especially at cryogenic temperatures. It can be computed from the elastic constants by

$$\Theta = \frac{h}{k} \left(\frac{3N}{4\pi V_a}\right)^{1/3} v_m \qquad (13)$$

where h = Planck's constant, k = Boltzmann's constant, N = Avogadro's number, V_a = atomic volume, and the mean acoustic-wave velocity is

$$v_m^{-3} = \frac{1}{3} \left(v_\ell^{-3} + 2v_t^{-3}\right) \qquad (14)$$

Using elastic data extrapolated to T = 0 K, the Debye Θ of the Cu-Cd-Cr alloy is 369 K; for copper, Θ = 344 K. The higher Debye Θ of the alloy follows directly from its higher shear modulus.

CONCLUSIONS

The following principal results and conclusions emerge from the

present study:

(1) All the elastic constants of the studied Cu-Cd-Cr precipitation-hardened alloy behave regularly during cooling from room temperature to liquid-helium temperature.

(2) Despite the differences in the elastic constants of Cu-Cd-Cr and Cu, the constants change similarly during cooling. This would be expected if the third-order and fourth-order elastic constants of the two materials were similar.

(3) The Debye temperature of the Cu-Cd-Cr alloy is seven percent higher than that of copper, reflecting the higher elastic shear modulus of the alloy.

ACKNOWLEDGMENTS

This work was supported by the Advanced Research Projects Agency of the U.S. Department of Defense. The PD 135 alloy was originally supplied by B. H. Wilson of the Phelps Dodge Copper Products Co. to Dr. J. M. Wells of the Westinghouse Research Laboratories who provided the material and its characterization to NBS.

REFERENCES

1. H. M. Ledbetter, submitted for publication.
2. W. Köster and H. Franz, Met. Rev. 6, 1-55 (1961).
3. E. R. Naimon, W. F. Weston, and H. M. Ledbetter, Cryogenics 14, 246-249 (1974).
4. W. F. Weston, J. Appl. Phys. 46, 4458-4465 (1975).
5. H. J. McSkimin, IRE Trans. Ultrasonics Engr. 5, 25-43 (1957).
6. J. Marx, Rev. Sci. Instrum. 22, 503-509 (1951).
7. Y. P. Varshni, Phys. Rev. 2, 3952-3955 (1970).
8. W. C. Overton and J. Gaffney, Phys. Rev. 98, 969-977 (1955).
9. Y. Hiki, J. F. Thomas, and A. V. Granato, Phys. Rev. 153, 764-771 (1967).

Table 1. Elastic constants of a precipitation-hardened copper-chromium-cadium alloy (PD 135) at selected temperatures. C_l = longitudinal modulus, C_t = transverse modulus, G = shear modulus, E = Young's modulus, B = bulk modulus, and ν = Poisson's ratio. Units are $10^{11} N/m^2$, except ν, which is dimensionless. C_l and C_t are the measured quantities, and their standard deviations are 0.009 and 0.014 based on 12 and 10 measurements, respectively.

T, K	C_l	$G=C_t$	E	B	ν
300	1.876	0.540	1.402	1.154	0.298
250	1.894	0.550	1.424	1.161	0.296
200	1.913	0.558	1.445	1.169	0.294
150	1.931	0.566	1.464	1.176	0.293
100	1.948	0.573	1.479	1.184	0.292
76	1.953	0.575	1.484	1.188	0.292
4	1.960	0.576	1.487	1.192	0.292

Table 2. Fitting parameters for the Varshni relationship, Eq. (9).

	Longitudinal	Transverse
C°, 10^{11} N/m^2	1.960	0.576
s, $10^{11} N/m^2$	0.0873	0.0652
t, K	211.1	313.0

Table 3. Temperature derivatives (1/C) (dC/dT) of the elastic constants C at room temperature, in units of 10^{-4} K^{-1}.

	B	E	G	ν
Cu-Cd-Cr (PD 135)	-1.24	-3.20	-3.51	1.34
Copper[a]	-1.02	-3.31	-3.70	0.85

a. Reference 8

LIST OF FIGURES

Fig. 1. Temperature dependence of the longitudinal modulus of a copper-based, cadmium-chromium, precipitation-hardened alloy (PD 135) compared to that of copper. The longitudinal modulus is defined in terms of the bulk and shear modulus in Eq. (10). The copper values are higher. Copper values were obtained from Overton and Gaffney[8] using a Voigt-Reuss-Hill averaging method.

Fig. 2. Temperature dependence of the shear, or transverse modulus of copper alloy PD 135. The copper values are lower.

Fig. 3. Temperature dependence of the Young's modulus of copper alloy PD 135.

Fig. 4. Temperature dependence of the bulk modulus, or reciprocal compressibility of copper alloy PD 135. Note that copper values are higher. Compare with the shear modulus shown in Fig. 2 where they are lower.

Fig. 5. Temperature dependence of the Poisson's ratio of copper alloy PD 135. The relatively large difference between this alloy and copper results because B and G are affected oppositely by precipitation-hardening.

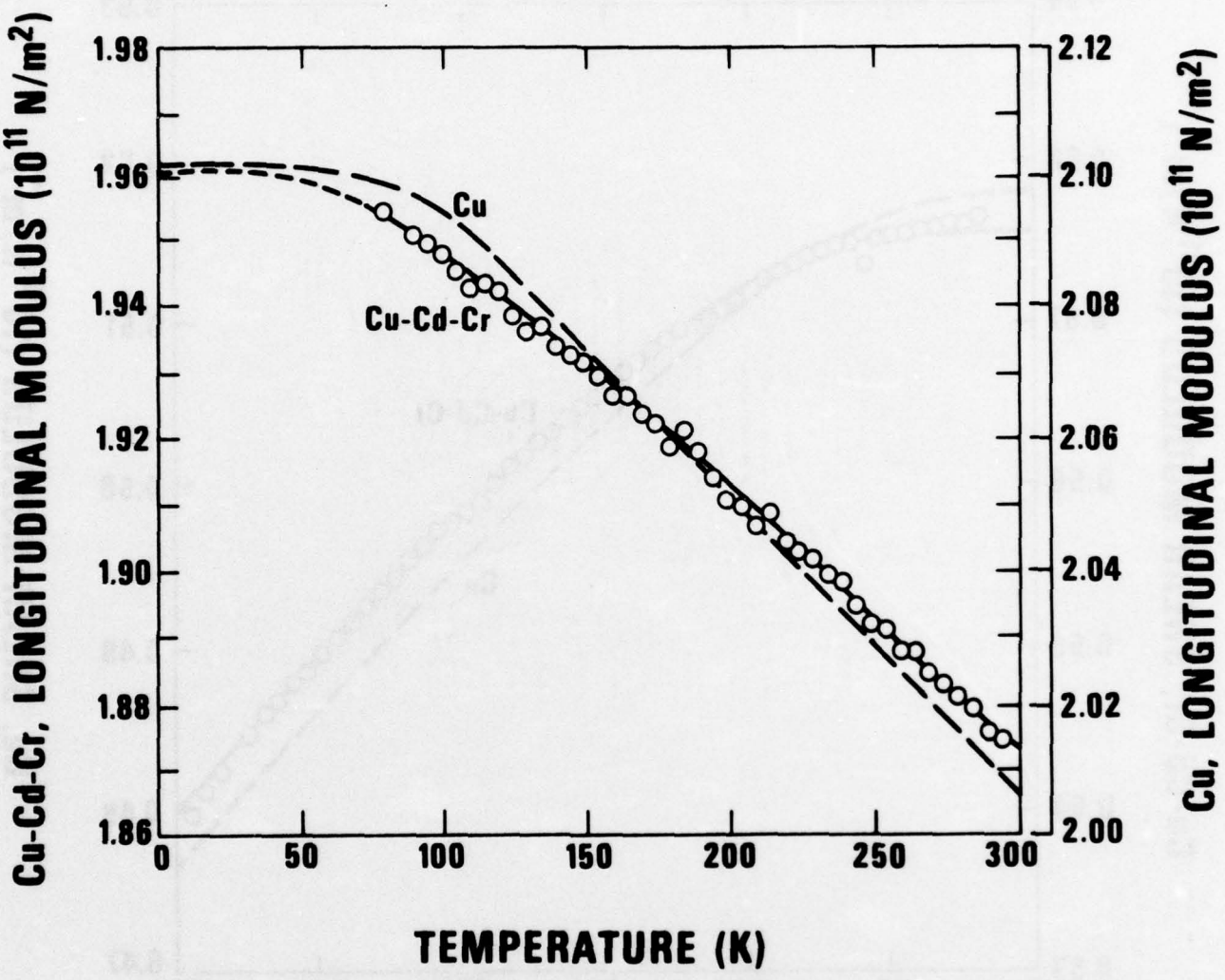


Fig. 1. Temperature dependence of the longitudinal modulus of a copper-based, cadmium-chromium, precipitation-hardened alloy (PD 135) compared to that of copper. The longitudinal modulus is defined in terms of the bulk and shear modulus in Eq. (10). Note copper values are higher.

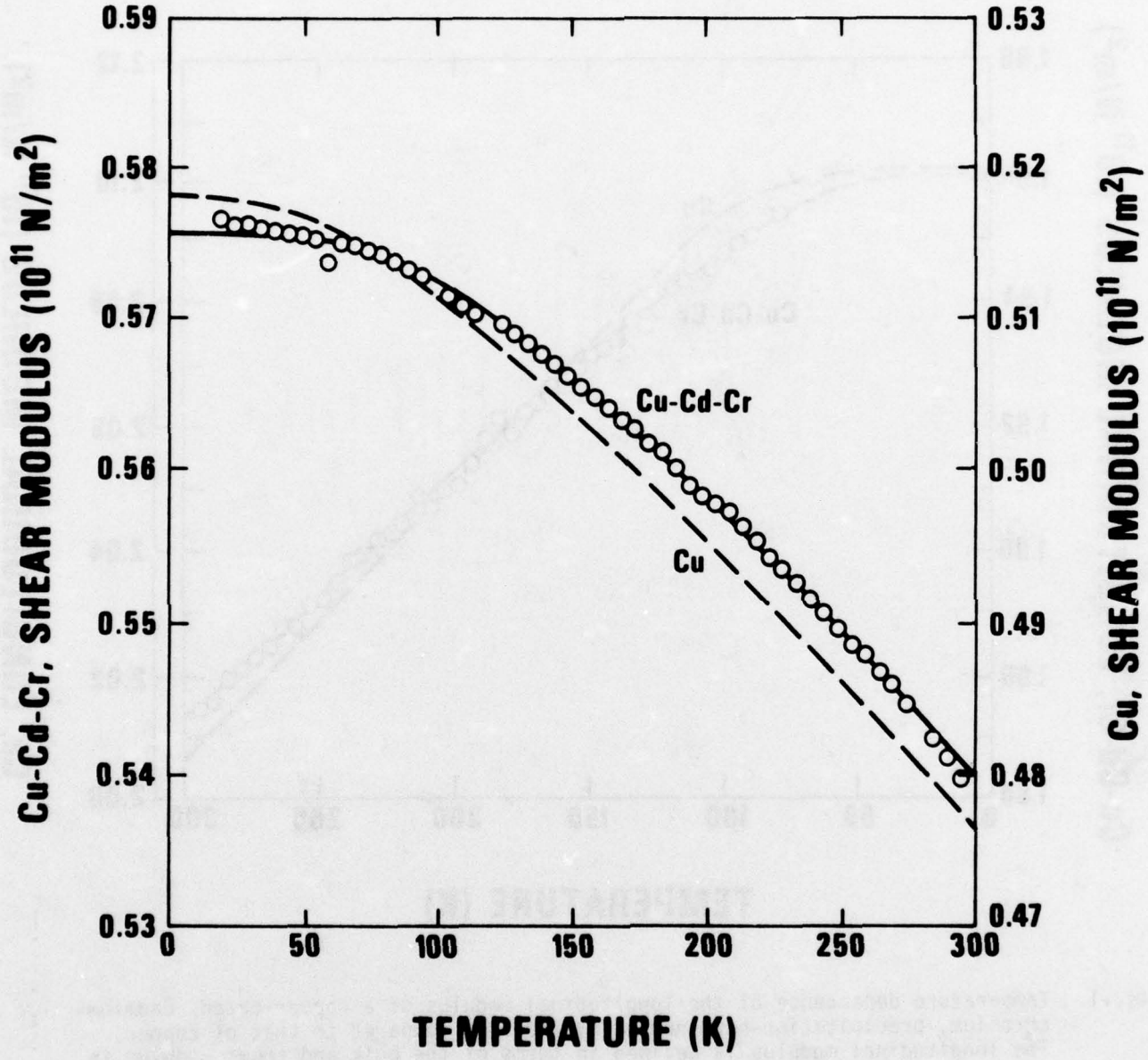


Fig. 2. Temperature dependence of the shear, or transverse, modulus of copper alloy PD 135. Note that copper values are lower.

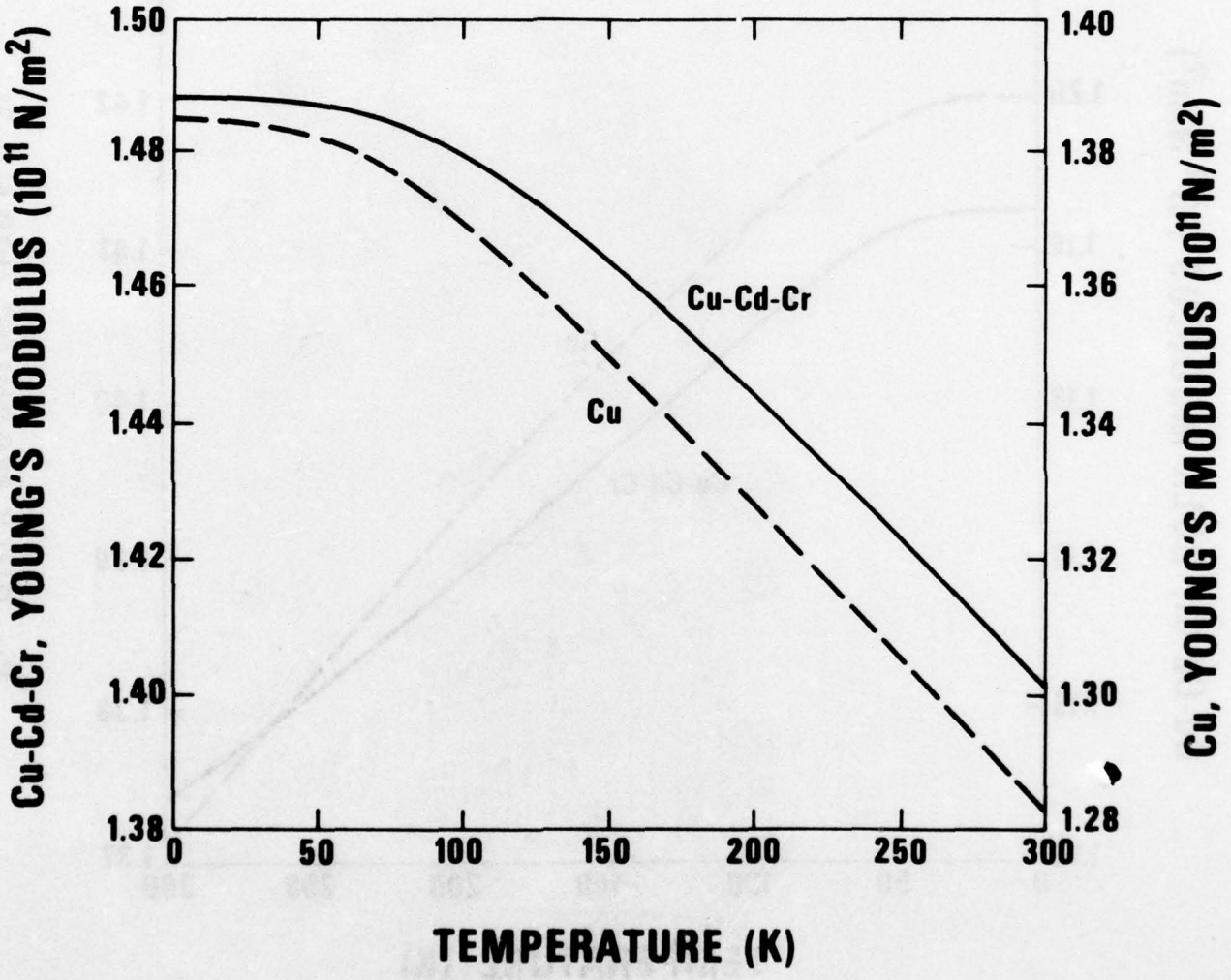


Fig. 3. Temperature dependence of the Young's modulus of copper alloy PD 135.

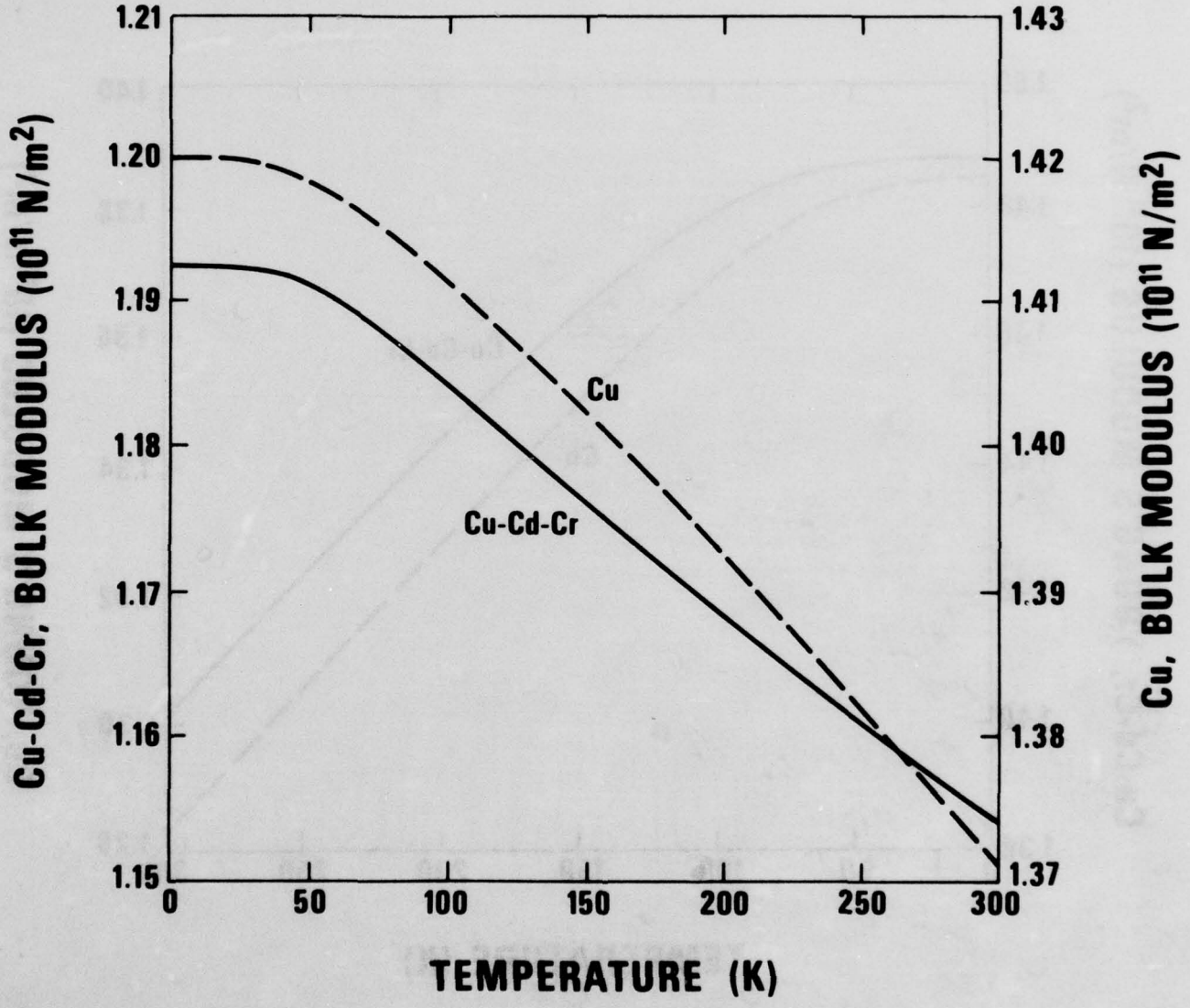


Fig. 4. Temperature dependence of the bulk modulus, or reciprocal compressibility, of copper alloy PD 135. Note that copper values are higher. Compare with the shear modulus shown in Fig. 2 where they are lower.

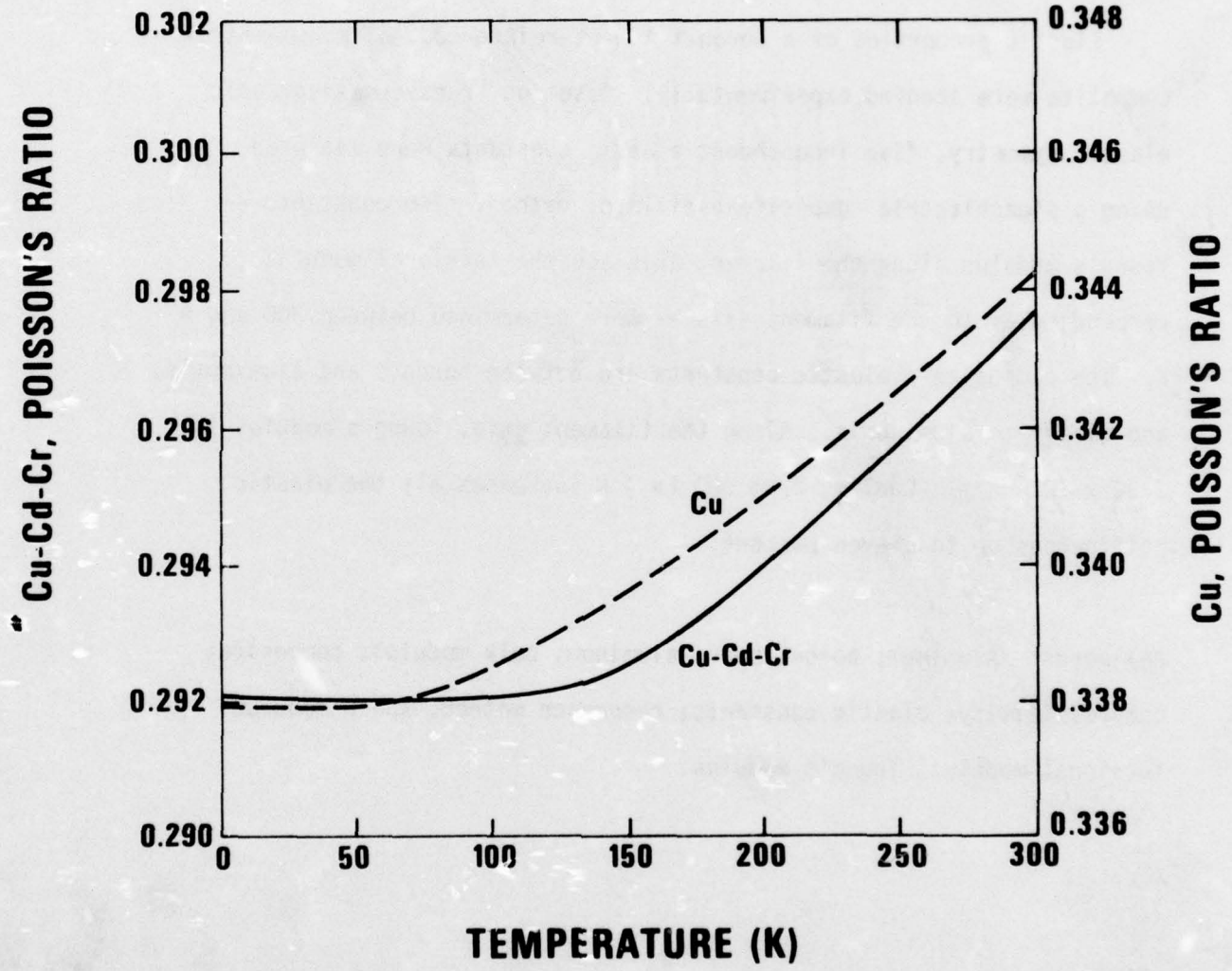


Fig. 5. Temperature dependence of the Poisson's ratio of copper alloy PD 135. The relatively large difference between the alloy and copper is due to B and G being affected oppositely by precipitation-hardening.

Elastic Properties of a Boron-Aluminum Composite at Low Temperatures+

D. T. Read* and H. M. Ledbetter

Cryogenics Division
Institute for Basic Standards
National Bureau of Standards
Boulder, Colorado 80302

ABSTRACT

Elastic properties of a boron-filament-reinforced, aluminum-matrix composite were studied experimentally. Assuming transverse-isotropic elastic symmetry, five independent elastic constants were measured using a piezoelectric composite-oscillator method. Two constants -- Young's modulus along the filament axis and the torsional modulus perpendicular to the filament axis -- were determined between 300 and 4 K. The composite's elastic constants are between boron's and aluminum's, and closer to aluminum's. Along the filament axis, Young's modulus is 2.30×10^{11} N/m^2. Cooling from 300 to 4 K increases all the elastic stiffnesses up to eleven percent.

Key words: Aluminum; boron; boron-aluminum; bulk modulus; composite; compressibility; elastic constants; resonance method; shear modulus; torsional modulus; Young's modulus.

+ Contribution of NBS, not subject to copyright.

* NRC-NBS Postdoctoral Research Associate, 1975-76.

INTRODUCTION

Boron-aluminum composites are useful because they have high elastic-modulus/density ratios (specific modulus) and high strength/density ratios (specific strength). These properties, together with comparatively high electrical conductivity, make boron-aluminum a candidate material for various structural applications: aerospace components; leisure products such as tennis rackets, bicycle frames, and golf shafts; orthotic and prosthetic devices; truck bodies; etc.

Elastic constants are important parameters in designing such components because they relate the mechanical load on a component to its resulting deflection. Elastic constants are also related to the basic structure of a material, to ultimate strengths, to melting points, and to phase stabilities. In a composite, elastic constants are due to both constituent properties and constituent interactions. Thus, besides describing the average stress-strain response of the composite, elastic constants provide tests of the mechanical and geometrical relationships between composite properties and constituent properties and a basis for improved material development.

EXPERIMENTAL

The studied boron-aluminum composite consisted of 0.14 mm (5.5×10^{-3} in)-diameter, uniaxial boron filaments in a matrix of aluminum alloy 6061. The aluminum alloy was in the F-tempered condition (as diffusion bonded). The composite, containing 48 percent filaments by volume, was fabricated as a plate measuring about 10 x 10 x 1.1 cm. The plate contained about 70 plies (as computed from an average ply thickness of 0.165 mm found by Kasen and Schramm[1] for a fifteen-ply sheet of the same material). This unusually thick composite was required for the elastic-constant measurements described below.

Elastic constants were measured by dynamic techniques. Such techniques have been used in our laboratory to obtain accurate values of complete sets of elastic constants of many polycrystalline materials, and to measure elastic-constant temperature dependencies between 300 and 4 K. There are two main dynamic techniques: pulse and resonance; each has many variations.

In the present study, a three-component composite-oscillator resonance technique[2] was used principally. A composite oscillator (consisting of a quartz-crystal driver, an identical quartz gage-crystal, and a specimen) was resonated by applying a sinusoidal voltage to electrodes plated on the drive crystal. The resulting oscillation amplitude was monitored by observing the voltage developed between electrodes plated on the gage crystal. The drive-signal frequency was varied until a sharp maximum indicating resonance was observed in the gage-voltage amplitude. The elastic constant was computed from the composite-oscillator resonant frequency, the specimen mass, the quartz-crystals' mass, the quartz-crystals' resonant frequency with no specimen attached, and the specimen's mass density and length. By using quartz crystals with orientations and electrode configurations appropriate for extensional oscillation, the Young's modulus, E, of the specimen was measured. Quartz crystals driven in torsional oscillation were used to measure the torsional (or shear) modulus, G.

Elastic constants at low temperatures were measured by enclosing the composite oscillator in a vacuum-tight container and lowering it gradually into a dewar containing liquid helium. As the composite oscillator cooled (about 2 K/min), its resonant frequency was measured. The oscillator temperature was monitored with a thermocouple. Data were obtained between 300 and 4 K using this technique, which was

described previously in more detail.[3]

ANISOTROPIC ELASTICITY

A boron-aluminum composite is macroscopically elastically anisotropic because the filaments affect the elastic modulus more strongly along the filament direction than in other directions. Using the notation indicated in Fig. 1, the Young's modulus along the filament direction, E_{33}, is expected to be larger than either E_{11} or E_{22}. Values of E_{11}, E_{22} and the Young's modulus along other directions in the 1-2 plane may be different. However, if the filaments are oriented randomly in the 1-2 plane, and if the matrix is elastically isotropic, then Young's modulus is invariant in the 1-2 plane (transversely isotropic). A hexagonal packing of filaments produces the same effect. The aluminum matrix in this composite is almost elastically isotropic. Based on the filament arrangement shown in Fig. 2, transverse isotropy was assumed. This assumption is often made for composites of this type, and it is not expected to introduce significant errors.

Elastic anisotropies of single crystals have been studied extensively; the theory[4] of materials with complete rotational symmetry about an axis and translational symmetry along that axis is used for hexagonal single crystals. This formalism also applies to macroscopic treatments of filament-reinforced composites that are transversely isotropic. In this theory, such a material has five independent elastic constants; all other elastic constants can be computed from these. At least five independent measurements are required to determine these five values. Four can be obtained by measuring Young's modulus along the filament direction (E_{33}), the torsional modulus about the filament direction ($G_{44} = G_{55}$), Young's modulus perpendicular to the filament direction (E_{11}), and the torsional modulus about an axis perpendicular

to the filament direction $2(G_{44}^{-1} + G_{66}^{-1})^{-1}$. The fifth elastic constant must be obtained from specimens oriented obliquely to the filament axis. Such off-axis specimens often exhibit coupling between the desired resonance mode and unwanted modes. This problem is analogous to pure and non-pure modes in transmitting ultrasonic pulses. This coupling can sometimes be avoided by appropriately choosing the angle between the filament axis and the specimen axis. Even if this coupling occurs, however, its effects can often be alleviated by allowing the specimen to vibrate unconstrained.

Six specimens were used. Four of these were cut either parallel or perpendicular to the filament axis. Two oblique specimens were prepared with filament-axis/specimen-axis angles of 78° and 45°. The specimen orientations are illustrated in Fig. 1. The 78° specimen was computed to have zero coupling between the desired resonance mode and other modes; zero coupling occurs when the elastic compliance S_{15} is zero in the coordinate system of the specimen. The 78° specimen had the disadvantage that its Young's modulus was quite insensitive to the fifth elastic constant, S_{13}. Therefore, a 45° specimen was prepared. For this orientation, Young's modulus is quite sensitive to S_{13}. Mode coupling in this specimen was minimized by allowing the sample to hang almost freely in resonance.

RESULTS

The six measured modulus values are given in Table 1. The subscripts indicate that the modulus was measured using specimens with filaments parallel, perpendicular, or at an angle Θ to the specimen axis. The elastic-compliance matrix S_{ij} was computed from these data by the relationships:

$$S_{33} = 1/E_{\parallel} \tag{1}$$

$$S_{11} = S_{22} = 1/E_{\perp} \tag{2}$$

$$S_{44} = S_{55} = 1/G_{\parallel} \tag{3}$$

$$S_{66} = 2/G_{\perp} - 1/G_{\parallel} \tag{4}$$

$$S_{13} = \frac{(1/E_{\theta}) - S_{33}\cos^4\theta - S_{11}\sin^4\theta}{2\cos^2\theta \sin^2\theta} - \frac{1}{2} S_{55} \tag{5}$$

$$S_{12} = S_{11} - \frac{1}{2} S_{66} \tag{6}$$

The two off-axis specimens gave slightly different S_{13} values. The value chosen was that producing the smallest total deviation of the two calculated and measured E_{θ} values. Room-temperature elastic compliances are given in Table 2.

The practical elastic constants can be calculated from the compliances using the relationships shown in Eq. (7), which reflects either transverse-isotropic or hexagonal symmetry:

$$
S_{ij} = \begin{array}{cccccc}
S_{11}=1/E_{11} & S_{12}=-\nu_{12}/E_{11} & S_{13}=-\nu_{31}/E_{33} & 0 & 0 & 0 \\
 & S_{11}=1/E_{11} & S_{13}=-\nu_{31}/E_{33} & 0 & 0 & 0 \\
 & & S_{33}=1/E_{33} & 0 & 0 & 0 \\
 & & & S_{44}=1/G_{44} & 0 & 0 \\
 & & & & S_{44}=1/G_{44} & 0 \\
 & & & & & S_{66}=1/G_{66}
\end{array} \qquad (7)
$$

Some other useful relationships are:

$$S_{ij} = S_{ji} \qquad (8)$$

$$\nu_{ij} = S_{ij}/S_{ii} \qquad (9)$$

$$\nu_{21}/E_{22} = \nu_{12}/E_{11} \qquad (10)$$

$$S_{66} = 2(S_{11} - S_{12}) = (1 + \nu_{12})/E_{11} \qquad (11)$$

The practical elastic constants measured in the present study are given in Table 3 together with data of Gieske and Allred[5] and of Schramm and Kasen.[1] The measured room-temperature Young's and shear moduli listed in Table 1 are estimated to have inaccuracies of less than one percent. The values listed in Tables 2 and 3 include additional uncertainties due to propagation of errors and to the assumption of transverse isotropy.

The Poisson's ratios ν_{13} and ν_{31} were obtained by indirectly measuring S_{13} using two off-axis specimens. The Young's moduli in these specimens are insensitive to S_{13}, and the values of ν_{13} and ν_{31} may have inaccuracies as high as twenty percent.

The $E_{\parallel}$ and $G_{\perp}$ temperature dependencies were measured between 300 and 4 K; and the results are given in Figs. 2 and 3 and, for selected temperatures, in Table 4. In these figures, most of the data-point deviations from the dashed curves are believed to be measurement artifacts and not real material behavior. However, the deviations in the region 0-30 K are believed to be real. The dashed curve is a three-parameter fit to the data using Varshni's[6] equation; it represents typical elastic-stiffness behavior of typical metals. The measured elastic-constant changes with temperature are believed to be inaccurate to less than 0.05 percent of the elastic constant.

DISCUSSION

As expected, the composite's room-temperature elastic stiffnesses are between aluminum's and boron's. Also as expected, the boron-filament contribution to Young's modulus is largest along the filament axis. But, two of the composite's Poisson's ratios are outside the boron and aluminum bounds. No reason for this is obvious.

The room-temperature elastic constants measured in the present study are compared with previously reported values, both dynamic and static, in Table 3. The two dynamic-study sets of results differ by five to fourteen percent. This disagreement is not surprising because different filament volume fractions and different measurement methods were used in these studies. Poisson's ratios disagree between the two sets of dynamic measurements; reasons for this are unclear, but they

are probably due to Poisson's ratio being measured indirectly, and less accurately. The two static elastic-stiffness values disagree about fourteen percent with the dynamic values, and in opposite senses. The static Poisson's ratios disagree considerably more. Reasons for this disagreement are unclear.

The composites elastic-constant temperature dependencies are expected to be between those of boron and aluminum. Aluminum's values are well known.[7] Boron's values have not been reported, but they are expected to be much lower than aluminum's because boron has a much higher Debye temperature (1362 K)[8] than aluminum (430 K).[7] The measured $E_{\parallel}$ and $G_{\perp}$, temperature dependencies shown in Table 4, are lower than the temperature dependencies of aluminum, as expected.

The measured stiffness-constant temperature dependencies of boron-aluminum shown in Figs. 2 and 3 show regular behavior; that is, the stiffnesses increase approximately linearly with decreasing temperature near room temperature, and increase less steeply with decreasing temperature. This regular behavior resembles aluminum's, and it shows that nothing exceptional occurs during cooling to the stiffnesses, except for a small rise below about 30 K.

The composite's geometry suggests that $E_{\parallel}$ is the elastic modulus that behaves most like boron's and least like aluminum's. The high value of $E_{\parallel}$ compared to the composite's other moduli shows this is so. Because $E_{\parallel}$ is most like boron's modulus, it must be the Young's moduli of boron-aluminum with the weakest temperature dependence because boron's temperature dependence is probably small. This explains why the change in $E_{\parallel}$ on cooling from 300 to 4 K is only four percent,

significantly less than the changes observed in aluminum during cooling and less than the temperature dependencies of boron-aluminum's other moduli. Similar considerations indicate that $E_{\parallel}$ and $G_{\perp}$ must have the strongest temperature dependencies of boron-aluminum's moduli, and that $G_{\parallel}$ should have a slightly weaker temperature dependence than $G_{\perp}$. Also, $E_{\perp}$ is expected to increase by ten percent or less upon cooling from 300 to 4 K. This increase must exceed four percent and is probably close to ten. Similarly, $G_{\parallel}$ should increase by up to, and probably close to, ten percent or less during cooling from 300 to 4 K. Thus, all the practical stiffness moduli of boron-aluminum increase eleven percent or less on cooling from 300 to 0 K, and Young's modulus along the fiber axis increases four percent on cooling.

CONCLUSIONS

The following principal findings and conclusions emerge from the present study:

1. Single-crystal methods can be used to study the anisotropic elastic properties of a composite such as boron-aluminum.

2. For dynamic studies of a composite's elastic constants, resonance methods have some distinct advantages over pulse methods. For example, the composite reported on here gave very poor, virtually unusable, pulse-echo patters in the 6-10 MHz region. However, the resonance peaks were well defined over a broad frequency range.

3. The elastic constants of a uniaxial boron-aluminum composite (48 percent volume fraction of filaments) are between those of boron and aluminum, and closer to aluminum's.

4. The composite's elastic stiffnesses increase by eleven percent or less during cooling from 300 to 4 K; Young's modulus along the

filaments increases four percent during this cooling.

5. Except for a non-zero slope at temperatures below 30 K, the composite's elastic constants show essentially regular behavior during cooling.

ACKNOWLEDGMENTS

This study was supported by the Advanced Research Projects Agency of the U.S. Department of Defense.

REFERENCES

1. R. A. Schramm and M. B. Kasen, in National Bureau of Standards Report No. NBSIR 75-828, 1975.
2. J. Marx, Rev. Sci. Instrum. 22, 503-509 (1951).
3. W. F. Weston, J. Appl. Phys. 46, 4458-4465 (1975).
4. J. F. Nye, Physical Properties of Crystals (Oxford U. P., Oxford, 1960), p. 141.
5. J. G. Gieske and R. E. Allred, Exper. Mech. 14, 158-165 (1974).
6. Y. P. Varshni, Phys. Rev. 2, 3952-3955 (1970).
7. E. R. Naimon, H. M. Ledbetter, and W. F. Weston, J. Mater. Sci. 10, 1309-1316 (1975).
8. K. A. Gschneider, in Solid State Physics, edited by F. Seitz and D. Turnbull (Academic, New York, 1964), Vol. 16, p. 370.

Table 1. Direct experimental elastic stiffnesses of a boron-aluminum composite containing 0.48 volume fraction of filaments, in units of $10^{11} N/m^2$.

Constant	Value
$E_{\parallel}$	2.30
$E_{\perp}$	1.39
$G_{\parallel}$	0.568
$G_{\perp}$	0.515
$E_{78°}$	1.41
$E_{45°}$	1.45

Table 2. Elastic-compliance matrix of boron-aluminum composite at 300 K as displayed in Eq. (7); matrix is symmetrical about main diagonal; derived from results in Table 1; units are 10^{-11} m^2/N.

0.719	-0.343	-0.074	0	0	0
	0.719	-0.074	0	0	0
		0.435	0	0	0
			1.755	0	0
				1.755	0
					2.123

Table 3. Practical elastic constants of boron-aluminum (0.48 volume fraction boron) at T = 295 K.

	Present	Gieske, Allred[a]	Schramm, Kasen[b]	Boron[c]	Aluminum[d]
E_{11} (10^{11} N/m^2)	1.39	1.34	--	4.41	0.703
E_{22} "	1.39	1.19	1.61	4.41	0.703
E_{33} "	2.30	2.11	2.00	4.41	0.703
G_{44} "	0.569	0.539	0.397	2.03	0.259
G_{55} "	0.569	0.542	--	2.03	0.259
G_{66} "	0.471	0.455	--	2.03	0.259
ν_{12} (dimensionless)	0.48	0.41	--	0.086	0.357
ν_{31} "	0.17	0.25	--	0.086	0.357
ν_{32} "	0.17	0.23	0.299	0.086	0.357

a. Linear interpolation of data between 0.34 and 0.54 volume fractions of boron.
b. Static test results, Ref. 1.
c. Ref. 8, polycrystalline, $\nu = (E/2G) - 1$.
d. Ref. 7, polycrystalline.

Table 4. Elastic stiffnesses of boron-aluminum at selected temperatures; in units of $10^{11} N/m^2$.

	300 K	200 K	100 K	0 K
$E_{\parallel}$	2.30	2.33	2.37	2.38
$G_{\perp}$	0.515	0.543	0.569	0.578

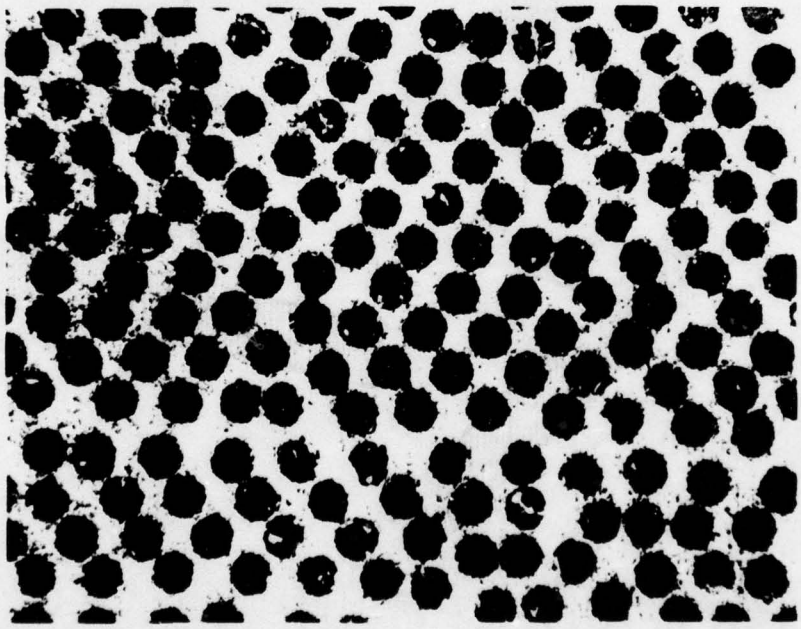


Fig. 2. Photomicrograph showing distribution of 0.14-mm-diameter boron filaments in aluminum matrix. Plane of photo is perpendicular to filaments.

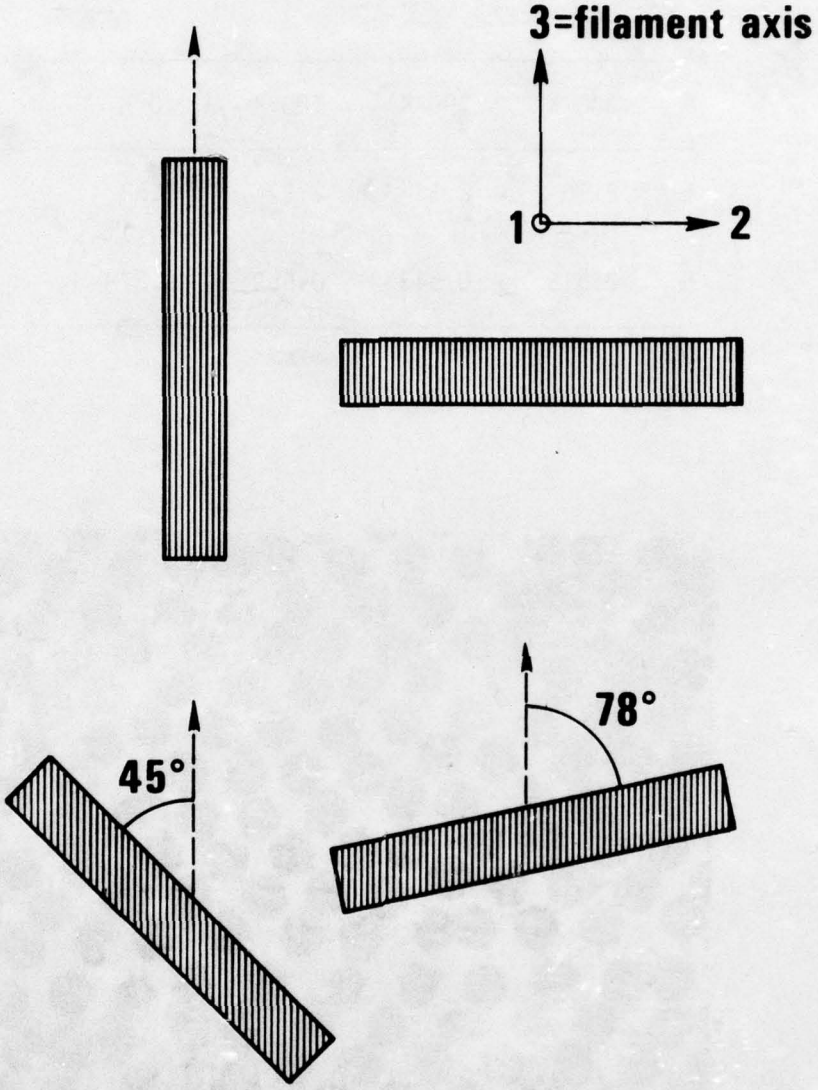


Fig. 1. Co-ordinate system, specimen geometries, and specimen orientations. Striping indicates filaments.

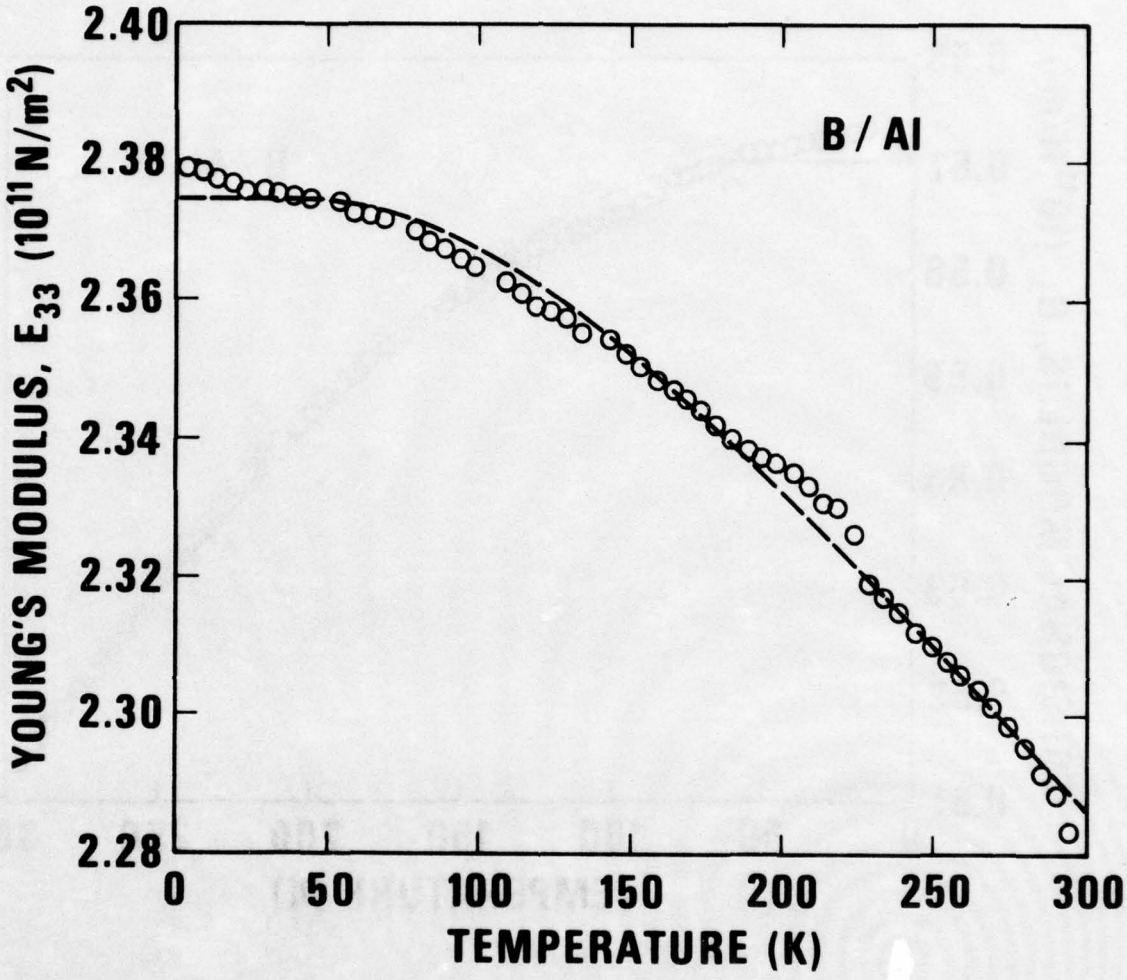


Fig. 3. Temperature dependence of Young's modulus $E_{\parallel} = E_{33}$ along the filament axis. Dashed curve is a semi-empirical three-parameter equation that is typical for most materials. Except for the rise below 30 K, data scatter are experimental artifacts.

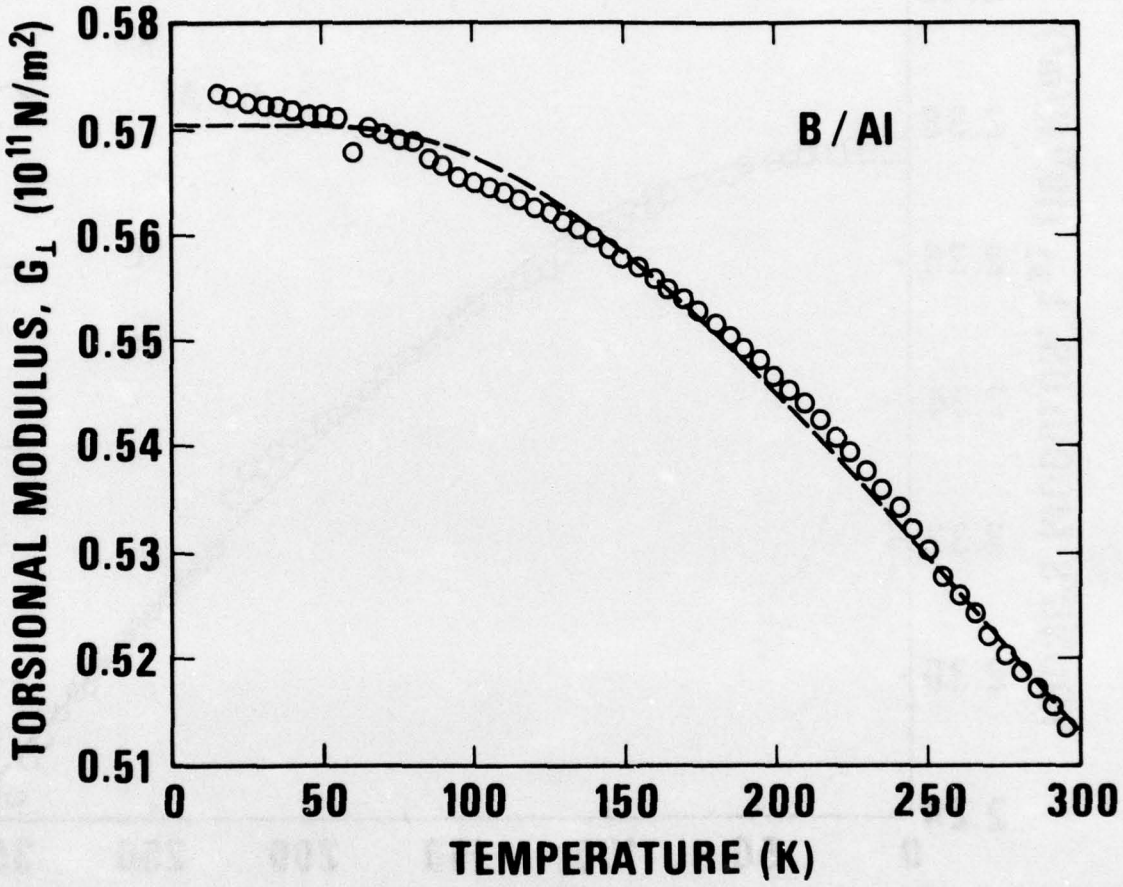


Fig. 4. Temperature dependence of the torsional (or shear) modulus about an axis perpendicular to the filament axis. See caption of Fig. 3.

ANOMALOUS LOW-TEMPERATURE ELASTIC BEHAVIOR OF A NITROGEN-STRENGTHENED CHROMIUM-MANGANESE STAINLESS STEEL[+]

H. M. Ledbetter
Institute for Basic Standards
National Bureau of Standards
Boulder, Colorado 80302

ABSTRACT

Elastic constants of an Fe-21Cr-6Ni-9Mn stainless steel were studied experimentally by both pulse and resonance methods. The room-temperature elastic constants are similar to those of AISI 304. During cooling to liquid-nitrogen temperature (76 K), all the elastic constants behave anomalously below 130 K. As in Fe-Mn alloys, these anomalies are probably due to a Néel transition. A further anomaly in the compressibility at 190 K suggests a second transition of unknown nature.

Key words: Bulk modulus; compressibility; elastic constants; Poisson's ratio; pulse method; resonance method; shear modulus; stainless steel; sound velocity; Young's modulus.

[+] Contribution of NBS, not subject to copyright.

ANOMALOUS LOW-TEMPERATURE ELASTIC BEHAVIOR OF A NITROGEN-STRENGTHENED CHROMIUM-MANGANESE STAINLESS STEEL

H. M. Ledbetter
Institute for Basic Standards
National Bureau of Standards
Boulder, Colorado 80302

Nitrogen-strengthened chromium-manganese stainless steels containing other alloying elements such as nickel and molybdenum are promising alloys for low-temperature applications.[1] They have high strength and toughness at cryogenic temperatures, and they resist stress-induced martensitic transitions that are often accompanied by undesirable property changes. Some low-temperature mechanical and physical properties of these materials have been reported.[1] And other low-temperature studies are in progress, including fatigue-crack growth rate and fracture toughness[2] and tensile and strength properties of weldments.[3]

The purpose of the study reported here was to determine the low-temperature elastic properties of a nitrogen-strengthened steel containing 21 chromium, 6 nickel, and 9 manganese, percent by weight. This steel is commonly called 21-6-9. The applicable elastic properties are: Young's modulus, the shear modulus, the bulk modulus (reciprocal compressibility), and Poisson's ratio. Besides characterizing a material, the elastic constants are also essential for computing either stress-induced deflections or thermo-elastic stresses. Elastic constants are inherent in fracture mechanics; for example, the plane-strain stress-intensity factor, K_{Ic}, is computed from the elastic-plastic fracture criterion, J_{Ic}, by using Young's modulus and Poisson's ratio.

In the presently reported study, the elastic constants were determined by measuring the velocities, v, of longitudinal waves and shear waves in a thin-rod resonance experiment near 60 kHz and in an infinite-plate pulse experiment with a carrier frequency near 10 MHz. Elastic-stiffness constants, C, are computed by

$$C = \rho v^2 \qquad (1)$$

where ρ is the mass density. Depending on the velocity mode -- longitudinal, shear, extensional, torsional, etc. -- different types of elastic-stiffness constants are determined. The dynamic elastic constants were obtained because the measurements were made at high frequencies. These differ very little from the more-familiar static elastic constants that result from stress-strain-type experiments. For the bulk modulus, the difference is zero at zero temperature, and it increases to a few percent at room temperature. For the shear modulus, the difference is zero at all temperatures. Depending on their relative shear and dilatational parts, all other elastic constants fall between these two behavior bounds. For example, Young's modulus behaves nearly like the shear modulus because volume is nearly unaffected by uniaxial elastic deformation.

EXPERIMENTAL

A. Material

The steel was provided by Lawrence Livermore Laboratories in the form of a 50 x 50 x 3.6 cm plate that was hot-rolled (1366-1089 K) from a 30.5 x 30.5 x 10 cm slab in twelve steps with 90° rotations of the slab between rollings. The plate was annealed 1.5 h at 1283 K,

air cooled, annealed 1.5 h at 1366 K, and water quenched. This material has a hardness of R_B = 92, an average grain diameter of 0.16 mm, and a mass density of 7.838 g/cm^3 (determined by hydrostatic weighing). Its chemical composition in weight percent is: 19.75 Cr, 7.16 Ni; 9.46 Mn, 0.019 C, 0.15 Si, 0.004 P, 0.003 S, 0.28 N, balance Fe.

B. Specimens

For ultrasonic-pulse measurements, cylindrical specimens were prepared 1.7 cm in diameter and 0.5 to 1.0 cm long. Opposite faces were ground flat and parallel within 3 μm.

For resonance measurements, cylindrical specimens were prepared 0.4 cm in diameter and 4.2 and 2.6 cm long for the extensional and torsional modes, respectively.

C. Methods

Experimental methods used in the present study were described previously[4,5]. Thus, only a brief outline is given here.

Room-temperature pulse measurements were made with a McSkimin[6] method. A quartz transducer with a fundamental frequency between 6 and 10 MHz was bonded to a specimen with phenyl salicylate. X-cut transducers were used for longitudinal waves and ac-cut transducers were used for shear waves. The pulse length was about one μs. The ultra-sound velocity was computed from

$$v = 2\ell/t \qquad (2)$$

where ℓ = specimen length and t = transit (round-trip) time. On an oscilloscope, t was the time between subsequent echoes. The oscilloscope was calibrated with a precision time-mark generator.

Low-temperature pulse measurements were made with a superposition method[6] where the envelope of the sum of the odd-numbered echoes is maximized by tuning the carrier frequency, f. Neglecting thermal contraction, the ultrasonic-velocity change is

$$\Delta v/v = \Delta f/f \tag{3}$$

Details of the specimen holder, cooling procedures, and temperature measurements were given previously.[4] Measurements were made at intervals of 5 K with a cooling rate of about 2 K/min.

Young's modulus and the shear (torsional) modulus were also measured with a composite-oscillator method[5] during cooling. The resonance frequency of the specimen is computed from

$$f_s^2 = f_o^2 + (f_o^2 - f_q^2)m_q/m_s \tag{4}$$

where m = mass and the subscripts s, o, and q denote specimen, oscillator, and quartz. For an extensional resonance, Young's modulus is

$$E = 4\rho(\ell_s f_s)^2 \tag{5}$$

where ρ = mass density and ℓ = length.

RESULTS

Room-temperature elastic constants are given in Table I for both pulse and resonance cases. Resonance values of many of the elastic constants are not shown because they are much more inaccurate than those obtained by a pulse method.

Temperature variations of the two experimentally determined elastic constants -- the longitudinal and shear moduli -- are shown in Fig. 1. The temperature variations of the derived elastic constants -- Young's modulus, the bulk modulus, and Poisson's ratio -- are shown in Fig. 2. Resonance-method temperature data are not reported here because they contain higher inaccuracies than the pulse-method data. The two sets of data were consistent within a few percent.

Based on several measurements, the 2σ uncertainties in the room-temperature elastic constants are estimated to be $\pm$ 3%. The point-to-point imprecision in the temperature-dependence measurements is estimated to be $\pm$ 0.1%.

DISCUSSION

Results shown in Figs. 1 and 2 are surprising; all the elastic constants of Fe-21Cr-6Ni-9Mn behave anomalously during cooling. The primary purpose of this section, then, is to explain this alloy's anomalous temperature behavior. Any fundamental model-explanation is precluded by the alloy's complexity -- four major components, all transition metals with incomplete d shells that exhibit either ferromagnetism, antiferromagnetism, or both. But several alternative types of "explanation" are possible. The problem is -- why doesn't 21-6-9 show regular temperature behavior (indicated by the dashed curves in Fig. 1): zero slope at zero temperature, a T^4 dependence at low temperatures; and a decreasing linear behavior at higher, increasing temperatures? In the simplest models of solids, Debye or harmonic, elastic constants are temperature independent. But, regular temperature behavior is predicted by a quasi-harmonic approximation,[7] in which the vibrational energy is volume dependent.

Changes of crystal structure cannot explain the present results. Both α and ε phases can be produced from the γ phase in 21-6-9 at low

temperatures by mechanical stress. However, the stress used in the present study was infinitesimal (the strain is typically 10^{-6}), and no stress-induced phases are possible. Athermal martensitic transition can also be excluded because such transitions in ferrous alloys are always accompanied by large temperature hysteresis.[8] No hysteresis was observed in the present studies; within experimental error, elastic-constant/temperature curves were identical in heating, in cooling and in successive runs. Available data[9] indicate that the γ-ε martensitic transition increases Young's modulus, contrary to present observations. Thus, the anomalous temperature behavior has no structural origin.

Neither can present results be explained by the familiar ΔE effect due to linear magnetostriction, arising from either ferromagnetism or antiferromagnetism. Such effects are not observed in a saturating magnetic field because domain-wall motions are prevented. While no magnetic field was used in the present study, the high frequencies (10 MHz) that were used are equivalent in suppressing the ΔE effect because the domain-wall displacements cannot follow the oscillating stress.[10]

It is useful to compare the present results with studies on more-familiar stainless steels, Fe-Cr-Ni alloys, which have low-temperature elastic anomalies due to paramagnetic-antiferromagnetic transitions. For present purposes, 21-6-9 is an AISI-304-grade stainless steel containing an additional nine percent Mn. The elastic constants of these two alloys are quite similar, with the Young's and shear moduli of 21-6-9 being about three percent higher than those of AISI 304. The elastic properties of AISI 304 were reported between room temperature and liquid-helium temperature by Ledbetter, Weston, and Naimon[11] together with similar data for AISI 310, AISI 316, and A286. All these stainless

steels have elastic-constant anomalies below about 80 K. These anomalies were interpreted by invoking the Döring effect. Döring[10] showed thermodynamically that either a paramagnetic-ferromagnetic (Curie) transition or a paramagnetic-antiferromagnetic (Néel) transition must be accompanied by a Young's-modulus anomaly due to volume magnetostriction, which is manifested as the difference between Young's modulus at constant magnetic field and at constant magnetization. However, Döring's analysis does not account for an anomalous change in the shear modulus, and it is inapplicable to 21-6-9. Thus, an important difference exists between the low-temperature elastic anomalies in Fe-Cr-Ni and Fe-Cr-Ni-Mn alloys. Fe-Cr-Ni alloys are anomalous in every elastic constant except the shear modulus. Fe-Cr-Ni-Mn alloys are anomalous in every elastic constant. This difference is important for developing models of elastic behavior, and it can be identified only when continuous, complete sets of elastic constants are available over a wide temperature region.

Since Fe-21Cr-6Ni-9Mn behaves differently from Fe-Cr-Ni alloys, it is appropriate to compare it with Fe-Mn alloys. Several authors[9,12-15] have reported low-temperature elastic constants of these alloys, which are often called manganese steels. The present alloy compares closely with Fe-Mn alloys in several respects: (1) all elastic constants are anomalous; (2) the anomaly consists of a lowering of the elastic stiffnesses during cooling; (3) little or no hysteresis; (4) a wide temperature range of transition; (5) frequency independence; and (6) a maximum-minimum-maximum behavior exhibited during cooling. Antiferromagnetism in Fe-Mn alloys was demonstrated first by Sedov,[16] who measured the

temperature dependence of the magnetic susceptibility of alloys containing 13.0 to 43.9 wt. pct. Mn. Elastic anomalies associated with the Néel transition in Fe-Mn alloys were reported first by Sokolov and Melker,[12] who measured the temperature dependence of Young's modulus of alloys containing 11.1 to 52.4 wt. pct. Mn. Young's modulus anomalies were also reported by Bogachev et al.[13,14] (13-44 and 14-38 wt. pct. Mn). Tanji[15] reported anomalies in both Young's modulus and the shear modulus of alloys containing 30 to 48 wt. pct. Mn. Tanji also reported very peculiar behavior of the bulk modulus in the vicinity of the Néel transition. Young's modulus anomalies were also reported by Lysek et al.[9], although they were complicated by the γ-ε structural transition. These previous studies can be summarized as follows: Fe-Mn alloys containing 13-48 pct. Mn undergo a Néel transition during cooling; both Young's modulus and the shear modulus decrease anomalously because of the transition; the bulk-modulus behavior during the transition may be peculiar, and further study is appropriate; no results have been reported for changes in Poisson's ratio. Thus, it is concluded that in Fe-21Cr-6Ni-9Mn the basic magnetic mechanism causing the elastic anomaly is the same as in Fe-Mn alloys.

Two additional results of the present study deserve mention. First, as shown in Fig. 2, Poisson's ratio is the most sensitive elastic-constant indicator of the transition, that is, a locater of the Néel temperature. Within the paramagnetic region, Poisson's ratio is almost linear over a wide temperature range. Since Poisson's ratio is not related simply to interatomic forces in solids, the physical implications of this behavior are unclear. Second, as also shown in Fig. 2, the bulk modulus has a maximum at 190 K, about 60 K above the suggested Néel transition. This

implies a second transition. The nature of this transition is unknown; but it also is probably magnetic, and magnetic-susceptibility measurements might elucidate its nature.

Several further studies are suggested by the present results: (1) Thermal expansion. Elastic-constant/temperature anomalies are often accompanied by anomalous thermal expansion, particularly in magnetic materials where they have a common cause -- magnetostriction. A weaker interatomic bond usually means a higher specific volume and lower elastic stiffnesses. Regions of negative thermal expansion are possible in this alloy since the magnetic effects may overcompensate for the usual thermal expansion. Alloys with both low thermal expansion and low temperature coefficients of the elastic constants are of considerable technological interest.[17] Also, thermal-expansion data would be useful for distinguishing among possible magnetic mechanisms. (2) Damping. Changes in elastic constants are always accompanied by increases in damping. The possibility of high damping over a temperature region (determined by Mn content) in a non-ferromagnetic material is an interesting possibility. (3) Compressibility. The variation of the compressibility in the vicinity of the Néel transition needs further, detailed study. Tanji's[15] results suggest that the compressibility is discontinous at the Néel temperature, implying a first-order phase transition. But, Néel transitions are known to be second-order. (4) Additional alloys. It would be useful to study other 21-6-9-type alloys to determine the more general validity and utility of the present results. In particular, effects of manganese content should be determined. (5) Magnetic susceptibility. Such measurements made continuously versus temperature would verify the occurrence of a Néel transition and possibly elucidate the nature of the transition that lowers the bulk modulus at 190 K.

CONCLUSIONS

The following principal results and conclusions emerge from the present study:

(1) At room temperature, an Fe-21Cr-6Ni-9Mn alloy has elastic properties similar to those of AISI 304; all the elastic constants except Poisson's ratio are slightly higher in 21-6-9.

(2) Upon cooling, all the elastic constants show anomalous behavior, which is reproducible and reversible, showing no hysteresis.

(3) These anomalies are believed to result from a paramagnetic-antiferromagnetic (Néel) transition, with a transition temperature near 130 K, as evidenced by drops in the shear modulus and in Young's modulus.

(4) Poisson's ratio is especially sensitive to the Néel transition. It is almost linear in the paramagnetic region, and the slope $d\nu/dT$ reverses sharply at the transition.

(5) This alloy's behavior resembles the Fe-Mn case rather than the Fe-Cr-Ni case, emphasizing the role of manganese in affecting properties.

(6) There may be a second transition in this alloy, evidenced by the drop in the bulk modulus upon cooling below 190 K.

(7) Such alloys may offer exceptional physical properties for non-ferromagnets, for example: high damping, low thermal expansion, and a small elastic-modulus change with temperature.

ACKNOWLEDGMENT

This work was supported by the Advanced Research Projects Agency of the U.S. Department of Defense.

REFERENCES

1. Handbook on Materials for Superconducting Machinery (Metals and Ceramics Information Center, Battelle, Columbus, Ohio, Nov. 1975).
2. R. L. Tobler, in National Bureau of Standards Rep. No. NBSIR 76-848 (1976).
3. J. M. Wells, R. Kossowsky, W. A. Logsdon, and M. R. Daniel, Westinghouse Research Rep. No. 76-9D4-CRYMT-R1 (1976).
4. E. R. Naimon, W. F. Weston, and H. M. Ledbetter, Cryogenics 14, 246-249 (1974).
5. W. F. Weston, J. Appl. Phys. 46, 4458-4465 (1975).
6. H. J. McSkimin, IRE Trans. Ultrasonics Engr. 5, 25-43 (1957).
7. G. Leibfried and W. Ludwig, in Solid State Physics, edited by F. Seitz and D. Turnbull (Academic, New York, 1961), Vol. 12, p. 383.
8. R. P. Reed and J. F. Breedis, in Behavior of Materials at Cryogenic Temperatures, ASTM STP 387 (Amer. Soc. Test. Mater., Philadelphia, 1966).
9. L. I. Lysek, S. P. Kondratev, Yu. N. Makogon, and B. I. Nikolin, Soviet Phys.-Doklady 18, 428-429 (1973).
10. R. M. Bozorth, W. P. Mason, and H. J. McSkimin, Bell Syst. Tech. J. 30, 970-989 (1951).
11. H. M. Ledbetter, W. F. Weston, and E. R. Naimon, J. Appl. Phys. 46, 3855-3860 (1975).
12. O. G. Sokolov and A. I. Melker, Soviet Phys.-Doklady 9, 1019-1021 (1965).
13. I. N. Bogachev, V. F. Egolaev, and B. A. Potekhin, Soviet Phys.-Doklady 12, 377-379 (1967).
14. I. N. Bogachev, V. F. Yegolayev, and T. L. Frolova, Fiz. Metal. Metalloved 29, 358-363 (1970).
15. Y. Tanji, J. Japan Inst. Met. 35, 1-5 (1971).
16. V. L. Sedov, Soviet Phys. JETP 15, 88-89 (1962).
17. G. Hausch and W. Warlimont, Z. Metallkd. 64, 152 (1973).

Table I. Elastic constants of an Fe-21Cr-6Ni-9Mn alloy at room temperature, compared to those of AISI 304.

	Fe-21Cr-6Ni-9Mn		AISI 304
	Pulse	Resonance	Pulse
ρ, g/cm^3	7.838		7.864
v_ℓ, 10^6 cm/s	0.571		0.563
v_t, 10^6 cm/s	0.310		0.306
C_ℓ, 10^{11} N/m^2	2.534		2.491
$G=C_t$, 10^{11} N/m^2	0.755	0.779	0.735
B, 10^{11} N/m^2	1.527		1.506
E, 10^{11} N/m^2	1.945	1.957	1.897
ν	0.288		0.290

LIST OF FIGURES

Fig. 1. Longitudinal and shear moduli variations with temperatures, as determined by an ultrasonic pulse-superposition method. Data are shown for a single cooling. Subsequent heatings and coolings reproduced these data within $\pm$ 0.1 percent. Dashed curves represent behavior expected for a typical material.

Fig. 2. Shear modulus (G), Young's modulus (E), Poisson's ratio (ν), and bulk modulus (B) computed from data in Fig. 1 by using standard formulas. Note that the bulk-modulus anomaly begins about 60 K higher than the shear-modulus anomaly.

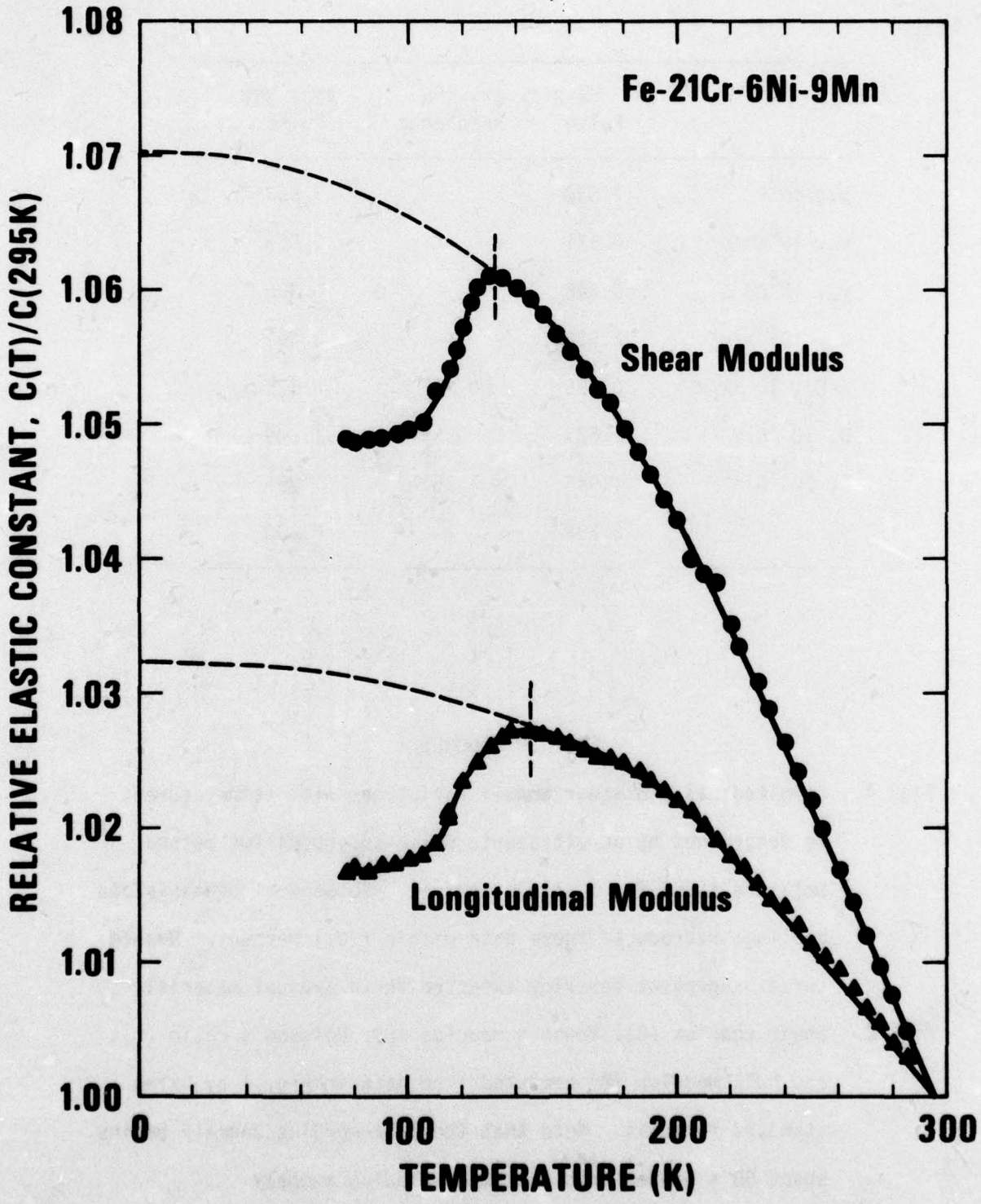


Fig. 1. Longitudinal and shear moduli variations with temperature, as determined by an ultrasonic pulse-superposition method. Data are shown for a single cooling. Subsequent heatings and coolings reproduced these data within ± 0.1 percent. Dashed curves represent behavior expected for a typical material.

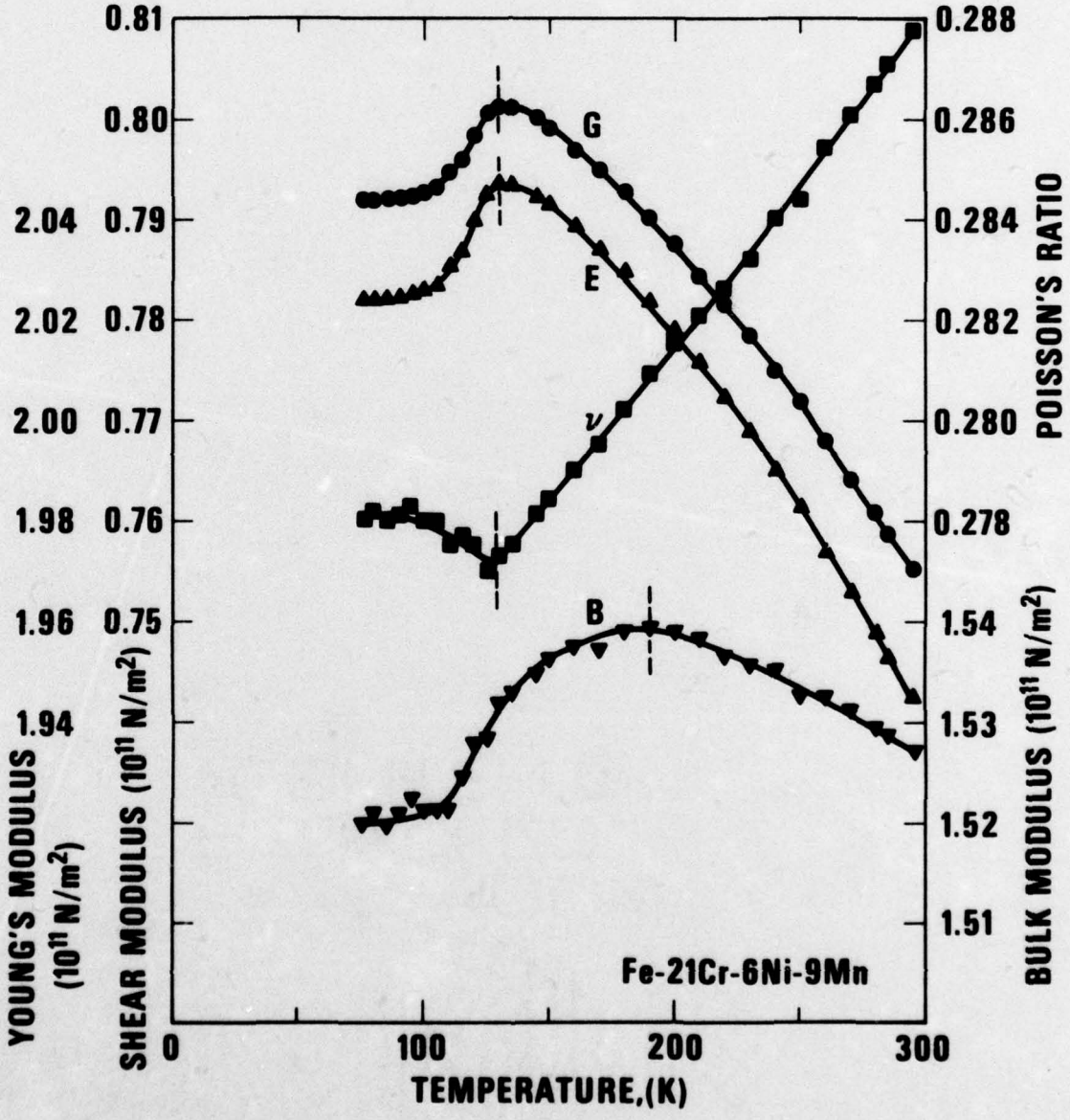


Fig. 2. Shear modulus (G), Young's modulus (E), Poisson's ratio (ν), and bulk modulus (B) computed from data in Fig. 1 by using standard formulas. Note that the bulk-modulus anomaly begins about 60 K higher than the shear-modulus anomaly.

PRECEDING PAGE BLANK-NOT FILMED

SEMI-ANNUAL REPORT ON MATERIALS RESEARCH IN SUPPORT OF SUPERCONDUCTING MACHINERY

FRACTURE MECHANICS PARAMETERS

R. L. Tobler, H. I. McHenry, R. P. Reed, and R. E. Schramm

Cryogenics Division
Institute for Basic Standards
National Bureau of Standards
Boulder, Colorado 80302

October 1976

NBS FRACTURE MECHANICS PROPERTIES STUDIES DURING ARPA SPONSORED PROGRAM, SEPTEMBER 1973 TO SEPTEMBER 1976.

	Material	Fracture Toughness	Fatigue Crack Growth
1.	Aluminum alloy 2014-T652	5,6	NA
2.	" " 2219-T87	5	NA
3.	" " 5083-0	6	6
4.	Inconel alloy 718	5	5
5.	Inconel alloy 750	2	2
6.	Maraging steel, 18Ni, 300 grade	6	6
7.	Iron-49% Ni	6	6
8.	Stainless steel Nitronic 40 (21-6-9)	5,6	6
9.	" " A 286	3	3,6
10.	" " AISI 304	1	1,6
11.	" " AISI 304L	NA	6
12.	" " AISI 310	2	2,6
13.	" " AISI 316	1	1,6
14.	Titanium alloy Ti-6Al-4V, Normal	1,3	1,3
15.	" " Ti-6Al-4V, ELI	3	3
16.	" " i-5Al-2.5Sn, Normal	2	2
17.	" " Ti-5Al-2.5Sn, ELI	NA	6

FRACTURE MECHANICS PARAMETERS FOR A 5083-O ALUMINUM ALLOY AT LOW TEMPERATURES†

R. L. Tobler and R. P. Reed

Cryogenics Division
Institute for Basic Standards
National Bureau of Standards
Boulder, Colorado 80302

ABSTRACT

The fatigue crack growth and fracture resistance of a 5083-O aluminum alloy plate were investigated at four temperatures in the ambient-to-cryogenic range -- 295, 111, 76, and 4 K. J-integral test methods were applied using compact specimens 3.17 cm thick, and the value of J required to initiate crack extension (J_{Ic}) is reported as an index of fracture toughness. The fracture toughness was orientation dependent, with anisotropy accounting for J_{Ic} variations of up to a factor of 2. For specimens having fracture planes parallel to the rolling direction, J_{Ic} increases progressively from 9 to 25 kJm^{-2} as temperature decreases between 295 and 4 K. In contrast, the fatigue crack growth rates (da/dN) are insensitive to specimen orientation. The fatigue crack growth rates at cryogenic temperatures are up to 10 times lower than in air at room temperature, but are virtually constant between 111 and 4 K. These results should be useful in fracture mechanics analyses of cryogenic structures, including liquified natural gas tankers.

Key words: Aluminum alloys; cryogenics; crack propagation; fatigue; fracture; low temperature tests; mechanical properties.

†Contribution of NBS, not subject to copyright.

INTRODUCTION

The aluminum alloy designated 5083-0 is strengthened by solid solution additions of magnesium and used in the annealed condition. Excellent formability, weldability, toughness, and relatively low cost are some advantages that make this alloy an attractive low temperature structural material. Applications include storage and transport tanks for cryogenic fluids. Currently, thousands of tons of 5083-0 alloy are destined for use in liquefied natural gas (LNG) tankers at service temperatures as low as 111 K. Emerging applications may include structural components for superconducting machinery. These structures are costly, and in the case of LNG tankers, the transported cryogen is flammable. Design engineers and regulatory agencies therefore require efficient and fail-safe design.

Extensive mechanical property data exist for 5083-0 aluminum [1-7]. Between room and liquid helium temperatures (295 to 4 K), the yield and ultimate strengths increase by 25% and 70%, respectively, with most of the improvement occurring at lower temperatures [2]. Ductility also improves at low temperatures, and precracked specimens retain the ability to deform prior to fracture. Nevertheless, quantitative fracture toughness data for this alloy are lacking. Several attempts to measure the critical stress intensity factor, K_{Ic}, have been unsuccessful. As defined by the ASTM testing method for plane strain fracture toughness of metallic materials (ASTM E 399-74), the parameter K_{Ic} applies to linear-elastic loading behavior. Kaufman, Nelson, and Wygonik [3] showed that 5083-0 alloys in section thicknesses up 20 cm remain sufficiently plastic to invalidate direct K_{Ic} measurements.

This study employs an alternative approach to fracture toughness characterization. The method is based on Rice's formulation of the J-integral [8], which is the rate of change of potential energy with respect to crack area. In applications of the J-integral, Begley and Landes identify a parameter denoted J_{Ic} which, unlike K_{Ic}, can be measured under nonlinear-elastic conditions [9,10]. Since experimental results for aluminum alloys support the hypothesis that J_{Ic} is a material constant [11,12], the J-resistance curve test method [10] was applied here to a 5083-0 aluminum plate. The J_{Ic} values and fatigue crack growth rates reported in this study should assist fracture mechanics analyses of 5083-0 structures at temperatures in the ambient-to-cryogenic range.

PROCEDURES

Material and Specimens

A 4.32 cm thick 5083-0 aluminum alloy plate was obtained from a commercial source and tested in the as-received condition. The microstructure is shown in Figure 1. The ASTM specification B 209-66 gives the chemical composition of this alloy in wt% as: 4.0-4.9 Mg, 0.3-1.0 Mn, 0.05-0.25 Cr, 0.4 max. Si, 0.4 max. Fe, 0.10 max. Cu, 0.25 max. Zn, 0.15 max. Ti, and 0.15 max. of other impurities.

After machining 0.44 cm of metal from each surface of the stock plate, 3.17 cm thick compact specimens were fabricated with the geometry shown in Figure 2. The specimen width, W, was 7.62 cm. The width-to-thickness ratio, W/B, was 2.4. Knife edges were machined integral to the notch to enable clip gage attachment and deflection measurements at the loadline. Most of the specimens were machined in the TL orientation (fracture plane normal to the long transverse direction), but

several specimens of the LT orientation (fracture plane normal to the longitudinal or rolling direction) were also tested.

Tensile tests of unnotched, longitudinally-oriented specimens were performed at room and liquid nitrogen temperatures, following ASTM Method E 8-69. Two tests were performed at each temperature. The yield and ultimate strengths, elongation, and reduction of area results, shown in Table 1, agree with other data for similar 5083-0 products [13].

Fatigue Crack Growth

A 100 kN servo-hydraulic test machine adaptable for cryogenic service was used in all fatigue and fracture tests. Room temperature tests were conducted in unconditioned air at a relative humidity, H, of approximately 30%. Low temperatures were achieved by enclosing the load frame, specimen, and clip gage in a dewar of liquid helium (4 K), liquid nitrogen (76 K), or nitrogen gas (111 $\pm$ 4 K). The low temperature apparatus and techniques were previously described [14,15]. The clip gage satisfied ASTM Method E 399-74 linearity requirements, and its sensitivity changed by no more than 5% over the temperature range investigated.

The compact specimens were precracked at their test temperatures using maximum fatigue stress intensity factors of from 10 to 22 $MPa \cdot m^{1/2}$. The minimum-to-maximum load ratio, R, was 0.1. Some fatigue crack growth rates were measured during precracking, but additional rates at relatively high stress intensity factors or R values were measured using specimens not intended for J-tests. All precracking and fatigue crack growth tests used sinusoidally-varying loads at a frequency of 20 Hz.

A correlation between crack length (a) and specimen compliance

(deflection per unit load, δ/P) was established using measurements from fractured specimens. Crack length was defined as the average of three measurements at the middle and quarter points of specimen thickness. The fatigue tests were then interrupted periodically to record compliance, and the inferred crack length was plotted as a function of load cycles, N. The fatigue crack growth rates, da/dN, were calculated by graphical differentiation of a-versus-N curves, while the corresponding stress intensity factor ranges, ΔK, were calculated from the maximum and minimum fatigue loads:

$$\Delta K = (P_{max} - P_{min})B^{-1}W^{-1/2}[f(a/W)], \quad (1)$$

According to ASTM Method E 399-74,

$$f(a/W)=29.6(a/W)^{1/2}-185.5(a/W)^{3/2}+655.7(a/W)^{5/2}-1017.0(a/W)^{7/2}+638.9(a/W)^{9/2}. \quad (2)$$

The uncertainty in crack growth rates is estimated at less than $\pm$ 25%.

Fracture Toughness

At each test temperature, a series of specimens having similar precrack lengths were loaded to selected deflections at the stroke rate of 0.05 mms^{-1}. These loadings were sufficient to cause stable crack extensions of up to 0.25 cm. Each specimen was then unloaded and refatigued using cyclic loads no greater than 70% of the maximum static load. After the refatigue crack was propagated several millimeters, the specimens were fractured into halves by a single loading.

The fracture surfaces showed, in succession: (1) a precrack zone, (2) a crack extension increment due to static loading, and (3) a refatigue

crack zone. The relatively coarse and less reflective increment of static crack extension was measured to the nearest 0.003 cm with a traveling microscope at the center and quarter points of specimen thickness, the three-point average being defined as Δa. The corresponding values of J were calculated for each test, using the approximate solution for deeply cracked compact specimens [16]:

$$J = 2A/Bb. \tag{3}$$

Here, A is the total area (energy) under the test record up to the point of unloading, and b is the original ligament depth ($b = W - a$). The uncertainty in J measurements was not greater than $\pm$ 2%.

To obtain critical J values, the resistance curves of J-versus-Δa were back-extrapolated to Δa = 0.005 cm. In tests of a 2219-T6 aluminum alloy, Read and Reed [12] suggested that defining J_{Ic} at 0.005 cm crack extension leads to reproducible results. The uncertainty in the J_{Ic} values obtained in this way for 5083-0 aluminum is estimated at $\pm$ 15%.

RESULTS AND DISCUSSION

Fatigue Crack Growth

Fatigue crack growth data at 4, 76, 111, and 295 K for 5083-0 aluminum specimens of the TL orientation at R = 0.1 are shown in Figure 3. The results span two orders of magnitude from 5 X 10^{-6} mm/cycle to 2.5 X 10^{-3} mm/cycle. For a given ΔK value, the rates of crack growth at 111, 76, and 4 K are equivalent within the degree of scatter among replicate tests. However, the rates at room temperature are up to 10 times faster than the rates at cryogenic temperatures.

As plotted on logarithmic coordinates, the low temperature fatigue crack growth data describe an approximately linear trend over the entire ΔK range, whereas the room temperature data do not. The linear approximation to the data at 111, 76 and 4 K, shown in Figure 3, is consistent with a Paris equation of the form:

$$\frac{da}{dN} = C(\Delta K)^n. \tag{4}$$

Here da/dN (mm/cycle) is a power law function of ΔK (MPa$\cdot m^{1/2}$). The constants C and n correspond to the ordinate intercept at $\Delta K = 1$, and the slope, respectively. A graphical solution for the equation of the line drawn through the 111, 76 and 4 K data yields:

$$\frac{da}{dN} = 1.3 \times 10^{-10}(\Delta K)^{5.2}. \tag{5}$$

The room temperature data fail to conform to a single power-law equation, due to the appearance of a "shoulder" on the da/dN-versus-ΔK plot at ΔK values between 10 and 15 MPa$\cdot m^{1/2}$. This shoulder brings the room and low temperature crack growth rates into closer agreement at higher ΔK values. Consequently, the room temperature fatigue crack growth resistance is only slightly inferior at stress intensity factor ranges greater than 15 MPa$\cdot m^{1/2}$.

Figure 4 shows additional crack growth data for the TL orientation at 295 and 111 K (R = 0.3), as well as data on specimens of the LT orientation at 111 K (R = 0.1). Scatterbands representing the data of Figure 3 are superimposed on Figure 4 for comparison. This comparison indicates that the change in R from 0.1 to 0.3 had no effect on the

room temperature fatigue crack growth rates, whereas, at 111 K, this change increased the rates by nearly a factor of 2. Also the data obtained for specimens of the LT orientation at 111 K fall within the band for TL orientations for the same stress ratio, R = 0.1. Thus, specimen orientation has no measureable effect on fatigue crack growth rates. Kaufman and Kelsey [17] also noted relatively isotropic fatigue crack growth in their tests of a 5083-0 aluminum alloy.

Comparisons of fatigue crack growth data reported in the literature for compact specimens of 5083-0 aluminum are shown in Figures 5 and 6. Although these data show considerable variance, most results can be rationalized in terms of the different test variables and procedures. Usually, higher R values lead to increased fatigue crack growth rates. Other significant factors to be considered include the procedure used to obtain a-versus-N data, and the relative humidity at room temperature.

In reference to Figures 5 and 6 note first that the present study yielded somewhat lower rates at a given ΔK value as compared with other investigations [4,17-19]. In our study, the crack length was defined as an average of measurements at the center and quarter points of thickness. Other studies used measurements of the crack at specimen edges. In our study the edge crack lengths were typically 5 to 8% shorter than the average crack lengths. If edge crack lengths had been used, tne f(a/W) values of Eq. (1) would have been reduced, and the ΔK value for a given growth rate would have been 10 to 17% lower than actually reported. This would shift the bands of Figures 5 and 6 into good agreement with the bulk of previously published results.

As shown in Figure 5, at least three other laboratories report a shoulder in room temperature fatigue crack growth rates [17-19]. This

shoulder occurs at rates near 3 X 10^{-4} mm/cycle, for tests conducted in air with appreciable moisture contents. Kelsey, Nordmark and Clark's [4] room temperature results at 90% relative humidity and R = 0.33 are nearly in agreement with Argy, Paris, and Shaw's [18] results at $\sim$ 50% relative humidity and R = 0.4. However, as the relative humidity is decreased to less than 10%, the shoulder is eliminated and fatigue crack propagation resistance at low ΔK is improved. Note in Figure 5 that the overall agreement of data is better at high ΔK values where differences in relative humidity are less influential.

Deleterious effects on the fatigue crack growth resistance of this alloy due to moisture are not surprising in view of the trends exhibited by other aluminum alloys [20]. Hartman and Schijve's [21] data for a 7075-T6 alloy demonstrate trends analogous to the behavior indicated in Figure 5. In dry air, their logarithmic plots of da/dN-versus-ΔK display a linear trend for growth rates in the range 10^{-5} to 10^{-3} mm/cycle; in moist air (relative humidity = 45%), a shoulder appears in the data at $\Delta K \simeq 15$ MPa$\cdot m^{1/2}$, and the rates at lower ΔK are accelerated by up to a factor of 10. Again, the rates at high ΔK are not sensitive to moisture.

Thus, the effects of moisture on the room temperature fatigue crack growth behavior of 5083-0 and 7075-T6 alloys are remarkably similar. The trend of the Kelsey et al. [4] data for 5083-0 aluminum in a dry air environment probably represents the true trend of room temperature results when moisture effects are practically eliminated. Note from Figures 5 and 6 that the rates reported by Kelsey et al. [18] for tests in dry air at 295 K are nearly equivalent to but slightly faster than their rates at 76 K. Based on these observations, it may be concluded

that moisture effects at 295 K are predominant, and temperature variations between 295 K and 4 K intrinsically have little effect on the fatigue crack propagation resistance of 5083-O aluminum. This is consistent with results for other face-centered cubic alloys which show only modest improvements of fatigue crack growth resistance at low temperatures [22].

Fracture Toughness

Plasticity and stable crack extension caused nonlinearity in the fracture test records at all temperatures, and unstable cracking was never observed. As expected, the linearity requirements of sections 9.1.2 and 9.1.5 of ASTM Method E 399-74 could not be satisfied using our specimens of aluminum alloy 5083-O, so it was appropriate to conduct J-integral tests. Table 2 lists the J-integral test results for both the LT and TL specimen orientations.

Resistance curves (J-versus-Δa graphs) for the TL orientation are shown in Figure 7. The results at 295, 111, 76, and 4 K show that higher J values are required for a given crack extension as temperature decreases. The J_{Ic} values obtained at Δa = 0.005 cm progressively increase from 9 to 25 kJm^{-2} between 295 and 4 K. Moreover, the rate of increase of J with respect to Δa is greater at 111, 76, and 4 K than at room temperature. Thus, greater energy is expended in fracture initiation and propagation at cryogenic temperatures. Kahn-type tear and dynamic tear tests render a similar conclusion [5-7, 23].

Figure 8 compares the J-resistance curves for the TL and LT orientations at 111 K, demonstrating the anisotropy of fracture toughness for this alloy. Based on these curves, J_{Ic} for the LT orientation is approximately 39 kJm^{-2} at 111 K, or twice the value for the TL orientation. The superiority of the LT orientation in comparison with the TL

orientation is typical of many alloys, and the tear test results and projected K_{Ic} values reported by Kaufman et al. [3,5,6] indicate a similar orientation dependence for 5083-O aluminum.

The fracture anisotropy is also evident in Figure 9, which shows TL and LT specimens that were tested at 111 K. The LT specimen was fatigue cracked and fractured in a single loading. The TL specimen was used in a J-test, and it shows an increment of crack extension, Δa, located between two fatigue cracks. The LT specimen displays shear fracture portions amounting to 30% of specimen thickness; delaminations are also visible at mid-thickness. In comparison, the TL specimen exhibits a flat fracture mode requiring less energy for crack extension. The fracture surface appearance of the TL orientation was not significantly influenced by test temperature.

The J_{Ic} data listed in Table 2 can be used to estimate K_{Ic} values by using the equation:

$$K_{Ic}^2 = \frac{EJ_{Ic}}{1 - \nu^2} \tag{6}$$

In this equation, E is Young's modulus of elasticity and ν is Poisson's ratio. The values of E and ν at temperatures between 295 and 4 K are known from Naimon, Weston, and Ledbetter's study [24]. The K_{Ic} estimates based on these data at 295, 111, 76 and 4 K are plotted in Figure 10, along with the corresponding J_{Ic} values.

As shown in Figure 10, the K_{Ic} estimates converted from J_{Ic} data range from 27.0 to 60.2 $MPa \cdot m^{1/2}$, depending on temperature and specimen orientation. For the TL orientation, the K_{Ic} estimates at 295 and 76 K are 27.0 and 43.4 $MPa \cdot m^{1/2}$, respectively. These are lower than Kaufman

and Kelsey's [17] projected K_{Ic} estimates of 49.5 MPa·$m^{1/2}$ at 295 K and 55 MPa·$m^{1/2}$ at 77 K. Kaufman and Kelsey's K_{Ic} estimates also pertain to specimens of the TL orientation, but their K calculations are based on the maximum load observed in fracture tests. Their procedure does not account for the fact that crack extension occurs prior to maximum load.

Finally, it should be noted that Merkle and Corten's method [25] of J calculation could have been used in this study. When applied to the 5083-0 aluminum experiments described in the text, that method amounts to replacing the coefficient 2 in Eq. (3) by higher factors from 2.2 to 2.3. The J_{Ic} values would have been increased by about 10%; the K_{Ic} estimates, by 5%. Read and Reed [12] found from measuring both K_{Ic} and J_{Ic} at 76 K for the aluminum alloy 2219-T87 that J_{Ic} as calculated from the measured K_{Ic} was about 40% greater than the measured J_{Ic}. Thus, the J_{Ic} data and K_{Ic} estimates reported here for 5083-0 may be considered conservative.

SUMMARY AND CONCLUSIONS

The fatigue crack growth behavior and J-integral fracture toughness of a 5083-0 aluminum alloy have been investigated at 295, 111, 76 and 4 K, a wider range of temperatures than previously studied. Specifically:

1. Fatigue crack growth resistance at 111 K was insensitive to specimen orientation, but improves at decreasing R ratios.

2. Although the fatigue crack growth rates in ambient air at room temperature exceed the rates at cryogenic temperatures by up to a factor of 10, the rates between 111 and 4 K are nearly equivalent. The high rates in ambient air can be attributed to the presence of moisture, rather than temperature effects per se.

3. Results for the TL orientation at decreasing temperatures between 295 K and 4 K indicate nearly a three-fold increase of J_{Ic} from 9 to 25 kJm^{-2}.

4. Anisotropy in rolled plate caused a J_{Ic} variation of a least 2:1 at the LNG temperature of 111 K.

5. In view of the favorable low temperature effects on tensile, fatigue, and fracture properties, it is apparent that the structural reliability of flawed or unflawed 5083-O alloy components will not be decreased by cryogenic temperatures.

ACKNOWLEDGMENTS

This work was sponsored by the Maritime Administration and the Advanced Research Projects Agency of the U.S. Department of Defense. The authors gratefully acknowledge the assistance of R. L. Durcholz and Dr. R. P. Mikesell in conducting the tensile tests. We also wish to thank Dr. R. A. Kelsey of the Alcoa Technical Center for reviewing the manuscript.

REFERENCES

1. Properties of Materials for Liquefied Natural Gas Tankage, ASTM STP 579, Amer. Soc. Test. Mater., Philadelphia, 1975, pp. 1-204.
2. Rice, L. P., Campbell, J. E., and Simmons, W. F., in Advances in Cryogenic Engineering, Vol. 8, 1963, pp. 671-677.
3. Kaufman, J. G., Nelson, F. G., and Wygonik, R. H., in Fatigue and Fracture Toughness -- Cryogenic Behavior, ASTM STP 556, Amer. Soc. Test. Mater., 1974, pp. 125-158.
4. Kelsey, R. A., Nordmark, G. E., and Clark, J. W., in Fatigue and Fracture Toughness -- Cryogenic Behavior, ASTM STP 556, Amer. Soc. Test. Mater., 1974, pp. 159-185.
5. Kaufman, J. G., Nelson, F. G., and Wanderer, E. T., Mechanical Properties and Fracture Characteristics of 5083-O Products and 5183 Welds in 5083 Products, Proceedings of the International Congress of Refrigeration, Washington, D.C., Vol. 1, 1971, pp. 651-658.
6. Nelson, F. G., Kaufman, J. G., and Wanderer, E. T., Tear Tests of 5083 Plate and of 5183 Welds in 5083 Plate and Extrusions, Paper D-1 in Adv. in Cryo. Eng., K. D. Timmerhaus, Ed., pp. 91-101.
7. Judy, R. J., Jr., and Goode, R. J., Fracture Resistance of Thick Plate 5083-O Alloy, Report of NRL Progress, December 1974, pp. 36-38.
8. Rice, J. R., J. Appl. Mechs., Trans. ASME, Vol. 35, 1968, pp. 379-386.
9. Begley, J. A. and Landes, J. D., in Fracture Toughness, ASTM STP 514, Amer. Soc. Test. Mater., 1972, pp. 1-39.
10. Landes, J. D. and Begley, J. A., in Fracture Analysis, ASTM STP 560, Amer. Soc. Test. Mater., 1975, pp. 170-186.

11. Griffis, C. A. and Yoder, G. R., Application of the J-Integral to Crack Initiation in a 2024-T351 Aluminum Alloy, Naval Research Report 7676, 1974, pp. 1-25.

12. Read, D. T. and Reed, R. P., Effects of Specimen Thickness on Fracture Toughness of Some Aluminum Alloys, submitted to Int. J. Fract. (1976).

13. Bogardus, K. O. and Malcolm, R. C., in Ref. 1, pp. 190-204.

14. Fowlkes, C. W. and Tobler, R. L., Fracture Testing and Results for a Ti-6Al-4V Alloy, Eng. Fract. Mechs., to be published.

15. Tobler, R. L., Mikesell, R. P., Durcholz, R. L., and Reed, R. P., in Ref. 1, pp. 261-287.

16. Rice, J. R., Paris, P. C., and Merkle, J. G., in Progress in Flaw Growth and Fracture Toughness Testing, ASTM STP 536, Amer. Soc. Test. Mater., 1973, pp. 231-244.

17. Kaufman, J. G. and Kelsey, R. A., in Ref. 1, pp. 138-158.

18. Argy, R., Paris, P. C., and Shaw, F., in Ref. 1, pp. 96-137.

19. Person, N. L. and Wolfer, G. C., in Ref. 1, pp. 80-95.

20. Wei, R. P., Eng. Fract. Mechs., Vol. 4, 1970, pp. 633-651.

21. Hartman, A. and Schijve, NLR Tech Note No. MP 68001 U, 1968; see also Fig. 11 of Reference 17.

22. Materials Research in Support of Superconducting Machinery, Vols. III, IV, and V, Reed, R. P., Clark, A. F., and van Reuth, E. C., Eds., National Bureau of Standards, Boulder, CO.

23. Zinkham, R. E. and Ashton, R. F., in ASTM STP 579, Ref. 1, pp. 159-175.

24. Weston, W. F., Naimon, E. R., and Ledbetter, H. M., in Ref. 1, pp. 397-420.

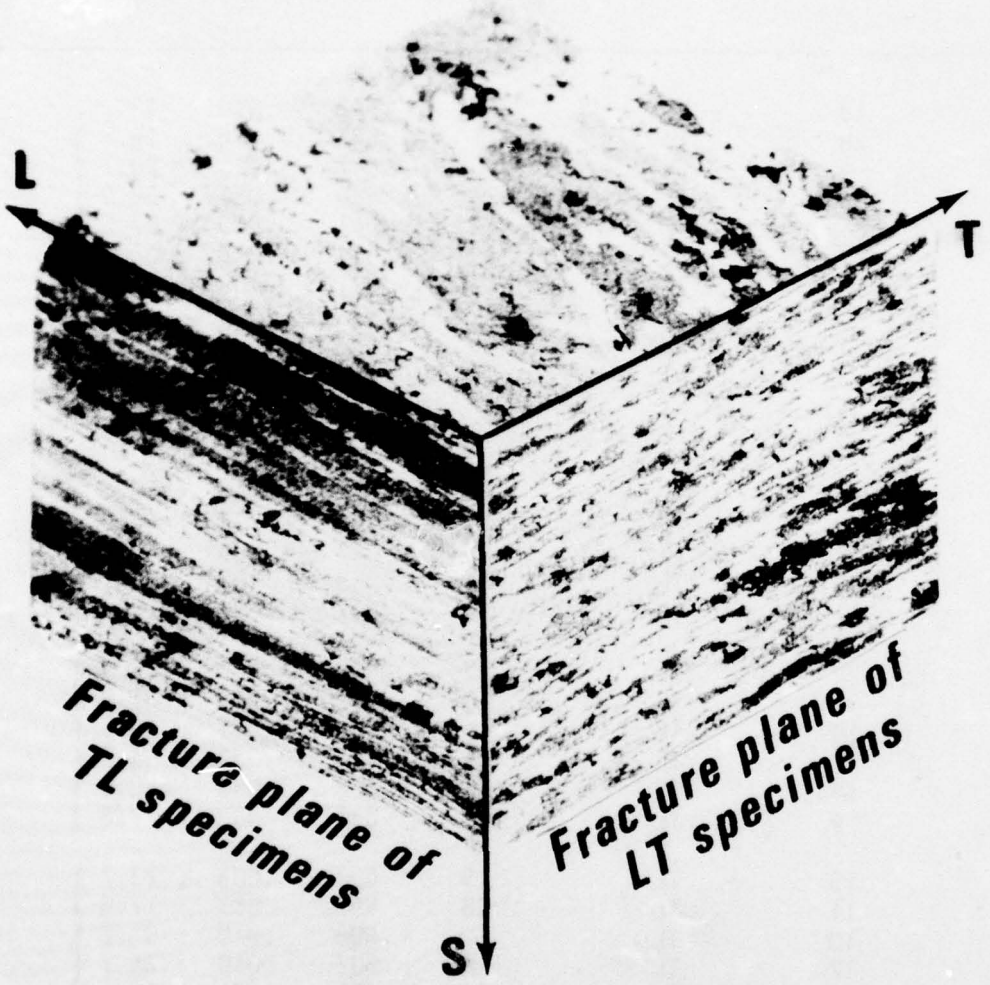
25. Merkle, J. G. and Corten, H. T., "A J-Integral Analysis for the Compact Specimen, Considering Axial Force as Well as Bending Effects," presented at the Pressure Vessels and Piping Conference with Nuclear Engineering and Mechanical Divisions, American Society of Mechanical Engineers, Paper No. 74-PVP-33, 1974.

Table 1. Tensile property results for 5083-0 aluminum alloy specimens in the longitudinal orientation (average values for two tests per temperature).

Temperature K	(°F)	0.2% Yield Strength MPa	(ksi)	Ultimate Strength MPa	(ksi)	Elongation (2.54 cm gage) %	Reduction of Area %
295	(70)	142	(20.6)	305	(44.2)	23.4	36.9
76	(-323)	150	(21.7)	404	(58.6)	34.1	36.7
4	(-452)	186	(27.0)	472	(68.5)	23.2	11.6

Table 2. J-integral test results.

Temperature K	Specimen	Orientation	K_{fmax} MPa·m$^{1/2}$	a/W cm	Δa cm	J kJm^{-2}	J_{Ic} kJm^{-2}
295	13	TL	14	.642	.010	10.3	
	28	TL	21	.647	.020	15.8	
	9	TL	15	.647	.029	20.1	
	8	TL	21	.620	.036	22.9	9
	31	TL	13	.641	.059	27.5	
	7	TL	15	.644	.070	30.5	
	14	TL	22	.611	.109	41.6	
111	2	LT	16	.622	.033	65.6	
	3	LT	18	.612	.019	54.2	41
	4	LT	18	.622	.033	60.8	
	5	LT	18	.619	.053	76.0	
111	30	TL	19	.622	.010	23.6	
	20	TL	13	.630	.023	36.4	
	22	TL	14	.617	.056	59.1	19
	10	TL	20	.629	.103	78.5	
	11	TL	20	.617	.253	122.4	
76	20	TL	15	.629	.010	27.9	
	17	TL	14	.623	.019	31.2	
	19	TL	16	.631	.026	40.5	21
	16	TL	14	.633	.039	54.7	
	14	TL	17	.628	.083	72.5	
	9	TL	21	.632	.093	77.3	
4	15	TL	19	.602	.003	13.7	
	11	TL	18	.597	.003	17.6	
	10	TL	20	.608	.010	30.2	
	17	TL	19	.602	.019	38.3	25
	16	TL	18	.602	.030	47.3	
	18	TL	18	.597	.056	61.4	



L—longitudinal or rolling direction
T—long transverse direction
S—short transverse or plate thickness direction

Figure 1. Microstructure of 5083-0 after rolling and annealing, 100X.

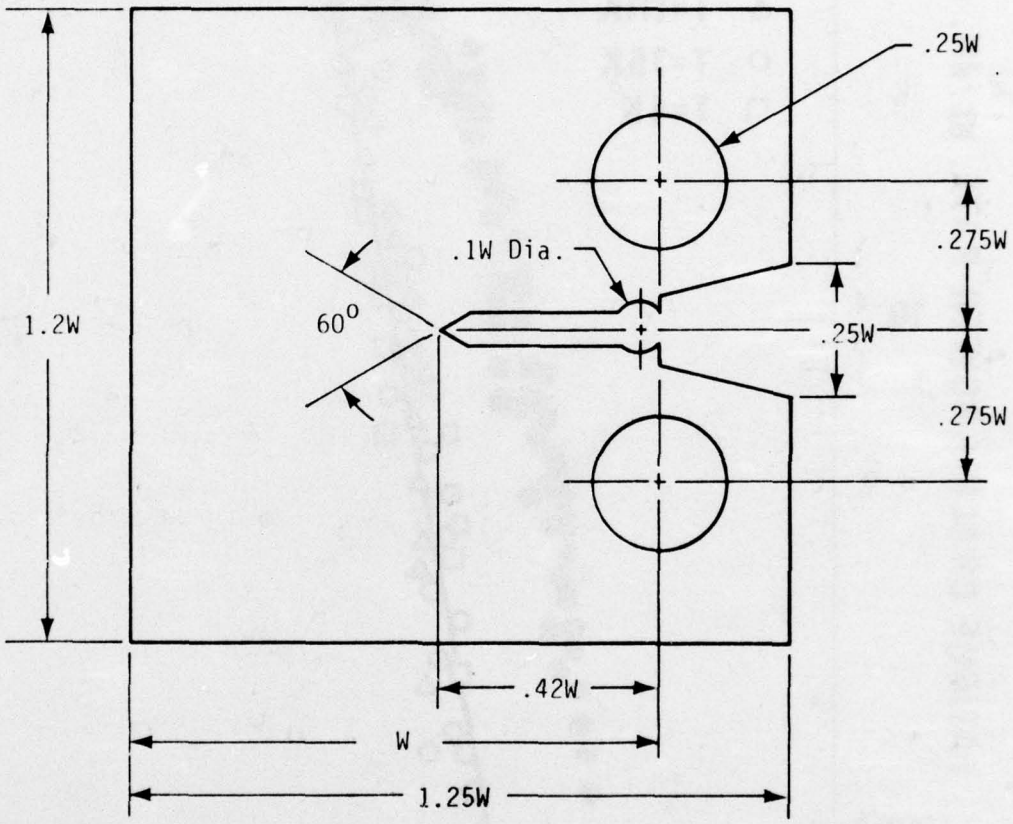


Figure 2. Compact specimen used in fatigue and fracture tests (thickness, B = 3.17 cm; dimensions are in cm).

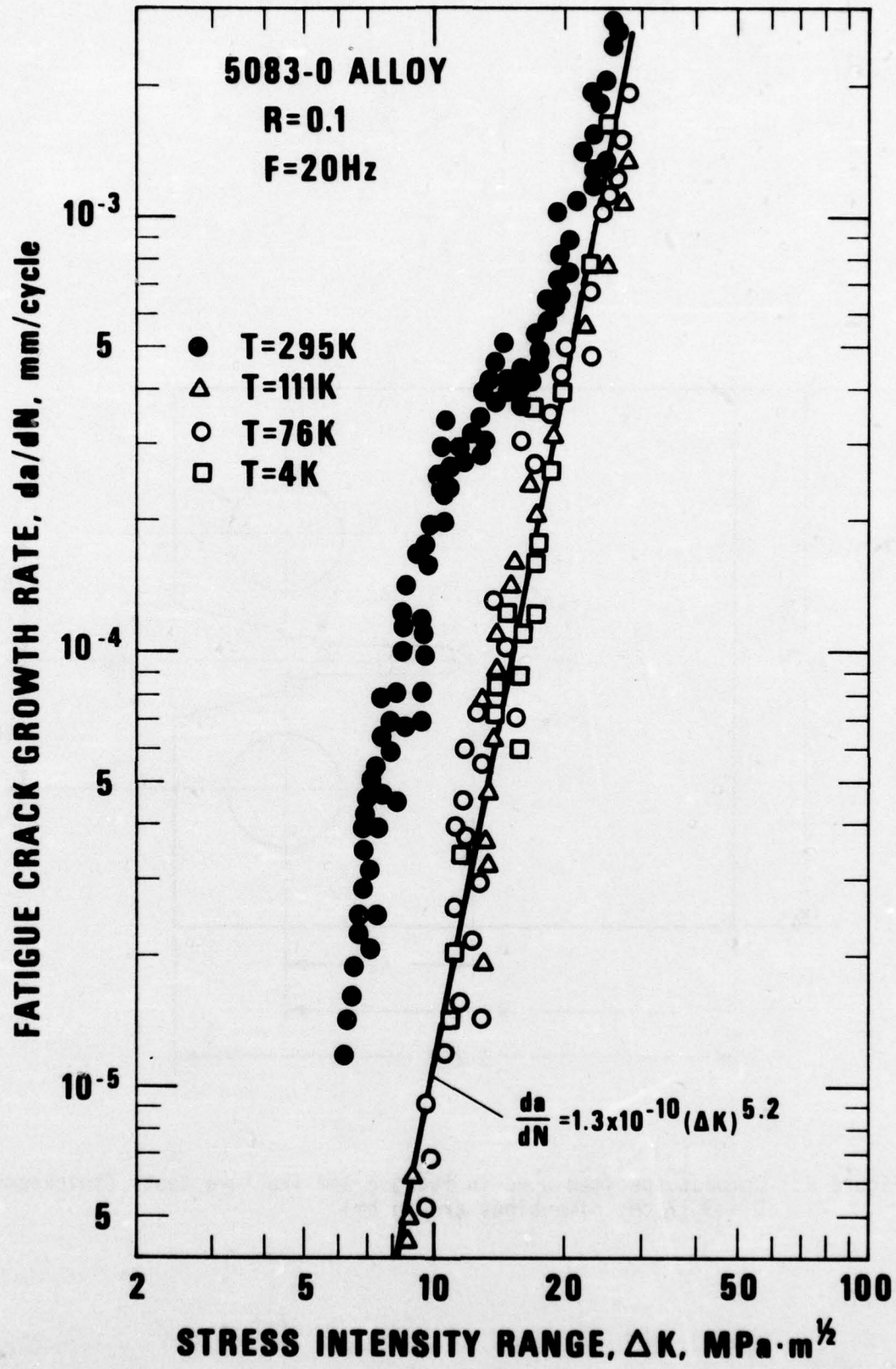


Figure 3. Fatigue crack growth rate results for TL orientations at 295, 111, 76 and 4 K.

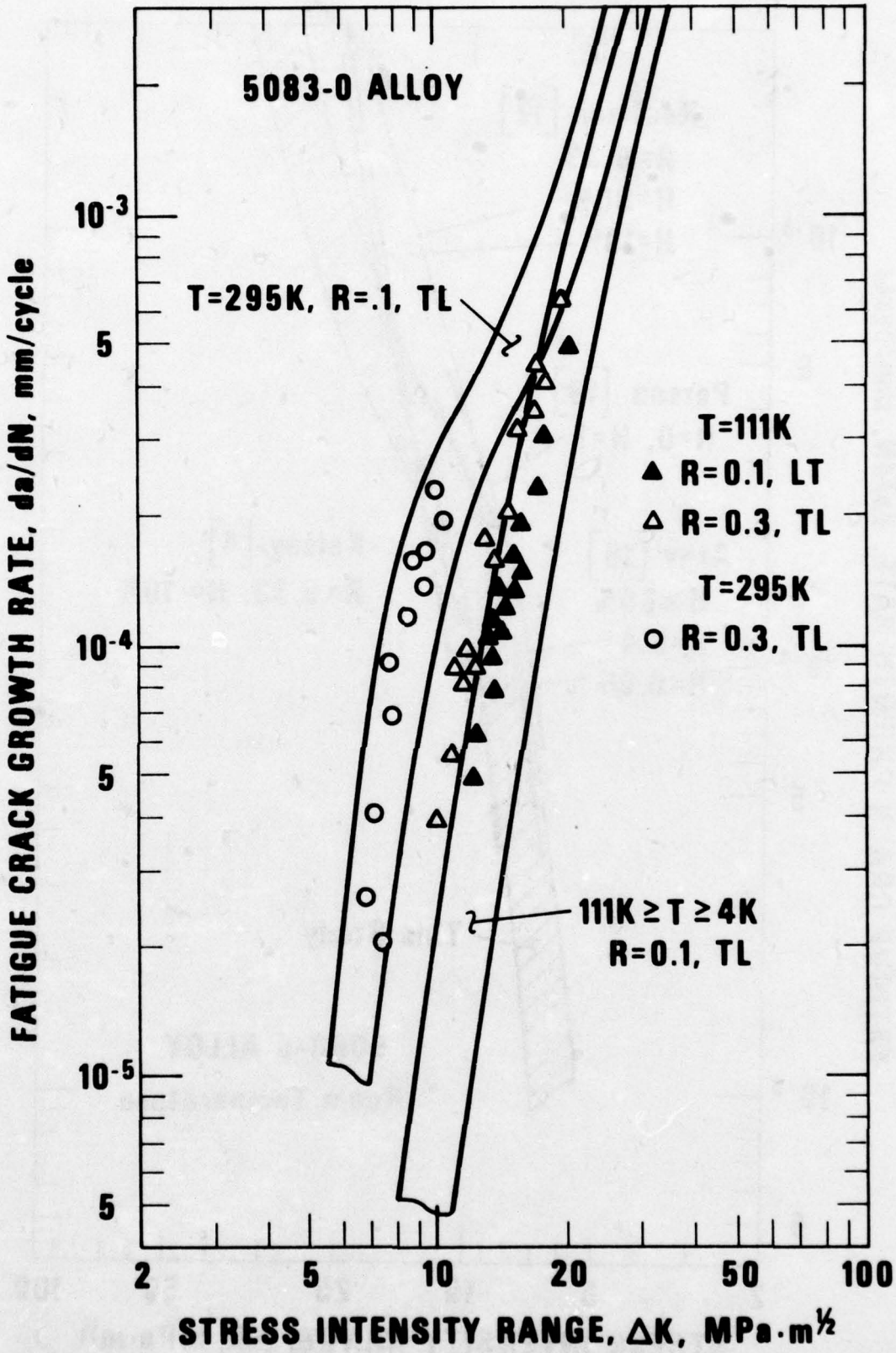


Figure 4. Fatigue crack growth rate results at 295 and 111 K, showing the effects of orientation and R ratio variations.

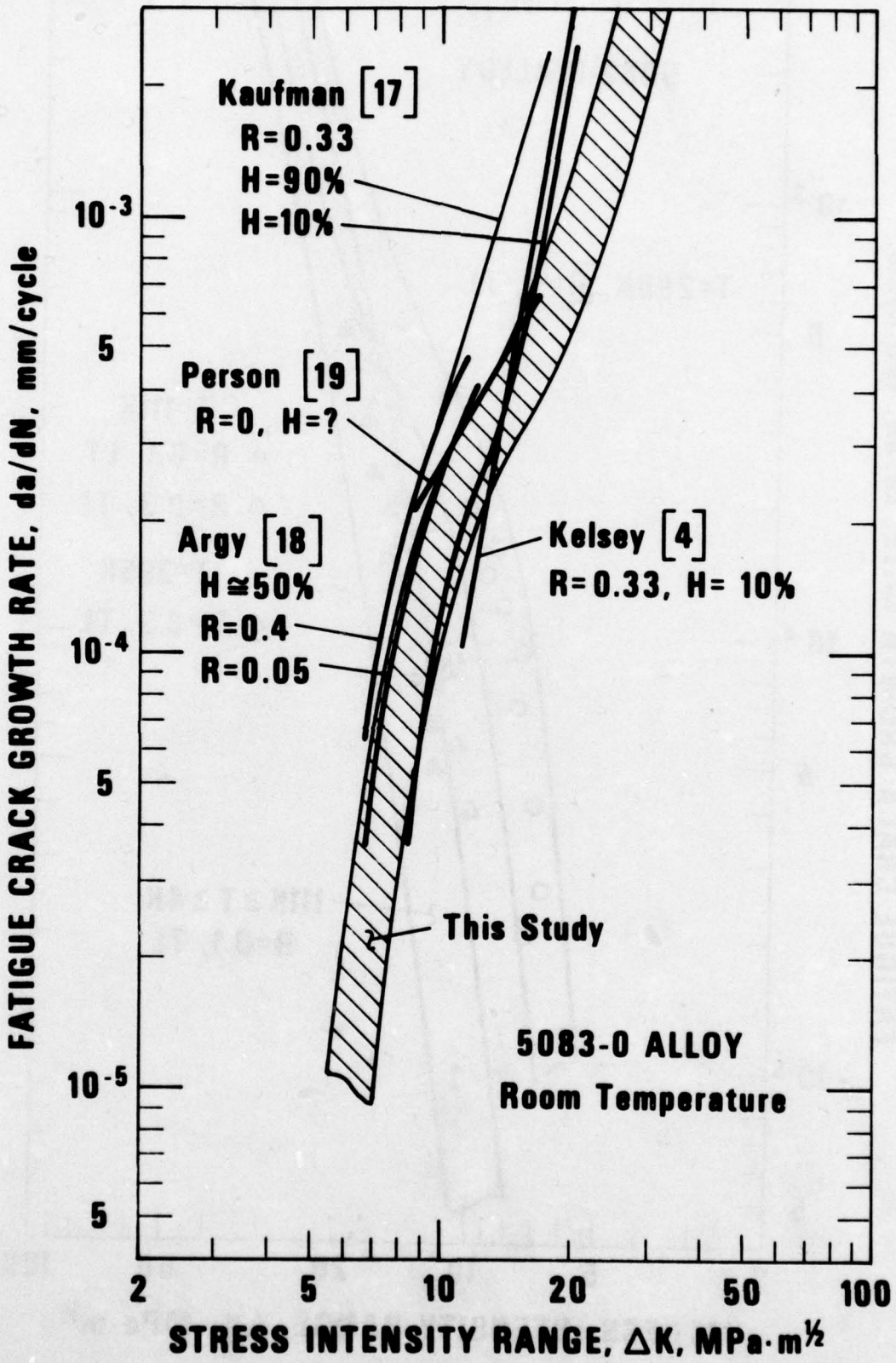


Figure 5. Comparison of fatigue crack growth data at 295 K.

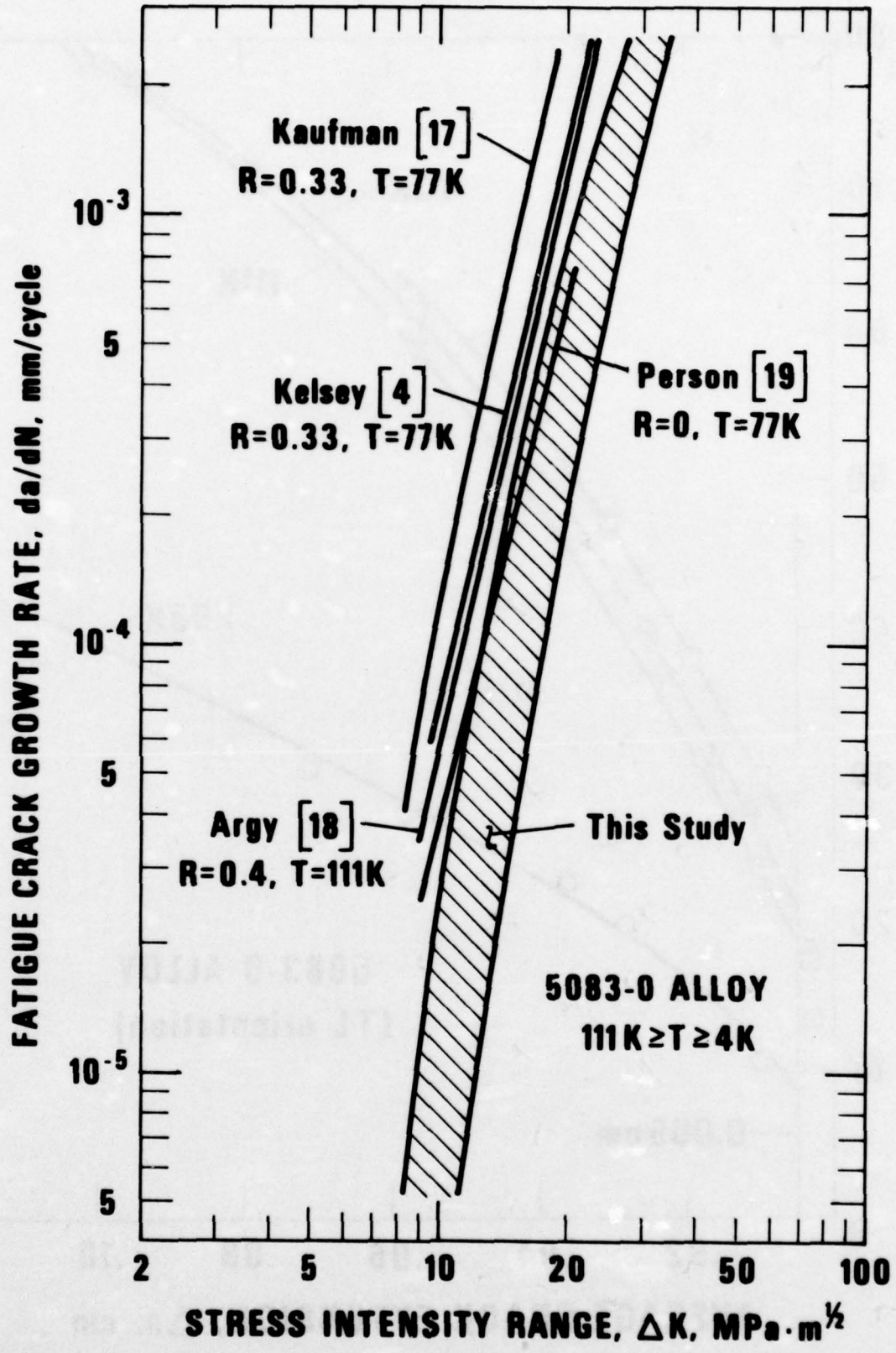


Figure 6. Comparison of fatigue crack growth data at low temperatures.

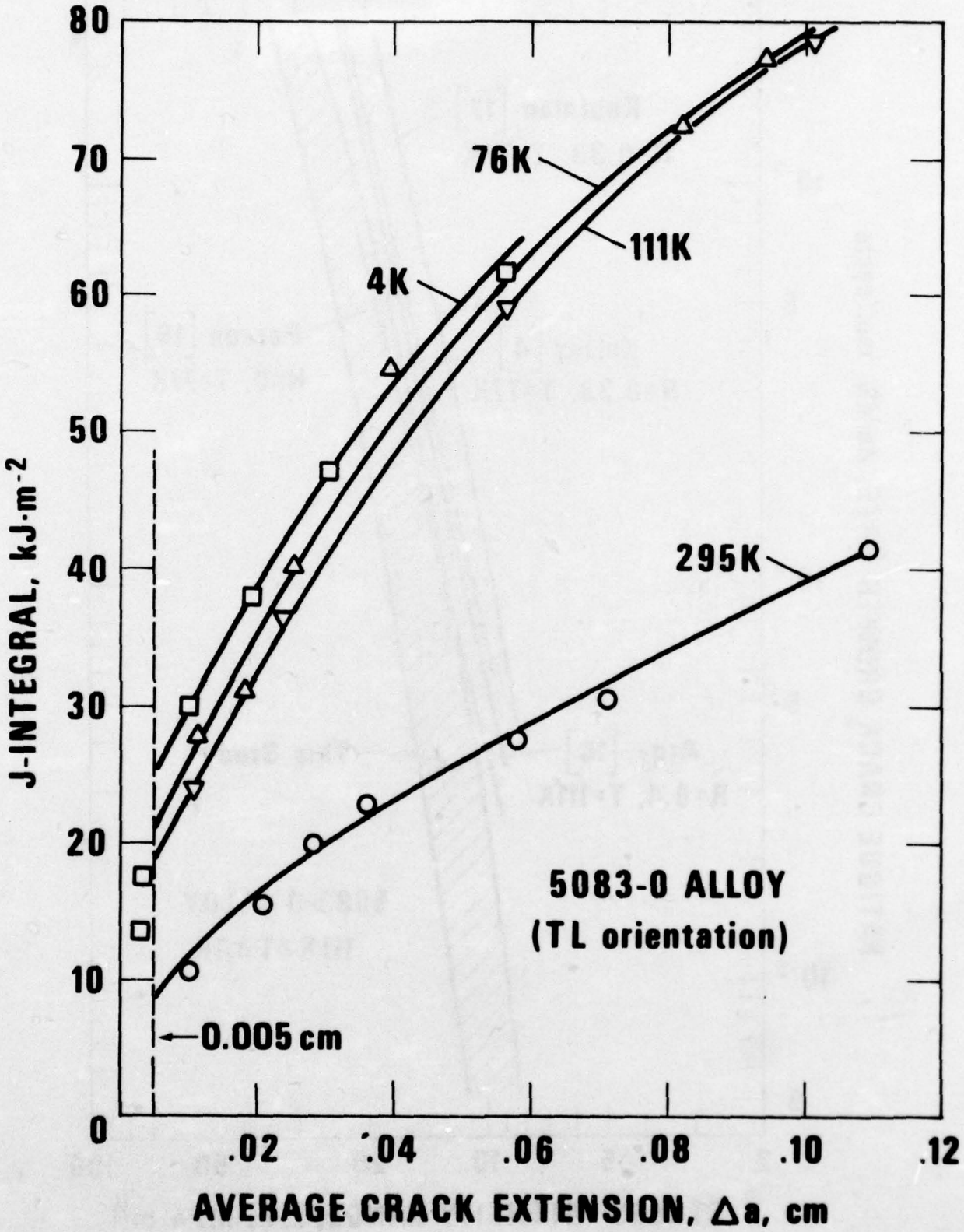


Figure 7. J-integral resistance curves for 5083-0 aluminum, showing the effect of temperature.

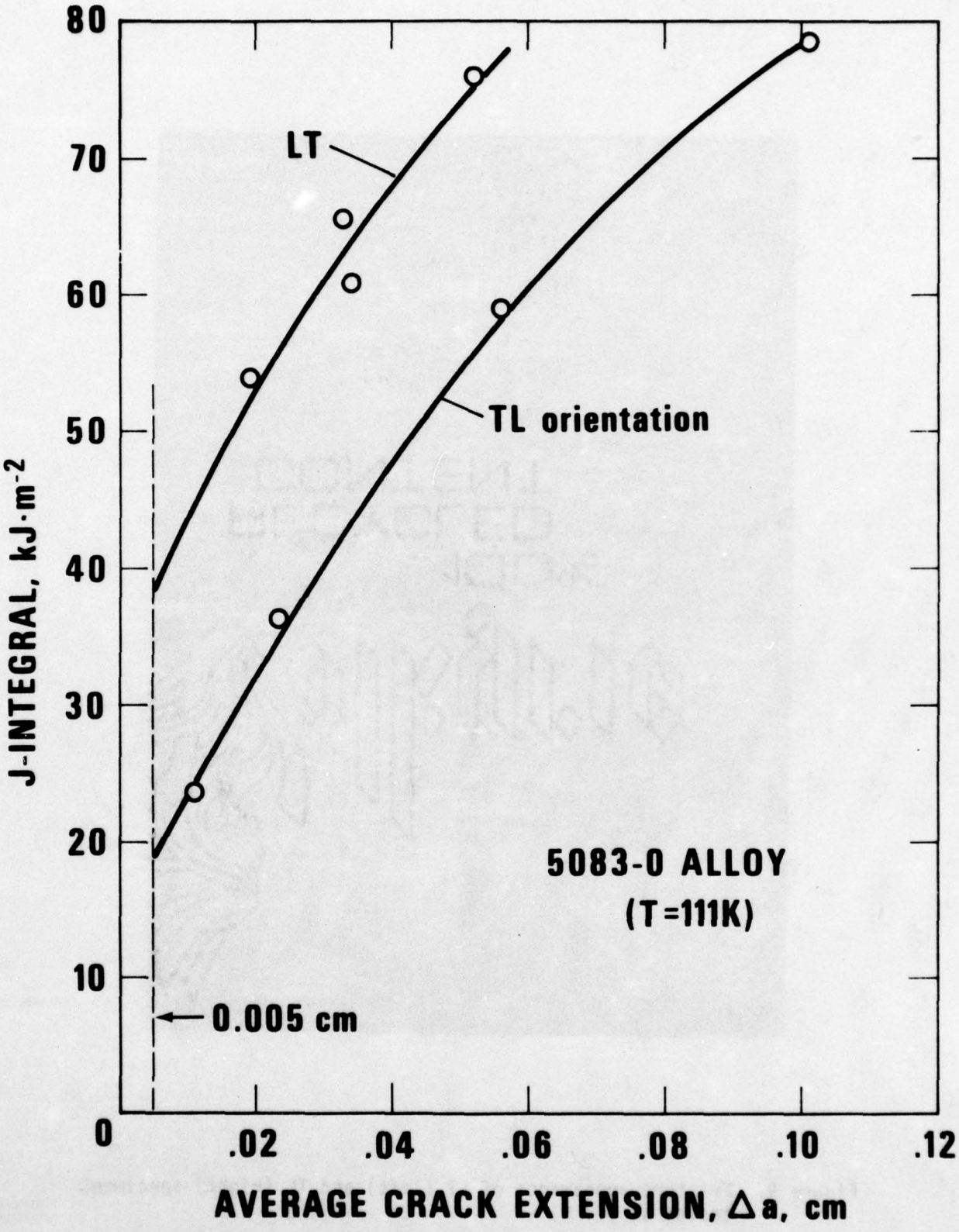


Figure 8. J-integral resistance curves for 5083-0 aluminum at 111 K, showing the effect of orientation.

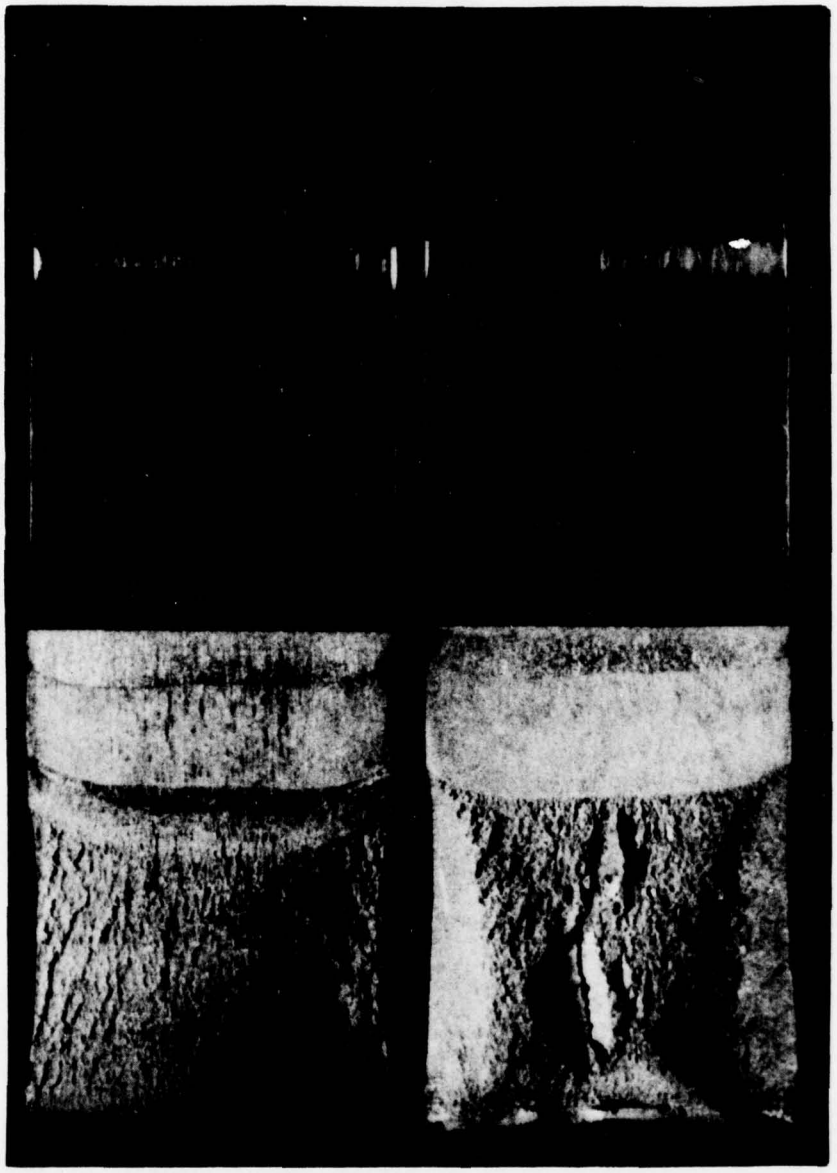


Figure 9. Fracture appearance of LT (left) and TL (right) specimens tested at 111 K.

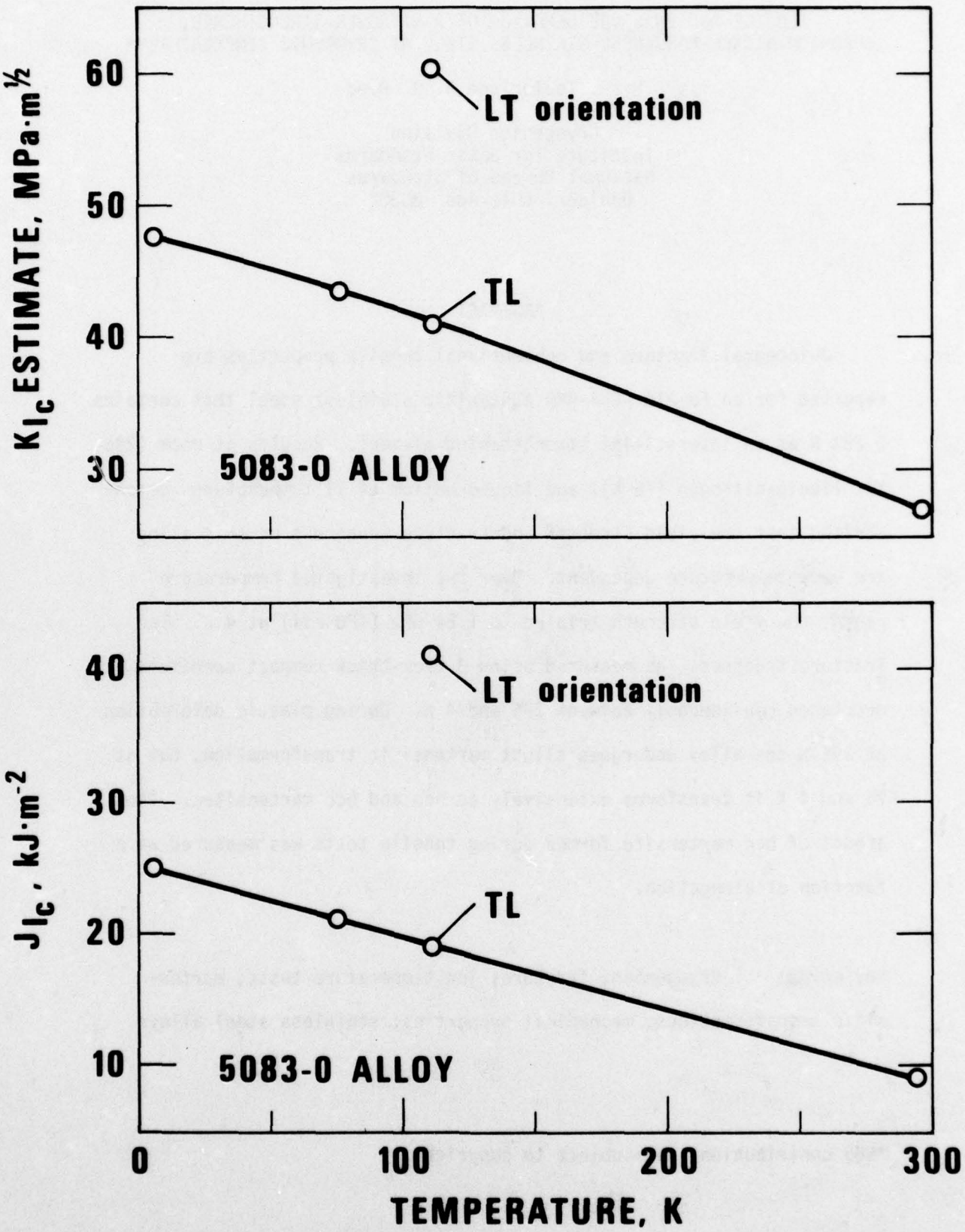


Figure 10. Temperature dependences of J_{Ic} data and K_{Ic} estimates.

TENSILE AND FRACTURE BEHAVIOR OF A NITROGEN-STRENGTHENED, CHROMIUM-NICKEL-MANGANESE STAINLESS STEEL AT CRYOGENIC TEMPERATURES*

R. L. Tobler and R. P. Reed

Cryogenics Division
Institute for Basic Standards
National Bureau of Standards
Boulder, Colorado 80302

ABSTRACT

J-integral-fracture and conventional tensile properties are reported for an Fe-21Cr-6Ni-9Mn austenitic stainless steel that contains 0.28% N as an interstitial strengthening element. Results at room (295 K), liquid-nitrogen (76 K), and liquid-helium (4 K) temperatures demonstrated that the yield strength and fracture toughness of this alloy are very temperature dependent. Over the investigated temperature range, the yield strength tripled to 1.24 GPa (180 ksi) at 4 K. The fracture toughness, as measured using 3.8-cm-thick compact specimens, decreased considerably between 295 and 4 K. During plastic deformation at 295 K the alloy undergoes slight martensitic transformation, but at 76 and 4 K it transforms extensively to hcp and bcc martensites. The amount of bcc martensite formed during tensile tests was measured as a function of elongation.

Key words: Cryogenics; fracture; low temperature tests; martensitic transformations; mechanical properties; stainless steel alloys.

*NBS contribution, not subject to copyright.

Introduction

Recently, austenitic stainless steel strengths have been increased considerably by the substitution of nitrogen and manganese for nickel. In addition to providing interstitial and solid solution strengthening, these elements serve to increase austenite stability with respect to martensitic transformations. Compared to nickel, these elements are more abundant and less expensive. The alloy studied in this report, Fe-21Cr-6Ni-9Mn-0.3N (21-6-9), has a room temperature yield strength nearly twice that of AISI 304. Available tensile and impact data[1-4] suggest that 21-6-9 retains good toughness at low temperatures, leading to consideration of its use for applications benefiting from high strength and toughness.

Accordingly, 21-6-9 is currently being considered for such critical components as the coil form for the prototype controlled thermonuclear reaction superconducting magnets and the torque tube for rotating superconducting machinery. To insure satisfactory service life and to compare with other candidate materials it is necessary to evaluate the fracture resistance of the alloy. This study presents the first fracture toughness data for this alloy.

Material

The 21-6-9 austenitic stainless steel plate was processed and donated by Lawrence Livermore Laboratories, Livermore, California. The chemical composition (in weight percent) of this heat is: 19.75 Cr, 7.16 Ni, 9.46 Mn, 0.019 C, 0.15 Si, 0.004 P, 0.003 S, and 0.28 N. This steel was hot rolled from 30.5 x 30.5 x 10 cm slabs to 50 x 50 x 3.6 cm plate using the following schedule:

soak for 4 hours at 1366 K;.

roll from 10 cm to 9.4 cm, screw down (compress) to 9.3 cm;

roll from 9.3 cm to 8.7 cm, screw down to 8.6 cm, rotate 90°;

roll from 8.6 cm to 8.0 cm, screw down to 7.9 cm;

roll from 7.9 cm to 7.4 cm, screw down to 7.3 cm, rotate 90°;

roll from 7.3 cm to 6.9 cm, screw down to 6.7 cm;

roll from 6.7 cm to 6.3 cm, screw down to 6.2 cm, rotate 90°;

roll from 6.2 cm to 5.9 cm, screw down to 5.7 cm;

roll from 5.7 cm to 5.4 cm, screw down to 5.3 cm, rotate 90°;

roll from 5.3 cm to 5.0 cm, screw down to 4.8 cm;

roll from 4.8 cm to 4.5 cm, screw down to 4.3 cm, rotate 90°;

roll from 4.3 cm to 4.2 cm, screw down to 4.0 cm;

roll from 4.0 cm to 3.8 cm, screw down to 3.6 cm.

The final plate temperature after this hot rolling was 1089 K. Each plate was then annealed at 1283 K for 1-1/2 hours and air cooled, followed by an anneal at 1366 K for 1-1/2 hours and a water quench. The resultant hardness was Rockwell B92 and the average grain diameter was 0.16 mm.

Procedure

Tensile

Tensile specimens were machined following ASTM specification E8-69[5]; the reduced section diameter was 0.5 cm and gage length was 2.54 cm. The tensile axis was oriented transverse to the final rolling direction. Tests were performed at a cross-head rate of 8.3×10^{-4} cm/s, using a 44.5 kN screw-driven machine that was equipped with the cryostat assembly designed by Reed.[6] The tests at 295 K were conducted in laboratory air, whereas tests at 76 K and 4 K used liquid nitrogen

and liquid helium environments, respectively. Load was monitored with a 44.5 kN commercial load cell while specimen strain was measured with a clip-on, double beam, strain gage extensometer. Yield strength was determined as the stress at 0.2% offset plastic strain.

Magnetic

To detect the amount of ferromagnetic, body-centered cubic (bcc) martensitic phase in the paramagnetic, fcc austenitic matrix a simple bar-magnet torsion balance was used.[7] Previous measurements on Fe-Cr-Ni austenitic steels established a correlation between the force required to detach the magnet from the specimen and the percent bcc martensite.[7] The same correlation was used for this study to estimate the amount of bcc martensite in the Fe-Cr-Ni-Mn alloy.

Fracture

The J-integral specimens were 3.78 cm thick compact specimens of a geometry described in ASTM E 399-74.[8] The specimen width, W, and width-to-thickness ratio, W/B, were 7.6 cm and 2.0, respectively. Other dimensions are shown in Figure 1. The notch, machined parallel to the final rolling direction of the plate, was modified to enable clip gage attachment in the loadline.

The J-integral specimens were precracked at their test temperatures, using a 100 kN fatigue testing machine and cryostat[9]. All fatigue operations were conducted using load control and a sinusoidal load cycle at 20 Hz. Maximum fatigue precracking loads (P_f) were well below the maximum load of J tests (P_{max}), as indicated in Table 1. The maximum stress intensities during precracking (K_f), the final relative crack lengths (a/W), and the edge-crack-to-average-crack-length ratios (a_e/a) at each temperature are also listed in Table 1. After precracking,

the specimens were transferred to a 267 kN (60,000 lb) hydraulic tensile machine for fracture testing. Thus, the 76 and 4 K fracture specimens were warmed to room temperature between precracking and J testing at 76 and 4 K. This was necessary since the load limitations of the 20 kN fatigue machine precluded loading this alloy to fracture at low temperatures.

The J-integral tests followed a resistance curve technique similar to that described originally by Landes and Begley.[10,11] A series of nearly identical specimens was tested at each temperature. Each specimen was loaded to produce a given amount of crack extension. The specimens were then unloaded and heat tinted to mark the amount of crack extension associated with a particular value of J. The oxidized zone of crack extension could be identified and measured after fracturing the specimen into halves.

Using the approximation for deeply cracked compact specimens,[12]

$$J = 2A/B(W-a), \qquad (1)$$

the value of J for each test was calculated from the total area, A, under the load-versus-record. The values of J obtained at each temperature were plotted versus crack extension, Δa, which was measured at five locations equidistant across the specimen thickness, and averaged.

The critical value of the J integral, J_{IC}, defined as the J value at the initiation of crack extension, was obtained by extrapolating the best fit J-Δa curve to the point of actual material separation. Conversion to the plane-strain fracture toughness parameter, K_{IC}, is made using:[10-12]

$$K_{IC}^2 = \frac{E}{1-\nu^2} (J_{IC}) \qquad (2)$$

where E is Young's modulus and ν is Poisson's ratio. At room temperature, E ≃ 195 GPa and ν ≃ 0.287; at 76 K and 4 K, E ≃ 203 GPa and ν ≃ 0.278, according to Ledbetter's measurements.[13]

Results and Discussion

Tensile

The yield and tensile strengths, elongation, and reduction of area were obtained for the 21-6-9 alloy at 295, 76, and 4 K. These data are summarized in Table 2. The results from this study are combined in Figures 2-4 with the unpublished results of Landon[1] for the same heat, also hot rolled and annealed, and with the results of Scardigno,[2] Malin,[3], and Masteller[4] for annealed bar stock. The spread of the Malin data represent results from both the longitudinal and transverse specimen orientations. Agreement is very good, except that the ultimate strength data of Masteller are consistantly higher than the average of the other data.

Typical stress-strain curves at each temperature are presented in Figure 5. The pronounced discontinuous yield behavior at 4 K probably is associated with adiabatic specimen heating. Significant local heating is indicated, as the flow stress drops to stress levels less than sustained at 76 K. Another indication of significant local heating is the rise of the reduction of area to values higher than obtained during 76 K tests. Specimens tested at 4 K developed very local areas of increased plastic deformation, which resulted in sizable specimen necking prior to fracture. These load drops should not be attributed to martensitic phase transformations for three reasons: (1) more

extensive transformation was detected in this alloy at 76 K than at 4 K (see later discussion) and no discontinuities in the stress-strain mode at 76 K were observed, (2) load drops have been observed in both metastable (e.g., AISI/304) and stable (e.g., AISI 310) austenitic stainless steels at 4 K and no distinction is apparent between the two alloy groups,[14] and (3) in austenitic steels the amplitude and frequency of the load drops at 4K are a function of the strain rate[14] which would be expected if local heating were responsible.

From the tensile data it is clear that the alloy 21-6-9 has a significant decrease of ductility below 195 K, and tensile elongation decreases progressively between 195 and 4 K.

A primary advantage offered by this alloy is its high yield strength compared to other austenitic alloys. At room temperature the yield strength of the 21-6-9 alloy is about 0.38 GPa (55 ksi), compared to AISI 300 series (Fe-Cr-Ni) steel values of 0.21 to 0.25 GPa (30-35 ksi). The yield strength of the 21-6-9 steel approximately triples to a value of 1.24 GPa (180 ksi) as the temperature is decreased to 4 K. The Fe-Cr-Ni austenitic alloys achieve values about double or triple their room temperature values (60-110 ksi) at 4 K. Thus, the strength advantage offered by the 21-6-9 alloy is greatest at low temperatures.

Fracture:

The load-versus-loadline deflection curves for compact specimens at 295, 76 and 4 K are shown in Figure 6. The curves at 295 K extended to larger deflections than indicated on the axis of the diagram. The fracture test data are tabulated in Table 3. There are no ASTM E 399-74 valid K_{IC} data. The 5% secant offset data are denoted K_Q because the ASTM E 399-74 thickness and crack front curvature criteria are not

satisfied. Using $B \geq 2.5\ (K_Q/\sigma_y)^2$, a specimen thickness of 4.2 cm at 4 K is required, slightly larger than the 3.8 cm thickness tested. The crack front curvatures shown in Figure 7, are slightly larger than allowed by ASTM E 399-74. The surface crack lengths are 88 to 89% of the average of internal crack lengths, while 90% is specified in the ASTM E 399-74 Method as the minimum deviation.

The J-versus-Δa results at room temperature are plotted in Figure 8. Ductile tearing or slow, stable crack extension occurred at this temperature. Large apparent crack extensions were observed due to plastic deformation at the crack tip; only in two specimens at the highest values of Δa was actual material separation noted. These two values fall on the same trend line as the specimen data that did not exhibit material separation. Therefore the response of this extremely ductile material to J-integral tests at room temperature is inconclusive, with no well-defined break from the linear portion of the plastic deformation curve observable.

According to the tentative size criterion suggested by Landes and Begley[11], the specimen thickness for valid J_{IC} measurements should satisfy the relationship:

$$B \geq \alpha(J/\sigma_f) \qquad (3)$$

where α is 25 and σ_f is the average of the yield and tensile strengths. In the tests at 295 K, the conditional critical J values are in the range 925 to 1350 kJm^{-2}. Using the flow stress value of 0.527 GPa (76.5 ksi), the J-integral results at room temperature are invalid for the specimen thickness tested here. A specimen thickness of 6.3 cm (2.5 inches) may be needed to insure valid data, according to Eq. (3).

The J-resistance curve at 76 K is also shown in Figure 8. The data fit a regular trend, with the exception of the point representing the largest observed crack extension (not shown). The curve drawn through the remaining data indicates that crack extension initiates at a J_{IC} value of about 340 kJm^{-2}. The corresponding value of $K_{IC}(J)$, estimated using Equation 2, is 275 $MPa \cdot m^{1/2}$ (250 ksi $in^{1/2}$), $\pm$ 5%.

At 4 K, the alloy approached linear-elastic behavior, but the results of the first three tests failed to satisfy the ASTM validity criteria[8] for direct K_{IC} measurements. Eight additional J tests were conducted and these results are included in Figure 8. The J-Δa curve at 4 K is nearly horizontal, indicating a J_{IC} value of about 150 kJm^{-2} $\pm$ 10; the K_{IC} estimate from Eq. (2) is 182 $MPa \cdot m^{1/2}$ (165 ksi$\cdot in^{1/2}$).

Phase Transformations

After tensile tests at 76 and 4 K, the deformed specimens were magnetic. Therefore, these specimens were measured, using bar-magnet torsion balance equipment,[6] to correlate magnetic attraction with specimen reduction of area. The magnetic readings were converted to percent bcc martensite and the reduction of area converted to elongation, assuming constant volume. These data are plotted in Figure 9 and typical microstructures are shown in Figure 10.

Although not positively identified, it is probable that hcp martensite was also formed in the 21-6-9 alloy during low temperature deformation. The microphotographs after deformation at 4 K (Figure 10) identify transformed regions which are parallel to the (111) slip band traces. These appear identical to the hcp areas identified in earlier research on AISI 304, an Fe-Cr-Ni alloy.[7,14]

The amount of bcc martensite formed is large and only slightly less than that which is formed in AISI 304 at the same temperatures[7,14]. Permeability values of the order of 10 were measured in heavily deformed specimen portions at 76 K, but it is difficult to identify bcc martensite in the Figure 10 photo-micrographs. Normally, in austenitic stainless steels the bcc martensitic product has an acicular, plate-like morphology with the habit plane of the plate not {111}. Examination of specimen microstructures, typified by Figure 10 indicate that only at {111} band intersections are the distinctive plate-like microstructures observed.

There is clear evidence that the amount of the transformation is suppressed, as a function of either stress or strain, as temperature is lowered from 76 K to 4 K. This is similar to the Fe-Cr-Ni (AISI 304) alloy martensitic transformation behavior[7,14], where formation of the hcp martensitic phase was suppressed at temperatures between 20 and 4 K. Apparently, in the complicated energy balance affecting martensitic transformation for these alloy systems at low temperatures, the increase of flow stress and the decrease of dislocation mobility more than offset the gradually increasing free energy difference between the structures.

Finally, it is not clear that martensitic transformations are deleterious to material application. Normally, the stress levels used in service are less than the yield strength, and no martensitic transformations should occur. The complexities and concern usually are discussed when one considers welds and weld techniques. Chemical segregation and stress concentraions are then more likely, rendering particular sections less stable and, locally, stressed above the yield

strength. In these situations martensitic products will form.

AISI 304 behaves in a similar manner; it is stable on cooling to low temperatures but transforms to hcp and bcc martensitic products during plastic deformation. But, unlike 21-6-9, the fracture toughness of AISI 304 remains extremely high at 4 K[15], implying that martensitic transformations are not harmful to the fracture toughness of the Fe-Cr-Ni stainless steel. This is not clear in the case of the Fe-Cr-Ni-Mn-N alloy, however, as the toughness is rapidly decreasing between 76 and 4 K. For appropriate safety of operation at 4 K, additional research is necessary to understand the effect of martensitic transformations on fracture toughness.

Conclusions

1. The fracture toughness of the 21-6-9 austenitic stainless steel exhibits a decided temperature dependence between 300 and 4 K, but retains a toughness of 150 kJ/m^2 (136 $ksi \cdot in^{1/2}$) at 4 K. Linear-elastic behavior was approached at 4 K.

2. The yield strength of the 21-6-9 alloy is also very temperature dependent, tripling from room temperature to 4 K, and reaching a value of 1.24 GPa (180 ksi) at 4 K.

3. During plastic deformation at 76 and 4 K, bcc martensite was identified and correlated with strain. Suppression at 4 K, compared to 76 K, of the amount of bcc martensite was found.

Acknowledgements

The authors thank D. P. Landon, Lawrence Livermore Laboratories for supplying the test material. Dr. R. P. Mikesell conducted the tensile tests, R. L. Durcholz contributed technical assistance to tensile, fracture, and metallographic preparation, and Dr. M. B. Kasen provided the photomicrographs.

References

1. P. R. Landon, Unpublished data, Lawrence Livermore Laboratories, Livermore, CA (1975).

2. P. F. Scardigno, Masters Thesis, Naval Postgraduate School, Monterey, CA, AD/A-004555 (1974).

3. C. O. Malin, NASA SP-5921(01), Technology Utilization Office, NASA, Washington, D.C. (1970).

4. R. D. Masteller, NASA CR-72638(N70-27114), Martin Marietta Corp., Denver, CO (1970).

5. Standard Methods of Tension Testing of Metallic Materials, ASTM E8-69, 1976 Annual Book of ASTM Standards, Part 10 (ASTM, Philadelphia, PA, 1976) p. 120.

6. R. P. Reed, Advances in Cryogenic Engineering, Vol. 7 (Plenum Press, New York, 1962) p. 448.

7. R. P. Reed and C. J. Guntner, Trans. AIME, 230, (1964) p. 1713.

8. Standard Method of Test for Plane-Strain Fracture Toughness of Metallic Materials, ASTM E 399-74, 1976 Annual Book of ASTM Standards, Part 10 (ASTM, Philadelphia, PA 1976) p. 471.

9. R. P. Reed, R. L. Tobler, and R. P. Mikesell, "Advances in Cryogenic Engineering - ICMC", Vol. 22 (Plenum Press, New York, 1976), to be published.

10. J. D. Landes and J. A. Begley, Westinghouse Research Laboratory Scientific Paper 73-1E7-FMPWR-P3, Pittsburgh, PA (1973).

11. J. D. Landes and J. A. Begley, "Fracture Analyses", ASTM STP 560, (American Society for Testing and Materials, Philadelphia, PA 1974) p. 170.

12. J. R. Rice, P. C. Paris, and J. G. Merkle, ASTM STP 536 (ASTM, Philadelphia, PA 1973) p. 231.

13. H. M. Ledbetter, personal communication.

14. C. J. Guntner and R. P. Reed, ASM Trans. 55, (1962) p. 399.

15. R. P. Reed, A. F. Clark and E. C. van Reuth, Eds. "Materials Research for Superconducting Machinery III", AD-A012365/3WM, National Technical Information Service, Springfield, VA (1975).

List of Figures

Figure 1. Compact specimen for fracture testing of Fe-19Cr-6Ni-9Mn alloy.

Figure 2. Summary of tensile and yield strength data as a function of temperature for the Fe-21Cr-6Ni-9Mn alloy.

Figure 3. Summary of tensile elongation as a function of temperature for the Fe-21Cr-6Ni-9Mn alloy.

Figure 4. Summary of tensile reduction of area as a function of temperature for the Fe-21Cr-6Ni-9Mn alloy.

Figure 5. Stress-strain curves for the Fe-21Cr-6Ni-9Mn alloy at 295, 76 and 4 K.

Figure 6. Typical load-deflection curves for compact specimens at 295, 76 and 4 K for annealed Fe-21Cr-6Ni-9Mn alloy.

Figure 7. Fracture characteristics of Fe-21Cr-6Ni-9Mn alloy at 295, 76 and 4 K.

Figure 8. The J-integral as a function of crack extension at 295, 76 and 4 K for annealed alloy Fe-21Cr-6Ni-9Mn.

Figure 9. Estimated percent bcc martensite that forms during tensile tests as a function of tensile elongation.

Figure 10. Microstructures of alloy 21-6-9 after deformation at 4 K. Bands lie on {111} austenite planes and probably represent hcp and bcc martensite, (a) 800X, (b) 1200X.

List of Tables

Table 1. Precracking parameters for J-integral specimens.

Table 2. Tensile properties of Fe-21Cr-6Ni-9Mn alloy.

Table 3. Fracture results for 3.8 cm thick compact specimens of alloy Fe-21Cr-6Ni-9Mn.

Table 1. Precracking parameters for J-integral test specimens.

Test Temperature (k)	P_f/P_{max} x100 (percent)	K_f ($MPa \cdot m^{1/2}$)	Relative Crack Length, a/W	a_e/a
295	40-45	48-54	0.638	0.90-0.91
76	22-27	52-63	0.640	0.87-0.90
4	30-35	52-63	0.64 to 0.795	0.88-0.89

Table 2. Tensile properties of Fe-21Cr-6Ni-9Mn alloy.

Temperature (K)	Yield Strength 0.2% offset GPa	Tensile Strength GPa	Elongation 2.5 cm gage length (%)	Reduction of Area (%)
295 K	0.350	0.696	61	79
	0.357	0.705	61	78
Average	0.353 (51 ksi)	0.701 (102 ksi)	61	78
76 K	0.913	1.462	42	32
	0.886	1.485	43	41
Average	0.899	1.474 (214 ksi)	43	37
4 K	1.258	1.633	16	40
	1.224	1.634		
Average	1.241 (180 ksi)	1.634 (237 ksi)	16	40

Table 3. Fracture results for 3.8 cm thick compact specimens of alloy Fe-21Cr-6Ni-9Mn.

Temperature (k)	a/W	K_Q[1] ($MPa \cdot m^{1/2}$)	J (kJm^{-2})	Δa (cm)	J_{IC} (kJm^{-2})
295	0.638	58	177	0.013[2]	
	0.636	61	744	0.051[2]	
	0.640	55	905	0.069[2]	1130±20%
	0.635	63	1355	0.097[3]	
	0.642	50	1423	0.112[3]	
76	0.612	134	261	0.0	
	0.634	153	413	0.028	
	0.640	131	499	0.053	
	0.637	137	674	0.079	337±10%
	0.645	130	788	0.091	
	0.643	130	698	0.198	
4	0.645	164	NA	NA	
	0.648	162	NA	NA	
	0.643	159	NA	NA	
	0.670	NA	100	0.0	
	0.655	167	147	0.020	
	0.670	158	149	0.080	
	0.656	160	162	0.076	
	0.750	NA	89	0.0	150±10%
	0.725	NA	191	0.0313	
	0.725	NA	274	0.105	
	0.755	NA	141	0.033	

1. Calculated from ASTM E 399-74 Method.
2. Apparent crack extension due to crack tip deformation only.
3. Crack extension due to deformation and material separation.

NOTES: 1 $in \cdot lb \cdot in^{-2} = 0.175\ kJm^{-2}$; 1 inch=2.54 cm; 1 $ksi \cdot in^{1/2} = 1.099\ MPa \cdot m^{1/2}$

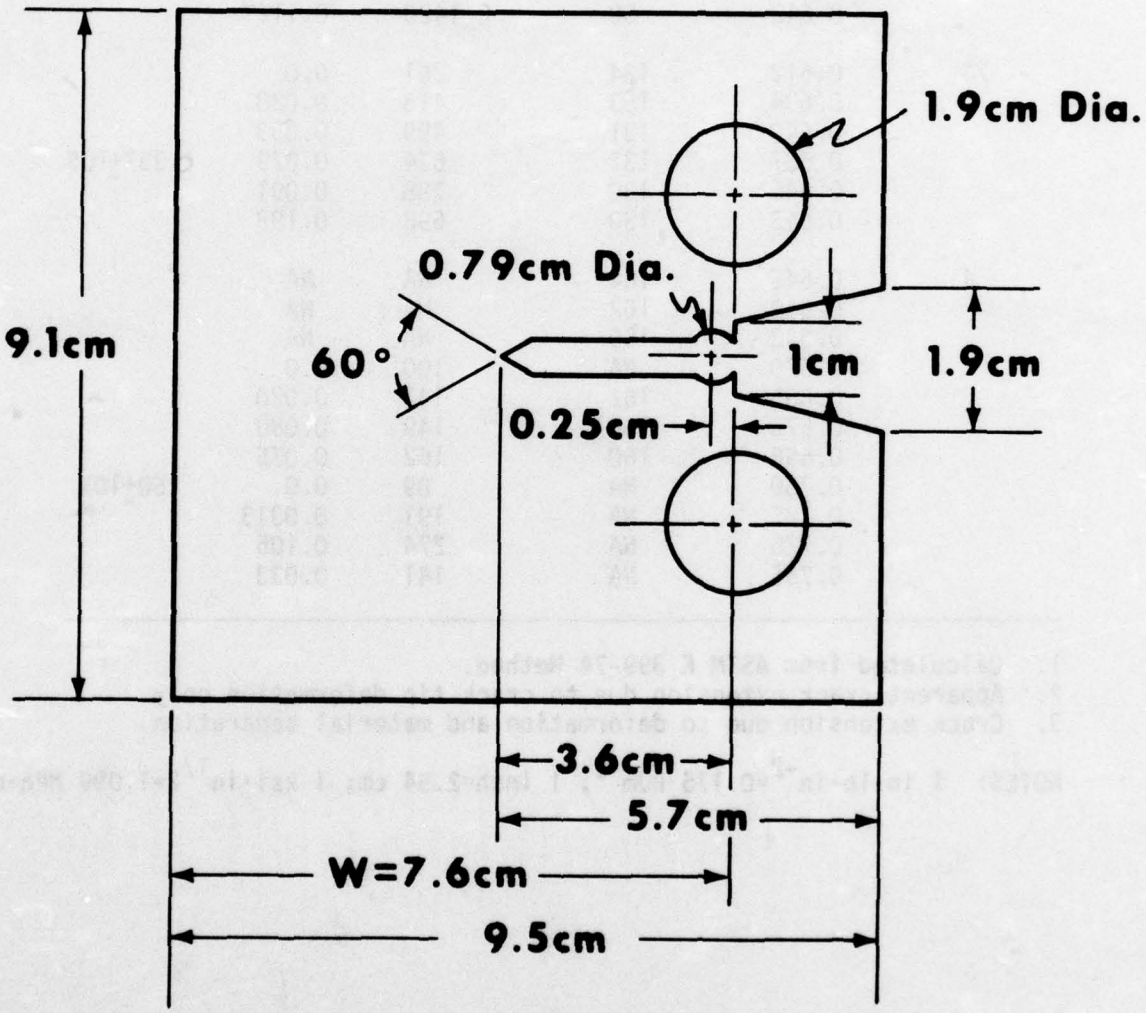


Figure 1. Compact specimen for fracture testing of Fe-19Cr-6Ni-9Mn alloy.

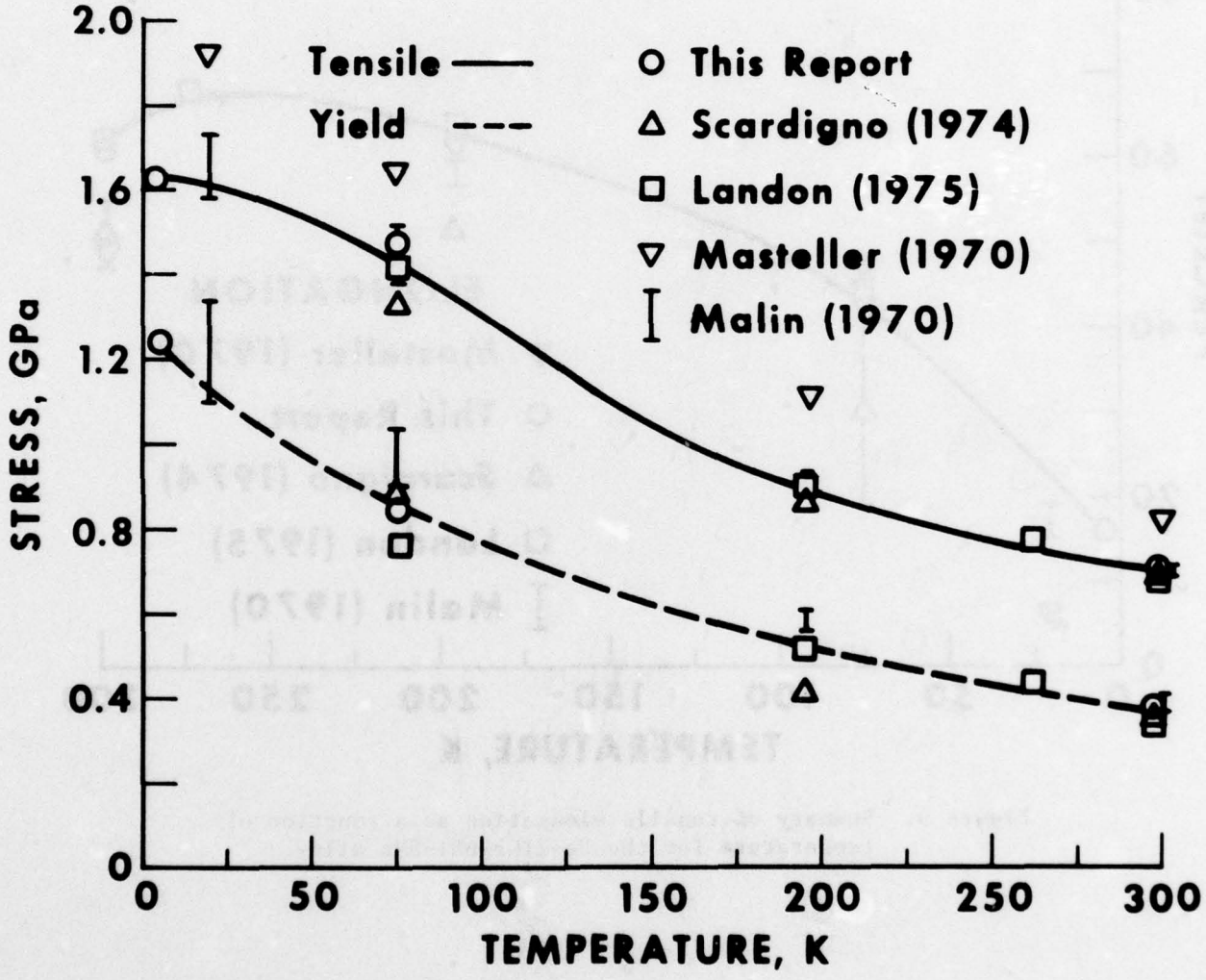


Figure 2. Summary of tensile and yield strength data as a function of temperature for the Fe-21Cr-6Ni-9Mn alloy.

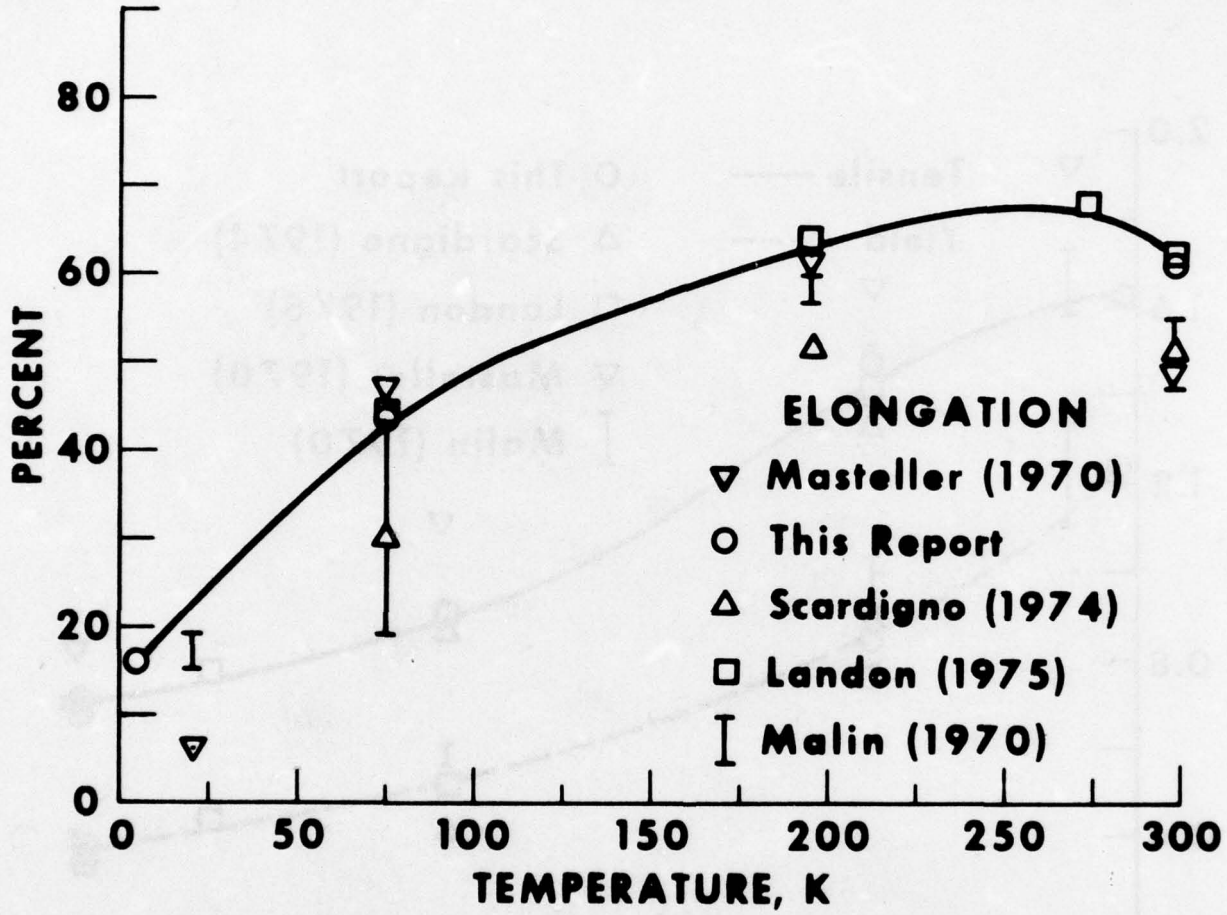


Figure 3. Summary of tensile elongation as a function of temperature for the Fe-21Cr-6Ni-9Mn alloy.

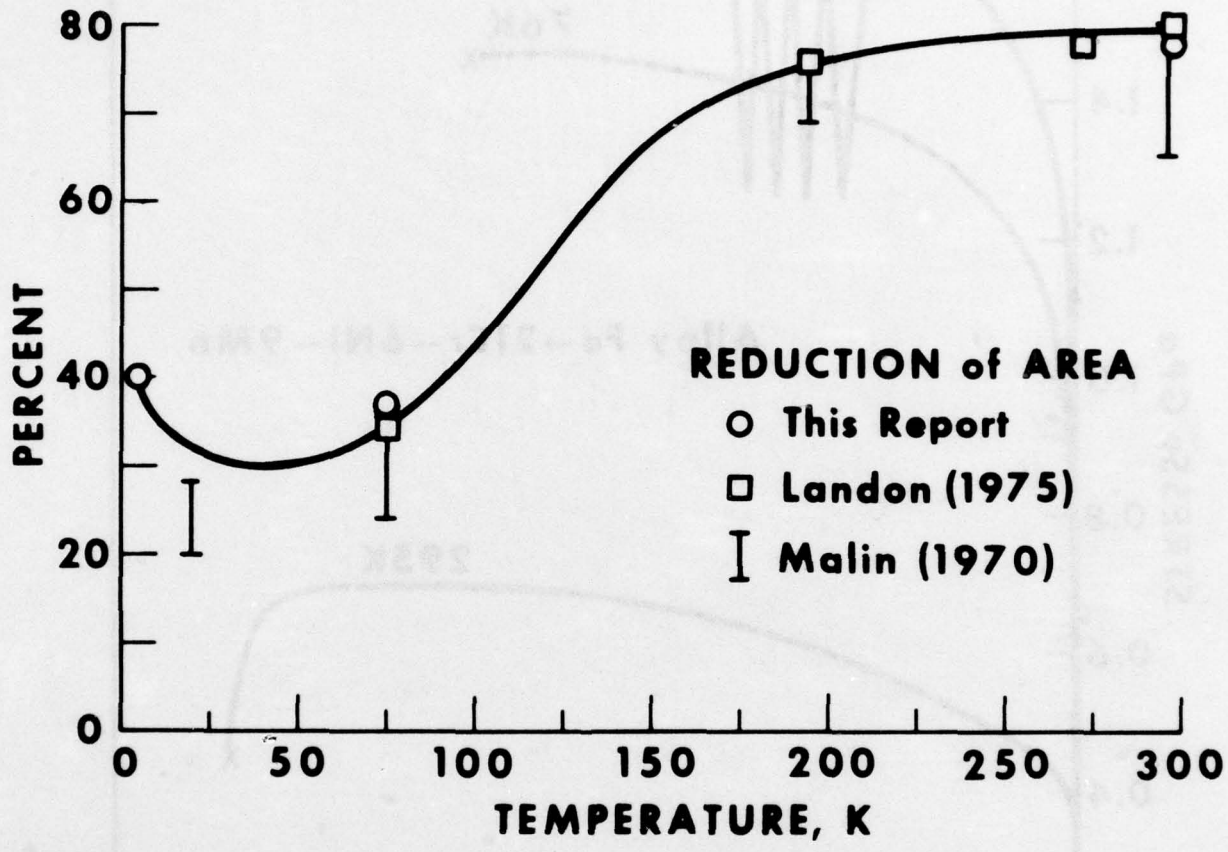


Figure 4. Summary of tensile reduction of area as a function of temperature for the Fe-21Cr-6Ni-9Mn alloy.

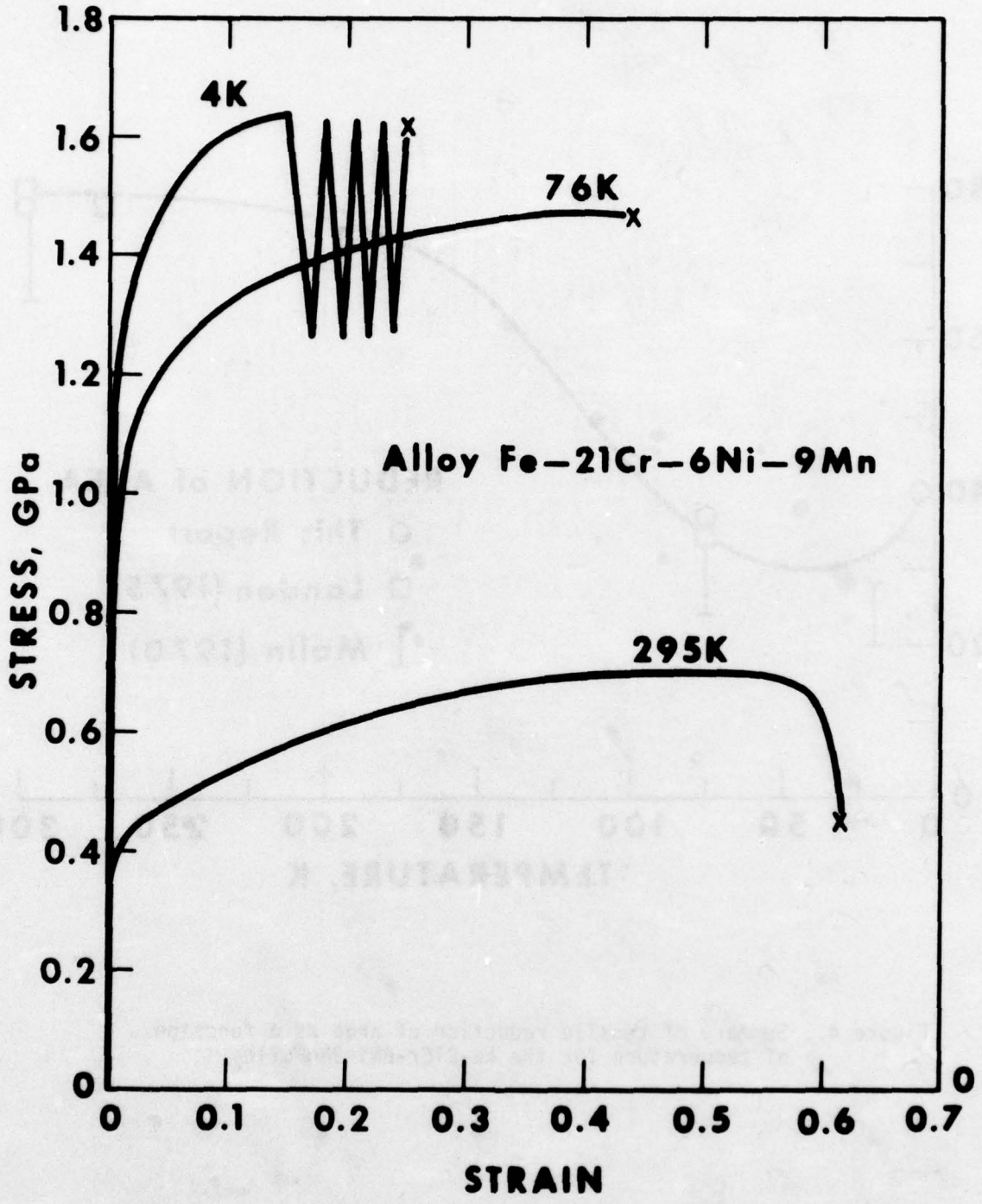


Figure 5. Stress-strain curves for the Fe-21Cr-6Ni-9Mn alloy at 295, 76, and 4 K.

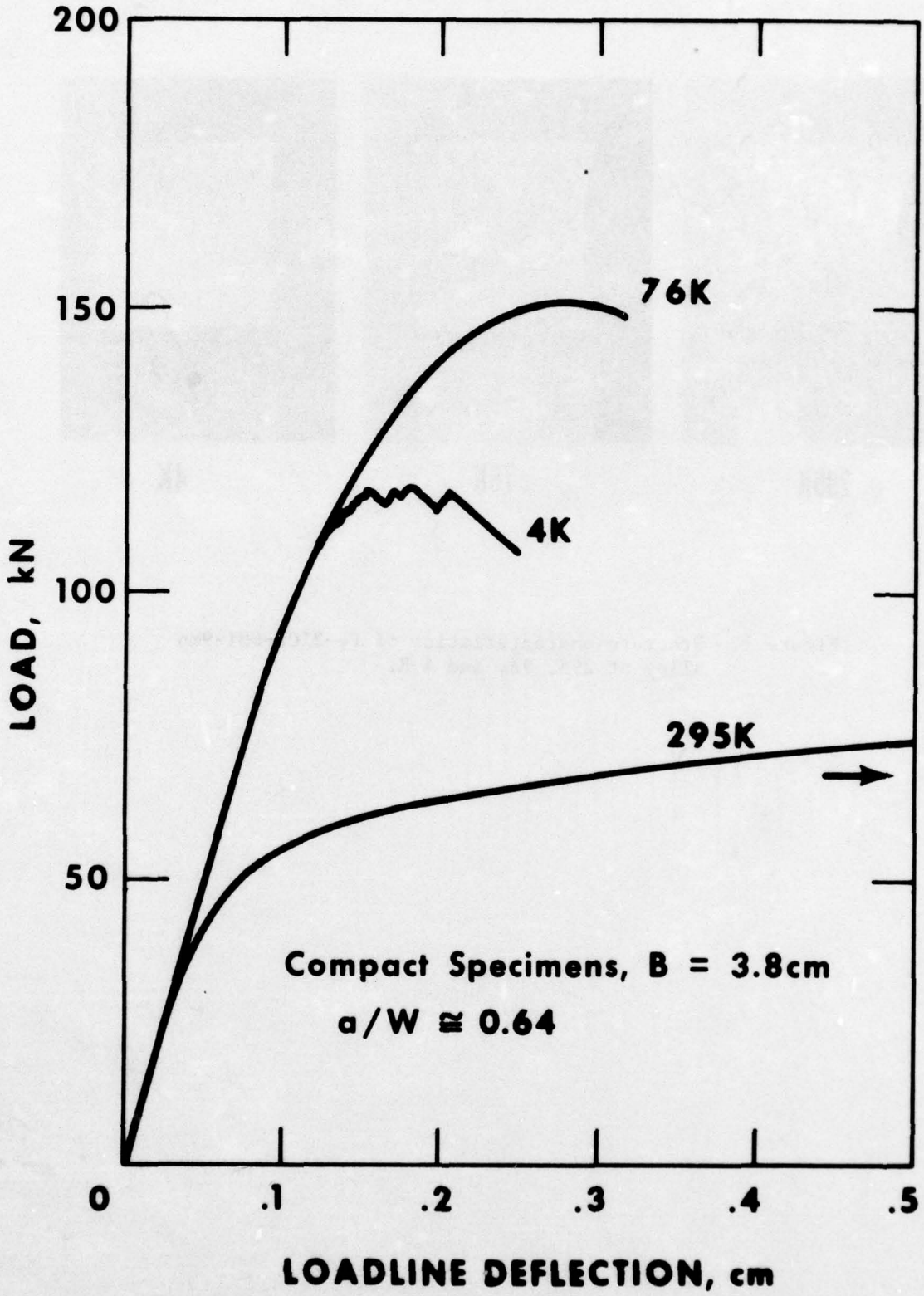


Figure 6. Typical load-deflection curves at 295, 76, and 4 K for annealed Fe-21Cr-6Ni-9Mn alloy.

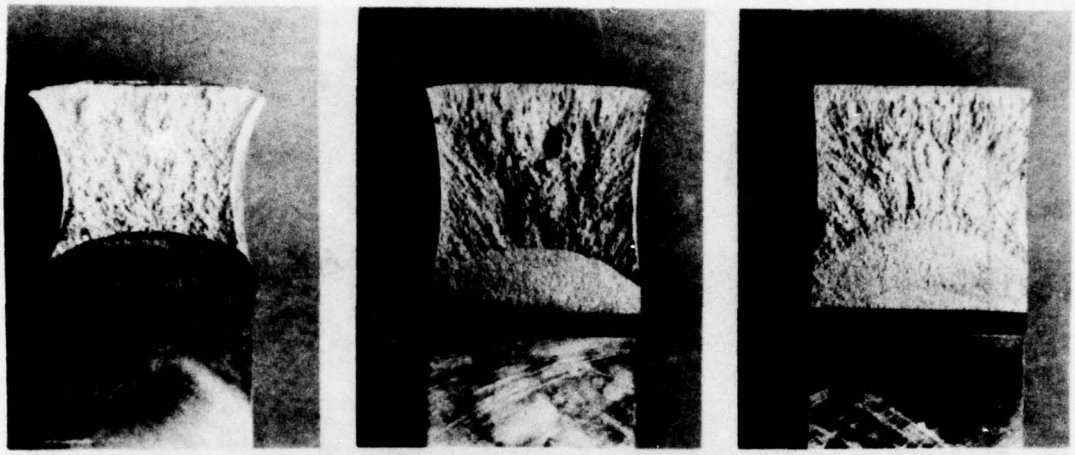


Figure 7. Fracture characteristics of Fe-21Cr-6Ni-9Mn alloy at 295, 76, and 4 K.

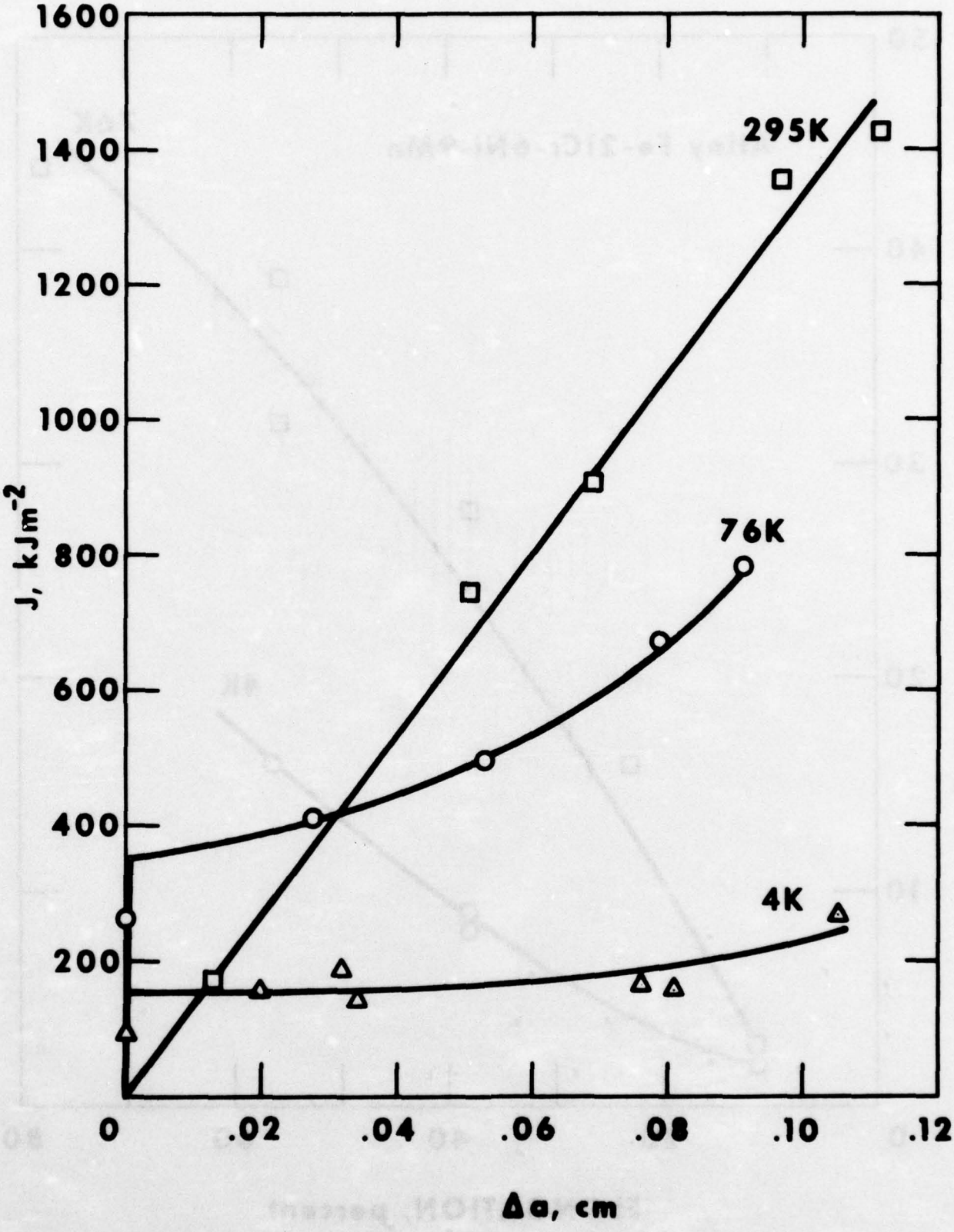


Figure 8. The J-integral as a function of crack extension at 295, 76, and 4 K for annealed alloy Fe-21Cr-6Ni-9Mn.

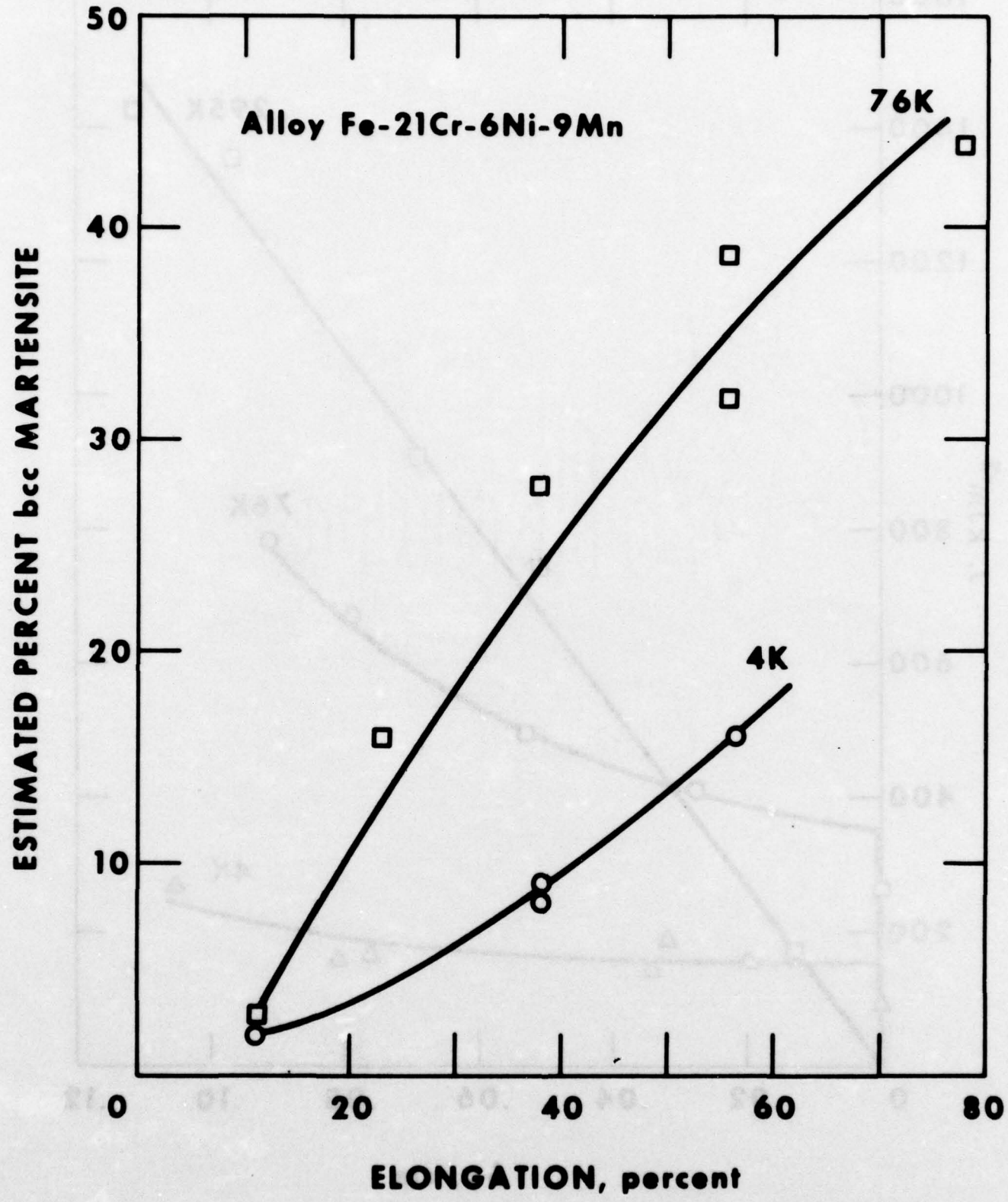
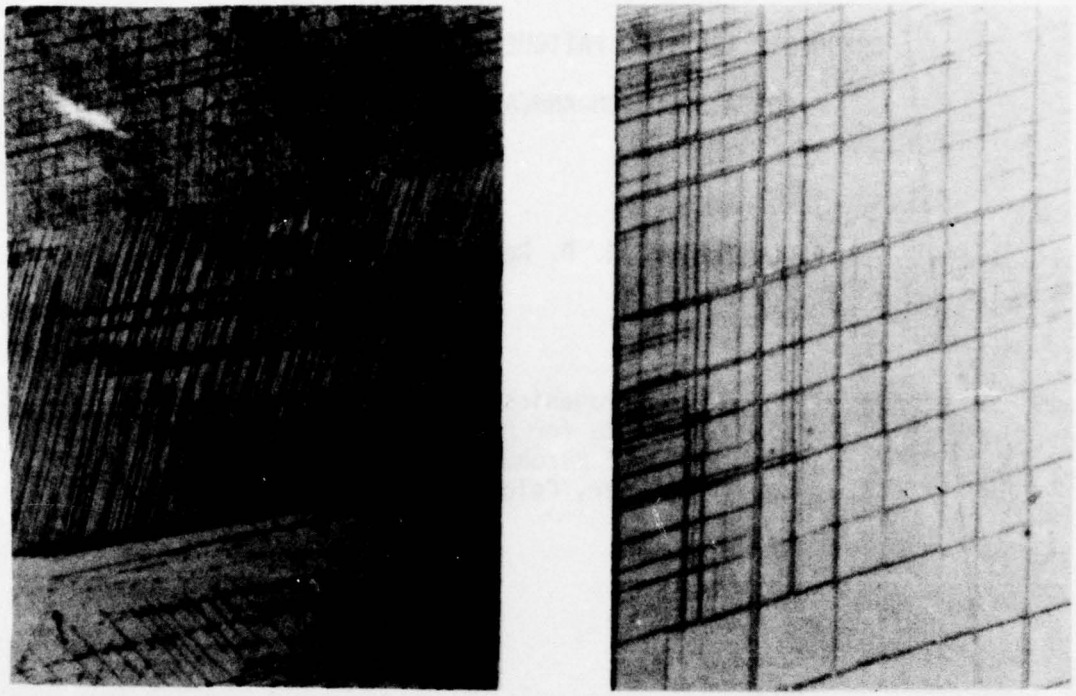


Figure 9. Estimated percent bcc martensite that forms during tensile tests as a function of tensile elongation.



(a) (b)

Figure 10. Microstructures of alloy 21-6-9 after deformation at 4 K. Bands lie on {111} austenite planes and probably represent hcp and bcc martensite, (a) 800X, (b) 1200X.

CRYOGENIC TENSILE, FATIGUE, AND FRACTURE PARAMETERS FOR A SOLUTION-ANNEALED MARAGING STEEL[+]

R. L. Tobler, R. P. Reed, and R. E. Schramm

Cryogenics Division
Institute for Basic Standards
National Bureau of Standards
Boulder, Colorado 80302

[+] Contribution of NBS, not subject to copyright.

ABSTRACT

The mechanical properties of an eighteen percent nickel, solution-annealed 300-grade maraging steel were measured to assist in the evaluation of this material for low-temperature structural applications. Tensile, fatigue-crack growth rate, and fracture toughness tests were performed in ambient air (295 K), liquid nitrogen (76 K), and liquid helium (4 K), with the following results: (1) the yield strength of this material increases from 848 MPa at room temperature to 1596 MPa at 4 K; (2) the tensile ductility is moderate, with elongation decreasing from 15.5 to 6.7% for this temperature region; (3) the plane strain fracture toughness (K_{Ic}) decreases from 165 MPa·m$^{1/2}$ at room temperature to 83 MPa·m$^{1/2}$ at 4 K; and (4) the fatigue-crack propagation resistance at intermediate stress intensity ranges is relatively insensitive to temperature. These results are compared with similar data for other cryogenic materials.

Key words: Fatigue; fracture; low temperature tests; maraging steels; mechanical properties; nickel alloys.

INTRODUCTION

The beneficial effect of nickel on the low temperature fracture resistance of steels is well known [1-2]. Concentrations of from 2 1/4 to 9% Ni are used in the 0.1 to 0.2% carbon ferritic steels that were specially developed for low temperature service [2]. For these steels, increasing nickel content correlates with reduced ductile-to-brittle transition temperatures. For the grade having the highest nickel content, ASTM A533-72a (9% Ni steel), the transition to low fracture toughness occurs at temperatures between 76 and 4 K. Emerging applications in the relatively new field of superconducting machinery would benefit from a commercially-available ferritic steel that retains high toughness at 4 K.

With this goal in mind, the 18% Ni maraging steels must be considered. Maraging steels are easily processed and are weldable. High nickel and low carbon contents ($\sim$ 0.003% C, max.) account for the relatively soft, platelet-like martensite that forms on cooling from the austenite field. Cobalt, molybdenum, titanium, and aluminum alloying contributes significantly to strengthening, and the ultra-high strengths obtained with fully aged 300 grade maraging steels represent an outstanding technological achievement [3,4]. However, low fracture toughness is often associated with high yield strength [5-8]. Therefore the fracture toughness of this material should be investigated before considering it a candidate for cryogenic structural applications. The literature contains numerous plain strain fracture toughness (K_{Ic}) and fatigue crack growth rate parameters for maraging steels [9-15], but low temperature studies are less common [10,13-15].

This paper describes the mechanical behavior of a solution-annealed 18% Ni, 300 grade maraging steel at temperatures in the ambient-to-extreme cryogenic range. The conventional tensile properties, fatigue crack growth rates, and fracture toughness values were measured at 295, 76, and 4 K, using state-of-the-art techniques. This alloy was tested in the solution-annealed condition, to maximize the fracture toughness.

Material

The 300 grade maraging steel tested in this study was supplied by the Morris Steel and Aluminum Corporation. The material was a 5.3 x 15.4 x 58 cm forged bar that had been solution-annealed at 1088 K and air cooled. The chemical analysis quoted by the supplier is, in weight percent: 18.41 Ni, 0.002 C, 0.01 Mn, 0.006 P, 0.003 S, 0.01 Si, 9.27 Co, 4.95 Mo, 0.59 Ti, 0.12 Al, and balance, Fe. This alloy was tested in the as-received condition which is a lath martensite having the body-centered cubic crystal structure and virtually no retained austenite [9].

Procedures

Tensile

Cylindrical tensile specimens having a reduced section 3.8 cm long and 0.51 cm in diameter were machined in the transverse orientation, such that the loading-axis/fracture-plane orientation matched that of the compact specimens described below. The tensile tests were conducted at a crosshead velocity of 0.008 mms^{-1}, using the 44.5 kN screw-driven machine and cryostat previously described [16]. The commercial load cell and clip-on strain gage extensometer outputs were autographically recorded, and the resultant load-versus-deflection curves were analyzed following the standard ASTM E8-69 Method [17].

Fracture

Compact specimens of the TL orientation [18] (notch plane normal to the long transverse forging direction) were used in all fatigue and fracture tests. The specimens were 2.3 cm thick (B) and 5.08 cm wide (W). The planar dimensions are shown in Figure 1. Knife edges were machined integral to the notch, permitting clip-gage placement and deflection measurements at the loadline.

Room temperature (295 K) tests were conducted in unconditioned air, using a 100 kN servo-hydraulic test machine and cryostat. Low temperature tests were performed with the specimen and clip gage completely submerged in liquid nitrogen (76 K) or liquid helium (4 K) environments. At each temperature, the clip-gage satisfied the ASTM E-399-74 Method linearity requirements [18]. The apparatus and low temperature techniques are described elsewhere in greater detail [19].

The test procedure involved precracking the specimens at their test temperatures and subsequently loading them to fracture by increasing the stress intensity at a rate of approximately 1 $MPa \cdot m^{1/2} s^{-1}$. At 76 K and 4 K, the ASTM E 399-74 requirements for valid, linear-elastic fracture toughness tests were fulfilled. Therefore, K_{Ic} was calculated directly using the solution for compact specimens [18]:

$$K_{Ic} = P_Q B^{-1} W^{-1/2} [f(a/W)] \qquad (1)$$

The calibration factor, f(a/W), is a function of relative crack length [18]:

$$f(a/W) = 29.6(a/W)^{1/2} - 185.5(a/W)^{3/2} + 655.7(a/W)^{5/2} - 1017.0(a/W)^{7/2} + 638.9(a/W)^{9/2} \qquad (2)$$

The load P_Q is derived from the test record using the secant offset procedure, and crack length is the average value of measurements at 25, 50, and 75% of specimen thickness. The uncertainty in K_{Ic} values obtained by this method is estimated at less than 5% [20].

Nonlinearity in the test records at room temperature precluded using the ASTM E-399-74 method. Therefore, K_{Ic} was estimated using the J-integral concept. J is the rate of change of potential energy with respect to crack area for nonlinear elastic materials, and it is a measure of the crack-tip strain field intensity for elastic-plastic fractures. The critical value, J_{Ic}, is the value of J at the onset of crack extenstion [21].

Since stable crack extension occurred in the solution-annealed maraging steel at room temperature, the resistance curve technique [21] was used to measure J_{Ic}. Seven nearly identical specimens ($a/W \simeq 0.6$) were loaded to cause crack extension increments of up to 0.4 cm. The specimens were then unloaded and heat-tinted to oxidize the crack surfaces. The specimens were then cooled to 76 K (to avoid subsequent plastic deformation) and fractured into halves. The straw/blue crack extension increments (Δa) created during the initial loading were measured to the nearest 0.001 cm with a travelling microscope at three points equidistant across the specimen thickness, and averaged. The J values at points of unloading were calculated using the approximation [22]:

$$J = 2AB^{-1}(W - a)^{-1} \qquad (3)$$

The pairs of J and Δa measurements were plotted and extrapolated to obtain J_{Ic} with an uncertainty of $\pm$ 10%. The room temperature K_{Ic} was then estimated from:

$$K_{Ic}^2 = EJ_{Ic}(1 - \nu^2)^{-1} \quad (4)$$

where E, Young's modulus for the material is 175.6 GPA (25.5 x 10^6 psi) and ν, Poisson's ratio is 0.325 [23].

Fatigue Crack Growth

Fatigue crack growth rates were measured during the precracking of fracture toughness specimens, but the maximum stress intensity factor was restricted to less than 50 MPa$\cdot m^{1/2}$, to insure that the precracking loads did not influence the fracture toughness test results. To obtain da/dN data at stress intensity factors greater than 50 MPa$\cdot m^{1/2}$, one additional specimen was tested at each temperature. The fatigue tests were conducted using controlled loads, a sinusoidal load cycle, a test frequency (F) of 20 Hz, and a minimum/maximum load ratio, R, of 0.1.

Crack length was inferred by elastic compliance or deflection-per-unit-load (δ/P) measurements. Following techniques previously described [24], correlations between average crack length and δ/P were obtained experimentally using data from fractured specimens. The a-versus-N curves were constructed from compliance readings taken periodically during the fatigue tests. Using a computer program, the a-versus-N curves were fitted with a third order polynomial and differentiated, yielding da/dN with an uncertainty of less than $\pm$ 20%. The stress intensity factor ranges were calculated based on Eqs. (1-2) and the fatigue load range:

$$\Delta K = K_{max} - K_{min} = (P_{max} - P_{min})B^{-1}W^{-1/2}[f(a/W)] \quad (5)$$

RESULTS AND DISCUSSION

Tensile

The uniaxial tensile property measurements for the solution-annealed 300 grade maraging steel are itemized in Table 1, and the average values of yield strength, ultimate strength, elongation, and reduction of area are shown in Figures 2 and 3. The results show that the strength and ductility parameters exhibit opposite temperature dependences. Between 295 and 4 K, the yield strength increases from 848 MPa to 1596 MPa, while reduction of area decreases from 70% to 47%. The room temperature yield strength is significantly lower than the 1790 to 2060 MPa range for aged 300 grade maraging steels [9], but ductility is higher. On the other hand, this solution-annealed 300 grade maraging steel offers a modest improvement over the yield and ultimate strengths and reduction of area values for a commercial 9% Ni steel in the quenched and tempered condition [25]. The yield strengths of several nickel alloy steels are compared in Figure 4.

Fracture Toughness

The fracture surfaces of compact specimens showed sizable shear-lip regions at room temperature, whereas the fractures at 76 and 4 K were relatively flat. "Type I" test records [18] having only slight nonlinear segments near the maximum load were obtained at these low temperatures. The fracture measurements at each temperature are summarized in Table 2.

Consider the room temperature results. The J-versus-Δa curve at room temperature, Figure 5, reveals a linear trend for Δa greater than 0.5 mm. At smaller Δa, apparent crack extension is caused by crack-tip geometry changes due to blunting instead of actual material

separation. The $J = 2\Delta a\sigma_{flow}$ line was constructed to account for this blunting, as recommended [21]. The J_{Ic} value taken at the intersection of the resistance curve and the flow line is 140 kJm^{-2}, and the corresponding K_{Ic} estimate from Eq. (4) is 165 $MPa \cdot m^{1/2}$.

The 76 K and 4 K results from the ASTM E 399-74 method satisfy the linear-elastic size criterion which requires:

$$a, W-a, B \geq 2.5 \frac{K_{Ic}}{\sigma_y}^2 \qquad (6)$$

The edge-crack-to-average-crack-length ratios were uniform, with values ranging from 0.96 to 0.98. The P_{max}/P_Q ratios were also acceptable, with values below 1.10. The data listed in Table 2 are therefore valid, and the average K_{Ic} at each temperature is shown in Figure 6.

As expected, there is a substantial improvement in fracture toughness over the values reported for aged 300 grade maraging steels. The room temperature K_{Ic} value for our solution-annealed material, 165 $MPa \cdot m^{1/2}$, is nearly threefold greater than values reported for the aged condition [3,9]. Low temperature data are scarce, but Antolovich [13] reports K_{Ic} values of 115 and 66 $MPa \cdot m^{1/2}$ for an aged 300 grade maraging steel at 295 and 77 K, respectively. Thus, the difference in K_{Ic} for the solution-annealed and aged conditions may be as large as a factor of 2 at liquid nitrogen temperature.

While it is true that low temperature effects on K_{Ic} for the maraging steels are adverse, our data indicate no abrupt fracture transitions such as usually observed for body-centered cubic materials, as shown in Figure 6. Nevertheless, there is a 48% reduction of K_{Ic} for the solution-annealed maraging steel between 295 and 4 K. At 4 K, the fracture toughness is

83 MPa·m$^{1/2}$, slightly higher than the 75 MPa·m$^{1/2}$ value reported [25] for quenched and tempered 9% Ni steel. The absence of transitional behavior in the maraging steel undoubtedly is related to the favorable influences of high nickel and low carbon contents on the deformation characteristics and cleavage resistance of steel [1].

The present results reinforce the view that plastic deformation and fracture processes are competitive, and that factors which tend to increase a material's resistance to slip also tend to enhance the probability of brittle fracture. In their studies of maraging steels at room temperature, Fischer and Repko [7], Jones and Brown [6], and Srawley [5] demonstrated decreases in toughness at higher yield strengths. They illustrated the inverse relationship by varying yield strength through metallurgical changes in alloying and heat treatment. In the present study, similar trends are noted on lowering the test temperature.

Fatigue Crack Growth Rates

Fatigue crack growth rates for the solution-annealed 18% Ni maraging steel are shown in Figure 7. The da/dN data define a scatterband approximately 10 MPa·m$^{1/2}$ wide. Within this range, the data at 76 K and 4 K are virtually equivalent, tending to be slightly lower than rates at room temperature. Since the improvement in rates at cryogenic temperatures never amounts to more than a factor of 2, all of the results at stress intensity factors between 20 and 55 MPa·m$^{1/2}$ can be specified by an upper bound equation:

$$\frac{da}{dN} = 6.6 \times 10^{-9}(\Delta K)^{3.0} \qquad (7)$$

Here da/dN and ΔK are given in SI units, mm/cycle and $MPa \cdot m^{1/2}$, respectively.

At ΔK values greater than 55 $MPa \cdot m^{1/2}$, the rates at 295 K and 76 K remain conservative with respect to Eq. (7), at least for the range of ΔK investigated. However, the rates at 4 K are accelerated and the fatigue crack propagation resistance becomes inferior as ΔK exceeds 75% of the reported K_{Ic} value at this temperature. The 4 K rates at stress intensity factors greater than 55 $MPa \cdot m^{1/2}$ are not specified by the upper bound equation, Eq. (7). Rather, the behavior at 4 K can be described as resulting from a transition in the power-law dependence on ΔK, i.e. a transition from an exponent of n = 3 to an exponent of n = 7.6 occurs at ΔK = 55 $MPa \cdot m^{1/2}$. Similar transitions to high values of n are known to occur in other steels as ΔK approaches K_{Ic}, due to the influence of static fracture modes on microcracking [25].

Figure 8 compares Eq. (7) for the solution-annealed 300 grade maraging steel with a band representing typical results for other steels at room temperature. Included in the band are: (1) Barsom's data [26] for non-nickel ferritic steels of various strengths, (2) our previously reported data [25] for 3.5, 5, and 9% Ni ferritic steels, and (3) some data for the 300 grade maraging steels tested by Bathias and Pelloux [11], and Antolovich, Saxena, and Chanai [12]. All of these sources report power-law equation exponents in the range 2.5 to 3.5. Evidently, the present results are typical for steels at room temperature. Bathias and Pelloux reported that their rates for a solution-annealed 300 grade maraging steel were indistinguishable from rates for the same alloy in the aged condition, for $30 \leq \Delta K \leq 50$ $MPa \cdot m^{1/2}$. However, it would be speculative to assume that this would be true at extreme cryogenic temperatures, and data at 4 K for the aged condition are unavailable.

In Figure 9, the upper bound representation of Eq. (7) is used again in comparing the behavior of this maraging steel with bands representing rates for austentic nickel-base superalloys and austenitic stainless steels tested at temperatures in the range 295 to 4 K. Included in the band for austenitic stainless steels are results for AISI types 304, 304L, 310, 310S, and 316 as well as Kromarc 58, A-286, and an Fe-21Cr-6Ni-9Mn alloy [27,28]. Included in the band for nickel base superalloys are data for Inconel alloys 750, 718, 706 and a low expansion alloy, LEA [29]. The fatigue-crack growth resistance of the solution-annealed maraging steel is intermediate when compared with these potential competitor alloys, suggesting that yield strength and fracture toughness comparisons should be the primary considerations governing alloy selection for cryogenic purposes.

CONCLUSIONS

Relatively few mechanical properties relevant to the problem of fracture-resistant design have been measured for maraging steels at low temperatures. In this study, conventional tensile properties and fracture mechanics parameters were measured for an 18% Ni, 300 grade maraging steel in the solution-annealed condition, since the toughness of aged alloys at low temperatures is marginal. The fracture toughness of the solution-annealed alloy is an inverse function of yield strength between 295 K and 4 K, with K_{Ic} decreasing from 165 MPa$\cdot$m$^{1/2}$ to 83 MPa$\cdot$m$^{1/2}$, and yield strength increasing from 848 MPa to 1596 MPa. These strengths compare favorably with some alloys frequently used in cryogenic environments, such as the austenitic stainless steels. The solution-annealed maraging steel can be considered for cryogenic uses, although the fracture toughness at 4 K is only about 8% greater than that of a commercially available and less expensive 9% Ni alloy steel (ASTM A 553).

ACKNOWLEDGMENTS

This study was sponsored by the Advanced Research Projects Agency of the U.S. Department of Defense. The contributions of Dr. R. P. Mikesell and R. L. Durcholz in conducting the tensile tests are gratefully acknowledged.

REFERENCES

1. Johnson, R. J., Metals Eng. Quart. 15 (1975) 1.
2. Pense, A. W. and Stout, R. D., in Fracture Toughness and Related Characteristics of the Cryogenic Nickel Steels, WRC Bulletin 205 reprint (Int. Nickel Co., New York, 1976) 1.
3. Zackay, V. F., in Alloy Design for Fatigue and Fracture Resistance, Conference Proceedings No. 185, AGARD-CP-185 (North Atlantic Treaty Organization, 1976) AD A021486.
4. Floreen, S., Metallurgical Reviews 126 (1968) 115.
5. Srawley, J. E., in Fracture, 1969 (Chapman and Hall, London, 1969) 131.
6. Jones, M. H. and Brown, W. F., in Review of Developments in Plane Strain Fracture Toughness Testing, ASTM STP 463 (Amer. Soc. Test. Mater., Philadelphia, 1970) 63.
7. Fischer, D. M. and Repko, A. J., J. Materials, JMLSA 7 (1972) 167.
8. Psioda, J. A. and Low, J. R., NASA Tech. Report No. 7 (Dept. Mater. Science, Carnegie-Mellon University, 1975) NASA-CR-143501. 9.
9. 18% Nickel Maraging Steels, Data Bulletin (International Nickel Co., 1969).
10. Cryogenic Materials Data Handbook, AFML-TDR-64-280 (Martin Marietta Co., 1964).

11. Bathias, C. and Pelloux, R. M., Met. Trans. 4 (1973) 1265.

12. Antolovich, S. D., Saxena, A., and Chanai, G. R., Met. Trans. 5 (1974) 623.

13. Antolovich, S. D., private communication.

14. Vishnevsky, C. and Steigerwald, E. A., in Fracture Toughness Testing at Cryogenic Temperatures, ASTM STP 496 (Amer. Soc. Test. Mater., Philadelphia, 1970) 3.

15. Shoemaker, A. K. and Rolfe, S. T., J. Basic Eng. Trans. ASME, 91 (1969) 512.

16. Reed, R. P., in Advances in Cryogenic Engineering 7 (1962) 448.

17. Standard Methods of Tension Testing of Metallic Materials, designation E8-69, in 1974 Annual Book of ASTM Standards, Part 10 (Amer. Soc. Test. Mater., Philadelphia, 1974) 90.

18. Standard Method of Test for Plane Strain Fracture Toughness of Metallic Materials, designation E 399-74, in 1974 Annual Book of ASTM Standards, Part 10 (Amer. Soc. Test. Mater., Philadelphia, 1974) 432.

19. Fowlkes, C. W. and Tobler, R. L., Eng. Fract. Mechs. 8 (1976) 487.

20. Antolovich, S. D. and Chanai, G. R., in Third International Conference on Fracture (Vereiu Deutscher Eisenhuttenleute, Dusseldorf, 1975) II-242.

21. Landes, J. D. and Begley, J. A., in Fracture Analysis, ASTM STP 560 (Amer. Soc. Test. Mater., Philadelphia, 1974) 170.

22. Rice, J. R., Paris, P. C., and Merkle, J. G., in Progress in Flaw Growth and Fracture Toughness Testing, ASTM STP 536 (Amer. Soc. Test. Mater., Philadelphia, 1973) 231.

23. Ledbetter, H. M., private communication.

24. Tobler, R. L., Mikesell, R. P., Durcholz, R. L., and Reed, R. P., in Properties of Materials for Liquified Natural Gas Tankage, ASTM STP 579 (Amer. Soc. Test. Mater., Philadelphia, 1975) 261.

25. Tobler, R. L. and Reed, R. P., to be published.

26. Barsom, J. M., J. Eng. Industry, Trans. ASME (1971) 1190.

27. Logsdon, W. A., Wells, J. M., and Kossowsky, R., in Proceedings of the Second International Conference on Mechanical Behavior of Materials (Amer. Soc. Metals, Ohio, 1976) 1283.

28. Tobler, R. L., in Proceedings of the Second International Conference on Mechanical Behavior of Materials (Amer. Soc. Metals, Ohio, 1976) 573.

29. Logsdon, W. A., Wells, J. M., and Kossowsky, R., in Materials Research for Superconducting Machinery; Reed, R. P., Ledbetter, H. M., and van Reuth, E. C., Eds. (National Bureau of Standards, Boulder, CO, 1976).

LIST OF FIGURES

Figure 1. Planar dimensions of compact specimens for fatigue and fracture tests.

Figure 2. Yield and ultimate strengths for solution-annealed 300 grade maraging steel, showing 88% and 64% increases for the temperature range 295 to 4 K.

Figure 3. Reduction of area and elongation values for solution-annealed 300 grade maraging steel, showing gradually decreasing tensile ductility at low temperatures.

Figure 4. A yield strength comparison of solution-annealed maraging steel and some ferritic nickel alloy steels.

Figure 5. The J resistance curve for solution-annealed maraging steel at room temperature, showing a typical data trend.

Figure 6. The effect of temperature on K_{Ic} for solution-annealed maraging steel, which does not show the transitional behavior exhibited by other nickel-alloy steels. (Data for the 3.5, 5, and 9% Ni steels are published elsewhere [24,25]).

Figure 7. Fatigue crack growth rates for the solution-annealed 300 grade maraging steel at 295, 76, and 4 K.

Figure 8. The fatigue crack growth data [Eq. (7)] for solution-annealed 300 grade maraging steel versus room temperature data for other steels [11,12,25,26].

Figure 9. The fatigue crack growth data [Eq. (7)] for solution-annealed 300 grade maraging steel versus data for austenitic superalloys and stainless steels tested at 295 and 4 K [27-29].

Table 1. Tensile property results for solution-annealed 18% Ni 300 grade maraging steel.

Temperature (K)	0.2% Yield Strength MPa (ksi)	Ultimate Strength MPa (ksi)	Elongation[a] (%)	Reduction in Area (%)
295	904	1069	15	71.3
	791	1068	16	70.3
	848 (123.0)	1068 (155.0)	15.5	70.8
76	1295	1569	12.6	60.4
	1302	1552	13.0	59.7
	1299 (188.4)	1560 (226.2)	12.8	60.1
4	1609	1759	5.6	44.7
	1583	1756	7.8	49.5
	1596 (231.5)	1758 (255.0)	6.7	47.1

a. 2.54 cm gage length

Table 2. Fracture toughness results for solution-annealed 18% Ni 300 grade maraging steel (2.3 cm thick compact specimens).

Temperature (k)	Specimen	a/W	J (kJm^{-2})	Δa (cm)	J^a_{Ic} kJm^{-2}	$K_{Ic}(J)^b$ ($MPa \cdot m^{1/2}$)	K^c_{Ic} ($MPa \cdot m^{1/2}$)
295	4	0.612	199	0.166			
	5	0.599	68	0.001			
	6	0.597	183	0.105			
	15	0.660	206	0.126	140±10%	165±5%	NA
	16	0.595	272	0.392			
	17	0.598	129	0.001			
	19	0.606	159	0.006			
76	2	0.471	NA	NA	NA	NA	125.5
	3	0.498					131.0
	14	0.542					107.0
	18	0.548					117.5
							Avg = 120.2
4	7	0.466	NA	NA	NA	NA	94.1
	11	0.514					78.8
	20	0.483					79.1
	21	0.507					80.1
							Avg = 83.0

a. obtained from extrapolation, see Fig. 4
b. Calculated using Eq. (3)
c. Obtained using the ASTM E 399-74 Method

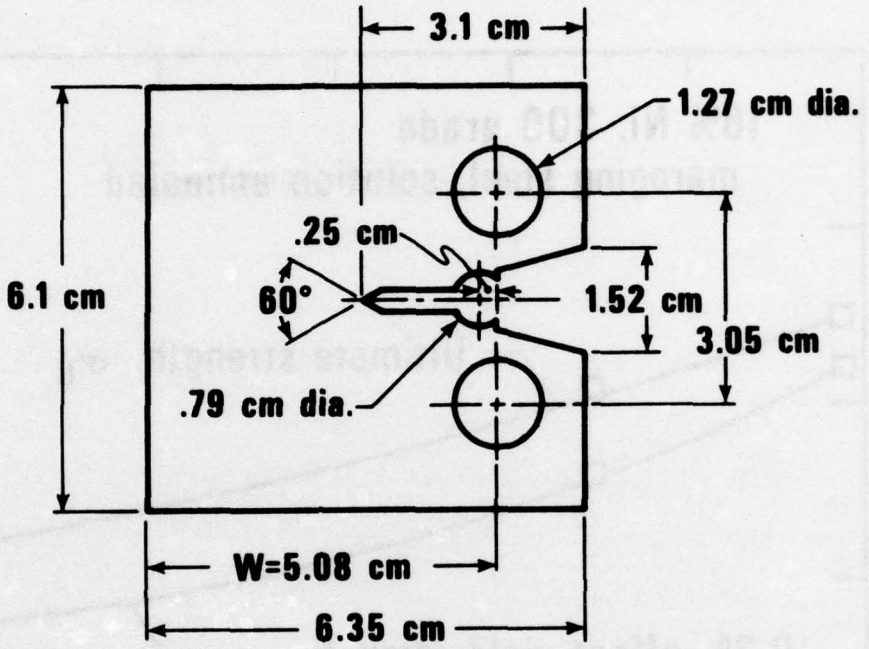


Figure 1. Planar dimensions of compact specimens for fatigue and fracture tests.

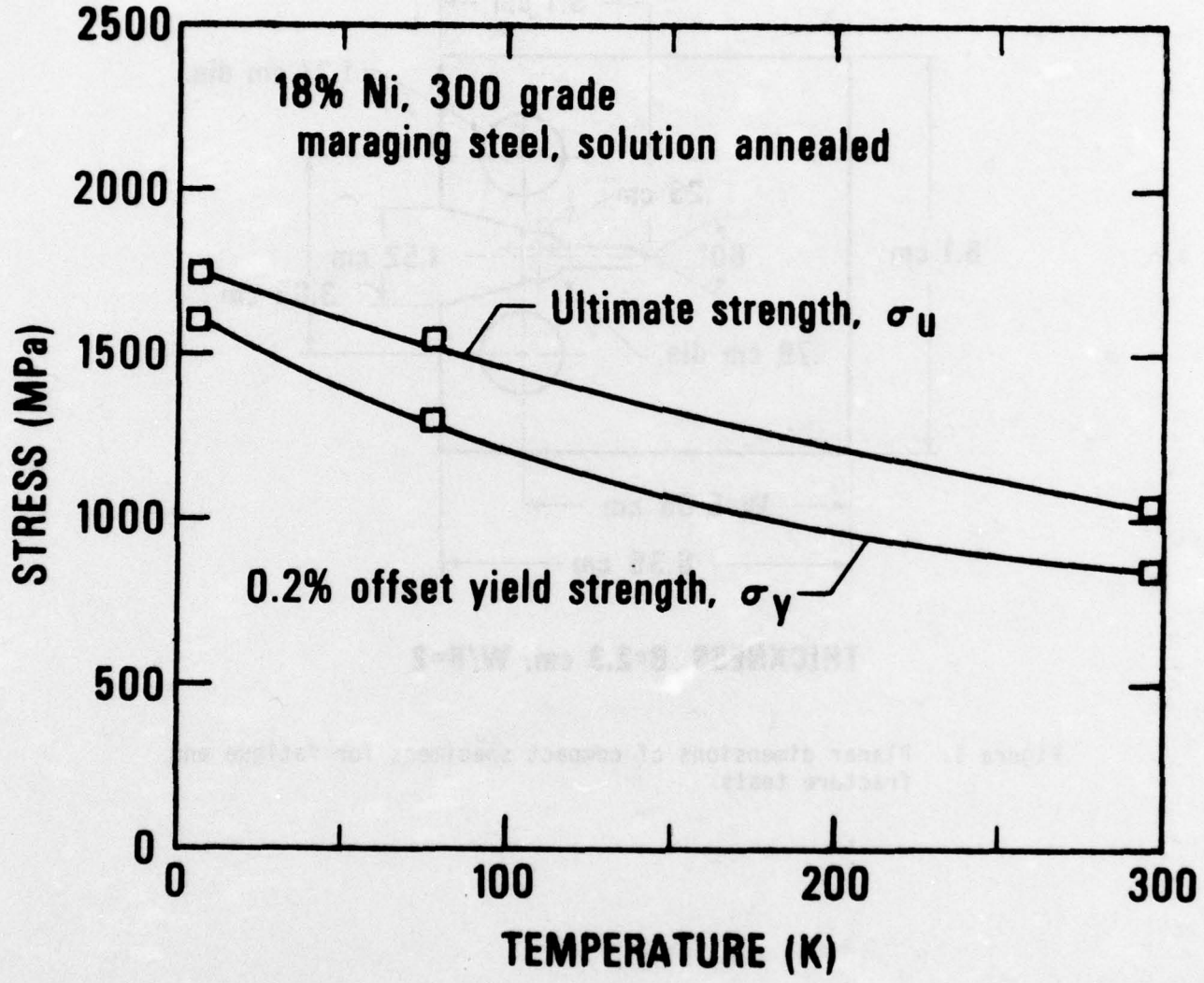


Figure 2. Yield and ultimate strengths for solution-annealed 300 grade maraging steel, showing 88% and 64% increases for the temperature range 295 to 4 K.

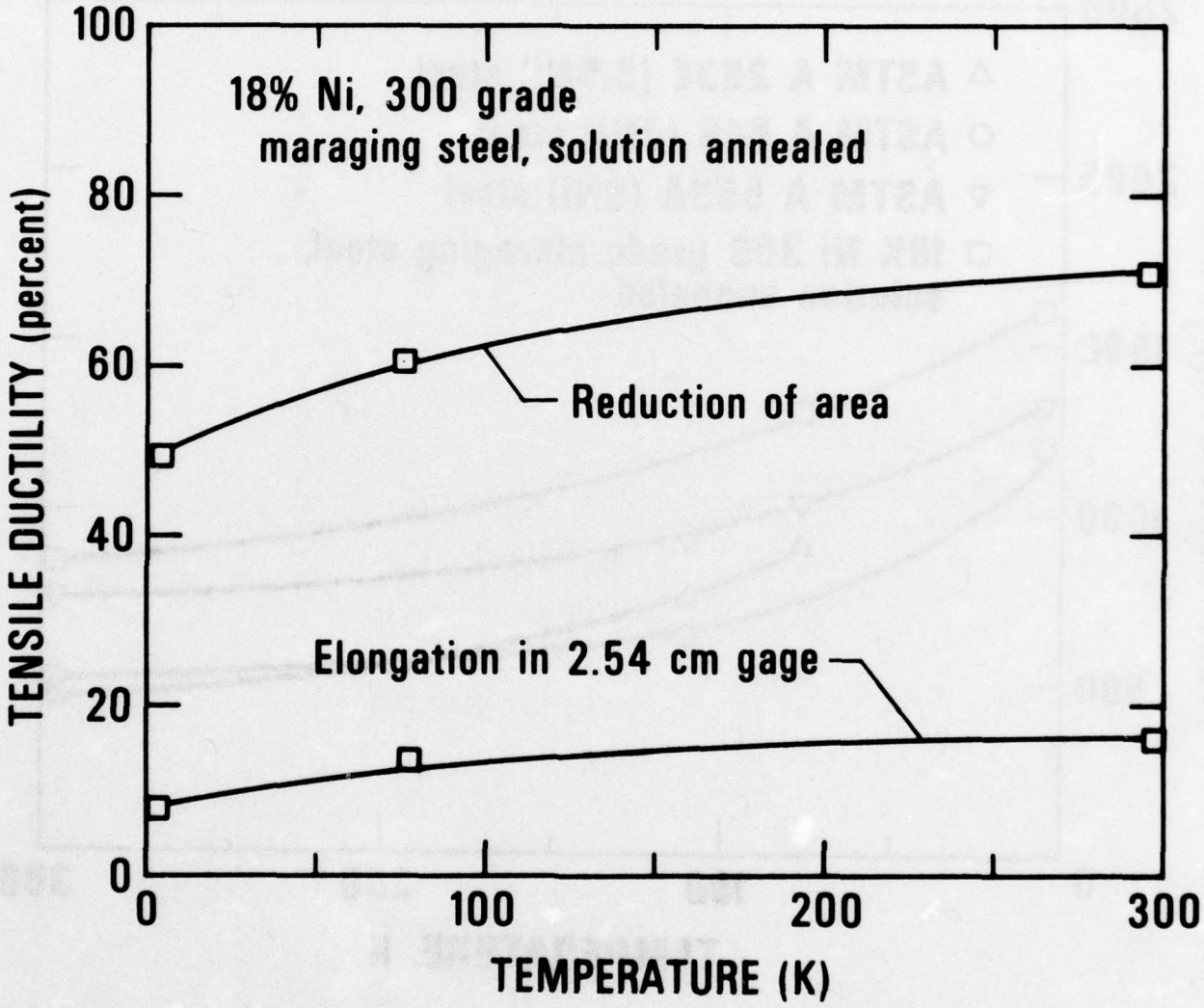


Figure 3. Reduction of area and elongation values for solution-annealed 300 grade maraging steel, showing gradually decreasing tensile ductility at low temperature.

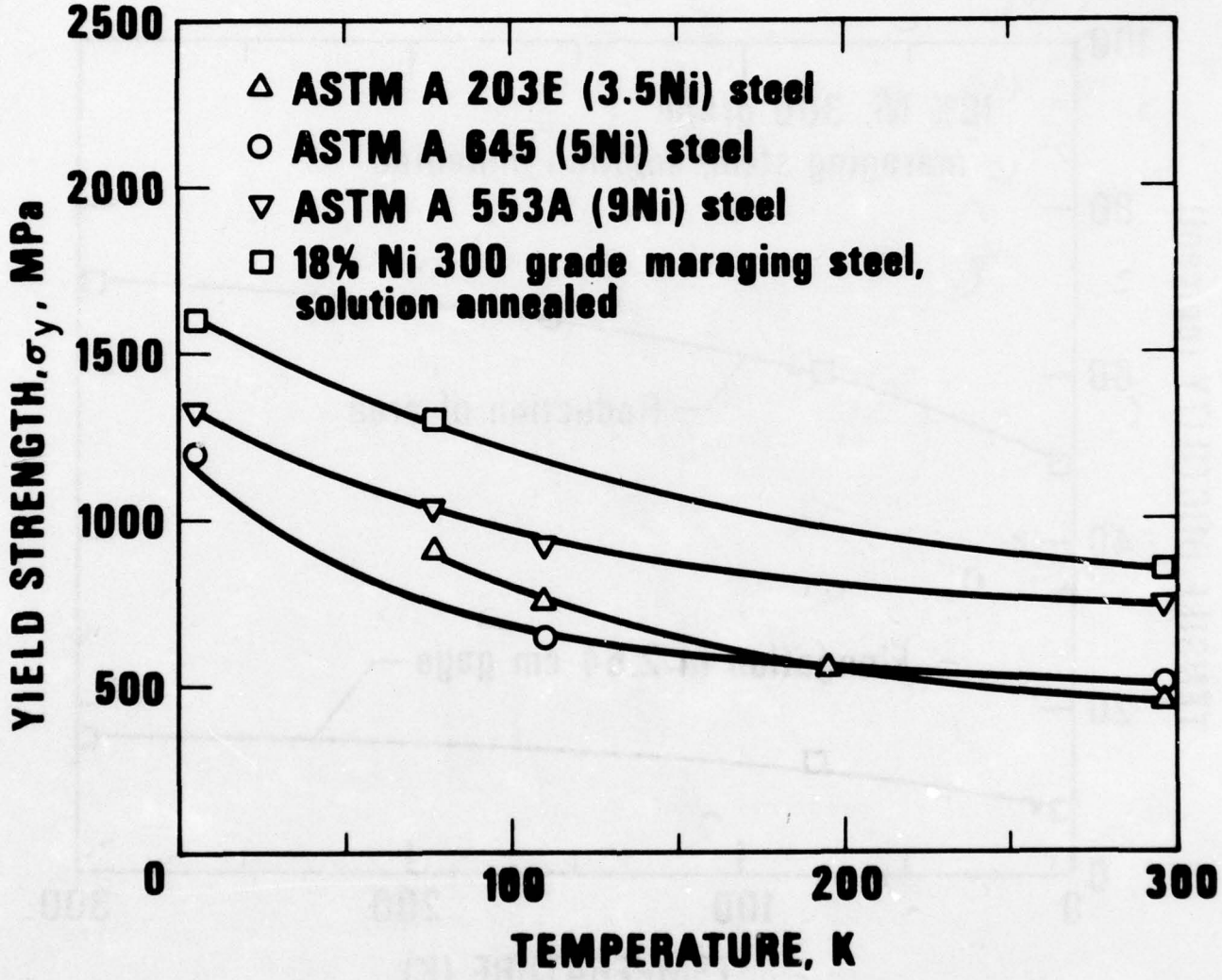


Figure 4. A yield strength comparison of solution-annealed maraging steel and some ferritic nickel alloy steels.

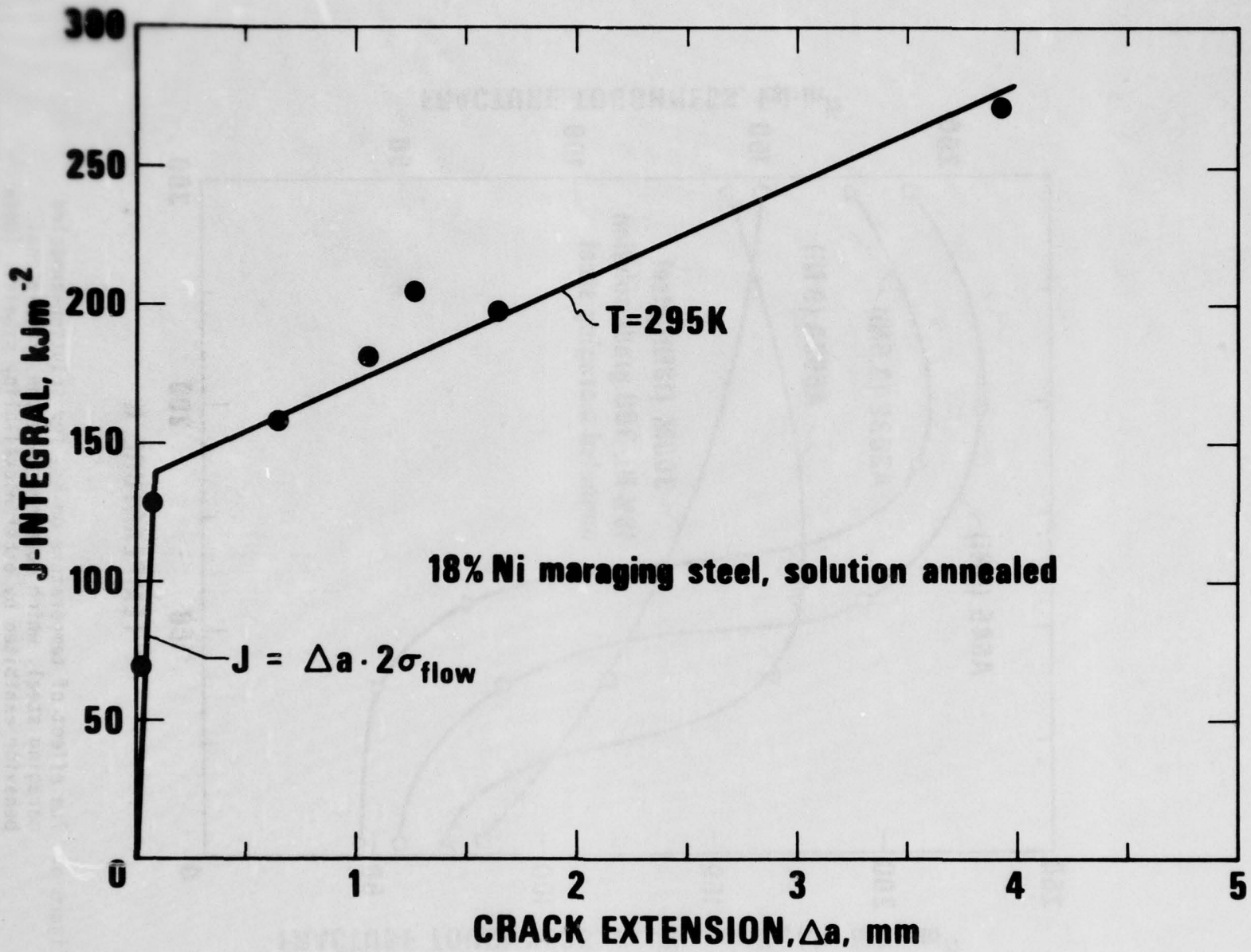


Figure 5. The J resistance curve for solution-annealed maraging steel at room temperature, showing a typical data trend.

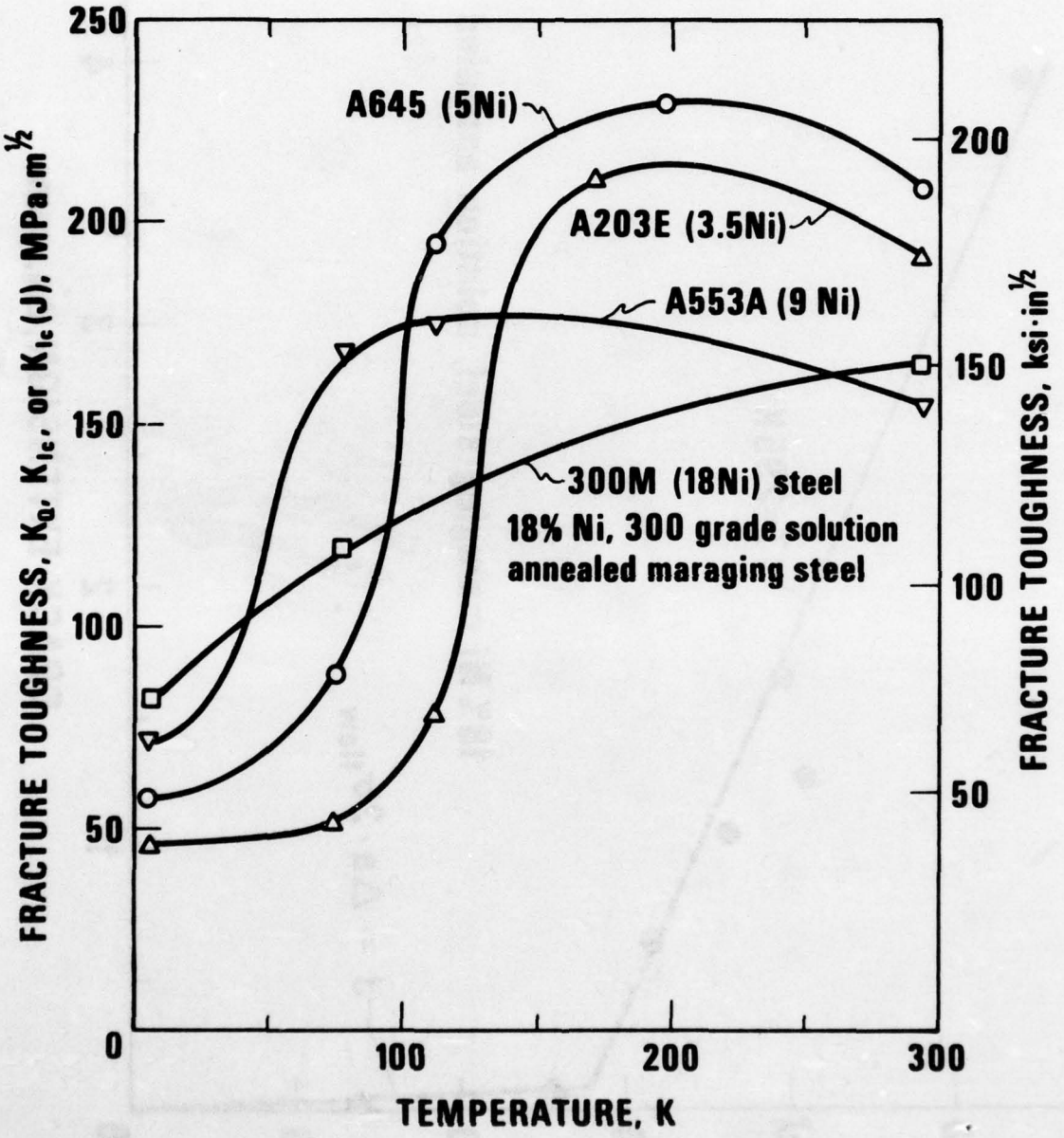


Figure 6. The effect of temperature on K_{Ic} for solution-annealed maraging steel, which does not show the transitional behavior exhibited by other nickel-alloy steels. (Data for the 3.5, 5, and 9% Ni steels are published elsewhere [24,25].

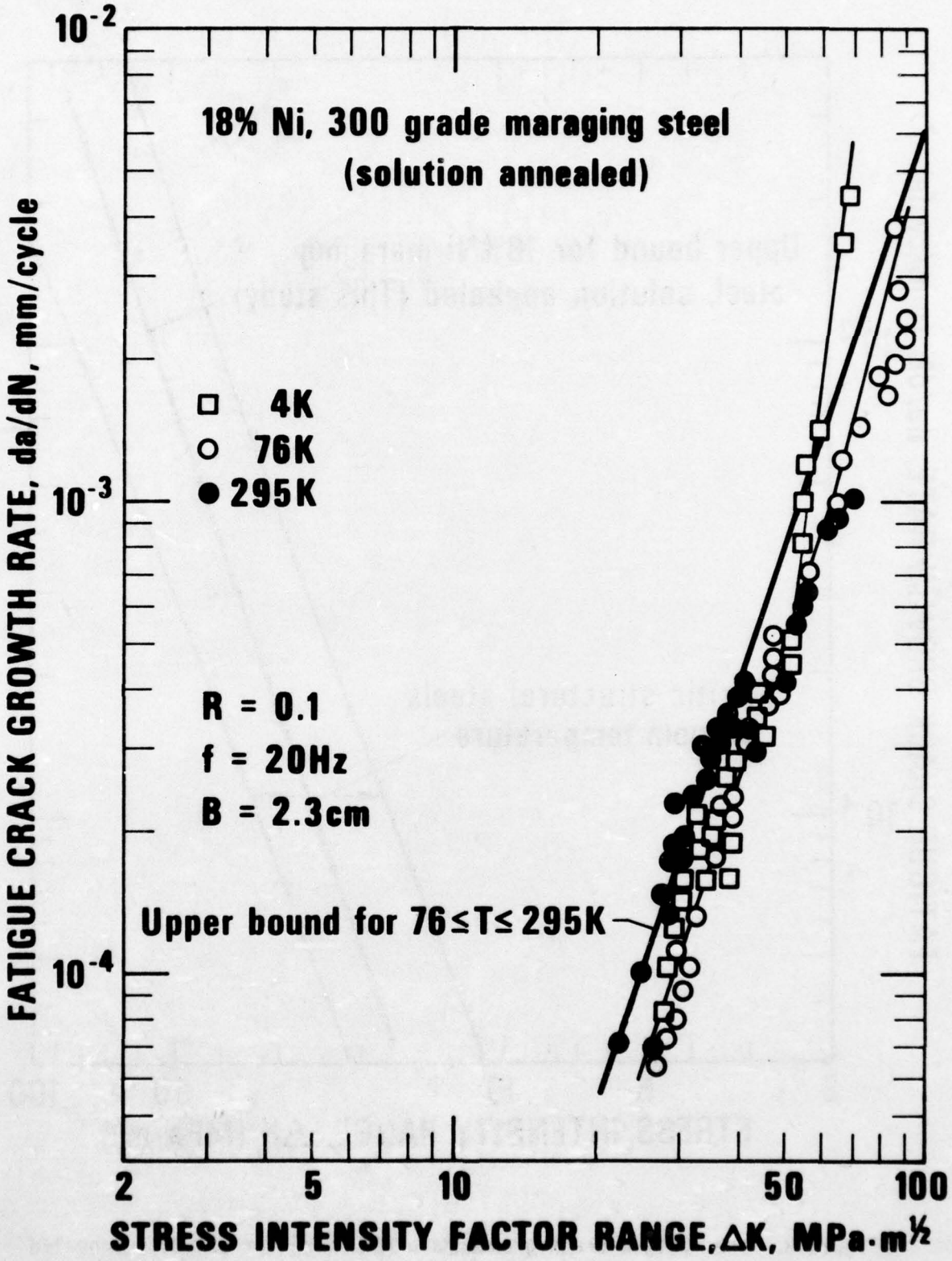


Figure 7. Fatigue crack growth rates for the solution-annealed 300 grade maraging steel at 295, 76 and 4 K.

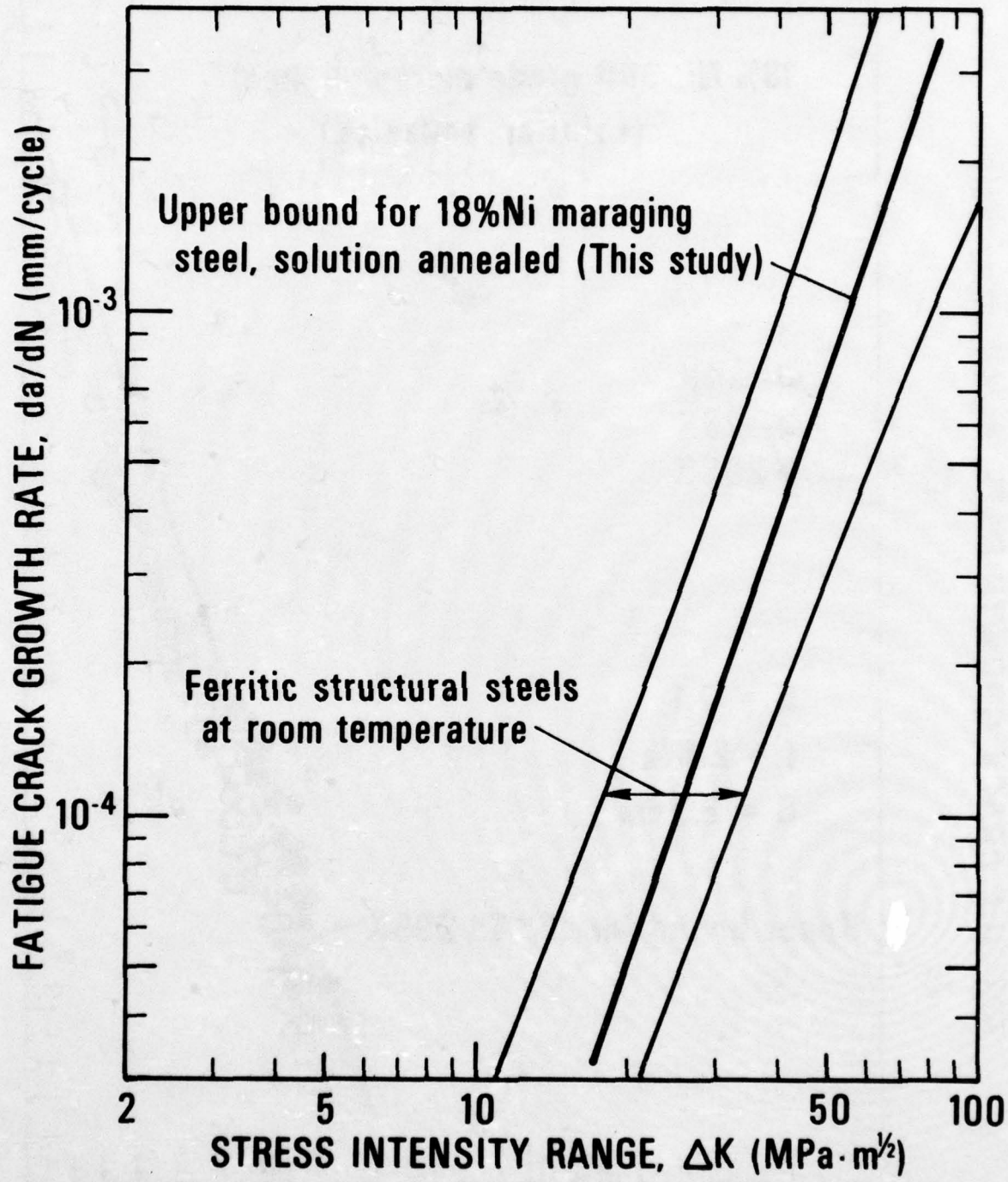


Figure 8. The fatigue crack growth data [Eq. (7)] for solution-annealed 300 grade maraging steel versus room temperature data for other steels [11, 12, 25, 26].

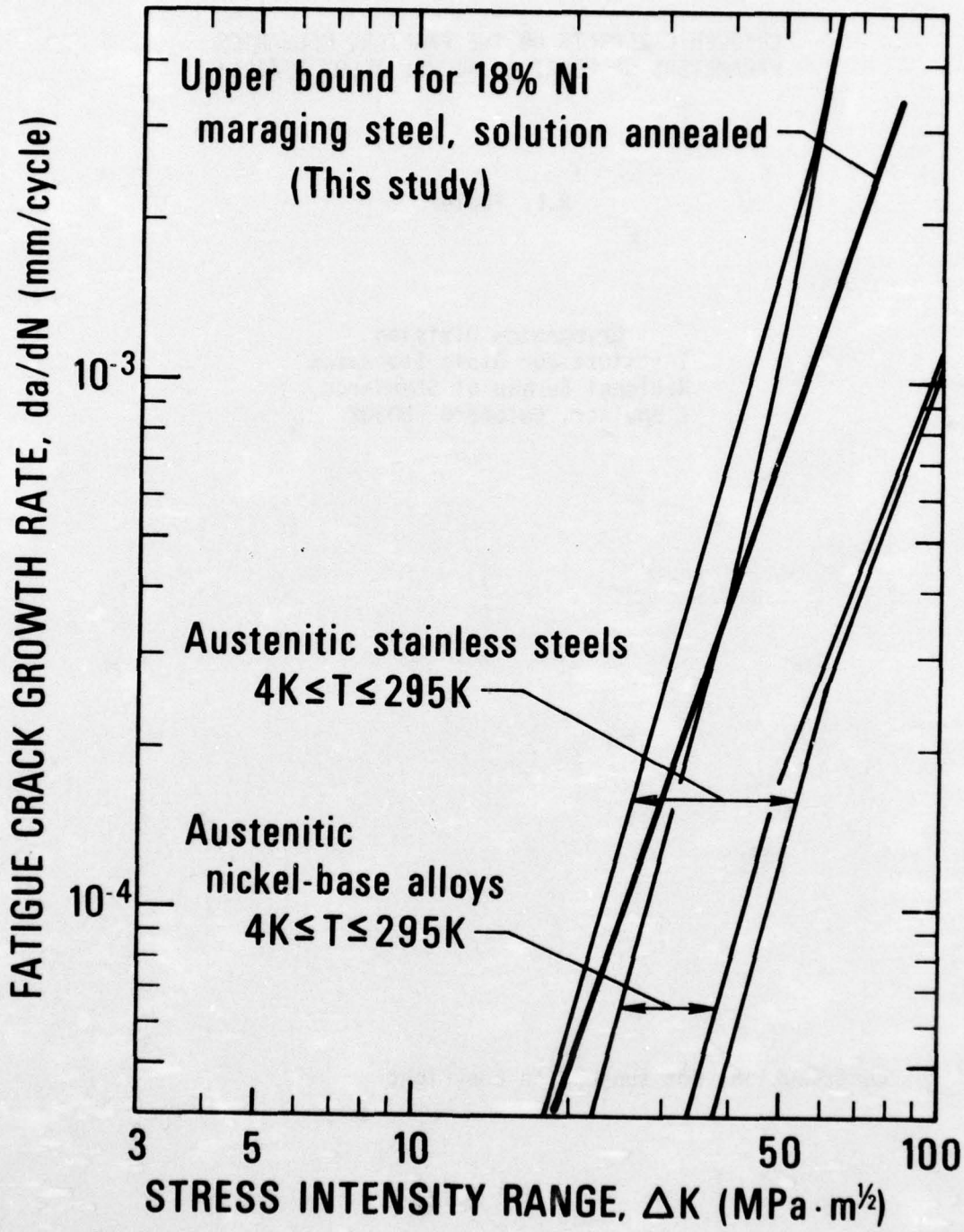


Figure 9. The fatigue crack growth data [Eq. (7)] for solution-annealed 300 grade maraging steel versus data for austenitic superalloys and stainless steels tested at 295 and 4 K [27-29].

CRYOGENIC EFFECTS ON THE FRACTURE MECHANICS PARAMETERS OF FERRITIC NICKEL ALLOY STEELS+

R.L. Tobler

Cryogenics Division
Institute for Basic Standards
National Bureau of Standards
Boulder, Colorado 80302

+ NBS contribution, not subject to copyright.

ABSTRACT

Fracture toughness data (K_{IC}, J_{IC}) and fatigue-crack growth rates (da/dN) are reported here for quenched and tempered low carbon ferritic 3.5 Ni and 9 Ni steels at temperatures between 295 K and 4 K. Such data are needed for cryogenic fluid containment and superconducting machinery design. The tests were performed using 25 and 31 mm thick compact specimens having fracture planes normal to the long transverse plate dimension. The fracture toughness results for both steels showed qualitatively similar trends: at decreasing temperatures below 295 K, J_{IC} increased by about 20%, prior to the onset of classical ductile-to-brittle transitions involving cleavage. The transitions occurred between 172 K and 100 K for 3.5 Ni steel, and between 76 K and 4 K for 9 Ni steel. The transitional behavior was also evident in fatigue-crack growth resistance. At room temperature, the fatigue crack growth rates for these nickel steels are typical of many other ferritic materials; however the rates at sub-transition temperatures are drastically accelerated, due to cleavage. Data comparisons between 3.5 and 9 Ni steels tested here and other nickel alloy steels are included in discussion.

Key words: Fatigue; fracture; low temperature tests; mechanical properties; nickel alloys; steels.

INTRODUCTION

Low-carbon ferritic 2 1/4 to 9% nickel alloy steels were developed to provide low-cost alternatives to the more heavily-alloyed austenitic stainless steels which are too expensive for use in many large-tonnage cryogenic structural applications. Since 1947, the effects of nickel on the mechanical properties of the ferritic steels have been studied and reviewed [1-9], one major finding being that increased nickel content leads to progressively lower ductile-to-brittle transition temperatures. Construction costs are minimized by selecting the appropriate nickel content for the intended service temperature range. For example, 3.5 Ni steel (ASTM A 203 grade E) has a minimum use temperature of 172 K (-150°F), and is used for liquid acetylene, ethelene, and propane tankage. On the other hand, 9 Ni steel (ASTM A 553 grade A) is used for liquified natural gas and nitrogen tankage at temperatures as low as 76 K (-321°F).

The tensile and impact properties of these steels are well-researched, but such data are insufficient to insure fail-safe design according to modern techniques of fracture mechanics analyses. The fracture parameters currently needed for more accurate material selection and design efficiency are: K_{IC}, the critical plane-strain stress intensity factor; J_{IC}, the critical value of the J-integral; and da/dN, the fatigue-crack growth rate where a is crack length and N is fatigue cycles. The parameters K_{IC} and J_{IC} characterize the magnitude of crack-tip elastic stresses or plastic strains, during monotonic loading, respectively, while da/dN governs sub-critical flaw growth cyclic loading. This paper investigates the temperature dependence of these parameters for quenched and tempered 3.5 Ni and 9 Ni steels tested at room temperature and reduced temperatures approaching absolute zero.

Materials and Specimens

A 2.54 cm thick plate of ASTM A 203 grade E steel (3.5 Ni), and a 3.2 cm thick plate of ASTM A 553 grade A Type I steel (9 Ni) were obtained from commercial sources. Both steels were received and tested in the quenched and tempered conditions. The 3.5 Ni steel had been tested at 1172 K for 1 h, and water quenched, followed by tempering at 896 K 1 h, and water quenched. The 9 Ni steel was heated at 1064 K for 1.5 h, and water quenched, followed by tempering at 877 K for 1.25 h and air-cooled. The mill chemical analyses for both steels are listed in Table 1, and the uniaxial tensile properties at selected test temperatures are listed in Table 2.

Compact specimens for fatigue and fracture tests were machined in the TL orientation, having planar dimensions proportional to specimen width, W, according to the ASTM E 399-74 method [10]. The 3.5 Ni steel specimens were 2.5 cm thick, and the width-to-thickness ratio, W/B, was 2.0. The 9 Ni steel specimens were (diagrammed elsewhere [11]) were 3.1 cm thick, with W/B = 2.4. Attached to knife edges at the loadline was a double-cantilever beam-type clip gage that satisfied the ASTM E 399-74 Method linearity requirements at each test temperature.

PROCEDURES

The environments studied here were room temperature air at 295 K, nitrogen vapor at 111 K or 172 K, liquid nitrogen at 76 K, and liquid helium at 4 K. Two 3.5 Ni steel fatigue tests were also performed in an alcohol/dry ice bath at 195 K. The low temperature apparatus included a 100 kN servo-hydraulic test machine and cryostat previously described [11,12].

Fracture Toughness

Direct K_{IC} measurements for nickel alloy steels are seldom

reported because the ASTM E 399-74 thickness criterion for valid linear-elastic tests is difficult to satisfy. The specimen thickness criterion requires that:

$$B \geq 2.5 \left(\frac{K_{IC}}{\sigma_y}\right)^2 \qquad (1)$$

where σ_y is the yield strength of the material. In this study J-integral and ASTM E 399-74 test methods were used alternatively, depending on the type of load-deflection (P-δ) behavior encountered. Examples of P-δ records for 9 Ni steel specimens are shown in Fig. 1.

Nonlinear, Plastic Fractures

Where ductile fractures by stable tearing occurred (9 Ni steel at 295 and 111 K; 3.5 Ni steel at 295 and 172 K), J-resistance curves were determined using Landes and Begley's method [13]. J as a function of crack extension was determined by heat-tinting experiments in which a series of precracked specimens at each material/temperature combination were loaded to cause crack extensions of between zero and 0.49 cm. After unloading, tinting, and complete fracturing, crack extension was measured to the nearest 0.001 cm at three thickness locations, and averaged. J values were calculated from the approximation:

$$J = \frac{2A}{B(W - a)} \qquad (2)$$

where A is the total area (energy) under the P-δ curve. J_{IC} was then obtained by extrapolating the J-versus-Δa plots back to the critical point of material separation, Δa_c. (Crack extensions less than Δa_c are

apparent crack extensions due only to plastic deformation or blunting.) Several reasonable extrapolations were examined to account for scatter. Finally, estimates of K_{IC} denoted $K_{IC}(J)$ were derived from the relation:

$$K_{IC}(J) = \frac{EJ_{IC}}{(1-\nu^2)}^{1/2} \qquad (3)$$

Young's modulus (E) and Poisson's ratio (ν) for these steels at low temperatures are known from the work of Weston, Naimon, and Ledbetter [14].

Linear-Elastic or Unstable Fractures

Where fast fracture occurred (9 Ni steel at 76 and 4 K; 3.5 Ni steel at 111, 76 and 4 K), conditional fracture toughness values denoted K_Q were calculated according to ASTM E 399-74. Some of the K_Q results approached nearly accurate K_{IC} determinations, but none were valid according to a strict interpretation of ASTM E 399-74.

In the case of 3.5 Ni steel at 76 K and 4 K, excessive crack front curvature proved unavoidable in combination with the restriction that the precracking stress intensity factor had to remain below 0.6 K_{IC}. For 3.5 Ni steel at 111 K, Eq. (1) was not satisfied, and the K_Q data decidedly invalid. For 9 Ni steel at 76 K, Eq. (1) was not satisfied, but the P-δ curve was sufficiently linear that J_{IC} could be calculated at maximum load, assuming sub-critical crack growth was negligable. At 4 K, the 9 Ni steel test records exhibit a unique saw-toothed appearance, as shown in Fig. 1, due to multiple pop-ins (unstable crack extensions) and arrests. The P_{max}/P_Q ratios at 4 K exceeded 1.10, but heat-tinting experiments confirmed that the nonlinearity was due to cracking, not plasticity.

Fatigue-Crack Growth Rates

Fatigue-crack growth was monitored using the compliance method

previously described [11,12]. Rates at stress intensity factors, K_f, as high as 50 MPa·m$^{1/2}$ were measured during the precracking stages of fracture specimen preparation, while rates at higher stress intensities were measured with specimens not used for fracture toughness tests. At least two specimens were tested per temperature.

All tests used a sinusoidal load cycle at 20 Hz, and a R ratio (P_{min}/P_{max}) of 0.1. The a-versus-N curves were fitted to a third-order polynomial and differentiated by computer, leading to an uncertainty in da/dN results of less than ± 25%. The da/dN data were plotted as a function of the stress intensity factor ranges which were calculated using the ASTM E 399-74 solutions for K and f(a/W):

$$\Delta K = K_{max} - K_{min} = \frac{(P_{max} - P_{min})}{BW^{1/2}}[f(a/W)] \qquad (4)$$

RESULTS

Fracture Toughness

Table 3 lists the fracture toughness results for 3.5 Ni steel at 295, 172, 111, 76, and 4 K. The J-resistance curves at 295 K and 172 K, shown in Figure 2, yield J_{IC} values of 163 kJm^{-2} and 193 kJm^{-2}, respectively. The corresponding K_{IC} estimates from Eq. (1) are 190 MPa·m$^{1/2}$ at 295 K and 219 MPa·m$^{1/2}$ at 172 K. Although the ASTM E 399-74 results for this steel at lower temperatures are invalid, due primarily to excessive crack-front curvature, it appears that K_{IC} approaches 30 to 50 MPa·m$^{1/2}$ near absolute zero.

The fracture toughness results for 9 Ni steel at 295, 111, 76, and 4 K are listed in Table 4. The J-resistance curves for this steel at 295 K and 111 K (Fig. 3) yielded J_{IC} values of 117 kJm^{-2} and 140 kJm^{-2},

respectively, and the K_{IC} estimates are 156 MPa·$m^{1/2}$ at 295 K and 174 MPa·$m^{1/2}$ at 111 K. Between 111 K and 76 K, $K_{IC}(J)$ is reduced slightly to 167 MPa·$m^{1/2}$, and it appears that the ductile-to-brittle fracture transition is just beginning at 76 K. Below 76 K the fracture toughness rapidly decreases, and at 4 K nearly all of the ASTM E 399-74 criteria for K_{IC} measurements are satisfied. The sole criticism that can be levelled against the 4 K results for 9 Ni steel is that the a/W ratios of about 0.6 slightly exceed the preferred range of 0.45 to 0.55. The statement "$K_Q \simeq K_{IC}$" in Table 4 indicates that these 4 K data are believed to be nearly accurate K_{IC} results.

The temperature effects on K_{IC} estimates for the 3.5 Ni and 9 Ni steels are shown in Fig. 4, along with results for a 5 Ni steel [11] that was tested using compact specimens (3.1 cm thick) and similar procedures. The 5 Ni steel was in the austenitized, temperized, and reversion annealed condition, which tends to decrease the transition temperature slightly compared to the quenched and tempered condition. In the range 295 to 4 K, all three steels exhibit: (1) an "upper shelf" temperature region showing an initial enhancement of fracture resistance at decreasing temperatures, (2) a transition range of abruptly decreasing toughness, and (3) a temperature-insensitive sub-transition range. For each steel, absolute zero is a sub-transition temperature. Within the transition range, K_{IC} increases by factors from 2.2 to 3. An interesting point seldom noted is that each steel exhibits a maximum fracture resistance within the upper shelf range, just prior to undergoing the fracture transition. The 6 Ni steel tested in a previous study also showed this type of behavior between 295 K and 76 K [11]. For these materials, the peak $K_{IC}(J)$ value is about 10 to 15% higher than the value at room temperature.

Nickel's beneficial effects on fracture resistance in the transition and sub-transition regions are attributed to favorable effects on the deformation characteristics and cleavage resistance of iron, combined with a tendency to promote the formation of retained austenite [3,7-9]. As indicated in Figure 4, the transition temperature intervals correlate with nickel content, lying approximately in the ranges:

1. $4\ K < T < 76\ K$ for 9 Ni steel
2. $\sim 60\ K < T < 111\ K$ for 5 Ni steel, and
3. $\sim 100\ K < T < 172\ K$ for 3.5 Ni steel.

The fracture toughness at sub-transition temperatures also increases with nickel content, with the K_{IC} values at 4 K ranging from 30 $MPa \cdot m^{1/2}$ for 3.5 Ni steel to 80 $MPa \cdot m^{1/2}$ for 9 Ni steel. On the otherhand, the upper shelf toughness is apparently more sensitive to heat treatment and metallurgical factors other than nickel content; 5 Ni steel exhibits the highest upper shelf fracture toughness, perhaps due to the uniform distribution of carbides and other benefits [7] associated with austenitizing, temperizing, and reversion annealing [7].

Fatigue-Crack Growth Rates

Over the range of stress intensity factors investigated (20 to 80 $MPa \cdot m^{1/2}$) the fatigue-crack growth rates for the 3.5 and 9 Ni steels conform to equations of the type proposed by Paris and Erdogan [15]:

$$\frac{da}{dN} = C(\Delta K)^n \qquad (5)$$

where n and C are material and temperature dependent empirical constants. Log-log plots of the da/dN-versus-ΔK were constructed to reveal linear trends from which the n and C values were determined as

the slopes and ordinate intercepts at $\Delta K = 1$, respectively. Table 5 lists the n and C values for each material/temperature combination.

Consider the room temperature results, shown in Fig. 5. Here, "Paris equation" equivalents representing the 3.5 Ni and 9 Ni steels of this study and the 5, 6, and 9 Ni steels of a previous study [11] are superimposed on a scatterband for commercially available construction steels where nickel is not a major alloying element [16-20]. The data spread for the nickel alloy steels is nearly equivalent to that for the non-nickel steels, with fatigue-crack growth rate variations approaching a factor of 4. However, the data for two 9 Ni steel alloys, show that heat-to-heat differences can account for fatigue-crack growth rate variations of at least a factor of 2 or three. It appears that the fatigue-crack growth resistances of nickel alloy steels at room temperature are typical of ferritic steels in general, and there seems to be no simple correlation between fatigue-crack growth rates and yield strength or nickel content.

The results in Fig. 6 reveal no dramatic temperature effects on the fatigue crack growth resistance of 3.5 Ni steel, as long as the temperature remains within the upper shelf region identified by the J_{IC} tests. The fatigue crack growth rates at 195 K and 172 K are nearly equivalent or slightly improved compared to the rates for this steel at room temperature. On the otherhand, further temperature reductions to 76 K greatly accelerate the rates to values well above those at room temperature. As indicated earlier, 76 K is a sub-transition temperature for this steel; inferior fatigue-crack growth resistance at this temperature is associated with the appearance of cleavage-type cracking modes, and a single increase of the Paris equation exponent from n = 3.2 at 295 K to n = 7.6 at 76 K.

The fatigue-crack growth behavior of 9 Ni steel is analogous to that of 3.5 Ni steel in that low temperature effects are moderate until the sub-transition range is approached. Data for the 9 Ni steel at 295, 111, 76, and 4 K are shown in Fig. 7. The rates decrease as temperature is lowered from 295 K to 111 K, but between 111 K and 76 K the trend is reversed. Thus, for ΔK greater than 40 $MPa \cdot m^{1/2}$, the rates at 76 K exceed those at 295 K. Previous tests of a second heat of 9 Ni steel also revealled higher rates at 76 K than at 295 K [11]. At more extreme cryogenic temperatures, the present data at 4 K confirm that the fatigue crack propagation resistance continues to deteriorate. Thus, for the ΔK range investigated, the fatigue crack growth resistance of 9 Ni steel is at a maximum near 111 K, the same temperature at which a peak in the static fracture toughness was observed.

DISCUSSION

Strain-rate, section thickness, and notch severity are three factors that usually influence the transition temperatures. Nevertheless, recent reports indicated the fracture toughness of 5 and 9 Ni steels to be unimpaired by dynamic loading [9]. Therefore the relatively thick and sharply-cracked compact specimens used for static fracture tests may provide a more severe test of crack tolerance than traditional tests based on Charpy impact energies.

Any comparison between the data of this report and the literature must carefully take into account the differences in measurement procedures. Standard K_{IC} determinations from the ASTM E 399-74 Method provide the most reliable comparisons, but valid K_{IC} data are rare. Pense and Stout [9] indicated that most authors reported "K_C" or "K_{max}"

values. The wide variety of test variables and data reduction schemes makes "K_C" data comparisons difficult. In the present study, the J-integral at initiation of crack extension is reported, rather than a K value calculated at the maximum load point. Huettich, Pense and Stout [4] report a K_{IC} measurement of 43 MPa$\cdot m^{1/2}$ for a quenched and tempered 3.5 Ni steel tested at 89 K (-300°F). Based on the data trend of Fig. 4, our 3.5 Ni steel indicates 30% higher toughness. This difference could be due to test procedures, since Huettich et al. precracked their specimens at room temperature.

In reference to 9 Ni steel, Syn, Jin, and Morris [5] reported a K_{IC} value of 78 MPa$\cdot m^{1/2}$ for a double-normalized and tempered grade at 6 K, nearly agreeing with the present result of 75 MPa$\cdot m^{1/2}$ for a quenched and tempered grade tested at 4 K. Our $K_{IC}(J)$ results for 9 Ni steel are up to 16% lower than results for a second heat tested at 295 K and 76 K [11]. The difference in fracture toughness for these two heats may be attributed to material variability since: (1) the J-integral test procedures were equivalent, and (2) the fracture surface topographies reveal distinctly different features, especially at room temperature, as shown in Fig. 8.

The 9 Ni steel of this study displayed highly uniform crack fronts, as compared to results from other studies. As listed in Tables 3 and 4, the edge crack lengths for the 9 Ni steel were typically 97% as long as the average crack lengths at central thickness. Similar values for 5, 6, and 9 Ni steels (see Fig. 8) ranged from 88 to 90% [11]. These crack-front curvature effects should not greatly influence the da/dN comparisons, since the compliance method of crack growth measurement is sensitive to through-the-thickness variations.

As indicated in Table 5, the Paris equation exponents for most nickel steels are nearly 3.0 at room temperature, which is expected for ferritic steels, based on Barsom's findings [16]. The Paris equation exponents tend to increase, depending on the severity of the temperature reduction. For example, the 9 Ni steel, shows a progressively increasing exponent from n = 2.7 at room temperature to n = 5.3 at 4 K. As long as the temperature remains in the upper shelf range, fatigue crack growth resistance is satisfactory. The rates for 9 Ni steel at 111 K and 76 K, and for 3.5 Ni steel at 195 K and 172 K deviate from their 295 K trends by margins not greater than observed in the scatterband shown in Fig. 5. Thus, variations in fatigue crack growth resistance due to temperature variations in the upper shelf ranges are of the same magnitude as variations induced by metallurgical effects in other ferritic steels at room temperature. It appears that the trend of decreasing fatigue crack growth resistance with decreasing temperatures is caused by the incidence of brittle cleavage modes which become predominant as the maximum fatigue stress intensity factor approaches K_{IC} at low test temperatures. Knott and Ritchie correlated high n values with steels of low fracture toughness, indicating that n is likely to exceed 4.0 if K_{IC} is 80 MPa$\cdot m^{1/2}$ or lower [21]. Lindley and Richards also associate high n values with brittle crack propagation modes such as occur in static fracture tests [22].

SUMMARY

The onset of cleavage fracture modes which account for transitions to low fracture toughness in ferritic steels also lead to a deterioration of fatigue-crack growth resistance. The quenched and tempered 3.5

Ni and 9 Ni steels exhibit low temperature fatigue-crack growth and fracture toughness data trends that are believed to be representative, qualitatively, of ferritic steels in general. Initially, the resistance to crack extension under monotonic loading increases at decreasing temperatures below 295 K, reaching a maximum prior to the ductile-to-brittle transition. The transition for 3.5 Ni steel lies between 172 and 110 K, and the transition for 9 Ni steel lies between 76 and 4 K. Based on observations for these and previously tested nickel steels, the ratios of the peak K_{IC} values to the minimum K_{IC} values exhibited near absolute zero are between 2.5:1 and 5:1. The fatigue-crack growth resistance of ferritic steels at room temperature apparently is not measurably influenced by nickel content. Reduced temperatures in the upper shelf range may improve the fatigue-crack growth resistance slightly, but fatigue cracking at sub-transition temperatures is drastically accelerated by cleavage such that the rates at normal temperatures may be exceeded by an order of magnitude.

CONCLUSION

The fracture mechanics properties reported here for familiar cryogenic tankage steels are of practical design value for existing and future structural applications. The data clearly illustrate general behavior trends for ferritic steels tested over the complete ambient-to-cryogenic range. In the future, it may be possible to improve the fracture resistance of the 3.5 Ni and 9 Ni steels by applying heat treatments analogous to the austenitized, temperized, and reversion annealing treatment applied to 5 Ni steel [7]. As regards superconducting machinery developments, these steels would not be ideal for use

in tensile-loading (Mode I) applications at 4 K, unless they can be reprocessed to eliminate the fracture transition as discussed by Syn, Jin, and Morris in reference to 9 Ni steel [5].

ACKNOWLEDGMENTS

Test materials for this program were donated by the Lukens Steel and Armco Steel Corporations. The program was sponsored by the National Maritime Administration and the Advanced Research Projects Agency of the U.S. Department of Defense. The assistance of Dr. R. P. Mikesell and R. L. Durcholz in conducting tests is gratefully acknowledged.

REFERENCES

1. Yeo, R. B. G. and Miller, O. O., "A History of Nickel Steels from Meteorites to Maraging," Sorby Centennial Symposium on History of Metallurgy, ASM, Cleveland, OH, October 21-23, 1963.
2. Properties of Materials for Liquefied Natural Gas Tankage, ASTM STP 579, (Amer. Soc. Test. Mater., Philadelphia, 1975) 1-420.
3. Floreen, S., Hayden, H. W., and Devine, T. M., Cleavage Initiation in Fe-Ni alloys, Met. Trans. 2 (1971) 1403.
4. Huettich, N. J., Pense, A. W., and Stout, R. D., The Toughness of 2 1/4 and 3 1/2% Nickel Steels at Cryogenic Temperatures, WRC Bulletin No. 165 (Welding Research Council, 1974) 1.
5. Syn, C. K., Jin, S., and Morris, J. W., Jr., Cryogenic Fracture Toughness of 9% Ni Steel Enhanced Through Grain Refinement, Met. Trans., submitted for publication.
6. McHenry, H. I. and Reed, R. P., "Fracture Behavior of the Heat-Affected Zone in 5% Ni Steel Weldments," Welding Journal, submitted for publication.

7. Sarno, D. A., Havens, F. E., and Bowley, D. L., Transformations involved in Developing Notch Toughness in a New 5% Nickel Steel for Cryogenic Purposes (ASM Technical Report No. C70-39-2, American Society for Metals, 1970).

8. Johnson, R. J., The Role of Nickel in Carburizing Steels, Metals Eng. Quart., 15 (1975) 1.

9. Pense, A. W. and Stout, R. D., Fracture Toughness and Related Characteristics of the Cryogenic Nickel Steels, WRC Bulletin No. 205 (Welding Research Council, 1975) 1.

10. Standard Method of Test for Plane Strain Fracture Toughness of Metallic Materials, E 399-74 Annual Book of ASTM Standards, Part 10 (Amer. Soc. Test. Mater., Philadelphia, 1976) 471.

11. Tobler, R. L., Mikesell, R. P., Durcholz, R. L., and Reed, R. P., "Low Temperature Fracture Behavior of Iron-Nickel Alloy Steels," Ref. 1, 261.

12. Fowlkes, C. W. and Tobler, R. L., Fracture Testing and Results for a Ti-6Al-4V Alloy at Liquid Helium Temperature, Eng. Fract. Mechs. 8 (1976) 487.

13. Landes, J. D. and Begley, J. A., Test Results from J-integral Studies: An Attempt to Establish a J_{IC} Test Procedure, in Fracture Analyses, ASTM STP 560 (Amer. Soc. Test. Mater., Philadelphia, 1973) 231.

14. Weston, W. F., Naimon, E. R., and Ledbetter, H. M., "Low Temperature Elastic Properties of Aluminum 5083-0 and Four Ferritic Nickel Steels," Ref. 1, 397.

15. Paris, P. C. and Erdogan, F., A Critical Analysis of Crack Propagation Laws, Trans ASME, J. Basic Eng., 85 (1963) 528.

16. Barsom, J. M., Fracture-Crack Propagation in Steels of Various Yield Strengths, Trans. ASME, J. Eng. Ind. (1971) 1190.

17. Barsom, J. M., Imhof, E. J., and Rolfe, S. T., Fatigue Crack Propagation in High Yield Strength Steels, Eng. Fract. Mechs. 2 (1971) 301.

18. Wei, R. P., Talda, P. M., and Che-Yu Li, Fatigue Crack Propagation in Some Ultra-High Strength Steels, in Fatigue Crack Propagation, ASM STP 415 (Amer. Soc. Test. Mater., Philadelphia, 1967) 460.

19. Brothers, A. J. and Yukawa, S., Fatigue Crack Propagation in Low Alloy Heat Treated Steels, Trans. ASME, J. Basic Eng., 89 (1967) 19.

20. Miller, G. A., The Dependence of Fatigue-Crack Growth Rate on the Stress Intensity Factor and Mechanical Properties of Some High Strength Steels, Trans. ASM, 61 (1968) 442.

21. Ritchie, R. O. and Knott, J. F., Mechanisms of Fatigue Crack Growth in Low Alloy Steel, Acta Met., 21 (1973) 639.

22. Richards, C. E. and Lindley, T. C., The Influence of Stress Intensity and Microstructure on Fatigue Crack Propagation in Ferritic Materials, Eng. Fract. Mechs., 4 (1972) 951.

LIST OF TABLES

Table 1. Mill chemical analyses of test materials.

Table 2. Tensile properties of test materials.

Table 3. Fracture toughness results for ASTM A 203 E (3.5% Ni) steel (specimen thickness = 2.54 cm).

Table 4. Fracture toughness results for ASTM A 553 A (9% Ni) steel (specimen thickness = 3.1 cm).

Table 5. Comparison of Paris equation parameters for nickel alloy steels.

Table 1. Mill chemical analyses of test materials, wt%.

Material	Fe	Ni	C	Mn	P	S	Si
ASTM A203-E (3.5 Ni steel) quenched and tempered	bal.	3.62	0.10	0.46	0.015	0.013	0.20
ASTM A553-A (9 Ni steel) quenched and tempered	bal.	8.99	0.08	0.62	0.010	0.010	0.19

Table 2. Tensile properties of test materials.

Material	Temperature K	0.2% Yield Strength[a] MPa	Ultimate Tensile Strength[a] MPa	Elongation in 2.54 cm gage[a] %	Reduction of Area[a] %	Young's Modulus[b] GPa	Poisson's Ratio[b]
ASTM A 203-E (3.5 Ni steel)	295	488.2	549.5	33.6	71.8	204	0.288
	194	564.6	659.8	36.2	69.4	209	0.285
	111	776.7	867.7	NA	NA	214	0.283
	76	900.8	911.1	35.1	57.8	214	0.282
ASTM A 553-A (9 Ni steel)	295	740.5	788.7	24	64.1	192	0.292
	111	913.5	1075.2	NA	NA	200	0.287
	76	1028.7	1202	NA	NA	201	0.286
	4	1329.3	1381.7	NA	NA	202	0.286

a. Average values from duplicate tests.
b. Data from Weston, Naimon, and Ledbetter [14].

Table 3. Fracture results for ASTM A 203 E (3.5 Ni) steel (specimen thickness = 2.54 cm).

Temperature K	Specimen	K_f MPa·m$^{1/2}$	a_e/a	a/W	P_{max}/P_Q	K_Q MPa·m$^{1/2}$	J kJm^{-2}	Δa cm	J_{IC} kJm^{-2}	$K_{IC}^a(J)$ MPa·m$^{1/2}$	K_{IC}
295	20	48	0.96	0.542	1.7	66	240	0.493			NA
	21	46	0.92	0.546	NA	65	124	0.064			NA
	22	50	0.90	0.552	1.5	69	317	0.838	163±10%	190±5%	NA
	24	48	0.94	0.544	1.6	67	174	0.135			NA
	27	50	0.93	0.552	1.7	60	254	0.457			NA
	27	50	0.93	0.552	1.7	60	254	0.457			NA
172	25	61	0.92	0.571	1.4	86	256	0.363			NA
	26	52	0.95	0.565	1.4	88	332	0.452			NA
	28	53	0.93	0.569	NA	82	70	0.000	193±10%	219±5%	NA
	29	67	0.94	0.585	1.4	89	214	0.150			NA
	30	75	0.93	0.596	1.4	90	231	0.321			NA
111	2	40	0.98	0.557	1.0	74.8	NA	NA	NA	NA	Invalid[b]
	31	45	0.85	0.530	1.4	81.0	NA	NA	NA	NA	Invalid[b,c,d]
76	10	34	0.90	0.582	1.0	63.4	NA	NA	NA	NA	Invalid[g]
	15	31	0.93	0.498	1.0	48.0	NA	NA	NA	NA	Invalid[e]
4	3[a]	50	0.85	0.475	1.0	60.2	NA	NA	NA	NA	Invalid[d,e,h]
	23[a]	44	0.88	0.545	1.0	49.9	NA	NA	NA	NA	Invalid[d,e,h]
	33[a]	32	0.76	0.523	1.0	53.9	NA	NA	NA	NA	Invalid[d]
	36[a]	29	0.75	0.530	1.0	32.2	NA	NA	NA	NA	Invalid[d,e,f]

a. Calculated using Eq. (3).
b. Insufficient specimen thickness.
c. Excessive P_{max}/P_Q ratio.
d. Excessive edge-crack-to-average crack length ratio, a_e/a.
e. Excessive precracking stress intensity factor, K_f.
f. Precracked at 76 K.
g. Precracked at 195 K.
h. Precracked at 295 K.

Table 4. Fracture results for ASTM A 553-A (9 Ni) steel (specimen thickness = 3.1 cm).

Temperature K	Specimen	K_f MPa·m$^{1/2}$	a_e/a	a/W	P_{max}/P_Q	K_Q MPa·m$^{1/2}$	J kJm^{-2}	Δa cm	J_{IC} kJm^{-2}	$K_{IC}^{a}(J)$ MPa·m$^{1/2}$	K_{IC} MPa·m$^{1/2}$
295	3	43	0.96	0.615	1.2	124	188	0.117			NA
	7	43	0.95	0.606	>1.17	120	116	0.043			NA
	11	41	0.94	0.611	NA	115	95	0.0	117±10%	156±5%	NA
	22	41	0.96	0.608	>1.2	113	155	0.100			NA
	23	43	0.96	0.608	>1.3	119	130	0.020			NA
	24	42	0.97	0.609	>1.3	110	153	0.071			NA
111	4	46	0.97	0.617	>1.28	119	130	0.011			NA
	6	48	0.95	0.616	>1.17	142	148	0.023			NA
	9	45	0.95	0.648	>1.25	144	218	0.084			NA
	15	41	0.97	0.607	>1.12	137	162	0.010	140±15%	174±8%	NA
	16	42	0.96	0.618	>1.19	136	232	0.114			NA
	18	45	0.96	0.606	>1.36	116	203	0.006			NA
76	21	40	0.95	0.613	1.07	147	99	NA	99	170	$K_Q \neq K_{IC}$[b]
	20	33	0.96	0.612	1.07	145	92	NA	92	164	$K_Q \neq K_{IC}$[b]
	17	37	0.97	0.611	1.09	144	97	NA	97	169	$K_Q \neq K_{IC}$[b]
4	14[c]	41	0.97	0.606	1.11	80.5	NA	NA	NA	NA	$K_Q \simeq K_{IC}$
	12[c]	33	0.98	0.608	1.15	67.3	NA	NA	NA	NA	$K_Q \simeq K_{IC}$
	5	43	0.98	0.617	1.09	78.2	NA	NA	NA	NA	$K_Q \simeq K_{IC}$

a. Calculated using Eq. (3)
b. Insufficient thickness.
c. Precracked at 76 K.

Table 5. Comparison of Paris equation parameters for nickel alloy steels (da/dN in mm/cycle).

Material	Temperature K	C	n	ΔK Region MPa•m$^{1/2}$
ASTM A 203-E	295	1.3×10^{-8}	3.2	18 to 60
(3.5 Ni steel)	195	1.3×10^{-8}	3.2	30 to 70
This study.	172	1.0×10^{-9}	3.2	30 to 60
	76	1.6×10^{-14}	7.6	20 to 30
ASTM A 645	295	1.1×10^{-8}	2.7	25 to 90
(5 Ni steel) [11]	111	1.1×10^{-8}	2.7	25 to 60
	76	2.0×10^{-10}	4.0	27 to 80
N-TUF Cr-196	295	3.7×10^{-9}	3.0	22 to 85
(5.5 Ni steel) [11]	111	3.7×10^{-9}	3.0	22 to 85
	76	4.2×10^{-9}	3.2	25 to 75
ASTM A 553-A	295	2.3×10^{-7}	2.0	27 to 100
(9 Ni steel) [11]	76	3.1×10^{-9}	3.3	27 to 100
ASTM A 553-A	295	2.0×10^{-8}	2.7	16 to 70
(9 Ni steel)	111	1.0×10^{-9}	3.4	17 to 80
This study.	76	4.8×10^{-11}	4.4	17 to 64
	4	1.4×10^{-11}	5.3	25 to 35

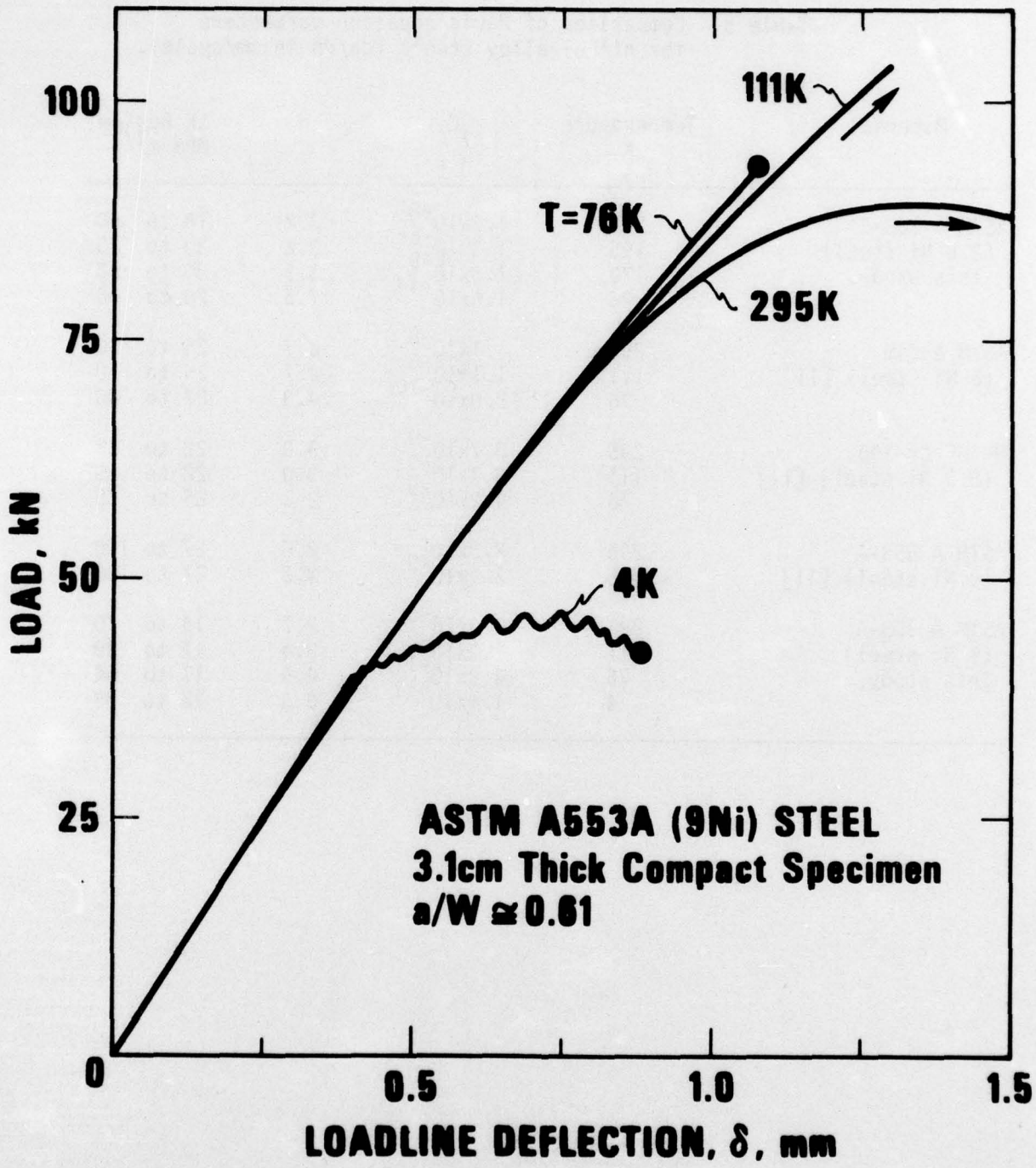


Figure 1. Load-versus-loadline deflection curves for 9 Ni steel.

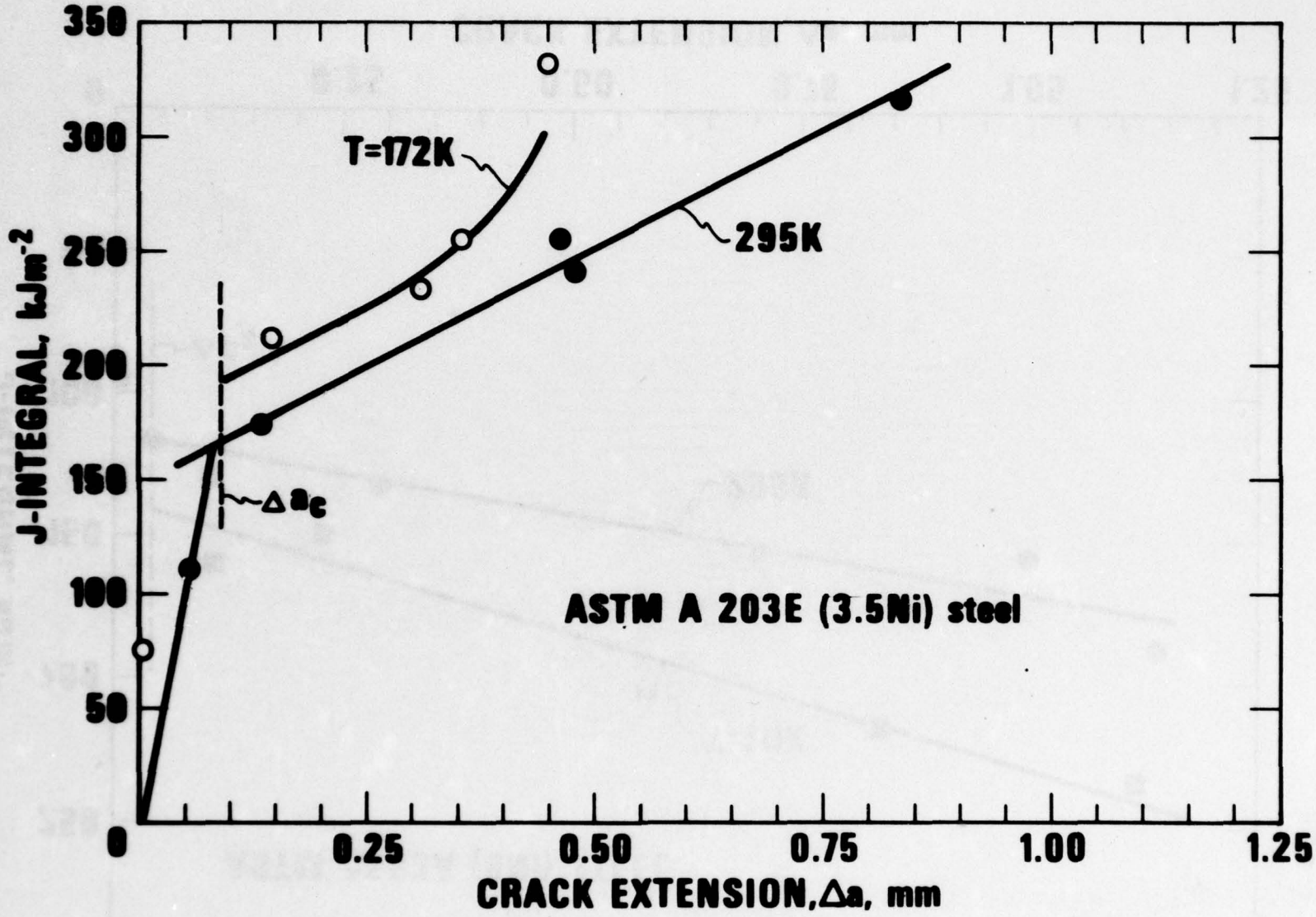


Figure 2. J-resistance curves for 3.5 Ni steel at room temperature (295 K) and the minimum use temperature (172 K).

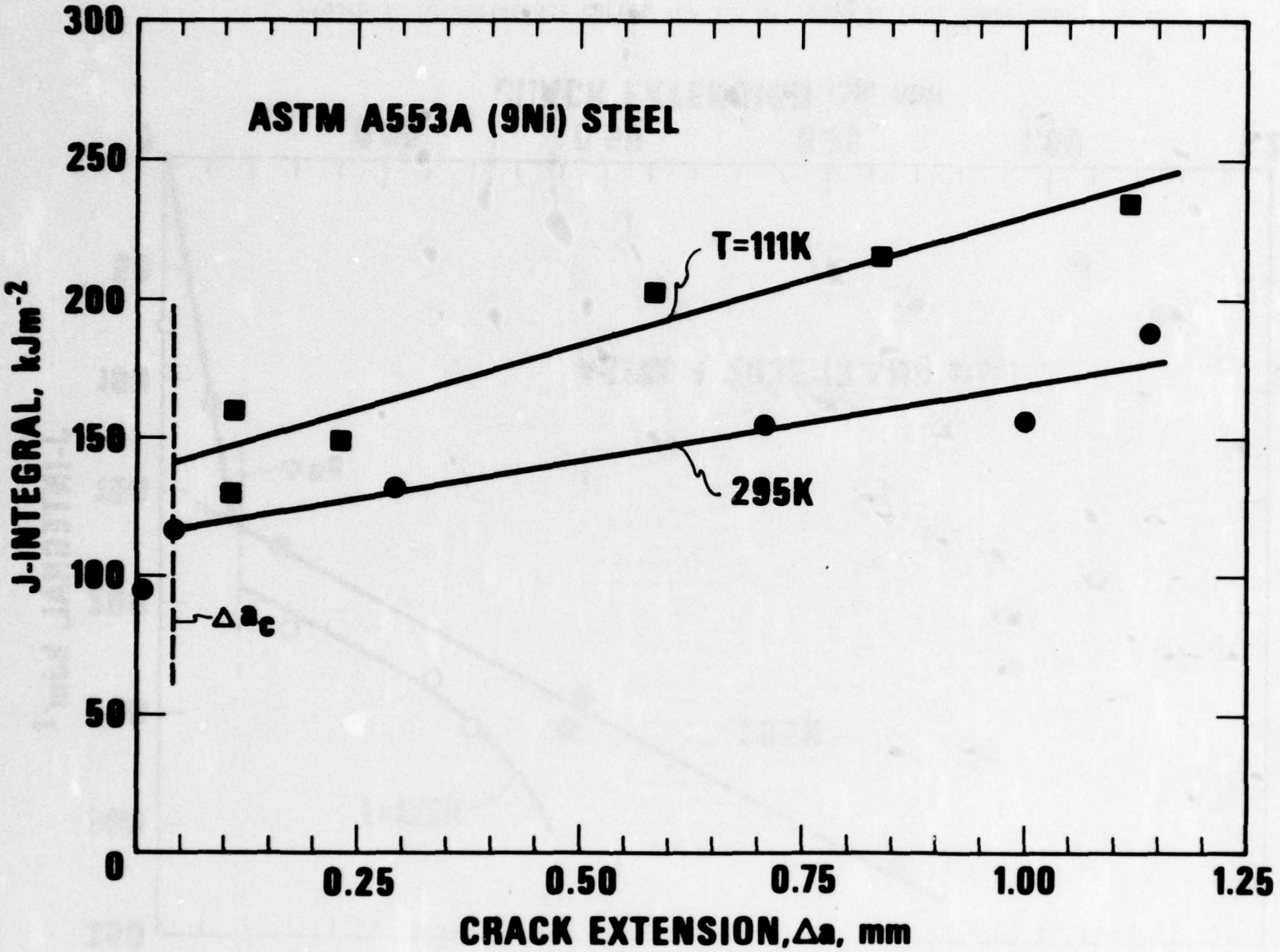


Figure 3. J-resistance curves for 9 Ni steel at room temperature (295 K) and liquified natural gas temperature (111 K).

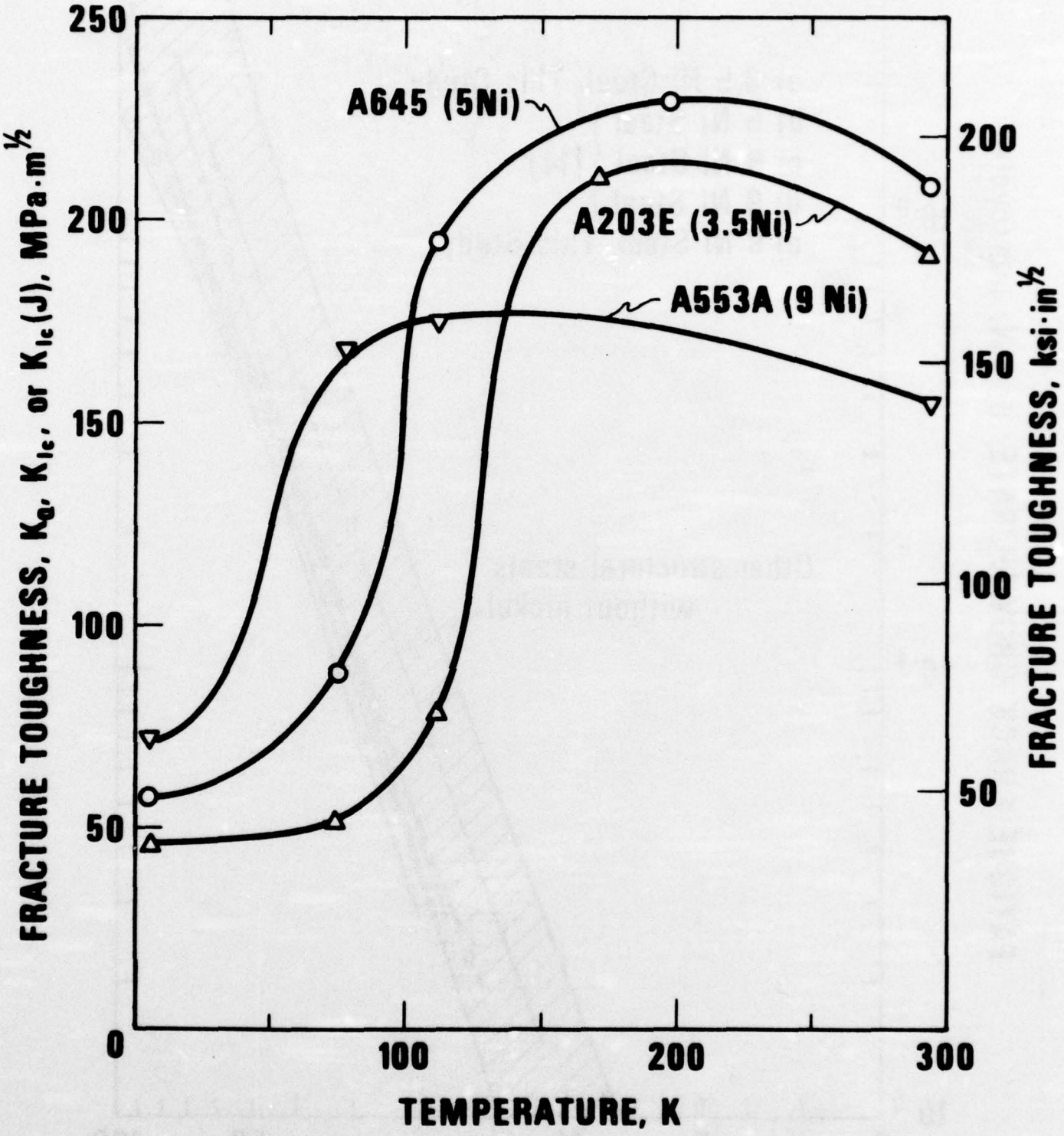


Figure 4. Temperature dependence of K_{IC} estimates obtained for the 3.5 Ni and 9 Ni steels of this study and the 5 Ni steel of a previous study [11].

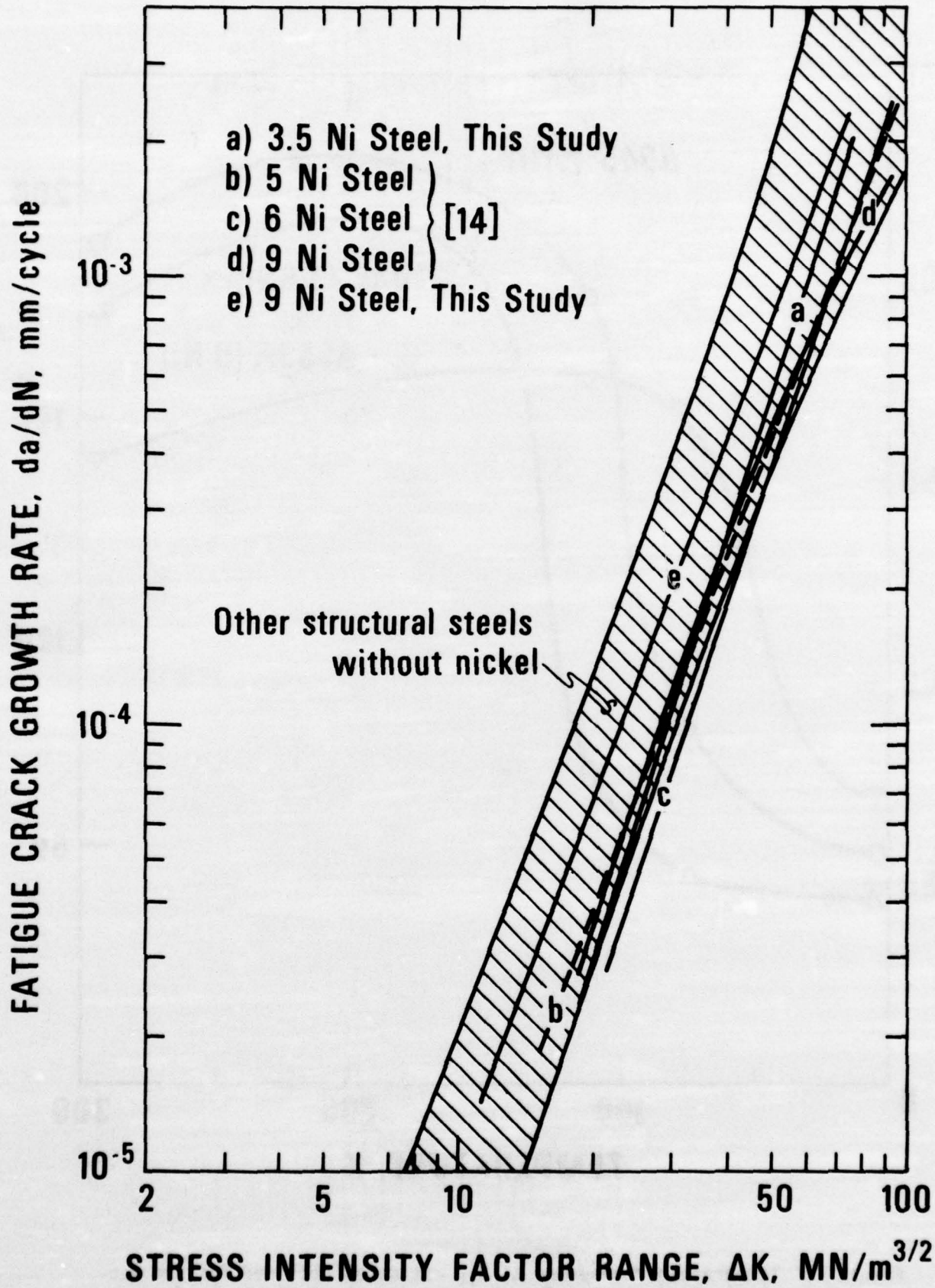


Figure 5. Room temperature fatigue crack growth data for the 3.5 Ni and 9 Ni steels of this study, the 5, 6, and 9 Ni steels of a previous study [11], compared to data for other ferritic structural steels without nickel [16-20].

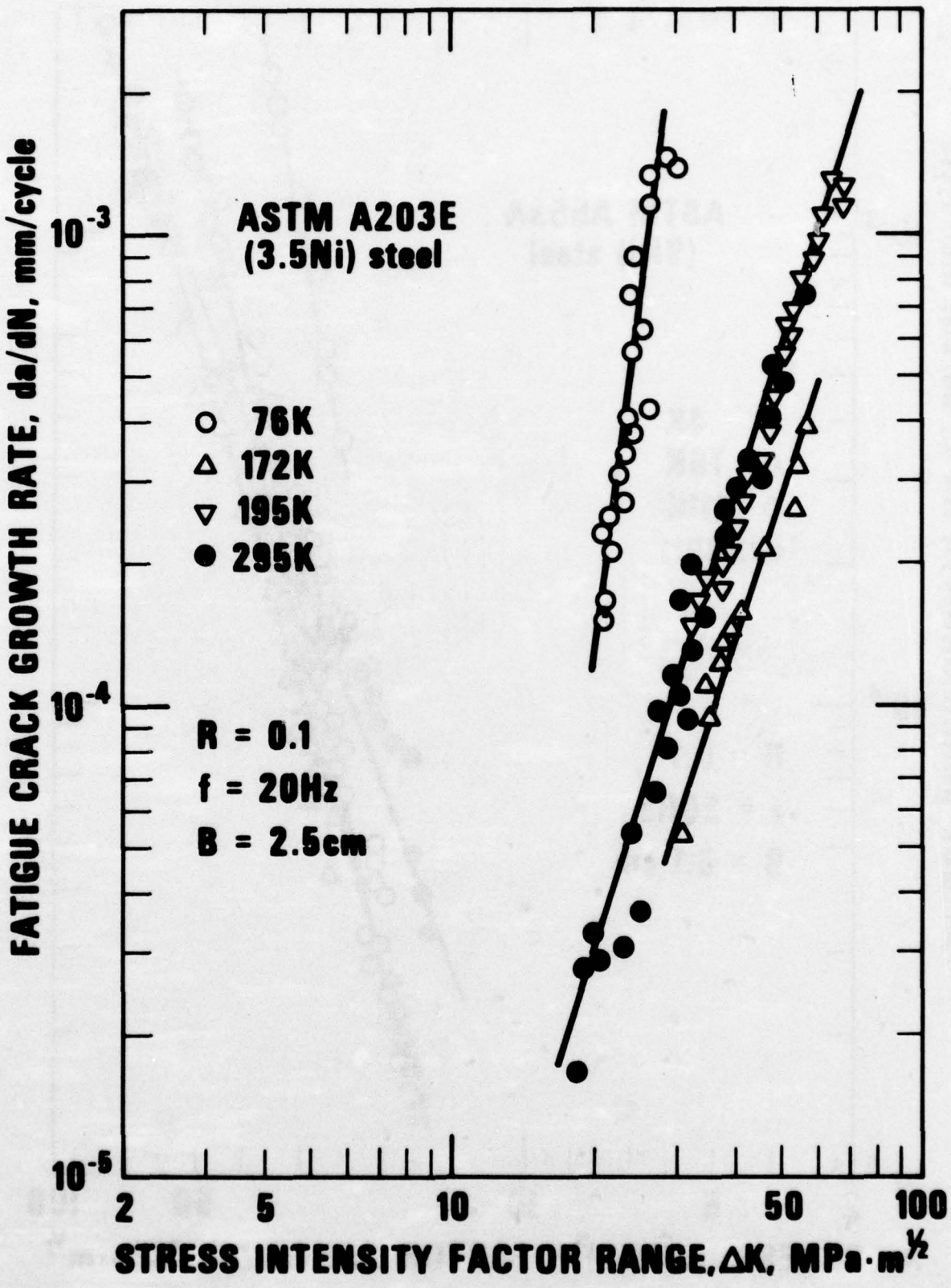


Figure 6. Fatigue-crack growth rates for 3.5 Ni steel at room and cryogenic temperatures.

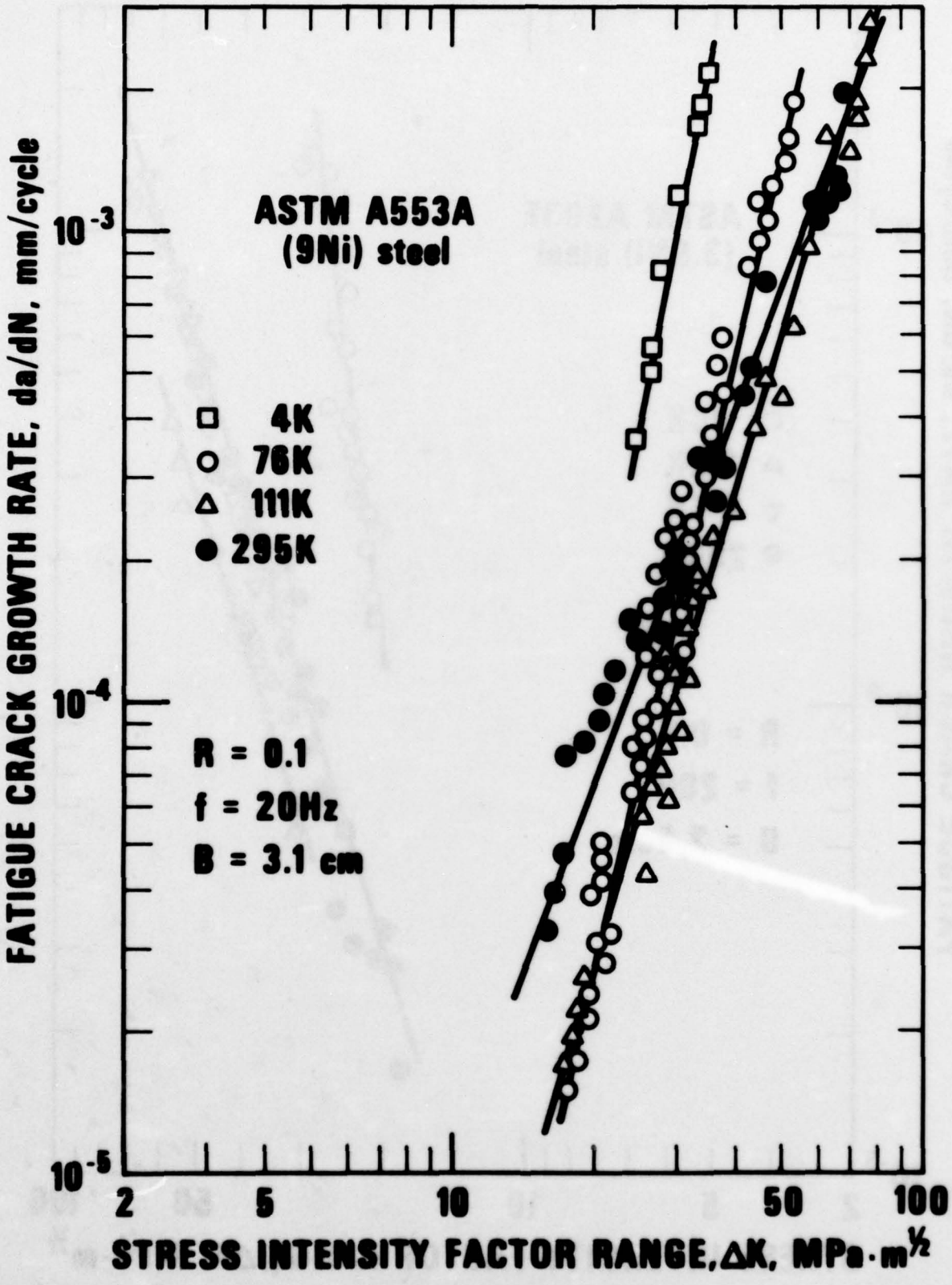


Figure 7. Fatigue-crack growth rates for 9 Ni steel at room and cryogenic temperatures.

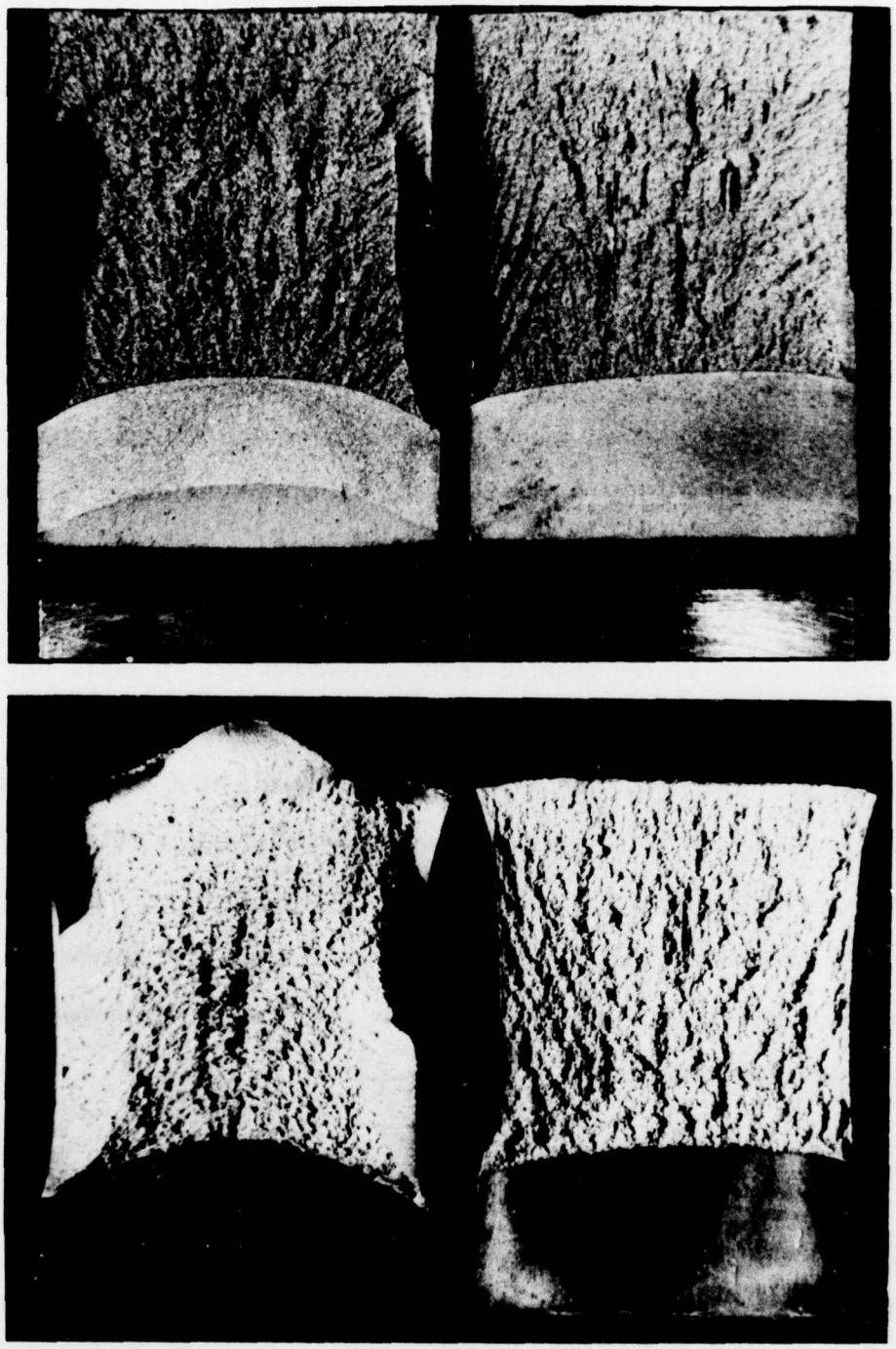


Figure 8. A comparison of the fracture surfaces of two different heats of 9 Ni steel fractured at 295 K (Top) and 76 K (Bottom) reveals heat-to-heat variability. The quenched and tempered 9 Ni steel of a previous study (left) displays a greater proportion of shear fracture at specimen edges, as well as a more pronounced degree of crack-front curvature.

NOTE ON THE FRACTURE PROPERTIES OF Fe-49Ni AT CRYOGENIC TEMPERATURES

H. I. McHenry and R. E. Schramm

The tensile, fatigue crack growth and fracture toughness properties of Fe-49 Ni were determined at room temperature, 76 K and 4 K. Tensile properties were determined with 25 mm gage length, 6.4 mm diameter specimens using the methods described previously by Reed [1]. Fatigue crack growth rates were determined with 25 mm thick, 51 mm wide compact tension specimens using the compliance method for crack length determinations; the test procedures and equipment were described previously by Fowlkes and Tobler [2]. Fracture toughness was determined with 25 mm thick, 51 mm wide compact tension specimens using the J-integral test procedures of Landes and Begley [3] and the cryogenic testing procedures and equipment described previously by Tobler et al. [4].

The results of the tensile tests are summarized in Table 1. The tensile and yield strengths at room temperature and 76 K are essentially the same as those obtained by Reed [5]. However, at 4 K the strength values obtained in this investigation are approximately 20% higher than those obtained by Reed [5].

The results of the fatigue crack growth tests are summarized in Figs. 1, 2 and 3. For each temperature, the line drawn through the data points has the form

$$\frac{da}{dN} = C(\Delta K)^n \qquad (1)$$

where da/dN is the fatigue crack growth rate in mm/cycle, ΔK is the stress intensity range in $MPa \cdot m^{1/2}$, and C and n are emperical constants. The

values for the intercept, C, the slope, n, and the coeficient of determination, R, were determined by least-squares regression analysis:

Temperature	C	n	R
Room Temp	7.7×10^{-9}	3.0	.977
76 K	8.4×10^{-10}	3.5	.981
4 K	1.6×10^{-10}	3.9	.995

A comparison of the data indicate that over the range of crack growth rates measured, the data at 4 K and 76 K are essentially the same and the growth rate at room temperature ranges from 1.4 to 2.5 times faster than the growth rate at the cryogenic temperatures.

The results of the fracture toughness tests are summarized in Table 2 and plotted in Figs. 4, 5 and 6. The J-integral value (J) for each test is calculated using the approximation of Rice, Paris and Merkle [6]:

$$J = \frac{2A}{B(W - a)} \tag{2}$$

where A is the area under the load displacement curve, B is the specimen thickness, W is the width and a is the crack length. For each temperature a curve of J vs Δa (crack extension) is constructed. On the same graph, the line defined by Eq. (3) is drawn:

$$J = 2\sigma_f \Delta a \tag{3}$$

where $\sigma_f = (\sigma_{ty} + \sigma_{tu})/2$, σ_{ty} = .2% offset yield strength and σ_{tu} = ultimate tensile strength. The intersection of the J-Δa plot and the $J/2\sigma_f$ line is defined as J_{IC}, the value of J at the onset of crack

extension. The values for J_{IC} are 1000 KJ/m^2 at 76 K and 870 KJ/m^2 at 4 K. At room temperature, J_{IC} was not defined because the curves did not intersect. It is reasonable to say that the room temperature toughness exceeds the J value for zero crack extension, i.e. 281 KJ/m^2.

Specimen size requirements for valid J_{IC} measurements have not yet been agreed upon by ASTM, however, Landes and Begley [3] suggest use of the following size criteria:

$$a, B, W-a \geq 25 J_{IC}/\sigma_f \qquad (4)$$

By these criteria, the measurement capacity of a 2.5 cm thick (W = 5 cm) compact tension specimen precracked to a/W = 0.62 would be determined by the ligament size, W-a = 1.9 cm. The calculated measurement capacities are 275, 464 and 568 KJ/m^2 at room temperature, 76 K and 4 K, respectively. At all temperatures, the measured J_{IC} values exceeded these limits. Thus, the specimen is not sufficiently large to assume that J characterizes the crack-tip field. If in fact the toughness does exceed the measurement capacity of the specimen, the toughness of Fe-49Ni is very high and not an important consideration in structural design.

Begley and Landes [7] have proposed that the plane strain fracture toughness, K_{IC}, is related to J_{IC} as follows:

$$K_{IC}(J) = \left(\frac{J_{IC}E}{1-\nu^2}\right)^{1/2} \qquad (5)$$

where E is Young's modulus and ν is Poisson's ratio. The values for E and

ν for Fe-49Ni were obtained from Ledbetter [8]: at 76 K E = 1.562×10^{11} N/m^2 (22.6×10^6 psi) and $\nu = .343$; at 4 K E = 1.569×10^{11} N/m^2 (22.8×10^6 psi) and $\nu = .343$. The values calculated for $K_{IC}(J)$ are 423 $MPa \cdot m^{1/2}$ (382 $ksi\sqrt{in}$) at 76 K and 396 $MPa \cdot m^{1/2}$ (396 $ksi\sqrt{in}$) at 4 K. These levels of toughness virtually preclude the possibility of brittle fracture in Fe-49Ni.

1. R. P. Reed, Advances in Cryogenic Engineering, Vol. 7 (Plenum Press, New York, 1962) p. 448.
2. C. W. Fowlkes and R. L. Tobler, Eng. Fract. Mechs. 8 (1976) 487.
3. J. D. Landes and J. A. Begley, "Test Results for J-Integral Studies -- An Attempt to Establish a J_{IC} Testing Procedure," Westinghouse Research Laboratory Scientific Paper 73-1E-7-FMPWR-P3, 1973.
4. R. L. Tobler, R. P. Mikesell, R. L. Durcholz and R. P. Reed, ASTM STP 579, 1975, p. 261.
5. R. P. Reed, National Bureau of Standards, Boulder, CO, to be published.
6. J. R. Rice, P. C. Paris and J. G. Merkle, ASTM STP 536, 1973, p. 231.
7. J. A. Begley and J. D. Landes, ASTM STP 514, 1972, p. 1.
8. H. M. Ledbetter, National Bureau of Standards, Boulder, CO, to be published.

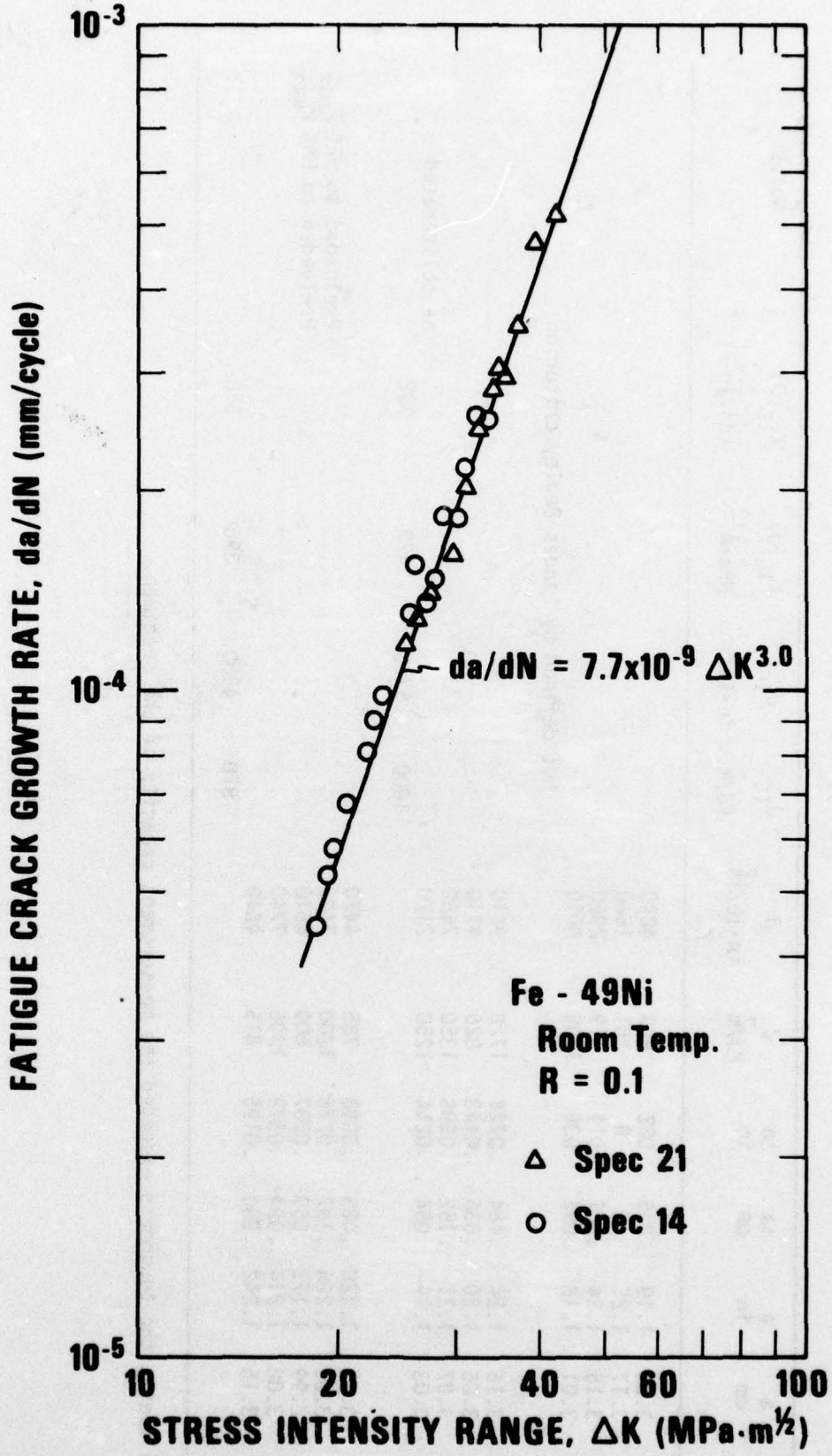
Table 1. Tensile property results for Fe-49Ni

Temperature K	Yield Strength MPa	(ksi)	Ultimate Strength MPa	(ksi)	Elongation % in 25 mm	Reduction of Area %
298	194	28.2	495	71.9	49	70
298	233	33.8	499	72.5	47	74
Average	214	31.0	497	72.2	48	72
76	351	51.0	841	122	57	72
76	365	53.0	845	123	56	72
Average	358	52.0	843	122	56	72
4	507	73.6	977	142	50	60
4	473	68.7	980	142	49	60
Average	490	71.1	978	[illegible]	49	60

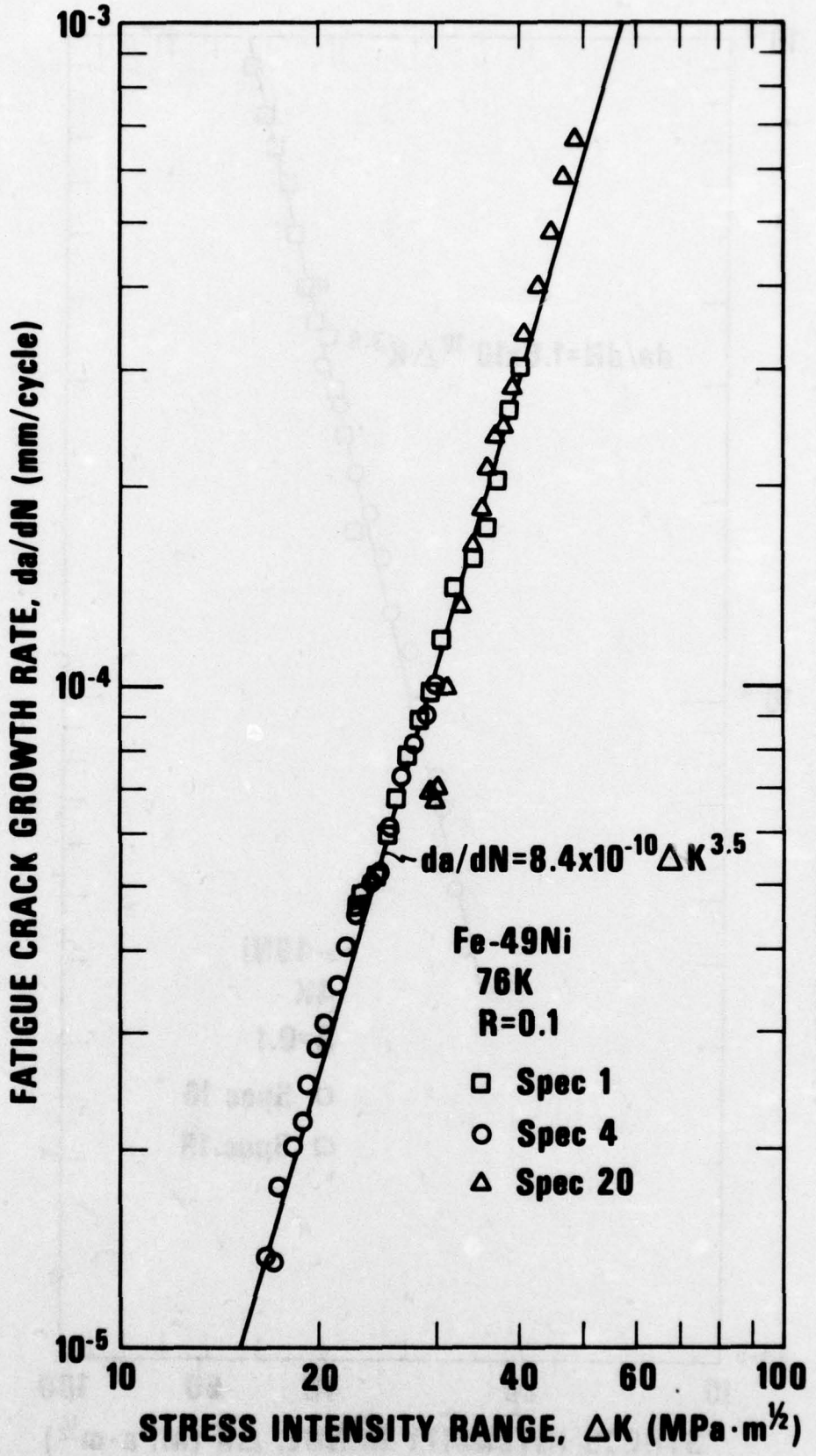
Table 2. Fracture toughness results for Fe-49Ni

Temp	Spec No	a cm	a in	Δa cm	Δa in	J KJ/m²	J in·lb/in²	J_{IC} KJ/m²	J_{IC} in·lb/in²	$K_{IC}(J)$ MPa·m$^{1/2}$	$K_{IC}(J)$ ksi$\sqrt{in}$	Notes
Rm Temp	12	3.03	1.19	.055	.022	849	4840					
	14	3.17	1.25	0	0	281	1600					
	22	3.15	1.24	.027	.011	519	2960					
	23	3.01	1.18	.092	.036	1405	8010					
								Not defined by Landes Begley criterion				
76 K	1	3.16	1.24	.184	.0724	1720	9810					
	4	3.06	1.20	.036	.0143	826	4710					
	6	3.07	1.21	.152	.0598	1350	7680					
	17	3.03	1.19	.054	.0214	1250	7120					Δa obliterated
								1000	5700	423	382	
4 K	5	3.12	1.228	.025	.0098	785	4470					
	7	3.06	1.206	.197	.0776	1300	7400					Preloaded to 92% P_{max}
	9	2.99	1.177	.053	.0207	809	4610					Preloaded to 88% P_{max}
	15	3.08	1.214	.094	.0372	1306	7740					
	16	3.15	1.242	.050	.0195	815	4640					
								870	4960	396	358	

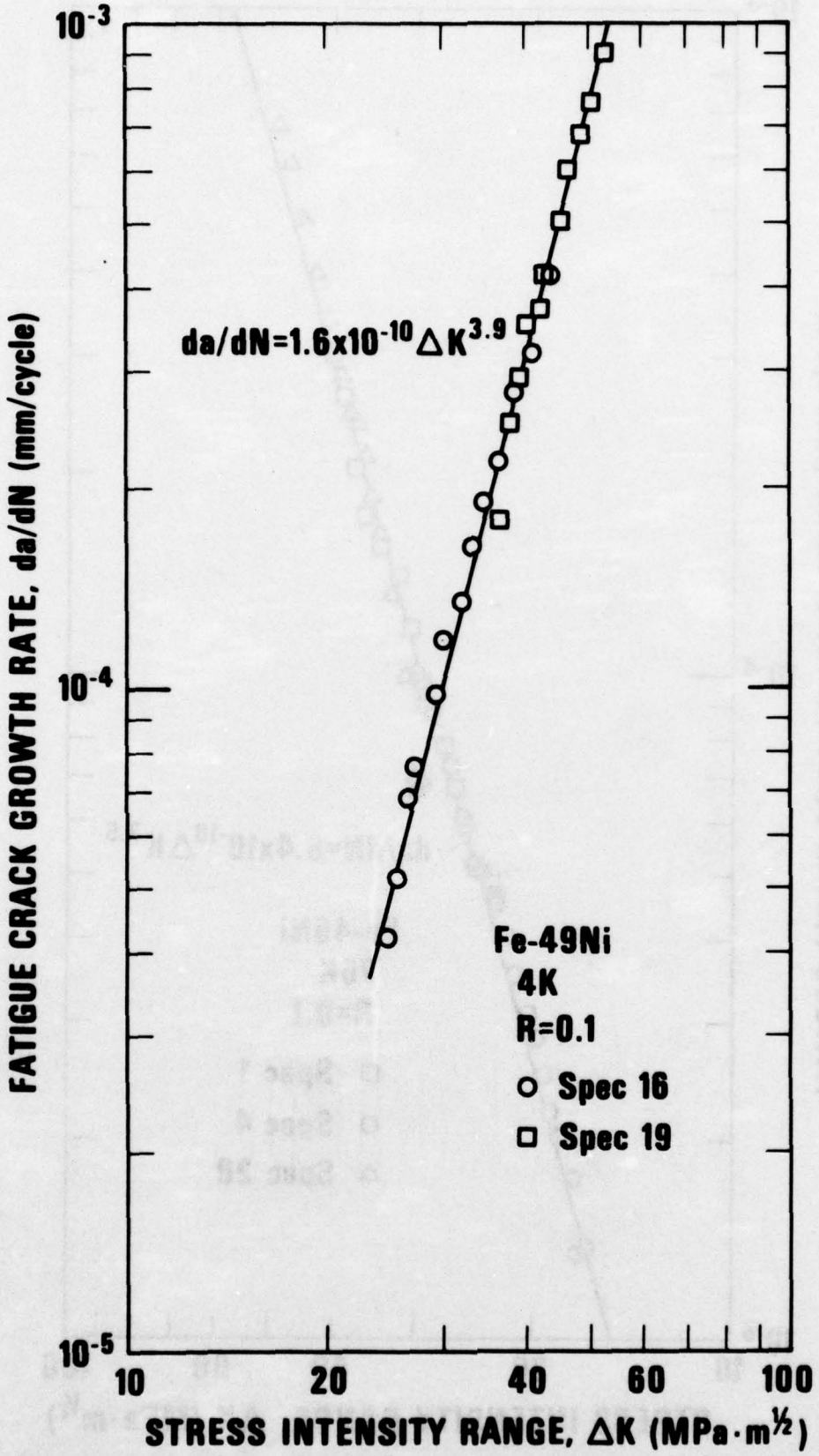
Note: In all tests, the toughness exceeded the measurement capacity of the specimen.



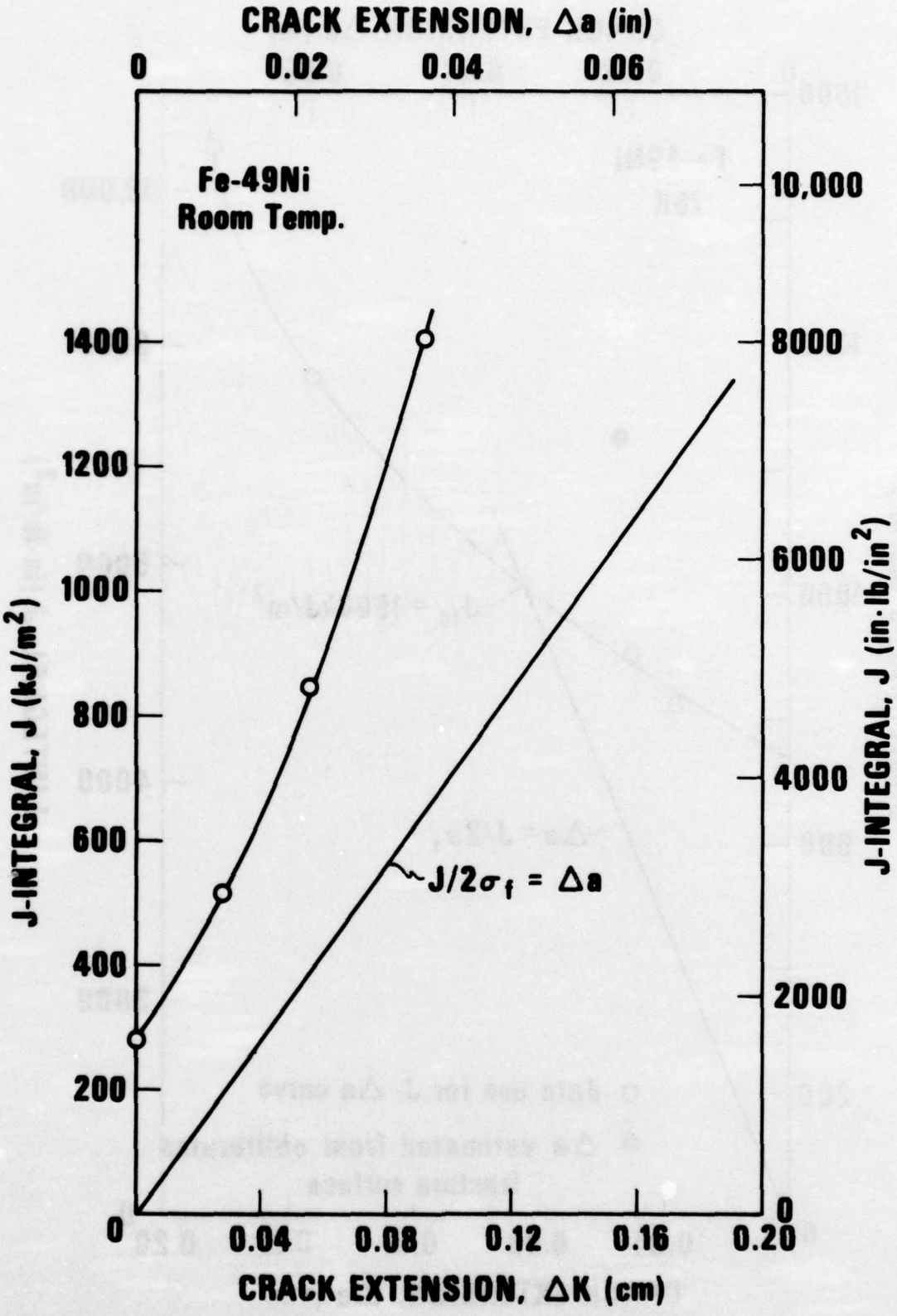
1. Fatigue crack growth rates in Fe-49 Ni at room temperature.



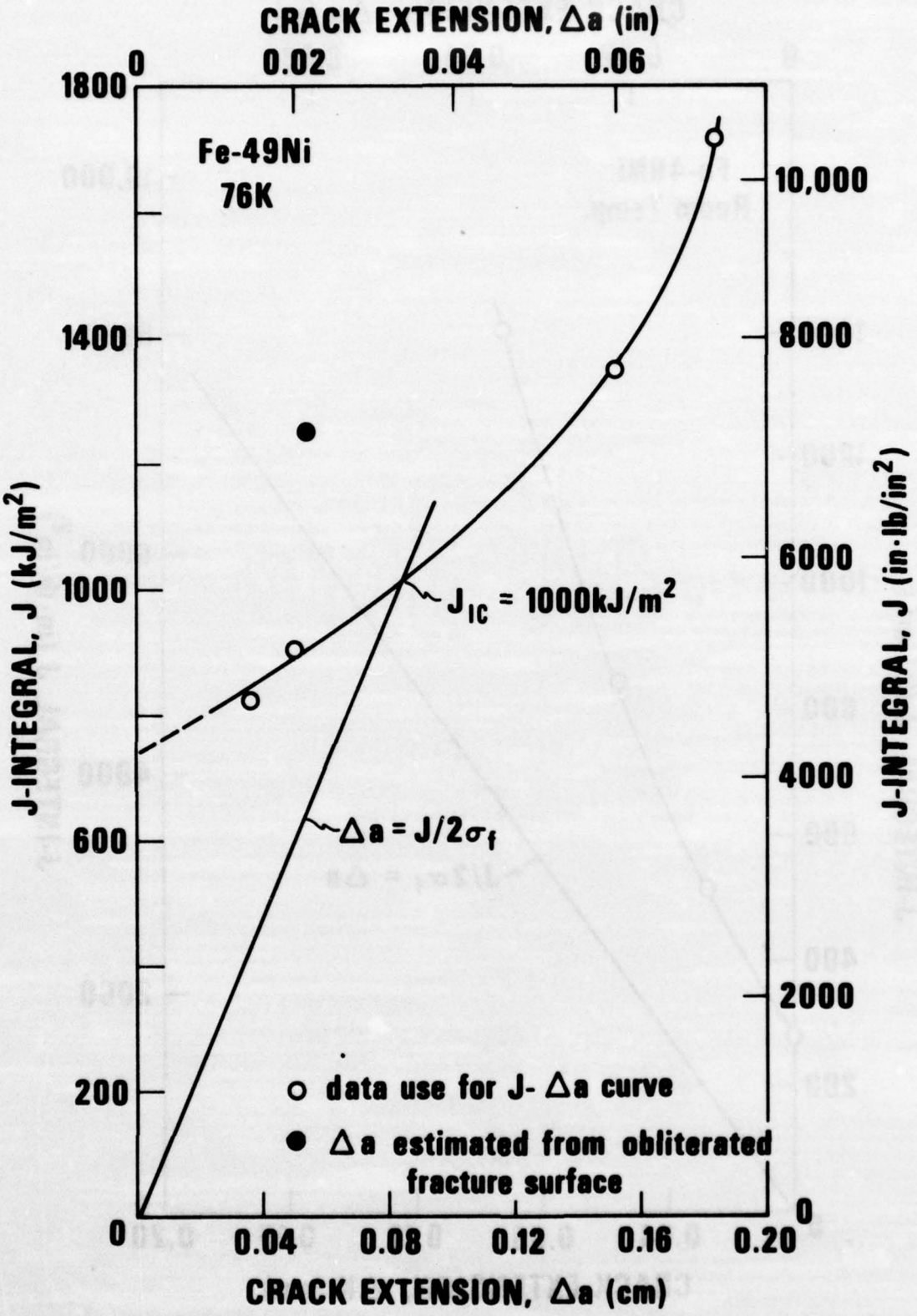
2. Fatigue crack growth rates in Fe-49 Ni at 76 K.



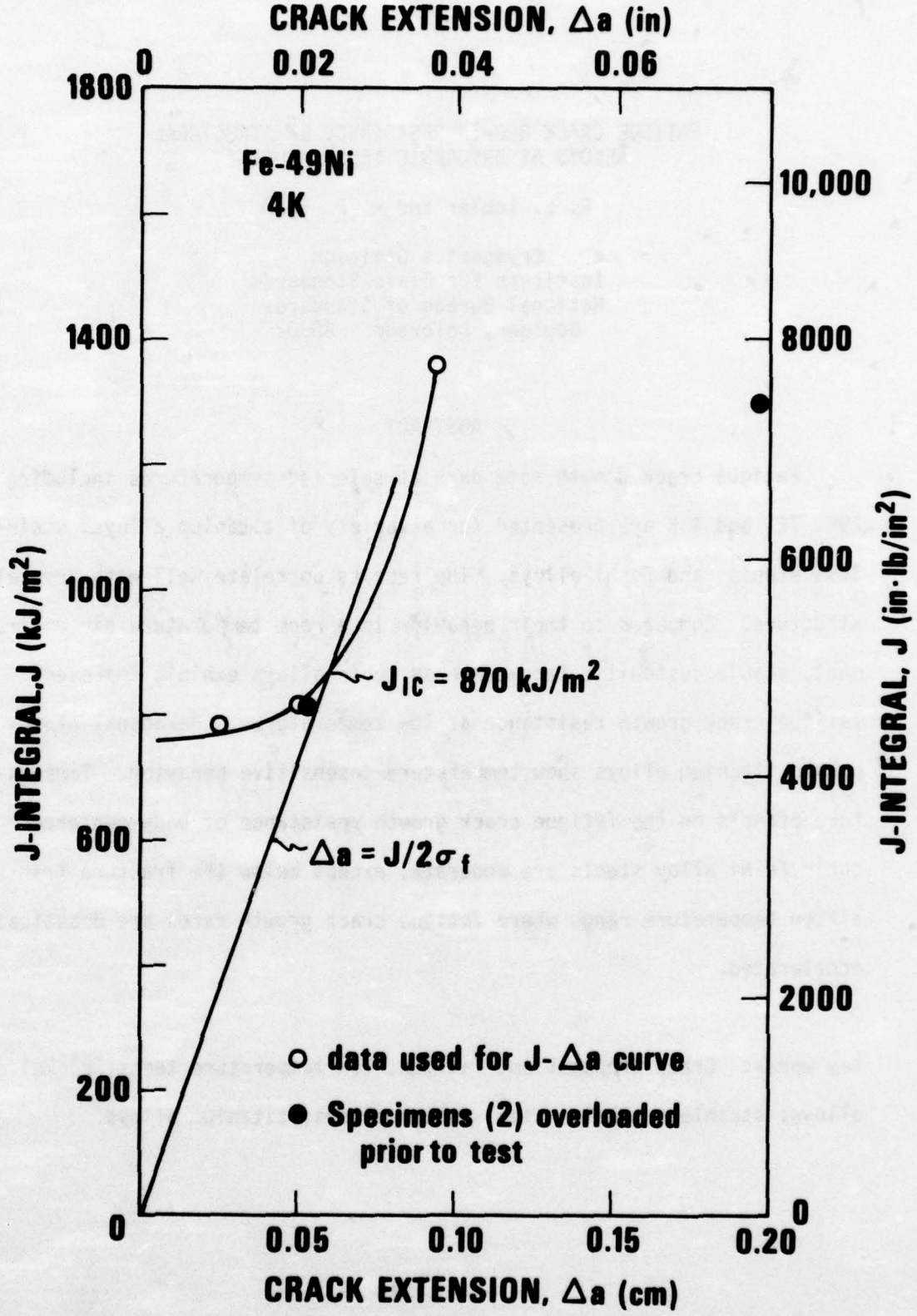
3. Fatigue crack growth rates in Fe-49 Ni at 4 K.



4. J-Δa fracture toughness curve for Fe-49 Ni at room temperature.



5. J-Δa fracture toughness curve for Fe-49 Ni at 76 K.



6. J-Δa fracture toughness curve for Fe-49 Ni at 4 K.

FATIGUE CRACK GROWTH RESISTANCE OF STRUCTURAL ALLOYS AT CRYOGENIC TEMPERATURES*

R. L. Tobler and R. P. Reed

Cryogenics Division
Institute for Basic Standards
National Bureau of Standards
Boulder, Colorado 80302

ABSTRACT

Fatigue crack growth rate data at selected temperatures including 295, 76, and 4 K are presented for a variety of titanium alloys, stainless steels, and Fe-Ni alloys. The results correlate well with crystal structure. Compared to their behavior in a room temperature air environment, stable austenitic face-centered cubic alloys exhibit improved fatigue crack growth resistance at low temperatures. Hexagonal close-packed titanium alloys show temperature-insensitive behavior. Temperature effects on the fatigue crack growth resistance of body-centered cubic Fe-Ni alloy steels are moderate, except below the fracture transition temperature range where fatigue crack growth rates are drastically accelerated.

Key words: Crack propagation; fatigue; low temperature tests; nickel alloys; stainless steels; steels; superalloys; titanium alloys.

*NBS contribution, not subject to copyright.

INTRODUCTION

Fatigue failure is a process of crack initiation, crack propagation, and fracture. Fracture occurs when the crack propagates to a critical size, and the structural component is no longer able to support the applied stress. The critical crack size is a function of the fracture toughness of the material and the component geometry, and can be calculated from a fracture mechanics analysis. The fatigue life is determined by the time required to initiate and propagate a crack to critical size.

Fatigue design data are essential to avoid catastrophic failure, overdesign, and inefficient selection of materials. Conventional stress-controlled S-N test data for several alloys at 295, 76, and 4 K are available from the work of Schwartzberg and Kiefer [1] and Nachtigall, Klima and Freche [2]. Nachtigall [3] also reports strain-controlled S-N test data at low temperatures. Such data pertain to smooth or notched bar specimens where the crack initiation phase is important and may account for up to 90% of the total fatigue lifetime, depending on the stress level. However, in many large engineering structures cracks already exist, or are assumed to exist, due to manufacturing and fabrication defects. In such cases, the life of the structure is determined solely by the crack growth rate, and a specific knowledge of fatigue crack growth rates (da/dN) is essential for accurate fatigue life predictions.

This paper summarizes our experimental results on the fatigue crack growth resistance of 14 commercial structural alloys tested at selected temperatures between 295 and 4 K. The data presented are

directly applicable to design. Many of the results are reported here for the first time, although some data alloys were previously tested and individually discussed in prior reports []. This collection and comparison of data leads to generalizations showing that temperature effects on da/dN-versus-ΔK behavior correlate well with alloy crystal structure.

EXPERIMENTAL

A list of alloys for which fatigue crack growth rates were measured is shown in Table 1. Included are the material forms, chemical analyses, heat treatments, and specimen orientations according to the ASTM E 399-74 notation [4]. The compact specimen geometry was chosen because it is standardized and much experience with it has been accumulated. Constant amplitude fatigue tests were performed using specimens 20 to 38 mm thick, a sinusoidal load cycle, test frequencies between 20 and 28 Hz, and a constant minimum-to-maximum load ratio, R, of 0.1. The compliance method of crack growth measurement was employed, using apparatus and techniques that were previously described in detail [5,6], producing fatigue crack growth rate data with uncertainties typically no greater than $\pm$ 20%.

RESULTS AND CONCLUSIONS

Fatigue crack growth rates at intermediate stress intensity factor ranges, ΔK, usually conform to Paris equations having the form [7]:

$$\frac{da}{dN} = C(\Delta K)^n \qquad (1)$$

where C and n are empirical constants that depend on material and test variables. Logarithmic plots of da/dN-versus-ΔK data that are in agreement with Eq. (1) reveal linear trends, n and C being the slope and

ordinate intercept at $\Delta K = 1$, respectively. Room temperature and cryogenic fatigue crack growth rate data for the alloys tested in this study are plotted in Figs. 1-13, and Paris equation parameters for each material/temperature combination are listed in Table 2. There are three distinct alloy groups:

I. HCP Titanium Alloys

Of all the alloys having mainly close-packed hexagonal crystal structures, the Ti-5Al-2.5Sn (single phase, HCP) and Ti-6Al-4V (two phase, HCP and some BCC) alloys are the most common for cryogenic service. These alloys offer high strength-to-weight ratios, while retaining adequate low temperature ductility and fracture toughness. As shown in Figs. 1 and 2, the fatigue crack growth data for annealed normal and low-interstitial grade Ti-5Al-2.5Sn alloys demonstrate temperature independent behavior between 295 K and 4 K. The Paris equation exponents for these alloys range from 4.0 to 4.8. Other results for the mill-annealed normal-interstitial and recrystallization-annealled, extra-low-interstitial Ti-6Al-4V alloys described in previous reports [9] also show temperature insensitive behavior. The results for those Ti-6Al-4V alloys are compared with the Ti-5Al-2.5Sn alloys in Fig. 3. Over most of the stress intensity range investigated, the fatigue crack growth resistances offered by the Ti-5Al-2.5Sn alloys are slightly superior to the Ti-6Al-4V alloys.

II. BCC Ferritic Steels

Fatigue crack growth rates for three ferritic steels containing 3.5, 5, or 9% nickel are shown in Figs. 4-6. Low temperature effects on this group of alloys are insignificant or slightly beneficial as long as

temperature reductions remain in the "upper shelf" range, which is defined as the region where dimpled rupture or fibrous fractures occur during static fracture toughness tests. However, these ferritic steels exhibit abrupt transitions to low fracture toughness involving cleavage at temperatures determined primarily by the nickel content. Cleavage cracking also leads to a drastic acceleration of fatigue crack growth rates at temperatures in the sub-transition ranges. Accelerated fatigue crack growth rates were observed for 3.5 Ni steel at 76 K (Fig. 4), and for 9 Ni steel at 4 K (Fig. 6). A reduced fatigue crack growth resistance is also evident in the data for 5 Ni steel (Fig. 5) between 111 and 76 K. Due to such adverse trends, ferritic or BCC alloys are of limited use in low temperature tensile applications, and are usually restricted to service temperatures in their upper shelf ranges. Of all alloys tested, the ferritic steels exhibit the most dramatic Paris equation exponent transitions, with the room temperature values near 3.0 increasing to as high as 7.6 at sub-transition temperatures.

III. FCC Austenitic Alloys

Although more expensive than the less alloyed ferritic steels, austenitic superalloys and stainless steels offer high fracture toughness and constitute the most important class of cryogenic materials. Extensive alloying is possible in austenitic alloys, and a large number of commercially available compositions exist. However, the structures of some alloys are unstable at low temperatures; stress-induced bcc and hcp martensitic phase transformations can occur, affecting fatigue crack growth resistance and other mechanical properties.

Figs. 7-9 illustrate fatigue crack propagation results for Inconel

750* (ASTM A 637), A-286 (ASTM A 453) and AISI 310 stainless steel, three austenitic alloys that remain stable with respect to martensitic transformations during fatigue tests at room and low temperatures. These alloys exhibit similar behavior: the fatigue crack growth rates at a given stress intensity factor are lower at 76 K and 4 K than at room temperature, but there is no measureable difference in the rates at the two cryogenic temperatures. Other stable FCC alloys such as 5083-O aluminum and Inconel 718 show similar trends [9]. Logsdon, Wells, and Kossowsky [8] also reported improved rates at 4 K compared to room temperature, in tests of the stable austenitic alloys Kromarc 58 and A-286.

The AISI 304, 304L, and 316 stainless steels and the Fe-21Cr-6Ni-9Mn stainless steel are unstable, undergoing significant martensitic phase transformations during fatigue tests at 76 K and 4 K. Evidence of martensite in crack-tip plastic zones was obtained metallographically, and by detection with a magnetometer. In comparison, the small amounts of martensite formed at 295 K are negligable. It can be assumed that transformations precede crack growth at 76 and 4 K, and that fatigue crack growth at these temperatures represents crack propagation through partially transformed austenite.

It is difficult to generalize regarding the effect of martensitic transformations on fatigue crack growth resistance. The results for AISI 316 and 304 stainless steels, shown in Figs. 10 and 11, reveal no pronounced temperature effects on fatigue crack propagation resistance,

---

*Tradenames are used for the sake of clarity, and do not imply endorsement or recommendation by NBS.

except perhaps at high rates approaching 2.5×10^{-3} mm/cycle. The AISI 304L stainless steel, having lower carbon content than AISI 304 (0.026C compared to 0.05C), shows behavior analogous to that observed for stable alloys. As shown in Fig. 12, there is a significant decrease in the rates for AISI 304L at cryogenic temperatures compared to room temperature, but and the data at 76 K and 4 K are equivalent. The lower carbon content should reduce the stability of AISI 304L relative to AISI 304. Thus, the dissimilar temperature dependences for these alloys may be due to differences in the quantity and properties of the martensites formed.

The fatigue crack growth rates for the Fe-21Cr-6Ni-9Mn alloy are shown in Fig. 13. The rates at 295 K and 76 K are equivalent despite appreciable martensitic transformations occurring at 76 K. This behavior is similar to that observed for AISI 304 and AISI 316. On the other hand, the rates at 4 K are definitely higher than at 295 K and 76 K. Pronounced cleavage-like facets were observed under magnification of the 4 K fatigue surfaces, so that the decreased fatigue crack propagation resistance at 4 K can be attributed to a transition in the fracture mode accompanying the martensitic transformation at this temperature. The results for this alloy represent the only case where the fatigue crack propagation resistance of an (initially) austenitic alloy decreases at cryogenic temperatures.

SUMMARY

Temperature effects on the fatigue crack growth resistance of alloys correlate well with crystal structure:

1. HCP titanium alloys exhibit temperature-insensitive behavior between 295 K and 4 K.

2. BCC ferritic steels exhibit weak temperature dependences at in their upper shelf temperature ranges, whereas at sub-transition temperatures fatigue crack growth resistance is markedly decreased, being associated with cleavage microfracture modes.

3. Stable FCC alloys exhibit improved fatigue crack growth resistances at cryogenic temperatures, as compared to their behavior in room temperature air. It is difficult to generalize on the trends for metastable FCC alloys since favorable, adverse, or temperature-insensitive behaviors are observed depending on alloy composition.

REFERENCES

1. F. R. Schwartzberg and T. Kiefer, "A Study of Fracture Behavior of Metals for Superconducting Applications," MCR-74-89 (Issue 4), in Materials Research for Superconducting Machinery, IV, R. P. Reed, A. F. Clark, E. C. van Reuth, Eds., (National Bureau of Standards, Boulder, Colorado, October 1975).

2. A. J. Nachtigall, S. J. Klima, and J. C. Freche, J. Mater. JMLSA 3 (1968) 425.

3. A. J. Nachtigall, in Properties of Materials for Liquified Natural Gas Tankage, ASTM STP 579 (Amer. Soc. Test. Mater., Philadelphia, 1975) 378.

4. Standard Method of Test for Plane Strain Fracture Toughness of Metallic Materials, ASTM E 399-74, in 1976 Annual Book of ASTM Standards, Part 10 (Amer. Soc. Test. Mater., Philadelphia, 1976) 471.

5. C. W. Fowlkes and R. L. Tobler, Eng. Fract. Mechs. 8 (1976) 487.

6. R. L. Tobler and R. P. Reed, in Advances in Cryogenic Engineering 22, R. P. Reed, Ed. (Plenum, New York, 1976) 35.

7. P. C. Paris and F. Erdogan, Trans. ASME, J. Basic Eng. 85 (1963) 528.

8. W. A. Logsdon, J. M. Wells, and R. Kossowsky, in Proceedings of the Second International Conference on Mechanical Behavior of Materials (Amer. Soc. Metals, Ohio, 1976) 1283.

9. Materials Research for Superconducting Machinery, Vols. I to V, R. P. Reed, A. F. Clark, H. M. Ledbetter, and E. C. van Reuth, Eds., (National Bureau of Standards, Boulder, Colorado, March 1974 to March 1976) AD780596, ADA004586, ADA012365, ADA019230, ADA030170.

Table 1. Fatigue crack growth rate test materials for the ARPA sponsored program ending September 30, 1976.

Material Form and Condition	Specimen Thickness (mm), & orientation	Mill Chemical Analyses, wt%
Ti-5Al-2.5Sn, normal-interstitial annealed bar	38, TS	Ti-5.28Al, 2.46Sn, 0.327Fe, 0.01C, 0.01N, 0.174O, 40 ppm H.
Ti-5Al-2.5Sn, low-interstitial, annealed bar	32, TL	Ti-5.25Al, 2.53Sn, 0.045Fe, 0.012C, 0.009N, 0.116O, 173 ppm H.
Ti-6Al-4V, normal-interstitial, mill-annealed bar	25, TL	Ti-6.24Al, 4.18V, 0.174Fe, 0.035C, 0.011N, 0.155O, 14 ppm H.
Ti-6Al-4V, extra-low-interstitial, recrystallization-annealed bar	20 to 25, TL	Ti-5.91Al, 3.94V, 0.103Fe, 0.018C, 0.014N, 0.11O, 52 ppm H.
ASTM A 203 E (3.5 Ni steel), quenched and tempered, 25 mm thick plate	25, TL	Fe-0.10C, 3.62Ni, 0.46Mn, 0.013S, 0.015P, 0.20Si.
ASTM A 645 (5 Ni steel), austenized, temperized and reversion-annealed, 32 mm thick plate	31, TL	Fe-0.08C, 5.03Ni, 0.6Mn, 0.3Mo, 0.08Al, 0.009S, 0.01P, 0.25Si, 0.010N.
ASTM A 553A (9 Ni steel, quenched and tempered, 32 mm thick plate	31, TL	Fe-0.08C, 8.99Ni, 0.62Mn, 0.01S, 0.01P, 0.19Si.
5083-O aluminum alloy, annealed 43 mm thick plate	32, TL	Al-4.0 to 4.9Mg, 0.3 to 1.0 Mn, 0.05 to 0.25Cr, 0.10Cu max, 0.25Zn max, 0.15Ti max, 0.40Si max, 0.40Fe max, 0.15 others, max.
Inconel 718, solution treated and double-aged forging	31, TS	Ni-18.1Cr, 18.5Fe, 0.90Ti, 0.05C, 0.10Mn, 0.002S, 0.01P, 0.10Si, 0.003B, 0.10Cu, 0.49Al, 0.17Co, 2.95Mo, 5.24 Nb+Ta.
Inconel 750, solution treated and double-aged forging	38, TS	Ni-15.16Cr, 6.58Fe, 2.51Ti, 0.04C, 0.20Mn, 0.007S, 0.25Si, 0.04Cu, 0.78Al, 0.89 Nb+Ta.
A-286, solution treated and aged forging	38, TS	Fe-0.05C, 13.96Cr, 24.97Ni, 1.52Mn, 0.54Si, 0.007S, 0.016P, 1.30Mo, 2.23Ti, 0.004B, 0.30V, 0.19Al.
AISI 310, annealed 38 mm thick plate	38, TL	Fe-0.038C, 24.65Cr, 20.4Ni, 1.41Mn, 0.72Si, 0.016S, 0.023P, 0.13Mo, 0.14Cu.
AISI 316, annealed 38 mm thick plate	38, TL	Fe-0.04C, 17.8Cr, 13.10Ni, 1.72Mn, 0.51Si, 0.019S, 0.019P, 2.18Mo.
AISI 304, annealed 38 mm thick plate	38, TL	Fe-0.052C, 18.33Cr, 9.82Ni, 1.6Mn, 0.75Si, 0.015S, 0.028P, 0.20Mo, 0.13Cu.
AISI 304L, annealed 38 mm thick plate	38, TL	Fe-0.026C, 18.84Cr, 10.18Ni, 1.65Mn, 0.82Si, 0.01S, 0.022P, 0.27Mo, 0.28Cu.
Fe-21Cr-6Ni-9Mn, annealed 38 mm thick plate	38, TL	Fe-0.019C, 19.75Cr, 7.16Ni, 9.46Mn, 0.15Si, 0.003S, 0.004P, 0.28N

Table 2. Paris equation parameters for alloys at room and cryogenic temperatures (da/dN in mm/cycle and ΔK in $MPa \cdot m^{1/2}$).

Material	Temperature, K	n	C	ΔK region investigated
Ti-5Al-2.5Sn, annealed				
1. normal-interstitial	295, 76, and 4	4.8	5.1×10^{-11}	14 to 30
2. low-interstitial	295, 76, and 4	4.0	4.9×10^{-10}	10 to 60
Ti-6Al-4V				
1. normal-int., mill-annealed,	295, 76, and 4	6.0	3.1×10^{-12}	14 to 30
2. ELI, recrystallization-annealed	295, 76, and 4	7.0	1.9×10^{-13}	10 to 20
	295 and 76	3.0	3×10^{-8}	20 to 60
ASTM A 203 E (3.5 Ni steel)	295	3.2	1.3×10^{-8}	18 to 60
quenched and tempered	195	3.2	1.3×10^{-8}	30 to 70
	172	3.2	1.0×10^{-9}	30 to 60
	76	7.6	1.6×10^{-14}	20 to 30
ASTM A 645 (5 Ni steel)	295	2.7	1.1×10^{-8}	25 to 90
austenitized, temperized, reversion	111	2.7	1.1×10^{-8}	25 to 60
annealed	76	4.0	2.0×10^{-10}	27 to 80
ASTM A 553 A (9 Ni steel)	295	2.7	2.0×10^{-8}	16 to 70
quenched and tempered	111	3.4	1.0×10^{-9}	17 to 80
	76	4.4	4.8×10^{-11}	17 to 64
	4	5.3	1.4×10^{-11}	25 to 35
5083-O aluminum	111, 76, and 4	5.2	1.3×10^{-10}	8 to 28
annealed				
Inconel 718	295	4.0	8×10^{-11}	20 to 70
solution treated, double-aged	4	4.0	4.8×10^{-11}	25 to 90
Inconel 750	295	3.0	2.4×10^{-9}	26 to 80
solution treated, double-aged	76 and 4	3.8	6.6×10^{-11}	30 to 92
ASTM A 453 (A-286)	295	3.0	2.5×10^{-9}	25 to 90
solution treated, aged	76 and 4	4.0	2×10^{-12}	32 to 90
AISI 310, annealed	295	4.4	3.5×10^{-11}	24 to 35
	295	3.0	4.7×10^{-9}	35 to 60
	76 and 4	3.7	1.1×10^{-10}	25 to 80
AISI 316, quenched	295 to 4	3.8	2.1×10^{-10}	19 to 60
AISI 304, quenched	295 to 4	3.0	2.7×10^{-9}	22 to $\sim$ 80
AISI 304L, annealed	295	4.0	2.0×10^{-10}	22 to 54
	76 and 4	4.0	3.4×10^{-11}	26 to 80
Fe-21Cr-6Ni-9Mn, annealed	295 and 76	3.7	1.9×10^{-10}	25 to 80
	4	4.4	3.6×10^{-11}	25 to 70

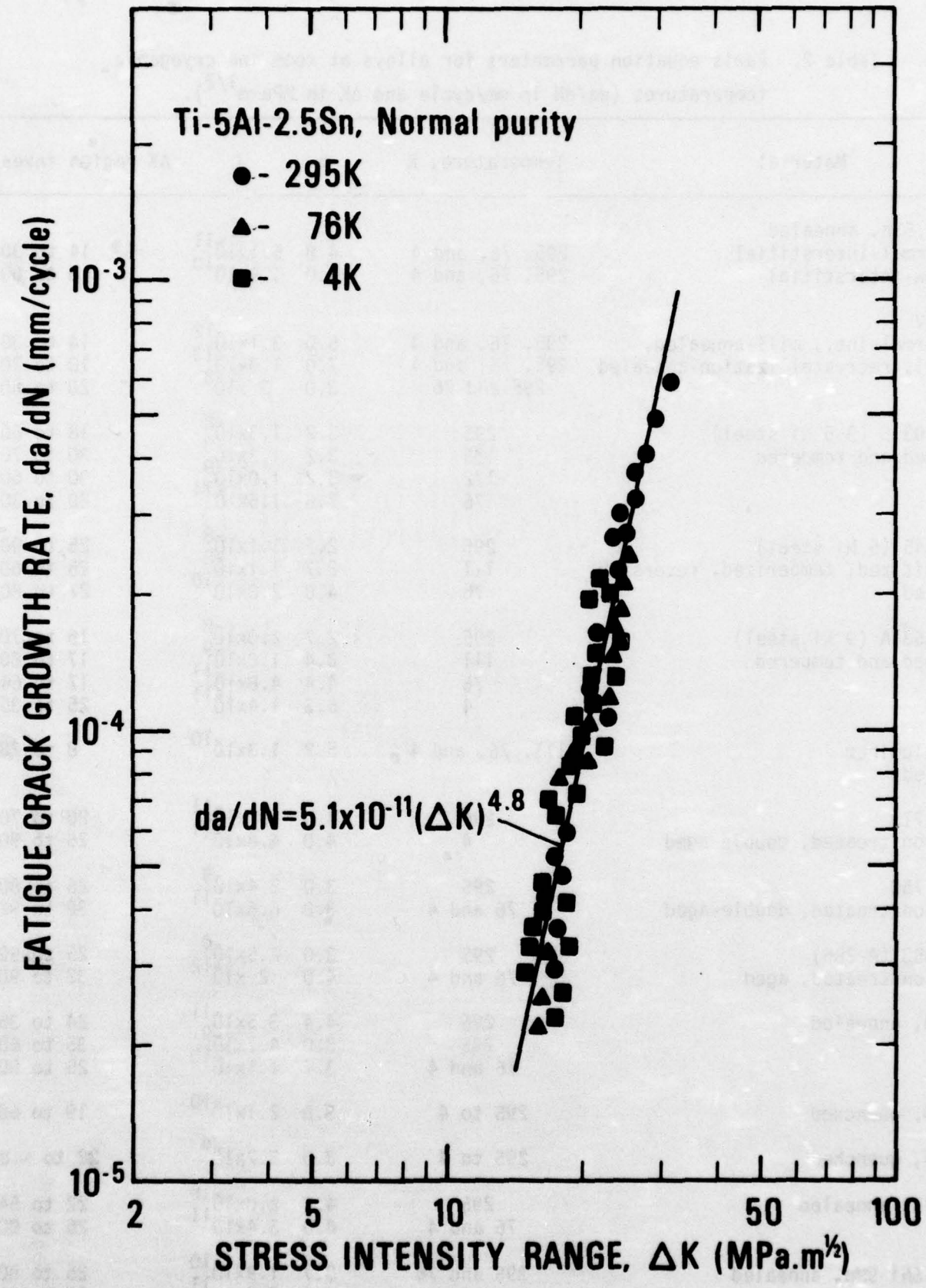


Figure 1. Fatigue crack growth data for a normal interstitial Ti-5Al-2.5 Sn alloy at 295, 76, and 4 K, showing temperature independent behavior.

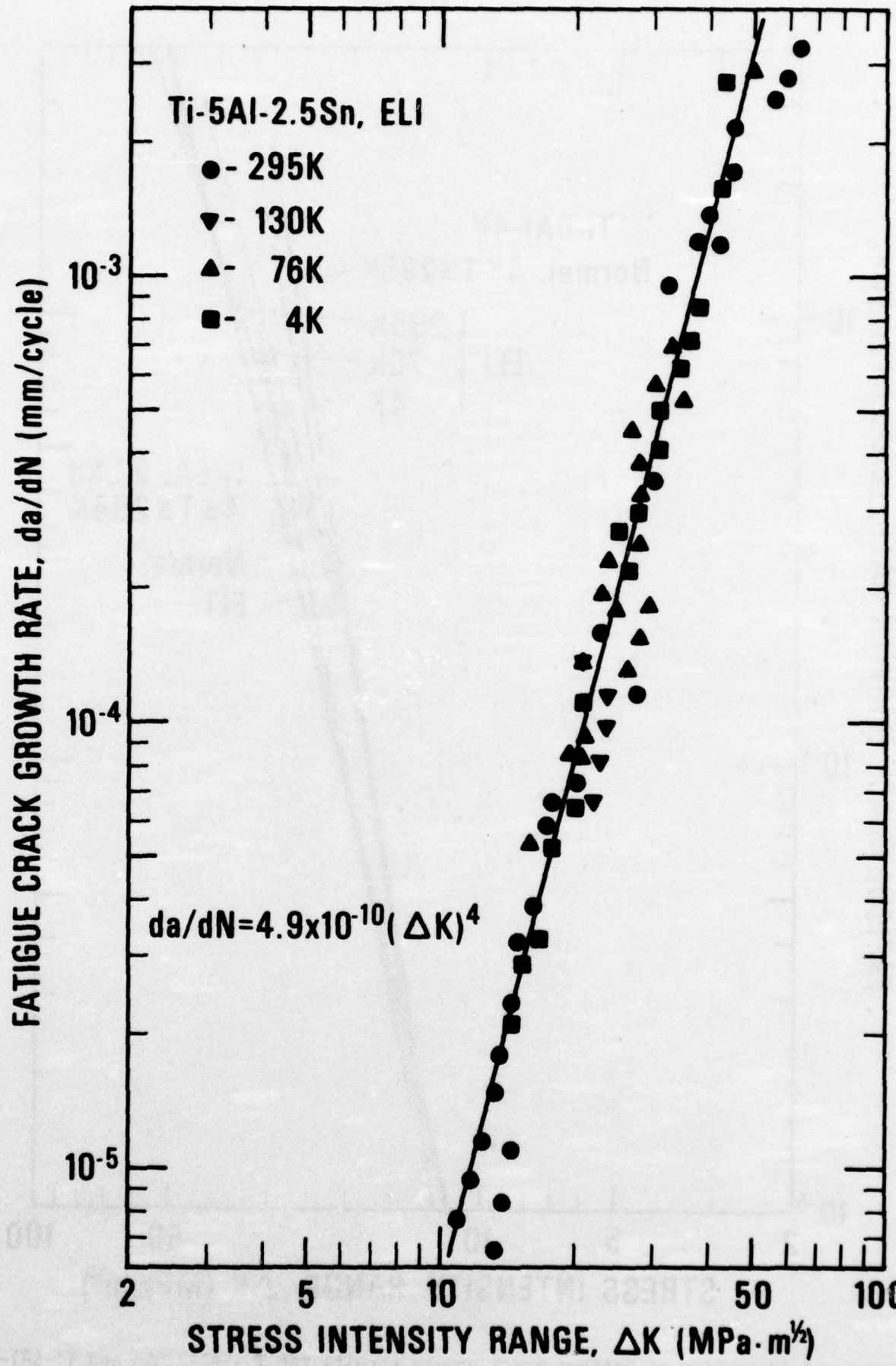


Figure 2. Fatigue crack growth data for a low-interstitial Ti-5Al-2.5Sn alloy at 295, 76 and 4 K, showing temperature independent behavior.

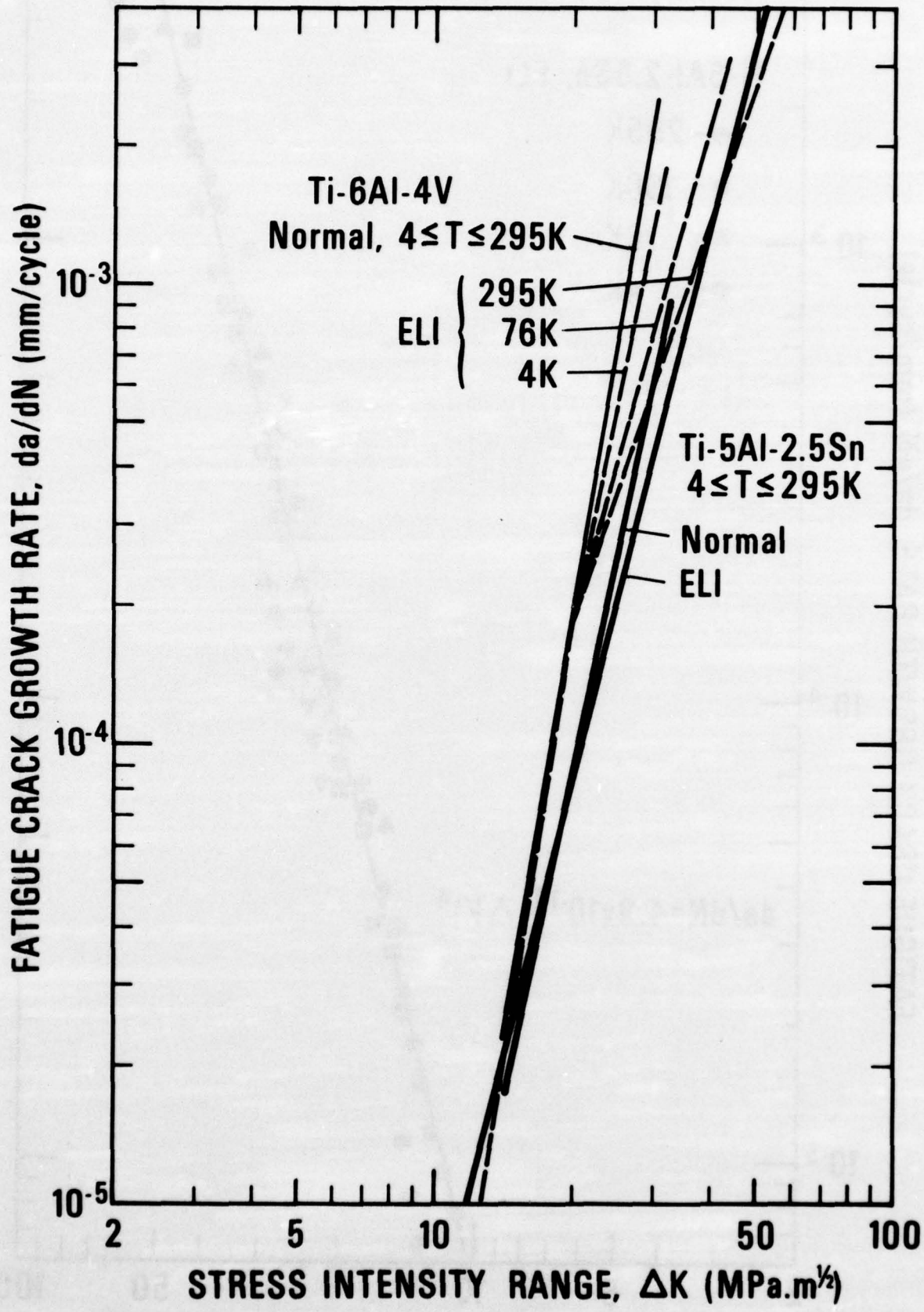


Figure 3. A comparison of fatigue crack growth results for Ti-5Al-2.5Sn and Ti-6Al-4V alloys indicating the slight superiority of Ti-5Al-2.5Sn alloys over most of the ΔK regions investigated.

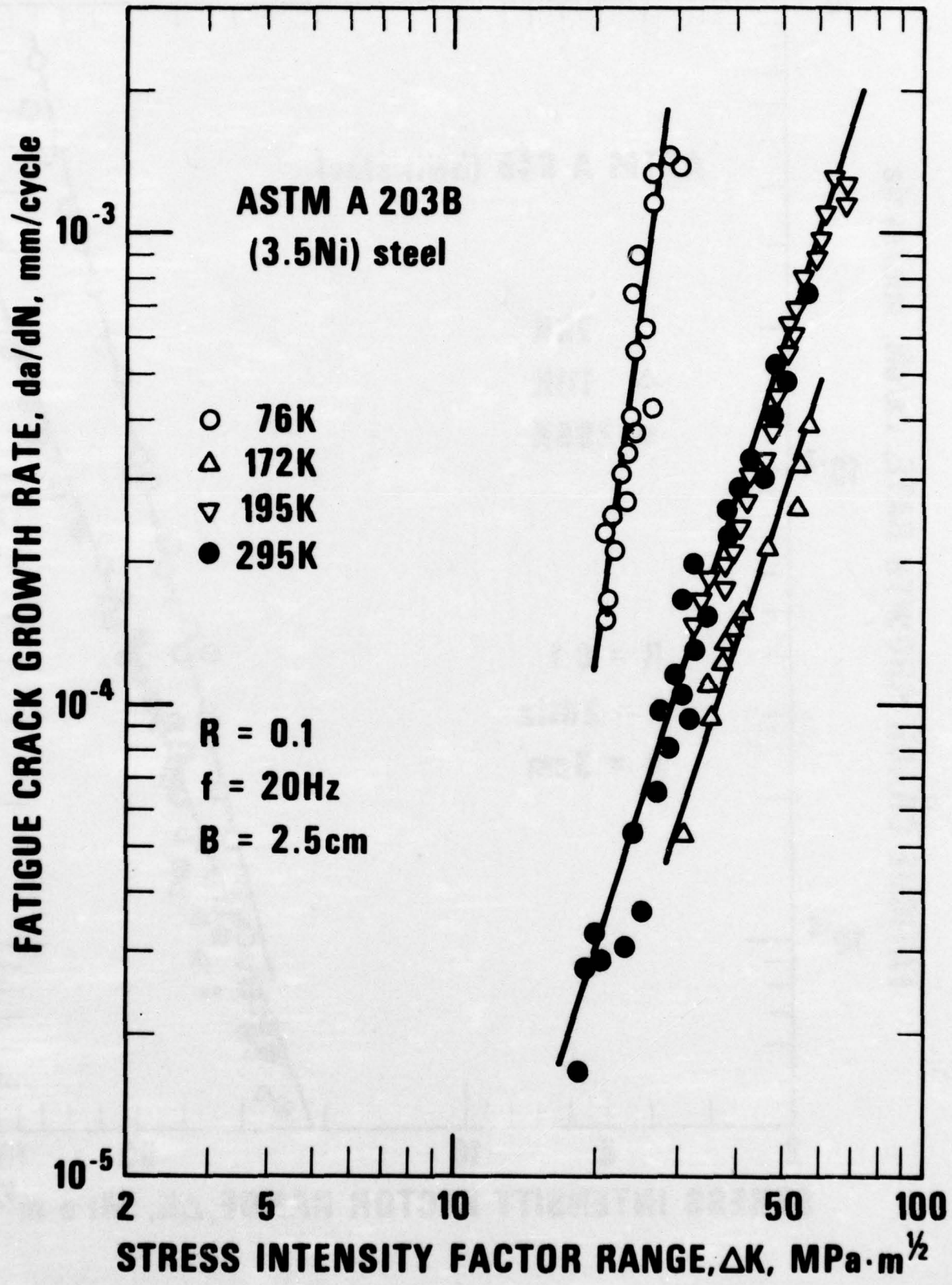


Figure 4. Fatigue crack growth data for a ferritic 3.5 Ni alloy steel at selected temperatures.

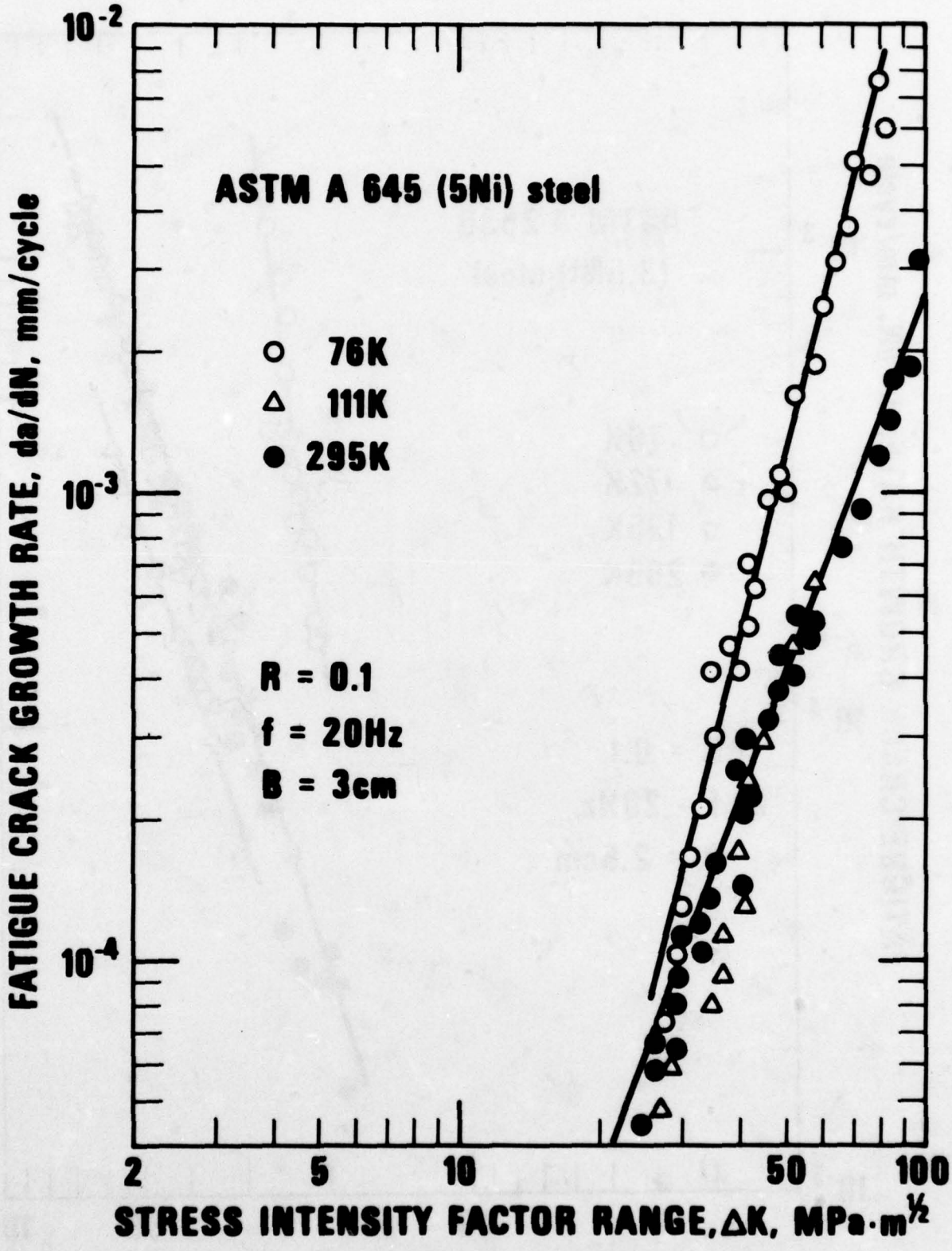


Figure 5. Fatigue crack growth data for a ferritic 5 Ni alloy steel at selected temperatures.

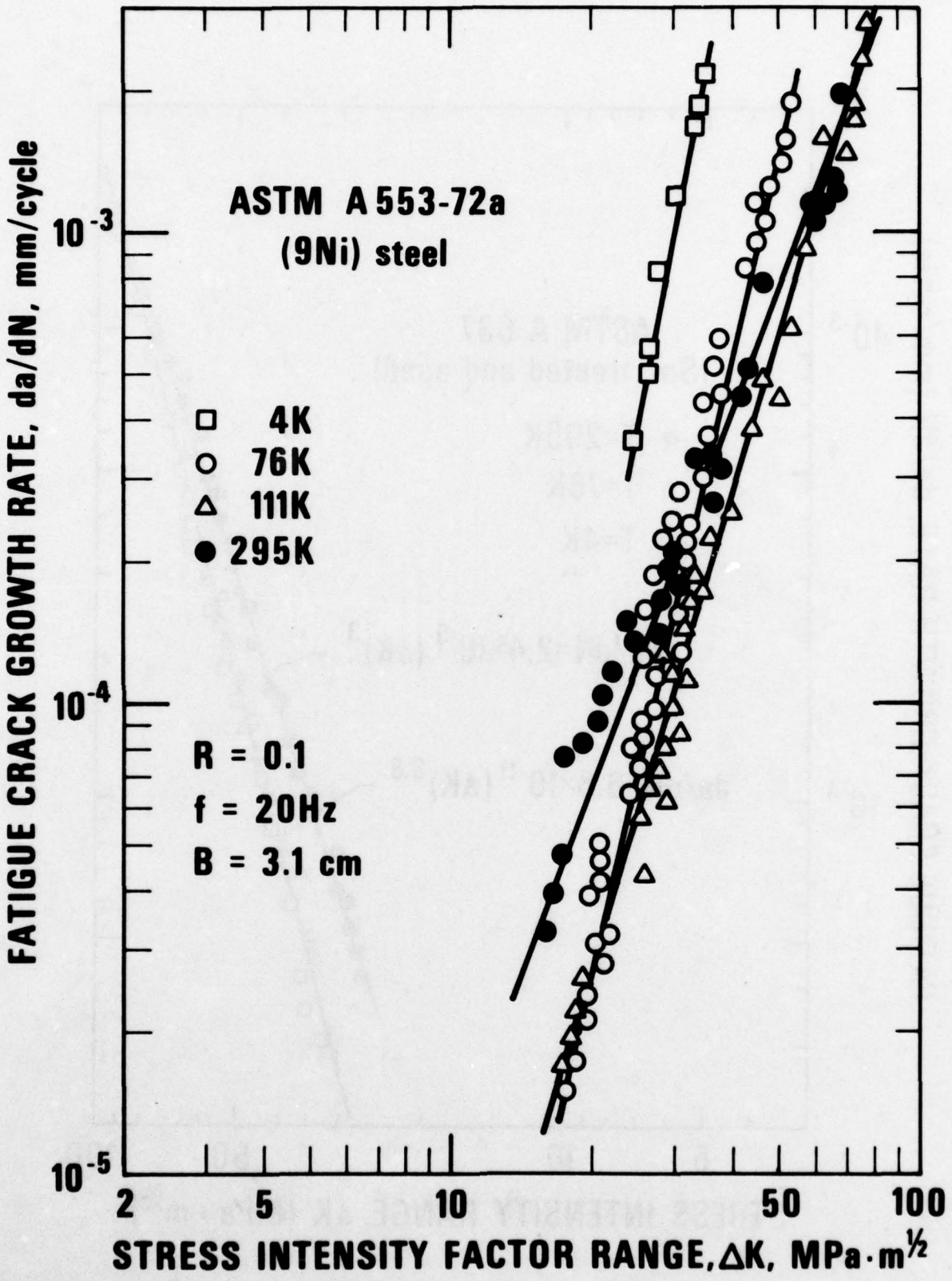


Figure 6. Fatigue crack growth data for a ferritic 9 Ni alloy steel at selected temperatures.

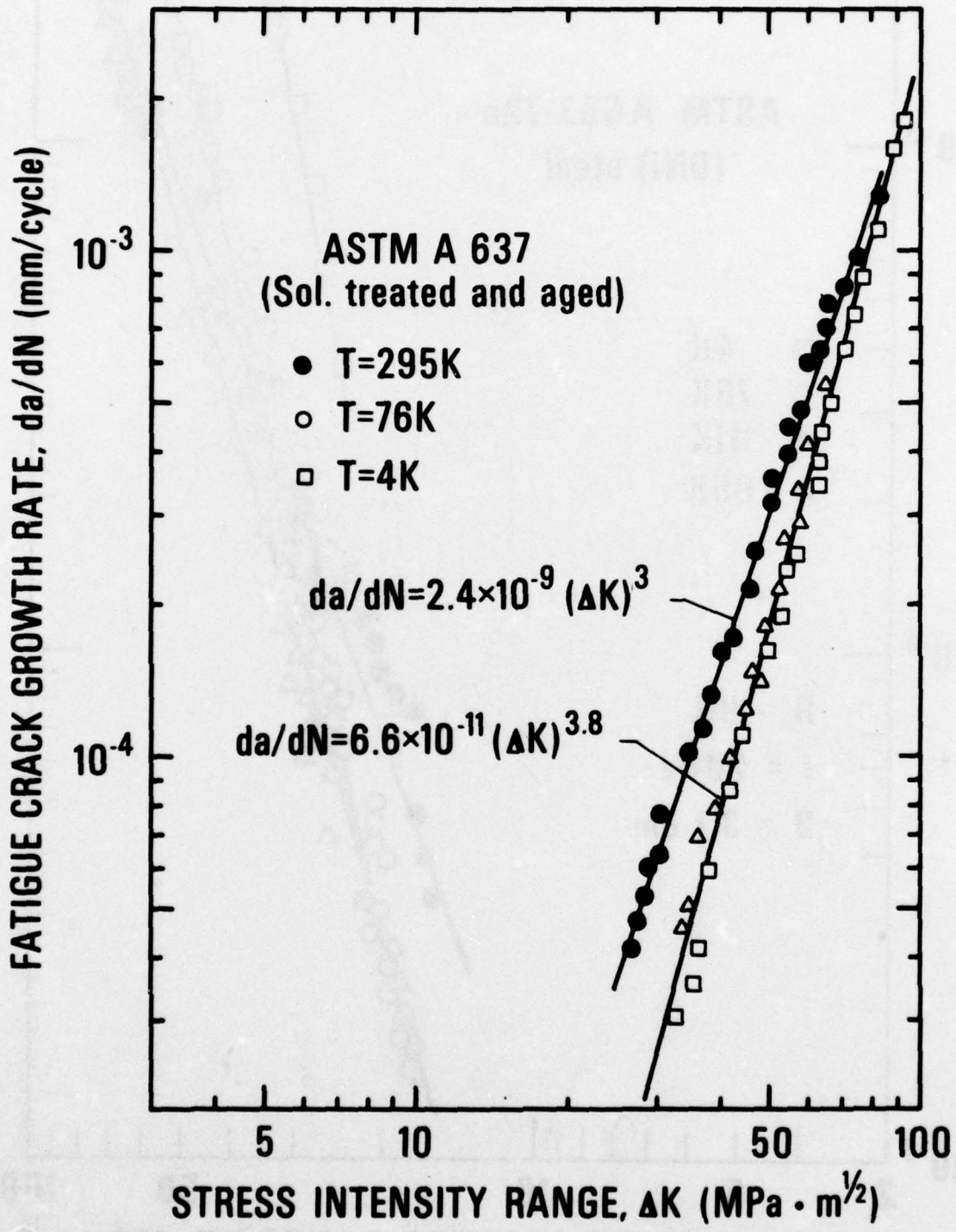


Figure 7. Fatigue crack growth data for a stable nickel-base austenitic superalloy at 295, 76 and 4 K.

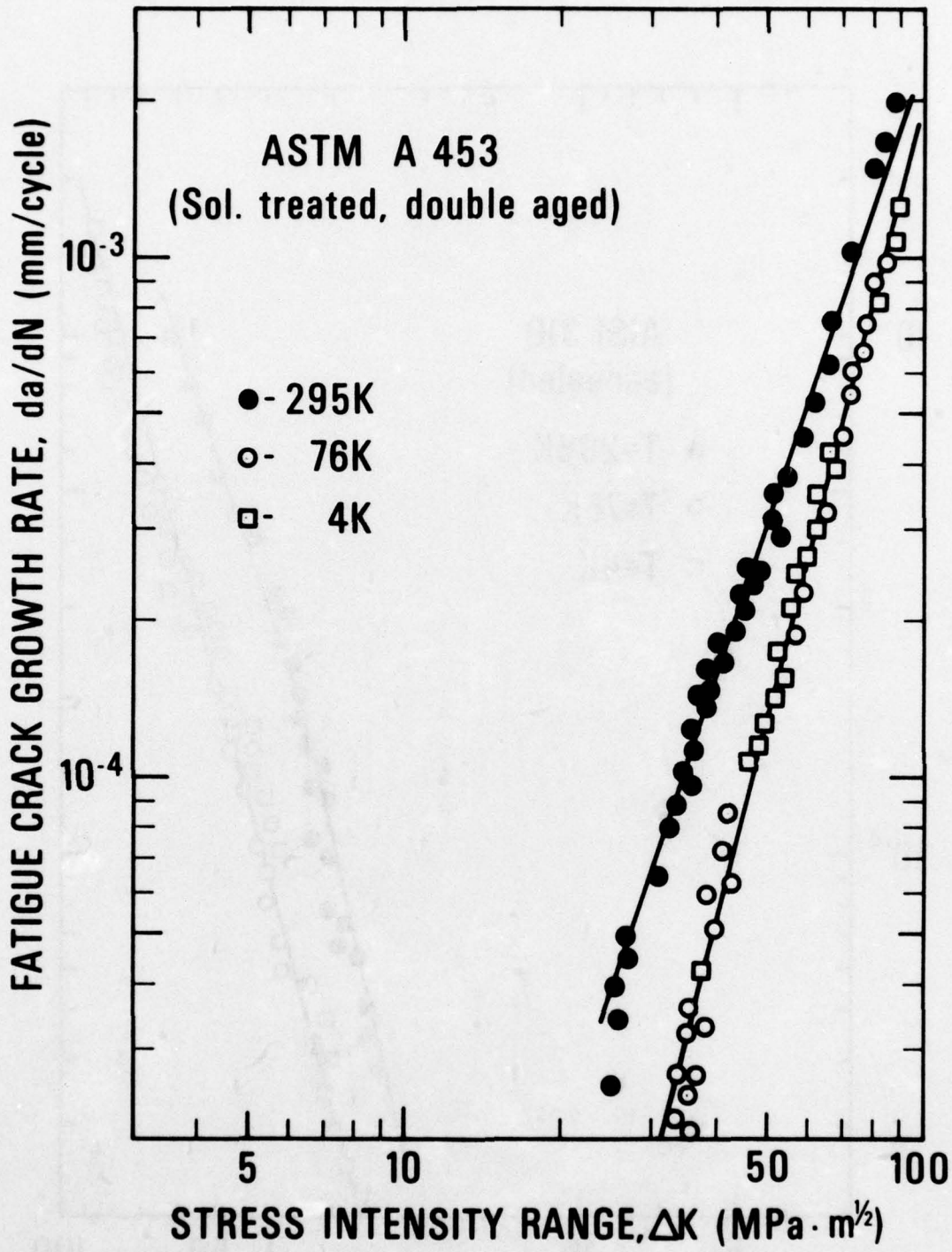


Figure 8. Fatigue crack growth data for a stable iron-base austenitic superalloy and stainless steel at 295, 76 and 4 K.

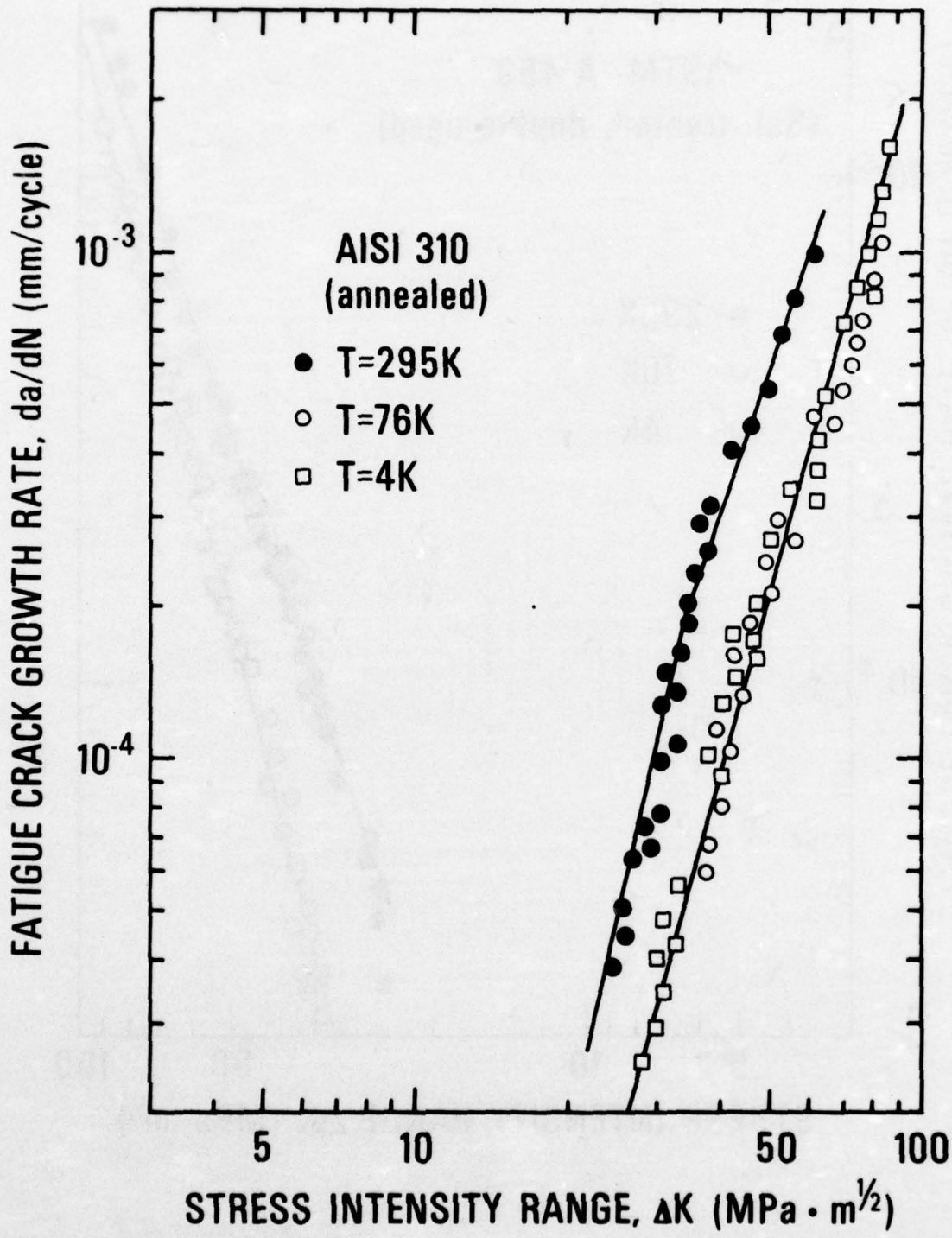


Figure 9. Fatigue crack growth data for a stable AISI 310 austenitic stainless steel at 295, 76 and 4 K.

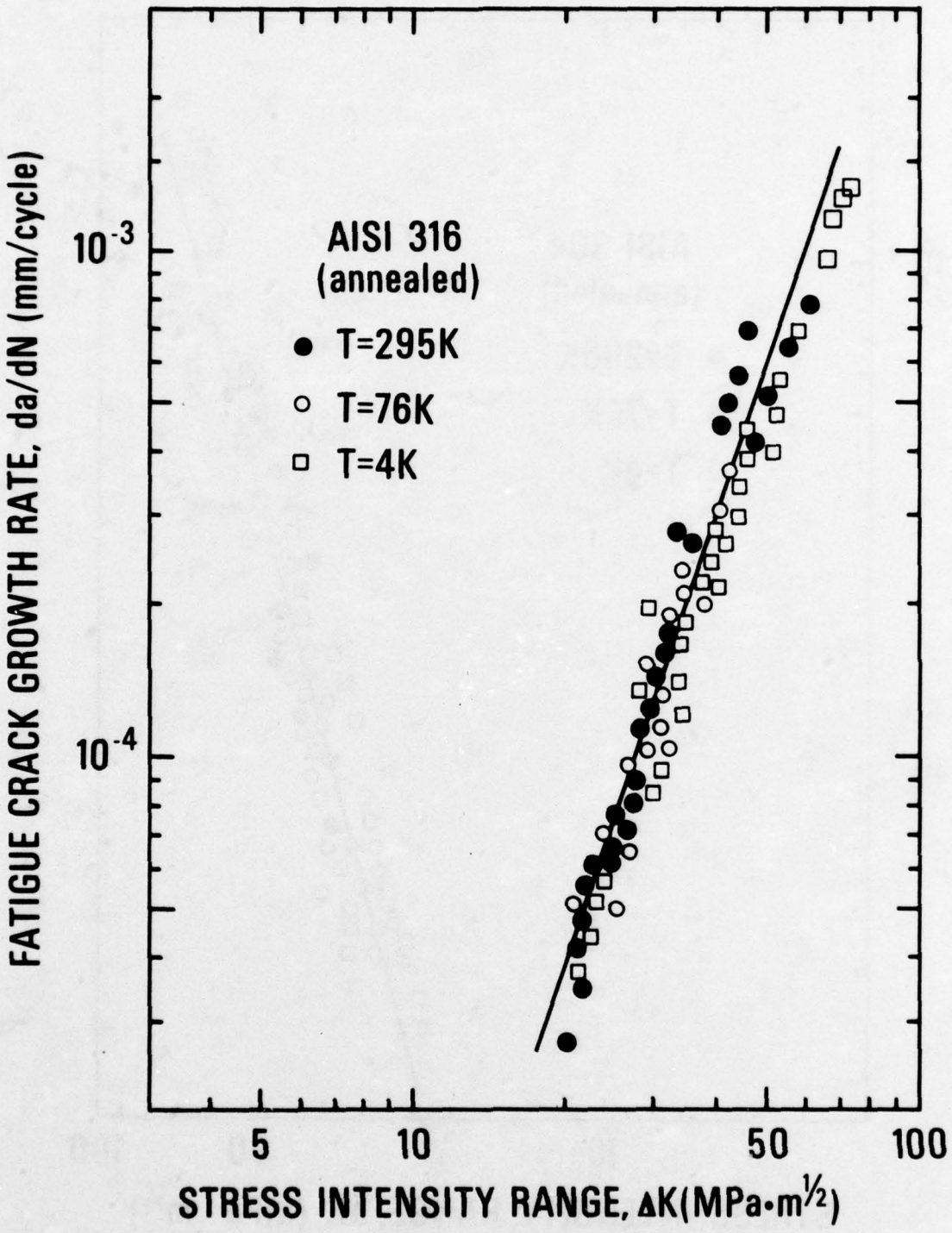


Figure 10. Fatigue crack growth data for a metastable AISI 316 stainless steel which exhibits martensitic transformations during fatigue loading at 76 and 4 K.

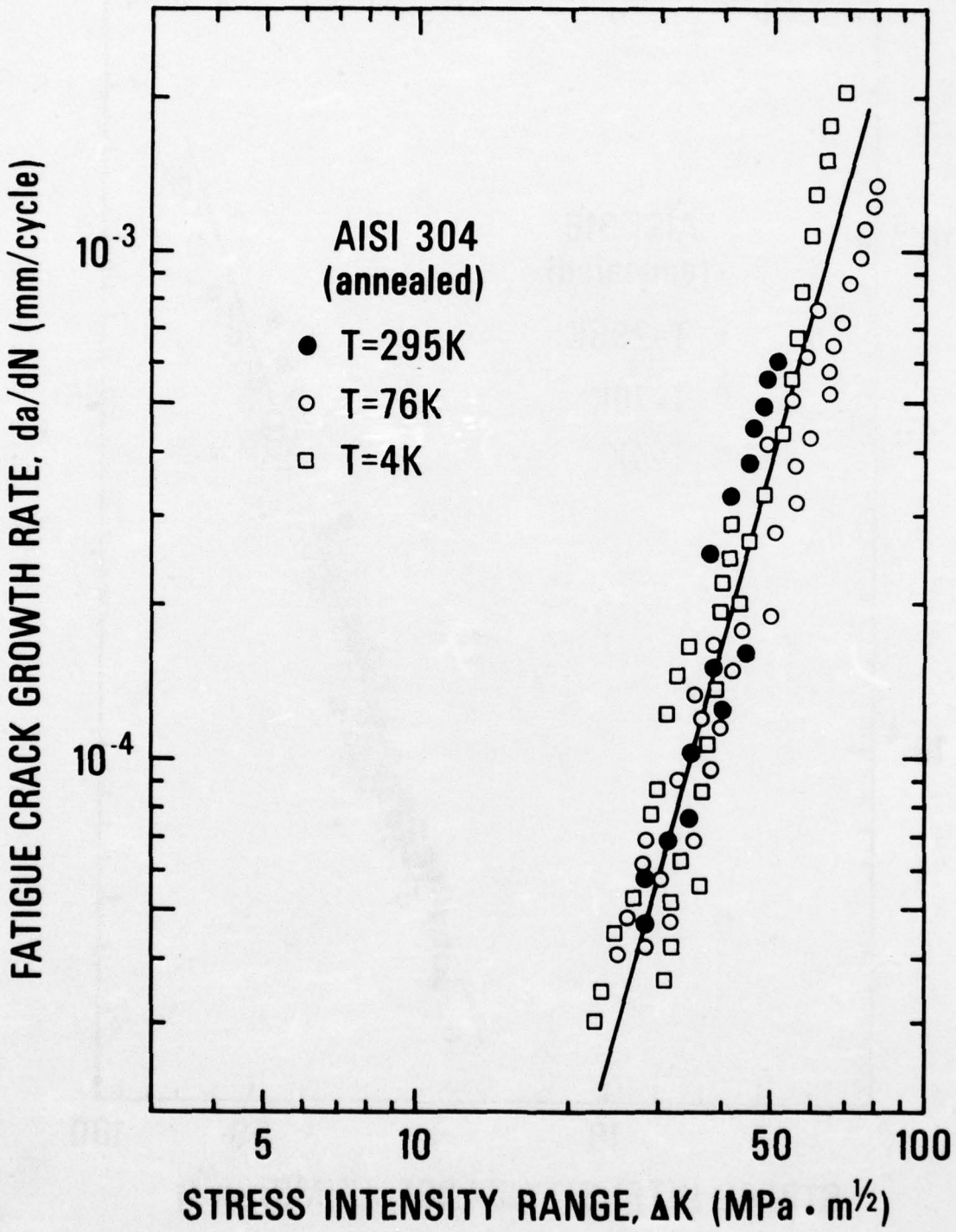


Figure 11. Fatigue crack growth data for a metastable AISI 304 stainless steel which exhibits martensitic transformations during fatigue loading at 76 and 4 K.

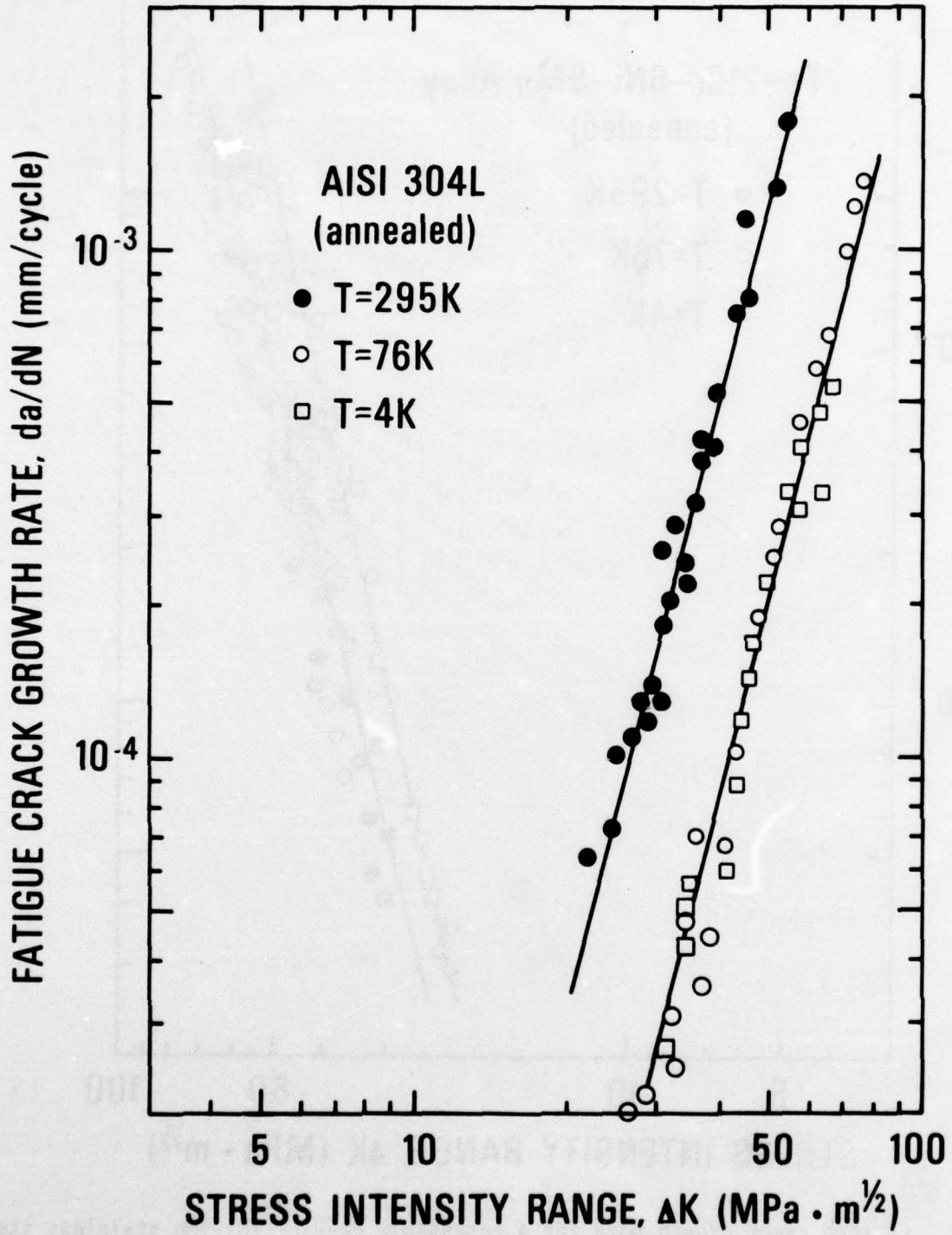


Figure 12. Fatigue crack growth data for a metastable AISI 304L stainless steel which exhibits martensitic transformations at 76 K and 4 K.

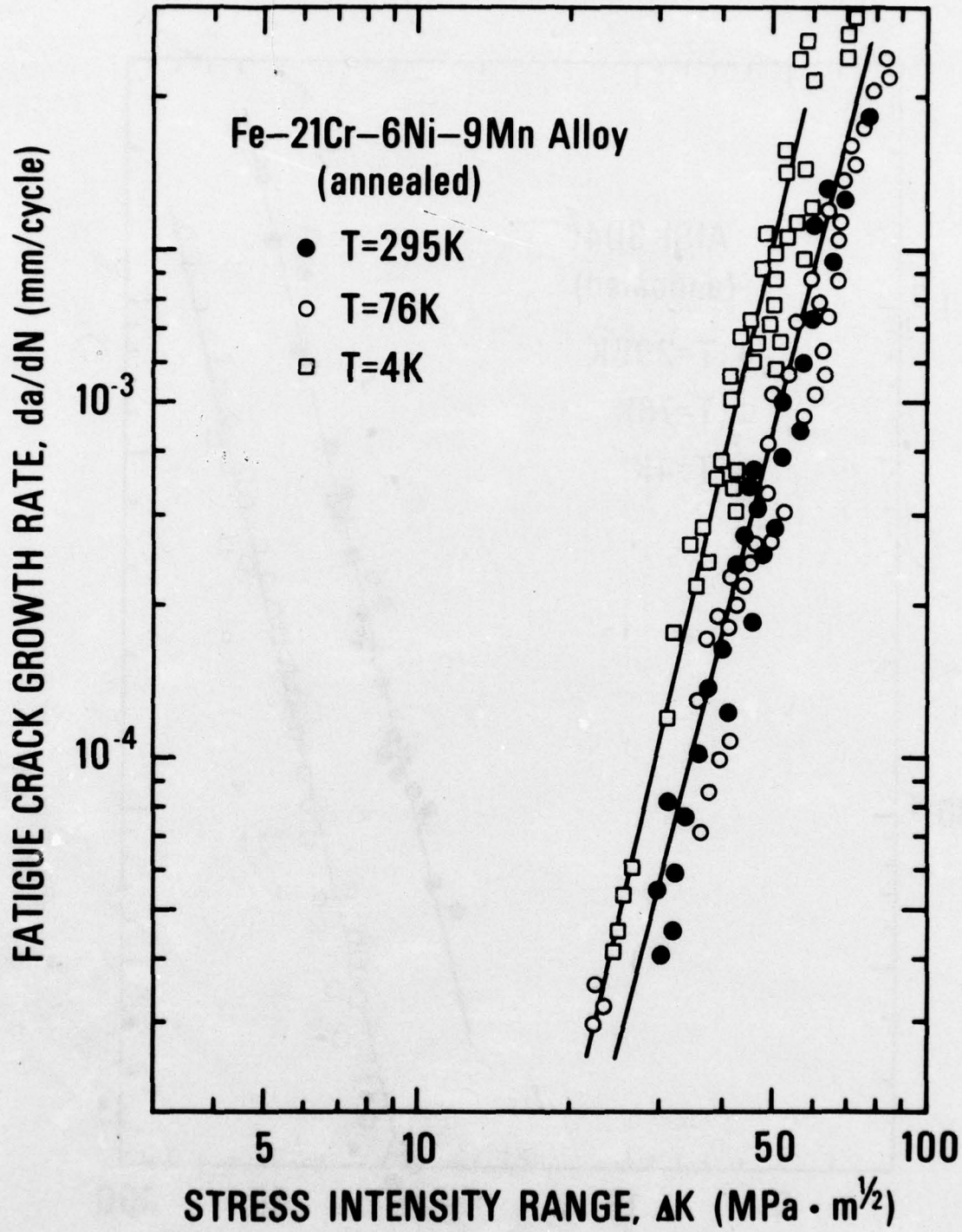


Figure 13. Fatigue crack growth data for a metastable Fe-21Cr-6Ni-9Mn stainless steel which exhibits martensitic transformations at 76 K and 4 K.

FRACTURE OF STRUCTURAL ALLOYS AT TEMPERATURES APPROACHING ABSOLUTE ZERO*

R. L. Tobler+

INTRODUCTION

Plastic deformation and fracture are often viewed as competitive processes. Factors that increase an alloy's resistance to slip usually tend to enhance the probability of brittle fracture. Temperature reductions can lead to pronounced increases in yield strength, while ductility may be decreased, resulting in flaw sensitive mechanical behavior. For this reason, alloys employed at normal temperatures may be unusable at low temperatures, and the fracture toughness of candidate alloys for extreme cryogenic service is a vital design consideration.

With the advent of superconducting electrical machinery we face for the first time a demand for fail-safe, efficiently designed structures that must be cooled with liquid helium to temperatures as low as 4 K. Fracture data are urgently needed to enable judicious material selection for a temperature extreme that previously was rarely experienced. Due to its inertness and proximity to absolute zero, liquid helium at 4 K provides a unique environment where the thermally-activated deformation processes of materials are suppressed, and lattice friction stresses are nearly maximized. Therefore, fracture tests in this environment should provide information of current scientific interest as well as data of engineering utility.

Previous studies of low temperature fracture were hampered by the lack of a quantitative parameter that could be applied to a broad range of material/temperature combinations. The traditional notched tensile and Charpy tests provide only qualitative indications of crack tolerance, while the K_{IC} test applies only to high strength alloys which fail in the elastic range. None of these parameters are well suited for characterizing the ductile and tough austenitic alloys, which, as this paper demonstrates, offer maximum fracture resistance at cryogenic temperatures.

In this study, J-integral and K_{IC} tests were used to characterize the fracture behavior of 14 alloys at temperatures from 295 to 4 K. The parameters measured, K_{IC} and J_{IC}, are complementary, being related in the linear-elastic case by the equation:

$$K_{IC}^2 = J_{IC}E(1 - \nu^2)^{-1} \qquad (1)$$

where E is Young's modulus and ν is Poisson's ratio.

---

* Contribution of NBS, not subject to copyright.
+ Cryogenics Division, National Bureau of Standards, Boulder, CO 80302.

J_{IC} is believed to be a material constant, applicable to either elastic or elastic-plastic fractures. Thus, the J_{IC} criterion offers a new method for comparing low, medium, and high strength alloys -- a task that was problemmatic in the past.

EXPERIMENTAL PROCEDURES

The commercial alloys listed in Table 1 were tested using compact specimens 20 to 38 mm thick. Where possible, K_{IC} was measured and J_{IC} was calculated by Eq. (1). Otherwise, J_{IC} was obtained directly using the resistance curve method, which required back extrapolation of J-vs-Δa data for a series of specimens [1]. Crack extension, Δa, was averaged at 25, 50, and 75% of specimen thickness, and the $J = 2A/Bb$ approximation was used. Although special cryostats were required to retain liquid helium, the test procedure at 4 K was similar to that at room (295 K) and intermediate temperatures.

The tensile properties of the alloys were also measured, following ASTM Method E8-69, and the elastic constants were obtained by Ledbetter et al., using ultrasonic methods [2]. The chemical analyses of these alloys and other procedural details are available in comprehensive reports [2].

RESULTS

Strength Level and Fracture Mode

Table 1 lists selected mechanical property results at 4 K. Following Tetelman and McEvily [3], it is convenient to classify these materials as low ($\frac{\sigma_y}{E} < 0.003$), medium ($0.003 < \frac{\sigma_y}{E} < 0.006$) and high strength ($\frac{\sigma_y}{E} > 0.006$) alloys. Decreasing the temperature from 295 K to 4 K serves to increase the strength level, with σ_y/E increasing by amounts ranging from 17% for 5083-0 aluminum to 245% for 21-6-9 stainless steel. Most of these alloys were plastic when fractured at 295 K in the thickness stated, necessitating J tests. However, at 4 K, the majority of alloys (all of the ferritic steels and titanium alloys, as well as several precipitation-hardened fcc alloys) were linear-elastic. It was noted that alloys having $\frac{\sigma_y}{E} > 0.006$ usually satisfied the ASTM E-399-74 specimen thickness requirement; exceptions were the ELI Ti-6Al-4V alloy at 295 K and the 21-6-9 stainless steel at 4 K.

Strength Versus Fracture Toughness

Although a combination of high yield strength and high fracture toughness would be ideal, in reality these properties are antithetical. It appears that designers must seek an alloy with the optimum combination of strength and toughness for a given application. An inverse relationship between

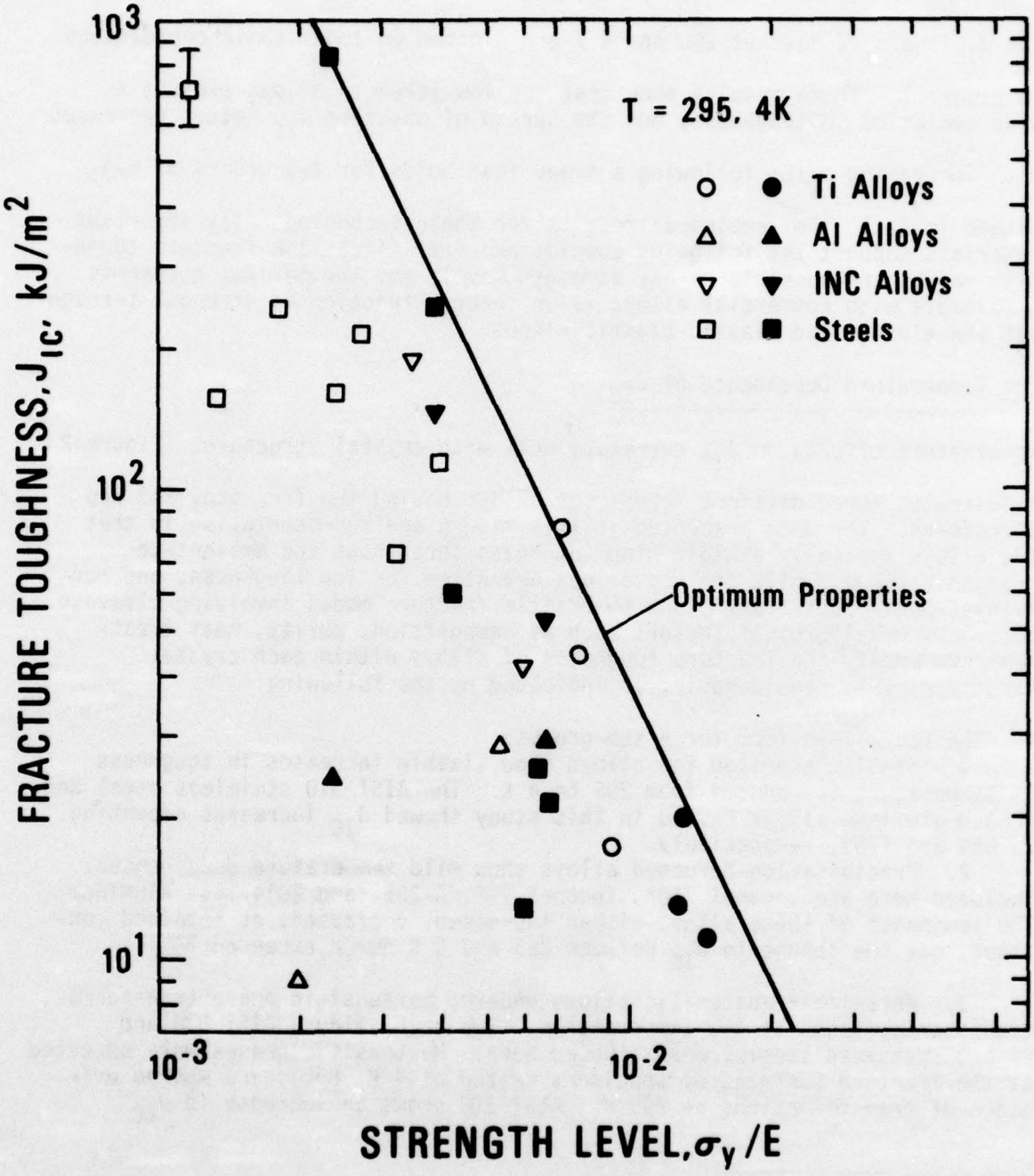


Figure 1. Fracture toughness-versus-σ_y/E for commercial structural alloys tested at 295 K and 4 K.

σ_y and K_{IC} at room temperature has been demonstrated for steel, aluminum, and titanium alloys [4]. It must be appreciated that a similar trade-off exists for alloys at cryogenic temperatures, and for elastic-plastic fractures as well.

The J_{IC} and σ_y/E data at 295 and 4 K are plotted on logarithmic coordinates in Figure 1. These results show that the low strength alloys exhibit a wide variation in toughness, but the spread of observed J_{IC} values decreases with increasing σ_y/E, following a trend that holds for two orders of magnitude in J_{IC}. The empirical results for these technologically important materials support the following conclusion: relatively low fracture toughness values are possible at any strength level, but the maximum toughness attainable with commercial alloys is an inverse function of strength throughout the elastic and elastic-plastic ranges.

The Temperature Dependence of J_{IC}

Temperature effects on J_{IC} correlate well with crystal structure. Figure 2 illustrates three distinct trends for alloys having the fcc, bcc, and hcp structures. The data presented in this figure are representative in that fcc alloys typically exhibit high toughness throughout the ambient-to-cryogenic range, while the hcp alloys are noted for low toughness, and bcc alloys show abrupt transitions to brittle fracture modes involving cleavage. Secondary metallurgical factors such as composition, purity, heat treatment can modify the fracture toughness of alloys within each crystal structure class considerably, as indicated by the following.

I. The fcc alloys form three sub-groups:

1. Stable, annealed fcc alloys show sizable increases in toughness as temperature is reduced from 295 to 4 K. The AISI 310 stainless steel and 5083-0 aluminum alloys tested in this study showed J_{IC} increases amounting to 55% and 175%, respectively.

2. Precipitation-hardened alloys show mild temperature dependences. Included here are Inconel 750*, Inconel 718, A-286, and 2014-T652 aluminum. The toughness of these alloys either increased, decreased, or remained constant, but the change in J_{IC} between 295 and 4 K never exceeded 30%.

3. Metastable austenitic alloys undergo martensitic phase transformations during tests at low temperatures. Two such alloys, AISI 316 and 21-6-9 stainless steels, were studied here. Martensitic phases were detected at the fracture surfaces of specimens tested at 4 K, but there was no evidence of transformations at 295 K. AISI 316 shows an increase in J_{IC}

---

* Tradenames are used for the sake of clarity, and do not imply recommendation or endorsement by NBS.

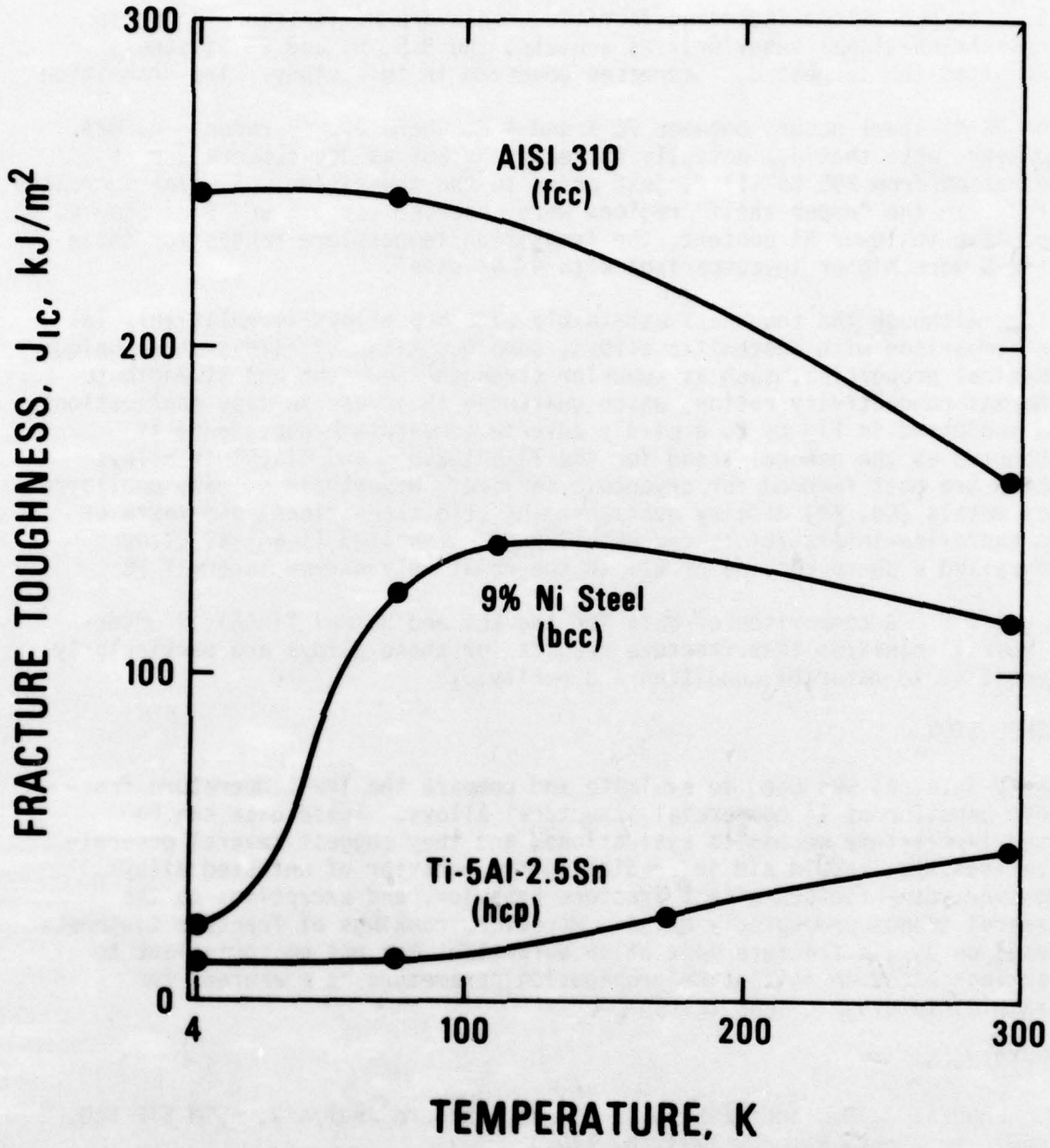


Figure 2. The temperature dependence of fracture toughness for alloys having three different crystal structures.

between 295 and 4 K, whereas 21-6-9 exhibits a sizable decrease. Thus it is difficult to generalize on the effects of phase transformations since favorable as well as adverse effects are possible.

II. The bcc alloys including ferritic steels are of limited use due to their transitional behavior. As a class, the 3.5, 5, and 9% Ni steels exhibited the largest J_{IC} decreases observed in this study. The transition for 9% Ni steel occurs between 76 K and 4 K, where J_{IC} is reduced by 82%. However, note that J_{IC} actually increases by 20% as the temperature is decreased from 295 to 111 K, just prior to the transition. Similar increases of J_{IC} in the "upper shelf" regions were observed for 3.5 and 5 Ni steels, but, due to lower Ni content, the transition temperature ranges for these steels were higher in comparison with 9% Ni steel.

III. Although the toughness attainable with hcp alloys is relatively low in comparison with austenitic alloys, some hcp titanium alloys offer unique physical properties, such as superior strength-to-weight and strength-to thermal conductivity ratios, which guarantee their use in many applications. As indicated in Figure 2, a mildly adverse temperature dependence is accepted as the general trend for the Ti-5Al-2.5Sn and Ti-6Al-4V alloys which are most favored for cryogenic service. Nevertheless, many unalloyed hcp metals (Cd, Zn) display ductile-to-brittle transitions, and tests of an extra-low-interstitial, recrystallization-annealed Ti-6Al-4V alloy revealled a sharp decline of K_{IC} in the relatively narrow interval $76 < T < 125$ K. A comparison of data for the ELI and normal Ti-6Al-4V grades (Table 1) confirms that fracture results for these alloys are particularly sensitive to material condition and purity.

CONCLUSION

The J-integral was used to evaluate and compare the low temperature fracture behavior of 14 commercial structural alloys. These data can be used in fracture mechanics evaluations, and they suggest several generalizations that should aid in predicting the behavior of untested alloys. However, many factors affect fracture behavior, and exceptions to the general trends undoubtedly exist. Moreover, rankings of fracture toughness based on J_{IC}, a fracture initiation parameter, may not be equivalent to rankings based on initiation/propagation parameters as measured, for example, in dynamic tear tests.

REFERENCES

1. LANDES, J. D., and BEGLEY, J. A., in Fracture Analysis, ASTM STP 560, Amer. Soc. Test. Mater., 1974, p. 170.
2. Materials Research in Support of Superconducting Machinery, Vol. 5 (and previous volumes), Reed, R. P., Ledbetter, H. M., and van Reuth, E. C., Eds., Nat. Bur. Stds., Boulder, CO.
3. TETELMAN, A. S., and McEVILY, A. J., Fracture of Structural Materials, Wiley, NY, 1967.
4. WOOD, H. A., in Fracture Mechanics of Aircraft Structures, AGARDograph No. 176, Liebowitz, H., Ed., North Atlantic Treaty Organization, 1974, p. 18, AD-777-641.

Table 1. Test Materials and Selected Results

Material and Condition	Spec. Thickness (cm) and Orientation	Yield Strength at 4K, σ_y(MPa)	Young's Modulus at 4K (GPa)	Poisson's Ratio at 4K, ν	K_{IC}(MPa·m$^{1/2}$) 295K	K_{IC}(MPa·m$^{1/2}$) 4K	J_{IC}(kJm^{-2}) 295K	J_{IC}(kJm^{-2}) 4K
5083-0 Aluminum (annealed)	3.2 TL	186	81.0	0.318	--	--	9.0	25.0
2014 Aluminum (T652 temper)	3.8, TL	547	83.8	0.330	50.0	53.4	29.2	30.3
Ti-6Al-4V, Normal (mill annealed)	2.5, TL	1792	122.0	0.309	47.0	38.5	17.8	11.0
Ti-6Al-4V, ELI (Recryst. annealed)	2.0, TL	1660	126.0	0.308	--	54.0	86.0	20.9
Ti-5Al-2.5Sn, Normal (annealed)	3.8, TS	1551	123.0	0.311	75.7	42.0	46.1	12.9
Inconel 718 (soln. treated & aged)	2.5, TS	1408	211.0	0.295	96.0	112.0	42.0	54.2
Inconel 750 (soln. treated & aged)	3.8, TS	869	219.0	0.296	--	--	193.0	149.0
A-286 (soln. treated & aged)	3.8, TS	889	212.0	0.281	--	--	74.5	61.2
AISI 310 (annealed)	3.8, TL	765	199.0	0.296	--	--	158.0	245.0
AISI 316 (annealed)	3.8, TL	545	234.0	0.281	--	--	~740.0	875.0
21-6-9 Stainless (annealed)	3.8, TL	1240	--	--	--	--	~245.0	150.0
A203-E (3.5% Ni Steel) (quenched & tempered)	2.5, TL	>900	215.0	0.282	--	~30.0	163.0	3.8
A645-74 (5% Ni Steel) (austenitized, temperized, & reversion annealed)	3.1, TL	1200	209.0	0.282	--	~50.0	222.0	13.3
A553-72A (9% Ni Steel) (quenched & tempered)	3.1, TL	1329	202.0	0.285	--	~73.0	117.0	23.2

PRECEDING PAGE BLANK-NOT FILMED

SEMI-ANNUAL REPORT ON MATERIALS RESEARCH IN SUPPORT OF SUPERCONDUCTING MACHINERY

MAGNETOTHERMAL CONDUCTIVITY

L. L. Sparks

Cryogenics Division
Institute for Basic Standards
National Bureau of Standards
Boulder, Colorado 80302

October 1976

MAGNETOTHERMAL-CONDUCTIVITY STUDIES DURING ARPA-SPONSORED PROGRAM, SEPTEMBER 1973 TO SEPTEMBER 1976

Material	Unified Numbering System Designation	ARPA Report Number
Inconel 718	N07718	3
AISI 304	S30400	4
AISI 310	S31000	3
Fe-47.5% Ni	--	6
Cu-28% Ni	C71500	6
Cu-0.5% Sn	--	6
OFHC-Cu	C10200	2
Hi Purity Cu	--	3
Al 1100-0	A91100	5
Ti-6Al-4V	--	6

Summary: Magnetothermal Conductivity

The magnetothermal conductivities have been determined for four alloys: Fe-47.47 wt % Ni, Ti-6Al-4V (ELI), Cu-0.5 at % Sn, and Cu-28 at % Ni. Data are presented in the temperature range 4 to 20 K and for magnetic fields up to 6366 kA/m (80 kOe). The effect of the magnetic field is to reduce the thermal conductivity of the Fe-Ni alloy and the Ti-Al-V alloy. The reduction due to 6366 kA/m field is 4.1% for the Fe-Ni specimen at 5 K and 2.2% at 20 K. The corresponding reductions for the Ti-Al-V specimen are 16% at 5 K and 1.6% at 20 K. Any magnetic field effect on the thermal conductivity of the two copper specimens was below the detectable limits of the system for temperatures below 20 K.

Contents: Magnetothermal Conductivity

		Page
1.	Introduction	290
2.	Procedures	290
	2.1 Apparatus	290
	2.2 Materials	290
3.	Results and Discussion	291
4.	References	292
	List of Figures	293

1. Introduction

The objective of the magnetothermal conductivity project has been to determine the effect of magnetic fields on the thermal conductivity of technically important metals. The need for this information arises from the development of rotating machinery which operates at cryogenic temperatures. The existing literature on magnetothermal conductivity, $\lambda(H)$, deals almost exclusively with pure materials and single crystals. A complete bibliography of the subject was given by Sparks and Fickett in a previous ARPA report [1].

The materials studied in this program are being used or are candidates for use in superconducting motors and generators. Optimum design of these machines, which must operate at low temperatures while in magnetic fields, requires a detailed knowledge of how the thermal properties of the constituent materials are affected by a magnetic field. Test specimens were chosen so that broad categories of materials were represented. The categories and the particular materials tested during the course of the ARPA work were:

(1) structural alloys -- UNS-N07718, UNS-S30400, UNS-S31000, Fe-47.47 wt % Ni, and Ti-6Al-4V;

(2) superconductor stabilizing materials -- oxygen-free copper, UNS-A91100, and high purity copper;

(3) superconductor cable constituents -- Cu-0.5 at % Sn and Cu-28 at % Ni.

Based on these data the magnitude of the magnetic field effect on the thermal conductivity can be estimated for similar materials.

Four specimens, Cu-0.5 at % Sn, Cu-28 at % Ni, Ti-6Al-4V, and Fe-47.47 wt % Ni, have been tested during this reporting period. Results for these materials are included in this report.

2. Procedures

2.1 Apparatus

The principal components of the $\lambda(H)$ system are shown schematically in Figure 1. The conventional longitudinal heat flow method of determining thermal conductivity [2] is utilized. A specimen is shown mounted with its axis parallel to the direction of the magnetic field. The longitudinal field effect is determined when the heat current and magnetic field are parallel.

The basic operation of the system has been described in previous reports [1,3], and the details of several system modifications were given in [4].

2.2 Materials

An extra low interstitial (ELI) form of Ti-6Al-4V was used for the $\lambda(H)$ specimen. This alloy was produced to AMS 4930 specifications; it was commercially annealed at 977 K for 2 hours, air cooled and descaled. The microstructure of this stock of material was primary alpha and beta with the average alpha grain diameter being 0.013 mm [5]. The chemical composition of the alloy in weight percent was: Al, 5.91; V, 3.94; Fe, 0.103; O, 0.110; C, 0.018; N, 0.014; H, 52 ppm; Ti, balance. The ratio of the electrical resistivity at the ice point to the electrical resistivity determined at a temperature just above the superconducting critical temperature was 1.16 ± 0.02. The ratio of area to length (A/l) for this specimen was 0.89 ± 0.01 mm.

A ferromagnetic specimen, Fe-47.47 wt % Ni, with an A/l equal to 0.852 ± 0.003 mm was tested in the hot rolled condition. Mill analysis of this alloy indicated the following composition in weight percent: C, 0.012; Mn, 0.33; Si, 0.25; P, 0.002; S, 0.004; Ni, 47.47; Fe, balance. Grain size, as determined using the intercept method was 0.12 mm, Rockwell hardness was B75, and the specimen density was 8.19×10^3 kg/m^3 [6]. The ratio (RRR) of the electrical resistivity at the ice point to that at liquid helium temperature was 2.40 ± 0.002 for this specimen.

Two copper alloys were made at NBS-Boulder using the drop casting technique described by Ekin and Deason [7]. The melting was done in a flowing hydrogen-argon atmosphere. Copper stock used in both alloys was from a 1.9 cm bar of oxygen-free copper (UNS-C10200). The tin content of the Cu-Sn alloy was 0.49 at % and A/l = 0.87 ± 0.01 mm. After machining, the specimen was annealed at 650°C for 2.5 hours at pressures not exceeding 6.4×10^{-3} Pa. The ratio of electrical resistivity at 295 K to the electrical resistivity at 4.2 K was 1.10 ± 0.01.

3. Results and Discussion

The Ti-6Al-4V specimen exhibited a superconducting phase in its electrical resistivity. The onset of superconducting behavior at zero magnetic field occurs when 5.2 K < T < 5.5 K as shown in Figure 2. The critical transition temperature is lowered as the magnetic field is increased until at 6366 kA/m (80 kOe) no transition is observed. Within the limits of precision of the measurement, the normal resistivity of the specimen was 1.43 ± 0.02 μΩ·m and was independent of both temperature (T ≤ 20 K) and magnetic field. Figure 3 shows the resistance of the specimen at 4.2 K as a function of magnetic field. The imprecision of the measurements at H = 0 is quite high as indicated by the scatter shown in the figure. It appears that the critical field is less than 3183 kA/m (40 kOe) when T = 4.2 K.

The thermal conductivity of Ti-6Al-4V is shown in Figure 4 as a function of temperature with magnetic field as a parameter. The relative change in thermal resistivity ($\Delta W/W_{H=0}$) is given by $(W_H - W_{H=0})/W_{H=0}$. When H = 6366 kA/m (80 kOe), $\Delta W/W_{H=0}$ is 19.8% at 5 K and 1.5% at 20 K. The normal to superconducting change is not evident in the thermal conductivity data since the primary mode of heat conduction in this material is due to phonons rather than the electrons. A marked decrease in conductivity would have been expected below the critical temperature (T_c) if the primary conduction mode were electronic. Electrons in the superconducting state have zero heat capacity and can, therefore, not carry thermal energy.

The thermal conductivity of the Fe-Ni alloy is shown in Figure 5 as a function of temperature with magnetic field as a parameter. As seen in this figure, essentially all of the reduction in conductivity due to magnetic field occurs when H ≤ 1592 kA/m (20 kOe). This saturating tendency is shown in Figure 6. A field of 6366 kA/m (80 kOe) causes $\Delta W/W_{H=0}$ = 4.79% at 5 K and $\Delta W/W_{H=0}$ = 2.27% at T = 20 K. Hust [8] measured the thermal conductivity of a similar Fe-Ni specimen at zero magnetic field and T = 7.42 K. His data indicate a conductivity of 1.47 W/m·K which is nearly identical to the data taken in the magnetothermal apparatus.

The thermal conductivities of the Cu-0.5 at % Sn and Cu-28 at % Ni at zero field are shown in Figures 7 and 8 respectively. The effect of magnetic field on the conductivity of these specimens is too small to be detected in the present system. Differences between the zero field thermal conductivity

data and the H = 3183 kA/m (40 kOe) and H = 6366 kA/m (80 kOe) data are shown in Figures 9 and 10. The differences in thermal conductivity used in these curves were obtained by subtracting the experimental thermal conductivities for $H \neq 0$ from the values read from the smooth curves shown in Figures 7 and 8. The electrical resistivity for these copper alloys did not change as a function of magnetic field or temperature for $H \leq 6366$ kA/m (80 kOe) and $T \leq 20$ K. This field independence has been observed previously at 4.2 K [9] on specimens from the same melts used for the $\lambda(H)$ specimens.

4. References

1. L. L. Sparks and F. R. Fickett; in Materials Research in Support of Superconducting Machinery-I; R. P. Reed, A. F. Clark, E. C. van Reuth (Eds.); Nat. Bur. Stds., Boulder, CO; March 1974; AD780596.

2. White, G. K., in Measurement of Solid Conductors at Low Temperatures, Tye, R. P. (Ed.), pages 88-94 (Academic Press, NY, 1969).

3. L. L. Sparks and F. R. Fickett; in Materials Research in Support of Superconducting Machinery-II; R. P. Reed, A. F. Clark, E. C. van Reuth (Eds.); Nat. Bur. Stds., Boulder, CO; October 1974; ADA004586.

4. L. L. Sparks; in Materials Research in Support of Superconducting Machinery-IV; R. P. Reed, A. F. Clark, E. C. van Reuth (Eds.); Nat. Bur. Stds., Boulder, CO; October 1975; ADA019230.

5. R. L. Tobler; in Materials Research in Support of Superconducting Machinery-III; R. P. Reed, A. F. Clark, E. C. van Reuth (Eds.); Nat. Bur. Stds., Boulder, CO; April 1975; ADA012365.

6. H. M. Ledbetter and D. T. Read; in Materials Research in Support of Superconducting Machinery-V; R. P. Reed, H. M. Ledbetter, E. C. van Reuth (Eds.); Nat. Bur. Stds., Boulder, CO; April 1976.

7. J. W. Ekin and V. A. Deason, Technique for Preparing Homogeneous Bulk Samples of Concentrated Alloys, Rev. Sci. Instrum. 46, No. 3, pp. 327 (March 1975).

8. J. G. Hust; in Materials Research in Support of Superconducting Machinery-VI; R. P. Reed, H. M. Ledbetter, E. C. van Reuth (Eds.); Nat. Bur. Stds., Boulder, CO; to be published.

9. F. R. Fickett, Nat. Bur. Stds., Boulder, CO, personal communication.

List of Figures

Figure 1. Schematic of magnetothermal conductivity probe and magnet.

Figure 2. Electrical resistivity as a function of temperature for Ti-6Al-4V (ELI).

Figure 3. Electrical resistance of Ti-6Al-4V (ELI) as a function of magnetic field at 4.2 K.

Figure 4. Thermal conductivity of Ti-6Al-4V (ELI) as a function of temperature with magnetic field as a parameter.

Figure 5. Thermal conductivity of Fe-47.47 wt % Ni as a function of temperature with magnetic field as a parameter.

Figure 6. Thermal conductivity of Fe-47.47 wt % Ni as a function of magnetic field with temperature as a parameter.

Figure 7. Thermal conductivity of Cu-0.5 at % Sn as a function of temperature at zero magnetic field.

Figure 8. Thermal conductivity of Cu-28 at % Ni as a function of temperature at zero magnetic field.

Figure 9. Deviation of thermal conductivities found in the zero and non-zero field tests on Cu-0.5 at % Sn.

Figure 10. Deviation of the thermal conductivities found in the zero and non-zero field tests on Cu-28 at % Ni.

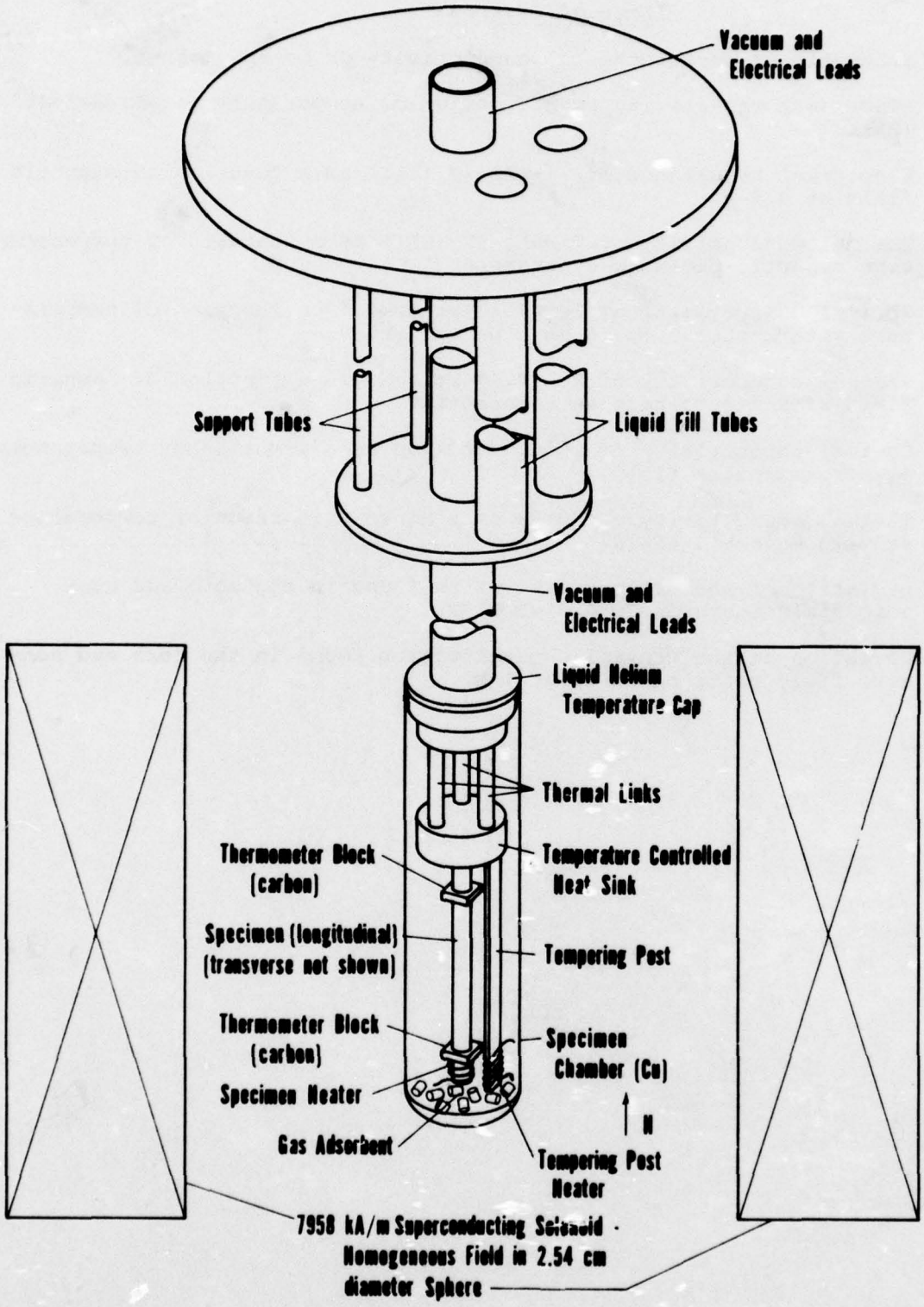


Figure 1. Schematic of magnetothermal conductivity probe and magnet.

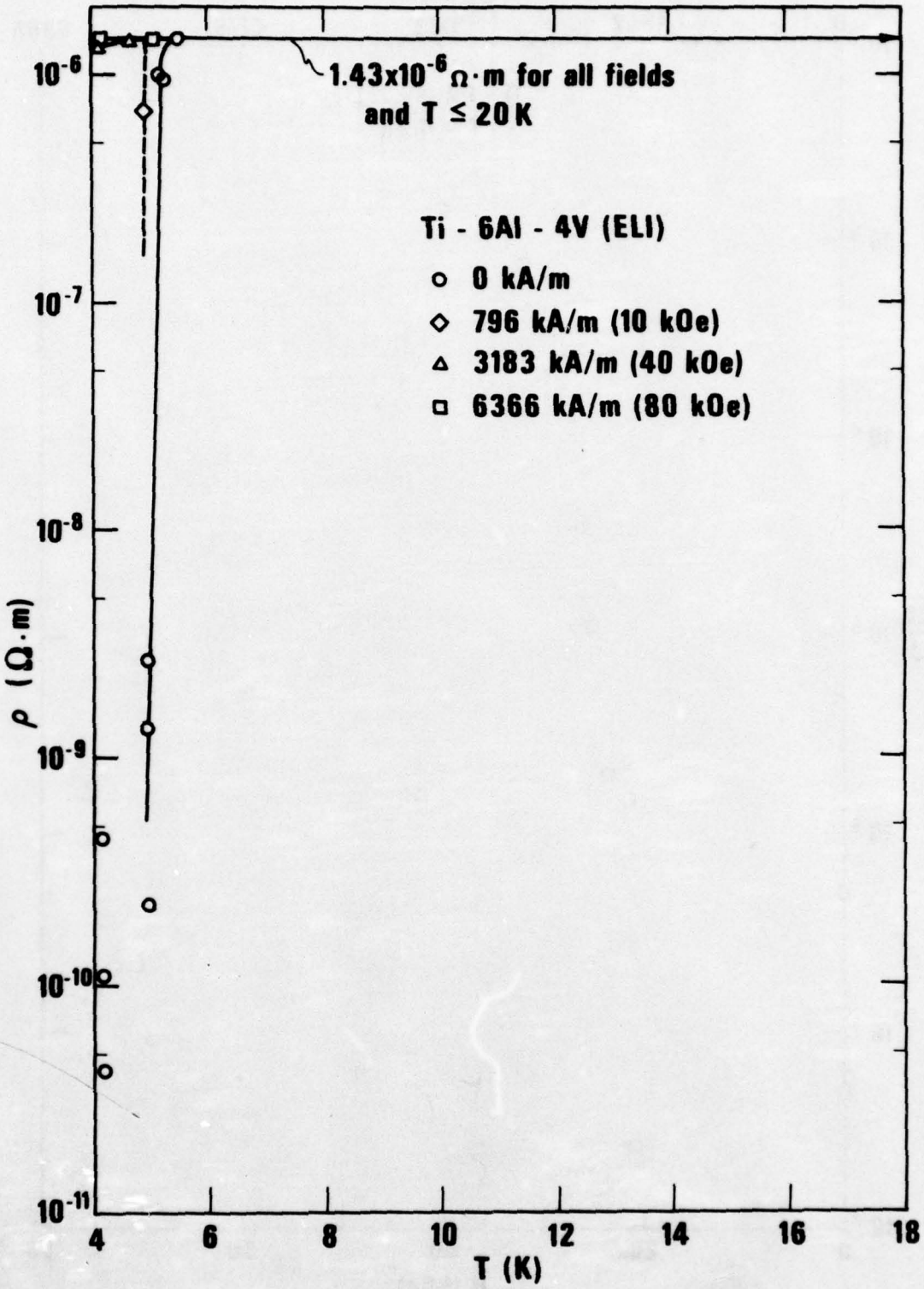


Figure 2. Electrical resistivity as a function of temperature for Ti-6Al-4V (ELI).

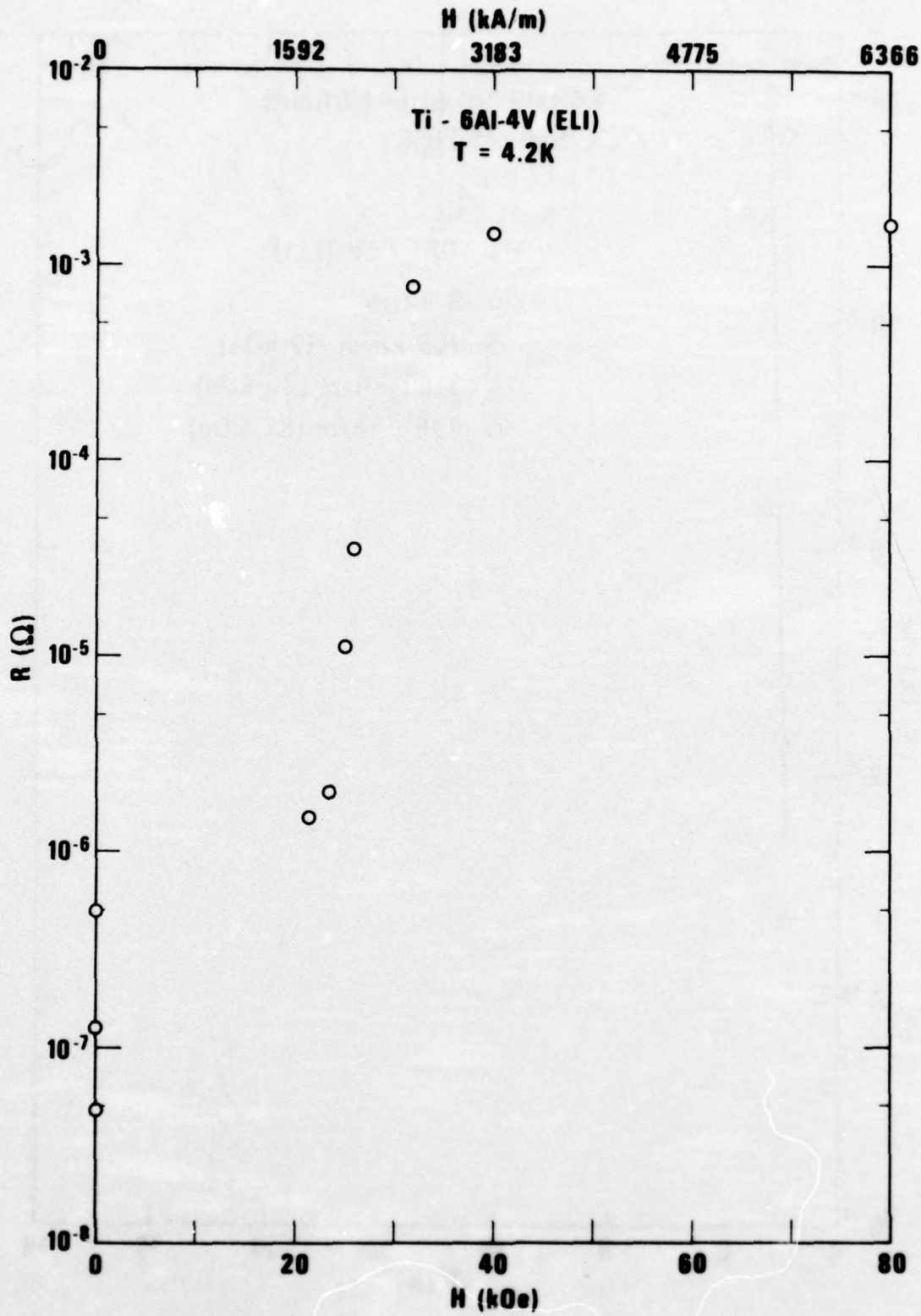


Figure 3. Electrical resistance of Ti-6Al-4V (ELI) as a function of magnetic field at 4.2 K.

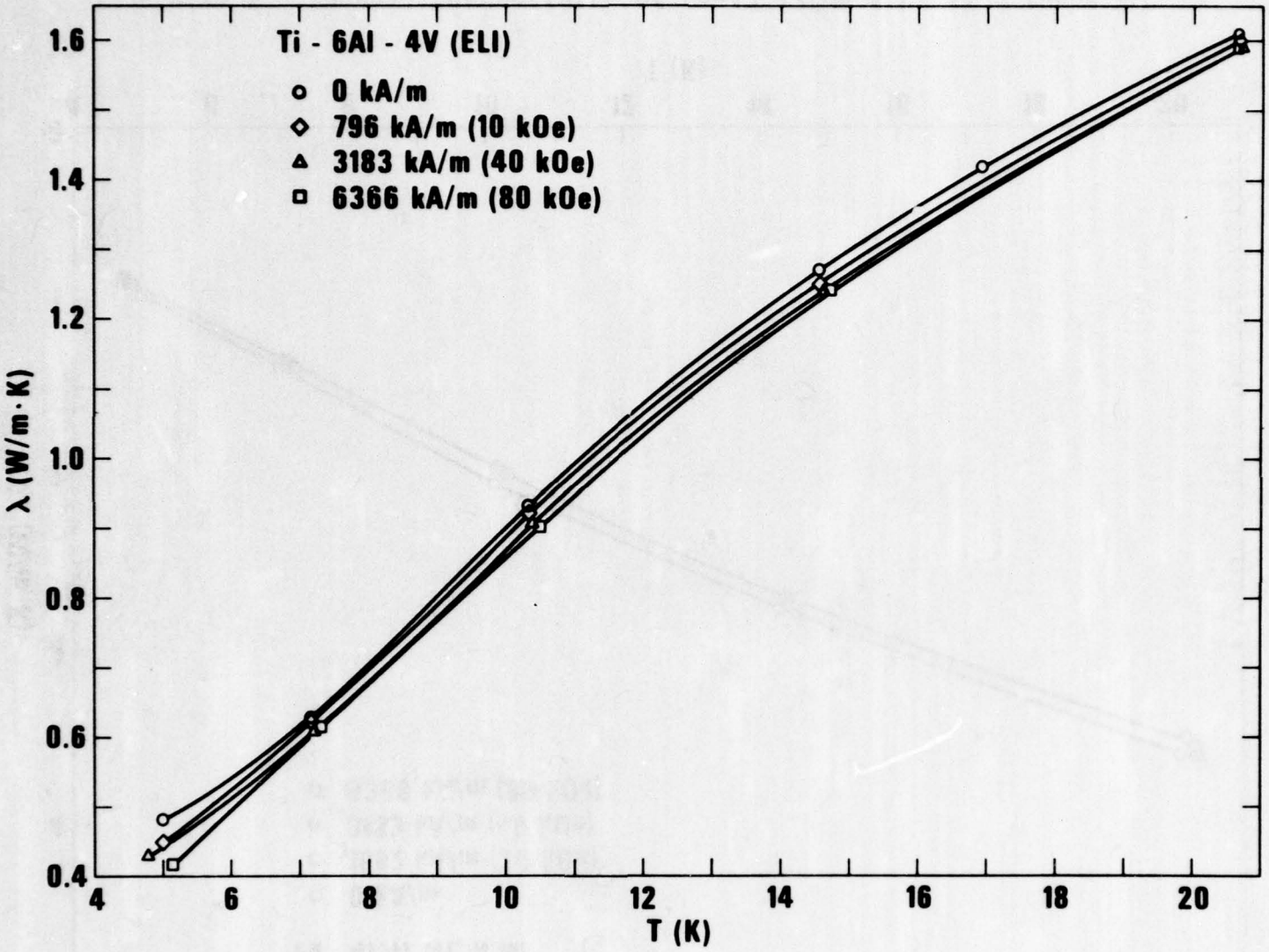


Figure 4. Thermal conductivity of Ti-6Al-4V (ELI) as a function of temperature with magnetic field as a parameter.

77 x 0647

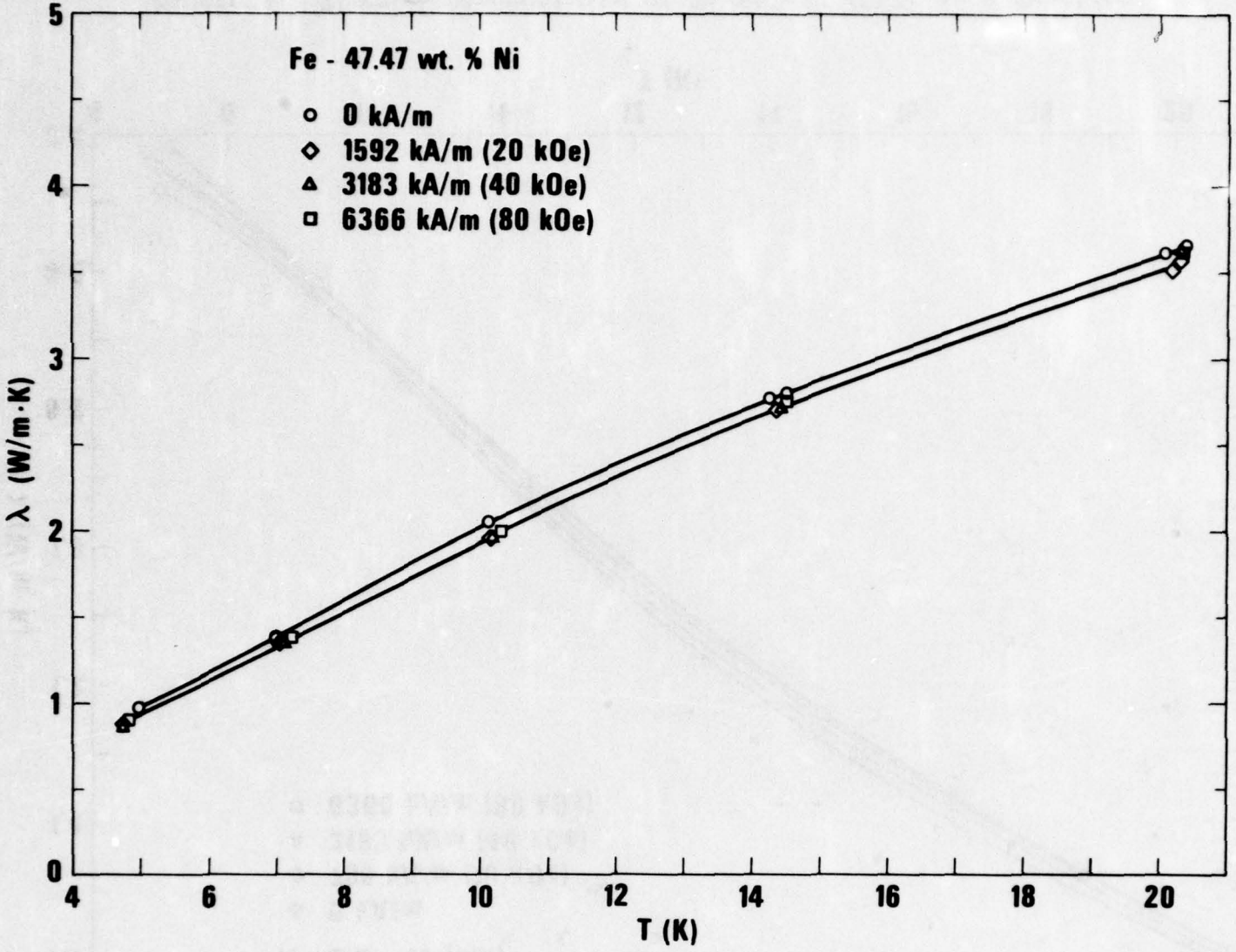


Figure 5. Thermal conductivity of Fe-47.47 wt % Ni as a function of temperature with magnetic field as a parameter.

77X 0648

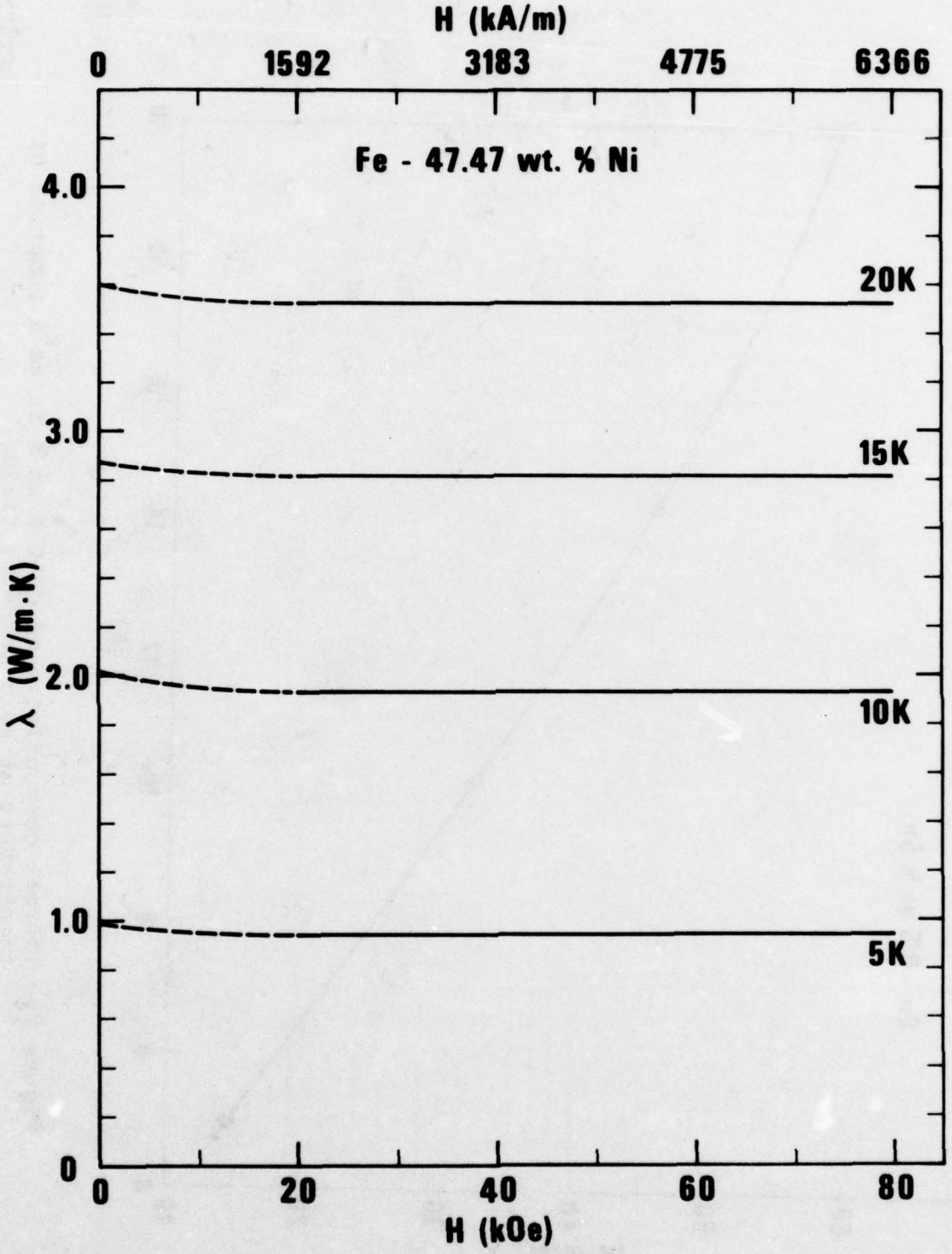


Figure 6. Thermal conductivity of Fe-47.47 wt % Ni as a function of magnetic field with temperature as a parameter.

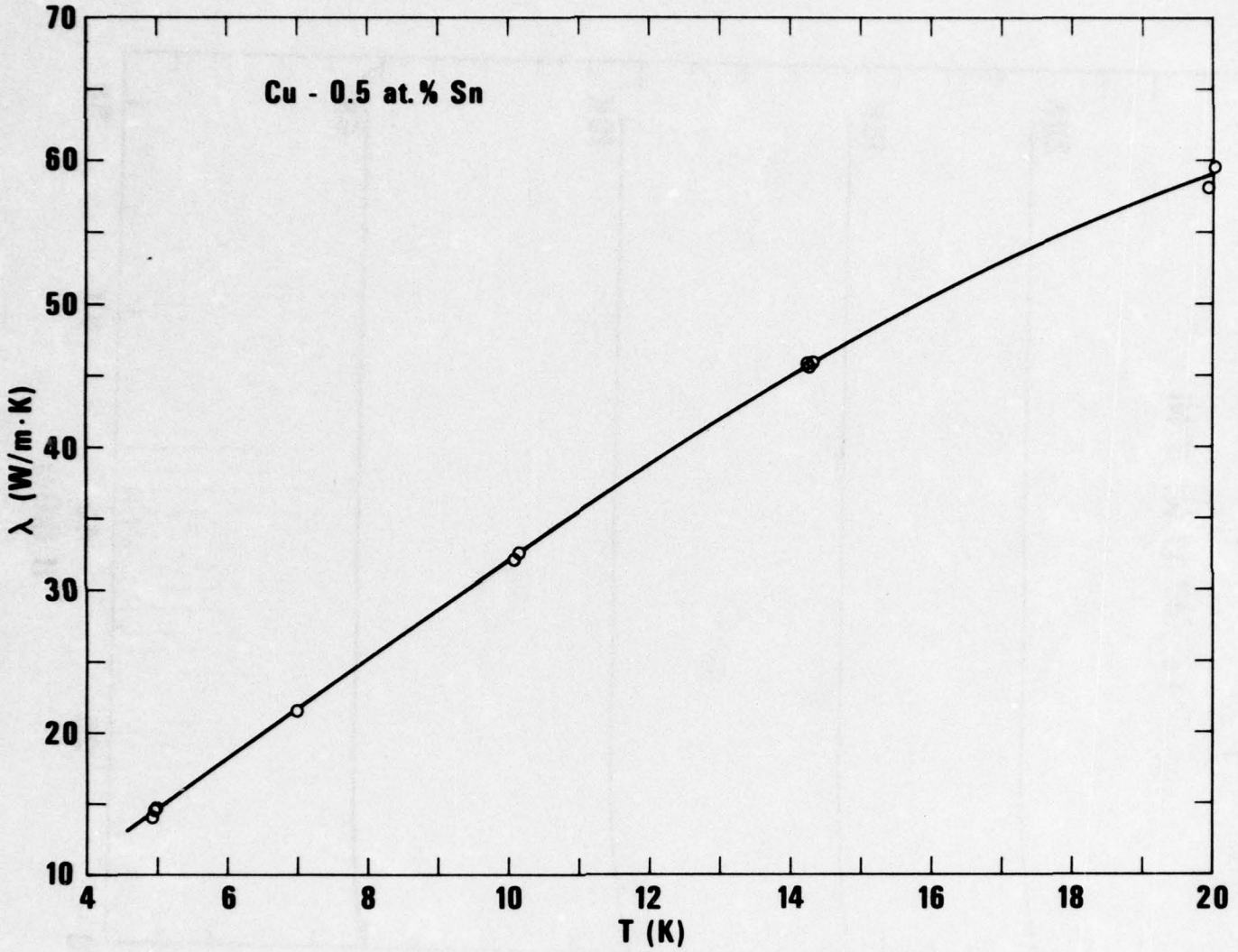


Figure 7. Thermal conductivity of Cu-0.5 at % Sn as a function of temperature at zero magnetic field.

77X0650

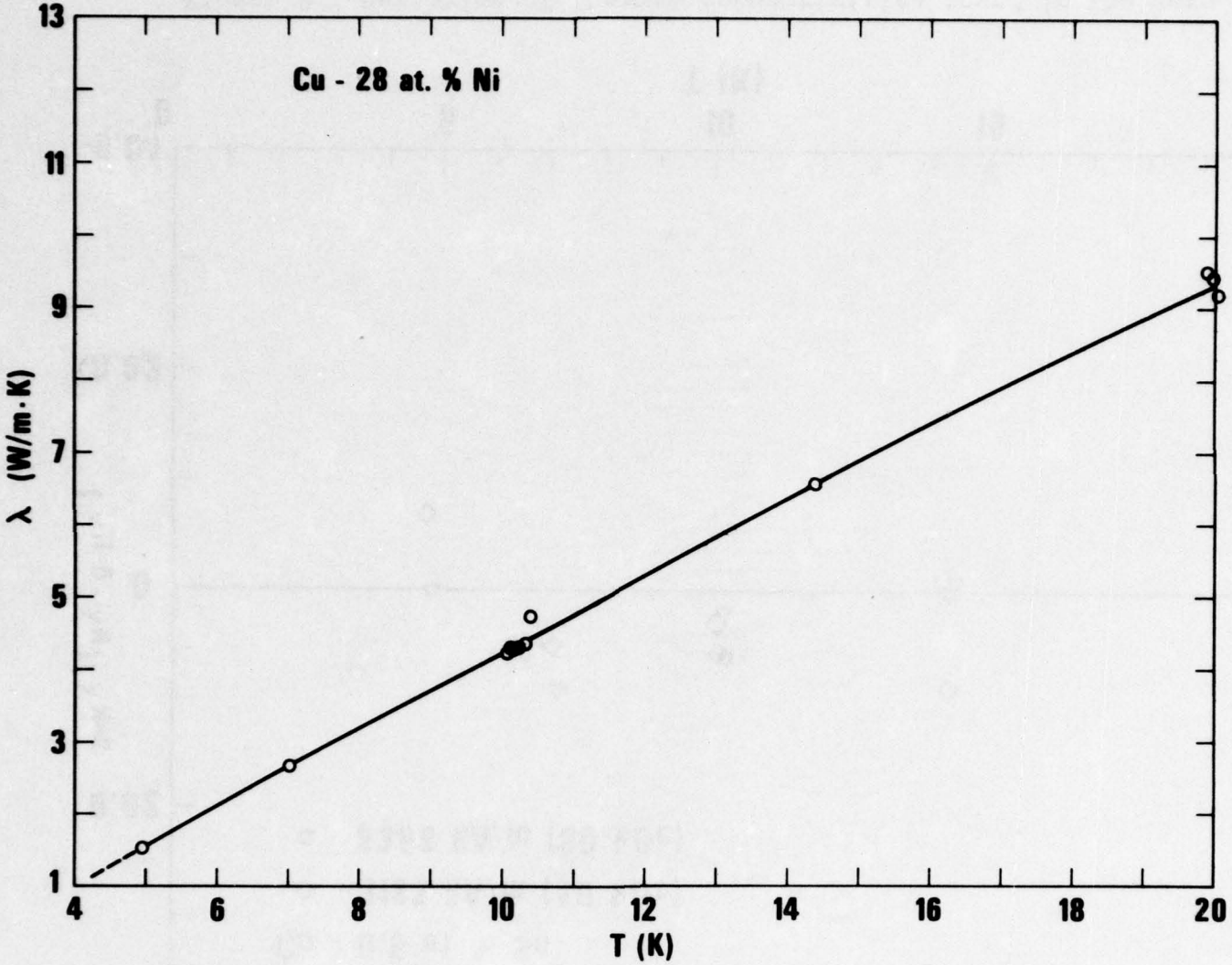


Figure 8. Thermal conductivity of Cu-28 at % Ni as a function of temperature at zero magnetic field.

77X 0649

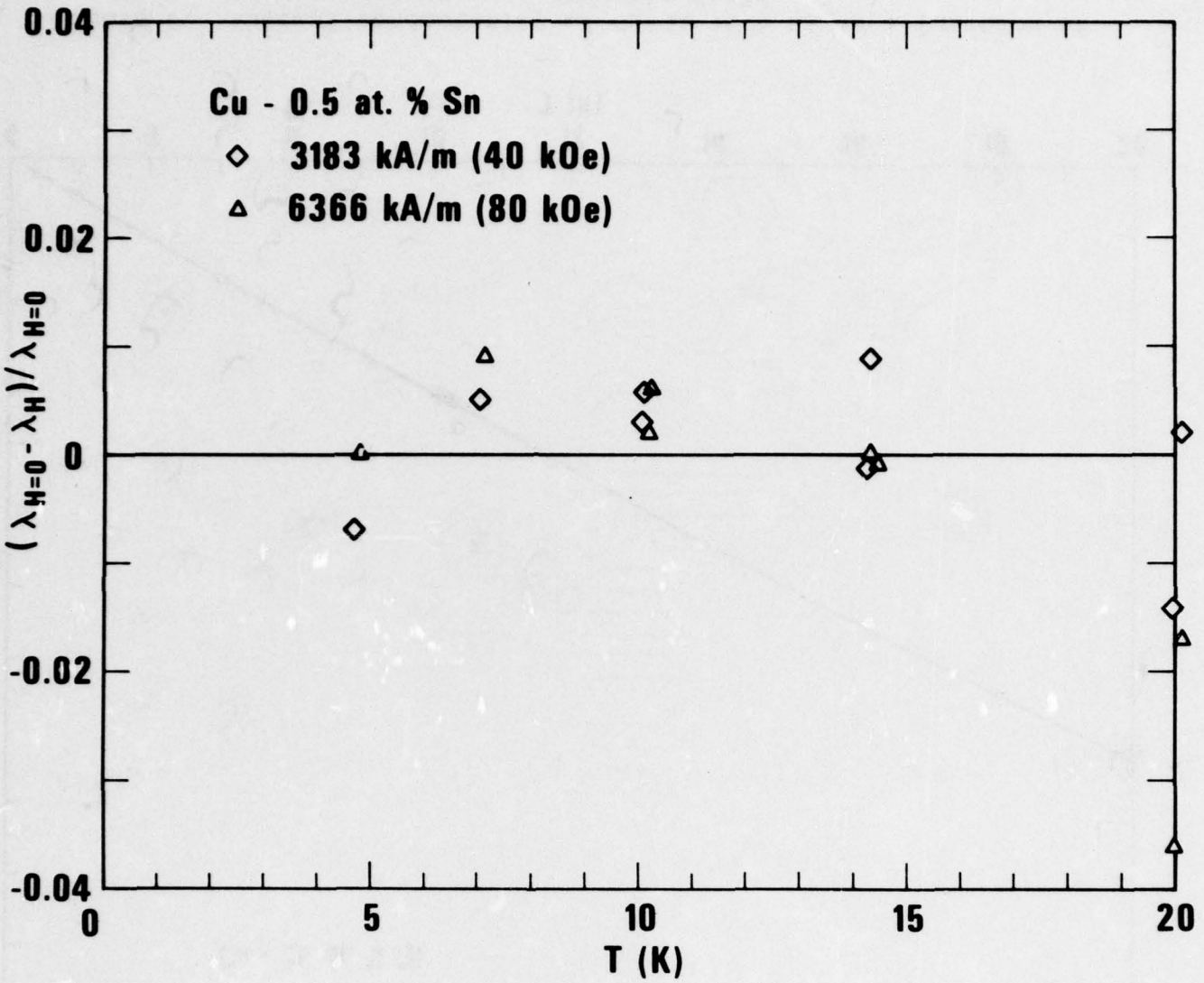


Figure 9. Deviation of thermal conductivities found in the zero and non-zero field tests on Cu-0.5 at % Sn.

77X 0645

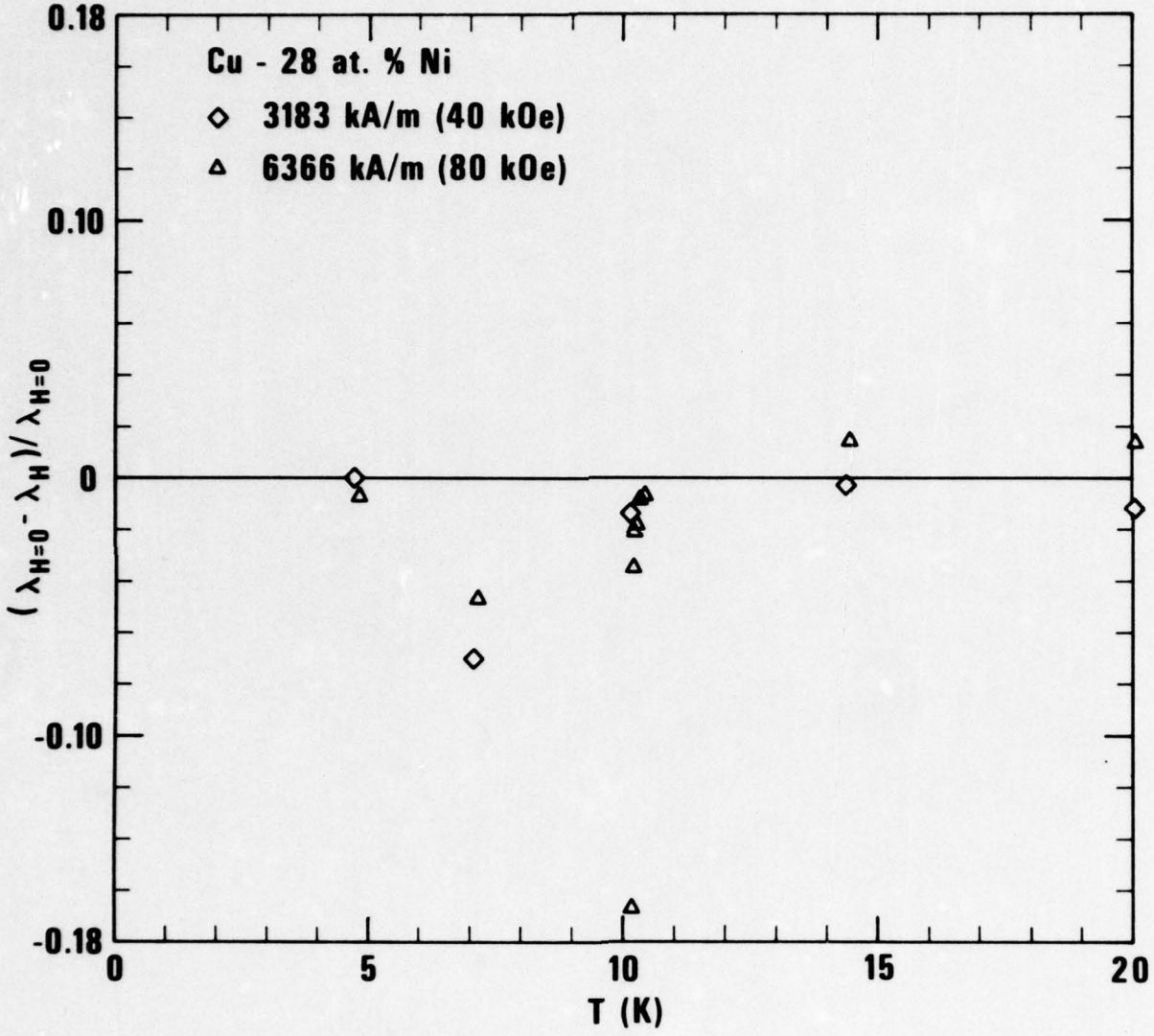


Figure 10. Deviation of the thermal conductivities found in the zero and non-zero field tests on Cu-28 at % Ni.

77 X 0646

PRECEDING PAGE BLANK-NOT FILMED

SEMI-ANNUAL REPORT ON MATERIALS RESEARCH IN SUPPORT OF SUPERCONDUCTING MACHINERY

THERMAL CONDUCTIVITY

J. G. Hust

Cryogenics Division
Institute for Basic Standards
National Bureau of Standards
Boulder, Colorado 80302

October 1976

THERMAL-CONDUCTIVITY MEASUREMENTS DURING ARPA-SPONSORED PROGRAM, SEPTEMBER 1973 TO SEPTEMBER 1976

Material	ARPA Report No.	Experimental Apparatus
OFHC Copper	2	variable temperature
Inconel X-750 (ST)	2	variable temperature
Inconel X-750 (STDA)	3	variable temperature
INCO LEA	2	variable temperature
Stainless Steel 310-S	2	fixed-point
Stainless Kromarc 58	2	fixed-point
Maraging Steel 300	6	fixed-point
Carpenter 49 Steel	6	fixed-point
Phenolformaldehyde	6	fixed-point
Graphite-epoxy	6	fixed-point
Boron-aluminum	6	fixed-point
Boron-epoxy	4,6	both

Summary: Thermal Conductivity

Thermal conductivity values are reported for those materials measured during the current reporting period. Specimens were measured of a high permeability steel (Fe-47.5Ni), maraging steel 300 (Fe-18Ni-9Co-5Mo), both in the rolling direction and perpendicular to the rolled plate, boron-aluminum, boron-epoxy, phenolformaldehyde, and graphite-epoxy composites. These data are compared to literature data for similar materials. A new thermal conductivity apparatus is also described. It is a fixed-point apparatus utilizing compressive thermal contacts to circumvent problems encountered with bonded thermal contacts.

THERMAL CONDUCTIVITY

J. G. Hust
Cryogenics Division
Institute for Basic Standards
National Bureau of Standards
Boulder, Colorado 80302

1. Introduction

Optimum design of superconducting machinery requires a knowledge of thermal properties of technically important materials at low temperatures. But, often, components extend from ambient temperatures to low temperatures, and, therefore, data are needed from 4 K to 300 K. Thermal conductivity of metals is a function of the host metal and its constituent elements and temperature; but it also depends on the microstructure of the material, strain, fatigue, and heat treatment; and in some cases environmental effects are important (e.g. in the case of superconducting machinery, magnetic field intensities may produce significant changes). Specific thermal conductivity data for particular components are required to limit heat losses and thermal stresses in machines. With such a myriad of parameters it is difficult (at best) to determine accurately, by experiment, the thermal conductivity of each machine component. Instead, we often rely on a limited number of measurements on specific types of materials, characterized according to the above parameters. Due to material variability effects these values are generally considered accurate to only about 10%.

It should be noted that accurate thermal conductivity measurements are much more expensive and time consuming relative to many other property measurements. The ease with which high accuracy can be obtained is primarily a function of temperature and the conductivity itself. The extremes of conductivity (both very high, such as in pure metals, and very low, such as in insulating materials) promote inaccuracies in measurement. Generally, low temperature data (below about 100 K) are more readily obtained with accuracy because radiation errors can be minimized.

For the above reasons, various methods of obtaining thermal conductivity data are used. The method used depends primarily on the accuracy dictated by the application. Usually accuracies of 10% are sufficient; in other cases values accurate to 50% suffice. The present state-of-the-art in thermal conductivity measurements is about 1% accuracy, but seldom is this required except in theoretical or standardization work.

In this laboratory three methods of data determination are used:

(a) A variable-temperature apparatus, capable of measuring at any temperature from 4 to 300 K, with an accuracy of about 2%. This apparatus also simultaneously measures electrical resistivity and thermopower for additional specimen characterization and subsequent predictions of similar materials. This apparatus is used to measure materials that have not been sufficiently measured and characterized previously and for accurate temperature dependence determinations.

(b) Two fixed point apparatus, capable of measuring near the fixed temperatures of various boiling fluids (such as liquid helium and liquid nitrogen) and melting or subliming solids (such as ice and CO_2). The accuracy of these apparatus is about 10%, depending mainly on the conductivity of the specimen.

(c) Predictive methods such as those described by Hust and Clark [1] and Hust and Sparks [2]. The latter paper also contains data for many metals and alloys, necessary to carry out such predictions.

2. Apparatus

During the current reporting period the fixed-point apparatus were used to determine thermal conductivity near the fixed-point temperatures of various cryogenic baths. As explained in a later section, difficulty was encountered in accurately measuring composite specimens using the fixed-point apparatus described in a previous report of this series [3]. The difficulty was caused by the differential thermal expansion between the composite specimens and the copper end pieces glued to the specimens for thermal contact. These epoxied bonds apparently cracked during cooldown and resulted in poor thermal contacts. During the last such run with a composite involving NASA resin 2 the end pieces actually fell off during the run. Because of these difficulties a new fixed-point probe was built in which the thermal contact to the specimen was obtained through a compressed indium contact. Otherwise, the operation was identical to the older probe. Figure 1 illustrates this compression type fixed-point apparatus.

The operation of this apparatus is the same as that previously described [3]. Prior to measuring any specimens several calibration runs were conducted to determine the amount of heat conducted by the compression bolts and the measuring wires which pass from the top block to the bottom block. These calibration runs, however, could not be conducted with an empty chamber, as before, because the thermal resistance between the two blocks is dependent on the existence of a force on the compression bolts. Therefore, the system was calibrated using three specimens of phenolformaldehyde rods of decreasing cross-sectional areas. The first was a solid rod of 1.91 cm diameter. The second was of the same outside diameter with a 1.27 cm hole through the center. The third was drilled with a 1.75 cm hole. For each of these specimens, curves of heat flow versus temperature gradient were experimentally determined. These curves were cross-plotted to obtain curves of heat flow versus cross-sectional area at constant gradient. The intersections of these curves (straight lines) with the A = 0 axis were used to determine the heat flow versus temperature gradient of the "empty" chamber. These data, given in Table 1, were used to correct the measured heat flow to obtain the heat flow actually conducted by the specimen at a given gradient.

Table 1. Heat flow of the empty chamber as a function heater block temperature at fixed upper block temperatures, i.e. the bath temperature.

Bath (temp)	$\dot{Q}$ (mW)	T (K)
liquid helium (4 K)	0.00	4.0
	0.44	6.5
	1.32	9.0
	2.89	12.0
	5.70	16.0
	9.05	20.0
liquid nitrogen (76 K)	0.0	76
	36.0	87
	77.7	99
dry ice and alcohol (192 K)	0.0	192
	83.5	204
	176.7	216
ice and water (273.15 K)	0.0	273
	149.0	285
	307.0	297

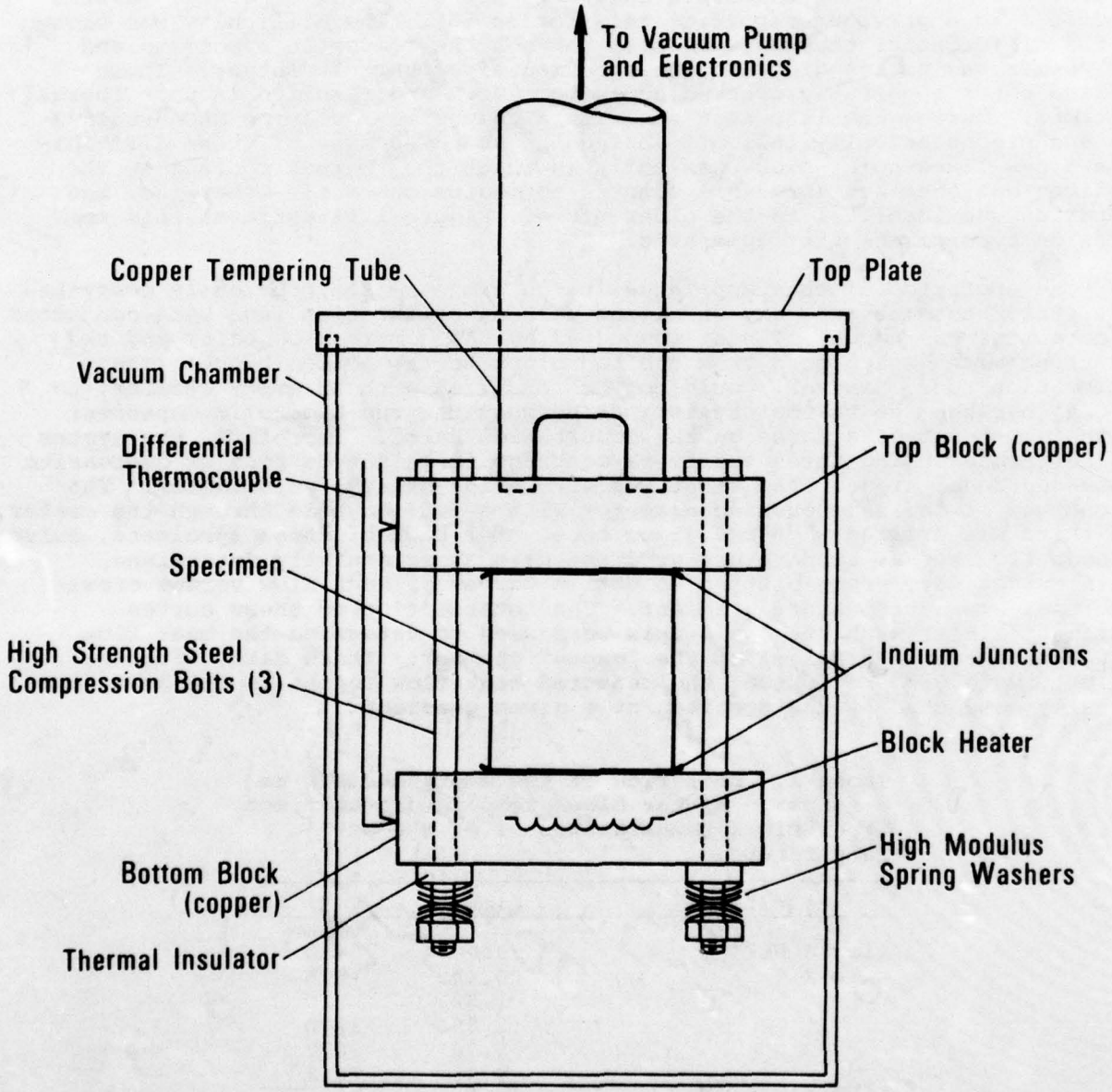


Figure 1. Compressive thermal contact fixed-point thermal conductivity apparatus.

Table 2. Thermal conductivity values for the materials measured during the current reporting period.

Specimen Identification	T (K)	λ ($W \cdot m^{-1} \cdot K^{-1}$)
High Perm 49 Fe-47.5 Ni (in rolling direction)	7.41	1.24
	84.0	10.4
	200	15.1
	280	16.9
SAME (perpendicular to plate)	7.42	1.47
	84.1	12.8
	199	18.2
	280	20.0
Maraging Steel-300 (in rolling direction)	85.2	6.93
	199	11.8
	279	14.4
SAME (perpendicular to plate)	7.45	0.712
	84.5	7.33
	199	12.5
	280	15.4
Boron-aluminum composite (longitudinal)	7.59	17.7
	78.4	75.1
	195	82.2
	276	89.6
SAME (transverse)	7.60	11.3
	78.3	51.3
	195	55.7
	276	60.6

These data obtained using bonded thermal contact apparatus.

Specimen Identification	T (K)	λ ($W \cdot m^{-1} \cdot K^{-1}$)
Phenolformaldehyde Composite	6	0.055
	8	0.070
	10	0.083
	80	0.38
	200	0.58
	300	0.54
Boron-epoxy (longitudinal)	5.98	0.248
	7.67	0.380
	10.84	0.672
	80.3	2.14
	198	2.24
	277	2.24
SAME (transverse)	5.96	0.128
	80.3	0.612
	196	0.940
	276	0.905
Graphite-epoxy (longitudinal deformed)	6.07	0.0388
	80.2	0.702
	196	2.36
	277	3.43
Graphite-epoxy (longitudinal) (high-temp. resin)	5.97	0.0466
	10.82	0.0724
	80.2	0.920
	195	3.19
	276	4.64

These data obtained using compressive thermal contact apparatus.

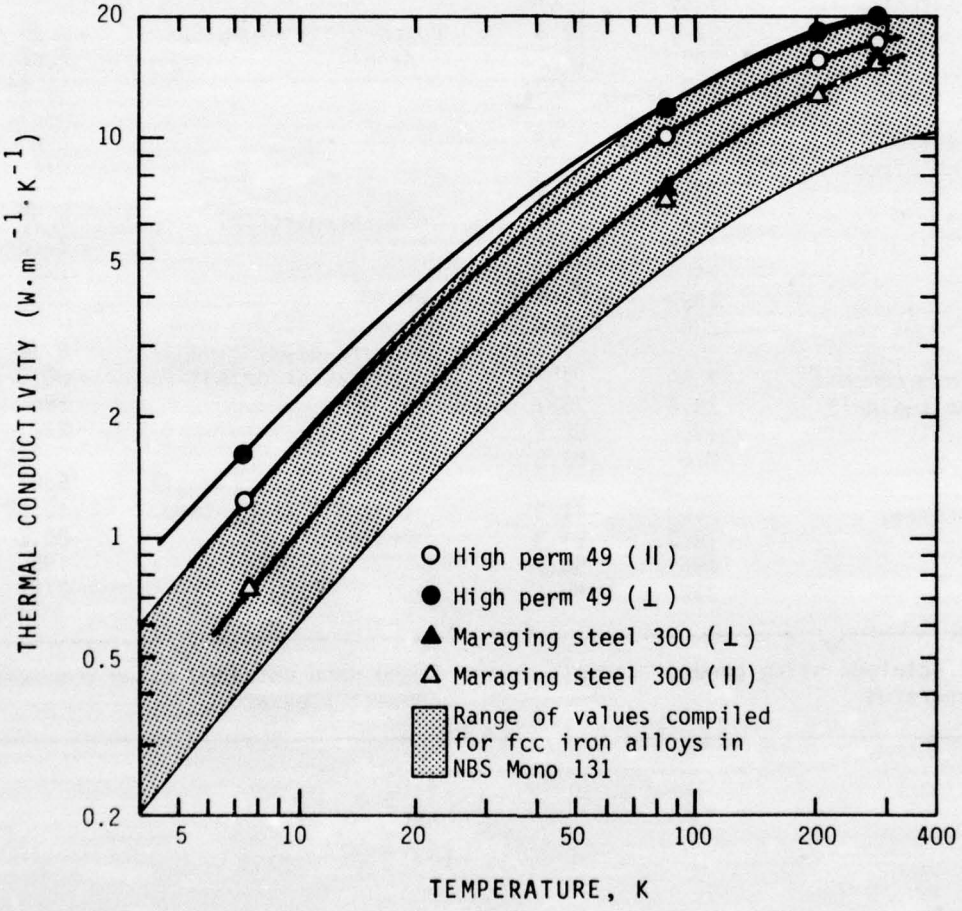


Figure 2. Thermal conductivity of High Perm 49 and Maraging Steel 300 compared to literature data [5] for fcc iron alloys.

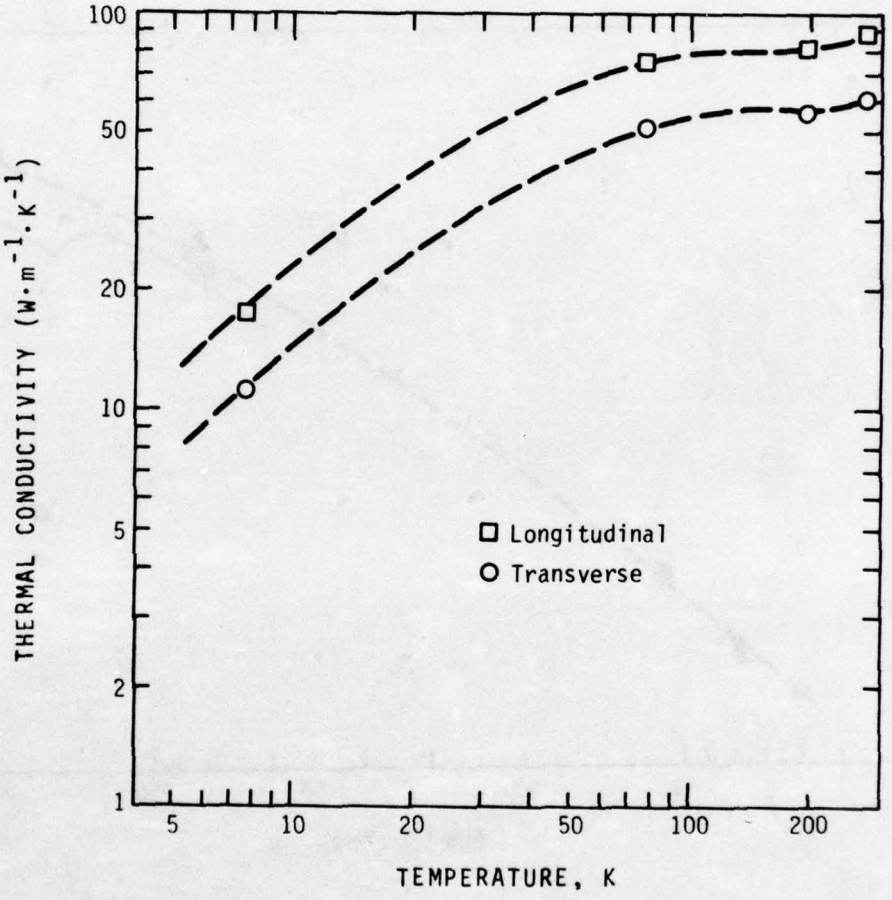


Figure 3. Thermal conductivity of boron-aluminum composite.

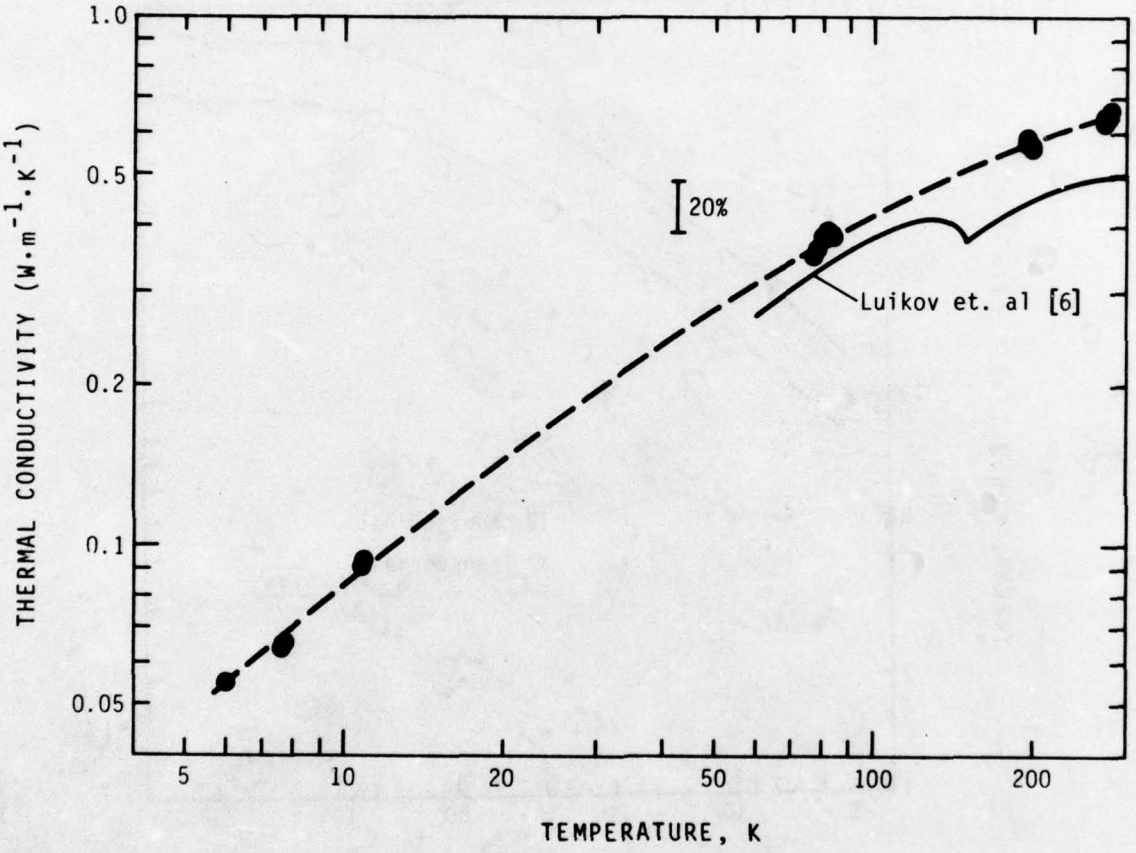


Figure 4. Thermal conductivity of phenolformaldehyde composite.

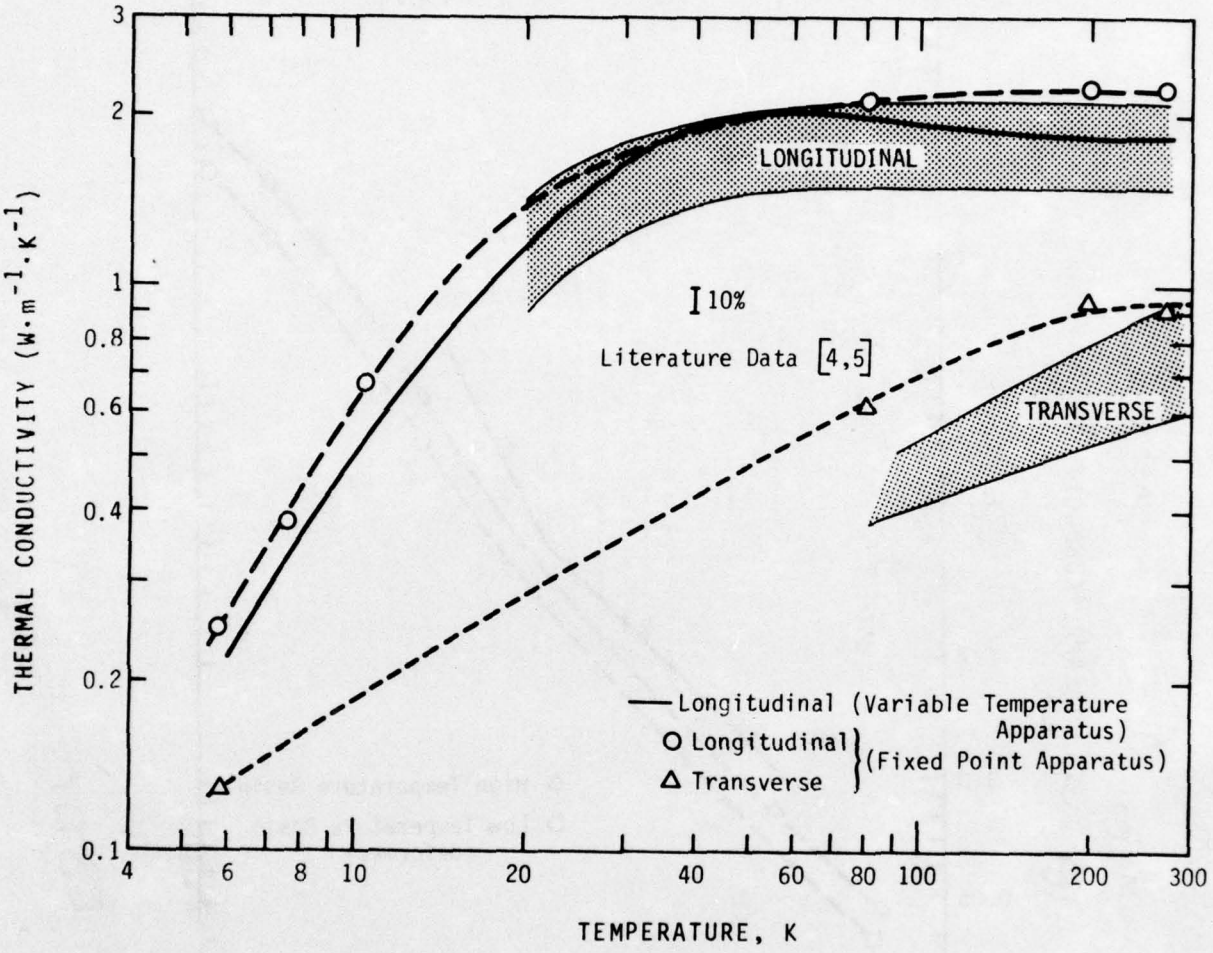


Figure 5. Thermal conductivity of longitudinal and transverse boron-epoxy composite specimens.

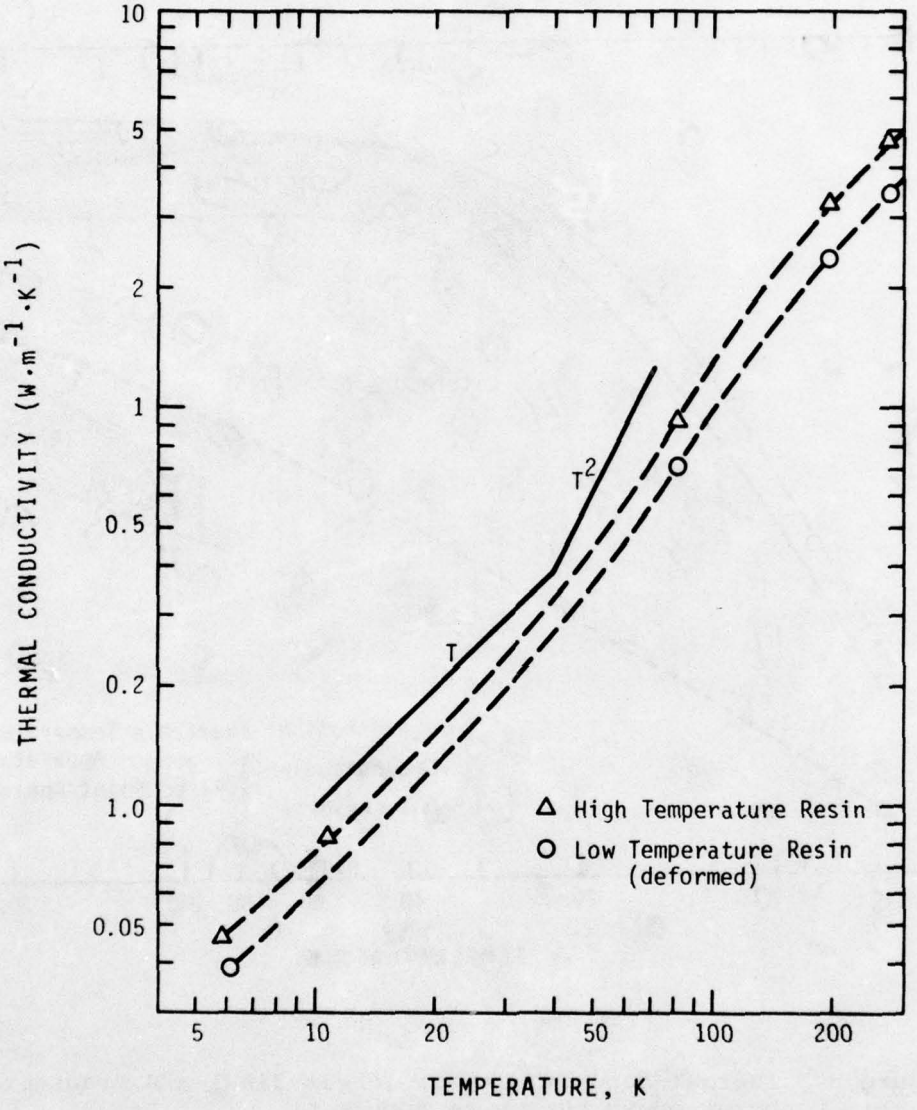


Figure 6. Thermal conductivity of two graphite-epoxy composite specimens (longitudinal).

3. Specimen Characterization

During the current reporting period specimens of high permeability steel (Fe-47.5Ni), maraging steel 300 (Fe-18Ni-9Co-5Mo), phenolformaldehyde, boron-epoxy, graphite-epoxy, and boron-aluminum composites were measured.

High Perm 49(Fe-47.5Ni):

The chemical composition by weight percent of this material is Fe(bal), Ni(47.47), Mn(0.33), Si(0.25), C(0.012), S(0.004), and P(0.002). The material was hot rolled and ground to a size of 9" X 4" X 20" long. The specimens measured were cut and ground from this plate. The density of the material is 8.19 ± 0.02 g/cm^3 and its Rockwell hardness is B73.

Maraging Steel 300:

The chemical composition is Fe(bal), Ni(18.41), Co(9.27), Mo(4.95), Ti(0.59), Al(0.12), Mn(0.01), Si(0.01), P(0.06), S(0.003), and C(0.002). Its density is 8.06 ± 0.02 g/cm^3 and its Rockwell hardness is B105.

Boron-Aluminum Composite:

This composite was fabricated with 5.6 mil boron fibers and 6061-F aluminum. The aluminum content by volume is 53% with a void content of less than 2%.

Phenolformaldehyde Composite:

This material is uncharacterized rod stock used for apparatus calibration as described earlier.

Boron-Epoxy Composite:

This is the same material as described in an earlier report of this series [4]. It was remeasured because of the aforementioned thermal contact problems.

Graphite-Epoxy Composite:

Measurements were performed on two graphite-epoxy formulations. One, designated as SP-288-T300, is composed of continuous graphite fibers with a PR-288 resin content of 50% by volume. The other is fabricated with NASA resin 2, also 50% by volume. The latter composite contains a highly flexibilized resin and was difficult to measure, as discussed later.

4. Results and Discussion

The results of the measurements conducted during the current reporting period are listed in Table 2 and illustrated in Figures 2 through 6. The uncertainty of these data is estimated to be ± 10%. The data obtained with poor thermal contacts are not listed. However, it may be interesting to note that the discrepancies resulted in values as small as one-third of the correct values. This illustrates the magnitude of the errors which can readily enter into thermal conductivity measurements and emphasizes the care which must be exercised to avoid them.

High Perm 49(Fe-47.5Ni) and Maraging Steel 300:

The results of these measurements are plotted in Figure 2. For comparison a shaded area is included which represents the range of reported values for fcc iron alloys [5]. The High Perm 49 values lie at the upper end of this range and the maraging steel values are near the middle. The differences between the longitudinal and transverse High Perm 49 specimens are slightly larger than measurement uncertainty while for maraging steel the differences are within measurement uncertainty. In either case, however, the differences are comparable to that one would expect from material variability.

Boron-Aluminum Composite:

The measured values of thermal conductivity for the longitudinal and transverse specimens of boron-aluminum composites are shown in Figure 3. An attempt was made to correlate these data with the pure component data. However, no data for aluminum 6061 in the F condition and boron fiber have been reported in the literature. Estimates could be made for both of these, but because of the high uncertainty of such estimates the resulting correlation would be of questionable value. Suffice it to say that the measured values are in reasonable correspondence for a similar aluminum alloy and the results estimated for boron fibers as reported previously in this series [4].

Phenolformaldehye Composite:

This material was not measured directly as part of this ARPA program but rather as a calibration material. However, because of its common usage, the results, illustrated in Figure 4, are considered useful. A. V. Luikov, L. L. Vasiliev and A. G. Shashkov [6] measured a similar material; their results are included in Figure 4. The agreement is considered good in view of the uncharacterized nature of these specimens. These results and the following were obtained with the compressive fixed-point apparatus. A smooth (dashed line) has been drawn through the present data, however, the data of Luikov et al [6] indicate there is a phase transition at 150 K. The point spacing of the present data would not reveal this transition but does not conflict with its potential existence.

Boron-Epoxy Composite:

This material was remeasured with the compressive thermal contact apparatus after the bonded thermal contact problem was discovered. The new results are illustrated in Figure 5 along with the previously reported values for the longitudinal specimen using the variable temperature apparatus. Contrary to the previously reported results using the bonded thermal contact fixed-point apparatus, the two longitudinal specimens are in reasonably good agreement. The poor thermal contacts reduced the apparent thermal conductivity by about 50%. The thermal contact to the transverse specimen was apparently also not good since the previously reported values are low by about 20-30%. The present values are slightly higher than the literature data for both specimen directions.

Graphite-Epoxy Composite:

As mentioned earlier, considerable difficulty was encountered in measuring this material. The first attempt to measure this material using the bonded thermal contact apparatus resulted in broken thermal contacts. The compressive thermal contact apparatus was then built and measurements attempted. Again, the results were questionable because of the deformation of the highly plasticized resin. Another specimen was fabricated using a less flexible resin and these results are considered reliable. The latter two sets of data are illustrated in Figure 6.

References

1. Hust, J. G. and Clark, A. F., The Lorenz ratio as a tool for predicting the thermal conductivity of metals and alloys, Materials Research and Standards 11, (No. 8), 22-4 (August 1971).

2. Hust, J. G. and Sparks, L. L., Lorenz ratios of technically important metals and alloys, Nat. Bur. Stand. (U.S.) Tech. Note 634, (February 1973) 133 pp.

3. Hust, J. G., in Semi-annual report on materials research in support of superconducting machinery, NBSIR 74-359 (1974) 308 pp; available from NTIS, AD 780-596/3WM.

4. Hust, J. G., in Semi-annual report on materials research in support of superconducting machinery, NBSIR 75-828 (1975) 186 pp.

5. Childs, G.E., Ericks, L.J., and Powell, R.L., Thermal conductivity of solids at room temperature and below, a review and compilation of the literature, Nat. Bur. Stand. (U.S.) Monograph 131, (1973) 608 pp.

6. Luikov, A.V., Vasiliev, L.L., and Shashkov, A.G., A method for the simultaneous determination of all thermal properties of poor heat conductors over the temperature range 80 to 500 K, Proceedings of the 3rd Symposium on Thermophysical Properties, Purdue University (1965) pp. 314-319.

Research Report 76-9D9-CRYMT-R1
Westinghouse Program 9D91-CRYMT
NBS Contract No. CST-8304

STRUCTURAL MATERIALS FOR CRYOGENIC APPLICATIONS

(Final Technical Report)

J. M. Wells, R. Kossowsky, W. A. Logsdon and M. R. Daniel

Westinghouse Electric Corporation
Research and Development Center
Pittsburgh, Pennsylvania 15235

October 9, 1976

The views and conclusions contained in this document are those of the authors and should not be interpreted as necessarily representing official policies,, expressed or implied, of the Advanced Research Projects Agency or the U.S. Government.

Approved

J. H. Bechtold, Research Div. Mgr.
Materials Science Division

R. C. Bates, Manager
Materials Evaluation and Application

This research was supported by the Advanced Research Projects Agency of the Department of Defense and was monitured by the Cryogenics Div., NBS, Boulder, CO under Contract No. CST-8304 Contract Amount $402,708.

Sponsored by Advanced Research Projects Agency ARPA Order No. 2569, Program Code No. 4D10

TITLE: STRUCTURAL MATERIALS FOR CRYOGENIC APPLICATIONS
(Final Technical Report - October 9, 1976)

CONTRACTOR: Westinghouse Electric Corporation
Research and Development Center
Pittsburgh, Pennsylvania 15235

Westinghouse Program Manager: Dr. J. M. Wells (412) 256-3467

Westinghouse Principal Investigators:

Mr. W. A. Logsdon (412) 256-3652
Dr. R. Kossowsky (412) 256-3684
Dr. M. R. Daniel (412) 256-3289
Dr. J. M. Wells (412) 256-3467

FY 74 Contract Start Date: September 10, 1973

FY 74 Contract Expiration Date: September 9, 1974

FY 75 Contract StarteDate: September 10, 1974

FY 75 Contract Expiration Date: September 9, 1975

FY 76 Contract Start Date: September 10, 1975

FY 76 Contract Expiration Date: October 9, 1976

TABLE OF CONTENTS

		Page
1.0	ABSTRACT	1
2.0	INTRODUCTION	3
3.0	INTERPRETIVE SUMMARY	6
	3.1 Program Status	6
	3.2 Alloy Selection and Utilization	7
	3.3 Mechanical and Fracture Mechanics Properties	7
	3.4 Effects of Processing	9
	3.5 Effects of Metals Joining	9
	3.6 Microstructural and Fractographic Analysis	10
	3.7 Magnetic Behavior and Electrical Resistivity	10
4.0	WESTINGHOUSE PROGRAM DESCRIPTION	25
	4.1 FY 76 Program Summation	26
	4.2 FY 75 Program Summation	26
	4.3 FY 76 Program Summation	27
5.0	GENERAL CRYOSTRUCTURAL MATERIALS/PROCESSING/FABRICATION CONSIDERATIONS	30
	5.1 Materials Selection and Utilization Considerations	31
	5.1.1 Overview	31
	5.1.2 Non-Austenitic Steels for Cryogenic Applications	36
	5.1.3 Dimension Instabilities	37
	5.2 Materials Processing Considerations	40
	5.2.1 Overview	40
	5.2.2 Property Variations in 21 Cr-6 Ni-9 Mn Alloy	44
	5.3 Materials Joining Considerations	46
	5.3.1 Overview	46
	5.3.2 Further Varestraint Weldability Considerations	51
6.0	MECHANICAL TESTING AND FRACTURE MECHANICS	75
	6.1 Tensile Results	76
	6.2 Fracture Toughness Results	79

TABLE OF CONTENTS (Cont'd)

		Page
6.3	Crack Growth Rate Results	84
6.4	Summary-Design Example	89
7.0	FRACTOGRAPHY AND MICROSTRUCTURAL ANALYSIS	134
7.1	Fatigue-Crack Growth, GTAW, Alloy IN 718	134
7.1.1	Results	134
7.1.2	Summary	135
7.2	A-286, Weld Specimens (STQ/GTAW)	135
7.2.1	Results	135
7.2.2	Summary	136
7.3	Pyromet 538 (21 Cr-6 Ni-9 Mn SS)	137
7.3.1	Results	137
7.3.2	Summary	140
7.4	Final Summary	141
8.0	MAGNETIC AND ELECTRICAL MEASUREMENTS	172
9.0	ACKNOWLEDGEMENTS	181

LIST OF TABLES

	Page
TABLE 3-1 - Structural Materials for Cryogenic Applications . .	11
TABLE 3-2 - Structural Materials for Cryogenic Applications . .	12
TABLE 5-1 - Candidate Materials for Advanced Cryogenic Structural Applications	55
TABLE 5-2 - Summary Chemical Composition of Ⓦ Program Materials (Weight Percent)	56
TABLE 5-3 - Summary of Material Documentation Data for Ⓦ Program Materials	57
TABLE 5-4 - Summary Processing and Heat Treatment Schedules for Ⓦ Program Materials	59
TABLE 5-5 - Test Specimen Identification System	61
TABLE 6-1 - Tensile and Notched Tensile Properties of A286 (UNS 66286) and Pyromet 538 (21Cr-6Ni-9Mn) Stainless Steel Baseplate and Weldments	100
TABLE 6-2 - Fracture Toughness Properties of Inconel X750 . . .	101
TABLE 6-3 - Fracture Toughness Properties of Inconel 706 . . .	102
TABLE 6-4 - Fracture Toughness Properties of Inconel 718 . . .	103
TABLE 6-5 - Fracture Toughness Properties of INCO Low Expansion Alloy (LEA)	104
TABLE 6-6 - Fracture Toughness Properties of KROMARC 58 Stainless Steel	105
TABLE 6-7 - Fracture Toughness Properties of AISI 310S Stainless Steel	106
TABLE 6-8 - Fracture Toughness Properties of A286 (UNS 66286) Stainless Steel	107
TABLE 6-9 - Fracture Toughness Properties of Pyromet 538 (21Cr-6Ni-9Mn) Stainless Steel	108
TABLE 6-10 - Fracture Toughness Properties of OFHC Copper and PD 135	109
TABLE 6-11 - Fatigue Crack Growth Rate Properties of Inconel X750	110
TABLE 6-12 - Fatigue Crack Growth Rate Properties of Three Nickel Base Superalloys	111
TABLE 6-13 - Fatigue Crack Growth Rate Properties of Four Stainless Steels	112

LIST OF TABLES (Cont'd) - 2

		Page
TABLE 6-14 -	Critical Flaw Sizes of Several Materials at -452°F (4K)	113
TABLE 6-15 -	Initial Allowable Flaw Sizes for Several Materials at -452°F(4K)	114
TABLE 7-1 -	Mode of Failure, Structural Materials for Cryogenic Applications	144
TABLE 8-1 -		176
TABLE 8-2 -		177
TABLE 8-2 -		178

LIST OF FIGURES

Page

FIG. 3-1 - Summary comparison of mechanical strength and ductility values for copper alloys including processing and fabricated joints at RT, 77K, and 4.2K . 13

FIG. 3-2 - Summary comparison of mechanical strength and ductility values for AISI 310S and Kromarc 58 stainless steels including processing and welded joints at RT, 77K and 4.2K 14

FIG. 3-3 - Summary comparison of mechanical strength and ductility values for Pyromet-538 (21 Cr-6 Ni-9 Mn) and A286 stainless steels including base metal and weldments at RT, 77K and 4.2K 15

FIG. 3-4 - Summary comparison of mechanical strength and ductility values for nickel based superalloys IN X750, 706 and LEA in various processed conditions at RT, 77K, and 4.2K 16

FIG. 3-5 - Summary comparison of mechanical strength and ductility values for Inconel X750 base metal, electron beam and GTA weldments and copper brazement at RT, 77K and 4.2K 17

FIG. 3-6 - Summary comparison of mechanical strength and ductility values for nickel base superalloys Udimet 718 and Inconel 718 in various processed and fabricated conditions at RT, 77K and 4.2K 18

FIG. 3-7 - Summary comparison of fracture toughness values at 4.2K for 310S, Kromarc 58, Inconel X750, Inconel 718, Inconel 706, INCO LEA, and A-286 materials including effects of processing and metals joinint . 19

FIG. 3-8 - Effect of processing conditions on yield strength and ultimate tensile strength ratios for OFHC copper, 310S and Kromarc 58 stainless steels and Inconel X750. In 718 and IN706 superalloys at RT, 77K and 4.2K 20

FIG. 3-9 - Effect of processing conditions on fracture toughness ratio for 310S, Kromarc 58, Inconel X750, and Inconel 718 at 4.2K 21

FIG. 3-10 - Effect of metals joining conditions on yield strength and ultimate tensile strength ratios for OFHC copper, 310S and K-58, Pyromet-538 and A-286 stainless steel at RT, 77K and 4.2K 22

FIG. 3-11 - Effect of metals joining conditions on yield strength and ultimate tensile strength ratios for Inconel X750, Inconel 718 and Inconel 706 at RT, 77K and 4.2K 23

LIST OF FIGURES (Cont'd) - 2

Page

FIG. 3-12 - Effect of metals joining conditions fracture toughness ratio for 310S, Kromarc-58, Pyromet-538 and A-286 stainless steels (Top) and IN X750, IN 718 and IN 706 (Bottom) at 4.2K 24

FIG. 4-1 - Ⓦ Program Outline - Structural materials for cryogenic applications 28

FIG. 4-2 - Westinghouse Program Organization - FY76 29

FIG. 5-1 - Photomicrograph of transverse section of varestraint sample 76-134. Mat. KROMARC 58SS, Cond. BM-STQ, ε = 2%; Note HAZ cracking 63

FIG. 5-2 - Photomicrograph of transverse section of varestraint sample 76-133. Mat. KROMARC 58SS, Cond.-Double Pass in Prior GTA Weld, ε = 2%, Note FZ cracking 64

FIG. 5-3 - Photograph of transverse section in varestraint specimen 76-130. Mat. Pyromet 538 (21Cr-6Ni-9Mn)SS, Cond. BM-STQ, ε = 2%; note no cracking. 65

FIG. 5-4 - Photomicrograph of transverse section of varestraint sample 76-154. Mat. Nitronic 33SS, Cond. BM-STQ, ε = 3%, note HAZ cracking 66

FIG. 5-5 - Photomicrograph of transverse section of varestraint sample 76-132. Mat. Nitronic 33, Cond. Single pass in prior 13-20Mn-CbGTAW, ε = 2%, note FZ cracking 67

FIG. 5-6 - Photomicrograph of transverse section varestraint sample 76-131. Mat. AISI 305SS, Cond. BM-STQ, ε = 2%, note FZ cracking 68

FIG. 5-7 - Photomicrograph of transverse section of varestraint sample 76-128. Mat. A-286(A), Cond. BM-ST(1800°F)OQ, ε = 2%, note both FZ and HAZ cracking 69

FIG. 5-8 - Photomicrograph of transverse section of varestraint sample 76-92. Mat. A-286(A), Cond. BM-ST(1800°F)QA, ε = 2%, note HAZ and FZ cracking 70

FIG. 5-9 - Photomicrograph of transverse section of varestraint sample 76-119. Mat. A-286(C), Cond. BM-ST(1800°F)QA, ε = 2%, note FZ and HAZ cracking 71

FIG. 5-10 - Photomicrograph of transverse section of varestraint sample 76-153. Mat. IN718, Cond. BM-AR, ε = 2%, note HAZ cracking and wide shallow nugget cross section 72

LIST OF FIGURES (Cont'd) - 3

Page

FIG. 5-11 - Photomicrograph of transverse section of varestraint sample 76-129. Mat. UD-718, Cond. BM-ST(1950°F), ε = 2%, note FZ and HAZ cracking 73

FIG. 5-12 - Photomicrograph of transverse section of restraint sample 76-121. Mat. UD-718, Cond. BM-ST(1950°F)DA, ε = 2%, note FZ and HAZ cracking 74

FIG. 6-1 - Tensile properties of A286 stainless steel baseplate and gas tungsten arc welds 115

FIG. 6-2 - Ductility of A286 stainless steel baseplate and gas tungsten arc welds 116

FIG. 6-3 - Tensile properties of Pyromet 538 (21Cr-6Ni-9Mn) stainless steel base plate, gas tungsten arc and shielded metal arc welds 117

FIG. 6-4 - Ductility of Pyromet 538 (21Cr-6Ni-9Mn) stainless steel baseplate, gas tungsten arc and shielded metal arc welds 118

FIG. 6-5 - The influence of processing and heat treatment on the -452°F(4K) J resistance curves of Inconel 718 (VIM-VAR) 119

FIG. 6-6 - J resistance curve for A286 stainless steel gas tungsten arc welds 120

FIG. 6-7 - J resistance curves for Pyromet 538 (21Cr-6Ni-9Mn) stainless steel gas tungsten arc and shielded metal arc welds 121

FIG. 6-8 - J resistance curve for PD 135 122

FIG. 6-9 - Fatigue crack growth rate properties of (VIM-VAR) Inconel 706 gas tungsten arc welds 123

FIG. 6-10 - Fatigue crack growth rate properties of (VIM-VAR) Inconel 718 gas tungsten arc welds 124

FIG. 6-11 - Fatigue crack growth rate properties of (VIM-VAR) Inconel 718 gas tungsten arc welds (heat affected zone 125

FIG. 6-12 - Comparison of the fatigue crack growth rate properties of (VIM-VAR) Inconel 718 base, gas tungsten arc weld and heat affected zone material 126

FIG. 6-13 - Comparison of the fatigue crack growth rate properties of (VIM-VAR) Inconel 718 and (VIM-VAR) Inconel 706 gas tungsten arc welds 127

LIST OF FIGURES (Cont'd) - 4

Page

FIG. 6-14 - Fatigue crack growth rate properties of A286 stainless steel gas tungsten arc welds 128

FIG. 6-15 - Fatigue crack growth rate properties of Pyromet 538 (21 Cr-6 Ni-9 Mn) stainless steel gas tungsten arc welds 129

FIG. 6-16 - Fatigue crack growth rate properties of Pyromet 538 (21 Cr-6 Ni-9 Mn) stainless steel shielded metal arc welds 130

FIG. 6-17 - Comparison of the fatigue crack growth rate properties of Pyromet 538 (21 Cr-6 Ni-9 Mn) stainless steel gas tungsten arc and shielded metal arc welds 131

FIG. 6-18 - Flaw shape parameter curves for surface and internal cracks 132

FIG. 6-19 - Cyclic life curves for several materials at -452°F(4K) 133

FIG. 7-1 - SEM micrographs, fatigue-crack growth specimen 6551 alloy IN718 GTAW weld fusion zone, tested at RT a) 280X, b) 700X, c) 700X, d) 1400X 148

FIG. 7-2 - EDAX data from Fig. 7-1d a: spots A, C b: spot B. 149

FIG. 7-3 - SEM micro-raphs, fatigue-crack growth specimen 6553 alloy I-718. GTAW fusion zone tested at 4.2K (a) 700X (b,c) 1400X 150

FIG. 7-4 - SEM micrographs fatigue-crack-growth specimen 6651 alloy IN-718 GTAW heat affected zone (HAZ) tested at RT (a) 700X, (b,c) 1400X 151

FIG. 7-5 - SEM micrographs, fatigue-crack-growth specimen 6653, alloy 718 GTAW heat-affected-zone (HAZ) tested at 4.2K a) 280X, b) 700X, c) 1400X . . . 152

FIG. 7-6 - SEM micrographs, fatigue-crack-growth specimen 7253 alloy 706 GTAW, fusion zone (used IN-718 filler wire), tested at 4.2K - 1400X 153

FIG. 7-7 - Light micrographs, STQ/GTAW, A-286 tensile specimen 50X a) tested at RT (9111), failed in base metal, b) tested at 4.2K (9113) failed in HAZ 154

FIG. 7-8 - SEM micrographs, A-286 STQ/GTAW tensile specimens a,b: Tested at RT (9111) 20X and 1000X, Base metal fracture c,d: Tested at 4.2K (9113) 20X and 200X, HAZ fracture 155

Page

FIG. 7-9 - SEM micrographs A-286 STQ/GTAW fatigue-crack-growth in fusion zone a,c: Tested at RT (9151) 700X and 2800X; b,d: Tested at 4.2K (9153) 1400X and 2800X 156

FIG. 7-10 - Light micrographs, Pyromet 538 cross sections of tensile specimen tested at RT (STQ 9211), a: 50X b: 100X, 10mm below fracture surface . . . 157

FIG. 7-11 - SEM micrographs of fracture surface, on Pyromet 538 base metal tensile specimen tested at RT (9211) a: 500 b: 500 c: 1000. EDAX of contaminants in (b) shown in Fig. 7-12 158

FIG. 7-12 - X-ray data (EDAX) from contaminants on fracture surface specimen 9211 (Fig. 7-11-b) 159

FIG. 7-13 - Light micrographs, cross sections of tensile specimen 9213-1 alloy Pyromet 538 tested at 4.2K, a. 50X and b. 100X. Note highly deformed matrix 160

FIG. 7-14 - Light micrograph cross sections of tensile specimen 9213-2, alloy Pyromet 538 tested at 4.2K. Note deformed matrix and possibly martensite (arrows) (1000X) 161

FIG. 7-15 - SEM micrographs, fracture surface, tensile specimen 9213-1 alloy Pyromet 538, tested at 4.2K. Note high degree of ductility dimpled fracture through the entire cross section a: 20X b: 500X c: 1000X 162

FIG. 7-16 - SEM micrographs, fracture surface, tensile specimen 9213-2, alloy Pyromet 538 tested at 4.2K. Note shear fracture (a) and heterogeneous deformation in details; a mix of dimpled and sheared areas. a: 20X b: 650X c: 250X d: 250X . 163

FIG. 7-17 - X-ray data, (a) typical composition of Pyromet 538 from area, Fig. 7-15-c. b: spot A, Fig. 7-16-b. Essentially no difference in composition 164

FIG. 7-18 - Cr-radiation, diffractometer traces of tensile specimens. (a) 9213-2, (b) 9213-1 Note the (110)-bcc peak in (a) which is not seen in (b) 165

FIG. 7-19 - Light micrographs, cross section of tensile specimens STQ/GTAW Pyromet 538 (a) 50X, tested at RT 9311; (b) 200X, tested at 4.2K (9313) both specimens failed in base metal 166

LIST OF FIGURES (Cont'd) - 6

Page

FIG. 7-20 - SEM micrographs of fracture surface tensile specimens STQ + GTAW 21-6-9SS a,b: Tested at 4.2K (9313-2) failed in fusion zone, 20X and 1000X; c,d: Tested at RT (9311-2) failed in base metal, 20X and 1400X 167

FIG. 7-21 - SEM micrographs, tensile specimen STQ/SMAW (9411) tested at RT base metal failure. (a) 30X, (b) 750X, (c) 1500X 168

FIG. 7-22 - SEM micrographs, tensile specimens, STQ + SMAW Pyromet 538 a,b: Tested at 77K (9412) 2400X and 1200X; c,d: Tested at 4.2K (9413) 2400X and 1200X both specimens failed in fusion zone 169

FIG. 7-23 - X-ray data (EDAX) from inclusions, Fig. 7-22-b (a) spot 2, (b) spot 1 170

FIG. 7-24 - SEM micrographs, fatigue crack growth specimens. Through the fusion zone Pyromet 538 GTAW a,b: Tested at RT (9351), 700X; c,d: Tested at 4.2K (9353) 600X and 1400X 171

FIG. 8-1 - The magnetic moment versus magnetic field for Pyromet 538 in strained and unstrained conditions . 179

FIG. 8-2 - The magnetic moment of Pyromet 538 base metal and weldments of 3 strain test temperatures 180

1.0 ABSTRACT

Interest in the engineering application of superconducting field windings in advanced cryogenic structures and devices has stimulated renewed interest in the mechanical and physical behavior of cryogenic structural support materials. Examples of such advanced cryogenic applications include such prototype devices as superconducting machinery and large s.c. magnets for Magnetohydrodynamic (MHD) and Controlled Thermonuclear Reactor (CTR) Type devices. The prior existing data base for structural materials in such applications was assessed as inadequate for effective materials selection and utilization in a high reliability design. Consequently, a program entitled, "Materials Research For Superconducting Machinery" was initiated by ARPA and NBS in FY 74.

The Westinghouse Research Laboratories (WRL) has been an active participant in the ARPA/NBS program throughout.

The Westinghouse Research Laboratories program has concentrated on three basic tasks, namely: I. The characterization and evaluation of candidate structural alloys, II. The investigation of metals processing considerations on the cryogenic behavior of selected alloys and III. The evaluation of fabricated joints for cryogenic structural applications. The evaluation procedures employed in the WRL program include mechanical and fracture mechanics testing, metallography, fractography and magnetic and electrical resistivity measurements from room temperature to 4K. Emphasis in the focused direction of this effort is placed upon: (A) utilizing modern fracture mechanics technology to evaluate the K_{IC} (J_{IC}) fracture toughness and fatigue crack growth rate (FCGR) of various alloy conditions, (B) evaluating various selected materials/processing and fabrication (MPF) techniques to elucidate the significant effects of MPF on the cryogenic behavior

of these alloys, (C) employment of metallographic and fractographic analysis techniques to characterize the microstructures and fracture surfaces of the tested materials, and (D) evaluating the general and specific structural materials considerations required to establish failure-safe design materials selection and utilization criteria.

During this sixth semi-annual reporting period (May to October 1976), final characterization, mechanical and fracture mechanics property and magnetic property determinations and metallurgical and fractographic evaluations on the FY76 materials, namely Pyromet 538 (21 Cr-6 Ni-9 Mn) and A286 stainless steels were completed. Some significant variations were observed in the tensile property data reported for Pyromet 538 between Ⓦ and NBS on material of identical chemical composition. The apparent cause of such tensile property variations were examined and attributed to implicit variations in plate processing techniques. Fracture toughness values at 4K for GTA Weldments in Pyromet 538 with matching composition filler material were only about 50% of that of the unwelded material, whereas K_{Ic} values for SMA Weldments in this material with nonmatching composition filler material were equal to the unwelded base material.

Strain induced martensite has been observed in the Pyromet 538 material deformed at both 77 and 4K in confirmation of the microstructural instability predictions made in the last reporting period. No such martensitic transformation has been observed in the A286 material, again in confirmation of earlier microstructural stability predictions. The fracture toughness of GTA Weldments in the A286 material was found to exceed that of the higher strength unweld base material. Summary compilations of all data generated in this program are presented along with overview discussions of the significance of such data with respect to the various interdisciplinary areas involved throughout this program.

2.0 INTRODUCTION

Work described in this report represents the most recent and final Westinghouse Research Laboratories contribution to the Advanced Research Project Agency Program entitled "Materials Research for Superconducting Machinery". This program is supported by DOD-ARPA under the direction of Dr. Edward C. vanReuth. Program management is administered by the Cryogenics Division of the National Bureau of Standards with Dr. Richard P. Reed as overall program manager and Dr. Alan F. Clark as contract monitor.

The present Westinghouse Research Laboratories (WRL) program has as its objectives:

(1) To select, characterize and evaluate candidate structural materials for suitability of use in advanced superconducting machinery.

(2) To investigate the influence of selected processing and fabrication/joining factors or techniques on the mechanical, fracture mechanics and physical (magnetic and electrical resistivity) properties of candidate structural materials.

(3) To develop engineering cryogenic mechanical and physical property data of direct usefulness to designers of prototype S.C. machinery.

(4) To help establish with designers of such systems, more specific criteria for selecting and improving the utilization of structural materials in S.C. machinery prototypes.

Five previous WRL semi-annual technical reports have been issued on this program as follows:

(a) WRL Report No. 74-9D4-CRYMT-R1, dated March 1, 1974
(b) WRL Report No. 74-9D4-CRYMT-R2, dated September 9, 1974
(c) WRL Report No. 75-9D4-CRYMT-R1, dated March 10, 1975
(d) WRL Report No. 75-9D4-CRYMT-R2, dated October 10, 1975
(e) WRL Report No. 76-9D4-CRYMT-R1, dated April 9, 1976.

These previous Westinghouse reports along with those of the other participating laboratories are included in the five corresponding NBS/ARPA overall program semi-annual technical reports as follows:

(1) Materials Research for Superconducting Machinery-I, by A. F. Clark, R. P. Reed, and E. C. VanReuth, Editors, Semi-Annual Technical Report, (Sept. 1973-March 1974), Order No. ARPA 2659, March 1974, NTIS Order No. A0780596.

(2) Materials Research for Superconducting Machinery-II, by A. F. Clark, R. P. Reed, and E. C. VanReuth, Editors, Semi-Annual Technical Report (March-Sept. 1974), Order No. ARPA 2569, Oct. 1974, NITS Order No. ADA004586.

(3) Materials Research for Superconducting Machinery-III, by A. F. Clark, R. P. Reed and E. C. VanReuth, Editors, Semi-Annual Technical Report (Sept. 1974-March 1975), Order No. ARPA 2569, April 1975, NITS Order No. ADA012365.

(4) Materials Research for Superconducting Machinery-IV, by A. F. Clark, R. P. Reed, and E. C. VanReuth, Editors, Semi-Annual Technical Report (March 1975-Sept. 1975), Order No. ARPA 2569, October 1975, NTIS Order No. ADA019230.

(5) Materials Research for Superconducting Machinery-V, by R. P. Reed, H. M. Ledbetter, and E. C. VanReuth, Editors, Semi-Annual Technical Report (Sept. 1975-March 1976), Order No. ARPA 2569, April 1976.

These unclassified reports are available from the National Technical Information Service, P.O. Box 1553, Springfield, VA 22161.

In addition, a comprehensive data compilation has been published by the Metals and Ceramics Information Center, Battelle Columbus Laboratories, P.O. Box 8128, Columbus, Ohio 43201 and identified as:

Handbook on Materials for Superconducting Machinery - First Edition, Nov. 1974 and First Supplement, Nov. 1975, Order No. MCIC-HB-04.

Four technical papers have been written by WRL staff members concerning work mainly accomplished during the Westinghouse FY 74 and FY 75 program. These papers are as follows:

1. Logsdon, W.A., "Cryogenic Fracture Mechanics Properties of Several Manufacturing Process/Heat Treatment Combinations of Inconel X750," Advances in Cryogenic Engineering, V. 22 (to be published in 1976).
2. Kossowsky, R., "Microstructure of Inconel X750 Materials for Cryogenic Structural Applications," Adv. in Cry. Engrg., V. 22 (to be published in 1976).
3. Wells, J.M., "Evaluation of Inconel X750 Weldments for Cryogenic Applications," Adv. in Cry. Engrg., V. 22 (to be published in 1976).
4. Logsdon, W.A., Wells, J.M., and Kossowsky, R., "Fracture Mechanics Properties of Austenitic Stainless Steels for Advanced Cryogenic Applications," Proc. of the Second Int. Conf. on Mechanical Behavior of Materials, Boston, MA, August 1976, pp. 1283-1289.

The first three papers were presented at the 1975 ICMC Conference at Kingston, Ontario and have been submitted for publication in Vol. 22 of Advances in Cryogenic Engineering.

Several additional technical papers pertaining to aspects of work conducted in this program are planned for presentation at the ICEC/ICMC conference in August 1977 at the University of Colorado in Boulder.

3.0 INTERPRETIVES SUMMARY

The purpose of this section is to provide for the casual as well as the involved reader both a continuing overall summation of the accumulated data and information developed in the Westinghouse program and an overall perspective of the significance of such information relative to the design and fabrication of advanced cryogenic machinery.

3.1 Program Status

A testing and evaluation status summary for the Westinghouse FY74, FY75 and FY76 program efforts are presented in Tables 3-1, 3-2 and 3-3, respectively. All testing and evaluation efforts planned and completed are so indicated in these tables. In addition, samples of several material, processing and fabrication conditions were shipped to Battelle, Columbus and NBS, Boulder for specific heat, thermal expansion and thermal conductivity, magnetic thermal conductivity, and elastic constant measurements, respectively. Such physical property data has been reported separately by these two laboratories and is considered to be particularly useful since it pertains to identical material otherwise characterized and evaluated in the present Ⓦ program.

While the present ARPA/NBS program is now terminating, it should not be inferred that "everything necessary has been done with respect to cryostructural materials for superconducting machinery". On the contrary, the technology area of advanced cryostructural materials evaluation and development is really quite embryonic--i.e., much remains to be done before failure-safe design and operation of such devices can be assured. It is true that considerable progress has been made in the past three years in improving both the materials data base and in understanding of the microstructural relationships with the mechanical and fracture mechanics behavior of selected candidate cryostructural materials. However, one should be aware that future SC machinery prototypes presently in the conceptual design

phase are much larger both in physical size and capacity (e.g., 300 and 1200 MVA).than existing fabricated prototypes of about 5MVA. The materials, processing and fabrication requirements for such larger SC machines are less well developed and yet most probably more severe than previously smaller prototype requirements and hence should be addressed specifically with a continuing materials technology support program similar to the presently terminating ARPA/NBS program.

3.2 Alloy Selection and Utilization

A total of ten different alloys in many different conditions have been evaluated as candidate cryostructural materials during the course of the Westinghouse program. Several of these materials have actually been utilized in earlier prototype SC machinery. Their initial selection for hardware utilization was actually made prior to the technical evaluations made in this program. Fortunately, the results of the present program have substantiated the earlier selection of these specific materials as being suitable (but not necessarily optimal) for their intended design purposes. A more systematic and objective materials selection and design utilization system is required and now appears possible with a continuing interaction between materials technologists and designers.

Several suggestions and comments have been made previously in the course of this program pertaining to the establishment of more specific criteria for selection and utilization of cryostructural materials. An overview of this area is presented in Section 5.1.1 of this report.

3.3 Mechanical and Fracture Mechanics Properties

Mechanical property data from RT to 4K has been obtained from both smooth and notched tensile (K_t = 10) tests for all candidate materials evaluated in this WRL program. Such data are graphically summarized in figures 3-1 through 3-6. Fracture toughness data expressed as either K_{Ic} or $K_{Ic}(J_{Ic})$ evaluated at 4K are graphically summarized in Fig. 3-7. Such data is also summarized in tabular form in Tables 6-1 through 6-10 of this report. In addition, fatigue crack growth rate (FCGR) data for all

materials, conditions and test temperatures evaluated is summarized in Tables 6-11 through 6-13 of this final report. Several summary comments pertaining to this data are appropriate to this section as follows:

1) Copper and Copper Alloys - Both OFHC and PD-135 copper have demonstrated temperature independent yield strength and reduction in area values. Ultimate tensile, notched ultimate, and total elongation values, on the other hand, were found to be inversely proportional to temperature for both materials. The ductility of the age hardenable PD-135 was found to be somewhat lower (yet still relatively high in absolute value) and all the strength levels significantly higher than that for the OFHC copper. The fracture toughness of PD-135 material at 4K was quite good ($\sim$165 MPa $\sqrt{m}$) while that of OFHC copper was found to exceed the measurement capacity of the 1/2TCT specimens used with J_{Ic} validity requirements. No FCGR data was obtained on either alloy.

2) Austenitic Stainless Steels - The yield, ultimate and notched tensile strength of all austenitic stainles alloys evaluated were found to be inversely temperature sensitive, i.e., strength increased with decreasing temperature. The A-286 material was the least temperature sensitive. Reduction in area values generally decreased with decreasing temperature while total elongation values were frequently higher at 77K than at either RT or 4K. Fracture toughness at 4K was highest for the 310S (262 MPa $\sqrt{m}$), and decreased in the following ranking order: Kromarc 58 (216 MPa $\sqrt{m}$), A-286 (180 MPa $\sqrt{m}$); and Pyromet 538 ($\sim$165 MPa $\sqrt{m}$). Interestingly, the Pyromet 538 would rank considerably higher at 77K based upon NBS reported data of K_{Ic} of $\sim$320 MPa $\sqrt{m}$. The decrease in K_{Ic} of 50% for this material from 77K to 4K is associated with the structural instability (i.e., $\gamma \rightarrow$ Md transformation) which occurs in this temperature range. No such structural instabilities were observed for the other three stainless alloys mentioned above in agreement with microstructural stability predictions made in previous report.

3) Nickel Base Superalloys - The nickel base superalloys X750, 718, 706 and LEA were generally inversely temperature sensitive with respect to yield, ultimate and notched tensile strength from RT to 4K. Reduction in area was directly temperature sensitive (i.e., decreased with decreasing temperature) for alloys X750 and 718 but remained relatively high and constant for alloy 706. Total elongation values for these alloys did not follow any systematic trend over this temperature range. Considerable variations in ductility were observed in these alloy types. Fracture toughness values at 4K also demonstrated considerable variation, both between different heats of the same alloy (e.g., $K_{Ic}(J_{Ic})$ of 239 MPa $\sqrt{m}$ for 40XX versus 76.6 MPa $\sqrt{m}$ for Code 31XX, both IN-X750 material), and between different alloys (e.g., $K_{Ic}(J_{Ic})$ of 168 MPa $\sqrt{m}$ for Code 71XX, IN706 versus 80.3 MPa $\sqrt{m}$ for Code 64XX, IN718 material). A direct temperature sensitivity of fracture toughness was indicated by the IN-LEA and the IN-X750 (Code 30XX) materials, whereas an inverse temperature sensitivity of fracture toughness was observed with IN706 and IN718 material. The fatigue crack growth rate data for these nickel base superalloys was significantly lower at 4K than at RT.

3.4 Effects of Processing

The effects of the various selected processing operations included in the WRL program on the yield and tensile strength and on the fracture toughness properties for several program alloys are summarized graphically in Figs. 3-8 and 3-9 of this report. An overview discussion of some of the more significant observations regarding processing effects is presented in Section 5.2.1 of this report.

3.5 Effects of Metals Joining

The effects of various selected metals joining processes including both brazements and fusion weldments on the yield strength and ultimate tensile strength are summarized graphically in Figs. 3-10 and 3-11. The fracture locations of the transverse composite weld tensile

specimens for the various alloys are indicated. Figure 3-12 presents a graphical comparison of the fracture toughness ratio of joint/unwelded base metal at 4K. It is obvious from Fig. 3-12 that the fracture toughness of weldments may be either superior, equal to or inferior to the unwelded base metal condition at 4K depending upon the materials and welding process involved. A summary overview discussion concerning the more significant observations pertaining to effects of metals joining conditions is presented in Section 5.3.1.

3.6 Microstructural and Fractographic Analysis

Microstructural and fractographic analyses on selected material conditions and fracture surfaces has provided a practical means of both characterizing the cause and mode of fracture and of correlating the microstructural features with mechanical and fracture mechanics test data to elucidate the effects of processing and metals joining relative to base metal behavior. Several examples of the usefulness of these analytical techniques to the current WRL program are described in Section 7.4 of this report.

3.7 Magnetic Behavior and Electrical Resistivity

Magnetic behavior and electrical resistivity of several alloy conditions has been evaluated in the temperature range of RT to 4K. An overview discussion of the significance of the results in this portion of the WRL is included in Section 8 of the present report.

TABLE 3-1 STRUCTURAL MATERIALS FOR CRYOGENIC APPLICATIONS

FY74 ⊛ Program Status As Of March 10, 1975

Material Code	Condition	Chem. Analy.	Metallography (1)	Metallography (2)	Physical Prop. Mag.	Physical Prop. Res.	Processing	Joining	Tensile R	Tensile N	Tensile H	Notched Tensile R	Notched Tensile N	Notched Tensile H	KIC R	KIC N	KIC H	J_{IC} (3) R	J_{IC} (3) H	FCGR R	FCGR N	FCGR H	Fractography (4) R	Fractography (4) N	Fractography (4) H
OFHC-Cu																									
10XX	A R	/1	2/1	1		1			1/1	1/1	1/1	1/1	1/1	1/1	1/2	1/2					/2	/3	1/1	3/3	3/3
11XX	S R		2/1	1			1/1		1/1	1/1	1/1	1/1	1/1	1/1	•/2	1/2					/2	/3			3/3
12XX	G M A W		3/2	1		1		3/2	2/2	2/2	2/2	2/1	2/2	2/2	•/2	→/2						/2	/1	/1	3/3
13XX	B		3/2	2				2/2	1/2	1/2	1/2	1/1	1/2	1/2	/2	→/2		4					/1	/1	2/2
14XX ◇	S		3/2	2				2/2	/2	/2	/2	/1	/2	/2	/2	/2							/1	/1	2/2
AISI 310S																									
20XX	S T Q	□/1	2/2	1	2/1	2/1	1/1		1/1	3/2	4/2	1/1	1/2	1/2	•/1	2/2	2/3	4		⊛/1	1/2	4/3	1/2	1/3	3/3
21XX	S T F C		1/1	1		1	1/1		1/1	1/2	2/2	1/1	1/2	1/2	•/1	2/2	2/3	5		⊛/1	2/2	2/3	1/2	1/3	3/3
22XX	S M W	□	2/2		1/1	1/1	2/2	2/2	2/1	2/2	2/2	2/1	2/2	2/2	•/2	→/3		6			2/2	2/2	/1	/3	3/3
Inconel X750																									
30XX	S T	2/1	3/2	3	2/2	2/2	2/2		1/1	2/2	2/2	1/1	2/2	2/2	→/1	4/2	2/3	5	4	2/2	/2	2/3	2/2	2/3	4/4
31XX	S T D A		3/2	3	2/1	2/1	2/2		1/1	2/2	2/2	1/1	2/2	2/2	•/1	4/2	2/3		5	2/2	/2	4/3	2/2	2/3	2/3
32XX	S T/E B W		2/3	1			3/3	3/3	1/1	1/2	1/2	1/1	1/2	1/2	• /2	→/2			2		1/1	2/1	1/1	1/2	2/2
33XX	S T D A/E B W		2/3	1			3/3	3/3	1/1	1/2	1/2	1/1	1/2	1/2	• /2	→/2			2		1/1	1/1	1	1	2/2
34XX	E B W/S T D A		2/3				3/3	3/3	1/1	1/2	1/2	1/1	1/2	1/2	• /2	→/2			3		1/2	2/2	1	1	2/2
35XX	S T/G T W		3/3	1			3/3	4/3	1/1	1/2	1/2	1/1	1/2	1/2	•/2	→/2			6		1/1	2/2	1	1	2/2
36XX	S T D A/G T W		3/3	1			3/3	4/3	1/1	1/2	1/2	1/1	1/2	1/2	•/2	→/2			5		1/1	2/2	1	1	2/2
37XX	G T W/S T D A		3/3				3/3	3/3	1/1	1/2	1/2	1/1	1/2	1/2	•/2	→/2			5		1/1	2/2	1	1	2/2
38XX	B		2/2	2			2/2	2/2	2/2	2/2	2/2	1/1	1/2	1/2	1 2/2	2/2							1	2/2	2/2
40XX	M P 2/S T D A	◙/1	2/2	3			2/2		1/1	2/2	2/2	1/1	2/2	2/2	• /2	→/2		6		1	1	1	1	1	2/2
50XX	M P 3/S T D A	◙/1	2/2	3			2/2		1/1	2/2	2/2	1/1	2/2	2/2	• /2	→/2		7		1	1	1	1	1	2/2
60XX	H I P	2/2	2/2	3			5/2		2/1	2/2	2/2	2/1	2/2	2/2	• /2	→/2		7			2/2	2/2	1/1	2/2	2/2
61XX	H I P/S T D A	1	2/2	3	1	1	3/2		2/1	2/2	2/2	2/1	2/2	2/2	• /2	→/2		6			2/2	2/2	1	1	1/2
Kromarc 58																									
80XX	S T Q	1/1	1/2	2	1/1	1/1	2/2		1/1	2/2	2/2	1/1	2/2	2/2	•/2	→/3		5		1/2	1/2	2/3	1/2	1/3	2/3
81XX	C W		2/2	2	1/1	1/1	2/2		1/1	2/2	2/2	1/1	2/2	2/2	• /2	→/3		5		1/2	1/2	2/3	1/2	1/3	2/3
82XX	G T W	1/1	4/2	2	1	1	2/2	2/2	1/1	2/2	2/2	2/1	2/2	2/2	/2	→/3		6			2/2	2/2	1/1	1/3	2/3
83XX	C W/G T W		1/2		1	1	1/1	1/1	2/1	2/2	2/2	2/1	2/2	2/2	/2	→/3		6					1	1	2/2
84XX	G T W/C W		1/2		1	1	1/1	1/1	2/1	2/2	2/2	2/1	2/2	2/2	/2	→/2		6							2/2
85XX	G T W/C W/A N		10/2				3/1	1/1	1/1	1/1	1/1	/1	/2	/2	/2	→/2		4							2/2
86XX	GT W/C W/A N						1	1/1	1/1	1/1	1/1							5							2/2

Notes: 1 Optical Microscopy

2 Replicate and Transmission Electron Microscopy, X-Ray Dispersive and Microprobe Analysis to be Incorporated as Required

3 Elastic-Plastic (J_{IC}) Testing and Analysis Techniques to be Incorporated Where Linear-Elastic (K_{IC}) Data is Non-Valid

4 Macro-and Microfractographic (SEM) Examination Schedule to be Adjusted in Response to Exhibition of Unusual Material Behavior

• Available Specimen Size Invalid for Meaningful K_{IC} Interpretation - Test Eliminated

□ Certified Chemical Analysis from Supplier

◙ Ditto-Additional Interstitial Analysis Completed at ⊛

→ J_{IC} Tests Substituted for K_{IC}

◇ Solder Joints Not Suitable for Mechanical Tests, Tests Eliminated

TABLE 3-2—STRUCTURAL MATERIALS FOR CRYOGENIC APPLICATIONS

FY75 Program Status as of April 9, 1976

Material Code	Condition	Chem. Analysis	Metallography (1)	Metallography (2)	Physical Mag.	Prop.(3) Res.	Processing Operations	Plates Joined	Tensile R	Tensile N	Tensile H	Notched Tensile R	Notched Tensile N	Notched Tensile H	K_{IC} (J_{IC}) R	K_{IC} (J_{IC}) N	K_{IC} (J_{IC}) H	FCGR R	FCGR N	FCGR H	Fractography R	Fractography N	Fractography H
PD135 Copper																							
15XX	EXT/PHT	■	2/2		1/1	2/2	2/2		2/2	2/2	2/2	2/2	2/2	2/2			6/6		/2	/2	1/1	1/2	2/3
Inconel X750 HIP																							
62XX	GTAW/STDA(FZ)	□	2/2		1/1	1/1	2/2	2/2	*/2	*/2	*/2	*/2	*/2	*/2			*/6		*/2		*/1	*/1	*/3
63XX	GTAW/STDA(HAZ)		2/2				2/2	2/2				*/2	*/2	*/2			*/6		*/2		*/1	*/1	*/3
Inconel 718																							
64XX	STDA	■	4/4	4	2/2	1/1	2/1		2/2	2/2	2/2	2/2	2/2	2/2	6		5/6	1	1/2	2/2	1/1	2/2	3/3
65XX	ST/GTAW/STDA(FZ)		3/3	4	1/1	1/1	2/2	3/3	2/2	2/2	2/2	2/2	2/2	2/2		2	2/6	2		2/2	1/1	1/1	3/3
66XX	ST/GTAW/STDA(HAZ)		3/3	4			2/2	3/3				2/2	2/2	2/2		2	2/6	2		1/2	1/1	1/1	2/3
67XX	ST/CW/AN		2/3				2/3		2/2	2/2	2/2	2/2	2/2	2/2			5/6	1	1.	1	2	2	2/2
68XX	ST/CW/AN		2/3				2/3		2/2	2/2	2/2	2/2	2/2	2/2			4/6	1	1	1	2	2	2/2
69XX	ST/CW/AN		2/3				2/3		2/2	2/2	2/2	2/2	2/2	2/2			4/6	1	1	1	2	2	2/2
Inconel 706																							
(EFR) 70XX	STDA	■	4/4	4	1/1	1/1	1/1		2/2	2/2	2/2	2/2	2/2	2/2			5/6	1	2	1/2	1/1	1/1	2/3
(VAR)71XX	STDA	■	4/4	4	1/1	1/1	1/1		2/2	2/2	2/2	2/2	2/2	2/2	7		7/6	1	1	1/2	1/1	1/1	3/3
(VAR) 72XX	ST/GTAW/STDA		3/3	4	1/1	1	2/2	3/3	2/2	2/2	2/2	2/2	2/2	2/2			4/6	2		2/2	1/1	1/1	3/3
INCO LEA																							
73XX	STA	■	3/3	4	1/1	1/1	2/2		2/2	2/2	2/2	2/2	2/2	2/2	5		5/6	1	1/2	1/2	1/1	1/1	2/3
74XX	ST/GTAW/STA		2/2	3	1/1	1	2/2	2/2	*/2	*/2	*/2	*/2	*/2	*/2			*/6			*/2	*/1	*/1	*/3
Kromarc 58																							
87XX	STW/CW/θ*	□	1/1				2/2		2/2	2/2	2/2	2/2	2/2	2/2			6/6	1	1	1/2	1/1	1/1	1/3

Notes: (1) Standard optical microscopy
(2) Electron microscopy, microprobe & x-ray dispersive analysis incorporated as required
■ Certified chem. analysis from supplier, additional interstitial gas analysis by
□ Analysis conducted for this material in FY74 program
(3) Physical property determiniations also conducted on five materials (Fe - 9% Ni, Fe - 68% Ni, Fe - 3% Si, AISI 416SS and ARMCO Fe) requested by NBS
* Fracture mechanic testing and fractographic analysis of these specimens indefinitely postponed

FY 76 Program Status as of April 9, 1976

Material Code	Condition	Chem. Analysis	Metallography (1)	Metallography (2)	Physical Mag.	Prop. Res.	Processing Operations	Plates Joined	Tensile R	Tensile N	Tensile H	Notched Tensile R	Notched Tensile N	Notched Tensile H	K_{IC} (J_{IC}) R	K_{IC} (J_{IC}) N	K_{IC} (J_{IC}) H	FCGR R	FCGR N	FCGR H	Fractography R	Fractography N	Fractography H
A-286																							
90XX	STQA	■	6		2/2		1/1		2/2	2/2	2/2				5		5	1	1	1	2/2	2/2	2/2
91XX	STQ/GTAW	■	2/2				2/2	7/5	2/2	2/2	2/2	/2	/2	/2			5/6	1/1	1/1	1/1	2/2	2/2	2/2
Pyromet 538 (21-6-9 SS)																							
92XX	STQ	■	5/5	2	6/4		2/2		2/1	2/1	2/1	/1	/1	/1		/5					1/2	1/2	2/2
93XX	STQ/GTAW	■	2/2	2	6/2		2/2	2/2	2/2	2/2	2/2	2/2	2/2	2/2			5/6	1/1	1/1	2/1	2/2	2/2	2/2
94XX	STQ/SMAW	■	2/2	2	4/2		2/2	2/2	2/2	2/2	2/2	2/2	2/2	2/2			5/6	1/1	1/1	1/1	2/2	2/2	2/2

Notes: (1) Standard optical microscopy
(2) Electron microscopy, microprobe, x-ray dispersive analysis incorporated as required
■ Certified chemical analysis from supplier, additional interstitial gas analysis by
■ Chemical analysis conducted by

Curve 679865-B

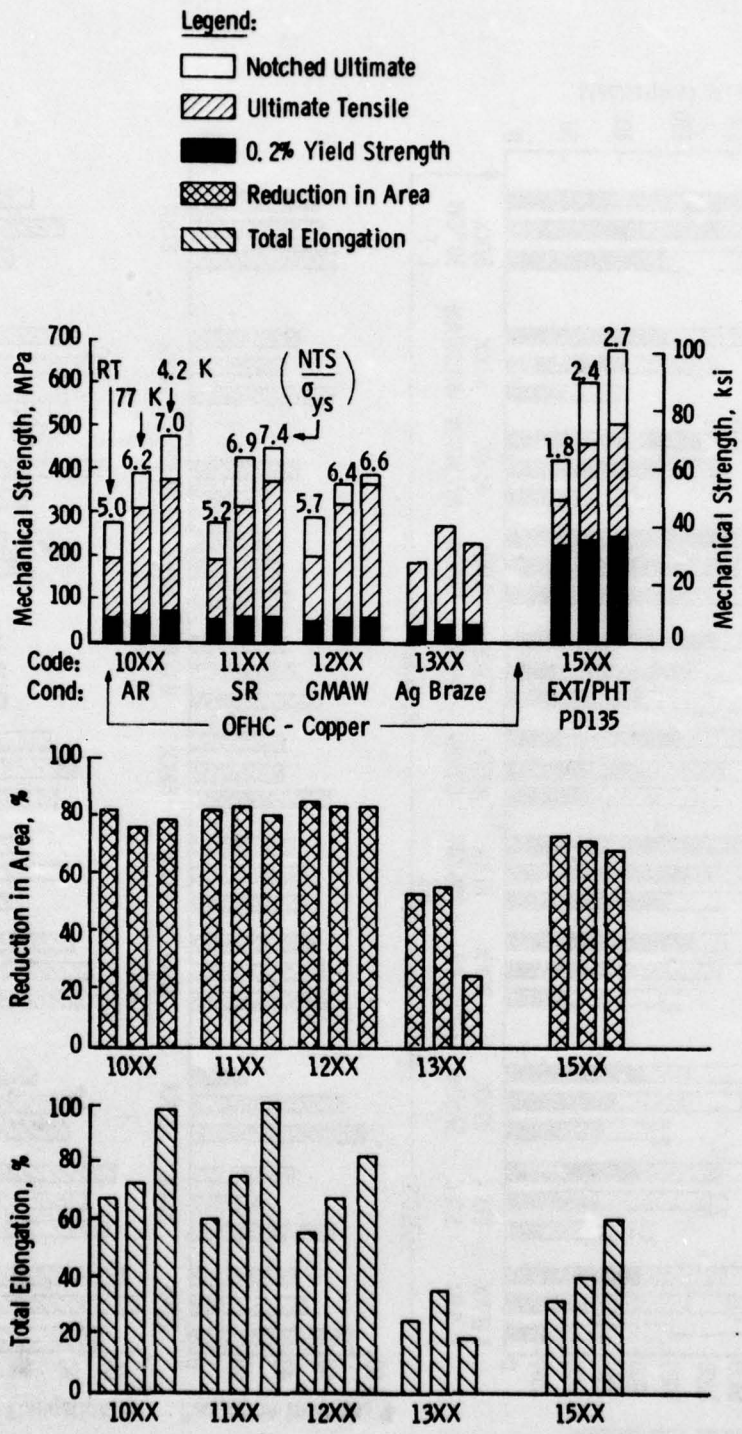


Fig. 3-1—Summary comparison of mechanical strength and ductility values for copper alloys including processing and fabricated joints at RT, 77K, and 4.2 K

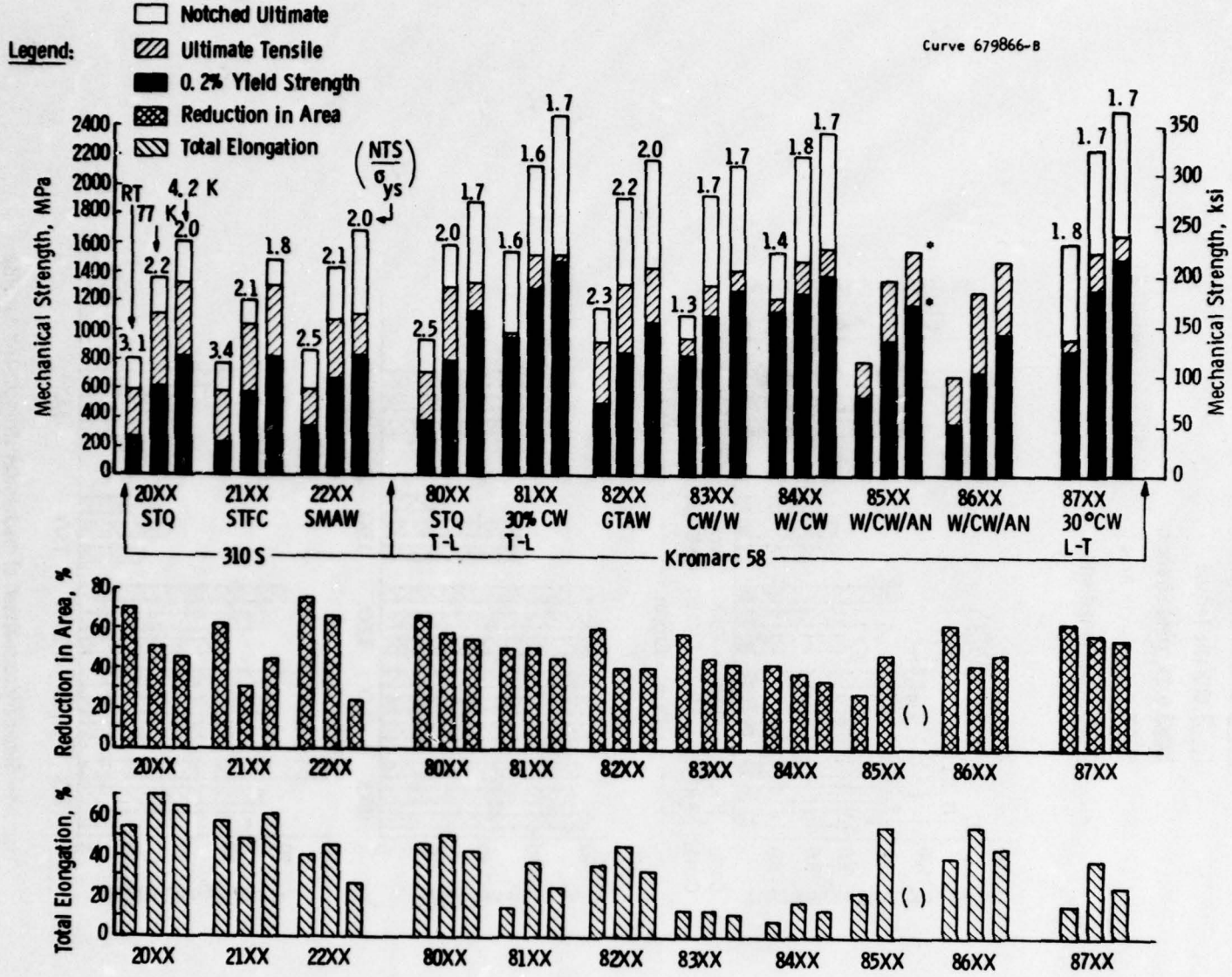


Fig. 3-2— Summary comparison of mechanical strength and ductility values for AISI 310 S and Kromarc 58 stainless steels including processing and welded joints at RT, 77 K and 4.2 K

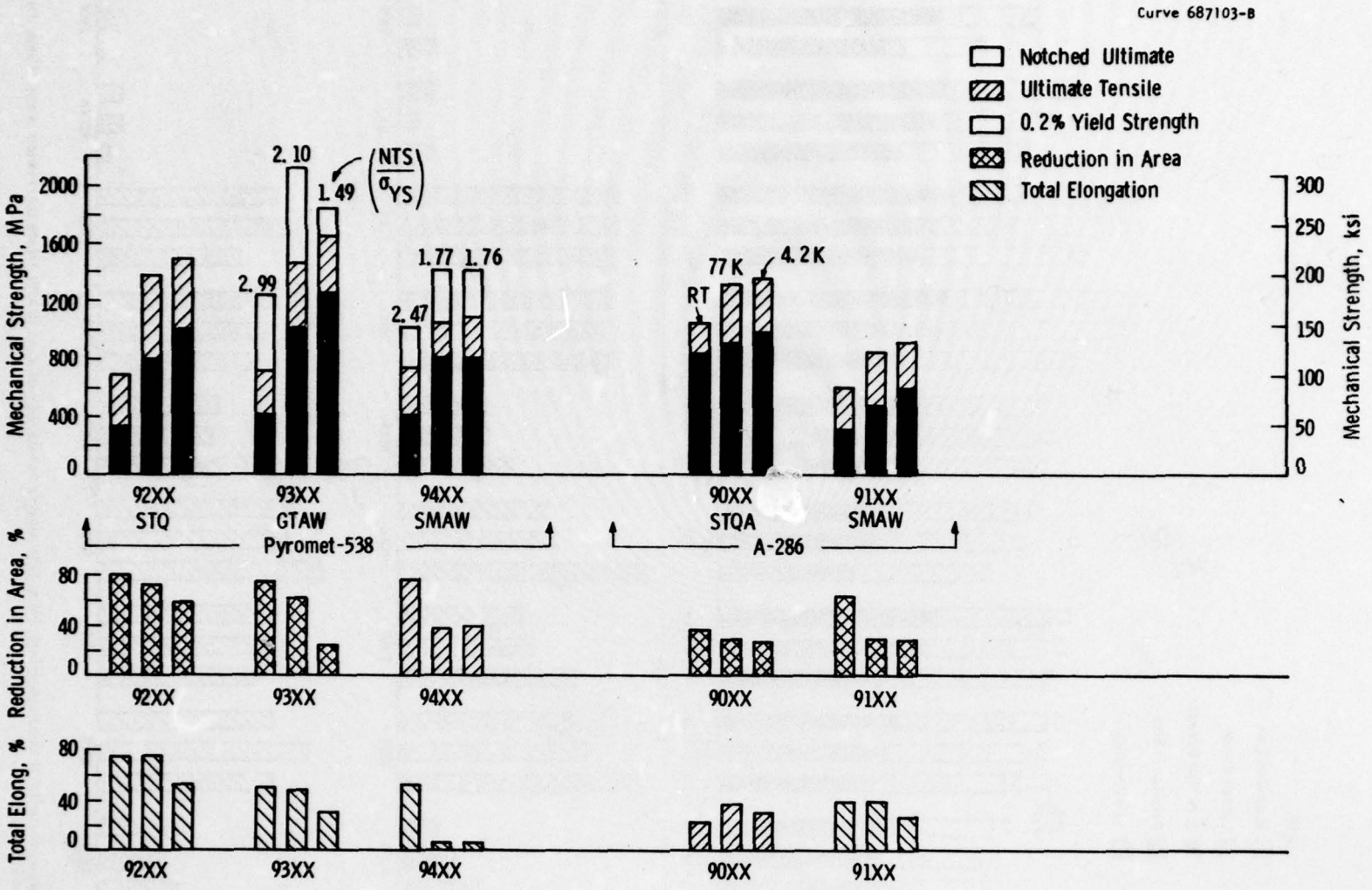


Fig. 3-3 — Summary comparison of mechanical strength and ductility values for Pyromet-538 (21Cr-6Ni-9Mn) and A-286 stainless steels including base metal and weldments at RT, 77 K and 4.2 K

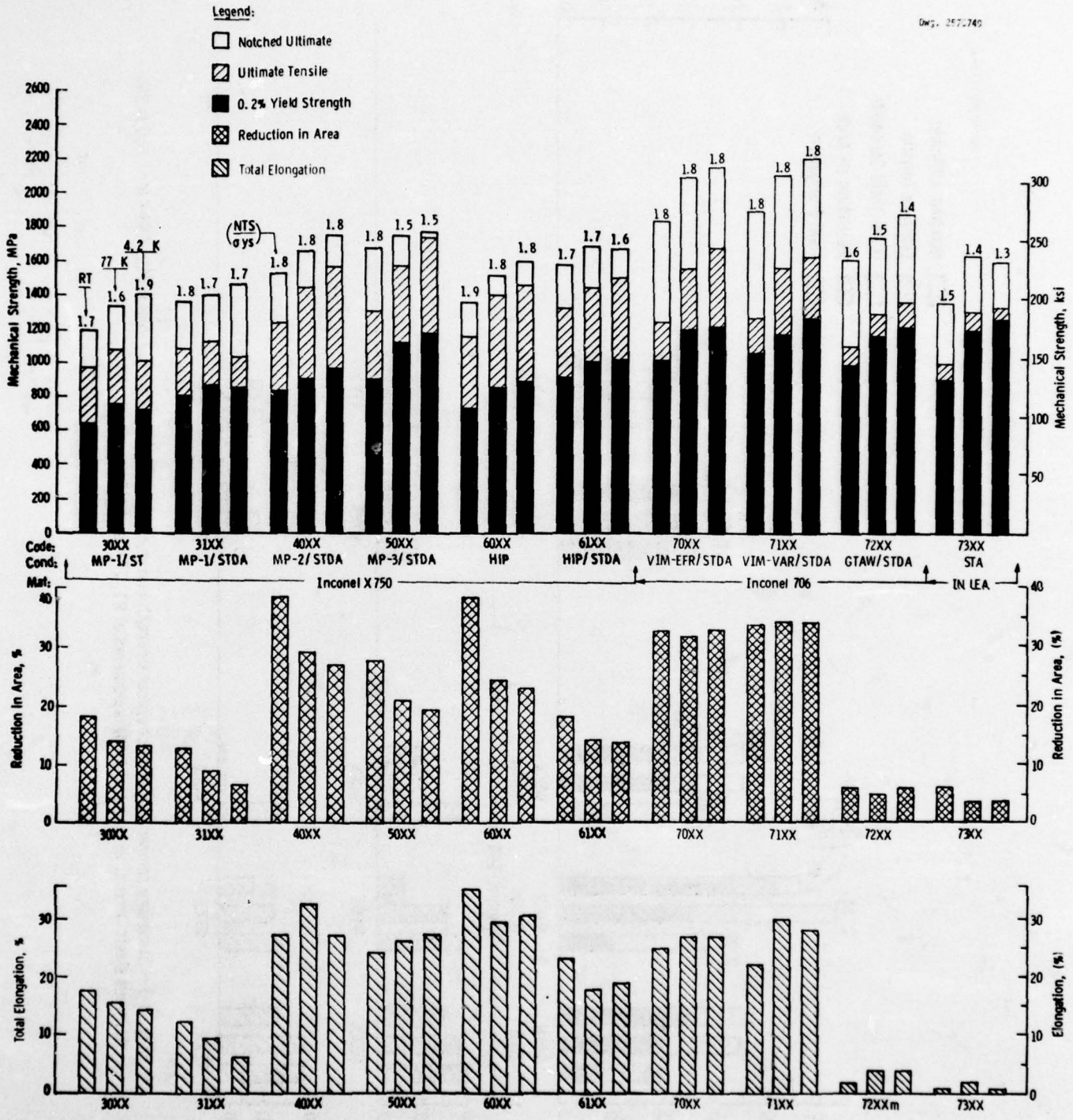


Fig. 3-4 – Summary comparison of mechanical strength and ductility values for nickel based superalloys IN X750, 706 and LEA in various processed conditions at RT, 77K, and 4.2K

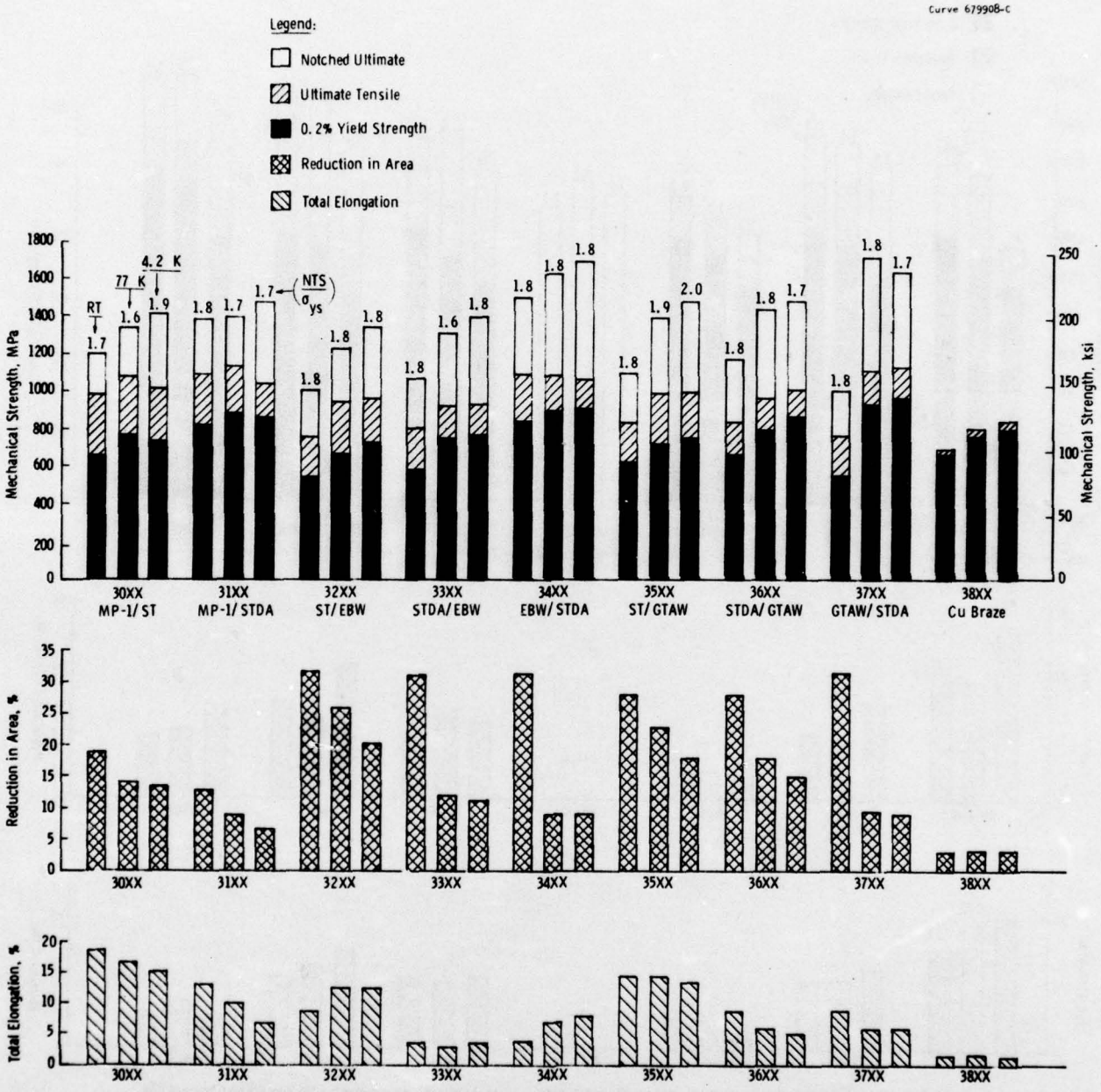


Fig. 3-5 —Summary comparison of mechanical strength and ductility values for Inconel X 750 base metal, electron beam and GTA weldments and copper brazement at RT, 77 K and 4. 2K

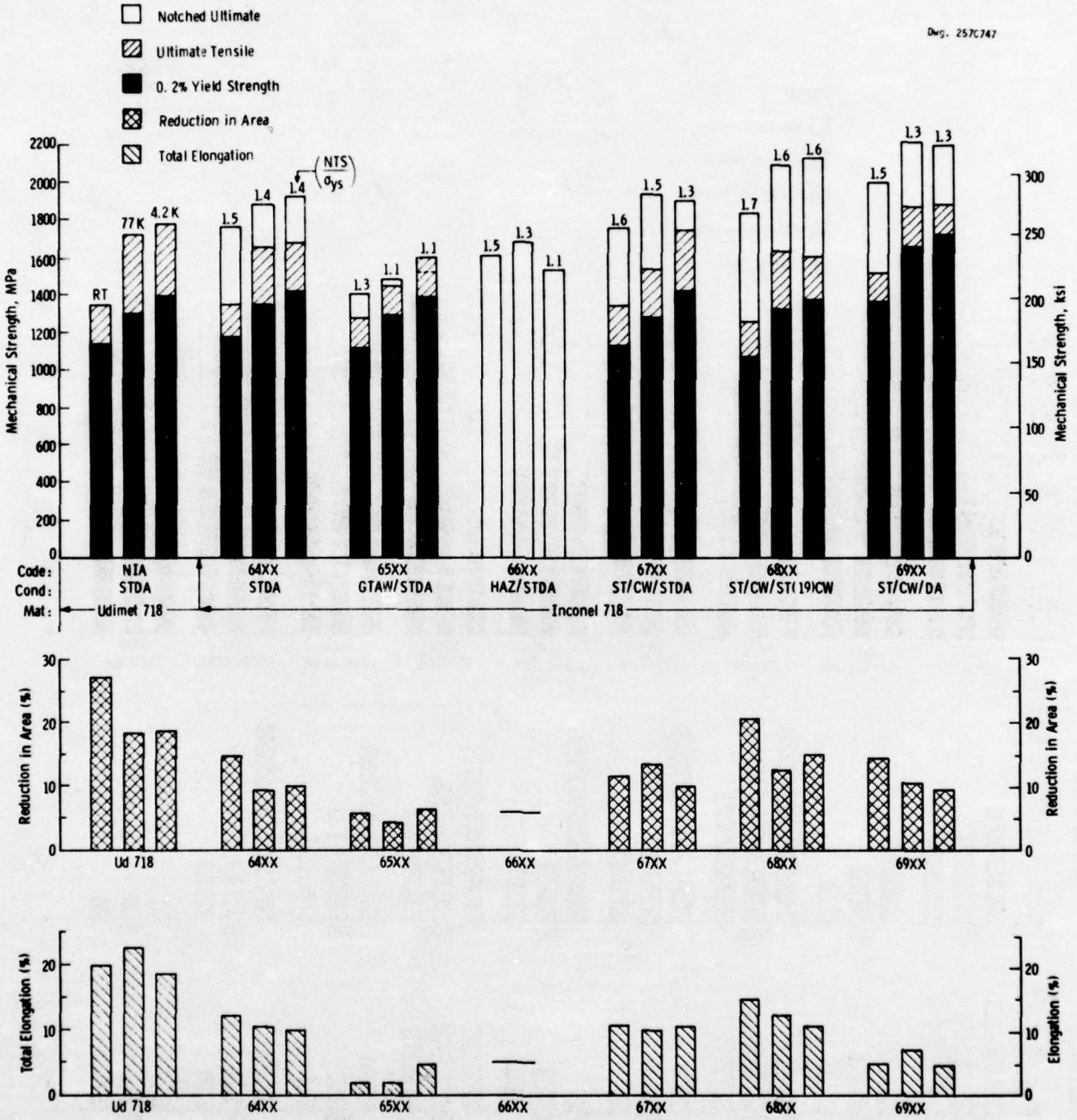


Fig. 3-6—Summary comparison of mechanical strength and ductility values for nickel base superalloys Udimet 718 and Inconel 718 in various processed and fabricated conditions at RT, 77K and 4.2K

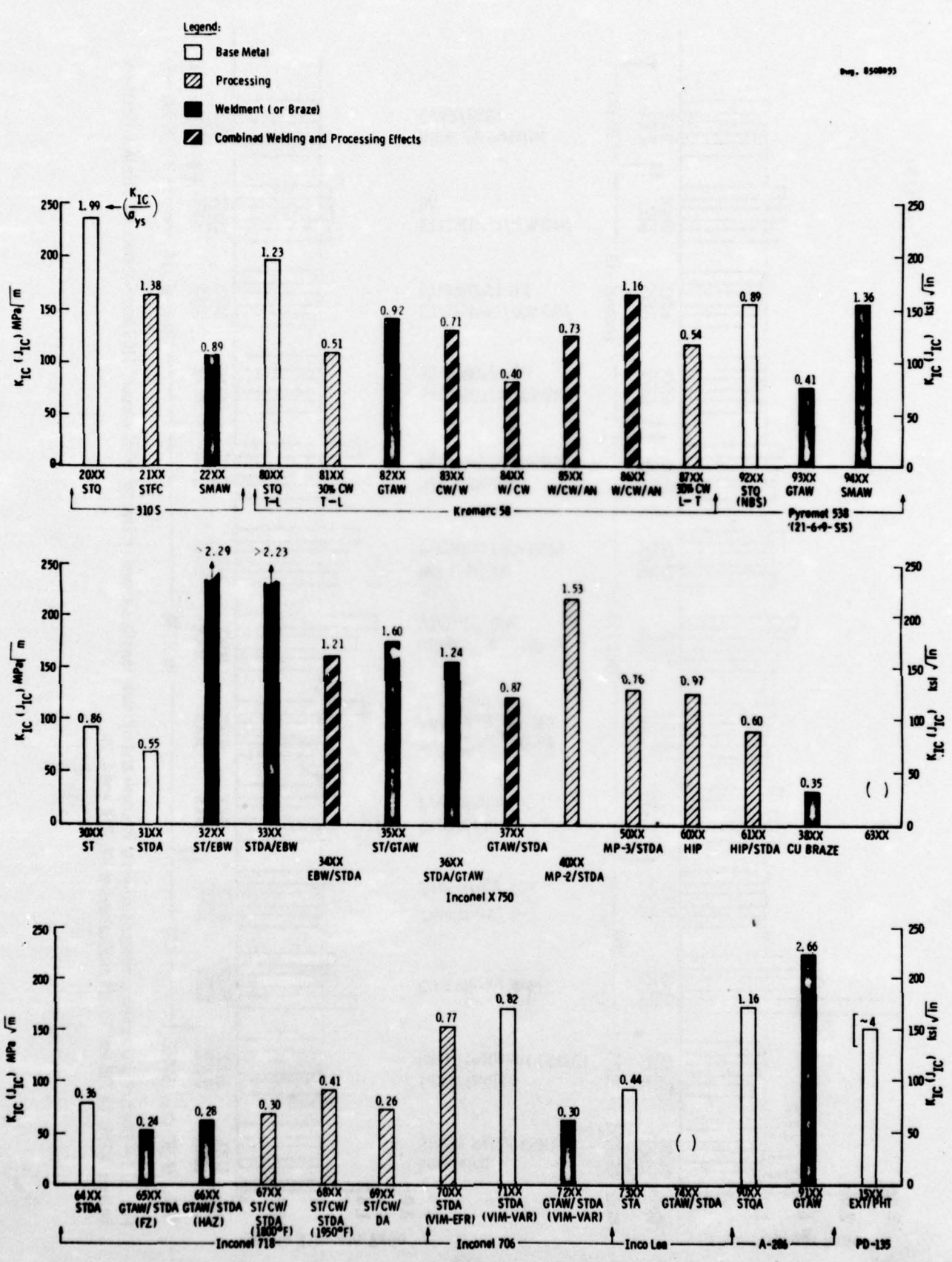


Fig. 3-7—Summary comparison of fracture toughness values at 4.2 K for 310S, Kromarc 58, Inconel X750, Inconel 718, Inconel 706, INCO LEA, and A-286 materials including effects of processing and metals joining

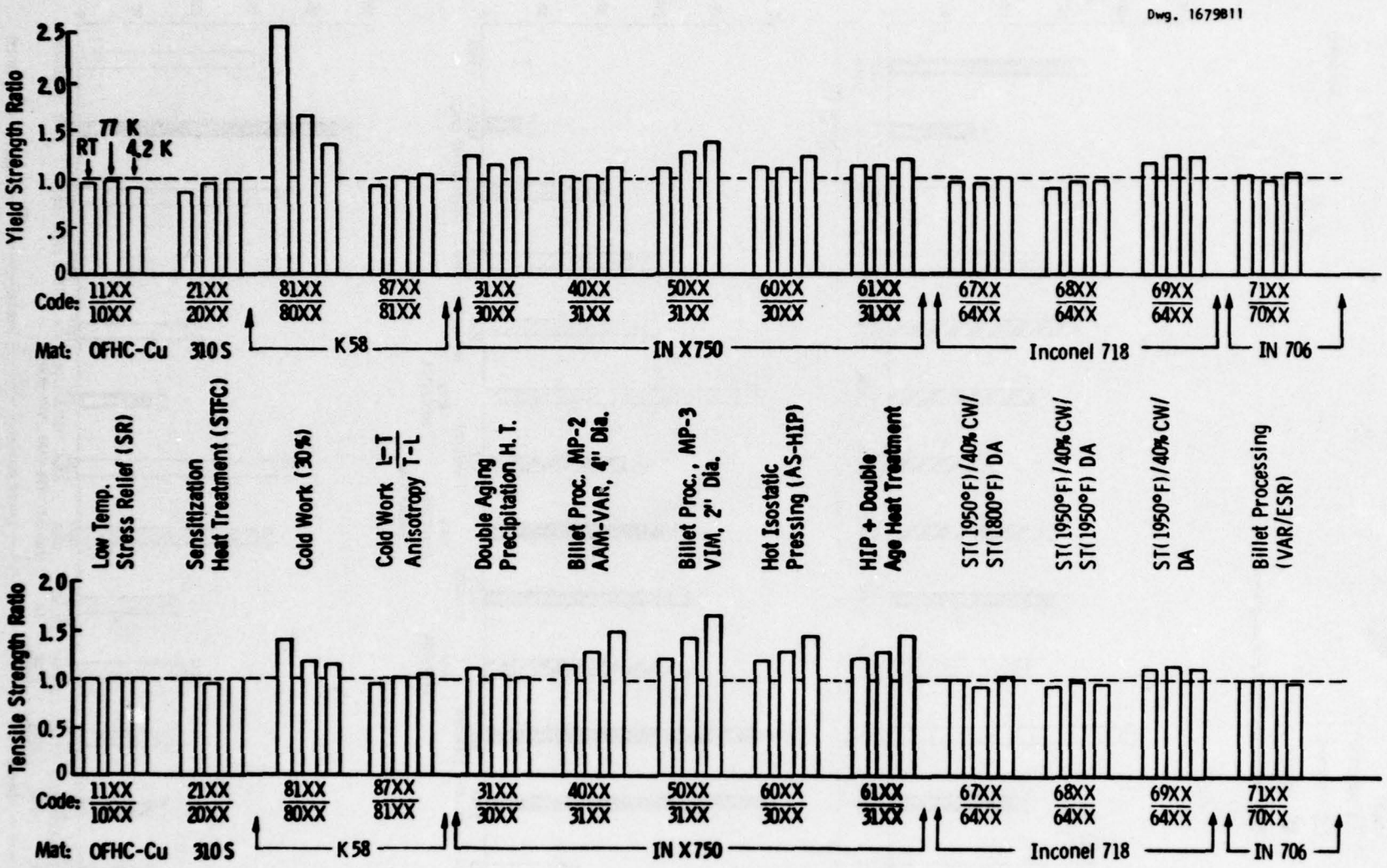


Fig. 3.8 — Effect of processing conditions on yield strength and ultimate tensile strength ratios for OFHC copper, 310S and Kromarc 58 stainless steels and Inconel X750, In 718 and In 706 superalloys at RT, 77K and 4.2K.

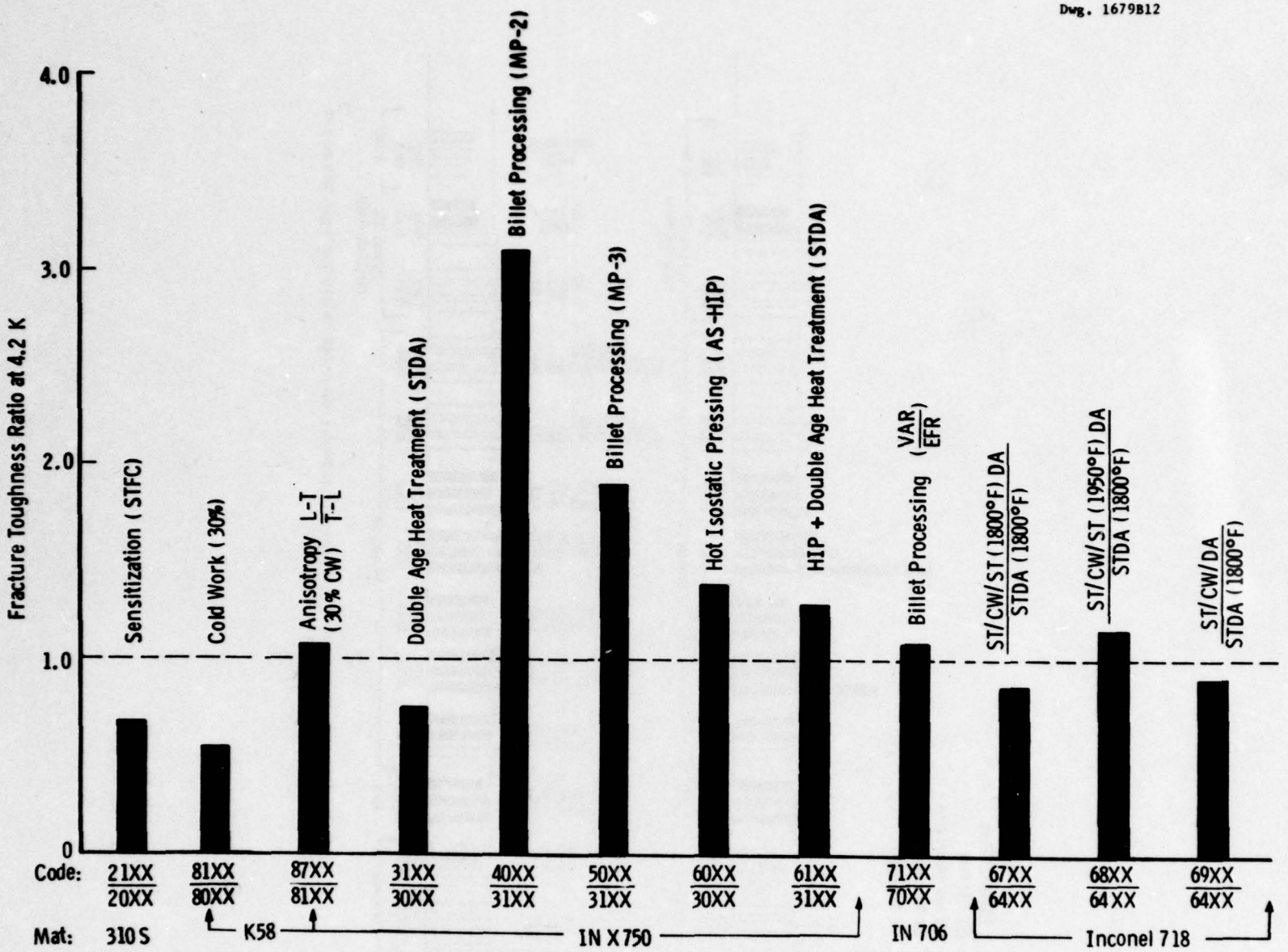


Fig. 3-9—Effect of processing conditions on fracture toughness ratio for 310S, Kromarc 58, Inconel X750, and Inconel 718 at 4.2K

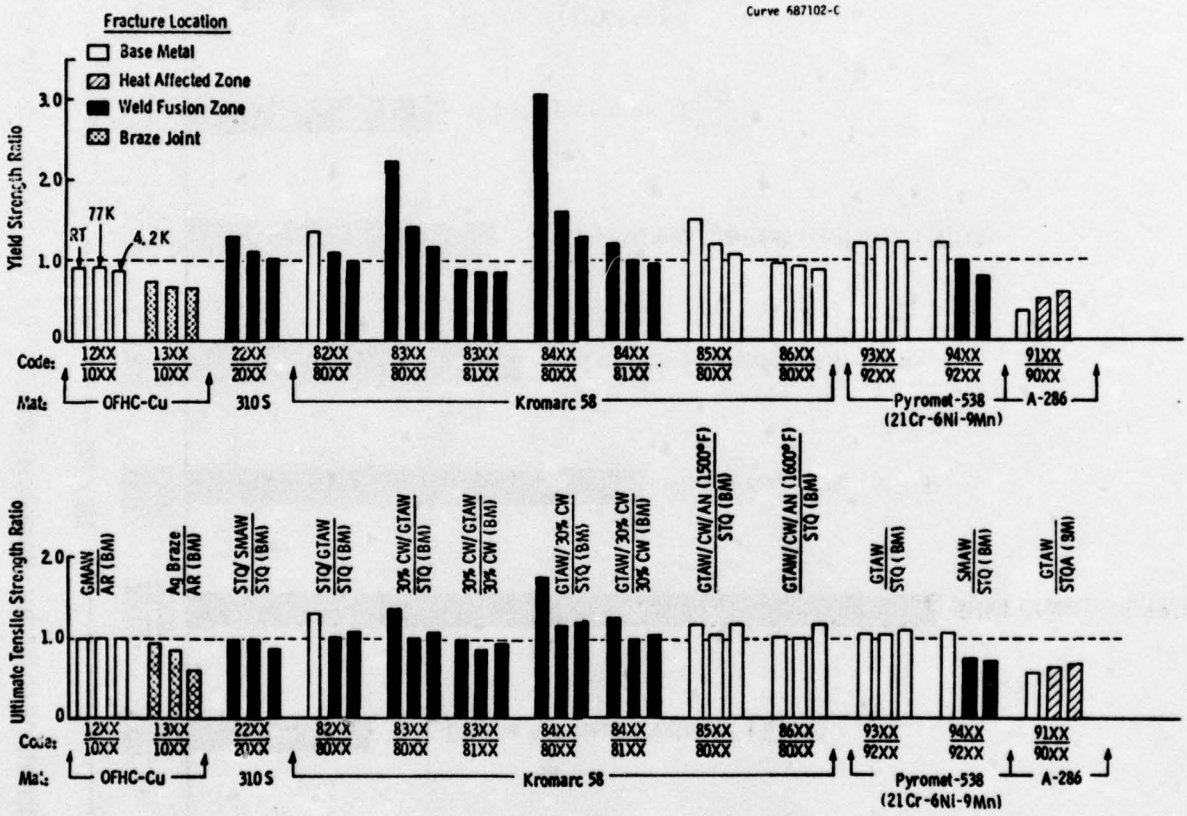


Fig. 3-10 – Effect of metals joining conditions on yield strength and ultimate tensile strength ratios for OFHC copper, 310S and K-58, Pyromet-538 and A-286 stainless steel at RT, 77 K and 4.2 K

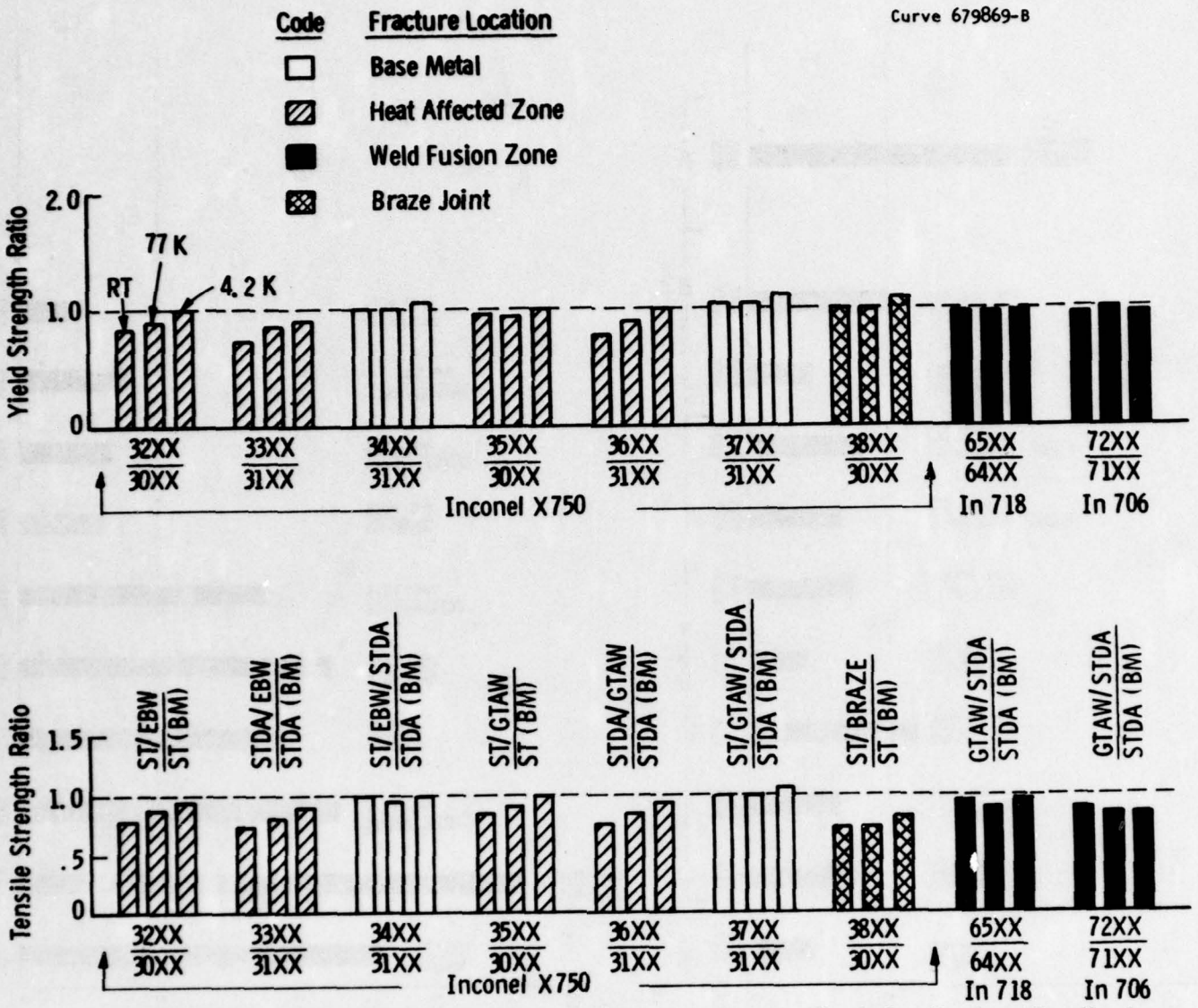


Fig. 3-11 – Effect of metals joining conditions on yield strength and ultimate tensile strength ratios for Inconel X750, Inconel 718 and Inconel 706 at RT, 77K and 4.2K

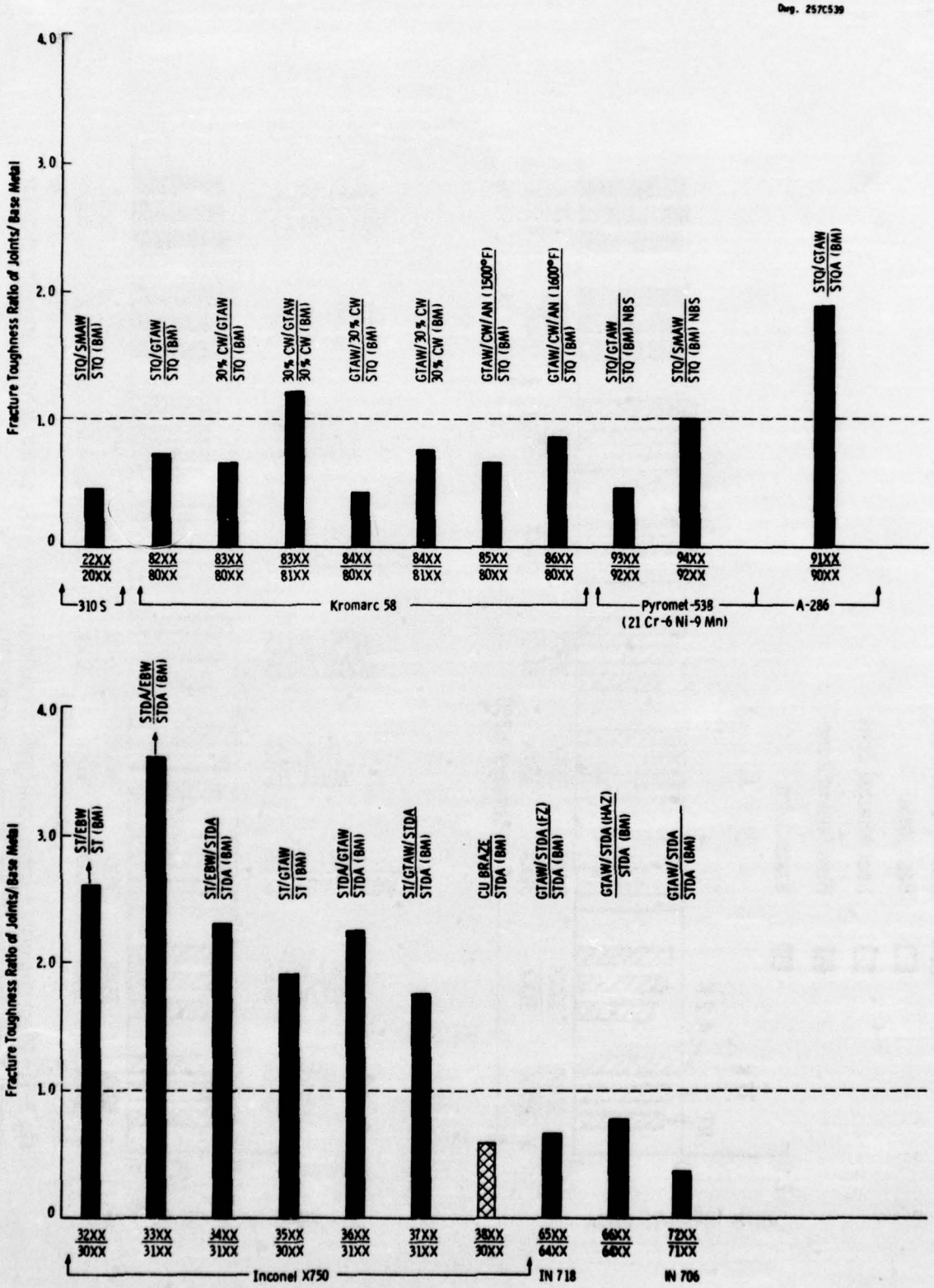


Fig. 3-12 – Effect of metals joining conditions fracture toughness ratio for 310 S, Kromarc-58, Pyromet-538 and A-286 stainless steels (Top) and IN X750, IN 718 and IN 706 (Bottom) at 4.2 K

4.0 WESTINGHOUSE PROGRAM DESCRIPTION

Interest in the engineering application of superconducting field windings in advanced cryogenic structures and devices has stimulated renewed interest in the mechanical and physical behavior of cryogenic structural support materials. Examples of such advanced cryogenic application areas include such prototype devices as superconducting motors and generators and large superconducting magnets for MHD and Tokomak and Mirror Type fusion power devices. The prior existing data base for structural materials in such applications was assessed as inadequate for material selection and utilization in a high reliability design.

This program represents the active participation of the Research Laboratories of the Westinghouse Electric Corporation under Contract CST-8304 in a comprehensive overall program for cryogenic structural materials for s.c. machinery monitored by the Cryogenics Division of the National Bureau of Standards. The overall program is sponsored by the Advanced Research Projects Agency (ARPA) of the Department of Defense. An overall outline for the Westinghouse portion of the ARPA-NBS program is shown schematically in Fig. 4-1. The principal personnel involved are listed in Figs. 4-2 according to their respective functional program responsibility areas.

A brief summation of the candidate materials evaluated, the processing considerations and the metals joining considerations included in each of the three years of the Westinghouse Program is presented below.

4.1 FY 74 Program Summation

- Candidate Materials Evaluated:

  OFHC Copper
  AISI 310S
  Kromarc 58
  Inconel X750

- Processing Considerations:

  Sensitization (STFC) in AISI 310S
  Melting Practice and Mill Processing in IN X750
  Hot Isostatic Pressed IN X750
  Cold Working in Kromarc 58

- Metals Joining Considerations:

  Gas Metal Arc Weldments in OFHC Copper
  Silver Brazements in OFHC Copper
  Solder joints in OFHC Copper
  Shielded Metal Arc Weldments in AISI 310S
  Gas Tungsten Arc Weldments in Kromarc 58
  Electron Beam and Gas Tungsten Arc Weldments in
  Inconel X750 with pre- and post-weld heat treatments.

4.2 FY 75 Program Summation

- Candidate Materials Evaluated:

  PD 135 Copper Alloy
  Inco Low Expansion Alloy
  Inconel 706
  Inconel 718

- Processing Considerations:

  Melting Practice in IN 706 (ESR vs VAR)
  Comparison of Inconel vs Udimet 718 Alloy
  Anisotropic CW texture in Kromarc 58

- Metals Joining Considerations:

  Copper Brazement in Inconel X750
  Gas Tungsten Arc Weldments in HIP X750
  Gas Tungsten Arc Weldments in INCO LEA
  Gas Tungsten Arc Weldments in IN 706
  Gas Tungsten Arc Weldments in IN 718 (FZ and HAZ)

4.3 FY 76 Program Summation

- Candidate Materials Evaluated:

  Pyromet 538 (21-6-9)
  A-286

- Processing Considerations:

  Plate fabrication from Pyromet 538 billet stock
  Cold working and recrystallization in IN 718
  Comparison of Armco versus Cameron Iron A-286 alloy
  Evaluation of predictive expressions for martensite formation in austenitic stainless steels

- Metals Joining Considerations:

  Evaluation of predictive expressions for delta ferrite formation in austenitic stainless steel weldments
  Gas Tungsten Arc Weldments in Pyromet 538
  Shielded Metal Arc Weldments in Pyromet 538
  Gas Tungsten Arc Weldments in A-286
  Varestraint weldability testing for microfissuring (hot cracking) in various austenitic stainless steel and nickel-base superalloys.

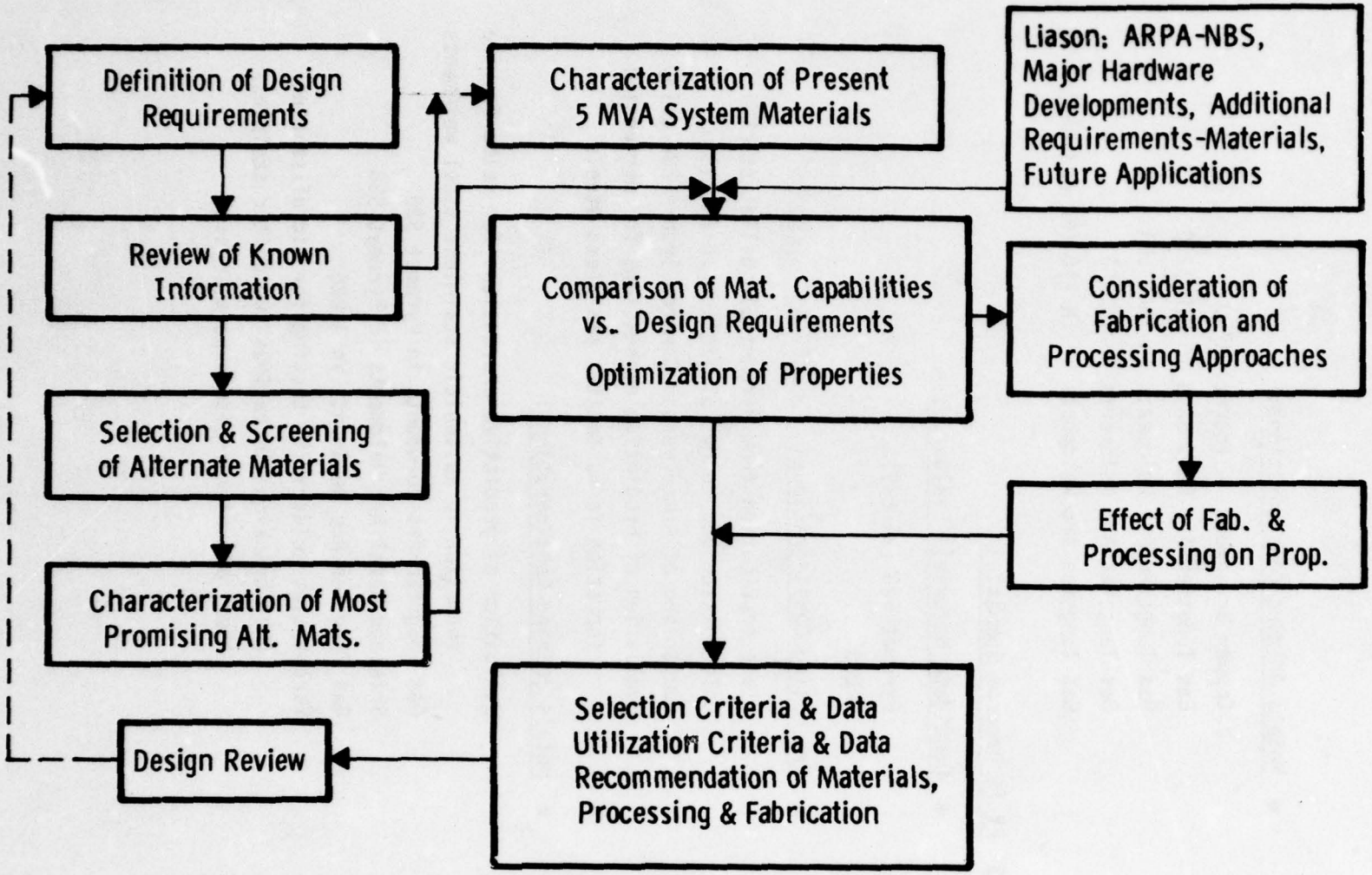


Fig. 4-1ⓦ Program Outline – Structural Materials for Cryogenic Applications

EVALUATION OF CRYOGENIC STRUCTURAL MATERIALS, NBS CONTRACT 8304

Functions	Task I Basic Characterization	Task II Processing Effects	Task III Joint Behavior
Metallurgy, Processing, Joining	•	•	•
Fracture Mechanics	•	•	•
Fractographic & Micro-Structural Analysis	•	•	•
Magnetic Properties	•	•	•

Westinghouse Program Organization

Management

Program Manager - J. M. Wells
Advisors - G. G. Lessmann
E. T. Wessel

Principal Investigators

Materials, Processing, Fabrication - J. M. Wells
Fracture Mechanics - W. A. Logsdon
Microstructural Analysis - R. Kossowsky
Magnetic Properties - M. R. Daniel

Fig. 4-2 Westinghouse Program Organization - FY76

5.0 GENERAL CRYOGENIC STRUCTURAL MATERIALS SELECTION/ PROCESSING/FABRICATION CONSIDERATIONS

The Westinghouse portion of the overall ARPA/NBS program entitled Materials Research for Superconducting Machinery is concerned with the selection, characterization and evaluation of several metal alloys in various processed and fabricated conditions for utilization as cryostructural (cryogenic structural) materials. A listing of several potential candidate cryostructural alloys for advanced cryogenic applications compiled by the present author (JMW) is included as Table 5-1. Those candidate alloys which have been investigated in this Westinghouse program for FY74, FY75 and FY76 are identified in Table 5-1 by a single, double or triple asterisk respectively. Documentation data for these Ⓦ program alloys including:

- Chemical composition
- Supplier source, heat number and product form
- Processing and heat treatment schedules
- Material hardness and ASTM grain size

have been included in Section 5 of the five prior semi-annual technical reports in this series[1-5]. A summary compilation of this program material documentation data is included herein in Tables 5-2 through 5-4. The material and test specimen identification code system employed throughout this program is presented in Table 5-5.

5.1 Materials Selection and Utilization Considerations

5.1.1 Overview

A significant objective of this program is to help designers of SC systems establish more specific criteria for selection and utilization of cryostructural materials. The practical need for such materials design criteria is obvious, but their explicit definition has been elusive, namely due to the following factors:

- The design of advanced superconducting machinery and devices is a relatively new and embryonic field. System performance criteria are still being defined in many cases and inadequate design effort has been expended on specific material property requirements.
- Considerable design differences exist between various SC devices of the same type as well as between different device categories such as between SC generators and large SC field magnets for fusion power. In addition, a given device or machine may contain several different component parts, any or all of which may have quite different specific materials design criteria.
- The detailed design of specific SC machines or devices is a difficult task aggravated by the extremely low temperature and high magnetic field conditions of service.
- Future systems under consideration are exotic, complicated and massive engineering structures for which design extrapolations from more conventional systems (i.e., nonsuperconducting) are often neither appropriate nor practical.

- Existing prototypes of SC machinery are relatively small in both physical size and capacity. They have been operated successfully but are conservatively designed and fabricated and have not been tested to the full extent required to assess lifetime reliability. Later generation prototypes presently in the conceptual design phase are significantly larger in size and capacity as to require appreciable modification of both design requirements and fabrication approaches with concurrent modifications in cryostructural materials selection and utilization criteria.

Thus, while the explicit definition of specific design criteria is elusive, progress has been made in establishing the more significant design considerations associated with cryostructural materials selection and utilization. These general materials considerations include the following:

a) Mechanical strength (yield strength, modulus)

b) Fracture toughness (linear elastic or elastic-plastic)

c) Fatigue crack growth rate

d) Microstructural stability (e.g., $\gamma \rightarrow M_s$ or M_d)

e) Dimensional stability (thermal expansion, creep, stress relaxation)

f) Magnetic behavior

g) Electrical resistivity

h) Thermal conductivity

i) Density

j) Specific heat

k) Fabricability

l) Joinability

m) Cost

n) Commercial availability.

In addition, significant progress has been achieved during this program in improving and extending the materials property data base which the designers are presently using as the best available data. Of equal significance, however, has been the impact of materials and mechanics specialists identifying and exploring areas within their respective specialities which although appearing quite subtle can have a significant influence, nevertheless, on the design and ultimate performance of SC machinery and devices. A few examples of such specialty areas which have been particularly relevant in the present program are the following:

- Materials Characterization - It is essential that test materials for which various property data become available are adequately characterized so one can assess the applicability of such property data to the actual materials incorporated into a given structure.
- Processing and Fabrication Effects - It is equally essential that the effects of various processing and fabrication consideration be appreciated to assess the probable attainment of desired material behavior in the final fabricated hardware.

- Predictive Capability - An understanding of materials composition-structure-property relationships leads to both qualitative and quantitative predictive capability of materials behavior under conditions for which explicit test data is often unavailable. In addition, lifetime reliability estimates can be made by employing both linear elastic and elastic-plastic fracture mechanics analytical techniques (and data) to assess the propagation of existing flaws to the critical size necessary for structural failure.

Previous reports in this series have discussed in considerable detail several aspects of materials selection and utilization considerations of interest to both materials and mechanics specialists as well as to SC system designers. While it is not practical to repeat all such discussions here in this final report, it does appear worthwhile to briefly list the following topical areas which were discussed in the prior reports indicated:

- First Semi-Annual Report (Ref. 1)

  Primary categories of cryogenic structural materials applications.
  Deficiencies of previously developed cryogenic materials data.
  Logic and objectives of establishing materials selection and utilization criteria.
  Listing of specific alloys, literature review and discussion of candidate materials for structural cryogenic applications.
  Review of processing and fabrication considerations.

- Second Semi-Annual Report (Ref. 2)

  Characterization as per the Materials Advisory Board (MAB) recommendations.

  Practical basis for materials selection, processing and fabrication data generation.

- Third Semi-Annual Report (Ref. 3)

  Definition and discussion of "Advanced" cryogenic structural applications.

  Suggested designer/materials specialist interaction on materials selection, processing and fabrication concerns toward achieving a failure-safe design.

  Literature review and discussion of non-austenitic steels for cryogenic applications.

- Fourth Semi-Annual Report (Ref. 4)

  Metal alloy designation terminology

  Variations in reported alloy property data

  Weldability considerations

- Fifth Semi-Annual Report (Ref. 5)

  Microstructural stability in austenite stainless alloys.

  Martensite formation in austenitic stainless alloys.

  Delta ferrite formation in austenitic stainless steels.

  Varestraint weldability testing.

A few additional technical areas are discussed in the following subsections to expand and clarify certain areas considered pertinent to this program

5.1.2 Non-Austenitic Steels for Cryogenic Applications

As discussed in an earlier report in this series[3], it is generally quite well known that the non-austenitic ferrous alloys such as carbon and low alloy steels experience a marked decrease in tensile ductility, notch toughness and fracture toughness at decreasing temperatures below 75F(298K). Alloy modifications (with nickel in particular) have been relatively effective in surpressing but not eliminating the ductile-to-brittle transition temperature[6-8]. Maximum service temperatures recommended[8] for the nickel steels are as follows:

Alloy Spec.	% Ni	Minimum Service Temperature
ASTM A203, Gr. A	2-1/4	-90°F(205K)
A203, Gr. D	3-1/2	-150°F(172K)
A645	5	-275°F(102K)
A553, Type II	8	-275°F(102K)
A553, Type I	9	-320°F(77K)
A353	9	-320°F(77K)

The potential for using ferromagnetic nickel steels for structural applications below 77K requires to a large extent the demonstration of the ability to both: (a) surpress the ductile-to-brittle transition temperature (DBTT) below 4K and (b) achieve an acceptable combination of mechanical and physical properties in an economical and commercially feasible alloy system.

Several authors have demonstrated that the DBTT can be surpressed to below 4.2K. In 1957, Basinski and Sleeswyk[9] demonstrated it for high purity iron by grain refinement and Smith and Rutherford[10]

have inhibited brittleness to 4.2K by using zone refined alpha iron. More recently Morris, et al.[12] have shown the suppression of the DBTT to 5K with a developmental 12% nickel 0.25% titanium alloy through microstructural control (grain refinement and introduction of some retained austenite). Morris, et. al[13] have also demonstrated that a similar microstructural control processing procedure is effective in reducing the DBTT of standard 9% nickel steel to 4K. Witzhe and Stephens[14] have demonstrated considerably improved ductility and toughness at 77K in 12 nickel developmental alloys by various reactive metal additions and annealing treatments.

Thus, sufficient data exists to have demonstrated the first of the above requirements, i.e., it is possible to suppress the DBTT to below 4.2K in non-austenitic steels. A recent review paper by Zackay[15] discusses much of the latest information available on the cause and effect relations between aspects of microstructure and fracture toughness for ferrous alloys. However, considerably more effort may be required to achieve a suitable combination of all significant mechanical, fracture mechanics and physical properties in a ferromagnetic alloy which will be both economically and technically suitable for advanced cryostructural applications.

5.1.3 Dimensional Instabilities

"Advanced" cryogenic structural applications are referred to herein as those cryogenic applications which require high integrity structural members to contain and restrain the active superconducting field winding. The mechanical restraint of the superconductor is important

for two basic reasons, namely: (1) Super-conductor motion leads to self quenching and (2) Superconductors experience irreversible mechanical damage and hence degraded current carrying ability at relatively low strain levels. It is therefore relevant to briefly consider here various aspects of cryostructural containment materials with respect to how the dimensions of such materials may change with time, stress, thermal, magnetic and radiation environment.

Structural dimensional changes or instabilities could arise due to a variety of causes. Some dimension instabilities are quite predictable (with an adequate data base available) such as thermal expansion or contraction and elastic strain at an applied stress level below the true onset of plastic deformation. Other causes of dimension change exist, however, which are, at present, neither well documented nor adequately appreciated to be incorporated into many current conceptual designs for advanced cryostructural applications.

One potential source of a significant dimensional instability is a microstructural instability with an inherent specific volume change. An example of such a microstructural change is the transformation of metastable austenite in many stainless steels to a less dense martensite phase. Such phase transformations are irreversible and depending on the specific alloy composition, may occur with or without strain at cryogenic temperatures. While considerable progress has been made in increasing our predictive capability of the likelihood of such transformations (see section 5.1.2 of Ref. 5), more work remains to be accomplished in assessing the magnitude and extent of such transformations. For example, at what true stress or strain levels do such transformations occur as a function

of temperature? What effect does residual elastic stress and applied magnetic field have on such transformations?

Since advanced cryostructural applications are intended for use in extremely large magnetic fields, the effect of such fields on the dimensional stability of the structural materials employed should be considered. A ferromagnetic material, for example, will experience a change in dimensions when exposed to a magnetic field, i.e., the magnetostriction effect. Alloys containing ferromagnetic phases (such as delta ferrite and martensite in austenitic stainless steels) might also be expected to experience a magnetostriction effect, although of a lesser magnitude depending upon their volume percentage of such ferromagnetic phases. In addition, one might question what affect large magnetic fields (steady or time varying) might have on dimensionally related properties such as thermal expansion or elastic modulus. Might not time varying magnetic fields be a source of heat generation through a cyclic magnetostriction effect? The trend of previous work in this program has been to consider the effect of materials composition and microstructural effect on magnetic properties. Perhaps the emphasis should now be changed to consider the effect of large magnetic fields on the mechanical and physical properties of the cryostructural materials.

An additional concern is that of time dependent plastic deformation at applied stress levels near the conventional engineering yield strength or stress level normally considered by structural designers. Although usually considered as high temperature phenomena, creep or stress relaxation can occur at cryogenic temperatures[16,17] and therefore should

be considered as additional factors in dimensional instability. Mugnier and Weil[16] and Voyer and Weil[17] have reported observations of logarithmic creep in times less than 15 hours for 18 Cr-10 Ni and 25 Cr-20 Ni type austenitic stainless steels at 20K and 77K. Interestingly, they find that for the 18-10 stainless alloy, the creep velocity at 20K is relatively high but decreases as the applied stress approaches the yield strength, due to the localized strain-induced formation of martensite. For the 25-20 stainless alloy which was microstructurally stable (i.e., no strain induced formation of martensite occurred), the creep velocity at 20K increased directly proportional to the applied stress level. Additional work in this area is considered important and recommended by the present author.

5.2 Materials Processing Considerations

5.2.1 Overview

The fact that both composition and microstructural variations in metal alloy systems demonstrate different mechanical, fracture mechanical and physical properties is quite well known. Also well known is the fact that conventional metals processing operations and techniques can produce a considerable variation in such property behavior in a given alloy composition. Nevertheless, data are often presented in the literature and employed by designers without adequate reguard for the effect of property variations in a particular alloy due to microstructural differences created by conventional processing practice. The consequences of such oversight are reflected in both an often unappreciated risk in structural design reliability and in an uneconomical utilization

of materials. Consequently, an effort has been made in this section of the Westinghouse program to explore and discuss selected examples of processing effects on certain candidate cryostructural alloys. While it is impractical to repeat all the pertinent data and discussion which has been presented in previous reports (see Refs. 1-5) pertaining to the above, a brief review or overview of the more important observations will be made.

Common commercial processing operations of interest which have been explored in the present program include mill processing and melting of practice, cold working and heat treating. Additional processing operations can and perhaps should be examined for major effects on critical property variations before using such operations in the construction of cryogenic structural hardware. Castings, for example, have not been well characterized or evaluated for utilization as large cryostructural members. Problems may also exist with high residual stress levels introduced by various machining generations. Hydrogen changing or embrittlement may occur in various electrochemical machining or electroplating operations. Other examples undoubtedly exist as well. The main point is, however, that what one ultimately must be concerned with are the properties of the various structural materials in the final processed condition and form actually used in-service hardware.

An excellent example of appreciable property variations experienced with material which had experienced both different melting practice and mill hot working schedules was demonstrated with the various sized billets of Inconel X-750 nickel based superalloy. While all material

was of comparable chemical composition and received identical heat treatment, considerable differences were observed in the tensile and fracture toughness properties at 4K of these different processed conditions (Codes 31XX, 40XX and 50XX) of the same commercial alloy. For example, variations of 38% in 0.2% yield strength, 67% in ultimate tensile strength, 330% in reduction of area, 346% in total elongation, 20% in notched tensile strength and 212% in fracture toughness were observed.

An example of the effect of cold working with and without recrystallization followed by an age-hardening heat treatment was explored with Inconel 718 nickel based superalloy billet material. In this case all material used was of identical mill processing and chemical composition but experienced differences in secondary (laboratory) cold working and heat treatment (Codes 64XX, 67XX, 68XX and 69XX). Intermediate level variations in tensile and fracture toughness properties at 4K were observed, somewhat less than with the X-750 material above. Nevertheless, variations of 25% in 0.2% yield strength, 18% in ultimate tensile, 36% in reduction of area, 55% in total elongation, 14% in notch tensile strength and 29% in fracture toughness were observed.

An example of mill processing and melting practice which produced relatively minor differences in tensile and fracture toughness data at 4K was experienced with Inconel 706 superalloy. VIM-VAR (Code 70XX) and VIM-EFR (Code 70XX) material of similar chemical composition and identical laboratory heat treatment was compared with relative property variations at 4K of 3.6% in 0.2% yield strength, 2.9% in ultimate tensile strength, 7.2% in reduction of area, 14% in total elongation, 3% in notched tensile strength and 9% in fracture toughness observed.

An example of the very significant effects of cold working on the tensile and fracture toughness properties of a structurally stable stainless steel was shown with 30% cold work in Kromarc 58 material. The 155% increase in 0.2% yield strength at room temperature due to the cold work greatly exceeds that at 4K of 34% while the corresponding 70% relative decrease in elongation at RT is only slightly greater than the corresponding 43% decrease at 4K. A difference of 44% in the fracture toughness values at 4K was observed between the solution treated and quenched (Code 80XX) and the cold worked (Code 81XX) Kromarc 58.

A final example to be mentioned here is the processing effect of a variation in cooling rate from the solution heat treatment temperature with a structurally stable 310S stainless steel. A slow furnace cooled condition (Code 21XX) was compared to a fast water quenched condition (Code 20XX). The microstructural effect of interest in the slow cooled sample anticipated and verified by subsequent metallography and fractography is, of course, grain boundary carbide sensitization. In these experiments, the variation in 0.2% yield strength was higher at RT (a decrease of 13.4%) compared to 5% at 77K and 0% at 4K. The relative changes in the other tensile properties were largest at 77K, i.e., decreases of 6% in UTS, 40% in RA, 32% in elongation and 12% in NTS. A difference in fracture toughness was only evaluated at 4K and amounted to a 31% decrease.

5.2.2 Property Variations in 21 Cr-6 Ni-9 Mn Alloy

A comparison of tensile test results in this Ⓦ program with those reported previously by Tobler and Reed[18] for Pyromet-538 (21 Cr-6 Ni-9 Mn) stainless steel shows some significant differences. These specific tensile data are presented and discussed in Section 6.1 of this report. Further discussion of these differences is presented here to explore the possible cause of such property differences since there is so much active interest in this material for cryostructural applications.

First, let us briefly consider the magnitude of the tensile property variations. If we compare the average value reported at 4K, we find the following relative differences between the NBS and the Ⓦ data:

Tensile Property	Actual Difference	Relative Difference
0.2% YS	32.9 ksi	-18.3% (Ⓦ value lower)
UTS	21 ksi	- 8.9% (Ⓦ value lower)
R.A.	18.6%	+46.5% (Ⓦ value higher)
Elong.	35.8%	+ 224% (Ⓦ value higher)

Secondly, let us examine the variations (actual and relative) in the two values at 4K reported which make up the average values reported for the Ⓦ and the NBS data.

Ⓦ Tensile Property	Actual Difference	Relative Difference
0.2% YS	31.9 ksi	24%
UTS	31.5 ksi	16%
R.A.	26.7%	37%
Elong.	2.1%	4.1%

NBS	Tensile Property	Actual Difference	Relative Difference
	0.2% YS	4.5 ksi	2.7%
	UTS	0.15 ksi	0.06%
	R.A.	Only 1 value reported	--
	Elong.	Only 1 value reported	--

It is apparent that the differences between these tensile properties are not trivial. A distinct high strength and lower ductility average behavior is observed in the NBS data relative to the Ⓦ data. There is little significant variation in the individual replicate values at 4K for the NBS data. The scatter in the 4K Ⓦ data, although significant with respect to the 0.2% YS, UTS and the R.A., is not adequate to explain the overall average differences. A similar trend in the average data exists as well when comparisons are made at 77K (i.e., strength is greater and ductility is lower for the NBS data relative to the Ⓦ data).

The most interesting aspect between the NBS and the Ⓦ data is that these significant tensile property variations occurred in the same heat of material. The main ostensible difference between the NBS and the Ⓦ material was therefore in the processing of that billet material to plate.

The NBS plate material was fabricated by the ORNL by hot cross rolling to 50 cm x 50 cm x 3.6 cm dimensions, the Ⓦ plate material was fabricated by Braeburn Alloy Steel by hot unidirectional rolling to random lengths 10 cm wide by 1.9 cm thick. Both the NBS and the Ⓦ plate material was given an identical final heat treatment of a 2000°F solution treatment

followed by a water quench. A comparison of hardness values showed only a minor difference, R_B 84 for the NBS plate and R_B 89 for the Ⓦ plate. The average ASTM grain size number for the NBS plate was 4.5 compared to 4.3 for the Ⓦ plate.

Thus, while there is at present no obvious explicit explanation for the significant differences in tensile property data between the NBS and the Ⓦ material, it is implicit that such differences are attributable to variations in the processing of the same starting material into plate. Further characterization of the two plate materials, although not presently planned, would be very helpful in explaining the above differences.

5.3 Metals Joining Considerations

5.3.1 Overview

The use of one or more of the three primary metals joining approaches namely: soldering, brazing and welding appears inevitable in the actual fabrication of advanced cryostructural support structures. Since such operations are often manual or only semi-automatic and may be required to be performed under adverse conditions such as limited access or field versus shop fabrication, one cannot assume the total absense of metallurgical defects. In fact, such assurance of absense of all defects can not always be made even for well controlled laboratory test weldments since many materials are hot cracking sensitive, especially under conditions of high restraint which are typically encountered in large structural fabrications. In addition, there are numerous combinations of welding processes (e.g., SMAW, GMAW, GTAW, EBW, EW, etc.), filler materials and process parameters (e.g., heat input, preheat, cooling rate, shielding gas,

pulsing, etc.) which can produce widely different microstructural and compositional features with significant variations resulting in mechanical and fracture mechanics behavior.

Several metals joining considerations have been investigated in the course of the present program (see Section 5.3 of Ref. 1-5), the details of which will not be repeated here. Included among those considerations were the following:

- Solder (90Pb-10Sn) joints in OFHC copper (Code 14XX)
- Brazed (B Ag-8) joints in OFHC copper (Code 13XX)
- GMA weldments in OFHC copper (Code 12XX)
- SMA weldments in AISI 310S stainless (Code 22XX)
- Electron beam weldments in IN X-750 (Codes 32XX to 34XX) (including pre- and post-weld heat treatments)
- GTA weldments in IN X-750 (Codes 35XX to 37XX) (including pre- and post-weld heat treatments)
- Copper brazed joints in IN X-750 (Code 38XX)
- GTA weldments in HIP IN X-750 superalloy (Codes 62XX, 63XX)
- GTA weldments in KROMARC 58 stainless (Codes 82XX to 86XX) (including various cold work and heat treatments)
- GTA weldments in Inconel 718 (Codes 65XX, 66XX) (Includes effects in both fusion and heat affected zones)
- GTA weldments in Inconel 706 superalloy (Code 72XX)
- GTA weldments in INCO low expansion alloy (Code 74XX)
- GTA weldments in A-286 stainless (Code 91XX)
- GTA weldments in Pyromet-538 stainless (Code 93XX)
- SMA weldments in Pyromet-538 stainless (Code 94XX)

In the case of the solder joints in OFHC copper (Code 14XX) the joint quality on the 1.3 cm thick samples was inadequate to justify further testing. Acceptable joints were made as Gas Tungsten Arc Weldments (GTAW) in the Hot Isostatic Pressed (HIP) Inconel X-750 (Codes 62XX and 63XX) and in the INCO Low Expansion Alloy (LEA, Code 74XX). However, because of funding and priority constraints, these weldments were not subjected to mechanical and fracture mechanics testing. All other fabrication conditions mentioned above were so tested and evaluated.

A summary of the actual data for these fabricated joint conditions can be found in Section 6, Tables 6.1 through 6.13 in this final report. A graphical summary comparison of the joint condition behavior relative to the respective all-base metal condition is presented in Figs. 3-10 through 3-12 in this report. Several detailed microstructural and fractographic observations have been made concerning the various joint conditions in Section 7 of the present and previous (1-5) reports in this series.

Some summary observations concerning the behavior of the metal joining conditions investigated are briefly made, as follows:

a) Solder joints of adequate section size and quality to make consistent comparisons with other metal joint conditions were not achieved and hence no data was generated.

b) Both brazed joint conditions evaluated exhibited inferior yield and/or tensile strength and fracture toughness levels than the corresponding base metal.

c) Shielded metal arc joints with matching composition filler wire (electrode) in 310S were comparable in strength but inferior in fracture toughness at 4K relative to the unwelded base metal. SMA joints with non-matching composition filler material in Pyromet 538 stainless steel were inferior in L.T. strength but equal in fracture toughness to the unwelded base metal. Fracture surfaces with both SMA weldments were observed to contain inclusions of Na, Al, Cl and K presumably introduced via the electrode coating.

d) Gas metal arc joints in OFHC copper were found to be slightly lower in yield strength and equal in ultimate tensile strength from RT to 4K. No fracture toughness data was obtained.

e) Gas tungsten arc weldments in both Kromarc 58 and Pyromet 538 stainless steels were superior or equal in strength to their respective base metal conditions. Both were inferior in cryogenic fracture toughness to their respective unwelded base metals, with the delta ferrite containing Pyromet-538 GTA weld fracture toughness being only about 46% of that reported by NBS for the unwelded base metal.

f) Gas tungsten arc and vacuum electron beam weldments in IN X-750 were both slightly inferior or equal in strength to their respective MP-1 base material, depending upon the absence or presence of a full post-weld heat treatment respectively. Fracture toughness values for both the VEB and the GTA weld fusion zones were considerably above that for the unwelded base metal, with the as-welded VEB joints most superior in fracture toughness.

g) Gas tungsten arc weldments in Inconel 718 and Inconel 706 nickel base superalloys using a 718 filler wire were slightly inferior in strength and greatly inferior in fracture toughness to their respective unwelded conditions. Extensive metal carbides were observed on the fracture surfaces of these welded samples and apparently significantly degraded the welded fracture toughness condition.

h) GTA welded joints in the A-286, precipitation hardenable stainless steel were considerable inferior in strength (as welded) but superior in fracture toughness to the unwelded base metal. Fracture was observed to strongly favor the heat-affected zone in the base metal where extensive microfissuring has been shown to occur.

In conclusion, it is obvious that weldments can <u>not</u> be classified as universally inferior or superior to their respective base metal conditions. Many specific considerations such as the process, the compositional and microstructural features and gradients and the presence of absence of defects such as porosity, cracking or microfissuring should all be addressed. Suffice it to say, that <u>if</u> properly designed, fabricated and inspected, a weldment can and will perform in a predictable and acceptable manner at cryogenic temperatures.

5.3.2 Further Varestraint Weldability Considerations

The varestraint test to evaluate the relative hot cracking tendency of both base metals and of prior deposited weld metal was discussed in Section 5.3.2 of the two previous reports[4,5]. Longitudinal sub-sized varestraint test data at augmented strain levels of up to 4.0 percent was presented[5] in both tabular and graphical form for several of the alloys of concern to this program. This data was reported as the number of cracks and as total crack length observed in the heat affected zone and weld fusion zone areas adjacent to the bend location. Such observations are made at 30X magnification on the top surface of the varestraint test specimen. Photomacrographs of these varestraint test specimen surfaces were presented as Figs. 5-22 through 5-32 in the previous report[5].

Subsequent to the above observations, selected varestraint samples were cross sectioned, polished, etched and examined metallographically on the Transverse cross section. Composite photomicrographs were taken of each cross section at 100X original magnification and are shown as Figs. 5-1 through 5-12 of this report. Several pertinent observations concerning these transverse sections of longitudinal varestraint samples can be made as follows:

1. A considerable variation exists in the size and shape of the weld fusion zone cross section. Nugget dimensions varied from 0.110 in. to 0.245 in. in width and 0.035 in. to 0.085 in. in depth, with fusion zone cross sectional area variations of from 0.020 sq in. to 0.057 sq in. observed. Since all varestraint test parameters were maintained at standardized conditions reported in Section 5.3.2 of reference 5, such appreciable dimensional variations were not anticipated and are not presently considered in the normal interpretation of varestraint test results.
2. Considerable weld fusion zone and heat affected zone cracking was observed in several of the transverse cross sections which

would not be detectable by top surface visual examination normally employed exclusively in examination of varestraint specimens. For example, HAZ microfissuring was observed in Kromarc 58 base metal at 2% augmented strain (see Fig. 5-1) in transverse cross section but was not observed in previous top surface examination of the as-tested sample. Similarly, HAZ microfissuring was observed in Nitronic 33 base metal at 3% augmented strain (see Fig. 5-4) in transverse section but was also not observed in previous top surface examination of the as tested sample. Considerable cracking was observed in the transverse section of the weld fusion zone of the AISI 305 stainless steel (see Fig. 5-6). While such fusion zone cracking had been previous observed in top surface examination of this sample, the cracking observed in Fig. 5-6 is quite extensive with a total crack length measurement in this single cross section greater than that observed on the entire top surface.

3. The fact that cracking is indeed observed below the top surface of the varestraint test specimen raises some interesting questions concerning the optimum effectiveness of this very useful testing technique. If cross sectional observations are not made, then in fact either fusion zone and/or heat-affected zone cracking may be present and neither observed nor reported. Furthermore, the strain level normally considered in this test is the longitudinal uniaxial strain on the sample top surface which is tensile in nature and at maximum amplitude on the top surface. However, the presence of subsurface cracking is indicative of appreciable transverse strains (e.g., solidification shrinkage strains) of a magnitude sufficient to induce cracking.

References (Section 5)

1. Lessmann, G.G., Logsdon, W.A., Kossowsky, R., Mathur, M.P. and Wells, J.M., "Structural Materials for Cryogenic Applications - First Semi-Annual Technical Report," Westinghouse Research Report 74-9D4-CRYMT-R1, March 1, 1974 (Unrestricted).

2. Lessmann, G.G., Logsdon, W.A., Kossowsky, R., Mathur, M.P. and Wells, J.M., "Structural Materials for Cryogenic Applications - Second Semi-Annual Technical Report," Westinghouse Research Report 74-9D4-CRYMT-R2, September 9, 1974 (Unrestricted).

3. Wells, J.M., Kossowsky, R., Logsdon, W.A. and Daniel, M.R., "Structural Materials for Cryogenic Applications - Third Semi-Annual Technical Report," Westinghouse Research Report 75-9D4-CRYMT-R1, March 10, 1975 (Unrestricted).

4. Wells, J.M., Kossowsky, R., Logsdon, W.A. and Daniel, M.R., "Structural Materials for Cryogenic Applications - Fourth Semi-Annual Technical Report," Westinghouse Research Report 75-9D4-CRYMT-R2, October 10, 1975 (Unrestricted).

5. Wells, J.M., Logsdon, W.A., Kossowsky, R., and Daniel, M.R., "Structural Materials for Cryogenic Applications - Fifth Semi-Annual Technical Report," Westinghouse Research Report 76-9D4-CRYMT-R1, April 9, 1976 (Unrestricted).

6. Haynes, A.G., Firth, K., Hollox, G.E., and Buchan, J., "Strength and Fracture Toughness of Nickel Containing Steels," Properties of Materials for Liquid Natural Gas Tankage, ASTM STP 579 (1975), pp. 288-323.

7. Pense, A.W. and Stout, R.D., "Fracture Toughness and Related Characteristics of the Cryogenic Nickel Steels," WRC Bulletin 205, May 1975.

8. Anon, "Low Temperature Properties of Nickel Alloy Steels," Bulletin A-1238, INCO (1975).

9. Basinski, Z.S. and Sleeswyk, A., "On the Ductility of Iron at 4.2°K," Acta Met., Vol. 5 (1957), pp. 176-179.

10. Smith, R.L. and Rutherford, J.L., " Journal of Metals, AIME (1957), p. 857.

11. Rosenberg, H.M., "The Mechanical Properties of Metals at Low Temperatures," Proc. of the 5th Int. Conf. on Low Temp. Physics and Chemistry,(1958), pp. 497-500.

12. Sungho Jin, Witaker, B., Morris, J.W., Jr., and Zackay, V.F., "Cryogenic Toughness Through Microstructure Control in an Iron-Nickel-Titanium Alloy," Properties of Materials for Liquid Natural Gas Tankage, ASTM STP 579, (1975), pp. 348-360.

13. Syn, C.K., Sunghu Jin, and Morris, J.W., Jr., "Cryogenic Fracture Toughness of 9 Ni Steel Enhanced Through Grain Refinement,"

14. Witzke, W.R. and Stephens, J.R., "Effect of Minor Reactive Metal Additions on Fracture Toughness of Iron-12 Percent Nickel Alloy at -196°C and 25°C," NASA TN D-8232, May 1976.

15. Zackay, V.F., "Fundamental Considerations in the Design of Ferrous Alloys," Alloy Design for Fatigue and Fracture Resistance, AGARD Conf. Proc. No. 185 (1976), pp. 5-1 to 5-20.

16. Mugnier, D. and Weil, L., "Creep and $\gamma \rightarrow \alpha$ Transformation in 18-10 Stainless Steel at Liquid Hydrogen and Nitrogen Temperatures," Adv. in Cryogenic Engrg., Vol. 9, (1963), pp. 98-103.

17. Voyer, R. and Weil, L., "Creep Properties of 18-10 and 25-20 Stainless Steels at Cryogenic Temperatures," Adv. in Cryogenic Engrg., Vol. 10, (1964), pp. 110-116.

18. Tobler, R.L. and Reed, R.P., "Tensile and Fracture Behavior of a Nitrogen Strengthened, Cr-Ni-Mn Stainless Steel At Cryogenic Temperatures," Materials Research for Superconducting Machinery-IV, ARPA/NBS, October, 1975, pp. 131-150.

TABLE 5-1 -- CANDIDATE MATERIALS FOR ADVANCED CRYOGENIC STRUCTURAL APPLICATIONS

Trade Name	UNS Designation
AUSTENITIC STAINLESS STEELS	
* AISI 310S	S31008
* Kromarc 58	--
Nitronic 33 (18-3Mn)	S24000
*** Nitronic 40 (21-6-9)†	S21900
Nitronic 50 (22-13-5)	S20910
Carpenter 20Cb-3	N08020
Carpenter 18-18 Plus	--
IRON BASE SUPERALLOYS	
*** A-286	K66286
W-545	K66545
Pyromet 860	--
Discaloy	K66220
NICKEL BASE SUPERALLOYS	
Inconel 625	N06625
** Inconel 718	N07718
** Inconel 706	N09706
* Inconel X750 (751)	N07750
Hastelloy C-276	N10276
Pyromet 680	N06002
Pyromet 102	--
OTHER SUPERALLOYS	
Haynes 188	R30188
Multiphase MP35N	R30035

Trade Name	UNS Designation
LOW EXPANSION ALLOYS	
**INCO(Unnamed) LEA	
Incoloy 903	
Pyromet CTX-1	
TITANIUM ALLOYS	
Ti-6Al-4V (ELI)	
Ti-5Al-2.5Sn (ELI)	
ALUMINUM ALLOYS	
2014	A92014
2219	A92219
5083	A95083
X2048	
COPPER AND COPPER ALLOYS	
* OFHC-Cu	C10200
Amzirc Cu (CW/HT)	C15000
Glidcop (Al_2O_3-D.S.)	
** PD-135 (Cu-Cr-Cd/PHT)	

* Materials characterized in Westinghouse FY 1974 program. ARPA/NBS Contract CST-8034.

** Materials included in Westinghouse FY 1975 Program.

*** Materials included in Westinghouse FY 1976 Program.

† Also available as Pyromet 538.

Dwg. 2609C19

TABLE 5-2 – SUMMARY CHEMICAL COMPOSITION OF ⓔ PROGRAM MATERIALS (WEIGHT PERCENT)

Code	Material	Cu	Cd	Cr	Sn	Si	Pb	P	Al	Mn	Zn	Residuals
Copper Alloys:												
10XX	OFHC (CDA # 102) Plate[1]	99.95	--	--	--	--		--	--	--	--	
	CU (CDA # 189) Wire[1]	(98.7)	--	--	0.6/0.9	0.15/0.40	.02 Max	.05 Max	.01 Max	0.10/0.30	.10 Max	<0.1
12XX	GTAW-As Deposited	Not Analyzed										
15XX	PD-135, t = 5/8"	Bal	.30	.43	--	--	<.01	--	--	<.01	--	4-27 ppm-O, 3 ppm-N
	t = 1"	Bal	.31	.33	--	--	<.01	--	--	<.01	--	--

	Stainless Steels:	C	P	S	Si	Mn	Ni	Cr	Mo	Ti	Al	V	Cu	N	Other
20XX	AISI 310S BM	.064	.017	.009	.74	1.70	19.66	24.40	.17	--	--	--	.15	--	Fe-Bal
	Weld Plate	.053	.027	.011	.48	1.70	20.80	25.00	.21	--	--	--	.14	--	Fe-Bal
	E310-16 Electrode[2]	.20 Max	.03 Max	.03 Max	.75 Max	2.5 Max	20.0/22.5	25.0/28.0	--	--	--	--	--	--	.70 Max, Fe-Bal
22XX	SMAW-As Deposited	Not Analyzed													
80XX	Kromarc-58 Plate	.030	.005	.005	.05	9.3	23.0	15.5	2.2	--	.02	.16	--	.17	Zr-.008, B-.016, Fe-Bal
	K-58 Filler Wire	.003	.001	.004	.09	11.5	21.4	15.3	2.18	--	--	.20	--	.15	Zr-<.002, B-.010, Fe-Bal
82XX	GTAW-As Deposited	Not Analyzed													
90XX	A-286 Billet	.036	.017	.0025	.57	1.72	25.8	14.9	1.31	2.35	.15	.31	--	--	Fe-Bal
	IN F-92 Filler Wire[4]	.04	--	.005	.07	2.17	70.19	16.20	--	2.72	--	--	--	--	Fe-8.30, Cu-0.10, (Cb + Ta) - 1.71
91XX	GTAW-As Deposited	.036	.037	.0023	.23	1.97	54.5	15.6	.49	2.71	.32	.16	--	.008	Fe-Bal
92XX	Pyromet-538 Billet	.018	.004	.0058	.15	9.46	7.16	19.75	--	--	--	--	--	.27	Fe-Bal
	21-6-9 Filler Wire	.022	.011	.006	.39	9.29	7.09	19.68	--	--	--	--	--	.223	Fe-Bal
93XX	GTAW-As Deposited[5]	.022	.012	.0034	.29	8.90	7.02	19.3	--	<.03	.019	--	--	.22	Fe-Bal
	IN 182 Electrode														
	.093" dia	.03	--	.007	.52	7.55	67.87	13.30		.34	--	--	.11	--	Fe-8.36, (Cb + Ta) - 1.87
	.125" dia	.04	--	.006	.58	6.79	67.93	14.08	--	.42	--	--	.10	--	Fe-8.30, (Cb + Ta) - 1.71
94XX	SMAW-As Deposited	.040	.009	.0086	.59	7.12	62.0	13.8	--	.52	.13	--		.043/.060	Fe-Bal

	Nickel Base Superalloys:	C	P	S	Si	Mn	Ni	Cr	(Nb + Ta)	Cu	Fe	Al	Ti	Co	O	N	H	
30XX	IN X-750 (MP-1, VIM/VAR)	.04	.003	<.001	.11	.089	73.0	15.2	.90	.022	6.47	.92	2.40	.017	.0016	.004	.00012	
	IN F69 (HT 00F 7XS)[3]	.03	--	.007	.14	.08	72.96	15.80	.92	.01	6.72	.71	2.60	--	--	--	--	
	(HT 21C8X)[3]	.03	--	.007	.17	.10	73.63	15.10	.92	.02	6.74	.70	2.54	--	--	--	--	
32XX	EBW - As Welded	Not Analyzed																
35XX	GTAW - As Deposited	Not Analyzed																
40XX	IN X-750 (MP-2, AAM/VAR)	.02	.004	.007	.24	.12	74.82	14.19	.95	.06	6.22	.73	2.62	.051	.0006	.004	.00007	
50XX	IN X-750 (MP-3, VIM)	.04	.004	.003	.27	.13	73.02	15.40	.89	.04	6.87	.68	2.64	.009	.0006	.007	.00010	
61XX	IN X-750 HIP (MP-1)	--	--	--	--	--	--	--	--	--	--	--	--	--	.013	.0060	.000022	
62XX	HIP/GTAW	Not Analyzed																
64XX	IN 718 (VIM/VAR)	.06	.010	.004	.27	.15	52.67	18.30	5.29	.17	18.47	.58	.97	.03	.0003	.0085	--	Mo-3.04
	IN F718 .045" dia[3]	.04	.011	.007	.19	.04	54.58	17.91	5.08	.05	17.60	.49	.99	.04	--	--	--	Mo-2.96
	IN F718 .062" dia[3]	.06	--	.007	.21	.07	53.49	17.99	5.12	.10	18.24	.59	1.00	.07	--	--	--	Mo-3.03
65XX	GTAW As-Deposited	Not Analyzed																
70XX	IN 706 (VIM/EFR)	.03	--	.002	.10	.10	41.49	16.09	2.95	.02	37.27	.27	1.66	--	.0005	.0050	--	
71XX	IN 706 (VIM/VAR)	.04	--	.007	.07	.13	41.80	16.33	2.96	.02	36.64	.20	1.78	--	.0005	.0044	--	
72XX	GTAW As Deposited	Not Analyzed																
73XX	IN LEA Billet	.01	--	.007	.12	.22	39.56	--	2.90	.04	55.44	.22	1.46	--	.0016	.0031	--	
74XX	GTAW As Deposited	Not Analyzed																

Notes: (1) Requirements of Standards Handbook, Part 2 - Alloy Digest, Copper Development Association, Inc NY 1973
(2) Analysis Certified from Supplier to AWS, A5.4-69, Class E310-16
(3) Analysis Certified from Supplier
(4) Analysis Certified from Supplier to AWS, A5.14-69, Class ERNICRFE-6
(5) Analysis Certified from Supplier to AWS, A5.11-69, Class ENICRFE-3

TABLE 5-3 - SUMMARY OF MATERIAL DOCUMENTATION DATA FOR Ⓦ PROGRAM MATERIALS

Material	Supplier Source	Heat No.	Form Received
Copper:			
• OFHC Cu (CDA #102)	Ⓦ RL Stock	Unknown	1/2 and 5/8" thick plate
CU Filler Wire (CDA #189)	Williams and Co., Inc.	E-Cu (Unknown)	Bare wire - 0.062" dia
• PD-135	Phelps Dodge	Unknown	Flat extrusion 5/8" thick x 4"w x 48"ℓ 1" thick x 4-1/4"w x 48"ℓ
Stainless Steel:			
• AISI 310S BM	McInnes Steel Company	500096	Forging Billet - Annealed
Weld Plate	Rolled Alloys, Inc.	20880	Plate - 5/8"t x 6"w x 18"ℓ, 4 PCS, HRAP
E310 - 16 Electrode	Arcos Corp.	(a) 3A17B-M9	SMAW Electrode - 1/8" dia
		(b) 2N10B-M16A	SMAW Electrode - 5/32" dia
		(c) 2N8B-M16	SMAW Electrode - 5/32" dia
• KROMARC 58 BM	Ⓦ RL Stock	HT-D8339	Plate - 1" thick
Filler Wire	Ⓦ RL Stock	HT-3736	Wire redraw stock - 0.287" dia
• Pyromet 538 BM	Carpenter Tech. Corp.*	89087	Forging Billet - 12 in. square
21-6-9 Filler Wire	Carpenter Tech. Corp.* * (via. LLL)	82287	Bare Filler Wire - 0.030" dia x 25 lb spool, VIM/ESR
IN 182 Electrode	INCO-Huntington Alloys+	HT 5022	SMAW Electrode - 0.093" dia x 9"ℓ, 10 lb
	INCO-Huntington Alloys+ + (via Williams and Co., Inc.)	HT 4916	SMAW Electrode - 0.125" dia x 12"ℓ, 20 lb (AWS, A5.11-69, Class ENICRFE-3)
• A-286	ARMCO Steel Corp.	4X0836	Forging Billet - 5-1/4" square
IN F92	INCO-Huntington Alloys, Inc.+	HT 1712MD	Bare Wire, 0.062" dia x 25 lb spool (AWS, A5.14-69, Class ERNICRFE-6)

TABLE 5-3 - SUMMARY OF MATERIAL DOCUMENTATION DATA FOR Ⓦ PROGRAM MATERIALS - p. 2

Material	Supplier Source	Heat No.	Form Received
Nickel Base Superalloys:			
Inconel X750			
• MP-1 (VIM/VAR)	INCO-Huntington Alloys Div.	HT56C1XY	Round, 10" dia, HFFQ
• MP-2 (AAM/VAR)	INCO-Huntington Alloys Div.	HT1250XV	Round, 4" dia, HFFQ
• MP-3 (VIM)	INCO-Huntington Alloys Div.	HT57F8XS	Round, 2" dia, HF
Powder for HIP	Federal-Mogul Corporation	HT56C1XY	Powder - 60 mesh, from MP-1
Weld Filler Wire 69	INCO-Huntington Alloys Div.	HT21C8X	Bare Wire, 0.093" dia
		HT00F7XS	Bare Wire, 0.062" dia
		HT21C8X	Bare Wire, 0.062" dia
• Inconel 718(VIM/VAR)	INCO-Huntington Alloys Div.	HT16G6EY	Round, 11-3/8" dia, HFFQ
Weld Filler Wire 718	INCO-Huntington Alloys Div.	HT52B0E	Bare Wire, 0.045" dia x 25 lb spool
	INCO-Huntington Alloys Div.	HT73C4E	Bare Wire, 0.062" dia x 25 lb spool
• Inconel 706 (VIM/EFR)	INCO-Huntington Alloys Div.	HT48C5HK	Round, 5-1/2" dia, HFFQ
(VIM/VAR)	INCO-Huntington Alloys Div.	HT79C0HY	Round, 11-3/8" dia, HFFQ
• INCO-LEA (AM/VAR)	INCO-Huntington Alloys Div.	HTY8798	Plate, 3" x 6.5" x 14"ℓ, HR
	INCO-Huntington Alloys Div.	HTY8798	Sheet, 1/8" t x 22"w x 26"ℓ (sheared in 1/8" sq strips for GTA filler rod)

Dwg. 2609C10

TABLE 5-4 SUMMARY PROCESSING AND HEAT TREATMENT SCHEDULES FOR Ⓦ PROGRAM MATERIALS

Material	Code	Condition			Hardness	ASTM Grain Size No.
Copper Alloys:						
OFHC Cu (CDA #102)	10XX	AR	As Received			
	11XX	SR	AR + 400°F (1 hr) Stress Relief			
	12XX	GMAW	AR + Preheat to 800/900°F, GMA Weld with ECu			
	13XX	BRAZE	AR + Vacuum Brazed with AWS BAg-8 @ 1435°F			
PD-135	15XX	EXT/PHT	Extruded from 8" dia. × 16" ℓ billet at 1750°F	τ = 5/8"	60 R30-T	5
			Followed by Precipitation Heat Treatment, 1100°F (1 hr)	τ = 1"	57.5 R30-T	5
Stainless Steels:						
AISI 310 S	20XX	STQ	Solution Treat @ 2000°F (1 hr), Water Quenched (W.Q.)		73 R_B	4.6
(25 Cr-20 Ni-2 Mn)	21XX	STFC	ST @ 2000°F (1 hr), Furnace Cool to 800°F, Air Cool		67.3 R_B	5
	22XX	SMAW	STQ, Then SMA Weld with E 310-16 Electrodes			
Kromarc 58	——	AR	As Received		93 R_B	9
(16 Cr-20 Ni-10 Mn-2 1/4 Mo)	80XX	STQ	ST @ 1800°F (1 hr), Water Quenched (W.Q.)		88 R_B	5.5
	81XX	CW	Cold Work ~ 30% Reduction in Thickness		33 R_C	9.5
	82XX	GTAW	STQ, Then GTA Weld with K-58 Filler Wire			
	83XX	CW/GTAW	STQ, 30% CW, Then GTAW with K-58 Filler			
	84XX	GTAW/CW	STQ, GTA Weld, Then Cold Work ~ 30%			
	85XX	GTAW/CW/PR	STQ, GTAW, 37% CW, Partially Recrystallize @ 1500°F (1 hr) W.Q.			
	86XX	GTAW/CW/FR	STQ, GTAW, 37% CW, Fully Recrystallize @ 1600°F (1 hr), W.Q.			
	87XX	STQ/CW (L-T)	STQ, 37% CW - Specimens Oriented in L-T Direction vs T-L			
Pyromet 538	——	AR	As Received Billet (LLL)		84 R_B	3.5 ¢
(21 Cr-6 Ni-9 Mn)	——	AR	3/4"τ HR Plate Produced by Braeburn Alloy Steel for Ⓦ RL		96 R_B	
	——	AR	1 1/2"τ HR Plate Produced by ORNL for NBS		84 R_B	4.5
	92XX	STQ	Ⓦ Plate, ST @ 2000°F (1 hr), Water Quenched		89 R_B	4.3
	93XX	STQ/GTAW	STQ, GTA Welded with 21-6-9 Bare Filler Wire			
	94XX	STQ/SMAW	STQ, SMA Welded with In 182 Covered Electrode			
A-286	90XX	STQA	ST @ 1650°F (5 hrs), Oil Quench, Age @ 1325°F (20 hrs), A.C.		30 R_C	4.2
	91XX	STQ/GTAW	STQ and GTAW with In 92 Bare Filler Wire			

Dwg. 7609C11

TABLE 5-4 SUMMARY PROCESSING AND HEAT TREATMENT SCHEDULES FOR ⓦ PROGRAM MATERIALS (Continued)

Material	Code	Condition		Hardness	ASTM Grain Size No.
Nickel Base Superalloys:					
Inconel X750	——	AR	As Received 11 3/8" Diam. Forging Round	29.3 R_C	~3.5
MP-1 (VIM/VAR)	30XX	ST	Solution Treat at 1800°F (1 hr), Air Cool (MP-1 Material)	29.5 R_C	~3.5
	31XX	STDA	ST, Then Double Age @ 1350°F (8 hrs), F.C. to 1150°F (8 hrs), A.C.	35.7 R_C	~3.5
	32XX	ST/EBW	ST, Then Vacuum Electron Beam Weld, No Filler Material		
	33XX	STDA/EBW	STDA, Then VEB Weld		
	34XX	EBW/STDA	Vacuum EB Weld, Then STDA Heat Treatment		
	35XX	ST/GTAW	ST, Then Gas Tungsten Arc Weld With In 69 Filler		
	36XX	STDA/GTAW	STDA, Then GTA Weld With In 69 Filler Wire		
	37XX	GTAW/STDA	GTA Weld (F69) Then STDA Heat Treatment		
	38XX	ST/Cu Braze	ST, Then Vacuum Brazed 2050°F (~10 Minutes) With Cu Plated Filler		
MP-2 (AAM/VAR)	40XX	STDA	STDA (Same as for 31XX) - MP-2 Material	36.0 R_C	6.5
MP-3 (VIM)	50XX	STDA	STDA (Same as for 31XX) - MP-3 Material	38.5 R_C	9
	60XX	HIP	Hot Isostatic Press at 1200°C (2192°F) & 10,000 psi (2 hrs)	35.0 R_C	8
	61XX	HIP/STDA	HIP, Then STDA (Same as for 31XX)	41.0 R_C	8
	62XX	HIP/GTAW/STDA (FZ)	HIP, GTA Weld With F69 Filler and STDA Post Weld h.t.		
	63XX	HIP/GTAW/STDA (HAZ)	HIP, GTA Weld With F69 Filler and STDA Post Weld h.t.		
Inconel 718 (VIM/VAR)	——	AR	As Received 11 3/8" Dia. Forging Round	23 R_C	4 to 5
	——	ST	Solution Treat at 1800°F (1 hr), Air Cool	38 R_C	4 to 5
	64XX	STDA	Solution Treat at 1800°F (1 hr), A.C., Double Age 1325°F (8 hrs), F.C. to 1150°F (8 hrs), A.C.	44 R_C	4 to 5
	65XX	ST/GTAW/STDA (FZ)	ST, Then GTA Weld with 718 filler, then STDA as for 64XX		
	66XX	ST/GTAW/STDA (HAZ)	Same as for 65XX		
	67XX	ST/CW/ST (1800°F) DA	ST @ 1950°F (1 hr), A.C., Cold Work ~40%, ST @ 1800°F (1 hr), A.C., Then D.A.	40 R_C	8
	68XX	ST/CW/ST (1950°F) DA	ST @ 1950°F (1 hr), A.C., Cold Work ~40%, ST @ 1950°F (1 hr), A.C., Then D.A.	39 R_C	2.9
	69XX	ST/CW/DA	ST @ 1950°F (1 hr), A.C., Cold Work ~40%, Then Direct Double Age	44 R_C	5.6
Inconel 706 (VIM/EFR)	——	AR	As Received 5 1/2" dia. Forging Round	26 R_C	4 to 5
	——	ST	ST @ 1800°F (1 hr), A.C.	87 R_B	5 to 7
	70XX	STDA	ST @ 1800°F (1 hr), A.C., Double Age 1350°F (8 hrs) F.C. to 1150°F (8 hrs), A.C.	40 R_C	5 to 7
Inconel 706 (VIM/VAR)	——	AR	As Received 11 3/8" dia. Forging Round	88 R_B	2 to 5
	——	ST	ST @ 1800°F (1 hr), A.C.	79 R_B	4 to 5
	71XX	STDA	ST @ 1800°F (1 hr), A.C., Double Age 1350°F (8 hrs) FC to 1150°F (8 hrs), A.C.	41 R_C	4 to 5
	72XX	ST/GTAW/STDA	ST, GTA Weld with 718 Bare Wire, Then Postweld STDA h.t.		
INCO LEA (AM/VAR)	——	AR	As Received	93 R_B	3 to 4
	——	ST	ST @ 1800°F (1 hr), A.C.	84 R_B	4
	73XX	STA	ST @ 1800°F (1 hr), A.C., Then Age @ 1225°F (8 hrs), A.C.	36 R_C	4
	74XX	ST/GTAW/STA	ST, GTA Weld with LEA Filler Strip, Then Postweld STA h.t.		

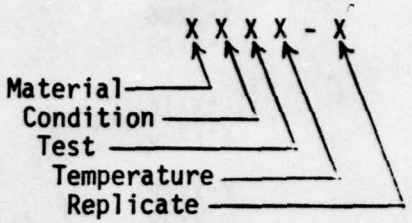
TABLE 5-5

TEST SPECIMEN IDENTIFICATION SYSTEM

Material	Condition	Code No.
OFHC Copper	As Received, AR	10XX-X
	Stress Relieved, SR	11XX-X
	GMAW	12XX-X
	Braze, B	13XX-X
	Solder, S	14XX-X
PD 135 Copper	EXT/PHT	15XX-X
AISI 310S	Sol'n Treated & Quenched, STQ	20XX-X
	Sensitized, STFC	21XX-X
	SMAW	22XX-X
Inconel X750 MP-1 (VIM-VAR)	Solution Treated, ST	30XX-X
	ST + Double Age, STDA	31XX-X
	ST/EBW	32XX-X
	STDA/EBW	33XX-X
	EBW/STDA	34XX-X
	ST/GTAW	35XX-X
	STDA/GTAW	36XX-X
	GTAW/STDA	37XX-X
	ST/Cu-Braze	38XX-X
X750, MP-2 (AAM-VAR)	STDA	40XX-X
X750, MP-3 (VIM)	STDA	50XX-X
X750, HIP	HIP	60XX-X
	HIP/STDA	61XX-X
	HIP/GTAW/STDA (FZ)	62XX-X
	HIP/GTAW/STDA (HAZ)	63XX-X

Specimen ID System

4 Digits + Dash No.



Test (3rd Digit)

Smooth Tensile	XX1X
Notched Tensile	XX2X
K_{IC}	XX3X
J_{IC}	XX4X
FCGR	XX5X

Temperature (4th Digit)

Room Temp. (293 K)	XXX1
LN_2 (77 K)	XXX2
LHe (4 K)	XXX3

TABLE 5-5 (CONTINUED)

Material	Condition	Code No.
Inconel 718	STDA (VIM-VAR)	64XX-X
	ST/GTAW/STDA (FZ)	65XX-X
	ST/GTAW/STDA (HAZ)	66XX-X
	ST/CW/1800 ST/DA	67XX-X
	ST/CW/1950 ST/DA	68XX-X
	ST/CW/DA	69XX-X
Inconel 706	STDA (VIM-EFR)	70XX-X
	STDA (VIM-VAR)	71XX-X
	ST/GTAW/STDA	72XX-X
Inco LEA	STA	73XX-X
	ST/GTAW/STA	74XX-X
Kromarc 58	STQ	80XX-X
	CW	81XX-X
	STQ/GTAW	82XX-X
	CW/GTAW	83XX-X
	GTAW/CW	84XX-X
	GTAW/CW/(Partially Recrystallized)	85XX-X
	GTAW/CW/(Fully Recrystallized)	86XX-X
	STQ/CW (Anisotropy L-T)	87XX-X
A-286	STQA	90XX-X
	STQ/GTAW	91XX-X
Pyromet 538 (21-6-9)	STQ	92XX-X
	STQ/GTAW	93XX-X
	STQ/SMAW	94XX-X

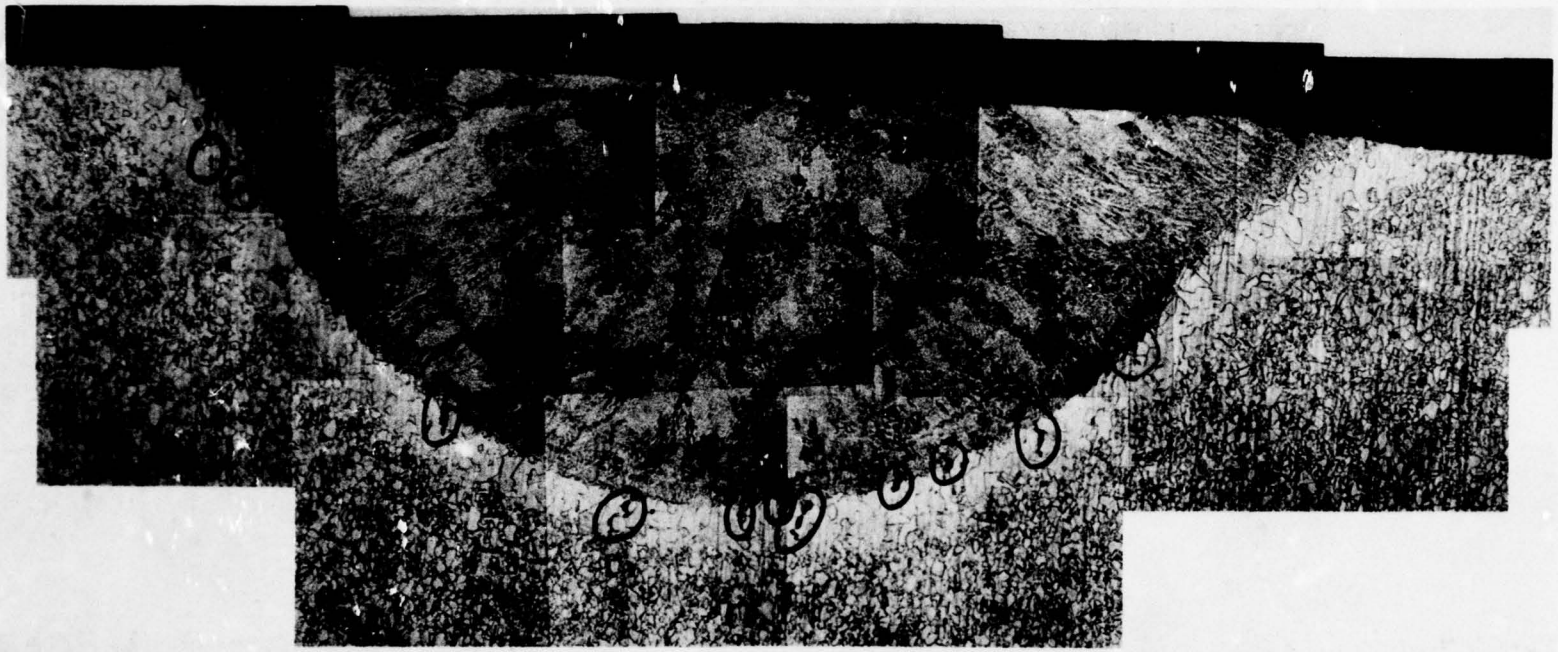


FIG. 5-1 - Photomicrograph of Transverse Section of Varestraint Sample 76-134.
Mat. KROMARC 58SS, Cond. BM-STQ, ε = 2%; Note HAZ Cracking.



FIG. 5-2 - Photomicrograph of Transverse Section of Varestraint Sample 76-133. Mat. KROMARC 58SS, Cond.-Double Pass in Prior GTA Weld, ε = 2%, Note FZ Cracking.

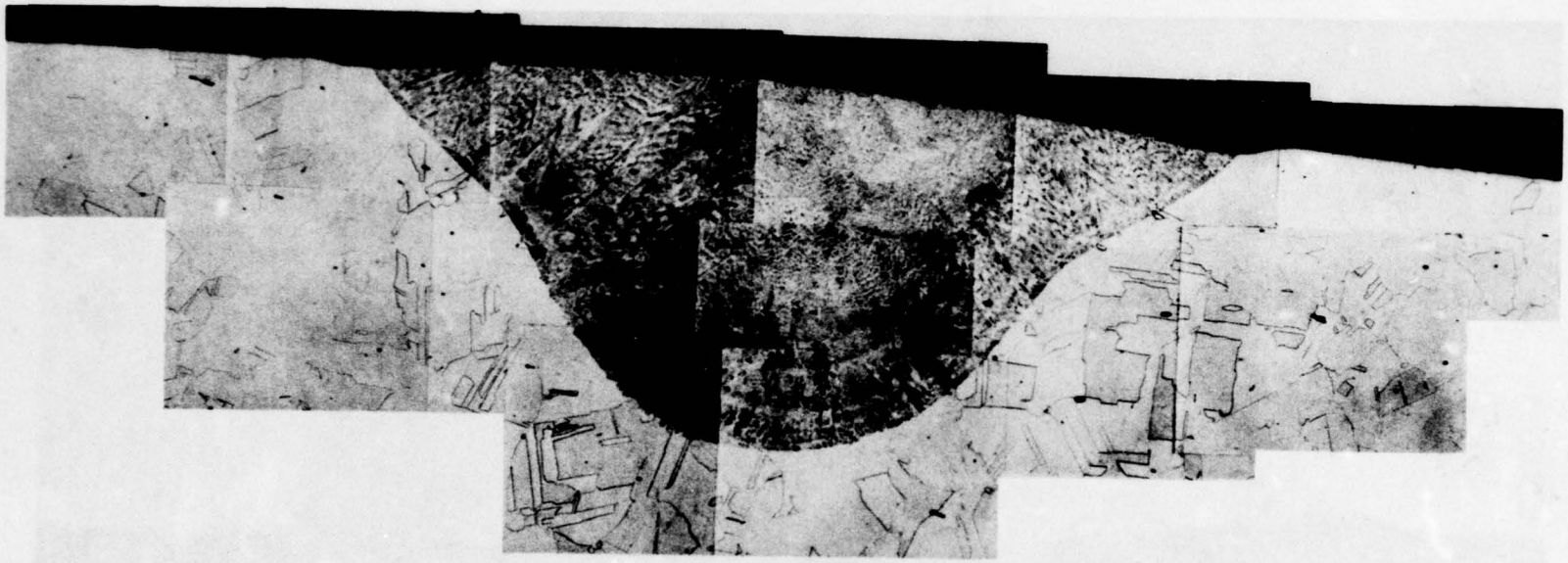


FIG. 5-3 - Photomicrograph of Transverse Section in Varestraint Specimen 76-130. Mat. Pyromet 538 (21Cr-6Ni-9Mn)SS, Cond. BM-STQ, ε = 2%, Note No Cracking.

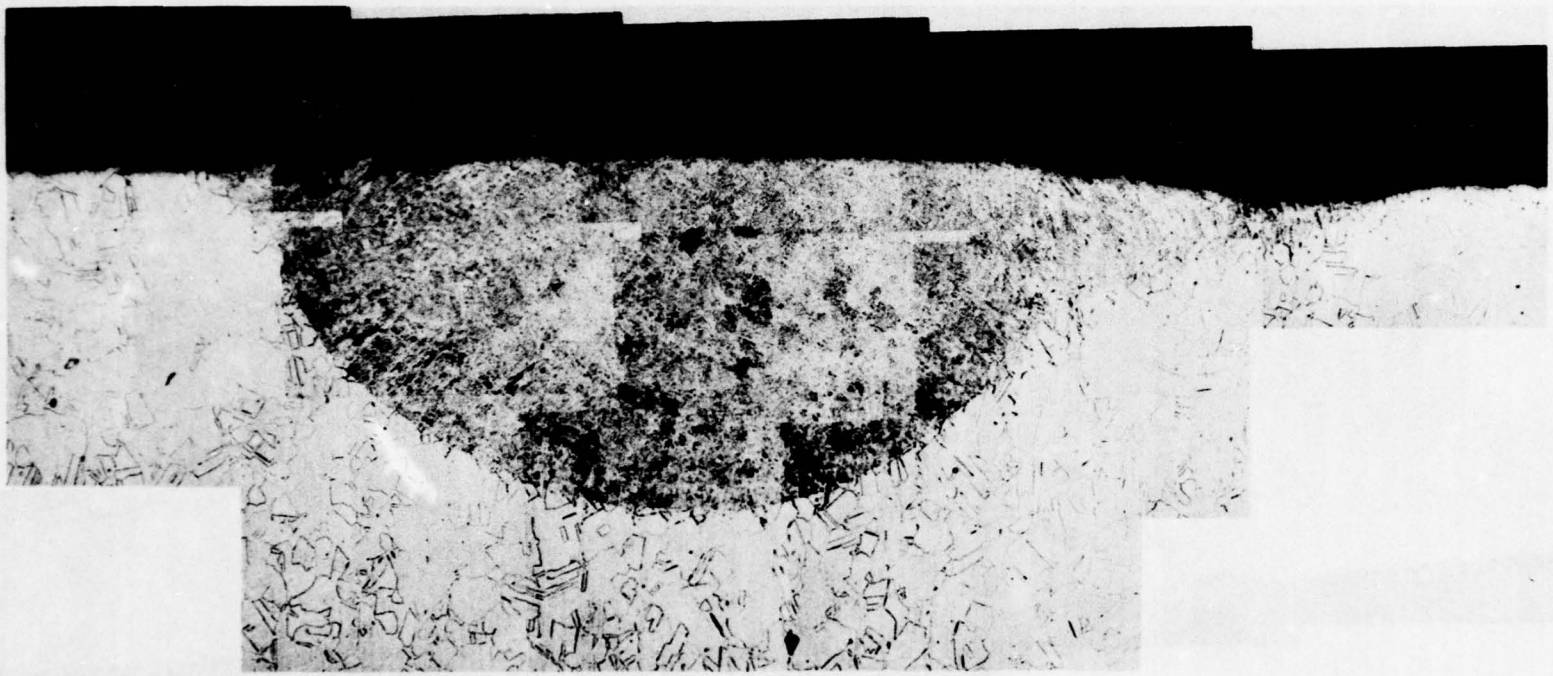


FIG. 5-4 - Photomicrograph of Transverse Section of Varestraint Sample 76-154.
Mat. Nitronic 33SS, Cond. BM-STQ, ε = 3%, Note HAZ Cracking.



FIG. 5.5 - Photomicrograph of Transverse Section of Varestraint Sample 76-132. Mat. Nitronic 33, Cond. Single Pass in Prior 13-20Mn-CbGTAW, ε = 2%, Note FZ Cracking.

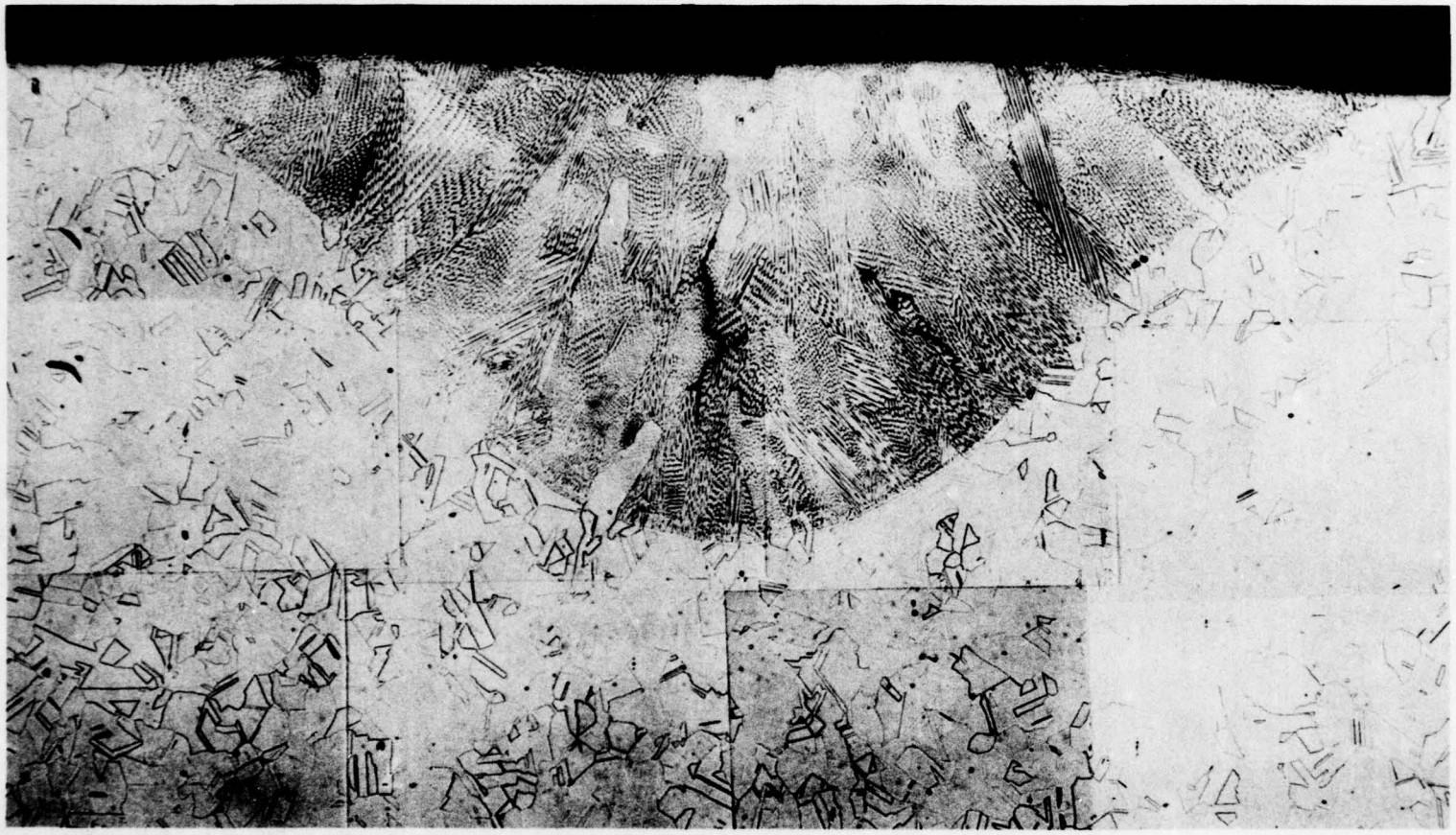


FIG. 5-6 - Photomicrograph of Transverse Section Varestraint Sample 76-131.
Mat. AISI 305SS, Cond. BM-STQ, ε = 2%, Note FZ Cracking.

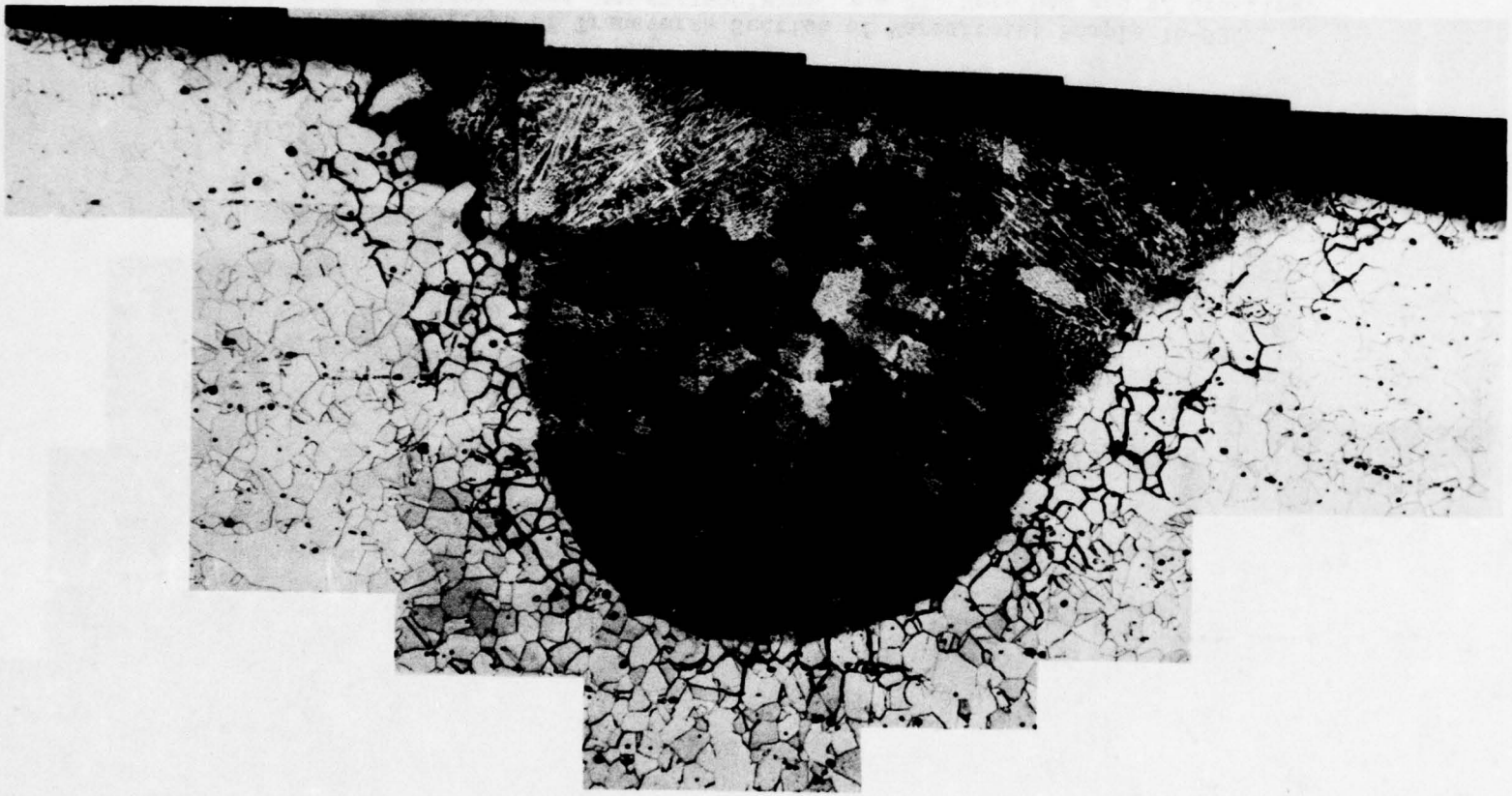


FIG. 5-7 - Photomicrograph of Transverse Section of Varestraint Sample 76-128. Mat. A-286(A), Cond. BM-ST(1800°F)OQ, ε = 2%, Note both FZ and HAZ Cracking.



FIG. 5-8 - Photomicrograph of Transverse Section of Varestraint Sample 76-92.
Mat. A-286(A), Cond. BM-ST(1800°F)QA, ε = 2%, Note HAZ and FZ Cracking.

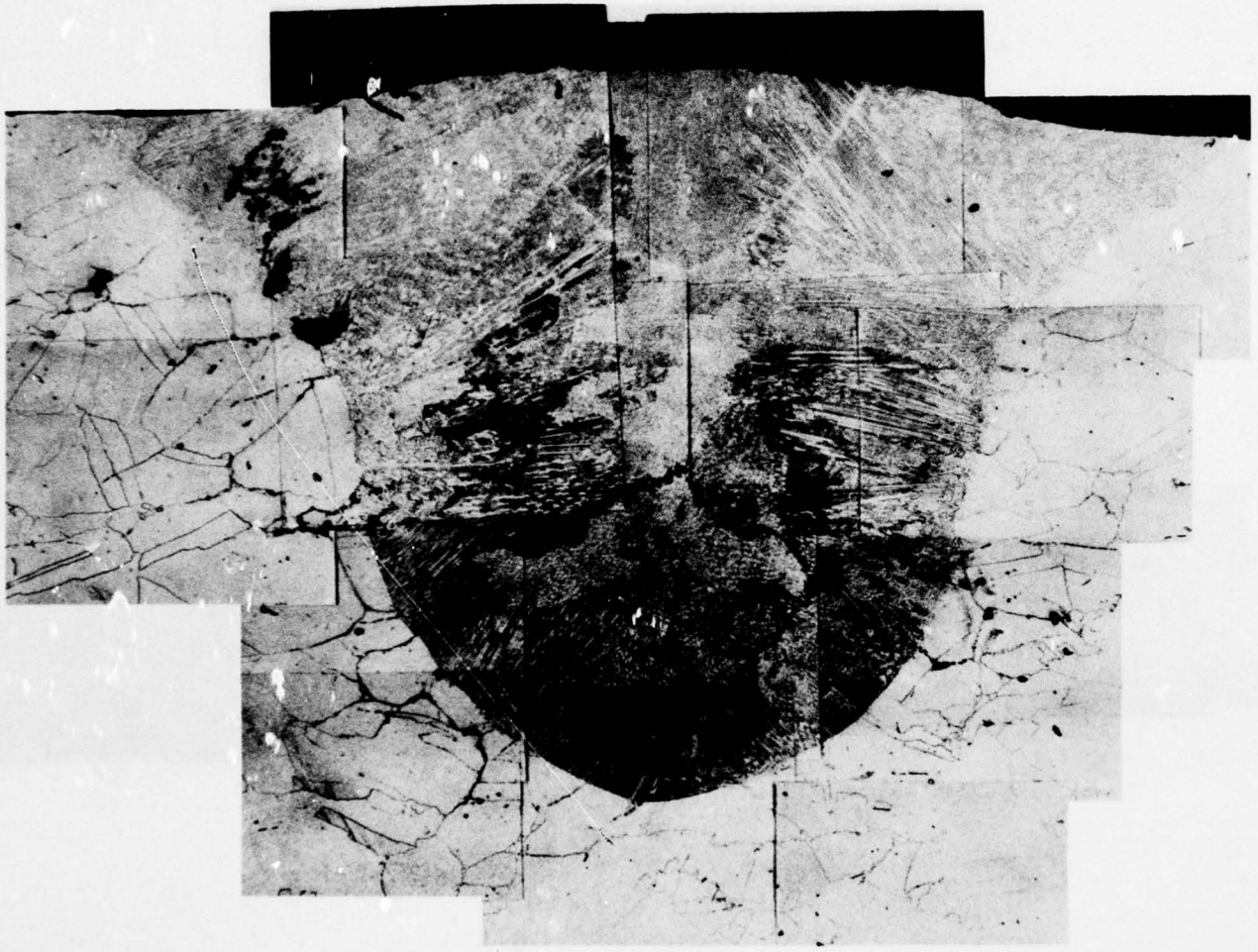


FIG. 5-9 - Photomicrograph of Transverse Section of Varestraint Sample 76-119.
Mat. A-286(C), Cond. BM-ST(1800°F)QA, ε = 2%, Note FZ and HAZ Cracking.

FIG. 5-10 - Photomicrograph of Transverse Section of Varestraint Sample 76-153. Mat. IN718, Cond. BM-AR, ε = 2%, Note HAZ Cracking and Wide Shallow Nugget Cross Section.

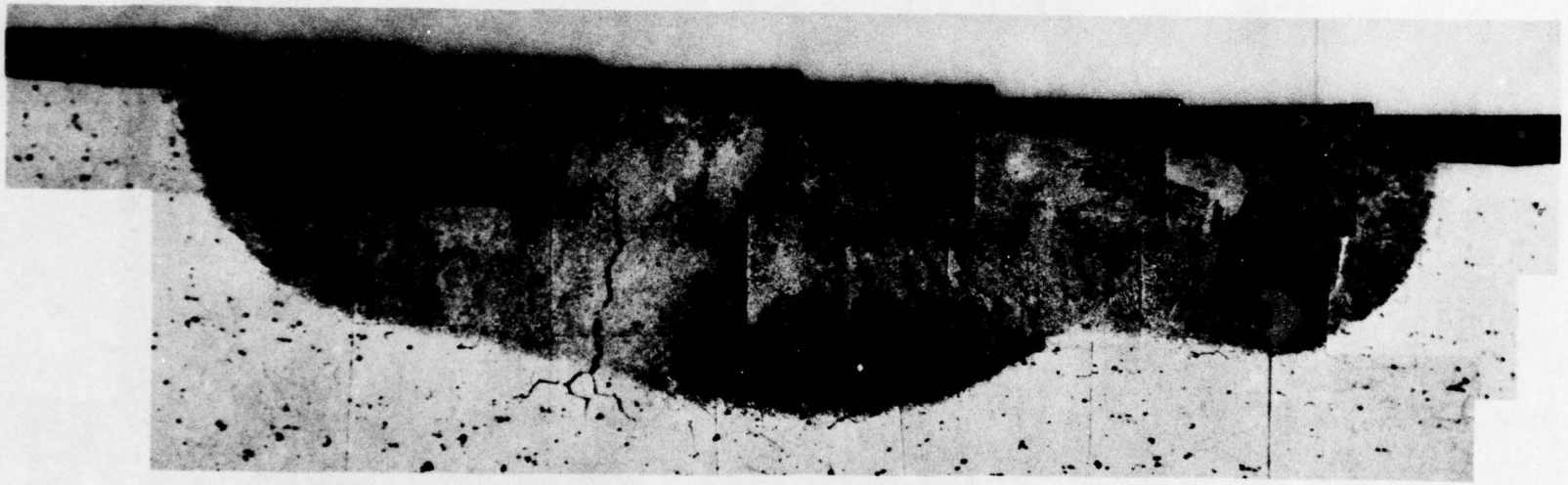


FIG. 5-11 - Photomicrograph of Transverse Section of Varestraint Sample 76-129.
Mat. UD-718, Cond. BM-ST(1950°F), ε = 2%, Note FZ and HAZ Cracking.

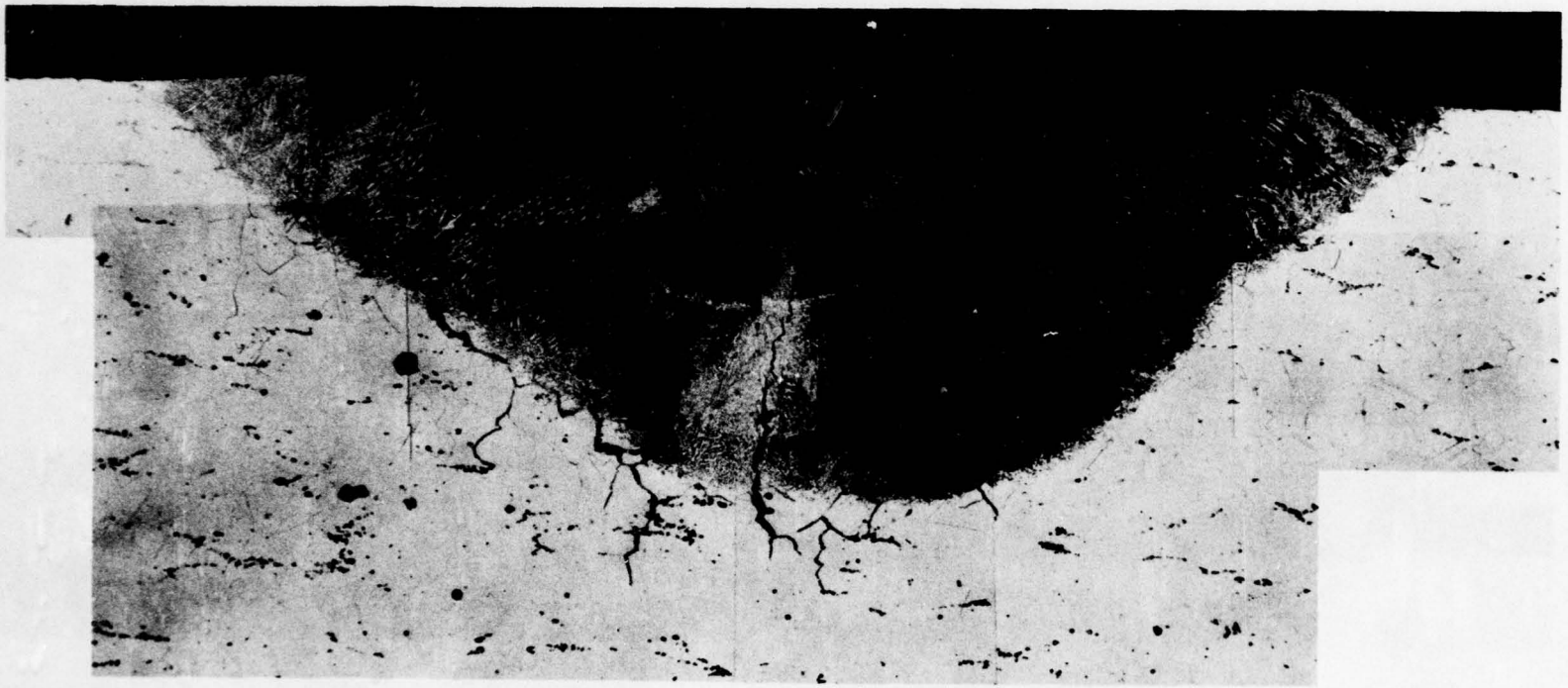


FIG. 5-12 - Photomicrograph of Transverse Section of Restraint Sample 76-121.
Mat. UD-718, Cond. BM-ST(1950°F)DA, ε = 2%, Note FZ and HAZ Cracking.

6.0 MECHANICAL TESTING AND FRACTURE MECHANICS

Introduction

The development of increasingly more cryogenic or superconducting devices and the almost total lack of low temperature fracture mechanics material properties (especially relative to the austenitic materials so ideally suited for low temperature structural applications) has created a strong demand by designers for the material properties data required to insure immunity from structural failure of these systems. Naturally, the cryogenic environment has placed severe restrictions on the development of these required material properties, especially those in the area of fracture mechanics technology. Recent advances in fracture mechanics technology, especially in the area of elastic-plastic fracture, have now made it possible to determine the required fracture mechanics material properties (specifically fracture toughness and crack growth rate) necessary to permit the application of fracture mechanics technology to structures and components subjected to cryogenic environments, thus insuring their structural performance.

This section of the Westinghouse final technical report presents the material properties (tensile, notched tensile, fracture toughness and fatigue crack growth rate) generated throughout the second half of the Westinghouse FY76 ARPA/NBS program. In addition, a comprehensive section is included which summarizes all the fracture toughness and fatigue crack growth rate data generated throughout this program. A basic, parametric fracture mechanics analysis is also included which outlines the design related procedures for utilizing this large amount of fracture data to insure the failsafe performance of a structure or component operating in a cryogenic environment.

6.1 Tensile Results

The tensile properties of A286 (UNS K66286) stainless steel base material and gas tungsten are welds (GTAW) are presented in Figures 6-1 and 6-2 as well as Table 6-1. The A286 base metal tensile specimens were oriented with their loading directions parallel to the longitudinal or rolling direction while the gas tungsten arc weldment specimens were oriented with their loading axis perpendicular (transverse) to the rolling direction and weld bead. The yield and ultimate strengths of A286 base material decreased only moderately with increasing temperature, especially when compared with other austenitic stainless steels, namely Kromarc 58 and AISI 310 S.[1] Whereas the strength superiority of A286 was modest at best at liquid helium temperature, its strength advantage increased significantly as temperature increased toward ambient. The yield and ultimate strengths of A286 gas tungsten arc welds, although considerably below that of the base metal, also demonstrated this moderate temperature dependence. Ductility of the A286 weldments is similar to that of the base metal at cryogenic temperatures but substantially superior at room temperature.

The tensile properties of Pyromet 538 (21Cr-6Ni-9Mn) stainless steel baseplate, gas tungsten arc (GTAW) and shielded metal arc welds (SMAW) are illustrated in Figures 6-3 and 6-4 and summarized in Table 6-1. Tobler and Reed (National Bureau of Standards Cryogenics Division) recently investigated the tensile and fracture properties of Pyromet 538 baseplate and reported the following mechanical properties.[2]

Test Temperature		Yield Strength		Ultimate Strength		Reduction in Area	Elongation
°F	K	ksi	MPa	ksi	MPa	%	%
75	297	51	351.6	102	703.3	78	61
-320	77	130	896.3	214	1475.5	37	43
-452	4	180	1241.1	237	1634.1	40	16

The Westinghouse baseplate tensile specimens were oriented with their loading axis parallel to the final plate rolling direction. The Westinghouse weldment and NBS baseplate tensile specimens were oriented with their loading axis perpendicular (transverse) to the final plate rolling direction. Although some differences in mechanical property behavior would be expected due to the orthogonal orientations, two obvious variations in mechanical behavior are immediately visible. First, the Westinghouse material retains significantly greater ductility at cryogenic temperatures. Secondly, whereas the strength level of the NBS material is slightly superior throughout, at liquid helium temperature the NBS material demonstrates a substantially greater yield strength. All Westinghouse reported mechanical properties are the average of two or more test samples. The individual test results for Pyromet 538 baseplate at -452°F (4K) are as follows:

Specimen Number	Yield Strength ksi	Yield Strength MPa	Ultimate Strength ksi	Ultimate Strength MPa	Reduction in Area %	Elongation %
9213-1	130.6	900.5	200.5	1382.4	72.0	50.7
9213-2	162.5	1120.4	232.0	1599.6	45.3	52.8

The mechanical properties obtained via specimen 9213-2 approach those reported by Tobler and Reed and other than elongation, are quite different from those of specimen 9213-1. Specimens 9213-1 and 9213-2 experienced completely opposite ductile and shear type fractures, respectively. Structural transformation to martensite was experienced by specimen 9213-2 but not by specimen 9213-1. Tobler and Reed have reported that during plastic deformation at room temperature, Pyromet 538 undergoes little martensitic phase transformation but at cryogenic temperatures it transforms extensively to bcc martensitic products.[2] More details on these specimens is available in Section 7 on Microstructural Analysis.

Room temperature strength and ductility of both the gas tungsten arc and shielded metal arc welds are essentially equivalent with the weldment strength and ductility slightly superior and inferior, respectively,

in comparison to Pyromet 538 baseplate. At cryogenic temperatures the gas tungsten arc welds demonstrated strength superiority while the baseplate displayed the maximum ductility.

One Pyromet 538 gas tungsten arc weld tensile specimen tested at liquid helium temperature failed in the weld fusion zone while the remaining specimens all failed in the base material. A direct comparison of the two -452°F (4K) gas tungsten arc weld tensile specimens is shown below.

Specimen Number	Yield Strength ksi	Yield Strength MPa	Ultimate Strength ksi	Ultimate Strength MPa	Reduction in Area %	Elongation %	Failure Zone
9313-1	178.5	1230.7	245.0	1689.2	24.2	29.8	Base
9313-2	181.0	1248.0	232.5	1603.0	24.2	31.6	Weld

Note the strength and ductility of these two tensile specimens are essentially equivalent.

Only the room temperature Pyromet 538 shielded metal arc weld tensile specimens failed in the base material. All shielded metal arc weld tensile specimens tested at cryogenic temperatures experienced weld fusion zone failures. This accounts for the poor elongation exhibited by the shielded metal arc welds at cryogenic temperatures. Obviously, the tensile specimens were deformed solely in the weld fusion zone which in effect implies the elongation was measured only over a small gauge length equivalent to the weld fusion zone thickness. A more realistic comparison of relative ductility between the two Pyromet 538 weldments would be to compare their area reductions. Under these conditions the shielded metal arc welds are more ductile at liquid helium temperature than the gas tungsten arc welds. This will become clearer when we compare the -452°F (4K) fracture toughness properties of these two weldments.

6.2 Fracture Toughness Results

The well documented linear elastic (K_{Ic}) fracture criterion with its inherent plane strain specimen size limitation cannot produce valid fracture toughness results (per the ASTM Test for Plane Strain Fracture Toughness of Metallic Materials, E399-74) on tough austenitic materials unless specimens of very large thickness are employed, which in turn are not representative of the cross-sectional thicknesses found in the majority of actual cryogenic structures. Furthermore, if a failure should occur, proper design of cryogenic structures or components would cause these structures or components to fail plastically (elastic plastic fracture) as opposed to catastrophically (linear elastic fracture). Therefore, where applicable, all our fracture toughness values were obtained via the elastic plastic (J_{Ic}) fracture criterion[3,4] and the associated resistance curve test technique for determining elastic plastic fracture toughness values.[5]

All the fracture toughness values generated at Westinghouse throughout the three year ARPA/NBS program are summarized in Tables 6-2 through 6-10. For comparison purposes, the ratios K_{Ic}/σ_{ys} and $(K_{Ic}/\sigma_{ys})^2$ are also included. Typically, the material with the highest K_{Ic}/σ_{ys} ratio is the toughest material for a given application.[6] The plane strain crack size factor $(K_{Ic}/\sigma_{ys})^2$ provides a measure of toughness that accounts in a single parameter for the interactions of K_{Ic} and strength on crack size tolerance.[7,8]* Stated alternatively, when conducting a parametric fracture mechanics analysis (that is, the applied stress is considered to be a fixed percentage of the particular material's yield strength) the critical defect size for failure in one cycle of loading will be proportional to the crack size factor.[6]

---

*The crack size factor is not related to critical crack size at a stress equal to the yield strength but only under small-scale yielding, that is, at applied stresses appreciably below the yield strength.[7,8]

Details relative to the fracture toughness properties of four materials not presented in a previous technical report follow. These included the influence of processing and heat treatment on the fracture toughness of Inconel 718, plus, in addition, the fracture properties of A286 stainless steel gas tungsten arc welds, Pyromet 538 gas tungsten arc and shielded metal arc welds and PD135.

The Inconel 718 precipitation hardening superalloy evaluated in the Westinghouse program was obtained as an 11 3/8 in. (29 cm) diameter hot finished forging billet, vacuum induction melted-vacuum arc remelted (VIM-VAR). Briefly, it was found that in the as-received conditions, a pronounced contiguous grain boundary network existed at the stock centerline position while at the 5 1/4 in. (13.3 cm) location such contiguous particles were not observed at the equiaxed matrix grain boundaries but rather at prior "ghost" grain boundaries.[9] The relatively low ductility and fracture toughness demonstrated by this 1800°F (1255K) solution treated and double aged Inconel 718 were attributed to thin carbide films or an agglomeration of very small carbide particles within the grain boundaries.[9] Carbide chains in the grain boundaries also proved detrimental to the ductility and fracture properties of (VIM-VAR) Inconel X750.[10,11]

Therefore, it appeared that either a higher solution treatment temperature to dissolve such carbides or a final working treatment followed by a heat treatment to break up this network and recrystallize the entire structure would be necessary to achieve optimum cryogenic material properties with the present Inconel 718 billet material. As a result, the effect of a higher solution treating temperature followed by cold work with a subsequent recrystallization heat treatment in reducing or removing this contiguous carbide grain boundary network as well as to modify the base metal grain size was examined. The various processing and heat treatment details are covered in References 9 and 12. After a 1950°F (1339K) solution treatment followed by cold working the Inconel 718 was subjected to one of three heat treatment schedules: (a) 1800°F (1255K) solution treatment and double age; (b) 1950°F (1339K) solution treatment

and double age; and (c) double age. The influence of processing and heat treatment on the mechanical properties of Inconel 718 were presented in Reference 13. Figure 6-5 illustrates the J resistance curves relative to Inconel 718 while Table 6-4 summarizes the fracture toughness properties of Inconel 718 baseplate and gas tungsten arc weldments.

The poorest fracture toughness was demonstrated by the cold worked plus 1800°F (1255K) solution treated and double aged Inconel 718 (Code 67XX), whose liquid helium temperature fracture toughness was 13 percent below that of the original solution treated and double aged Inconel 718 (Code 64XX). Surprisingly, the high strength Inconel 718 which was double aged but not resolution treated after cold working (Code 69XX) yielded a superior fracture toughness compared with that of the cold worked plus 1800°F (1255K) solution treated and double aged Inconel 718 (Code 67xx). The highest fracture toughness was demonstrated by the cold worked and 1950°F (1339K) solution treated and double aged Inconel 718 (Code 68XX). This improved fracture toughness was expected since prior microstructural analysis had revealed that the carbide network in the higher solution treated temperature Inconel 718 material was appreciably reduced at the matrix grain boundaries and the ghost boundary network was no longer observed.[9] Despite these various processing and heat treatment schedules the fracture toughness of Inconel 718 still fell below that of a solution treated and double aged Udimet 718, which demonstrated no carbide chains or films and had a static fracture toughness of 82.1 ksi$\sqrt{in.}$ (90.0 MPa$\sqrt{m}$) at -320°F (77K).[13]

The J resistance curve for A286 stainless steel gas tungsten arc welds is illustrated in Fig. 6-6 while Table 6-8 summarizes all the fracture toughness properties of A286 (UNS K66286) stainless steel base metal and weldments. All the A286 base metal and weldment fracture toughness specimens were oriented with their notch perpendicular (transverse) to the rolling direction (orientation L-T per ASTM E399-74). The liquid helium temperature fracture toughness of A286 gas tungsten arc welds was not only substantially greater than that of the A286 base metal but superior to that of all the stainless steel weldments

investigated throughout this program, including gas tungsten arc welds in Kromarc 58 and Pyromet 538 as well as shielded metal arc welds in AISI 310 S and Pyromet 538.

The J resistance curves and fracture toughness properties of Pyromet 538 (21Cr-6Ni-9Mn) stainless steel gas tungsten arc and shielded metal arc welds are presented in Fig. 6-7 and Table 6-9, respectively. The liquid helium temperature fracture toughness of the Pyromet 538 shielded metal arc welds proved twice that of the gas tungsten arc welds. Also, in general, the steeper the slope of the J resistance curve the greater the ability of a particular material to resist fracture (i.e., more energy is required for an increment of additional crack extension). The slope of the J resistance curve relative to Pyromet 538 gas tungsten arc welds is extremely shallow and approaches zero, indicating these welds have little ability to sustain loads greater than that corresponding to the critical value of J (J_{Ic}).

Microstructural examination of the shielded metal arc weld fusion zone revealed no evidence of delta ferrite whereas an appreciable ferrite level was observed in the gas tungsten arc weld fusion zone.[13] Filler materials for the gas tungsten arc and shielded metal arc weldments were respectively a matching 21Cr-6Ni-9Mn composition bare wire and a high nickel content Inconel 182 covered electrode. Apparently, the gas tungsten arc welds transformed structurally under deformation at cryogenic temperatures, although no x-ray analysis work was completed to varify this microstructural transformation. On the other hand, due in part to the high nickel content electrode the shielded metal arc welds did not appear to transform structurally and retained excellent cryogenic fracture toughness.

The cryogenic fracture toughness properties of Pyromet 538 baseplate as developed by Tobler and Reed are presented below.[2]

Test Temperature		K_{Ic}	
°F	K	ksi$\sqrt{in.}$	MPa$\sqrt{m}$
-320	77	239	263
-452	4	161	177

The room temperature fracture toughness was too high to measure with the available sized specimens. At liquid helium temperature the base metal J resistance curve slope was very shallow and quite similar to that relative to the gas tungsten arc weldments, even though the base metal yielded a reasonably high fracture toughness. According to Tobler and Reed, the Pyromet 538 base metal did transform structurally to bcc martensite at cryogenic temperatures.[2] This becomes obvious when one considers how the Pyromet 538 base material fracture toughness rapidly decreased with decreasing temperature, unlike structurally stable austenitic materials, whose fracture toughness remains relatively constant and often increases with decreasing temperature. Therefore, although the shielded metal arc welds apparently did not undergo a structural transformation at cryogenic temperatures, it is possible that the surrounding Pyromet 538 base metal did transform structurally.

The -452°F (4K) J resistance curve relative to PD135 is illustrated in Fig. 6-8 while Table 6-10 summarizes all the fracture toughness data generated throughout this program on OFHC copper and copper alloys. PD135 is a heat treatable, oxygen free copper-chromium-cadmium alloy which offers a considerable strength advantage over OFHC copper while still maintaining a high level of conductivity and toughness.

Some explanation is in order concerning the PD135 resistance curve. Experience in J testing on several low strength, highly ductile materials such as various aluminum alloys, copper alloys and even some austenitic stainless steels at elevated temperatures has revealed that the blunting line, developed to account for apparent crack extension due to deformation in elastic-plastic fracture toughness testing of medium and high strength steels and given by the equation $J = 2\sigma_f \Delta a$, where σ_f is a flow stress midway between a material's yield and ultimate stresses, is not always applicable. This is obvious upon viewing the PD135 resistance curve where all the J versus Δa data points fall to the left of the blunting line. If the blunting line is assumed not applicable to this material and the data points best fit with a straight line extrapolated back to zero crack growth (Δa), the corresponding value of

fracture toughness equals 133.3 ksi$\sqrt{in.}$ (147.6 MPa$\sqrt{m}$). A second way to interpret this data is described in an as yet unpublished standard test method to be submitted to the American Society for Testing and Materials on elastic plastic fracture toughness testing, which calls for the construction of an optional blunting line if two or more J versus Δa data points fall on a straight line extrapolated back through the origin. This is the case of PD135. If the optional blunting line is constructed and the remaining data points properly fitted, the corresponding fracture toughness equals 166.8 ksi$\sqrt{in.}$ (184.6 MPa$\sqrt{m}$). From a design standpoint the more conservative fracture toughness value should be employed until an accepted standard test procedure is finalized for obtaining the elastic plastic fracture toughness of low strength, highly ductile materials. Even the conservative liquid helium temperature fracture toughness value for PD135 results in a plane strain crack size factor equal to 12.98, which is the highest crack size factor developed through this program for any material at cryogenic temperatures. Therefore, from a fracture toughness standpoint, PD135 looks very attractive for cryogenic structural applications.

6.3 Crack Growth Rate Results

All the fatigue crack growth rate (FCGR) tests conducted at Westinghouse throughout the three year ARPA/NBS program were performed on a universal hydraulic fatigue machine under sinusoidal tension loading. The maximum alternating load (ΔP) was maintained constant throughout each individual test. Stress ratios, R, (where $R = \sigma_{min}/\sigma_{max} = K_{min}/K_{max}$) equaled 0.10. Test frequency equaled 10 hertz.

Instantaneous crack length in both the cryogenic and room temperature environments was determined by first measuring test specimen crack opening displacement by utilizing either a linear variable differential transformer (LVDT) or clip gauge attached to the specimen front face and finally transforming this crack opening displacement value via specimen compliance into crack length. Test specimen compliance was determined by employing a procedure originally developed by Novak and Rolfe.[14]

The raw test data of crack length (a) versus number of elapsed cycles (N) was subsequently translated into the crack growth rate (da/dN) versus stress intensity factor range (ΔK) data required to conduct a fracture mechanics failure prevention analysis. These crack growth rates were established by means of a computerized curve-fitting analysis of the crack length versus number of elapsed cycles data obtained directly from the FCGR experiments.[15]

A nearly linear relationship between log da/dN and log ΔK data was obtained in all cases and is typical of most FCGR data. Since this linear relationship exists, the crack growth rate data was expressed in terms of the generalized FCGR law developed by Paris.[16] This crack growth rate law is expressed as:

$$\frac{da}{dN} = Co\Delta K^n$$

where da/dN is the rate of crack growth, Co is an intercept constant determined from the log da/dN versus log ΔK plot, n is the slope of the log-log plot and ΔK is the stress intensity factor range.

Several, more complicated expressions for describing log da/dN versus log ΔK behavior have been developed.[17,18] These various expressions are basically similar to the Paris relationship and are often characterized by the addition of various constants. Typically, these modified, more complicated expressions allow the basic relationship to account for nonlinearity. Nonlinearity can be accentuated by adverse environmental influences, stress ratio effects and, in addition, if the log da/dN versus log ΔK relationship spans a large stress intensity factor range, nonlinearity will be introduced by threshold effects and plasticity at low and high stress intensities, respectively. Since inert cryogenic environments are not aggressive enough to cause non-linearity and since our FCGR tests were conducted at a stress ratio equal to 0.10 over a limited range of ΔK, the basic Paris relationship is totally adequate to describe all the FCGR data developed by Westinghouse throughout the ARPA/NBS program.

It should be cautioned that when conducting a fracture mechanics failure prevention analysis, FCGR expressions should not be employed to calculate the growth rate of fatigue cracks in a structure or component unless the applied stress intensity level experienced by the structure or component falls within the stress intensity range spanned by the actual data. In other words, do not extrapolate the linear FCGR expression to cover higher or lower stress intensities.

All the FCGR properties generated at Westinghouse throughout the three year ARPA/NBS program are summarized in Tables 6-11 through 6-13. Details relative to the FCGR properties of five weldments not presented in a previous technical report follow. These include gas tungsten arc welds in Inconel 706, Inconel 718, A286 and Pyromet 538 (21Cr-6Ni-9Mn) as well as shielded metal arc welds in Pyromet 538. Each of the nickel base superalloy weldments were post weld heat treated (solution treated and double aged) while the stainless steel weldments were tested in the as-welded condition.

The FCGR properties of (VIM-VAR) Inconel 706 gas tungsten arc welds are illustrated in Fig. 6-9. Like the (VIM-VAR) Inconel 706 base metal, fatigue cracks in Inconel 706 gas tungsten arc welds will grow considerably faster at room temperature than at cryogenic temperatures. In addition, the growth rate of fatigue cracks in the Inconel 706 gas tungsten arc welds is significantly faster than in the Inconel 706 base metal.

The FCGR properties of (VIM-VAR) Inconel 718 gas tungsten arc welds, both the weld fusion and heat affected zones, are illustrated in Figures 6-10 and 6-11, respectively. Figure 6-12 compares the FCGR properties of Inconel 718 base, gas tungsten arc weld fusion zone and heat affected zone material. Like the Inconel 706 weldments and Inconel 718 base metal, fatigue cracks in Inconel 718 gas tungsten arc welds (both the fusion and heat affected zones) will grow significantly faster at room temperature than at cryogenic temperatures. At both room and liquid helium temperature, the most conservative FCGR properties were demonstrated by the Inconel 718 base metal. The growth rate of fatigue cracks is

fastest in the Inconel 718 gas tungsten arc weld fusion zone with the heat affected zone growth rate falling midway between that of the base metal and weld fusion zone. In addition, Forman has concluded that the FCGR for similar Inconel 718 gas tungsten arc welds was an order of magnitude greater than the growth rate for his Inconel 718 base metal.[19]

A comparison of the Inconel 706 and Inconel 718 gas tungsten arc weldment FCGR properties is illustrated in Figure 6-13. The FCGR properties demonstrated by these gas tungsten arc welds are nearly identical. Fracture toughness of the weldments was also very similar with a slight edge going to the Inconel 706 gas tungsten arc welds.[9] The most conservative FCGR properties were displayed by the Inconel 706 gas tungsten arc welds at -452°F (4K) and by the Inconel 718 heat affected zone material at room temperature. The growth rate of fatigue cracks was fastest in the Inconel 718 gas tungsten arc welds at both room and liquid helium temperature.

The FCGR properties of A286 (UNS K66286) stainless steel gas tungsten arc welds are illustrated in Figure 6-14. Again the growth rate of fatigue cracks is faster at room temperature than at cryogenic temperatures, although, unlike the A286 base metal, the growth rates at -320°F (77K) and -452°F (4K) are identical. The growth rate of fatigue cracks in A286 base metal was directly proportional to temperature; that is, the higher the temperature the greater the fatigue crack propagation rate.[13,20] Although the fracture toughness of A286 gas tungsten arc welds was significantly superior to that of the base metal, the weldment FCGR properties are substantially inferior.

The FCGR properties of Pyromet 538 (21Cr-6Ni-9Mn) stainless steel gas tungsten arc and shielded metal arc welds are displayed in Figures 6-15 and 6-16, respectively. Figure 6-17 compares the FCGR properties of both Pyromet 538 weldments.

Some unusual FCGR behavior is evident relative to these Pyromet 538 weldments. First, the growth rate of fatigue cracks in Pyromet 538 gas tungsten arc welds is faster at cryogenic temperatures than at room temperature. This behavior is unlike that experienced by any base metal

or weldment tested at Westinghouse throughout the three year ARPA/NBS program. A substantial data base exists which indicates that for structurally stable austenitic materials, the growth rate of fatigue cracks is faster at room temperature than at cryogenic temperatures.[1,11,21,22] Also, recall that the fracture toughness of these Pyromet 538 gas tungsten arc welds equaled only half that demonstrated by the shielded metal arc welds and, in addition, the resistance curve slope was very shallow, indicating the gas tungsten arc welds have little ability to sustain a load greater than that corresponding to the critical value of J. Furthermore, Tobler and Reed reported that Pyromet 538 base metal transformed structurally to bcc martensite when deformed plastically at cryogenic temperatures.[2] Therefore, the FCGR behavior demonstrated by the Pyromet 538 gas tungsten arc welds lends further proof that these weldments did indeed transform structurally. No x-ray analysis work was performed on these test specimens, however, to verify this structural transformation. Obviously, Pyromet 538 (either base metal or gas tungsten arc weldments) must be considered very carefully for structrual applications where cryogenic temperatures are involved, especially since Pyromet 538 is a borderline material which can but does not always experience a structural transformation when deformed plastically at cryogenic temperatures.

Interestingly, the growth rate of fatigue cracks in Pyromet 538 shielded metal arc welds is independent of temperature. This same FCGR behavior has been observed in (VIM) Inconel X750, a structurally stable austenitic material.[11] Combining this FCGR behavior with the excellent liquid helium temperature fracture toughness demonstrated by these welds indicates Pyromet 538 shielded metal arc welds do not transform structurally when deformed plastically at cryogenic temperatures. This behavior is most likely due to the high nickel content Inconel 182 covered electrode utilized for these weldments.

6.4 Summary - Design Example

To best summarize the voluminous fracture mechanics material properties data generated by Westinghouse throughout the three year ARPA/NBS program, a parametric, elastic fracture mechanics analysis is included in order to demonstrate the use of fracture mechanics concepts as they apply to a structure subjected to a cryogenic environment. This example will demonstrate to designers a method of applying this data to insure the failsafe structural performance and either predict the cyclic lifetime or initial allowable flaw sizes relative to a particular structure or component.

Successful use of fracture mechanics technology as a tool for design against failure requires basic information in three areas of concern: stress analysis, defect characterization and material properties. The pertinent nominal stress information required for a fracture mechanics analysis of a structure subjected to cyclic loading includes knowledge of the maximum nominal applied stresses developed in the structure as well as the alternating stresses. For this example, the applied nominal stresses and alternating (cyclic) stresses were assigned parametric values equivalent to a specific percentage (75 percent) of the particular material's yield strength ($\sigma/\sigma_{ys} = 0.75$).

Regarding defect characterization, information is required relative to the size, shape, location and orientation of the most critical defects which exist or are likely to develop in the structure of concern. The defect geometry considered was a 10 to 1 length to depth ratio elliptical surface crack oriented with the major crack plane perpendicular to a uniform tension stress field (worst case condition). An example of this defect geometry would be a long, shallow surface crack intersecting the axial bore or inside diameter of a superconducting generator rotor with the major plane of the crack normal to the trangential bore stresses. The pertinent stress intensity expression for this configuration is[23]

$$K_I^2 = \frac{1.21\ a\pi\sigma^2}{Q} \qquad (1)$$

Where K_I = nominal stress intensity factor

a = surface crack depth

σ = applied nominal stress

Q = flaw shape parameter (from Fig. 6-18).

The flaw shape parameter (Q) permits evaluation of defect severity by accounting for surface or internal defects with various length to depth ratios. The flaw shape parameter is obtained from Fig. 6-18, which also illustrates prototype surface and internal defects and the necessary dimensions required for obtaining length to depth ratios. For the case of a 10 to 1 length to depth ratio elliptical surface defect where σ/σ_{ys} equals 0.75, Q equals 0.98.

The pertinent material properties (yield strength, fracture toughness and fatigue crack growth rate) required for the calculations are presented in Tables 6-2 through 6-13. To keep the failure analysis as conservative as possible, the weakest link (whether base metal, weldment or heat affected zone) in terms of fracture toughness or fatigue crack growth rate will be utilized in this analysis. We will assume that the hypothetical structure operates only at liquid helium temperature. This eliminates undue complications which must be considered if the structure experiences both ambient and liquid helium temperatures. Recall, the growth rate of fatigue cracks is greater at room temperature than at cryogenic temperatures for structurally stable austenitic materials, which includes all the nickel base superalloys and stainless steels investigated by Westinghouse with the exception of Pyromet 538.

Concerning Inconel X750, the poorest fracture mechanics material properties were demonstrated by solution treated and double aged (VIM-VAR) Inconel X750 base material. Continuous carbide films in the grain boundaries of this particular (VIM-VAR) Inconel X750 material are the primary reason for these poor fracture properties.[10] Since these

grain boundary carbides were not observed in the (AAM-VAR) and (VIM) Inconel X750 materials, it may be argued that the fracture properties of (VIM-VAR) Inconel X750 are not representative of a typical Inconel X750. Since grain boundary carbides may occur in actual Inconel X750 structures or components, however, we feel justified in employing the fracture properties of (VIM-VAR) Inconel X750 in the analysis. Fracture properties of the Inconel X750 electron beam and gas tungsten arc welds were equal to or superior to those of most manufacturing process/heat treatment combinations of Inconel X750 base material and, as such, these weldments will not be a weak link from a fracture toughness or fatigue crack growth rate standpoint.

Gas tungsten arc welds are the limiting design factor relative to Inconel 706 and Inconel 718 from both a fracture toughness and fatigue crack growth rate standpoint. It should be pointed out that an Inconel 718 filler wire was utilized in the Inconel 706 gas tungsten arc welds. If an Inconel 706 filler wire were employed fracture properties of the Inconel 706 weldments may have approached those of the corresponding base metal. In addition, like (VIM-VAR) Inconel X750, chains of grain boundary carbides were observed in the Inconel 718 baseplate and weldments (including the Inconel 706 weldments), which undoubtedly contributed to their poor fracture properties.[9]

Dynamic fracture toughness was developed for a Udimet 718 material at -320°F (77K).[13] Although dynamic and static cryogenic fracture toughness values of this structurally stable austenitic nickel base superalloy were essentially equivalent, this may not be the case for materials such as Pyromet 538, which transform structurally when deformed plastically at cryogenic temperatures. Consequently, additional dynamic fracture toughness tests must be conducted to observe whether rapid loading decreases the fracture toughness of materials at cryogenic temperatures. If dynamic loading proves detrimental at cryogenic temperatures, dynamic fracture toughness values must be utilized in any thorough fracture mechanics failure prevention analysis.

Regarding Kromarc 58 stainless steel, the lowest fracture toughness was demonstrated by the cold worked baseplate while the growth rate of fatigue cracks was greatest in the gas tungsten arc weldments. Therefore, both Kromarc 58 baseplate (cold worked) and gas tungsten arc welds (STQ/W) will be included in the analysis. Although a common question relative to cold working is whether an anisotropic texture exists in the as cold rolled plate sufficient to cause an appreciable degradation of mechanical or fracture properties under specific orientations of load application, Kromarc 58 was cold worked without creating any specially oriented planes with exceptionally low resistance to catastrophic fracture or fatigue crack propagation.

The lowest fracture toughness and least conservative fatigue crack growth rate properties relative to AISI 310 S stainless steel were displayed by the shielded metal arc welds. Consequently, the fracture properties of these weldments will represent AISI 310 S stainless steel.

Fracture toughness of the A286 gas tungsten arc welds was significantly superior to the A286 baseplate but the growth rate of fatigue cracks in the weld fusion zone was much faster. Therefore, since it is impossible to predict whether the baseplate or weldment will be the limiting design factor in an A286 structure or component operating at cryogenic temperatures, both solution treated, quenched and aged A286 baseplate and A286 gas tungsten arc welds (STQ/W) will be included in the analysis.

Pyromet 538 (21Cr-6Ni-9Mn) stainless steel gas tungsten arc welds, which transformed structurally at -452°F (4K) based on the available fracture toughness and fatigue crack growth rate data, clearly demonstrated the poorest fracture mechanics material properties relative to Pyromet 538 and as such will represent this material in the failure prevention analysis.

Since no weldment data was generated on the Inco low expansion alloy (LEA) or various copper and copper alloys including PD135, these materials will not be included in the example analysis.

The initial step in conducting a fracture mechanics analysis is to calculate the critical flaw sizes necessary to cause failure of the hypothetical structure in one cycle of loading when subjected to a liquid helium environment at applied stress levels equivalent to 75 percent of the appropriate material's yield strength. If the terms in Eq. (1) are rearranged and K_I and "a" are respectively set equal to K_{Ic} and a_{cr}, the following critical flaw size expression is obtained

$$a_{cr} = \frac{K_{Ic}^2 Q}{1.21 \pi \sigma^2} \qquad (2)$$

Substituting the appropriate values of applied stress (see Table 6-14), K_{Ic} and Q (0.98) into the above expression yields the critical flaw sizes presented in Table 6-14.

By combining the critical flaw size with the -452°F (4K) fatigue crack growth rate properties of a particular material, it is possible to compute the number of elapsed cycles (start up - shut down cycles) for an existing subcritical flaw to grow to failure. Wilson has developed a generalized cyclic life expression which readily determines the number of cycles required for an existing defect to grow to the critical flaw size.[6] This expression is presented below

$$N = \frac{2}{(n-2)C_o M^{n/2} \Delta\sigma^n} \left[\frac{1}{a_i^{(n-2)/2}} - \frac{1}{a_{cr}^{(n-2)/2}}\right] \text{ for } n \neq 2$$

$$N = \frac{1}{C_o M \Delta\sigma^2} \ln \frac{a_{cr}}{a_i} \text{ for } n = 2 \qquad (3)$$

where N = number of cycles to failure

n = slope of the log (da/dN) vs log ΔK curve

C_o = intercept constant from log (da/dN) vs log ΔK curve

a_i = initial flaw size

a_{cr} = critical flaw size

$\Delta\sigma$ = alternating stress range

M = flaw shape and geometry parameter [for surface defects, $M = (1.21\ \pi/Q)$].

The above expression is applicable to those loading situations where the relationship between applied load, flaw size and stress intensity factor has the form of $K_I = \sigma(Ma)^{1/2}$. In addition, it is assumed that the cyclic stress range ($\Delta\sigma$) remains constant throughout the component life and that the mean stress does not influence the results.

Solving this expression for N at the various cyclic stress ranges of interest and for a_i values ranging from the minimum detectable flaw size to the appropriate critical flaw size developed cyclic life curves which relate the maximum initial allowable flaw size to the number of cycles required to cause failure at different stress levels. Naturally, any inspection technqiues must be capable of locating and defining some defect smaller than the specified initial allowable flaw size, the exact size of which depends on the safety factors desired.

Resulting cyclic life curves for the various materials at liquid helium temperature are presented in Fig. 6-19. These cyclic life curves represent the most convenient form of presenting fatigue life information because either: (a) the total life can readily be determined from a knowledge of the defect size known or assumed to be present at the start of life or; (b) the initial allowable flaw sizes can be ascertained based on a desired cyclic structural lifetime. For example, initial allowable flaw sizes based on structural lifetimes of 20 and 700 cycles of alternating applied stress are included in Table 6-15.

First let us consider the two materials (namely A286 and Kromarc 58) where it was not possible to predict whether the base metal or weldments would be the limiting design factor from a structural reliability standpoint. Subjected to the particular stress and defect characterization parameters considered in the example, for cyclic lifetimes less than 400 cycles the A286 baseplate is the weaklink while in applications requiring greater than 400 lifetime cycles the A286 gas tungsten arc welds proved to be the weaklink. Compared with the Kromarc 58 gas tungsten arc welds, cold worked Kromarc 58 baseplate proved inferior throughout and as such is the limiting factor in design.

From a total fracture mechanics structural reliability standpoint, A286 stainless steel is clearly the logical choice followed by AISI 310 S and Kromarc 58 stainless steels. The poor fracture toughness and fatigue crack growth rate properties demonstrated by Inconel 706 and Inconcel 718 gas tungsten arc welds make these materials rather unattractive for cryogenic structural applications where similar weldments are required. These poor Inconel 706 and Inconel 718 weldment fracture properties as well as the fracture properties of (VIM-VAR) Inconel X750 base metal were greatly influenced by the grain boundary carbides discovered throughout these materials. Fortunately, Inconel 706 weldment fracture properties would probably improve significantly and approach those of Inconel 706 base metal if an Inconel 706 filler wire were available and utilized instead of the Inconel 718 filler wire employed in this program.

The critical and initial allowable flaw sizes relative to Pyromet 538 are also quite small. As previously mentioned, Pyromet 538 gas tungsten arc welds should be utilized with caution in a structure exposed to cryogenic temperatures due to the somewhat unpredictable behavior (possible structural transformation) demonstrated by these gas tungsten arc welds when deformed plastically at cryogenic temperatures. Fracture mechanics properties of the Pyromet 538 shielded metal arc welds are far superior to those of the gas tungsten arc welds, however, and as such much greater cyclic lifetimes would be realized.

Please note this parametric elastic analysis is strictly an example and in no way should a designer attempt to apply the critical or initial allowable flaw sizes generated herein to a random structure or component. Although this analysis serves to relate the fracture behavior of these materials in a hypothetical cryogenic structural application, no provision is made for materials which may be attractive due to a particularly high yield strength, mechanical and fracture properties which are relatively constant with temperature or any other of several design considerations including elastic, thermal and magnetic properties as well as ease of fabricability. This example analysis does demonstrate in a very simplistic way, however, how fracture mechanics technology can be applied to insure the failsafe performance and either predict the cyclic lifetime or initial allowable flaw sizes relative to a particular structure or component which operates at cryogenic temperatures.

REFERENCES - SECTION 6

1. Logsdon, W. A., Wells, J. M. and Kossowsky, R., "Fracture Mechanics Properties of Austenitic Stainless Steels for Advanced Cryogenic Applications," proceedings of the Second International Conference on Mechanical Behavior of Materials, Boston, Massachusetts, August 1976, pp. 1283-1289.

2. Tobler, R. L. and Reed, R. P., "Tensile and Fracture Behavior of a Nitrogen-Strengthened, Chromium-Nickel-Manganese Stainless Steel at Cryogenic Temperatures," proceedings of the Second International Conference on Mechanical Behavior of Materials, Boston, Massachusetts, August 1976, pp. 1206-1210.

3. Begley, J. A. and Landes, J. D., "The J Integral as a Fracture Criterion," Fracture Toughness, Proceedings of the 1971 National Symposium on Fracture Mechanics, Part II, ASTM STP 514, American Society for Testing and Materials, 1972, pp. 1-20.

4. Landes, J. D. and Begley, J. A., "The Effect of Specimen Geometry on J_{Ic}," Fracture Toughness, Proceedings of the 1971 National Symposium on Fracture Mechanics, Part II, ASTM STP 514, American Society for Testing and Materials, 1972, pp. 24-39.

5. Landes, J. D. and Begley, J. A., "Test Results from J-Integral Studies: An Attempt to Establish a J_{Ic} Testing Procedure," Fracture Analysis, ASTM STP 560, American Society for Testing and Materials, 1974, pp. 170-186.

6. Wessel, E. T., Clark, W. G. and Wilson, W. K., "Engineering Methods for the Design and Selection of Materials Against Fracture," U. S. Army Tank-Automotive Center Report AD No. 801005, June 1966.

7. Brown, W. F., Jr. and Srawley, J. E., "Commentary on Present Practice," Review of Developments in Plane Strain Fracture Toughness Testing, ASTM STP 463, American Society of Testing and Materials, 1970, pp. 216-248.

8. Vishnevsky, C. and Steigerwald, E. A., "Plane Strain Fracture Toughness of Some Cryogenic Materials at Room and Subzero Temperatures," Fracture Toughness Testing at Cryogenic Temperatures, ASTM STP 496, American Society for Testing and Materials, 1971, pp. 3-26.

9. Wells, J. M., Logsdon, W. A., Kossowsky, R. and Daniel, M. R., "Structural Materials for Cryogenic Applications, Fourth Semi-annual Technical Report," Westinghouse Research Report 75-9D4-CRYMT-R2, October 1975.

10. Kossowsky, R., "Microstructure of Inconel X750 Materials for Cryogenic Structural Applications," presented at the International Cryogenic Materials Conference, Kingston, Ontario, July 1975.

11. Logsdon, W. A., "Cryogenic Fracture Mechanics Properties of Several Manufacturing Process/Heat Treatment Combinations of Inconel X750," presented at the International Cryogenic Materials Conference, Kingston, Ontario, July 1975.

12. Wells, J. M., Logsdon, W. A., Kossowsky, R. and Daniel, M. R., "Structural Materials for Cryogenic Applications, Third Semi-annual Technical Report," Westinghouse Research Report 75-9D4-CRYMT-R1, March 1975.

13. Wells, J. M., Logsdon, W. A., Kossowsky, R. and Daniel, M. R., "Structural Materials for Cryogenic Applications, Fifth Semi-annual Technical Report," Westinghouse Research Report 75-9D4-CRYMT-R1, April 1976.

14. Novak, S. R. and Rolfe, S. T., "Modified WOL Specimen for K_{Iscc} Environmental Testing," Journal of Materials, JMLSA, Vol. 4, No. 3, September 1969, pp. 701-728.

15. Federowicz, A. J. and Powell, B. A., "A Computer Program to Obtain a Min-Max Regression Model by Linear Programming," unpublished Westinghouse Research data.

16. Paris, P. C., "The Fracture Mechanics Approach to Fatigue," Proc. Tenth Sagamore Army Materials Research Conference, August 1963, Syracuse University Press, 1964.

17. Gallagher, J. P., "Fatigue Crack Growth Rate Laws Accounting for Stress Ratio Effects," ASTM Task Force E24.04.04 Report No. 1, 1975.

18. Collipriest, J. E., Ehret, R. M., "A Generalized Relationship Representing the Sigmoidal Distribution of Fatigue Crack Growth Rates," Rockwell International Space Division, Paper No. SD 74-CE-0001, March 1974.

19. Forman, R. G., "Crack-Growth Behavior in Thick Welded Plates of Inconel 718 at Room and Cryogenic Temperatrues," NASA Technical Note D-7665, National Aeronautics and Space Administration, Washington, D.C., May 1974.

20. James, L. A., "The Effect of Temperature on the Fatigue-Crack Propagation Behavior of A286 Steel," Hanford Engineering Development Laboratory, HEDL-TME 75-82, September 1975.

21. Tobler, R. L. and Reed, R. P., "Fatigue Crack Growth Rates of Structural Alloys at Four Kelvin," Presented at the International Cryogenic Materials Conference, Kingston, Ontario, July 1975.

22. Reed, R. P., Tobler, R. L. and Mikesell, R. P., "The Fracture Toughness and Fatigue Crack Growth Rate of an Fe-Ni-Cr Superalloy at 298, 76 and 4K," Presented at the International Cryogenic Materials Conference, Kingston, Ontario, July 1975.

23. Irwin, G. R., "Crack Extension Force for a Part-Through Crack in a Plate," Journal of Applied Mechanics, Vol. 29, Transactions ASME, Vol. 84, Series E, December 1962.

TABLE 6-1 - TENSILE AND NOTCHED TENSILE PROPERTIES OF A286 (UNS 66286) AND PYROMET 538 (21Cr-6Ni-9Mn) STAINLESS STEEL BASEPLATE AND WELDMENTS

Code	Material	Material Condition	Heat Treatment	Test Temperature °F	Test Temperature K	Yield Strength ksi	Yield Strength MPa	Ultimate Strength ksi	Ultimate Strength MPa	Reduction in Area %	Elongation %	NTS ksi	NTS MPa	NTS/σ_{ys} ksi/ksi
90XX	A286	Base	STQA	75	297	119.3	822.5	151.2	1042.5	34.8	23.5	--	--	--
				-320	77	131.4	906.4	191.6	1321.0	29.0	35.7	--	--	--
				-452	4	140.5	968.7	194.2	1339.0	26.0	29.7	--	--	--
91XX	A286	GTAW	STQ/W	75	297	44.3	305.4	87.7	604.7	63.0	39.0	--	--	--
				-320	77	68.6	473.0	122.8	846.7	28.7	39.2	--	--	--
				-452	4	84.6	583.3	132.6	914.2	27.1	27.1	--	--	--
92XX	Pyromet 538	Base	STQ	75	297	49.0	337.8	97.9	675.0	81.0	75.1	--	--	--
				-320	77	116.0	799.8	199.4	1374.8	72.8	76.4	--	--	--
				-452	4	146.6	1010.8	216.2	1490.6	58.6	51.8	--	--	--
93XX	Pyromet 538	GTAW	STQ/W	75	297	60.0	413.7	105.2	725.3	74.2	50.9	179.6	1238.3	2.99
				-320	77	146.3	1008.7	210.7	1452.7	61.2	48.3	307.4	2119.4	2.10
				-452	4	179.8	1239.7	238.8	1646.5	24.2	30.7	267.0	1840.9	1.49
94XX	Pyromet 538	SMAW	STQ/W	75	297	59.9	413.0	105.7	728.8	75.4	52.6	147.6	1017.7	2.47
				-320	77	116.1	800.5	151.6	1045.2	37.4	6.1	205.4	1416.2	1.77
				-452	4	116.7	804.6	157.5	1085.9	39.5	6.0	205.8	1418.9	1.76

Each value is the average of two samples per temperature.

TABLE 6-2 - FRACTURE TOUGHNESS PROPERTIES OF INCONEL X750

Code	Material Condition	Manu. Process	Heat Treatment	Test Temperature °F	Test Temperature K	Yield Strength ksi	Yield Strength MPa	J_{Ic} in.-lb/in.^{2}	J_{Ic} MN/m	K_{Ic} ksi$\sqrt{in.}$	K_{Ic} MPa$\sqrt{m}$	K_{Ic}/σ_{ys} $\sqrt{in.}$	$(K_{Ic}/\sigma_{ys})^2$ in.
30XX	Base	VIM-VAR	ST	-452	4	106.8	736.4	245	.043	92.2	102.1	.86	.75
30XX	Base	VIM-VAR	ST	75	297	96.2	663.3	320	.056	103.6	114.7	1.08	1.16
31XX	Base	VIM-VAR	STDA	-452	4	125.7	866.7	138	.024	69.2	76.6	.55	.30
40XX	Base	AAM-VAR	STDA	-452	4	141.3	974.2	1350	.236	216.0	239.1	1.53	2.34
50XX	Base	VIM	STDA	-452	4	173.2	1194.2	500	.088	131.5	145.6	.76	.58
60XX	Base	HIP	--	-452	4	130.1	897.0	465	.081	126.8	140.4	.97	.95
61XX	Base	HIP	STDA	-452	4	150.5	1037.7	233	.041	89.7	99.3	.60	.36
32XX	EBW*	VIM-VAR	ST/W	-452	4	106.0	730.8	>1696	>.297	>242.7	>268.7	>2.29	5.20
33XX	EBW*	VIM-VAR	STDA/W	-452	4	111.8	770.8	>1789	>.313	>249.2	>275.9	>2.23	4.97
34XX	EBW	VIM-VAR	ST/W/STDA	-452	4	132.5	913.6	738	.129	160.1	177.2	1.21	1.46
35XX	GTAW	VIM-VAR	ST/W	-452	4	108.8	750.1	875	.153	174.3	193.0	1.60	2.57
36XX	GTAW	VIM-VAR	STDA/W	-452	4	125.0	861.8	690	.121	154.8	171.4	1.24	1.53
37XX	GTAW	VIM-VAR	ST/W/STDA	-452	4	139.0	958.4	425	.074	121.5	134.5	.87	.76
38XX	Cu Braze	VIM-VAR	ST/B	-452	4	115.1	793.6	--	--	40.5	44.8	.35	.12
38XX	Cu Braze	VIM-VAR	ST/B	-320	77	108.4	747.4	--	--	35.3	39.1	.33	.11
38XX	Cu Braze	VIM-VAR	ST/B	75	297	94.5	651.6	--	--	34.7	38.4	.37	.13

*Toughness exceeds the measurement capacity of 1/2 TCT specimens. That is, the dimensional parameter of the 1/2 TCT specimens could not meet the size requirement necessary for a valid J test: a, B, b $\geq$ 25 (J/σ_f).

TABLE 6-3 - FRACTURE TOUGHNESS PROPERTIES OF INCONEL 706

Code	Material Condition	Manu. Process	Heat Treatment	Test Temperature °F	Test Temperature K	Yield Strength ksi	Yield Strength MPa	J_{Ic_2} in.-lb/in.^{2}	J_{Ic_2} MN/m	K_{Ic} ksi$\sqrt{in.}$	K_{Ic} MPa$\sqrt{m}$	K_{Ic}/σ_{ys} $\sqrt{in.}$	$(K_{Ic}/\sigma_{ys})^2$ in.
70XX	Base	VIM-EFR	STDA	-452	4	178.0	1227.3	550	.096	137.9	152.7	.77	.60
71XX	Base	VIM-VAR	STDA	-452	4	184.6	1272.8	664	.116	151.5	167.7	.82	.67
71XX	Base	VIM-VAR	STDA	75	297	154.2	1063.2	364	.064	110.2	122.0	.71	.51
72XX	GTAW	VIM-VAR	ST/W/STDA	-452	4	177.2	1221.8	--	--	53.0	58.7	.30	.09

TABLE 6-4 - FRACTURE TOUGHNESS PROPERTIES OF INCONEL 718

Code	Material Condition	Manu. Process	Heat Treatment	Test Temperature °F	Test Temperature K	Yield Strength ksi	Yield Strength MPa	J_{Ic} in.-lb/in.^{2}	J_{Ic} MN/m	K_{Ic} ksi$\sqrt{in.}$	K_{Ic} MPa$\sqrt{m}$	K_{Ic}/σ_{ys} $\sqrt{in.}$	$(K_{Ic}/\sigma_{ys})^2$ in.
64XX	Base	VIM-VAR	STDA	-452	4	203.9	1405.8	152	.027	72.5	80.3	.36	.13
64XX	Base	VIM-VAR	STDA	75	297	168.8	1163.8	120	.021	63.3	70.1	.38	.14
67XX	Base	VIM-VAR	ST/CW/ST*	-452	4	206.0	1420.3	114	.020	62.8	69.5	.30	.09
68XX	Base	VIM-VAR	ST/CW/ST**	-452	4	198.5	1368.6	189	.033	80.8	89.4	.41	.17
69XX	Base	VIM-VAR	ST/CW/DA	-452	4	248.7	1714.7	125	.022	65.7	72.7	.26	.07
65XX	GTAW	VIM-VAR	ST/W/STDA	-452	4	199.2	1373.4	--	--	47.1	52.1	.24	.06
65XX	GTAW	VIM-VAR	ST/W/STDA	-320	77	185.8	1281.0	--	--	46.5	51.5	.25	.06
66XX	GTAW(HAZ)	VIM-VAR	ST/W/STDA	-452	4	199.2	1373.4	--	--	55.4	61.3	.28	.08
66XX	GTAW(HAZ)	VIM-VAR	ST/W/STDA	-320	77	185.8	1281.0	--	--	60.2	66.6	.32	.10

*(1800°F, 1255 K)/DA

**(1950°F, 1339 K)/DA

TABLE 6-5 - FRACTURE TOUGHNESS PROPERTIES OF INCO LOW EXPANSION ALLOY (LEA)

Code	Material Condition	Manu. Process	Heat Treatment	Test Temperature °F	Test Temperature K	Yield Strength ksi	Yield Strength MPa	J_{Ic_2} in.-lb/in.^{2}	J_{Ic_2} MN/m	K_{Ic} ksi$\sqrt{in.}$	K_{Ic} MPa$\sqrt{m}$	K_{Ic}/σ_{ys} $\sqrt{in.}$	$(K_{Ic}/\sigma_{ys})^2$ in.
73XX	Base	AAM-VAR	STA	-452	4	185.9	1281.7	195	.034	82.1	90.9	.44	.20
73XX	Base	AAM-VAR	STA	75	297	133.2	918.4	263	.046	93.7	103.7	.70	.49

TABLE 6-6 - FRACTURE TOUGHNESS PROPERTIES OF KROMARC 58 STAINLESS STEEL

Code	Material Condition	ASTM E399 Orientation	Heat Treatment	Test Temperature °F	Test Temperature K	Yield Strength ksi	Yield Strength MPa	J_{Ic} in.-lb/in.^{2}	J_{Ic} MN/m	K_{Ic} ksi$\sqrt{in.}$	K_{Ic} MPa$\sqrt{m}$	K_{Ic}/σ_{ys} $\sqrt{in.}$	$(K_{Ic}/\sigma_{ys})^2$ in.
80XX	Base	T-L	STQ	-452	4	158.7	1094.2	1250	.219	195.4	216.3	1.23	1.52
81XX	Base	T-L	CW	-452	4	213.4	1471.3	388	.068	108.8	120.4	.51	.26
87XX	Base	L-T	CW	-452	4	215.8	1487.9	452	.079	117.5	130.1	.54	.30
82XX	GTAW	T-L	STQ/W	-452	4	153.8	1060.4	650	.114	140.9	156.0	.92	.84
83XX	GTAW	T-L	CW/W	-452	4	184.1	1269.3	552	.097	129.8	143.7	.71	.50
84XX	GTAW	T-L	W/CW	-452	4	201.4	1388.6	217	.038	81.4	90.1	.40	.16
85XX	GTAW	T-L	W/CW/AN*	-452	4	≈171†	≈1179†	515	.090	125.4	138.8	.73	.54
86XX	GTAW	T-L	W/CW/AN**	-452	4	142.4	981.8	895	.157	165.3	183.0	1.16	1.35

*(1500°F, 1089 K)

**(1600°F, 1144 K)

†Estimated

TABLE 6-7 - FRACTURE TOUGHNESS PROPERTIES OF AISI 310 S STAINLESS STEEL

Code	Material Condition	Heat Treatment	Test Temperature °F	Test Temperature K	Yield Strength ksi	Yield Strength MPa	J_{Ic_2} in.-lb/in.^{2}	K_{Ic} MN/m	K_{Ic} ksi$\sqrt{in.}$	K_{Ic} MPa$\sqrt{m}$	K_{Ic}/σ_{ys} $\sqrt{in.}$	$(K_{Ic}/\sigma_{ys})^2$ in.
20XX	Base	STQ	-452	4	118.5	817.0	1600	.280	236.3	261.6	1.99	3.98
21XX	Base	STFC	-452	4	118.5	817.0	765	.134	163.4	180.9	1.38	1.90
22XX	SMAW	ST/W	-452	4	120.2	828.7	325	.057	106.5	117.9	.89	.79

TABLE 6-8 - FRACTURE TOUGHNESS PROPERTIES OF A286 (UNS 66286) STAINLESS STEEL

Code	Material Condition	Heat Treatment	Test Temperature °F	Test Temperature K	Yield Strength ksi	Yield Strength MPa	J_{Ic} in.-lb/in.^{2}	J_{Ic} MN/m	K_{Ic} ksi$\sqrt{in.}$	K_{Ic} MPa$\sqrt{m}$	K_{Ic}/σ_{ys} $\sqrt{in.}$	$(K_{Ic}/\sigma_{ys})^2$ in.
90XX	Base	STQA	-452	4	140.5	968.7	815	.143	162.8	180.2	1.16	1.34
90XX	Base	STQA	75	297	119.3	822.5	692	.121	145.6	161.2	1.22	1.49
91XX	GTAW	STQ/W	-452	4	84.6	583.3	1660	.291	225.1	249.2	2.66	7.08

TABLE 6-9 - FRACTURE TOUGHNESS PROPERTIES OF PYROMET 538 (21Cr-6Ni-9Mn) STAINLESS STEEL

Code	Material Condition	Heat Treatment	Test Temperature °F	Test Temperature K	Yield Strength ksi	Yield Strength MPa	J_{Ic_2} in.lb/in.^{2}	K_{Ic} MN/m	K_{Ic} ksi$\sqrt{in.}$	K_{Ic} MPa$\sqrt{m}$	K_{Ic}/σ_{ys} $\sqrt{in.}$	$(K_{Ic}/\sigma_{ys})^2$ in.
93XX	GTAW	STQ/W	-452	4	179.8	1239.7	172	.030	74.4	82.4	.41	.17
94XX	SMAW	STQ/W	-452	4	116.7	804.6	783	.137	158.8	175.8	1.36	1.85

TABLE 6-10 - FRACTURE TOUGHNESS PROPERTIES OF OFHC COPPER AND PD 135

Code	Material	Material Condition	Heat Treatment	Test Temperature °F	Test Temperature K	Yield Strength ksi	Yield Strength MPa	J_{Ic} in.-lb/in.^{2}	J_{Ic} MN/m	K_{Ic} ksi$\sqrt{in.}$	K_{Ic} MPa$\sqrt{m}$	K_{Ic}/σ_{ys} $\sqrt{in.}$	$(K_{Ic}/\sigma_{ys})^2$ in.
10XX	OFHC Copper*	Base	AR	-452	4	10.2	70.3	--	--	--	--	--	--
11XX	OFHC Copper*	Base	SR	-452	4	9.2	63.4	--	--	--	--	--	--
12XX	OFHC Copper*	GMAW	W	-452	4	8.8	60.7	--	--	--	--	--	--
15XX	PD 135	Base	EXT/PHT	-452	4	37.0	255.1	754.1 to 1180.0	.132 to .207	133.3 to 166.8	147.6 to 184.6	3.60 to 4.51	12.98 to 20.32

*Toughness exceeds the measurement capacity of 1/2 TCT specimens. That is, the dimensional parameter of the 1/2 TCT specimens could not meet the size requirement necessary for a valid J test: a, B, b $\geq$ 25 (J/σ_f).

TABLE 6-11 - FATIGUE CRACK GROWTH RATE PROPERTIES OF INCONEL X750

Code	Material Condition	Manu. Process	Heat Treatment	Test Temperatures °F	Test Temperatures K	da/dN = Co ΔK^n (in./cycle, ksi$\sqrt{in.}$) n	da/dN = Co ΔK^n (in./cycle, ksi$\sqrt{in.}$) Co
30XX	Base	VIM-VAR	ST	75	297	7.00	4.83×10^{-16}
				-452	4	8.00	2.04×10^{-18}
31XX	Base	VIM-VAR	STDA	75	297	7.00	4.83×10^{-16}
				-452	4	8.00	2.04×10^{-18}
40XX	Base	AAM-VAR	STDA	75, -320	297, 77	3.45	2.52×10^{-11}
				-452	4	3.45	8.26×10^{-12}
50XX	Base	VIM	STDA	75, -320, -452	297, 77, 4	4.40	1.57×10^{-12}
60XX	Base	HIP	--	-320, -452	77, 4	3.90	6.72×10^{-12}
61XX	Base	HIP	STDA	-320, -452	77, 4	4.85	2.62×10^{-13}
32XX	EBW*	VIM-VAR	ST/W				
33XX	EBW*	VIM-VAR	STDA/W				
34XX	EBW	VIM-VAR	ST/W/STDA	-320, -452	77, 4	8.00	2.04×10^{-18}
35XX	GTAW	VIM-VAR	ST/W	-320, -452	77, 4	8.00	2.04×10^{-18}
36XX	GTAW	VIM-VAR	STDA/W	-320, -452	77, 4	8.00	2.04×10^{-18}
37XX	GTAW	VIM-VAR	ST/W/STDA	-320, -452	77, 4	8.00	2.04×10^{-18}

*Fatigue cracks grew into base material

TABLE 6-12 - FATIGUE CRACK GROWTH RATE PROPERTIES OF THREE NICKEL BASE SUPERALLOYS

Code	Material	Material Condition	Manu. Process	Heat Treatment	Test Temperatures °F	Test Temperatures K	da/dN = Co ΔK^n (in./cycle, ksi$\sqrt{in.}$) n	Co
70XX	Inconel 706	Base	VIM-EFR	STDA	75	297	4.11	4.20×10^{-12}
					-320	77	3.35	3.18×10^{-11}
					-452	4	3.12	4.72×10^{-11}
71XX	Inconel 706	Base	VIM-VAR	STDA	75	297	3.27	5.47×10^{-11}
					-320	77	3.50	1.57×10^{-11}
					-452	4	2.77	1.19×10^{-10}
72XX	Inconel 706	GTAW	VIM-VAR	ST/W/STDA	75	297	4.34	6.02×10^{-12}
					-452	4	4.35	1.57×10^{-12}
64XX	Inconel 718	Base	VIM-VAR	STDA	75	297	4.10	8.79×10^{-12}
					-320, -452	77, 4	4.55	4.42×10^{-13}
65XX	Inconel 718	GTAW	VIM-VAR	ST/W/STDA	75	297	4.02	2.19×10^{-11}
					-452	4	4.65	8.57×10^{-13}
66XX	Inconel 718	GTAW(HAZ)	VIM-VAR	ST/W/STDA	75	297	4.78	1.13×10^{-12}
					-452	4	4.64	6.62×10^{-13}
73XX	Inco LEA	Base	AAM-VAR	STA	75	297	3.97	1.39×10^{-11}
					-320	77	4.44	2.18×10^{-12}
					-452	4	4.07	4.56×10^{-12}

TABLE 6-13 - FATIGUE CRACK GROWTH RATE PROPERTIES OF FOUR STAINLESS STEELS

Code	Material	Material Condition	ASTM E399 Orientation	Heat Treatment	Test Temperatures °F	Test Temperatures K	da/dN = Co ΔK^n (in./cycle, ksi$\sqrt{in.}$) n	Co
80XX	Kromarc 58	Base	T-L	STQ	75	297	3.93	1.29×10^{-11}
					-320, -452	77, 4	3.00	1.04×10^{-10}
81XX	Kromarc 58	Base	T-L	CW	75	297	3.00	2.10×10^{-10}
					-320, -452	77, 4	3.00	1.04×10^{-10}
87XX	Kromarc 58	Base	L-T	CW	75	297	3.00	2.10×10^{-10}
					-320, -452	77, 4	3.00	1.04×10^{-10}
82XX	Kromarc 58	GTAW	T-L	STQ/W	-320, -452	77, 4	4.45	7.61×10^{-13}
20XX	AISI 310 S	Base	T-L	STQ	-320, -452	77, 4	3.75	7.90×10^{-12}
21XX	AISI 310 S	Base	T-L	STFC	-320, -452	77, 4	3.75	7.90×10^{-12}
22XX	AISI 310 S	SMAW	T-L	ST/W	-320, -452	77, 4	5.15	4.98×10^{-14}
90XX	A286 (ASTM A453)	Base	L-T	STQA	75	297	2.70	6.61×10^{-10}
					-320	77	2.18	1.76×10^{-9}
					-452	4	2.18	1.31×10^{-9}
91XX	A286 (ASTM A453)	GTAW	L-T	STQ/W	75	297	4.63	7.66×10^{-13}
					-320, -452	77, 4	5.00	1.16×10^{-13}
93XX	Pyromet 538 (21Cr-6Ni-9Mn)	GTAW	T-L	STQ/W	75	297	3.72	9.91×10^{-12}
					-320, -452	77, 4	6.36	5.47×10^{-15}
94XX	Pyromet 538 (21Cr-6Ni-9Mn)	SMAW	T-L	STQ/W	75, -320, -452	297, 77, 4	5.13	1.61×10^{-13}

TABLE 6-14 - CRITICAL FLAW SIZES OF SEVERAL MATERIALS AT -452°F (4K)

Code	Material	Material Condition	Heat Treatment	Applied Stress Level ksi	Applied Stress Level MPa	Critical Flaw Size Depth in.	Critical Flaw Size Depth cm	Critical Flaw Size Length in.	Critical Flaw Size Length cm
31XX	Inconel X750	Base	STDA	94.3	650.0	.139	.353	1.39	3.53
72XX	Inconel 706	GTAW	ST/W/STDA	132.9	916.4	.041	.104	.41	1.04
65XX	Inconel 718	GTAW	ST/W/STDA	149.4	1030.0	.026	.066	.26	.66
81XX	Kromarc 58	Base	CW	160.0	1103.5	.119	.302	1.19	3.02
82XX	Kromarc 58	GTAW	STQ/W	115.4	795.3	.384	.975	3.84	9.75
22XX	AISI 310 S	SMAW	ST/W	90.2	621.5	.359	.912	3.59	9.12
90XX	A286	Base	STQA	105.4	726.5	.615	1.562	6.15	15.62
91XX	A286	GTAW	STQ/W	63.4	437.5	3.250	8.255	32.50	82.55
93XX	Pyromet 538	GTAW	STQ/W	134.8	929.8	.079	.201	.79	2.01

TABLE 6-15 - INITIAL ALLOWABLE FLAW SIZES FOR SEVERAL MATERIALS AT -452°F (4K)

Code	Material	Material Condition	Heat Treatment	Initial Allowable Flaw Size 20 Cycles Depth in.	Depth cm	Length in.	Length cm	700 Cycles Depth in.	Depth cm	Length in.	Length cm
31XX	Inconel X750	Base	STDA	.124	.315	1.24	3.15	.054	.137	.54	1.37
72XX	Inconel 706	GTAW	ST/W/STDA	.027	.069	.27	.69	.005	.013	.05	.13
65XX	Inconel 718	GTAW	ST/W/STDA	.034	.086	.34	.86	.012	.030	.12	.30
81XX	Kromarc 58	Base	CW	.115	.292	1.15	2.92	.061	.155	.61	1.55
82XX	Kromarc 58	GTAW	STQ/W	.345	.876	3.45	8.76	.078	.198	.78	1.98
22XX	AISI 310 S	SMAW	ST/W	.338	.859	3.38	8.59	.128	.325	1.28	3.25
90XX	A286	Base	STQA	.612	1.554	6.12	15.54	.557	1.415	5.57	14.15
91XX	A286	GTAW	STQ/W	2.365	6.007	23.65	60.07	.408	1.036	4.08	10.36
93XX	Pyromet 538	GTAW	STQ/W	.045	.114	.45	1.14	.010	.025	.10	.25

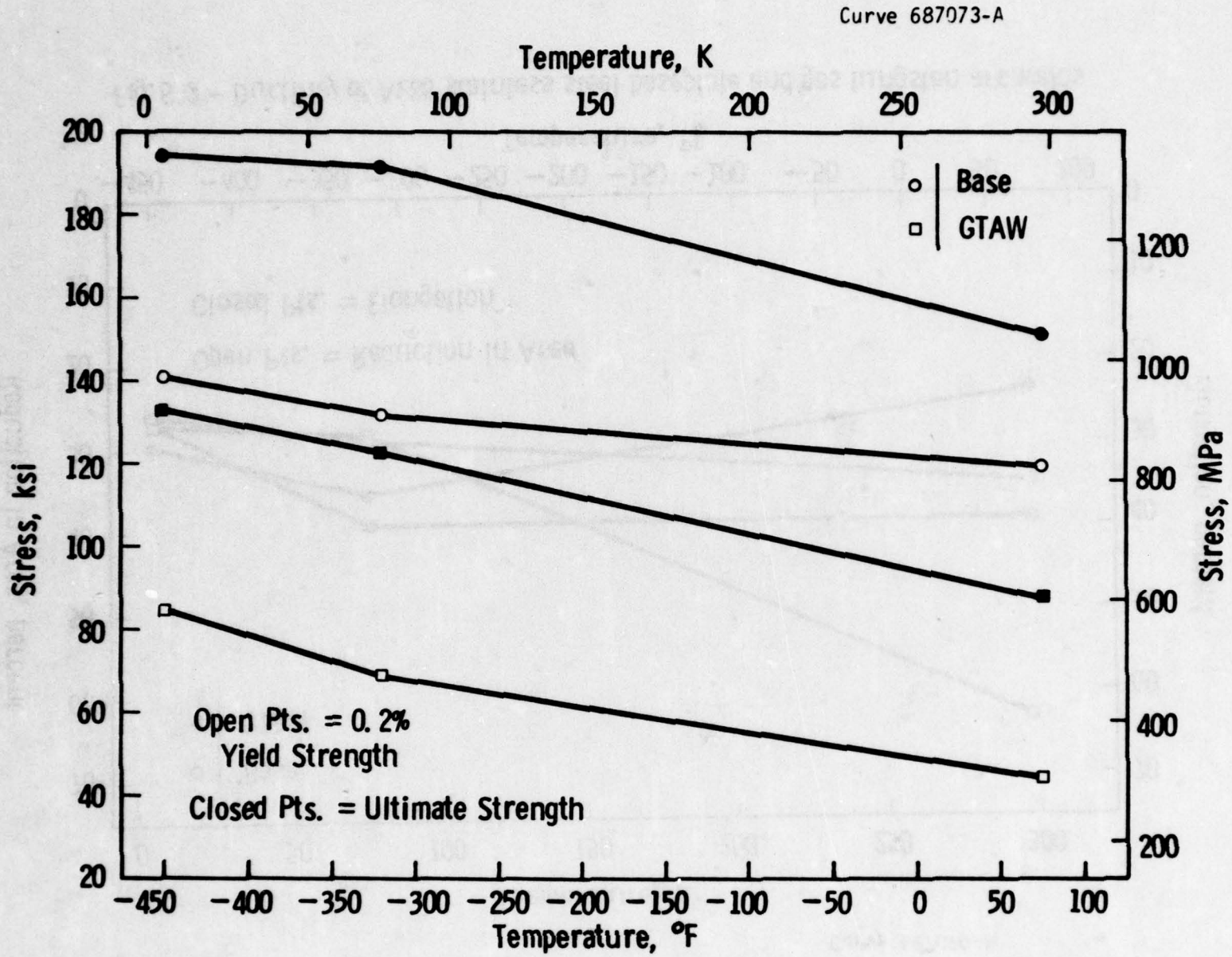


Fig.6-1 – Tensile properties of A286 stainless steel baseplate and gas tungsten arc welds

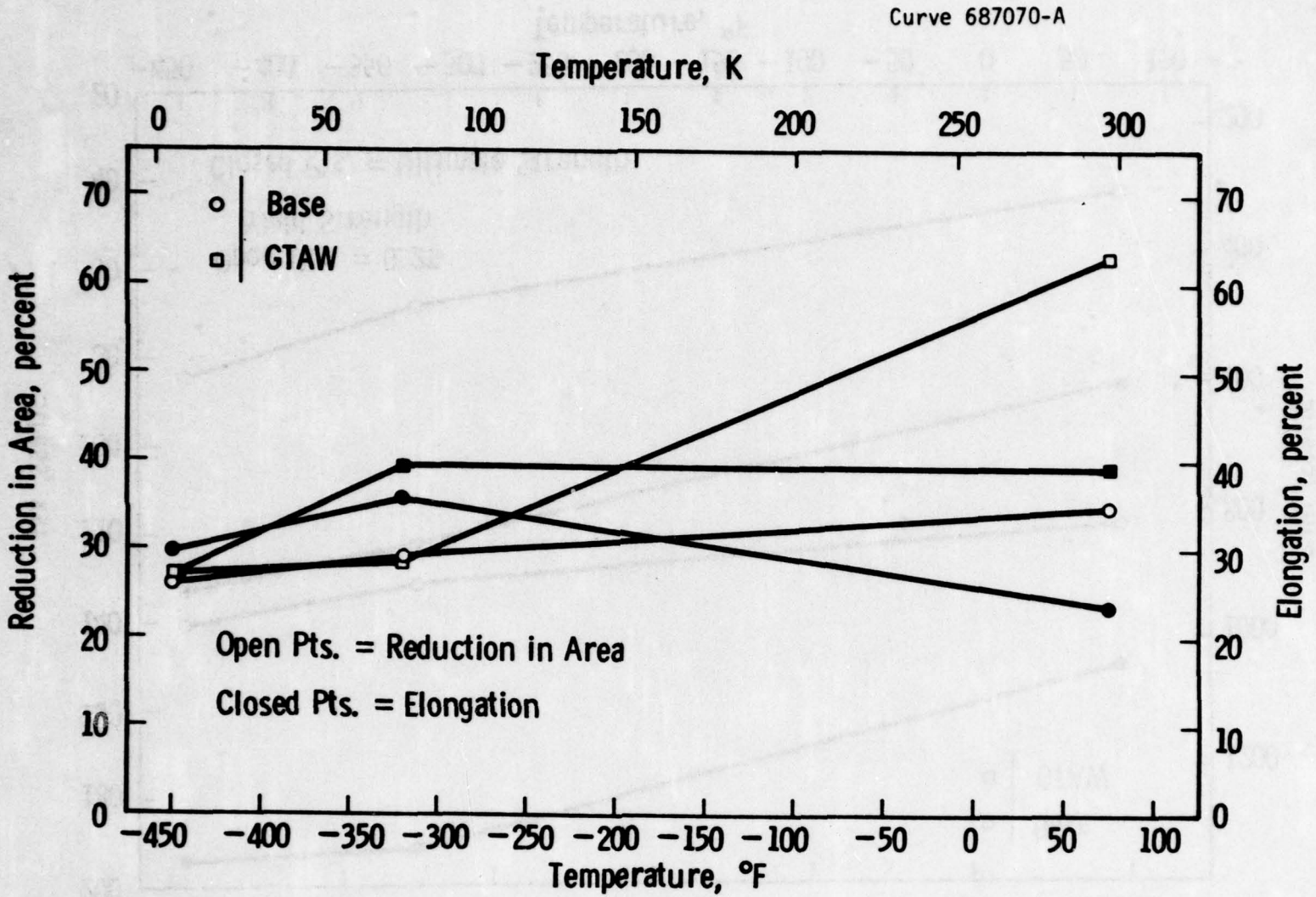


Fig. 6-2 — Ductility of A286 stainless steel baseplate and gas tungsten arc welds

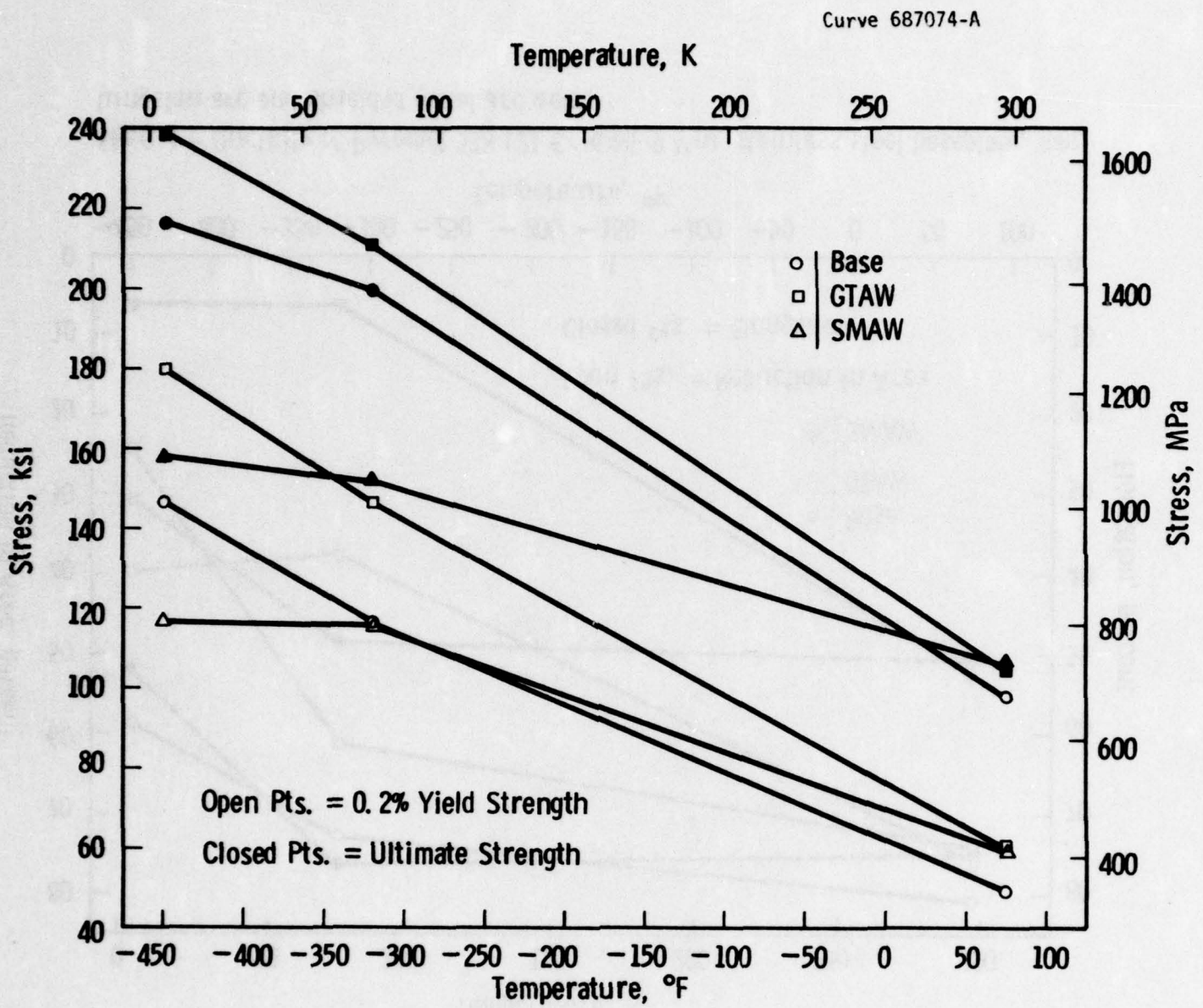


Fig.6-3 – Tensile properties of Pyromet 538 (21 Cr-6 Ni-9 Mn) stainless steel base plate, gas tungsten arc and shielded metal arc welds

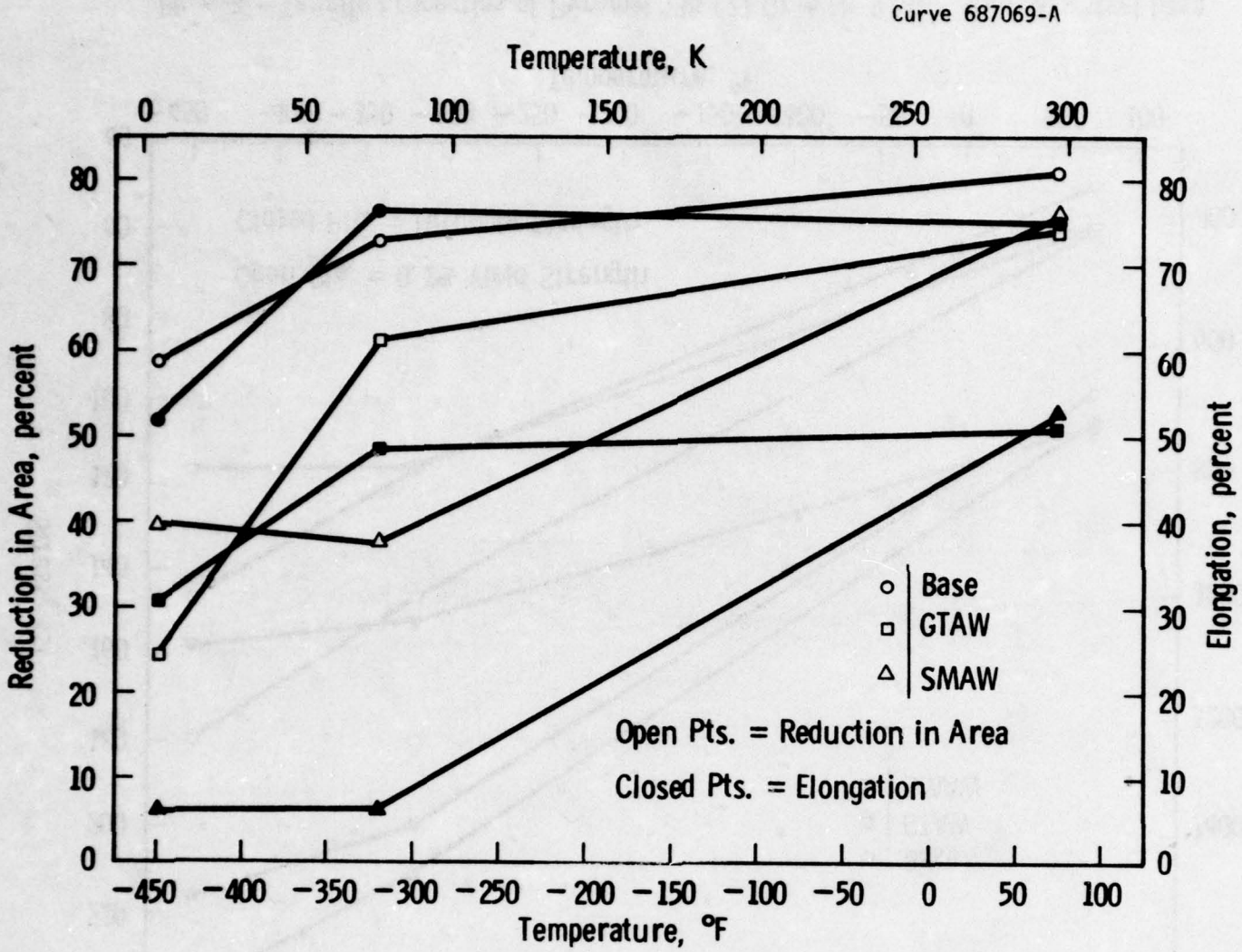


Fig.6-4 – Ductility of Pyromet 538 (21 Cr-6 Ni-9 Mn) stainless steel baseplate, gas tungsten arc and shielded metal arc welds

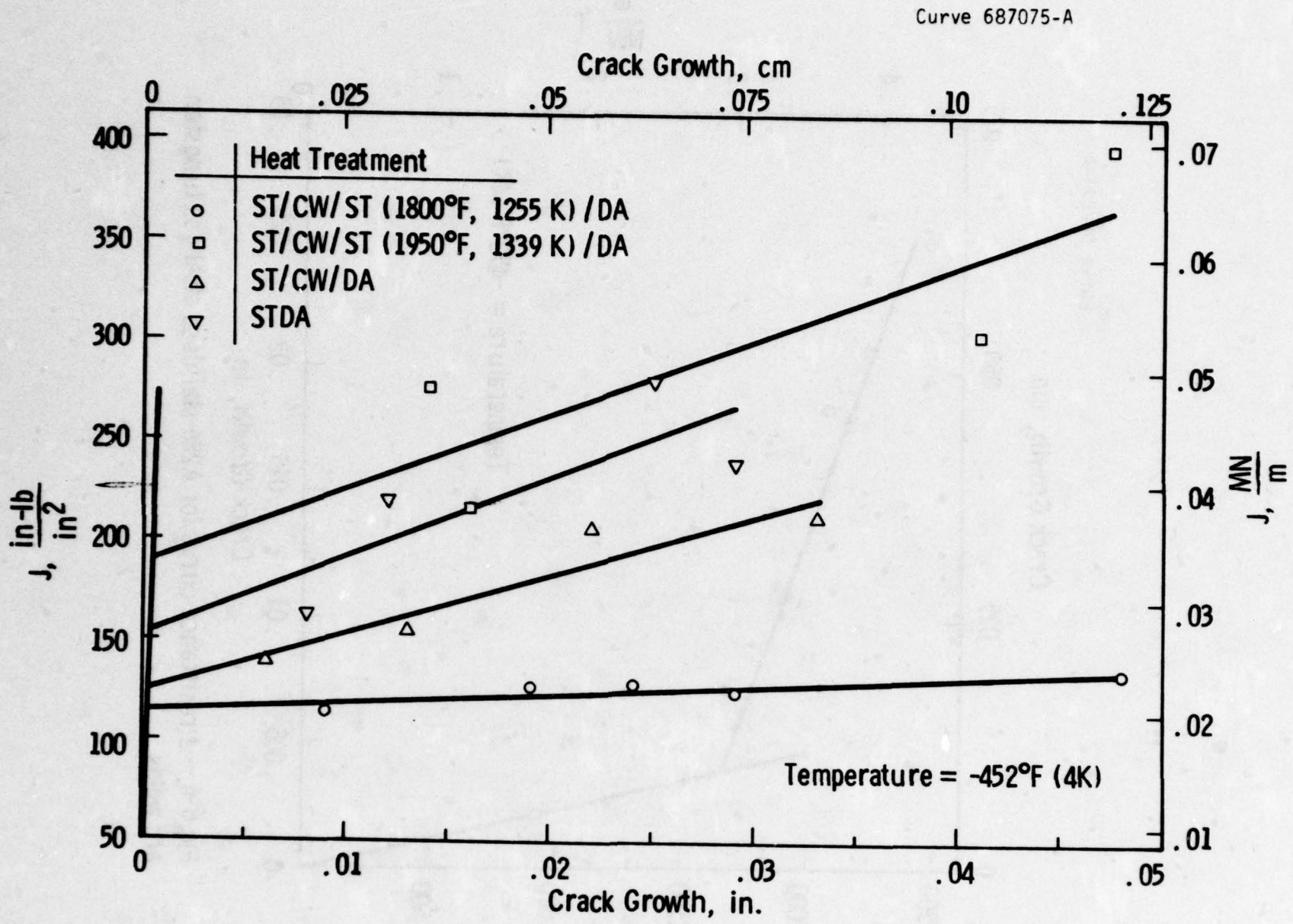


Fig.6-5 – The influence of processing and heat treatment on the -452°F (4K) J resistance curves of Inconel 718 (VIM-VAR)

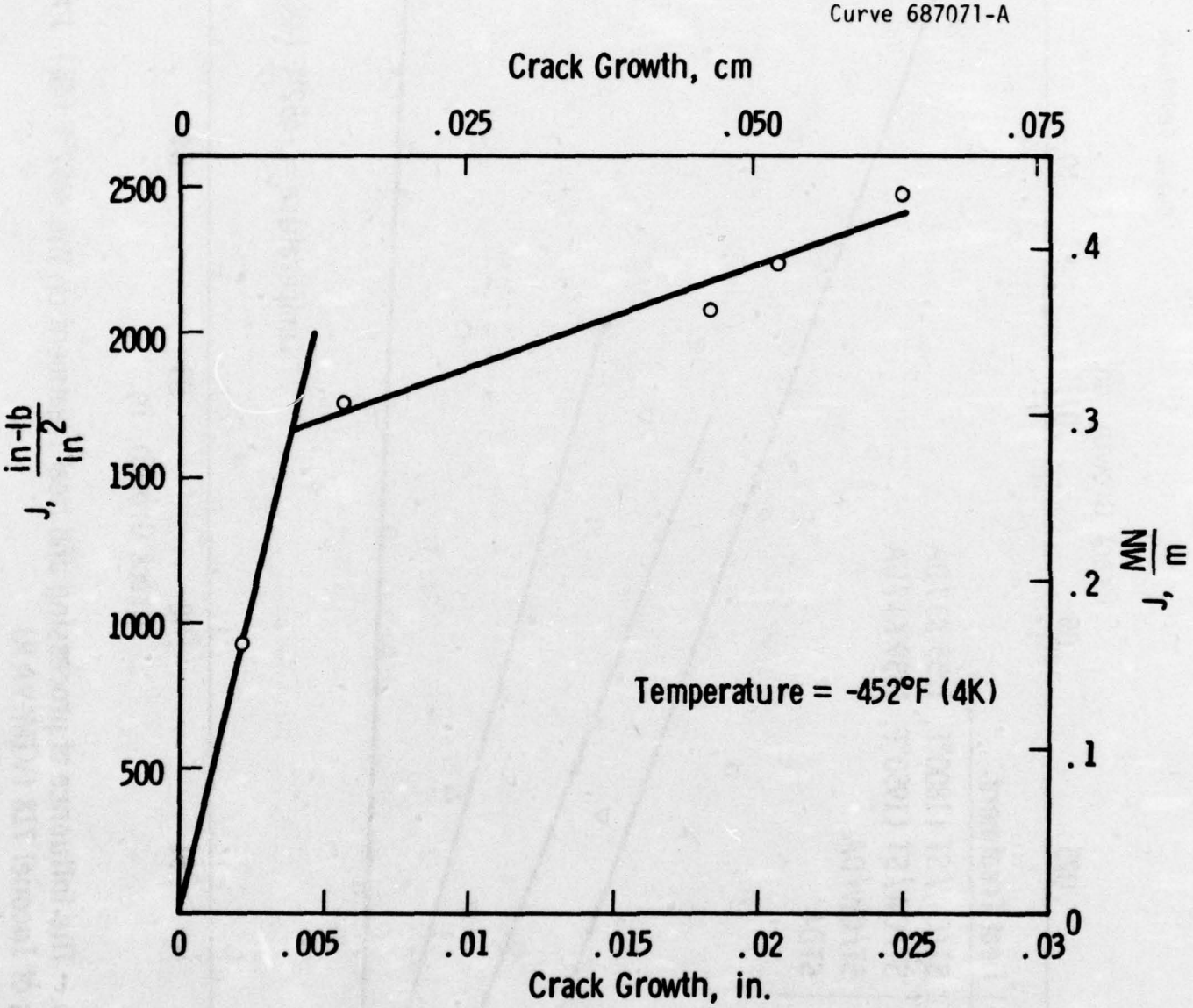


Fig.6-6 — J resistance curve for A286 stainless steel gas tungsten arc welds

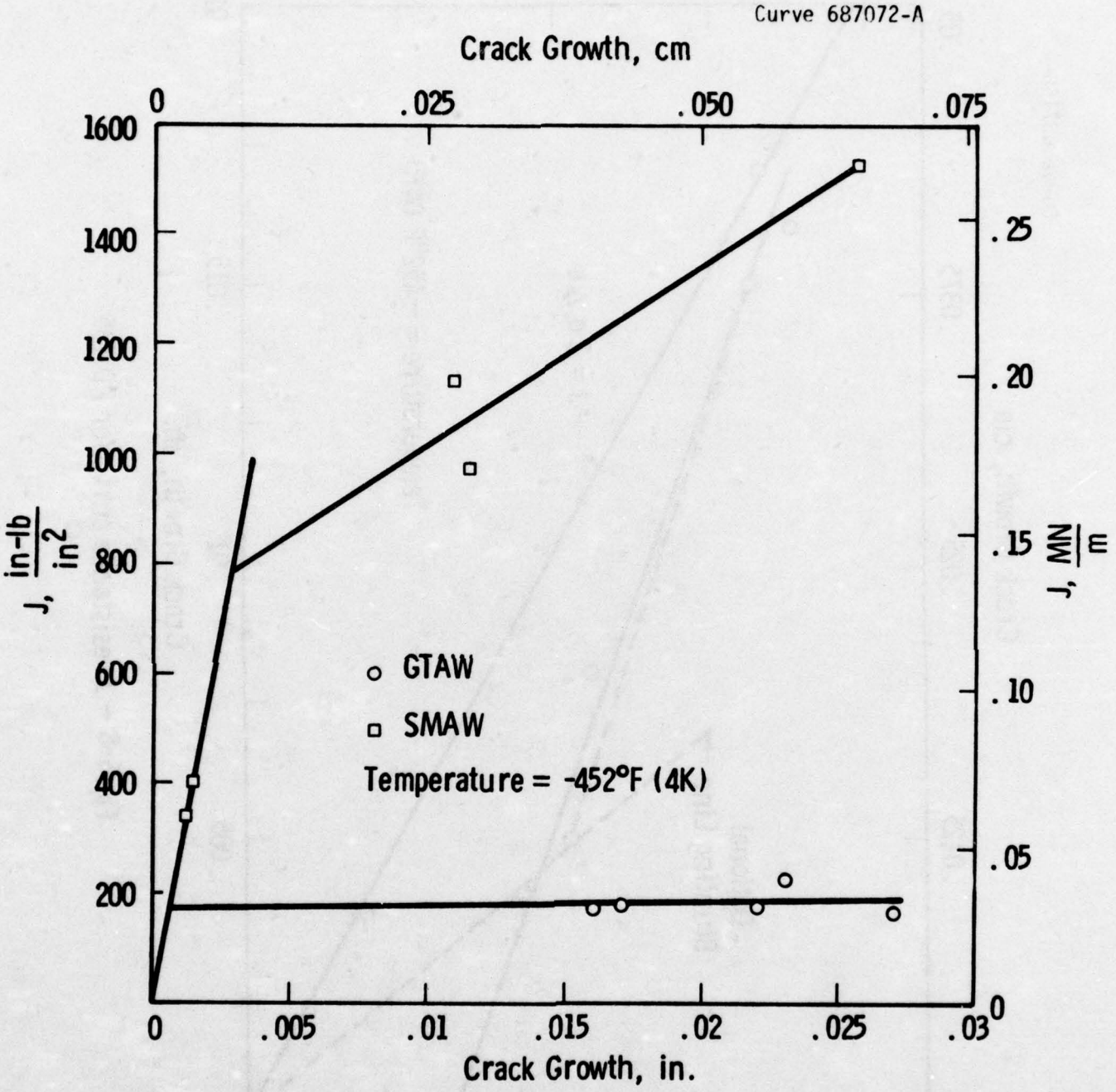


Fig.6-7 – J resistance curves for Pyromet 538 (21 Cr-6 Ni-9 Mn) stainless steel gas tungsten arc and shielded metal arc welds

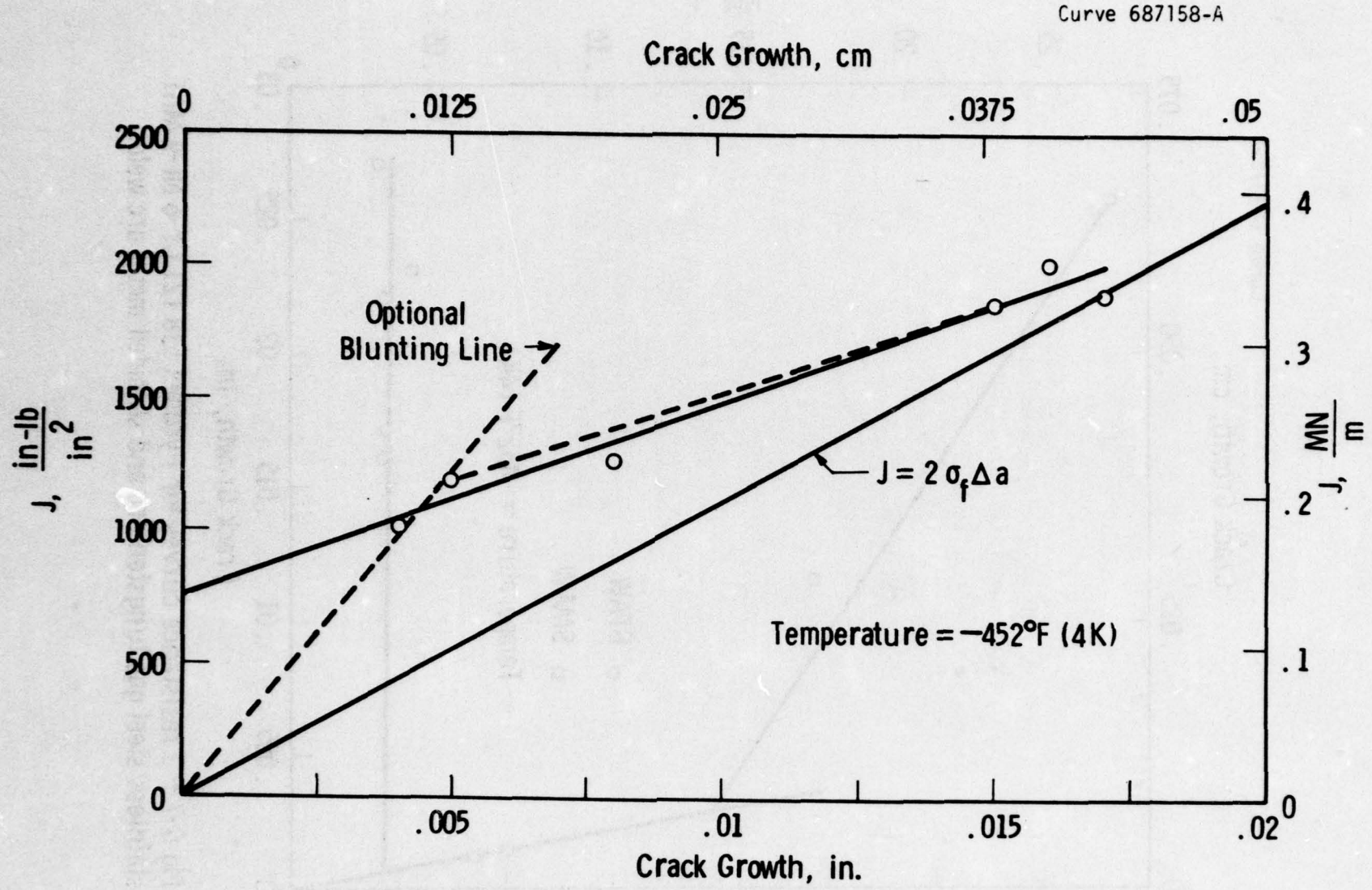


Fig.6-8 — J resistance curve for PD 135

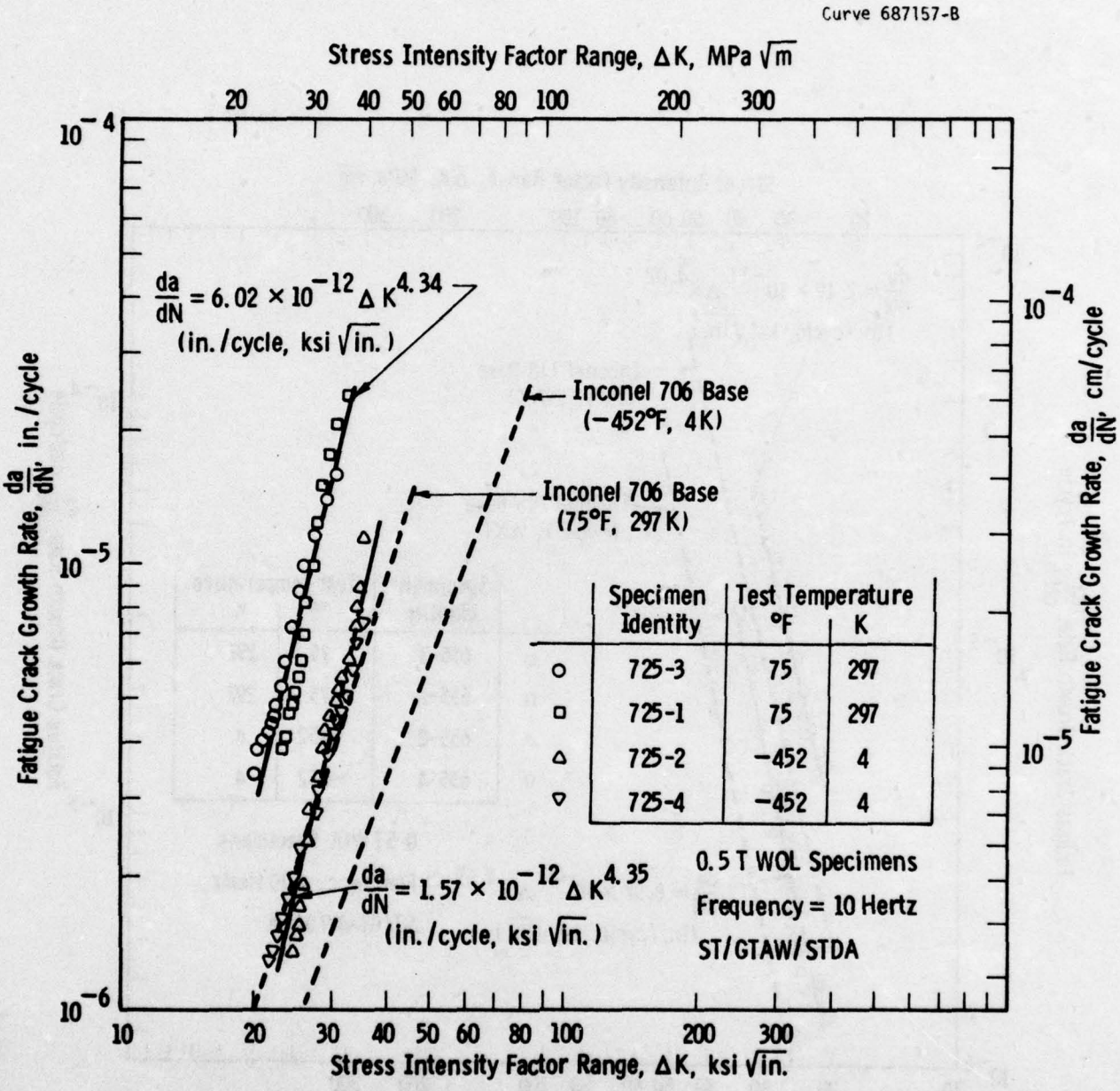


Fig.6-9 — Fatigue crack growth rate properties of (VIM-VAR) Inconel 706 gas tungsten arc welds

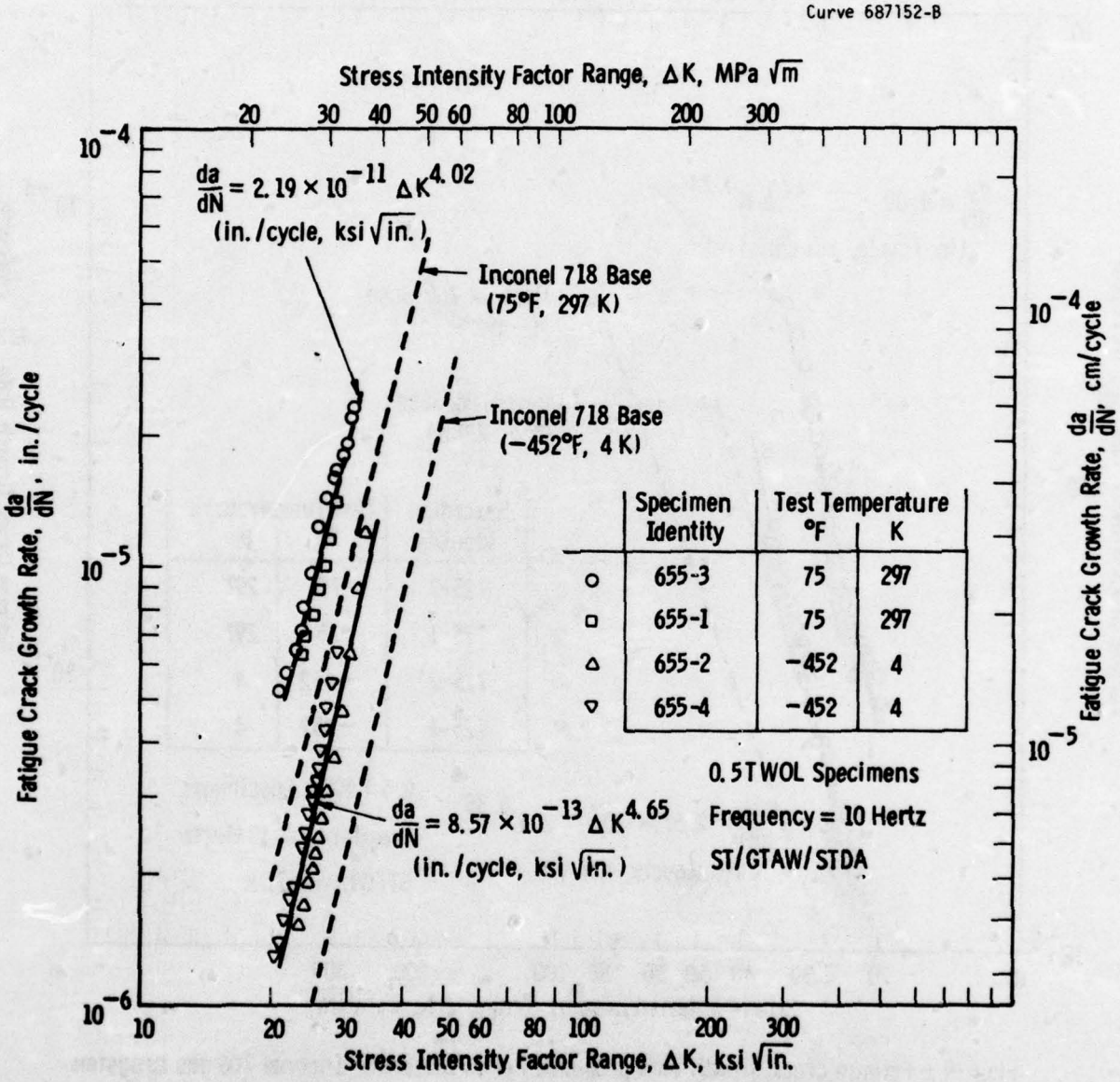


Fig. 6-10– Fatigue crack growth rate properties of (VIM-VAR) Inconel 718 gas tungsten arc welds

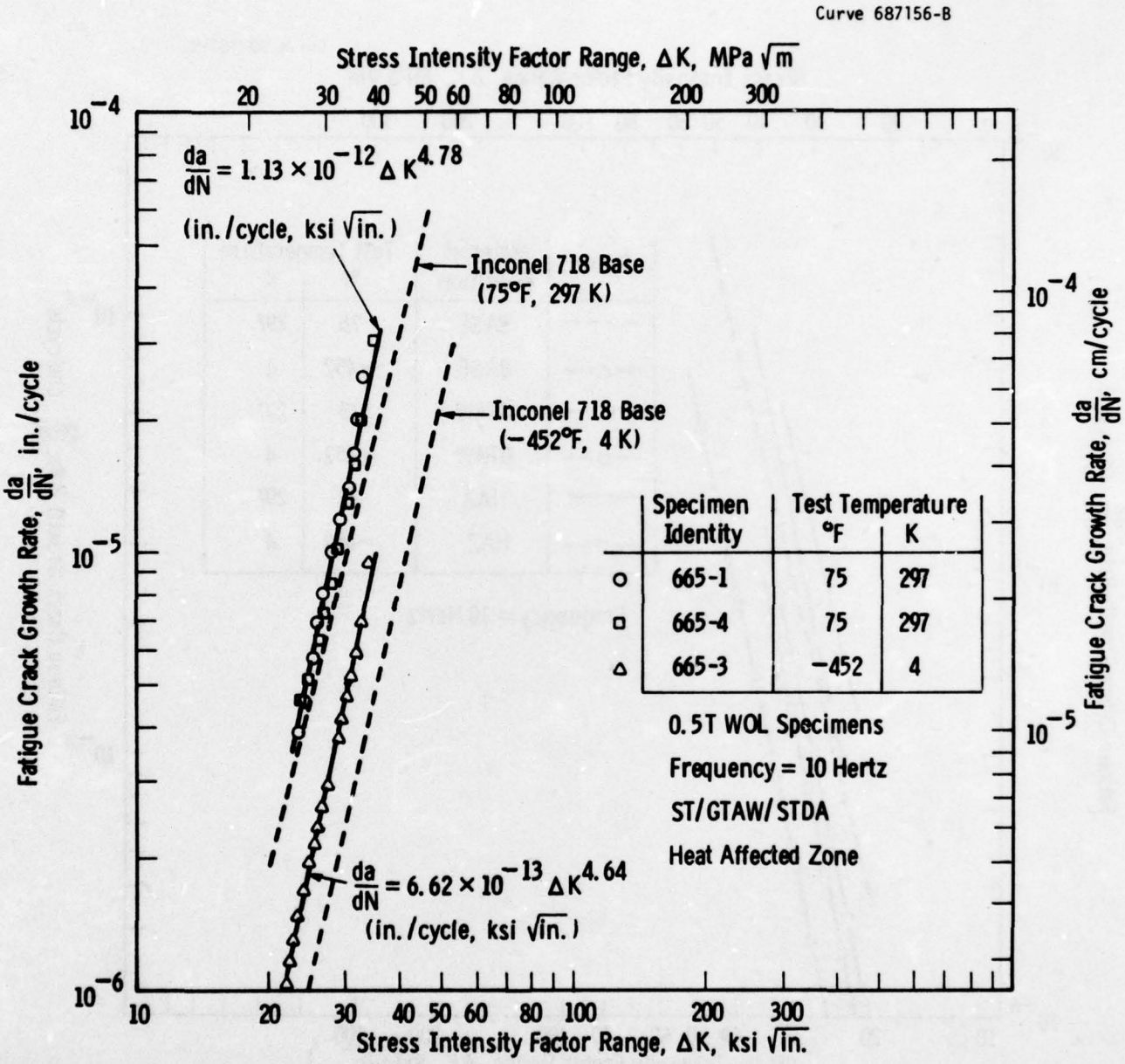


Fig. 6-11- Fatigue crack growth rate properties of (VIM-VAR) Inconel 718 gas tungsten arc welds (heat affected zone)

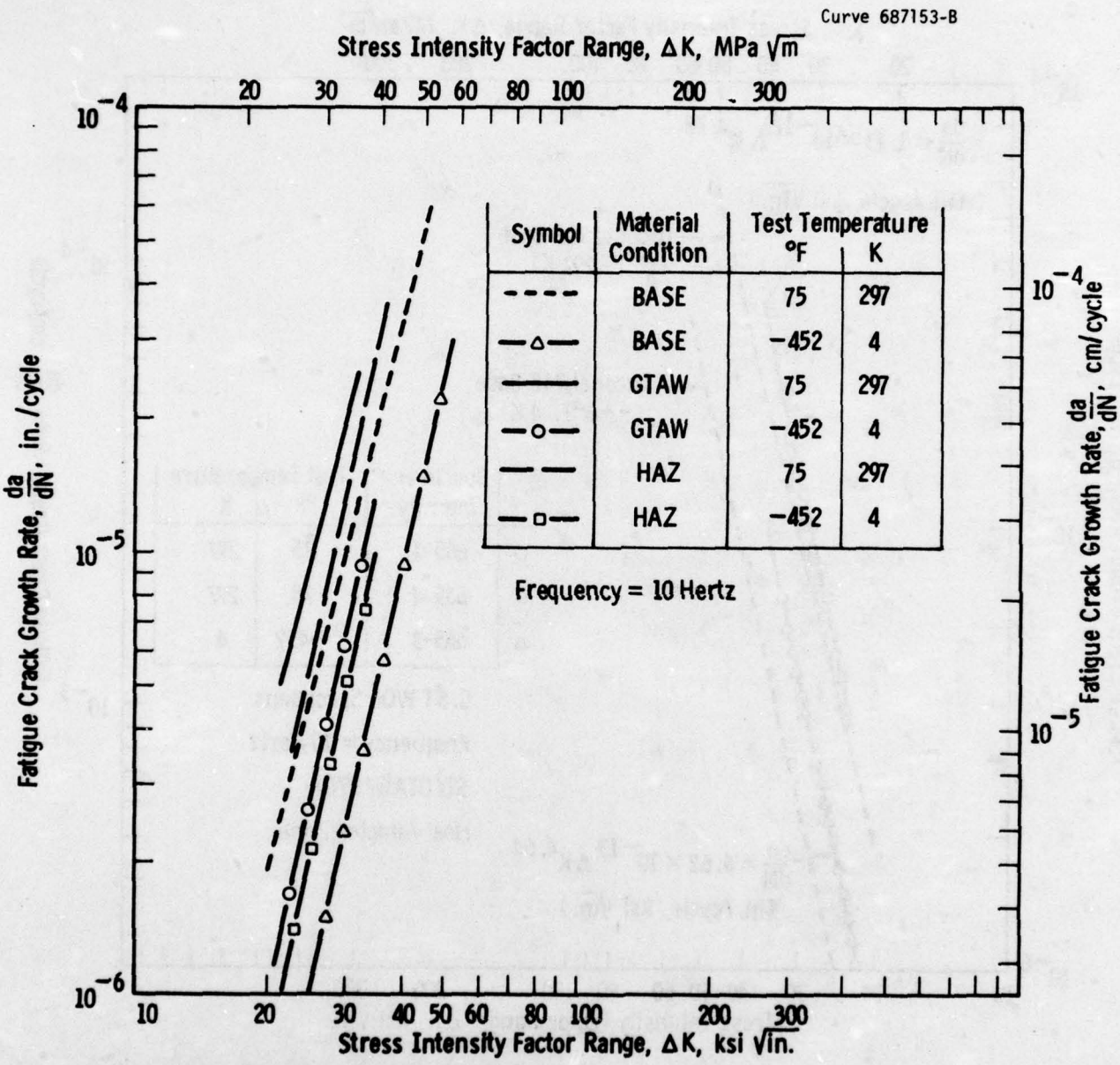


Fig. 6-12- Comparison of the fatigue crack growth rate properties of (VIM-VAR) Inconel 718 base, gas tungsten arc weld and heat affected zone material

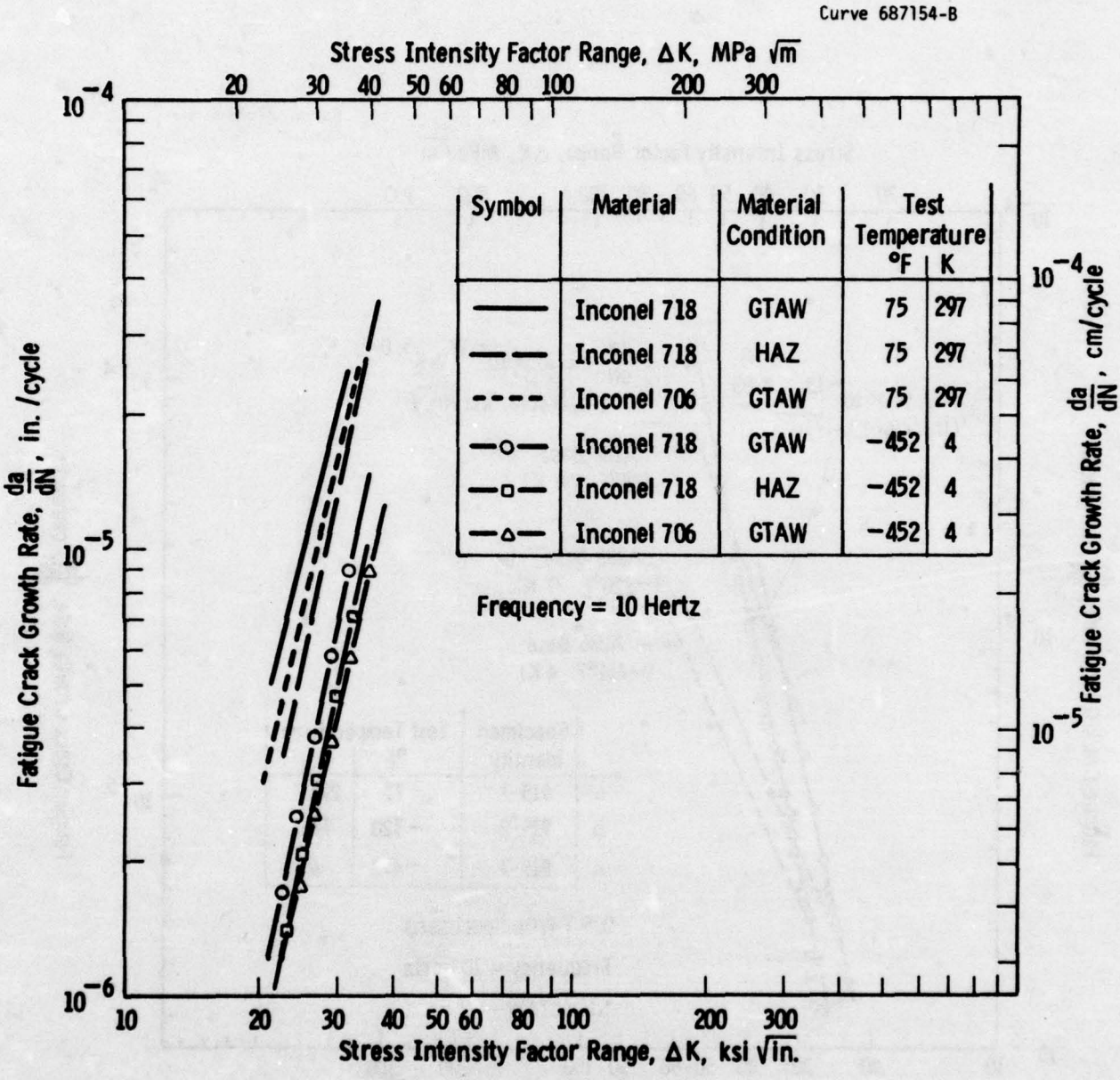


Fig.6-13– Comparison of the fatigue crack growth rate properties of (VIM-VAR) Inconel 718 and (VIM-VAR) Inconel 706 gas tungsten arc welds

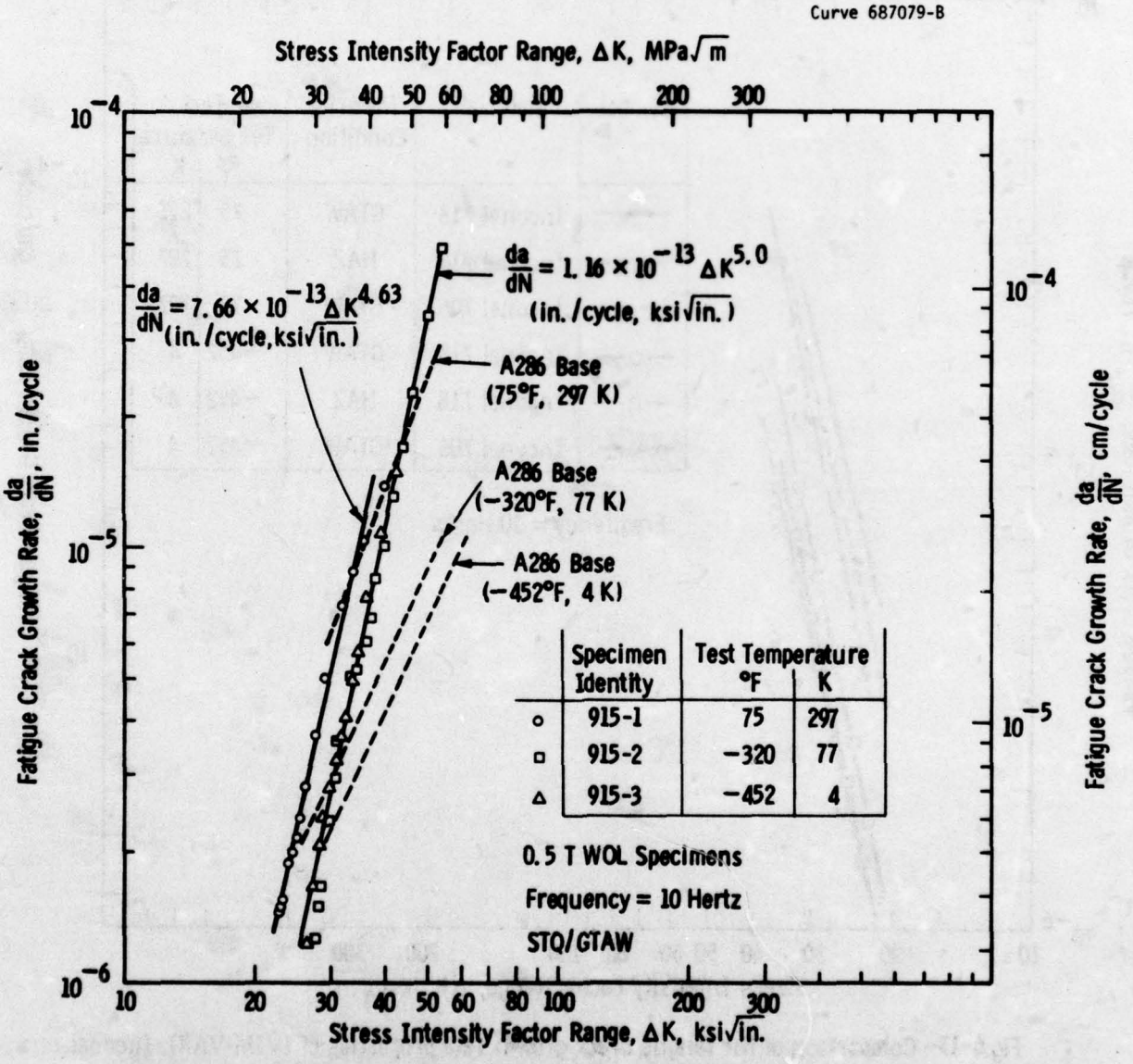


Fig.6-14– Fatigue crack growth rate properties of A286 stainless steel gas tungsten arc welds

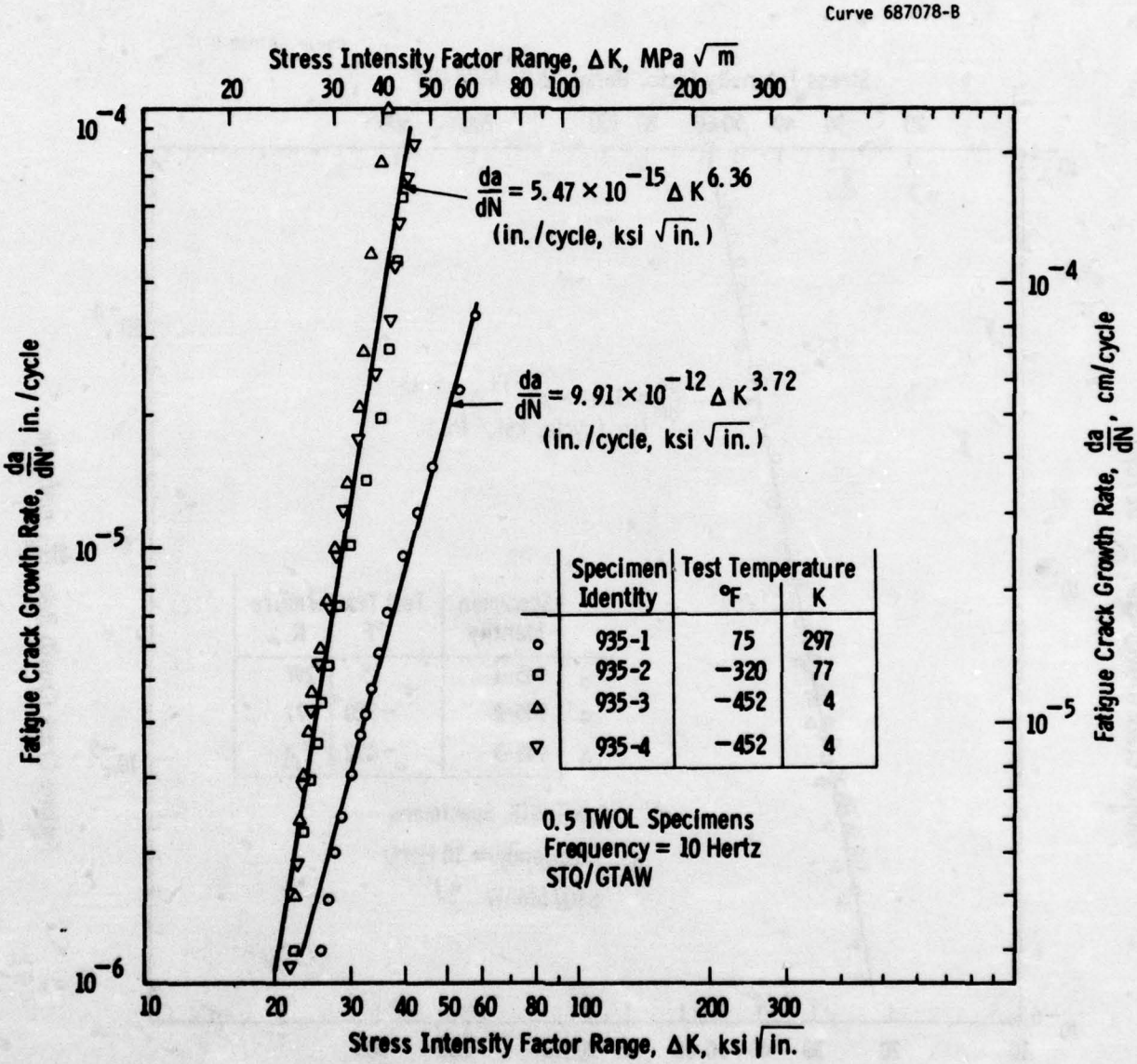


Fig.6-15— Fatigue crack growth rate properties of Pyromet 538 (21 Cr-6 Ni-9 Mn) stainless steel gas tungsten arc welds

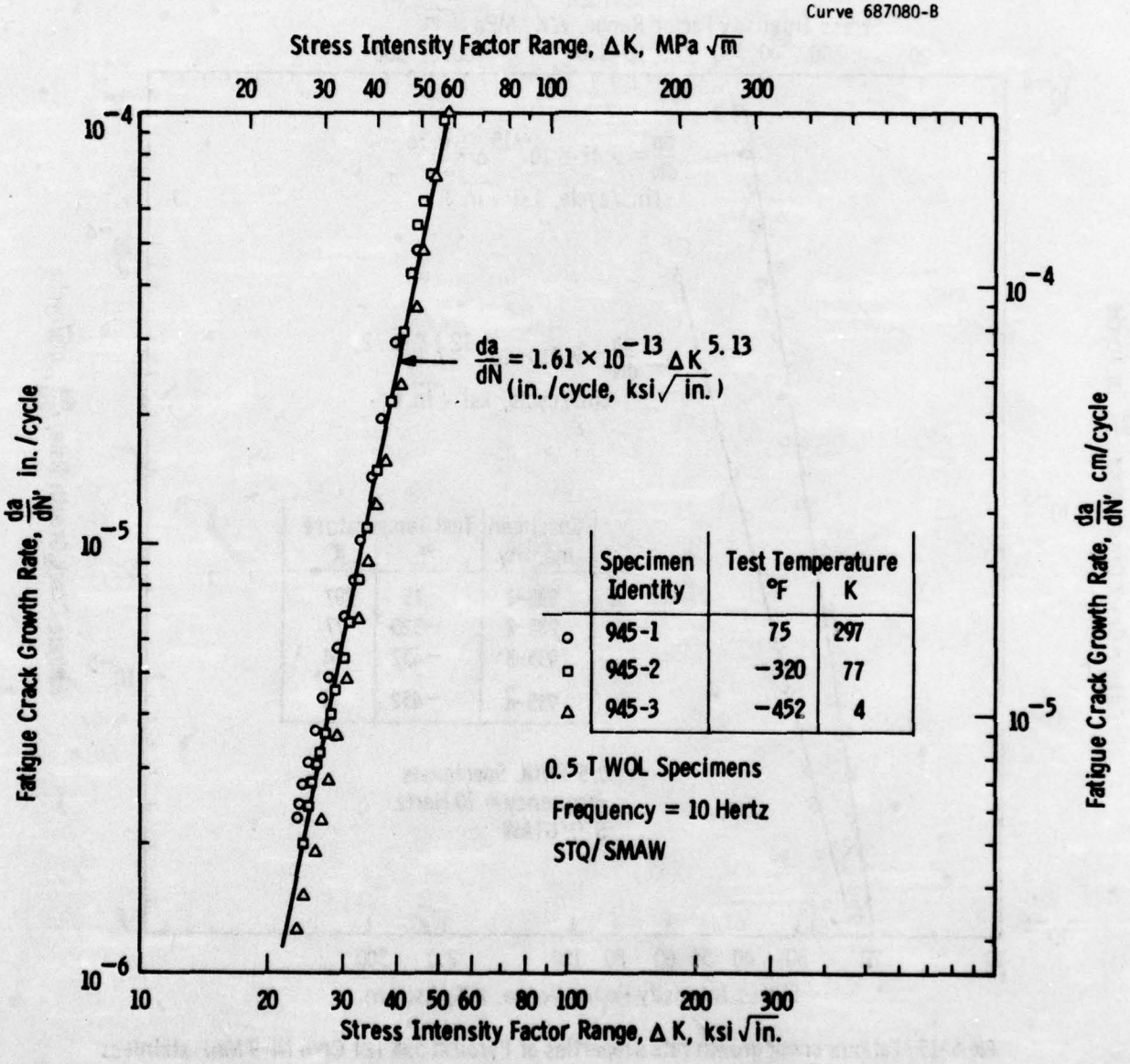


Fig.6-16– Fatigue crack growth rate properties of Pyromet 538 (21 Cr-6 Ni-9 Mn) stainless steel shielded metal arc welds

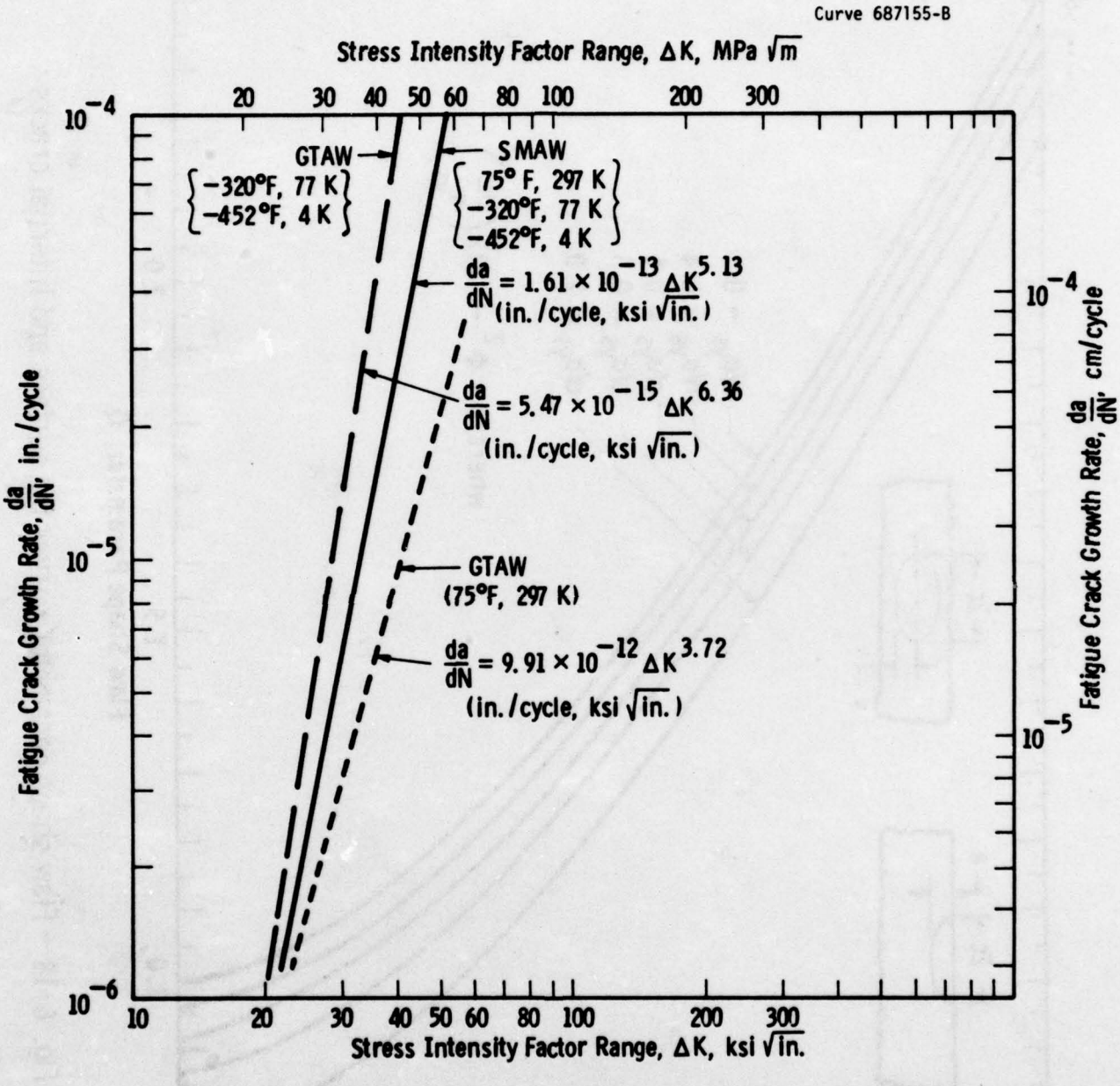


Fig.6-17— Comparison of the fatigue crack growth rate properties of Pyromet 538 (21 Cr-6 Ni-9 Mn) stainless steel gas tungsten arc and shielded metal arc welds

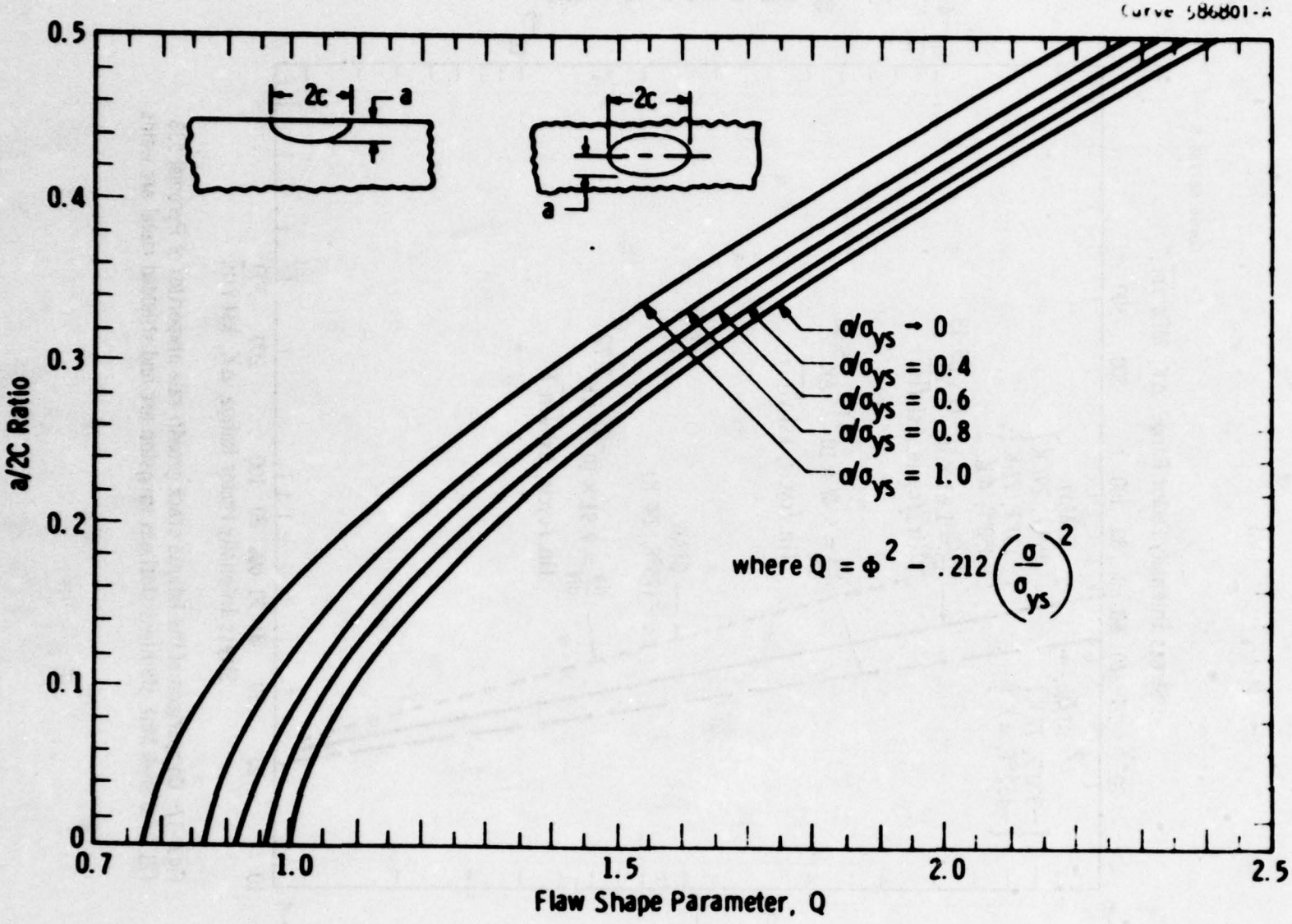


Fig. 6-18 — Flaw shape parameter curves for surface and internal cracks

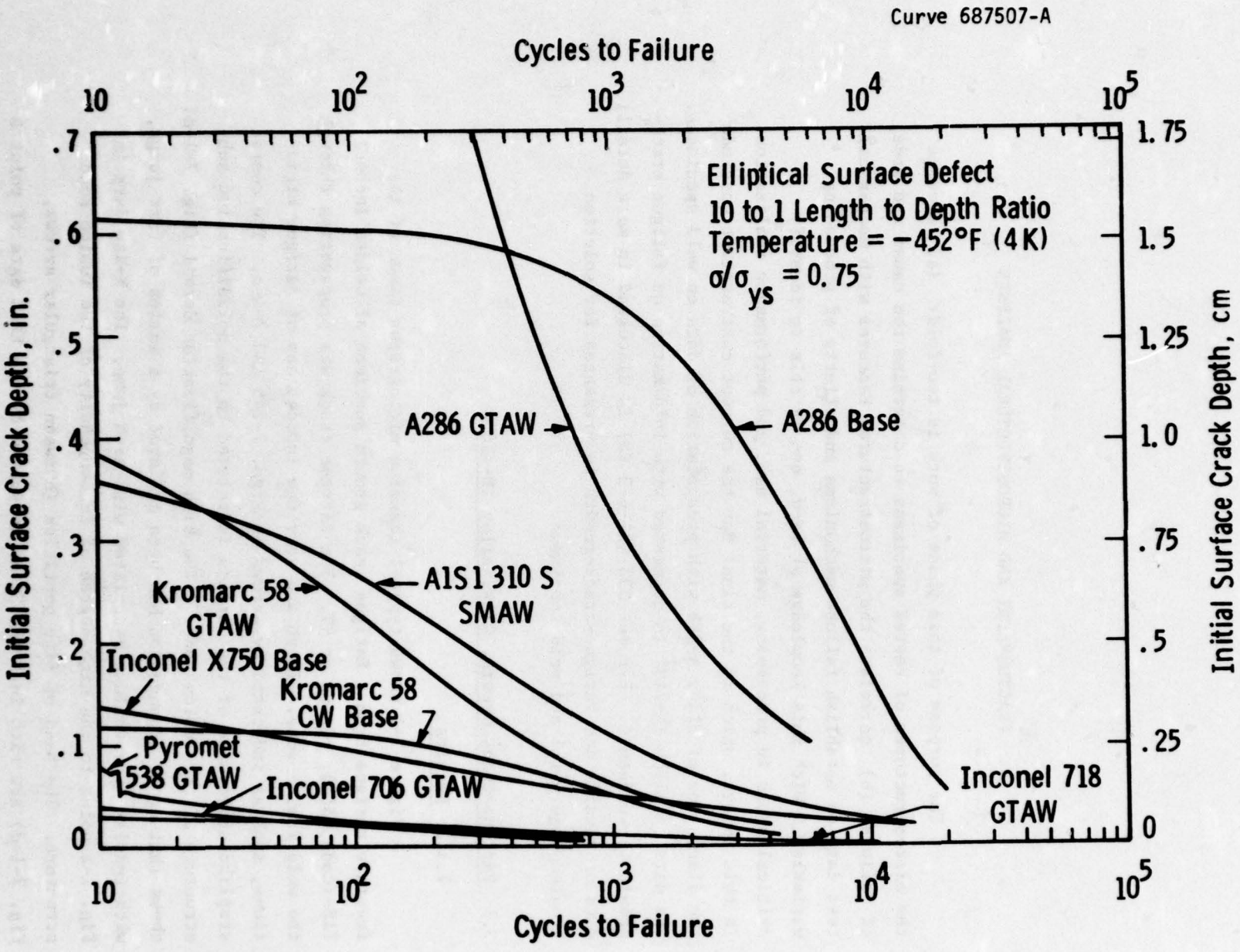


Fig. 6-19 — Cyclic life curves for several materials at −452°F (4 K)

7. FRACTOGRAPHY AND MICROSTRUCTURAL ANALYSIS

The purpose of this phase of work is two-fold: (a) Examine the microstructures of tested specimens to determine the cause and mode of failure, (b) correlate the microstructural features with mechanical test data to establish failure mechanisms and effects of processing variables. With this knowledge at hand, one is able to identify critical areas in processing, material use, and performance realization. In this report, which is the final for the current contract, we conclude the discussion of Alloy A-286 with presentation of data on weld specimens. The data on Alloy IN-718[1] is augmented with information on fatigue crack-growth in weldments. Pyromet 538 (21-6-9 SS) is discussed in more detail; data on tensile and fatigue-crack-growth is presented for solution treated base metal and weld specimens.

7.1 Fatigue-Crack Growth, GTAW, Alloy IN-718

7.1.1 Results

Figure 7-1 shows typical scanning micrographs taken of the fracture surface from a fatigue crack growth specimen of welded Inconel 718-(Code 6551), tested at RT. The fatigue crack was propagating through the weld fusion zone. There are very few indications of fatigue striations, such as indicated by arrows in Figs. 7-1-b and 7-1-c. The coarse steplike appearance of the surface is related to the solidification substructure of the fusion zone.[2] The high magnification detail (Fig. 7-1-d) shows that crack propagation has been achieved by a series of fast jumps, with tensile type failure associated with each jump. The X-Ray data in Fig. 7-2 point to the high degree of inhomogeneity of the fusion zone structure. The band of fine particles (between triangular arrows, Fig. 7-1-d) are rich in P and Si as indicated by the EDAX data of point B (Fig. 7-2-b).

The mode of crack propagation at low temperatures is not significantly different than at RT; this is demonstrated by the micrographs of a specimen tested at 4.2 K (Fig. 7-3). However, subcracking is noticed at low temperature, Fig. 7-3-a. The band of fine particles (A. Fig. 7-3-b) are rich in Si and P as before. The glassy inclusion in Fig. 7-3-c is rich in Mo, Cl, and K.

The mode of crack propagation in the heat-affected zone (HAZ) is typical of a tensile-shear combination. This is evident from the micrographs in Fig. 7-4. The high magnification detail also indicates that the crack front has moved in and out of the fusion zone. Secondary intergranular cracking is seen in detail b, Fig. 7-4. At 4.2 K the mode of failure of fatigue-crack growth specimens is a combination of intergranular cracking and transgranular propagation. This is shown in Fig. 7-5. Figure 7-5-b shows typical intergranular cracking while occasional fatigue striations are evident in Fig. 7-5-c. Note the mode of crack propagation in the fusion-zone of IN 706 welds is identical to that shown for IN-718. This is to be expected since IN 718 filler wire was used in the welding of IN 706 (see Ref. 1). The micrographs in Fig. 7-6 attest to the similarity of crack propagation mode.

7.1.2 Summary

Fatigue-crack-growth in the weld fusion zone in Alloy IN-718 is controlled by the solidification substructure. The crack is propagating by a tensile-shear mode across a dendritic interface, with apparent short arrest at the dendritic boundaries.

The mode of crack growth in the heat-affected zone is predominantly by tensile-shear and intergranular cracking. At 4.2 K there is evidence of localized transgranular crack propagation.

7.2 A-286, Weld Specimens (STQ/GTAW)

7.2.1 Results

The mode of failure of tensile-weld specimens is typical of superalloy, i.e., intergranular fracture. The location of failure and

the associated ductilities, however, are temperature dependent. At RT failure occurred in the base metal with a fair amount of ductility. At low temperature, failures occurred in the heat-affected zone, accompanied by a substantially lower ductility. The light micrographs in Fig. 7-7 show two typical examples. Note the elongated grains in Fig. 7-7-a, indicating large plastic deformation as compared to the relatively undisturbed grain shape in Fig. 7-7-b. Note grain boundary separation below the fractured surface. The orientation of some of the grain boundary openings parallel to the stress axis (arrow Fig. 7-7-b) suggest that these are the so-called "fissures" observed in the HAZ after welding. The deep groove seen in the SEM micrographs (Fig. 7-8-c, d) further support the conclusion that grain boundary cracking occurs in the HAZ of A-286 as a result of prior microfissures introduced during welding. The mechanism of fissuring has been debated in the literature for some time, and models have been advanced for particular systems. The need for a thorough scientific study of the mechanism of fissuring using such tools as TEM and Auger cannot be emphasized enough. The mode of crack propagation in the weld fusion zone of Alloy A-286 is quite different from that reported above for Alloy IN-718. Microfissuring was noted also in IN-718.[3] However, evidence of that was not noted on the fracture surface as in the case of A-286. The SEM micrographs in Fig. 7-9 show classical patterns of fatigue striations. One should also note that the solidification structure is reproduced by the crack front, and that secondary, interdendritic cracking occurs also (arrows).

7.2.2 Summary

Location of failure in A-286 STQ and welded specimens is temperature dependent. At RT, ductile failure occurs in the base metal. At 77 K and 4.2 K, low ductility failure occurs in the HAZ. There is also evidence of grain boundary fissures in the HAZ.

Fatigue crack growth proceeds in the transgranular manner with secondary cracking along dendritic boundaries.

7.3 Pyromet 538 (21Cr-6Ni-9Mn SS)

7.3.1 Results

7.3.1.1 Tensile Specimens

Cross sections of a tensile specimen in the solution treated and quenched condition (STQ, 9211) tested at RT are shown in Fig. 7-10. Appreciable necking has occurred and the grains are distorted due to the very high plastic strain (about78% elongation, see Table 6-1). Note also the very fine black dots that appear to be gas porosity holes (arrows, Fig. 7-10-b). The gas porosity is seen more clearly in the SEM micrographs, Fig. 7-11 (arrows). It seems that many dimples are associated with a hole located at the bottom of the dimple. It is quite likely that these holes represent nitrogen porosity. A more definitive statement could be made only after a specimen of this material is subjected to analysis by Auger Spectroscopy, equipped with gas-mass-analyzer.

The contaminations, shown in Fig. 7-11-b, were observed in many specimens and contain Na, Al, Cl, K and Ca, see Fig. 7-12.

Tensile data obtained on two specimens at RT and on two specimens at 77 K show close agreement between the duplicate results (see Section 6.1). There was, however, a significant variance between the two specimens tested at 4.2 K. Specimen 9213-1 yielded at 130,600 psi with 72% RA, while specimen 9213-2 yielded at 162,500 psi with 45% RA. Both specimens were therefore examined.

The light micrographs in Fig. 7-13 show the highly deformed gauge section of specimen 9213-1. The micrograph in Fig. 7-14 shows details of the deformation bands in specimen 9213-2. It is conceivable that features like the one marked by arrows indicate transformed martensitic needle. The highly deformed area precludes an unambiguous interpretation. Details of the fracture surface of specimen 9213-1 are illustrated by the SEM micrographs in Fig. 7-15. The fracture surface shows homogeneous, ductile dimpled fracture. The mode of fracture of the stronger specimen, 9213-2, is quite different, as shown by the micrographs in Fig. 7-16.

It is clear that shear dominates the fracture surface of specimen 9213-2. Frequently, cleavage steps are seen, Figs. 7-16-c and 7-16-d. Localized dimpled deformation is also seen. It is significant that no compositional differences could be detected by EDAX analysis on any feature on the fractured surface. For example, the cleaved area, A, Fig. 7-16-b, shows the same Cr-Fe-Ni rations as the surface of specimen 9213-1, or any other point on the surface of specimen 9213-2 (Fig. 7-17). It is quite likely that the cleaved features, Fig. 7-16, are the martensitic needles seen alluded to in Fig. 7-14.

Final verification of martensitic transformation in specimen 9213-2 was obtained by X-Ray diffraction. Both specimens (9213-1 and -2) were electropolished to remove cold work from the outer surface. Cr-radiation diffractometer traces are shown in Fig. 7-18. The d-2.03 (110) peak of the body-centered-cubic is quite evident in specimen 9213-2. We conclude that, indeed, martensitic transformation has occurred in this specimen, which is reflected in the strength, ductility, and mode of fracture of this specimen. It should also be noted that no variation in grain size has been noted among all 92XX specimens, nor was there any trace of martensite outside the deformed gauge section in specimen 9213-2. The martensitic transformation was, therefore, stress induced.

The gas-tungsten arc weld specimens, where a matchining 21-6-9 filler wire was used, showed an interesting consistency in their yield strength. There was less than 5% variance in duplicate test. All specimens but one failed in the base metal, significantly away from the heat-affected-zone. Specimen 9313-2 tested at 4.2 K failed in the fusion zone, displaying the same yield strength as the duplicate specimen 9313-1, which failed in the base metal. It is also of interest to note that at all temperatures the 93XX series had yield strengths higher by 25-30% than the base metal series, 92XX. Figure 7-19 and 7-20 show typical features of the fractures. All specimens displayed a ductile mode of failure, including specimen 9313-2 which failed in the fusion zone (Fig. 7-20-b).

Specimens of the series 94XX represent shielded-metal-arc-weld (SMAW) using IN-182 electrodes. The fusion zone has thus been converted to a higher Ni alloy than the original base 21-6-9. The tensile tests reflect the change in the weld metal composition (Table 6). The room-temperature specimens failed in the base metal, displaying strength levels identical with those of series 93XX. The other specimens tested at 77 K and 4.2 K failed in the fusion zone at strength levels significantly lower than the base metal specimens (92XX) or the GTAW specimens (93XX).

The room temperature fracture shows features typical of a ductile, dimpled deformation, similar to that shown in previous figures. This is shown in the SEM micrographs in Fig. 7-21.

The morphology of the fracture of the fusion zone in specimens 9412 and 9413 is illustrated in Fig. 7-22. The dominant features are deep dimples, indicative of ductile deformation. There are, however, localized areas of shear, Fig. 7-22-d, and in many instances certain portions of the fracture surface covered with inclusions. The X-Ray data in Fig. 7-23 show that the inclusions are rich in Al, Si, Cl and K. The probable source of these inclusions is the coating on the weld electrode.

7.3.1.2 Fatigue Crack Growth

One set of specimens was examined, i.e., STQ and GTAW (935X) at RT and 4.2 K. In both cases generally, a planar crack was propagating, showing fatigue striation. As in previous observations of fatigue crack growth in the fusion zone, the crack front reproduced, in general, the solidification pattern of the weld metal. Typical examples are shown in Fig. 7-24. Note also cleaved features in Figs. 7-24-d (arrows). Although there is no verification by chemistry or X-Ray diffraction, the cleaved features may represent transformed martensitic needles. The temperature dependence of the crack growth data indicates that the behavior of the fusion-zone material is more like a body-centered-cubic structure than like an austenitic structure (see also Sec. 6).

7.3.2 Summary

Pyromet 538 deformed in a ductile manner at all temperatures. At least one specimen showed evidence of stress-induced martensitic transformation at 4.2 K which resulted in shear-type, lower ductility deformation. There is also evidence of cleavage in the fusion zone of specimens welded with Pyromet 538 filler wire.

References Section 7

1. J. M. Wells, W. A. Logsdon, R. Kossowsky and W. R. Daniel, "Structural Materials for Cryogenic Applications," Fifth Semi-Annual Report, April 1976.

2. N. C. Binkley, R. G. Berggrer and G. M. Goodwin, "Microstructural Studies of Weldments of Stainless Steel," Welding Res. Suppl., Feb. 1974, p. 25.

3. J. M. Wells, W. A. Logsdon, R. Kossowsky and W. R. Daniel, Lo. cit Third Semi-Annual Report, April 1975.

7.4 Final Summary

The contribution of microstructural analysis to the Overall Program.

The microstructural analysis phase of this contract was designed to examine tested specimens representing as much as possible processing, temperature, and testing variables. We also attempted to correlate test results with material history and structural details, in particular, when seemingly similar materials exhibited varied mechanical properties.

7.4.1 Variabilities in As-Received X-750 Billets

IN X750 materials were received[3] in three processed conditions, designated MP-1, MP-2 and MP-3. The MP-1 material was melted by VIM-VAR process, then hot worked from a 50 cm billet to a 25 cm billet. MP-2 was melted by AM-VAR process, then press forged and hot worked for a 10 cm billet, MP-3 material was melted by VIM process only, then hot worked from 50 cm ingot to a 5 cm bar.

There were marked differences in mechanical properties among the three materials; MP-1 showing lower strength and half the fracture toughness of MP-3 and MP-2.

Using transmission electron microscopy and X-ray analysis of non-soluble residues, we showed that the resulting mechanical properties could be related to the microstructure produced by the three different processing schedules. In particular, we showed that:

- grain size has a small effect on the strength of X-750 at low temperatures.
- Residual dislocation density (in MP-3) and γ' morphology accounts for an increase in fracture toughness.
- Continuous carbide film in the grain boundaries in MP-1 material were the major cause for low strength, low ductility, and low fracture toughness of this material.

7.4.2 Variabilities in Alloy 718 Received from Different Sources

A factor of about 1.3 difference in fracture toughness and ~2 in. ductility between specimens prepared from IN-718 (received from Huntington Alloys) billets and specimens prepared from U-718 (received from Special Metals) billets were observed. There were no apparent reasons to account for the comparatively poor behavior of the IN-718 material. Both materials were received in the same billet size; their chemistry was well within the specification limits, and all test specimens received identical thermal treatment.

X-ray diffraction analysis of non-soluble residues, coupled with transmission electron microscopy, and Auger Spectroscopy showed that the low fracture toughness of IN-718 vs U-718 was due to

- Solutions annealed IN-718 contained five times more MC carbides than U-718.
- The standard heat treatment resulted in the precipitation of $\gamma+\gamma'$ in both alloys. However, in U-718 (Ni_3Nb) was also present while in IN-718 detrimental Laves phases were identified.
- Grain boundary agglomeration of carbides and Laves phases was detected in IN-718, while in U-718 the dominant phase in or near grain boundaries was γ'' (Ni_3Nb).
- Based on previous experience with Fe-Ni-Cr alloys we suggested that variability in Si content between U-718 and IN-718 can account for the precipitation of detrimental phases. This is true even though in both alloys the Si content present was within the range allowed. However, Si content in U-718 was at the lower level allowed with about 5 times higher Si content in IN-718.
- The effect of precipitating phases in the mechanical behavior of IN-718 was further demonstrated in the analysis of weldments. Low ductility in weldments that fail mostly in the fusion zone is aggrevated by cellular carbide films that dominate the fracture surface. The latter was clearly demonstrated by Auger Spectroscopy.

7.4.3 Properties of the Heat Affected Zone

Welding processes and significantly so high heat input welding such as GTAW and SMAW, result in structural modification of the heat affected zone. We conducted a thorough microstructural analysis that spotlighted the effect of the microstructure of the heat affected zone on subsequent mechanical behavior of welded specimens. Specifically, we showed that:

- For aging sensitive materials post welding thermal conditioning is essential. For superalloys following welding, the heat affected zone may deteriorate to conditions of solution annealed or over-aged material. In the case of stainless steels, the heat affected zone may become sensitized.
- Weakening of the heat affected zone is also a function of test temperature. In many cases (i.e., IN-718, A-286 and Pyromet 538), failures in the heat affected zone occurred only at low temperatures.
- Microstructural analysis defined the mechanisms of HAZ failures, which are specific for each alloy and the welding process. In superalloys, overaging or solutioning of γ' is the prime process. Precipitation of deleterious phases may occur in alloy 718. Precipitation of grain boundary carbides (sensitization) occurs in 310 stainless steel.

7.4.4 Fracture Characteristics

A complete summary of the observed fracture modes in the alloys studied during the program is given in Table 7-1. In this table, the features typical of tensile deformation and fatigue crack propagation were defined, and the effect of test temperature, heat treatment and processing histories are emphasized.

Summary, Table 7-1. Mode of Failure,
Structural Materials for Cryogenic Applications.

Material Code	Condition	Mode of Testing	Temperature	Fracture Characteristics
OFHC Cu				
111X	Stress relief	Tensile	RT,77K,42K	High ductility. Dimpled surface, all temperatures
1153	Stress relief	F.C.G.	4.2K	ductile, Stage I fatigue crack propagation.
1313	Ag brazed Cu	Tensile	4.2K	Braze-base metal interface failure. G.B. embrittlement.
310S				
2013	STQ	Tensile	4.2K	Ductile. Dimpled surface.
2053	STQ	F.C.G.	4.2K	Ductile. No systematic fatigue striation. Tearing.
2112	STFC	Tensile	77K	Ductile. Intergranular-to-cross granular mix. Carbides in grain boundaries evidence of sensitization.
2153	STFC	F.C.G.	77K	Secondary intergranular. Tearing. No systematic striation.
2213	SMW	Tensile	4.2K	Fusion zone failures. Ductile, dimpled fracture. Carbide in dimples. Deformation both in base metal and FZ.
2253	SMW	F.C.G.	4.2K	Only occasional striations. Mostly tearing mode. Alkaline rich inclusions on fracture surface.
I-X750; MP-1				
3013	S.T.	Tensile	4.2K	Ductile. Final failure intergranular.
3113	STDA	Tensile	4.2K	Ductile. Final failure, intergranular.
3113	STDA	F.C.G.	4.2K	Fatigue striations mixed modes of coarse and fine. Occasional secondary intergranular cracks.
321X	ST/EBW	Tensile	RT,77K,4.2K	Most failures in HAZ. Intergranular. Ductile.
331X	STDA/EBW	Tensile	RT,77K,4.2K	Most failures in HAZ. Ductile, intergranular.
341X	EBW/STDA	Tensile	RT,77K,4.2K	Base metal failure. Intergranular.
3452	EBW/STDA	F.C.G.	77K	Fatigue striations mixed with tearing.
351X	ST/GTAW	Tensile	RT,77K,4.2K	Failed in HAZ. Evidence of fissuring. High concentration of carbides. Dimples. Final failure intergranular.
361X	STDA/GTAW	Tensile	RT,77K,4.2K	Same as 35XX series. Failed in HAZ.
371X	GTAW/STDA	Tensile	RT,77K,4.2K	Base metal failure. Dimples. Final failure intergranular. Similar in all features to base metal, specimens. 31XX.
3751	GTAW/STDA	F.C.G.	RT	Ductile, tearing. Occasional striations.

Summary, Table 7-1. (Cont'd) - p. 2

Material Code	Condition	Mode of Testing	Temperature	Fracture Characteristics
3753	GTAW/STDA	F.C.G.	4.2K	Fatigue striations. Secondary cracking normal to crack front.
3812	Cu brazed	Tensile	77K	Failed in braze-metal interface. Evidence of incomplete wetting. Ductile fracture of Cu braze.
I-X750; MP-2 401X	STDA	Tensile	RT,77K,4.2K	Ductile. Final failure-mixed mode of cross-granular shear and intergranular cracking.
I-X750; MP-3 501X	STDA	Tensile	RT,77K,4.2K	Ductile. Final failure-mixed mode of cross-granular shear and intergranular cracking.
I-X750-HIP 611X	STDA	Tensile	RT,77K,4.2K	Ductile. Cross-granular shear, occasional secondary intergranular cracks.
6152	STDA	F.C.G.	77K	Wide range of striation spacings. Occasional tearing and secondary intergranular cracks.
I-718 641X	STDA	Tensile	RT,4.2K	Low ductility. Intergranular. Some deformation within the grain and secondary cracking evident cleaved (Nb-Ti) carbides prevalent on fracture surface.
6453	STDA	F.C.G.	4.2K	Striations. Secondary intergranular cracking.
651X	ST/GTAW/STDA	Tensile	RT,4.2K	All specimens but one failed in fusion low ductility zone. Cellular appearance. Carbides and oxides prevalent on fracture surface.
652X	As 65XX notched in FZ	Notch-bar Tensile	RT,4.2K	Low ductility. Mixed mode of cross granular shear and intergranular cracking. Sheared carbides evident.
662X	As 65XX notched in HAZ	Notch Tensile	RT,4.2K	Low ductility. Cross granular shear and intergranular cracking. Deep secondary intergranular crack. Sheared carbides evident.
671X	ST/CW/AN (fine g.s)	Tensile	RT,4.2K	Mixed modes of dimpled and shear fractures.

Summary, Table 7-1. (Cont'd) - p. 3

Material Code	Condition	Mode of Testing	Temperature	Fracture Characteristics
671X	ST/CW/AN (fine g.s.)	Tensile	RT,4.2K	Mixed modes of dimpled and shear fractures.
681X	ST/CW/AN (large g.s.)	Tensile	RT,4.2K	Mixed modes of dimpled shear and intergranular fractures. Carbides in fracture surfaces.
691X	Same as 68XX cold work not completely annealed	Tensile	RT,4.2K	Mixed mode of dimpled and shear fractures. Some evidence of secondary intergranular cracking. High concentration of carbides on fracture surfaces.
I-706				
701X 711X	EFR/STDA VAR/STDA	Tensile	RT,77K,4.2K	Ductile fracture. Mostly cross-granular shear, some evidence of intergranular cracking.
702X	EFR/STDA	Notched	RT,4.2K	Dimpled, cross-granular shear cracked carbides on fracture surface.
721X	ST/GTAW/STDA	Tensile	RT,77K,4.2K	Specimen failed in fusion zone. Mixture of dimpled and shear fractures. Strong evidence of fissuring in fusion zone. Fracture surface covered with carbides.
I-LEA				
73XX	STA	Tensile and notch tensile	RT,4.2K	Low ductility. Dimpled failure. High concentration of sheared (Nb,Ti) carbides intergranular cracking.
Kromarc 58				
80XX	STQ	Tensile and notch tensile	RT,4.2K	High ductility. Dimpled fracture. Occasional "Slag" particles on fractured surface.
821X	GTAW	Tensile	RT,4.2K	Failed in fusion zone. Usually, failure initiated at large inclusion. Dimpled fracture.
831X	CW/GTAW	Tensile	RT,4.2K	Features similar to 82XX group.
8352	CW/GTAW	C.G.R.	77K	Fine striations, irregular tearing. Crack front branching along crystallographic directions.

Summary, Table 7-1. (Cont'd) - p. 4

Material Code	Condition	Mode of Testing	Temperature	Fracture Characteristics
841X	GTAW/CW	Tensile	RT,4.2K	Base metal fracture. Characteristics similar to base metal specimens (80XX). Predominantly ductile, shear fracture.
85XX				--
A-286				
901X	STQA	Tensile	RT,77K,4.2K	Mixed modes of intergranular failure and cross granular shear. Dimples on grain surfaces.
905X	STQA	F.C.G.	77K,4.2K	Mixture of tearing and fatigue striations along crystallographic directions. Intergranular crack branching.
9111	STG/GTAW	Tensile	RT	Failed in base metal. Typical intergranular fracture.
9113	STG/GTAW	Tensile	4.2K	Low temperature failure in HAZ. Evidence of fissuring.
915X	STG/GTAW	F.C.G.	77K,4.2K	Transgranular fatigue growth, with secondary cracking along dendritic boundaries.
Pyromet 538 (21-6-9SS)				
921X	STQ	Tensile	RT,77K,4.2K	Ductile, dimpled shear deformation. One specimen showed evidence of stress induced martensitic transformation at 4.2K. Evidence of gas porosity.
9311	STQ/GTAW	Tensile	RT	Failed in base metal. Ductile, dimpled fracture.
931X	STQ/GTAW	Tensile	77K,4.2K	Failed in fusion zone. Mixed dimpled and shear.
9351	STQ/GTAW	CGR	RT	Irregular striations, mostly tearing.
9353	STQ/GTAW	CGR	4.2K	Striation. Evidence of cleaved surfaces, possibly martensite.
9411	STQ/SMAW	Tensile	RT	Failed in base metal. Ductile, dimpled.
941X	STQ/SMAW	Tensile	77K,4.2K	Failed in fusion zone. Mixed mode of dimpled and shear deformation.

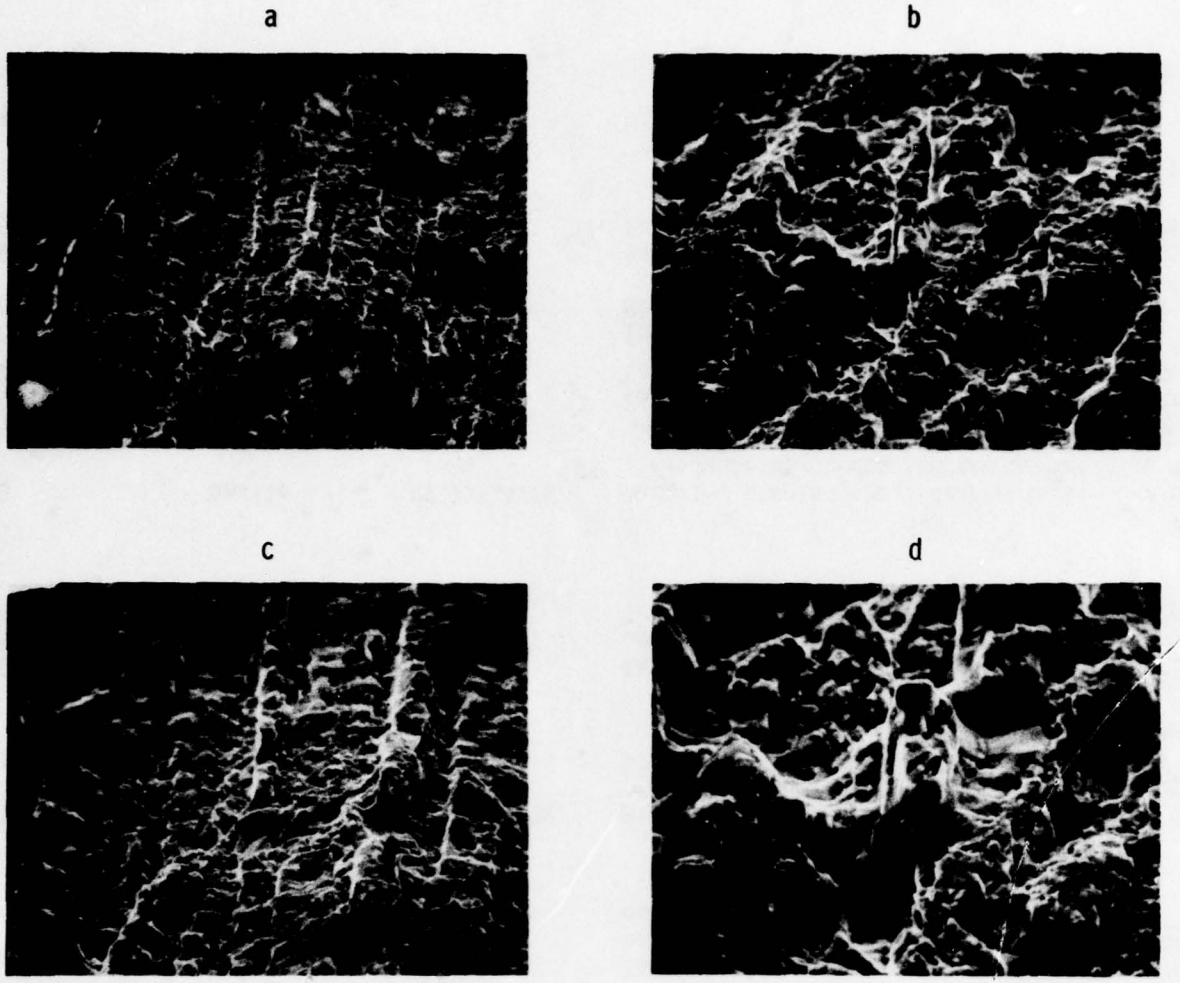
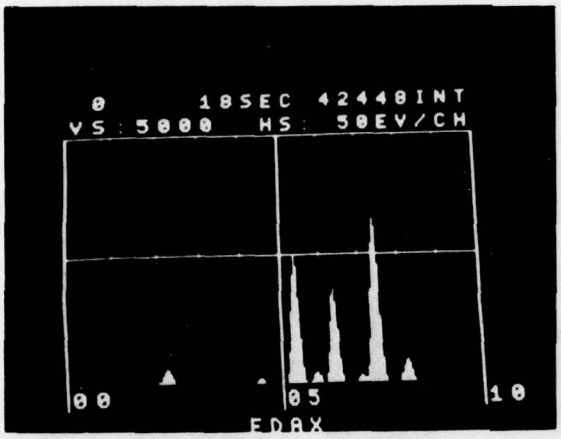
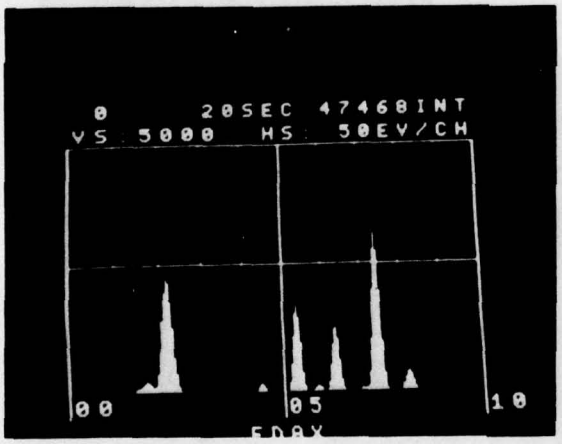


Fig. 7-1 — SEM micrographs, fatigue-crack growth specimen 6551 alloy IN-718 GTAW weld fusion zone, tested at RT a: 280X b: 700X c: 700X d: 1400X




```
NEXT? 0
(A,B,C,D)? A
     2.21      317P   S,Mo
     4.45      140P   Ti
     5.36     2564P   Cr
     5.88      258P   Cr, + Mn
     6.34     1871P   Fe
     7.03      159P   Fe
     7.41     3397P   Ni
     8.19      462P   Ni
```




```
NEXT? 0
(A,B,C,D)? B
     1.10       38P
     1.71      239P   Si
     2.16     2323P   P
     .
     4.45      188P   Ti
     5.35     1697P   Cr
     5.87      143P   Cr + Mn
     6.33     1324P   Fe
     7.05       80P
     7.40     3135P   Ni
     8.19      419P
```

Fig. 7-2 — EDAX data from Fig. 7-1-d a: spots A, C b: spot B

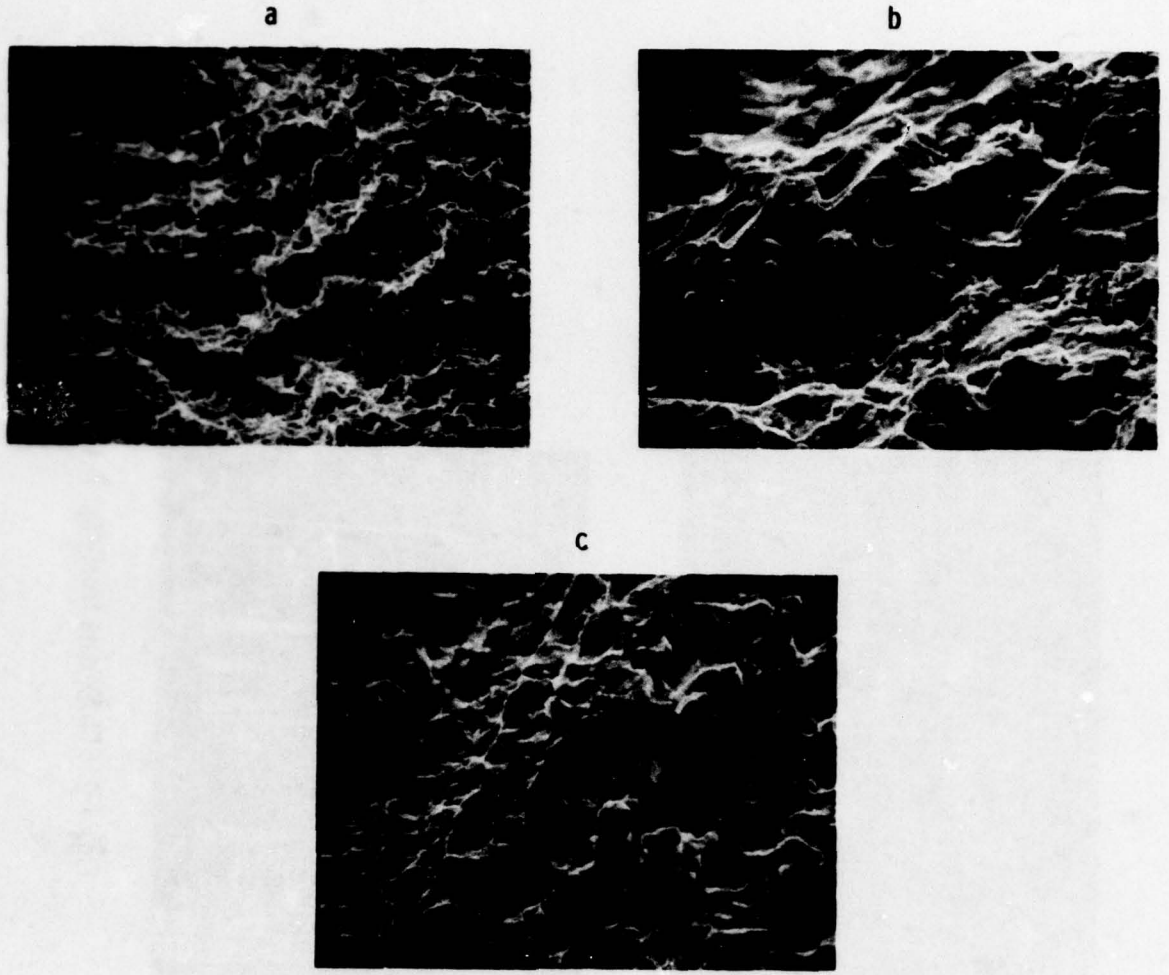


Fig. 7-3 – SEM micrographs, fatigue-crack growth specimen 6553 alloy I-718. GTAW fusion zone tested at 4.2 K (a) 700X (b,c) 1400X

RM-69384

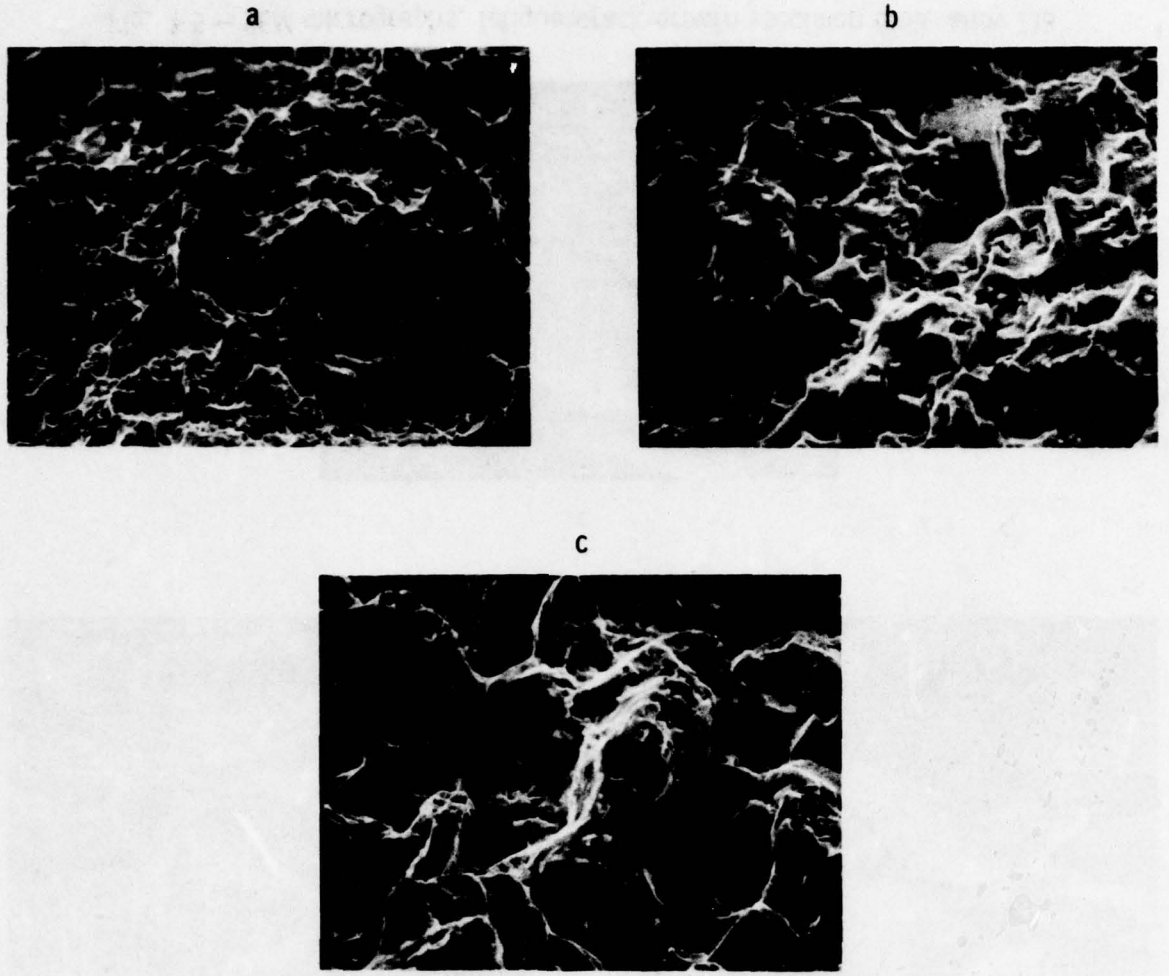


Fig. 7-4 – SEM micrographs fatigue-crack-growth specimen 6651 alloy IN-718 GTAW heat affect zone (HAZ) tested at RT (a) 700X (b, c) 1400X

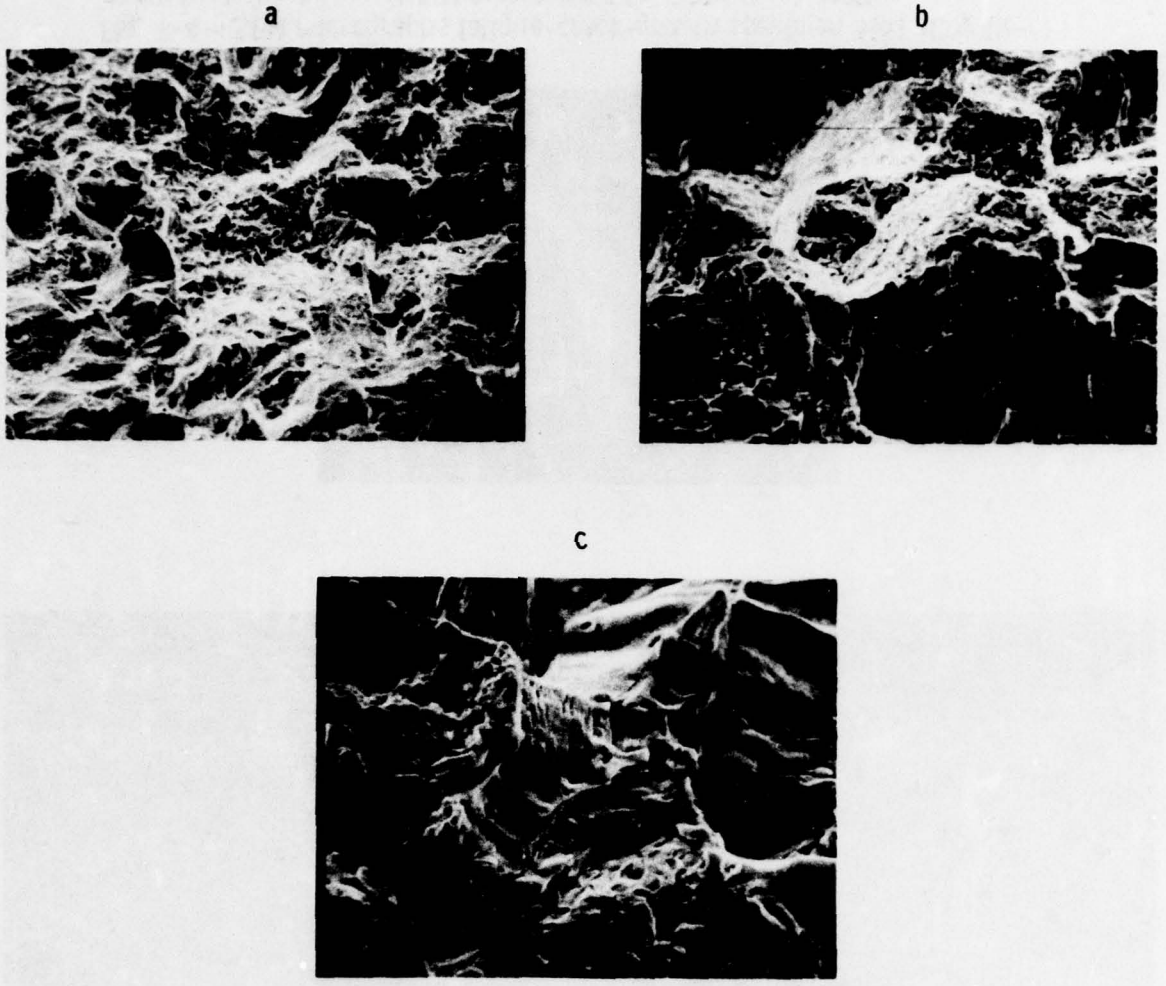


Fig. 7-5 — SEM micrographs, fatigue-crack-growth specimen 6653, alloy 718 GTAW heat-affected-zone (HAZ) tested at 4.2 K a: 280X b: 700X c: 1400X

RM-69386

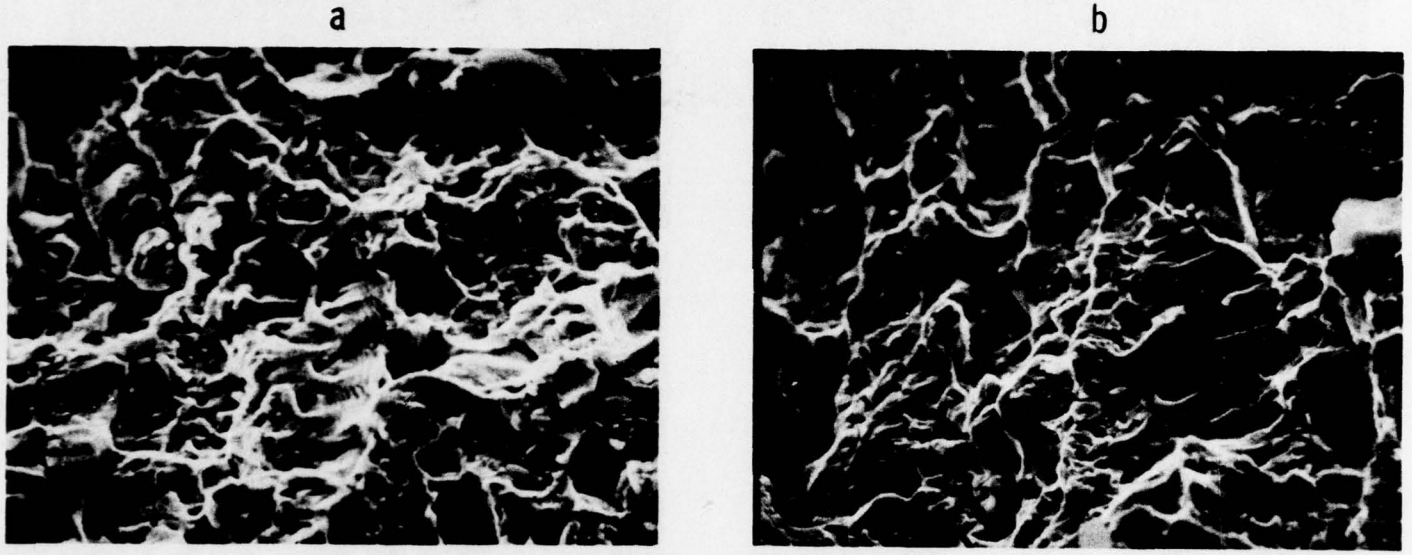


Fig. 7-6 — SEM micrographs, fatigue-crack-growth specimen 7253 alloy 706 GTAW, fusion zone (used IN-718 filler wire), tested at 4.2 K 1400X

RM-69387

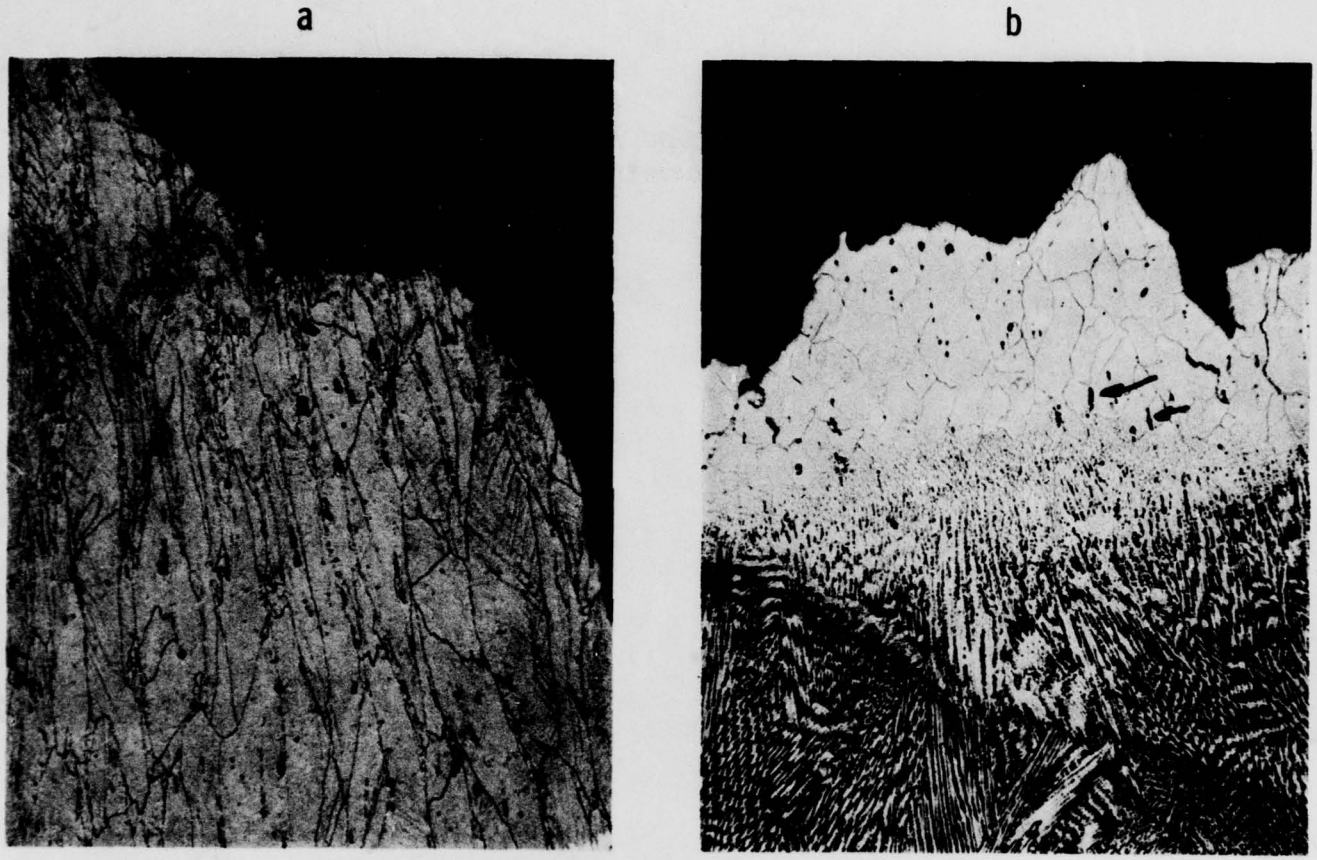


Fig. 7-7 – Light micrographs, STQ/GTAW, A-286 tensile specimen 50X a) tested at RT (9111), failed in base metal b) tested at 4.2 K (9113) failed in HAZ

RM-69388

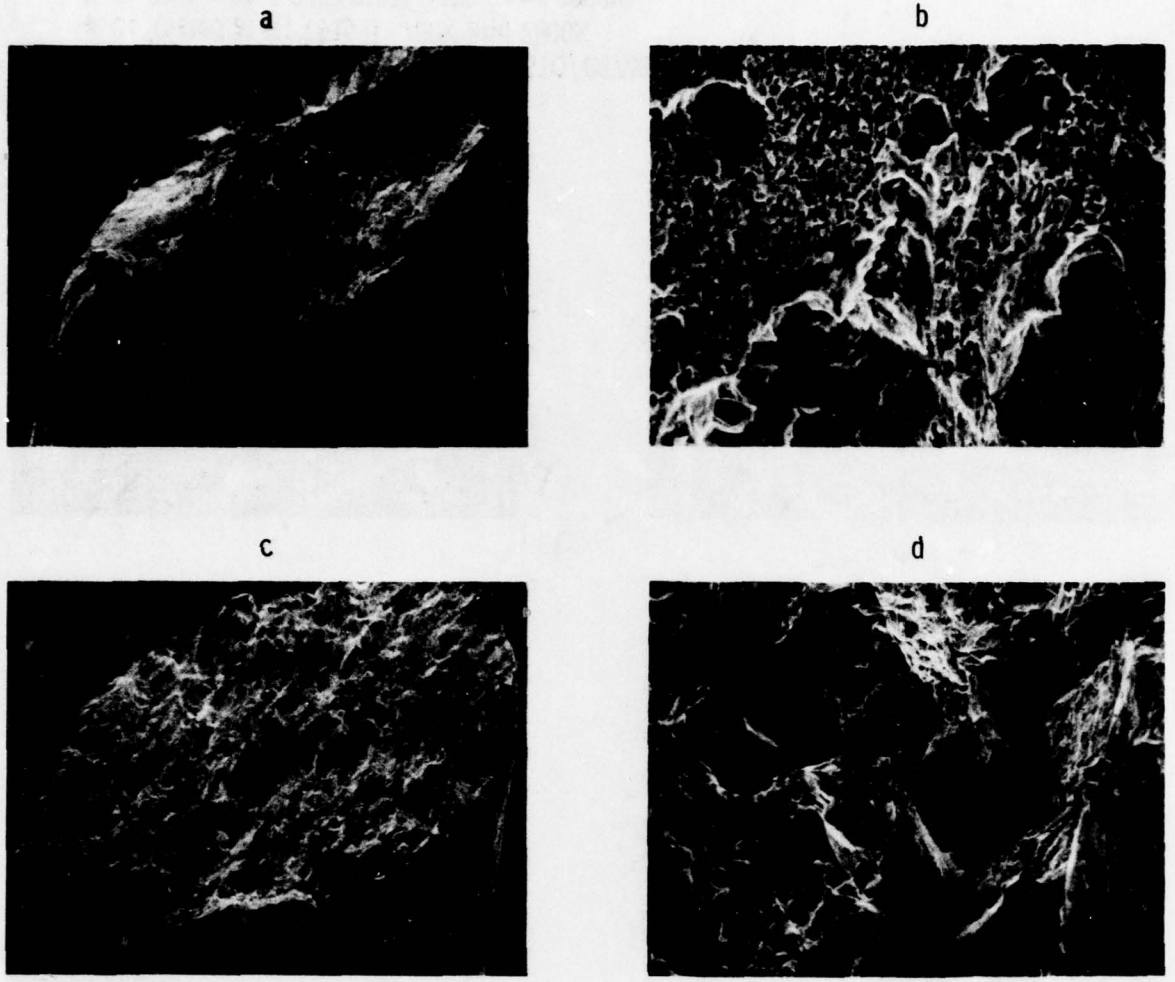


Fig. 7-8 — SEM micrographs, A-286 STQ/GTAW tensile specimens
a,b: Tested at RT (9111) 20X and 1000X, Base metal fracture
c,d: Tested at 4.2 K (9113) 20X and 200X, HAZ fracture

RM-69389

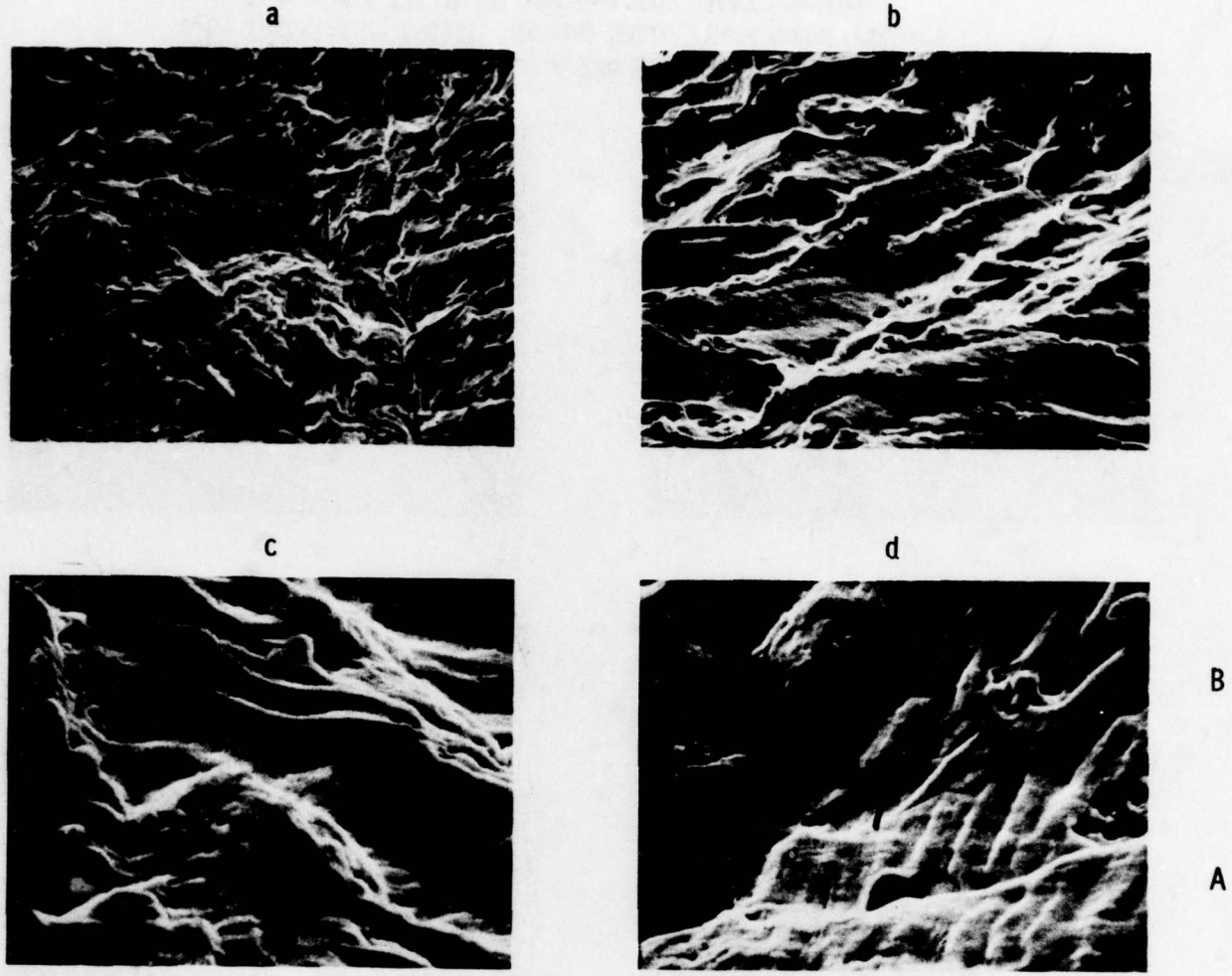


Fig. 7-9 — SEM micrographs A-286 STQ/GTAW fatigue-crack-growth in fusion zone
a, c: Tested at RT (9151) 700X and 2800X
b, d: Tested at 4.2 K (9153) 1400X and 2800X

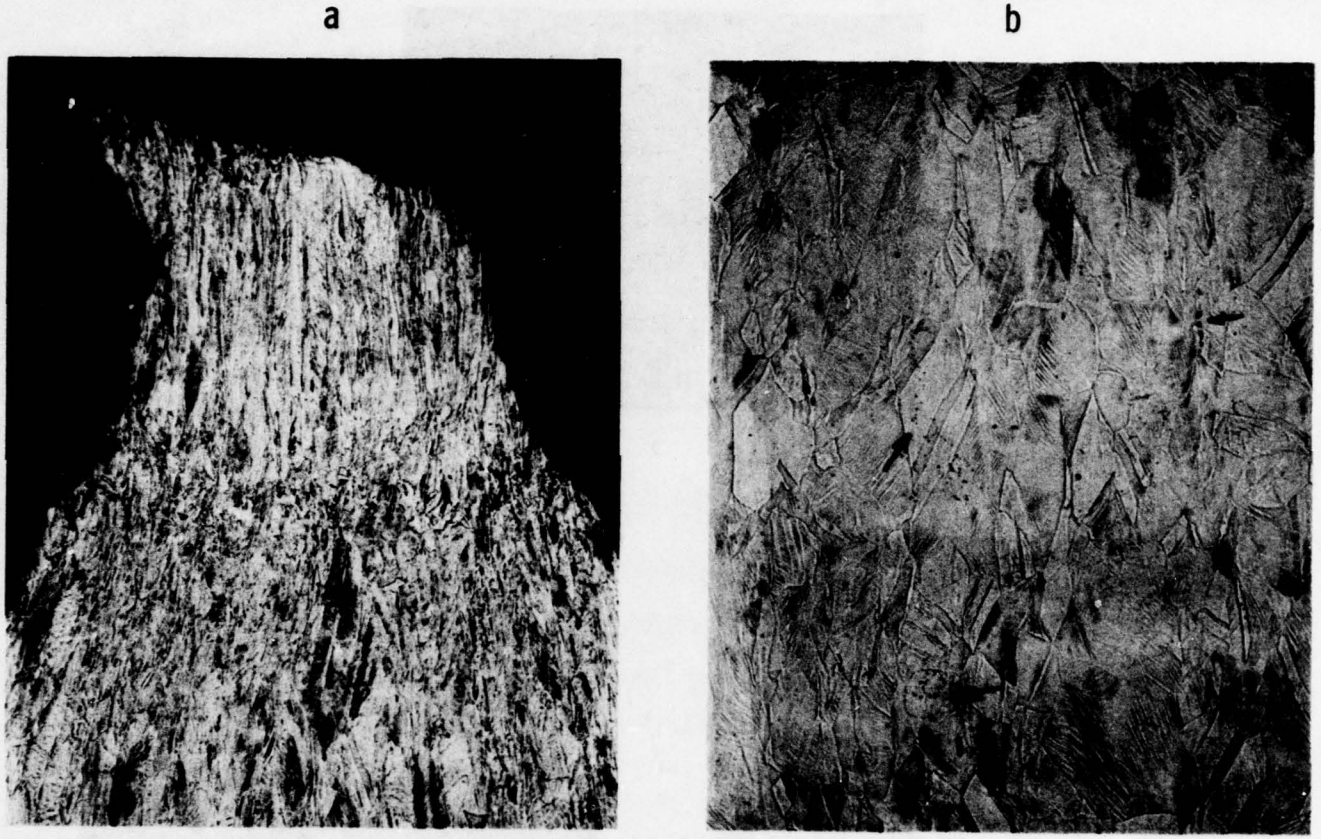


Fig. 7-10 — Light micrographs, Pyromet 538 cross sections of tensile specimen tested at RT (STQ 9211). a: 50X b: 100X, 10mm below fracture surface

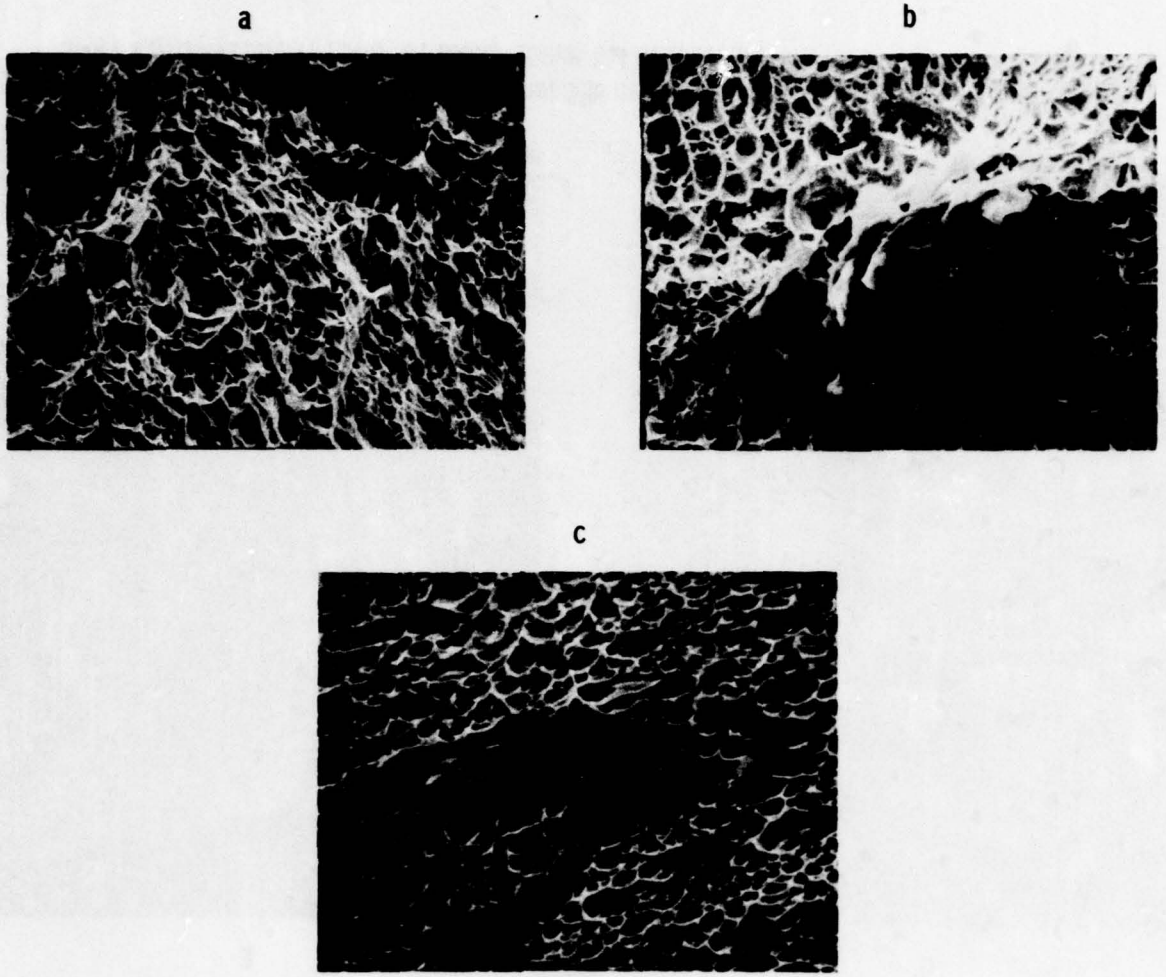
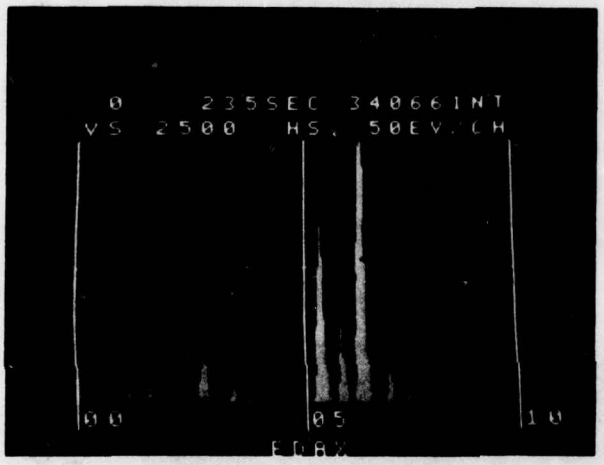


Fig. 7-11 – SEM micrographs of fracture surface, on Pyromet 538 base metal tensile specimen tested at RT (9211) a: 500 b: 500 c: 1000. EDAX of contaminants in (b) shown in Fig. 7-12




```
NEXT? 0
(A,B,C,D)? B
     1.07      193P  Na
     1.51      263P  Al
     2.30       70P  S
     2.62      508P  Cl
     3.30      189P  K
     3.61       52P  Ca
     5.38     1876P  Cr
     5.87      833P  Cr + Mn
     6.37     3293P  Fe
     7.01      371P  Fe
     7.46      149P  Ni
     8.20       12P  Ni
```

Fig. 7-12 — X-ray data (EDAX) from contaiminants on fracture surface specimen 9211 (Fig. 7-11-b)

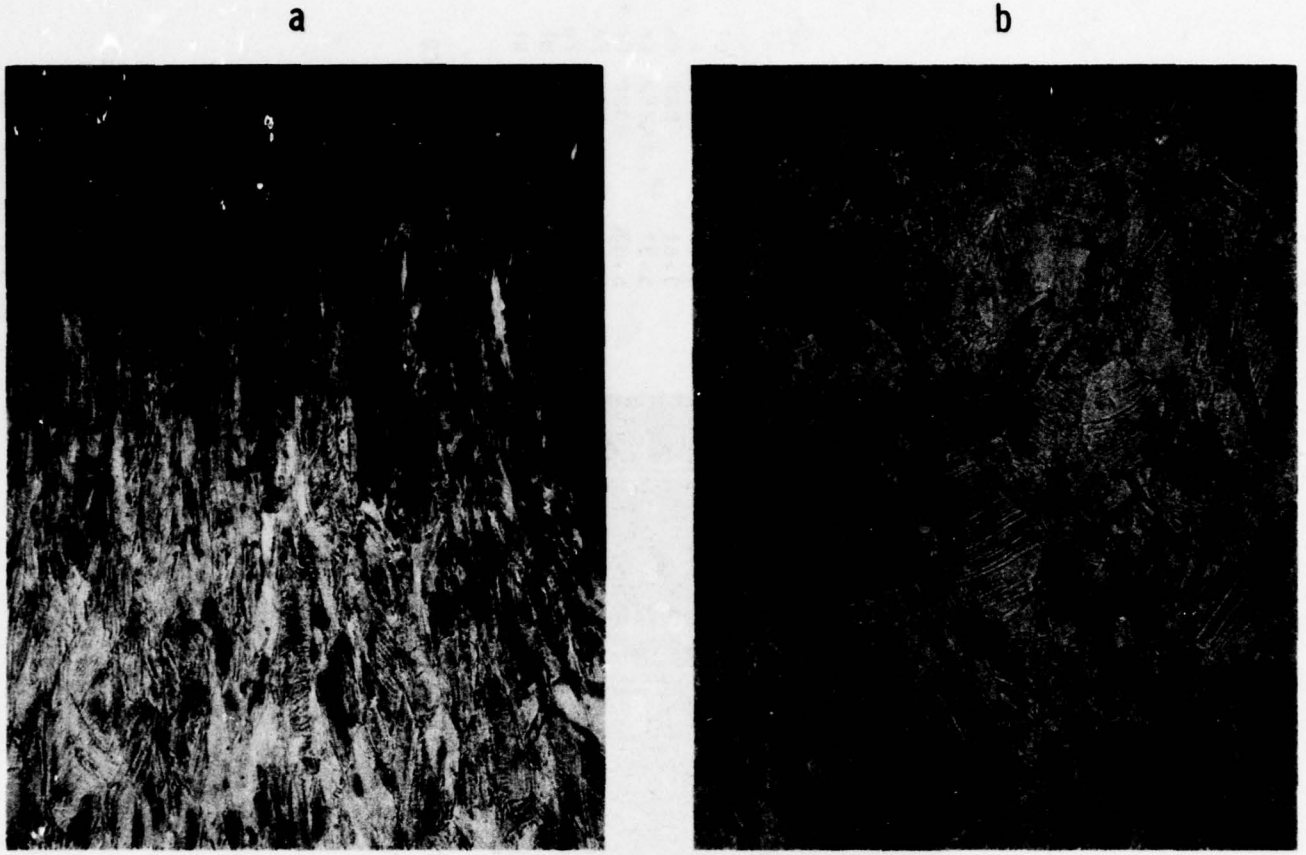


Fig. 7-13 — Light micrographs, cross sections of tensile specimen 9213-1 alloy Pyromet 538 tested at 4.2 K, a. 50X and b. 100X. Note highly deformed matrix

RM-69394

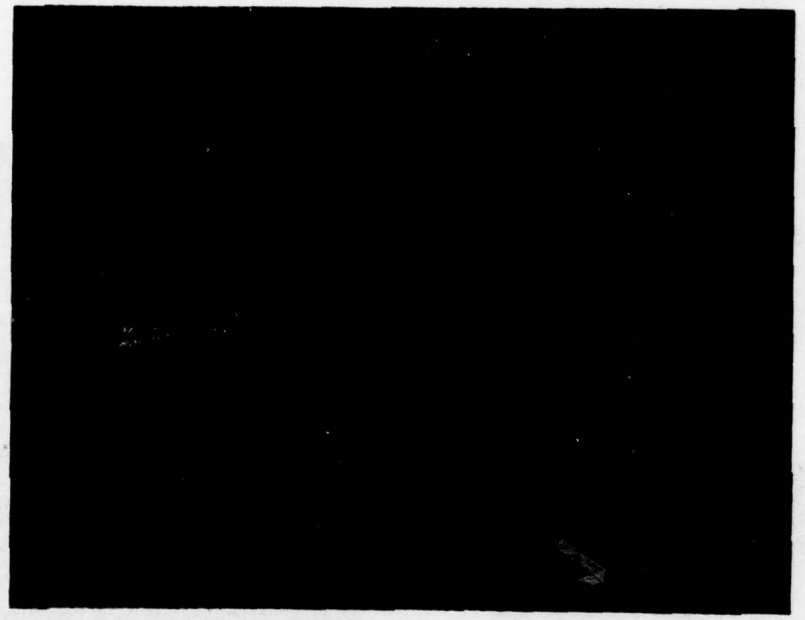


Fig. 7-14 — Light micrograph cross sections of tensile specimen 9213-2, alloy Pyromet 538 tested at 4.2K. Note deformed matrix and possibly martensite (arrows) (1000X)

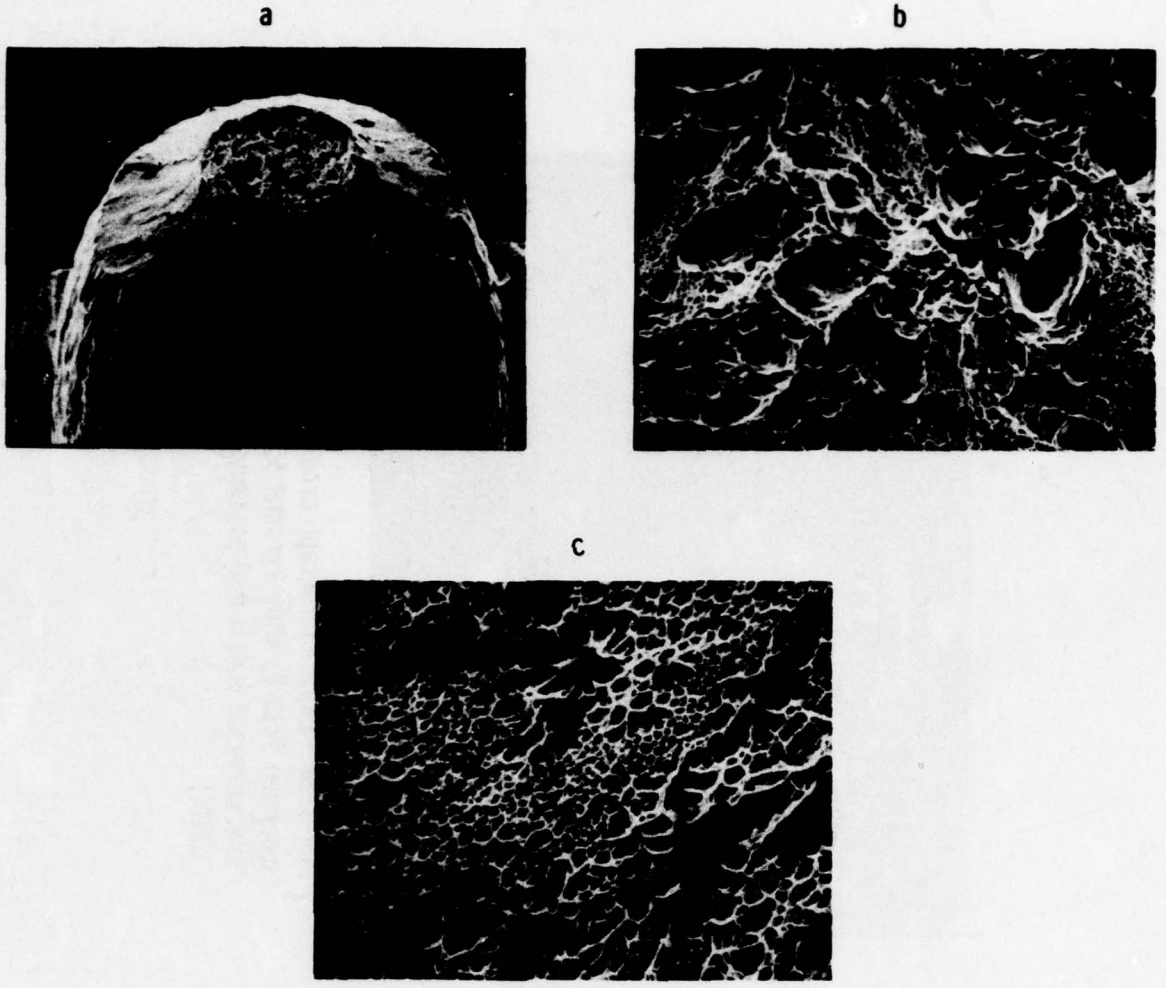


Fig. 7-15 — SEM micrographs, fracture surface, tensile specimen 9213-1 alloy Pyromet 538, tested at 4.2 K. Note high degree of ductility dimpled fracture through the entire cross section a: 20X b: 500X c: 1000X

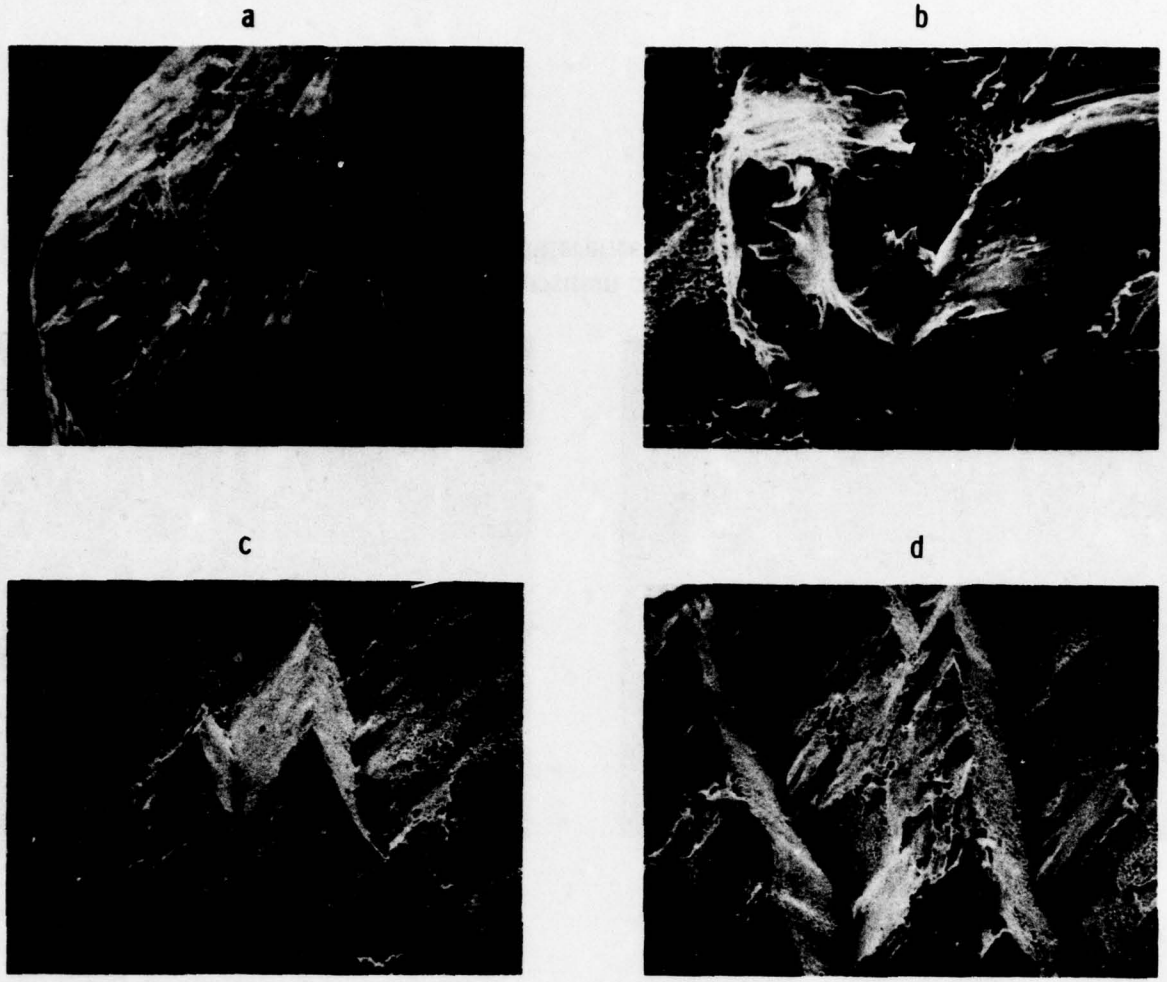


Fig. 7-16 — SEM micrographs, fracture surface, tensile specimen 9213-2, alloy Pyromet 538 tested at 4.2 K. Note shear fracture (a) and heterogeneous deformation in details; a mix of dimpled and sheared areas. a: 20X b: 650X c: 250X d: 250X

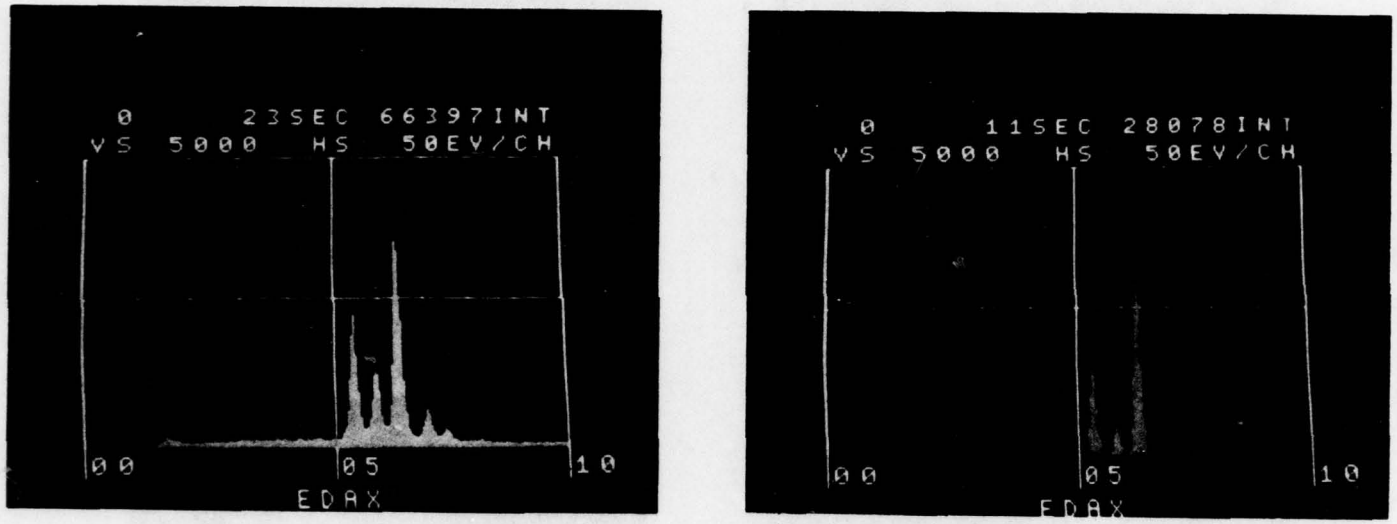


Fig. 7-17 — X-ray data, (a) typical composition of Pyromet 538 from area, Fig. 7-15-c. b: spot A, Fig. 7-16-b. Essentially no difference in composition

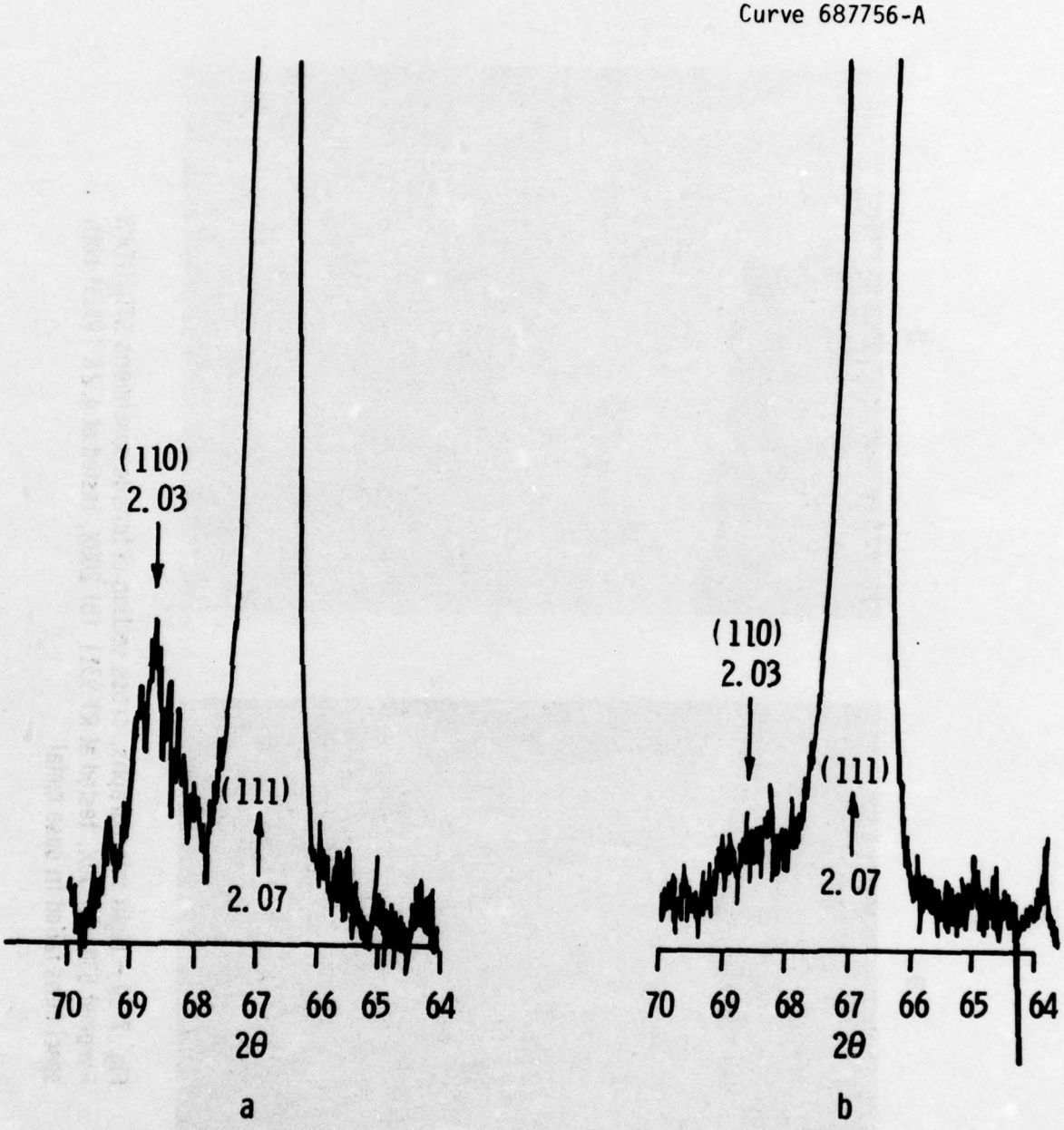


Fig. 7-18 — Cr — radiation, diffractometer traces of tensile specimens. (a) 9213-2 (b) 9213-1 Note the (110)-bcc peak in (a) which is not seen in (b)

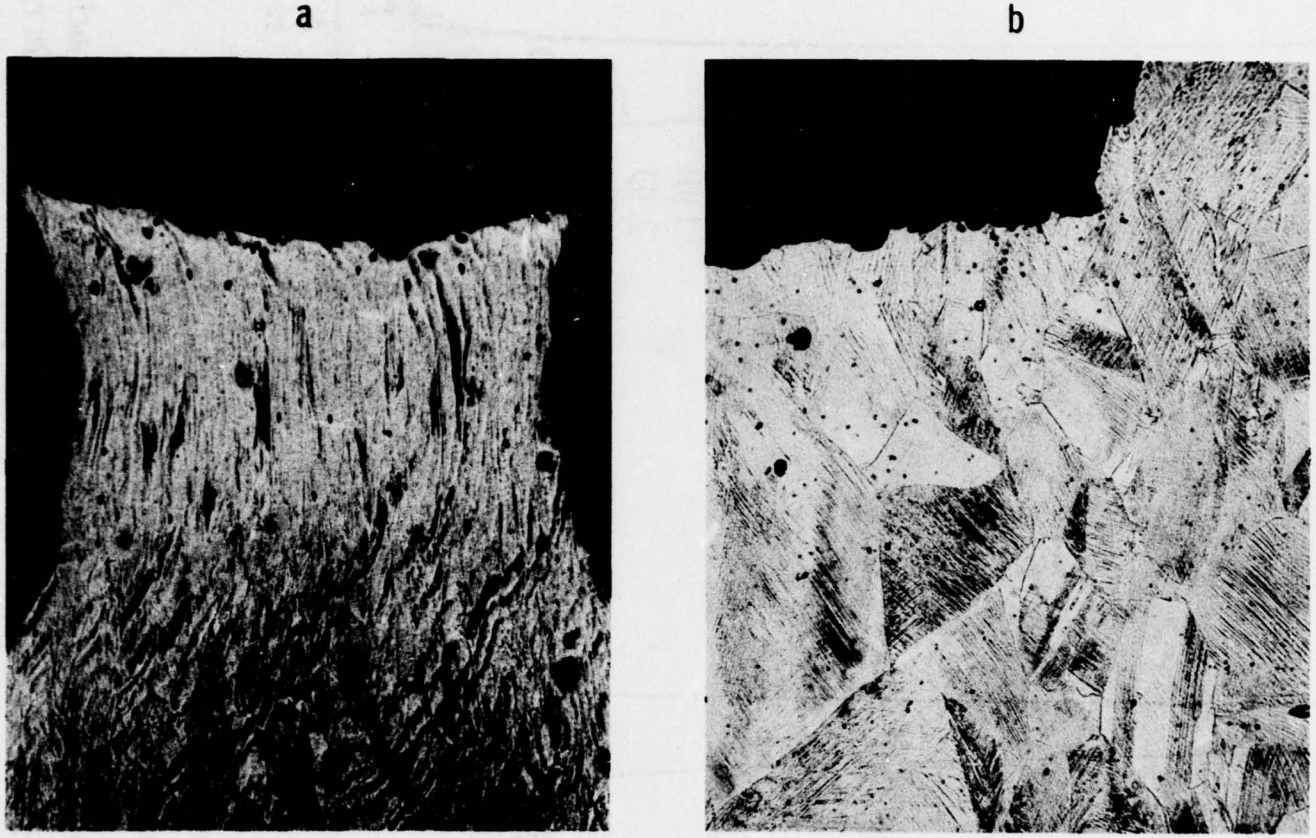


Fig. 7-19 — Light micrographs, cross section of tensile specimens STQ/GTAW Pyromet 538 (a) 50X, tested at RT 9311 (b) 200X, tested at 4.2K (9313) both specimens failed in base metal

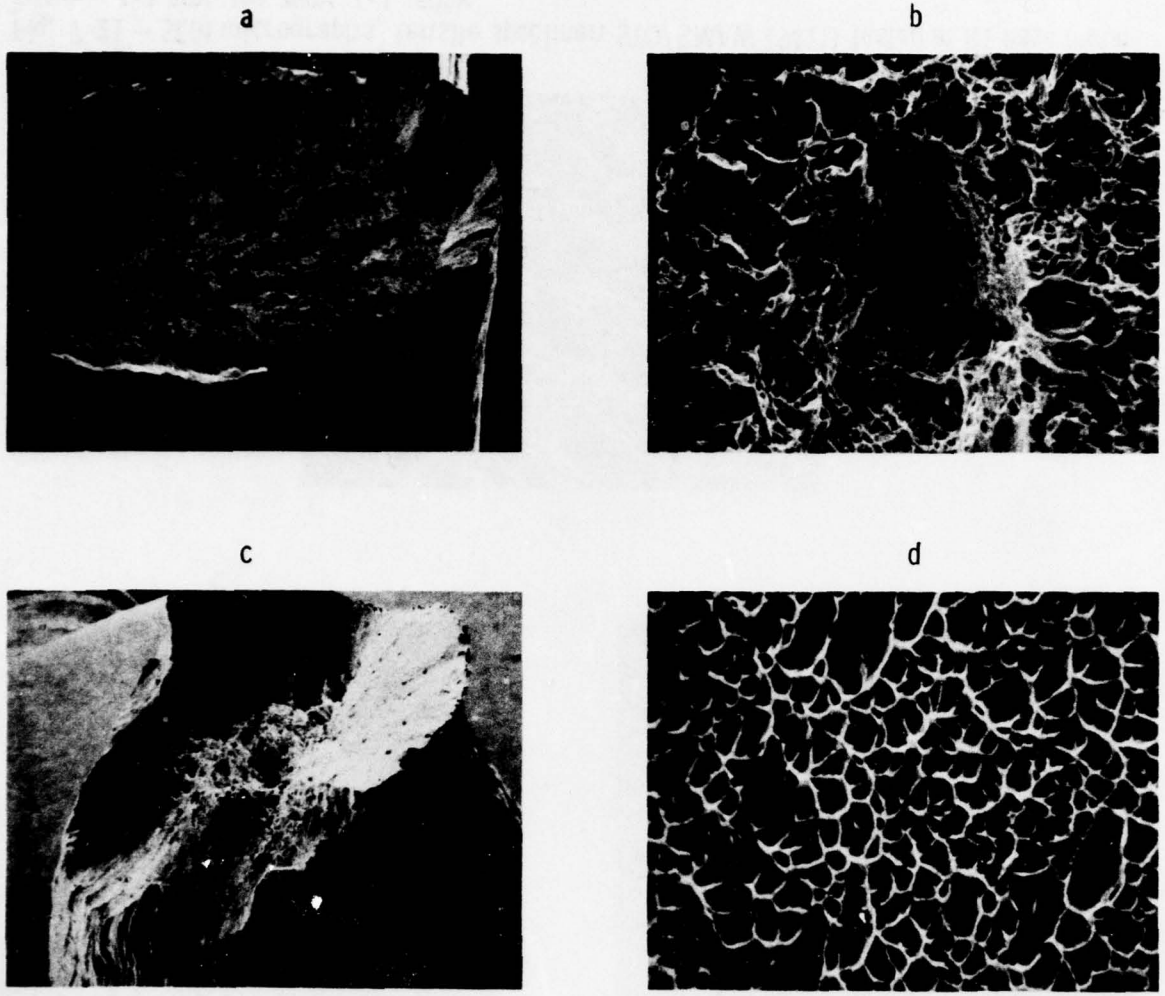


Fig. 7-20 — SEM micrographs of fracture surface tensile specimens STQ +GTAW 21-6-9 SS
a, b: Tested at 4.2 K (9313-2) failed in fusion zone, 20X and 1000X
c, d: Tested at RT (9311-2) failed in base metal, 20X and 1400X

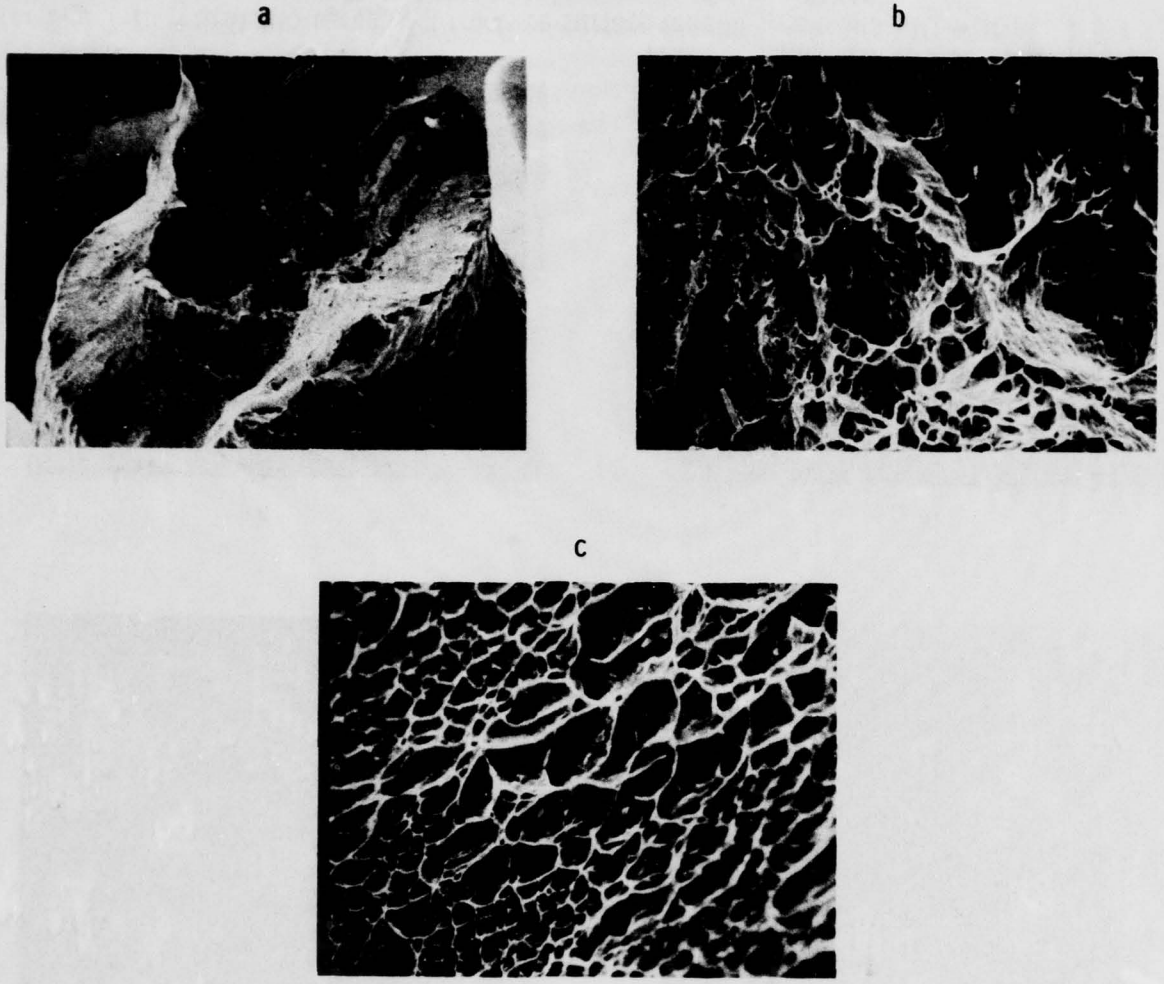


Fig. 7-21 — SEM micrographs, tensile specimen STO/SMAW (9411) tested at RT base metal failure. (a) 30X (b) 750X (c) 1500X

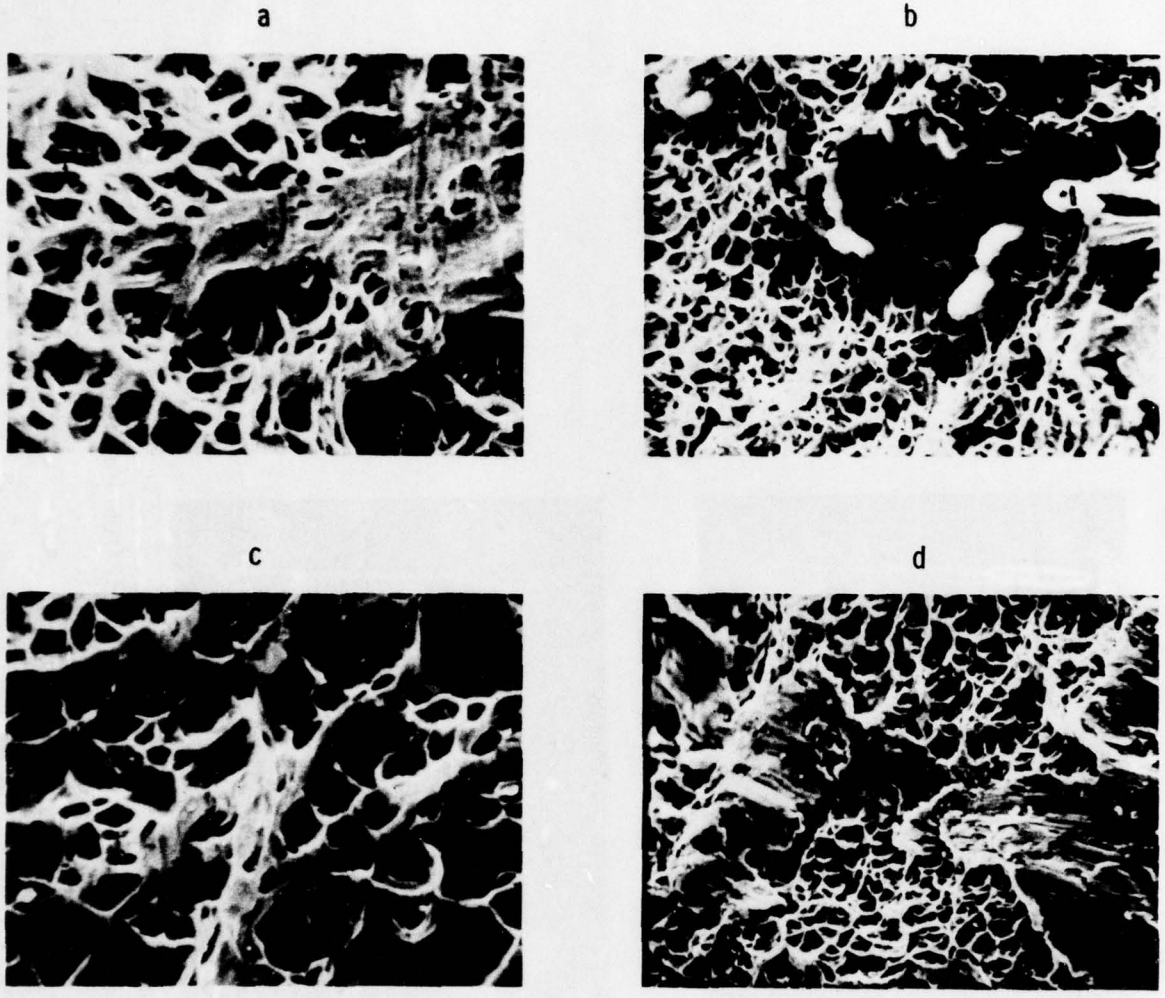
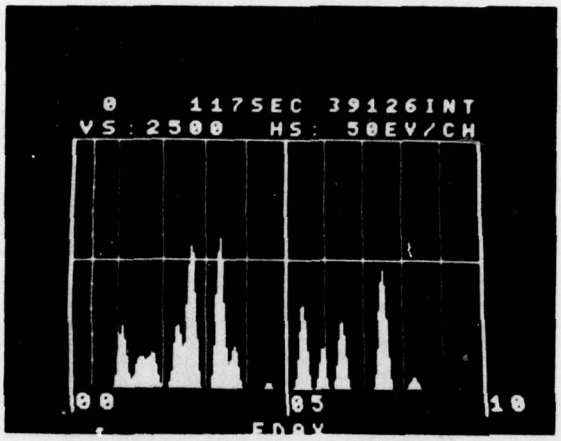
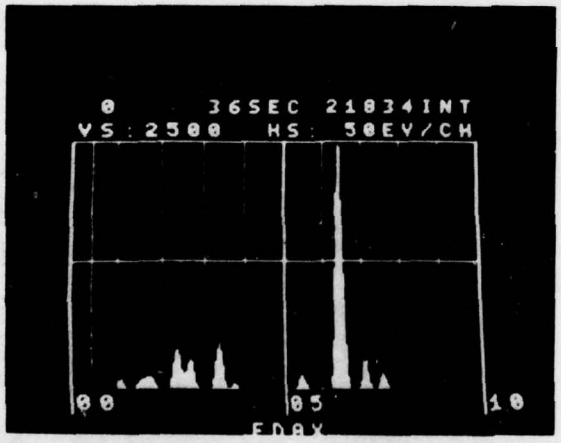


Fig. 7-22 — SEM micrographs, tensile specimens, STQ + SMAW Pyromet 538
a, b: Tested at 77 K (9412) 2400X and 1200X
c, d: Tested at 4.2 K (9413) 2400X and 1200X both specimens failed in fusion zone




```
NEXT? 0
(A,B,C,D)? B
     1.10      633P   Na
     1.53      334P   Al
     1.75      353P   Si
     2.34      648P   S
     2.66     1464P   Cl
     3.34     1533P   K
     3.70      420P
     4.55       73P   Ti
     5.44      875P   Cr
     5.93      443P   Cr + Mn
     6.43      720P   Fe
     7.10       20P
     7.50     1187P   Ni
     8.27      133P
```




```
NEXT? 0
(A,B,C,D)? A
     1.10      122P   Na
     1.70      136P   Si
     2.34      402P   S
     2.65      298P   Cl
     3.35      455P   K
     3.71       75P
     5.43      159P   Cr
     5.93       35P
     6.42     2711P   Fe
     7.08      331P
     7.51      185P   Ni
     8.26       23P
```

Fig. 7-23 — X-ray data (EDAX) from inclusions. Fig 7-22-b
(a) spot 2 (b) spot 1

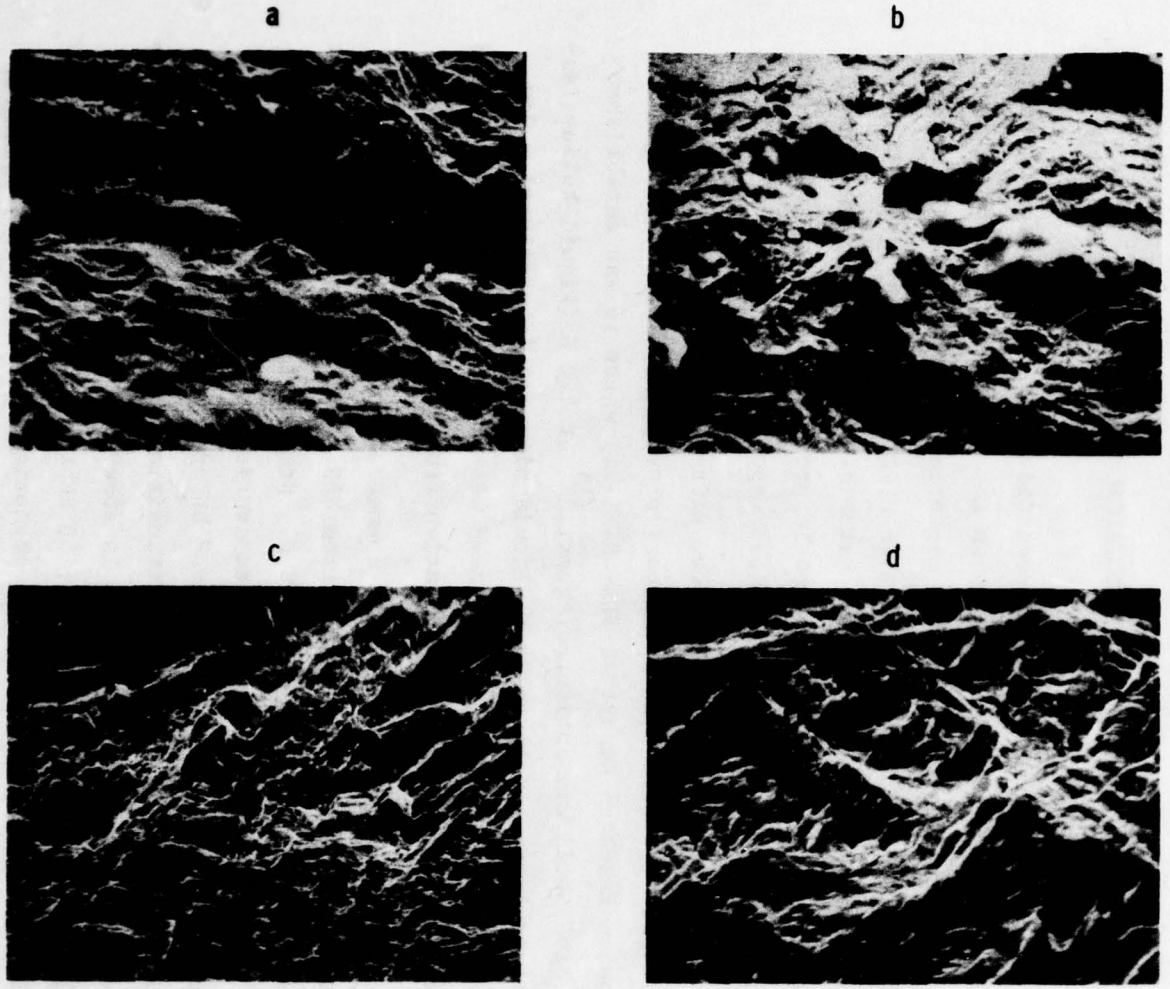


Fig. 7-24 SEM micrographs, fatigue crack growth specimens. Through the fusion zone Pyromet 538 GTAW a,b: Tested at RT (9351), 700X c,d: Tested at 4.2 K (9353) 600X and 1400X

8.0 MAGNETIC AND ELECTRICAL MEASUREMENTS

The magnetic measurements reported on in this section of the final report concentrated exclusively on the alloy Pyromet 538. This material showed the most interesting magnetic effects of all the materials examined since the inception of this program in FY 74. However, it should be cautioned that some of the materials examined previously may indeed exhibit the same striking magnetic properties when subject to the same strain tests as was the Pyromet 538 reported on here.

The magnetic condition of the 21Cr-6Ni-9Mn alloy (Pyromet 538) was first reported on in the report previous to this one (Westinghouse Research Report 76-9D4-CRYMT-R1) where it was established that the base metal was antiferromagnetic[1] at 4.2 K (liquid helium temperature) and certainly up to 78 K (liquid nitrogen temperature). However, the weldments GTAW and SMAW showed weak ferromagnetism[1] which was attributed to ferromagnetic contamination from the filler metal.

Measurements reported here commenced on two tensile specimens of Pyromet 538 (#1 and #5) received from NBS. No. 1 had been strained at 300 K (room temperature) and #5 at 78 K. Samples from the unstrained sections of both and from the strained section of #1 showed the same antiferromagnetic condition as observed before. However, material from the strained section of #5 showed a transition had occurred from antiferromagnetism to ferromagnetism. This is shown in Figure 8.1 where it is strikingly evident that at a field of 50 kG the transition involves a change of about a factor of forty in magnetic moment. Information from NBS suggested that the strained section of #5 contained up to 40% martensite. The ability of strain or deformation to raise the martensitic transformation temperature (M_d) of an alloy of this composition and similar ones has already been discussed in the report R1 referred to above

(see pages 19 through 24 of R1 for example). The results reported here on the NBS material and on the Westinghouse samples of Pyromet 538 discussed below are consistent with the predictions of Figure 5-1 in R1.

Measurements on ☺ tensile samples of Pyromet 538 are reported in Tables 8.1 through 8.3 and in Figure 8.2 for tensile test temperatures of 300 K, 78 K and 4.2 K. The magnetic transition is evident in the base metal (Table 8.1) and in the weldments (Tables 8.2 and 8.3) at test temperatures of 78 K and 4.2 K. The magnitude of the induced magnetic moment is variable though. For example in Table 8.1 for the base metal, the tensile test at 78 K induces a greater moment than the tensile test at 4.2 K. This situation is reversed in Table 8.2 for the GTAW weldment. A further complication occurs for the 300 K tensile test specimens and the unstrained sections of some of the 78 K and 4.2 K test specimens. A small but measureable ferromagnetic moment was detectable in addition to a predominantly (and anticipated) antiferromagnetic condition. The origin of this is presently unexplained. The NBS samples #1 and #5 did not show this small moment probably because there was a good separation (several inches) between the strained and unstrained sections. Later samples were much smaller -- maybe only 1/2 inch in length -- and the possibility of some strain extending to the nominally unstrained region is real. This explanation is clearly only applicable to the 78 K and 4.2 K tensile test materials. The small remnant ferromagnetic moment in the 300 K test specimen may indicate the onset of the magnetic transition at this temperature.

In conclusion the presence of an antiferromagnetic to ferromagnetic transition has been found in the strained sections of tensile specimens of Pyromet 538 strained at temperatures of 78 K and below. In a magnetic field of 50 kG the transition causes a sample to change its magnetic moment by about a factor of forty. The transition is attributed to the formation of a ferromagnetic martensite consistent with an elevated M_d temperature in the presence of strain as discussed previously in report R1.

Overview

Magnetic Measurements

With the exception of Cu-PD135 all the materials examined in this program were found to be either ferromagnetic or antiferromagnetic at cryogenic temperatures. The ferromagnetic strengths ranged all the way from weak, i.e., almost nonmagnetic to strong, i.e., iron-like. The majority of the materials were ferromagnetic and it has been possible to correlate the presence of the rarer antiferromagnetic condition to the Mn content of a particular alloy in these austenitic stainless steels. If this content exceeds 5 or 6%, the material will be found to exhibit an antiferromagnetic state. For Mn contents less than 5 or 6%, the ferromagnetic condition results. Thus if a nonmagnetic, i.e., paramagnetic material was essential for some application, a 5 or 6% Mn content should guarantee it. This statement is made only with respect to austenitic stainless steel alloys having a principal composition of the four magnetic elements Mn, Cr, Ni, and Fe. A striking transition from an antiferromagnetic to a ferromagnetic state was observed in the strained section of a tensile specimen of Pyromet 538 which had undergone a tensile test at liquid nitrogen temperatures or below. The possibility of a similar such transition is very likely in the other antiferromagnetic material Nitronic-33 but not, however, in Kromarc 58 (see report R1).

In an engineering application wherein strong magnetic fields are generated by superconducting coils (field windings, armatures, or solenoids) the magnetic condition of structural and support materials can cause one or more of four effects.

(a) Antiferromagnetic and ferromagnetic materials will experience an induced moment in the magnetic field and hence a mechanical torque;

(b) in a field gradient they will experience a translational force;

(c) they may perturb the magnetic field generated by the superconducting coils and;

(d) ferromagnetic materials will cause hysteresis losses (heating for example) in time varying fields.

Whether any of these effects is critical to any specific proposed application has not been addressed during this contract period. Experience at Westinghouse during the design and construction of 5 and 10 MVA superconducting generators suggests the magnetic condition of the structural and support materials for these devices is of secondary importance. This may well be untrue for larger generators and the structures to be built for fusion. This program has made a start by identifying the magnetic conditions and strengths of a number of candidate structural materials for these applications.

Electrical Measurements

Although done routinely during the earlier part of this program, these measurements were not continued throughout its duration. It was evident from the data already accumulated that the electrical resistivity was a fairly composition independent quantity in these commercial alloys. In summary, it was found the resistivity was about 100 μΩcm to within 30% at 4.2 K and did not change by more than 30% up to 300 K. This is characteristic of a residual resistance or impurity dominated mechanism.

References

1. For an explanation of the difference between anti- and ferromagnetism and the various ferromagnetic strengths see J. M. Wells, W. A. Logsdon, R. Kossowsky, and M. R. Daniel, "Structural Materials for Cryogenic Applications," Westinghouse Research Laboratories Report 75-9D4-CRYMT-R2 (October 1975).

Table 8-1

Pyromet 538 Base Metal			
Unstrained†			
Strain Test Temperature in K	Temperature in K	Ferromagnetic Moment ($4\pi M_s$) in G	Antiferromagnetic Moment at 50 kG in G
4.2	4.2	---	103
	20	---	104
	75	---	111
78	4.2	26	137
	20	24	140
	75	24	149
300	4.2	7	113
	20	7	115
	75	7	123
Strained*			
4.2	4.2	940	---
	20	967	---
	75	953	---
78	4.2	5830	---
	20	5800	---
	75	5720	---
300	4.2	7	125
	20	7	119
	75	7	126

†Unstrained samples taken from grip ends of tensile specimens.

*Strained samples taken from the tensile gage length sections adjacent to the fracture surfaces.

Table 8-2

Pyromet 538 - GTAW			
Unstrained - Base Metal[†]			
Strain Test Temperature in K	Temperature in K	Ferromagnetic Moment ($4\pi M_s$) in G	Antiferromagnetic Moment at 50 kG in G
4.2	4.2	---	103
	20	---	105
	75	---	113
78	4.2	---	106
	20	---	110
	75	---	116
300	4.2	---	108
	20	---	113
	75	---	121
Strained - Weldment[*]			
4.2	4.2	4150	---
	20	4150	---
	75	4100	---
78	4.2	151	---
	20	150	---
	75	153	---
300	4.2	83	202
	20	80	200
	75	80	200

[†]Unstrained samples taken from grip ends of tensile specimens.

[*]Strained samples taken from the tensile gage length sections of the composite weldments adjacent to the fracture surfaces.

Table 8-3

Pyromet 538 - SMAW			
Unstrained - Base Metal[†]			
Strain Test Temperature in K	Temperature in K	Ferromagnetic Moment ($4\pi M_s$) in G	Antiferromagnetic Moment at 50 kG in G
78	4.2	---	106
	20	---	106
	75	---	113
Strained - Weldment[*]			
78	4.2	867	---
	20	870	---
	75	650	---

[†]Unstrained samples taken from grip ends of tensile specimens.

[*]Strained samples taken from the tensile gage length sections of the composite weldments adjacent to the fracture surfaces.

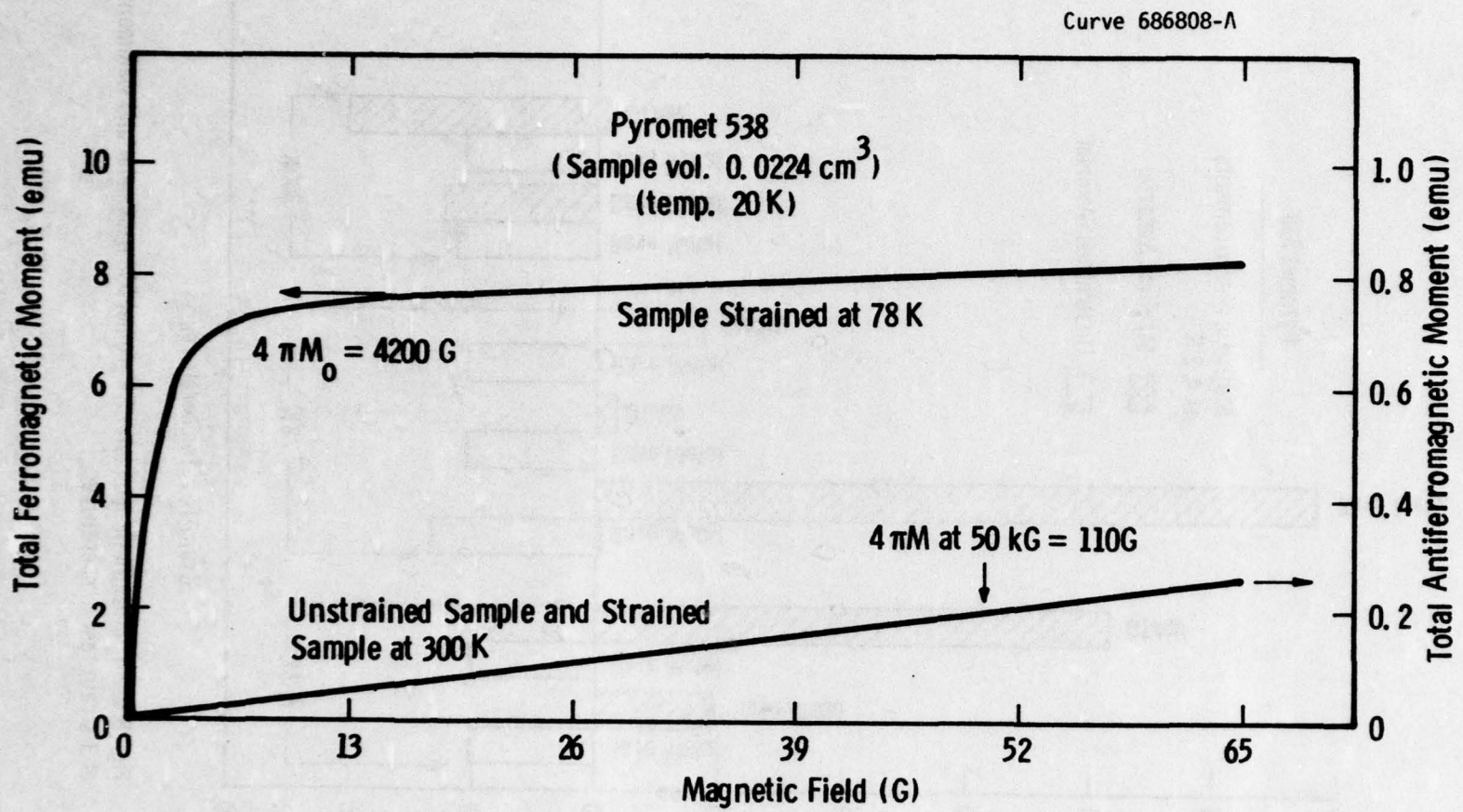


Fig. 8.1 — The magnetic moment versus magnetic field for Pyromet 538 in strained and unstrained conditions.

Curve 687095-B

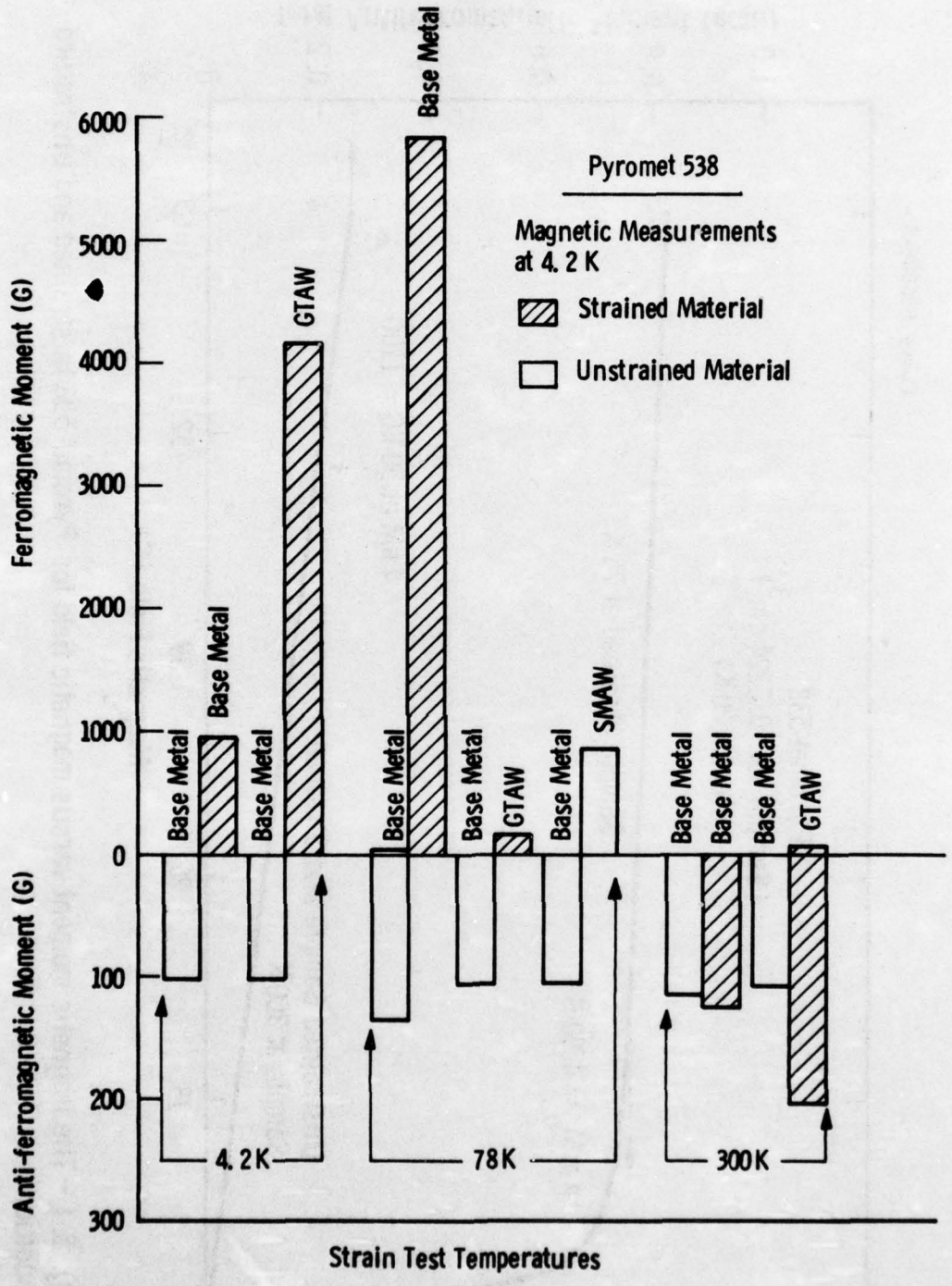


Fig. 8.2 — The magnetic moment of Pyromet 538 basemetal and weldments at 3 strain test temperatures.

9. ACKNOWLEDGEMENTS

The authors wish to greatfully acknowledge the following Westinghouse personnel for their respective advice, contributions, and cooperation and encouragement in the conduct of this work:

Dr. J. H. Parker, Jr.
J. L. McCabria
D. C. Litz
G. D. Cooper
G. G. Lessmann
G. E. Grotke
J. E. Smith
W. R. Kuba
E. T. Wessel
W. A. Pryle
D. R. Young
R. R. Hovan
A. R. Petrush
W. H. Halligan
R. C. Brown

In addition, special acknowledgement is extended to:

(1) The Huntington Alloys Product Division of the International Nickel Company, for providing the Low Expansion Alloy.

(2) To the Phelps Dodge Copper Products Company for providing the PD-135 Copper Alloy.

(3) The USAF/APL Contract F33615-71-C-1591, under which support the data for the Udimet 718 and Cameron Iron A-286 materials were obtained.

(4) Dr. P. R. Landon of the Lawrence Livermore Laboratory for providing the Pyromet 538 billet material.